ISBN 978-82-326-7554-8 (printed ver.)
ISBN 978-82-326-7553-1 (electronic ver.)
ISSN 1503-8181 (printed ver.)
ISSN 2703-8084 (electronic ver.)

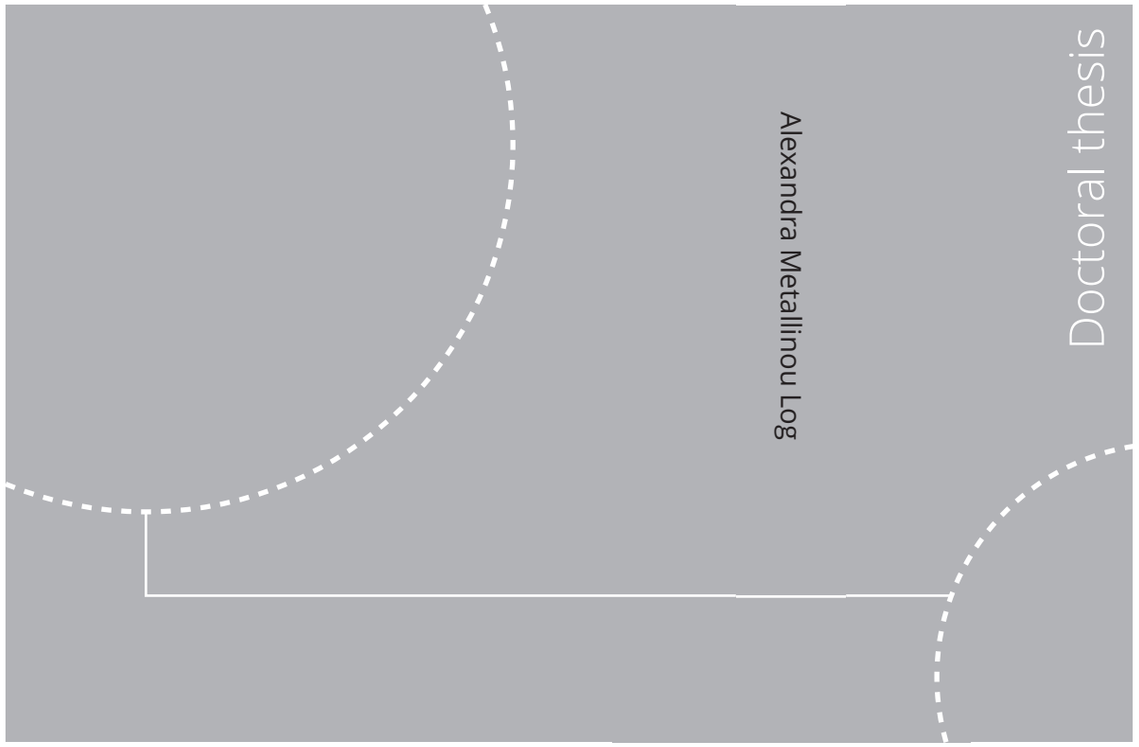

Doctoral theses at NTNU, 2023:427

Alexandra Metallinou Log

Depressurization of CO2 in pipes: Analysis of experiments and non-equilibrium flashing flow models

NTNU
Norwegian University of
Science and Technology
Thesis for the degree of
Philosophiae Doctor
Faculty of Engineering
Department of Energy and Process Engineering

NTNU
Norwegian University of
Science and Technology

Doctoral theses at NTNU, 2023:427

NTNU

NTNU
Norwegian University of
Science and Technology

Alexandra Metallinou Log

Depressurization of CO2 in pipes: Analysis of experiments and non-equilibrium flashing flow models

Thesis for the degree of Philosophiae Doctor

Trondheim, December 2023

Norwegian University of Science and Technology
Faculty of Engineering
Department of Energy and Process Engineering

NTNU
Norwegian University of
Science and Technology

NTNU
Norwegian University of Science and Technology

Thesis for the degree of Philosophiae Doctor

Faculty of Engineering
Department of Energy and Process Engineering

ISBN 978-82-326-7554-8 (printed ver.)
ISBN 978-82-326-7553-1 (electronic ver.)
ISSN 1503-8181 (printed ver.)
ISSN 2703-8084 (electronic ver.)

Doctoral theses at NTNU, 2023:427

PRINTED IN NORWAY
NO - 1598

NORDIC SWAN ECOLABEL
Printed matter
2041 0731

Printed by Skipnes Kommunikasjon AS

Abstract

CO_2 capture and storage is expected to play a vital role in reaching net zero emissions by 2050. In this context, large-scale CO_2 pipeline transportation networks must be deployed. In order to perform safety analyses and ensure efficient operation of large-scale CO_2 transportation systems it is key to predict the flow, in particular during depressurization events. This includes intentional depressurizations, e.g., the opening of a pressure relief valve, and accidental depressurizations, e.g., caused by a pipe fracture. High-capacity CO_2 pipelines will be operated in the dense-phase region, meaning that the CO_2 will boil during depressurization. This kind of boiling is denoted as *flashing*, and flashing often occurs delayed, i.e., at a lower pressure than the saturation pressure, out of equilibrium. The resulting pressure evolution and mass flow is highly dependent on the flashing process. Therefore, the focus of the present thesis is to gain more knowledge of this phenomenon through experiments and coupled thermo and fluid dynamics modeling.

In this work, a series of full-bore pipe depressurization experiments were conducted and analyzed, physics-based models for the mass-transfer during flashing have been investigated, and novel numerical methods have been developed for the simulation of non-equilibrium two-phase flows. The effect of homogeneous and heterogeneous bubble nucleation on the maximum attained superheat in the experiments has been investigated. It is found that homogeneous nucleation determines the superheat at warm conditions, i.e., near the critical point, and heterogeneous nucleation dominates otherwise. Homogeneous nucleation can be modeled by classical nucleation theory. This theory is applied herein to account for delayed boiling for flow through orifices and nozzles, and to improve the fluid curve in the Battelle two-curve method for the assessment of pipeline designs with respect to running ductile fracture. It is found that the combination of the crevice model and bubble growth for heterogeneous nucleation can explain the attained superheat at colder temperatures. A

main result from this work is a homogeneous flashing model (HFM) for flashing flows. The mass-transfer model in the HFM accounts for bubble nucleation, coalescence, breakup and growth. The key finding from the analysis of this model is that *both* homogeneous and heterogeneous nucleation must be included in flashing flow models to capture the flow behavior during depressurization at warm conditions, including the relevant operating region of CO_2 transportation pipelines. The present findings for flashing flows are general and relevant for other industrial applications including refrigeration systems and water cooling for pressurized water (nuclear) reactors.

Sammendrag

Det forventes at CO_2-fangst og lagring vil spille en avgjørende rolle for å nå netto nullutslipp av klimagasser innen 2050. I denne sammenhengen må det etableres rørsystemer for storskala CO_2-transport. For å gjennomføre sikkerhetsanalyser og sørge for effektiv drift av CO_2-transportsystemer er det viktig å predikere strømningen, spesielt under trykkavlastning. Dette innebærer både tilsiktede situasjoner, f.eks. ved åpning av en trykkavlastningsventil, og utilsiktede situasjoner som trykkavlastning som forårsakes av et brudd i røret. Høykapasitets CO_2-rør vil ha superkritiske trykk og CO_2-en vil koke under trykkavlastning. Denne typen koking refereres til som "flashing" (hurtigfordamping) og flashing skjer ofte forsinket, ved et lavere trykk enn metningstrykket og en høyere temperatur enn kokepunktet, ute av likevekt. Trykkutviklingen og massestrømmen avhenger av kokeprosessen. Fokuset i avhandlingen er derfor å utvikle en bedre forståelse for dette fenomenet gjennom eksperimentelt arbeid og termo- og fluiddynamisk modellering.

I dette arbeidet har det blitt gjennomført en rekke trykkavlastningseksperimenter, fysikkbaserte modeller for masseoverføring under flashing har blitt undersøkt og nye numeriske metoder har blitt utviklet for simulering av tofasestrømning ute av likevekt. Det har blitt undersøkt hvordan homogen og heterogen nukleering av bobler påvirker maksimal overheting oppnådd i eksperimentene. Resultatene viser at homogen nukleering definerer grensen for overheting ved varme temperaturer, dvs. nær kritisk punkt, og heterogen nukleering dominerer ellers. Homogen nukleering kan modelleres med klassisk nukleeringsteori. Denne teorien har blitt anvendt i arbeidet for å ta hensyn til forsinket koking for strømning gjennom blender og dyser, og for å forbedre fluidkurven i Battelle tokurvemetoden for evaluering av rørdesign for å unngå løpende brudd. Kombinasjonen av crevice-modellen og boblevekst for heterogen nukleering kan forklare grensen for overheting ved kalde temperaturer. Et hovedresultat av dette arbeidet er en homogen kokemodell (HFM) for kokende

strømning. Masseovergangsmodellen i HFM inkluderer boblenukleering, koalesens, oppsprekking og vekst. Hovedfunnet fra analysen av denne modellen er at både homogen og heterogen nukleering må inkluderes i modeller for kokende strømning for å beskrive trykkavlastning utført ved varme temperaturer. Dette inkluderer det relevante driftsområdet for CO_2-transport i rør. Resultatene fra dette arbeidet er generelle og relevante også i andre industrielle sammenhenger, inkludert kuldeteknikk og kjølesystemer for trykkvannsreaktorer.

Preface

The work presented in the thesis has been performed at the Department of Energy and Process Engineering at the Norwegian University of Science and Technology. The research was conducted as part of the Norwegian CCS Research Centre (NCCS) activity on CO_2 transport, and was funded by the Research Council of Norway (257579) and industry. Through NCCS, I was also granted a three months mobility stay at the École nationale supérieure de techniques avancées (ENSTA) in Paris.

I would like to acknowledge Prof. Armin Hafner for his supervision and support during this work. To my co-supervisors, Dr. Svend Tollak Munkejord and Dr. Morten Hammer, thank you for all the detailed feedback, support and suggestions for interesting research directions. I would also like to acknowledge Dr. Han Deng and Dr. Anders Austegard who helped me with all the experimental work. My sincere gratitude goes to Dr. Marcia Huber for her openness for collaboration and all the supportive e-mails. I must also thank Dr. Marica Pelanti for inviting me to stay at ENSTA, and for the interesting discussions. I had a wonderful time as a visitor.

Thanks to my office mates and researchers at the refrigeration group at NTNU who included me in various social events, and even a trip to visit CERN, and for the fun discussions and memories. I would also like to thank the graduate students and researchers at ENSTA Paris, who made my stay abroad such a memorable experience.

Finally, I would like to thank my family and friends for their support, encouragement and endless patience regarding my ramblings on the mysteries of heterogeneous bubble nucleation.

Trondheim, November 2023,
Alexandra Metallinou Log

Contents

Nomenclature

Latin letters

a_{int}	Interfacial area density	$\text{m}^2\,\text{m}^{-3}$
A	Cross-sectional area	m^2
c	Speed of sound	$\text{m}\,\text{s}^{-1}$
$\tilde{C}_p$	Heat capacity at constant pressure	$\text{J}\,\text{K}^{-1}$
C_p	Specific heat capacity at const. press.	$\text{J}\,\text{K}^{-1}\,\text{kg}^{-1}$
C_v	Specific heat capacity at const. vol.	$\text{J}\,\text{K}^{-1}\,\text{kg}^{-1}$
E	Total energy	$\text{J}\,\text{m}^{-3}$
e	Specific internal energy	$\text{J}\,\text{kg}^{-1}$
$\boldsymbol{F}$	Flux vector	-
$\mathcal{F}$	Friction force	$\text{N}\,\text{m}^{-3}$
G	Free energy	J
g	Gravitational acceleration	$\text{m}\,\text{s}^{-2}$
$\mathcal{H}$	Heat transfer rate	$\text{J}\,\text{s}^{-1}\,\text{kg}^{-1}$
h	Specific enthalpy	$\text{J}\,\text{kg}^{-1}$
$\mathcal{I}$	Mechanical relaxation rate	$\text{m}^3\,\text{m}^{-3}\,\text{s}^{-1}$
J	Nucleation rate	$\text{m}^{-3}\,\text{s}^{-1}$
K	Kinetic prefactor	$\text{m}^{-3}\,\text{s}^{-1}$
k_{B}	Boltzmann's constant	$\text{J}\,\text{K}^{-1}$
L	Latent heat	$\text{J}\,\text{kg}^{-1}$
m	Mass	kg
n_{bub}	Number density of bubbles	bubbles m^{-3}
p	Pressure	Pa
$\mathcal{Q}$	Heat transfer from surroundings	$\text{W}\,\text{m}^{-3}$
q_{int}	Heat transfer to liquid-vapor interface	$\text{W}\,\text{m}^{-3}$
r	Radius	m
R	Gas constant	$\text{J}\,\text{K}^{-1}\,\text{mol}^{-1}$
s	Specific entropy	$\text{J}\,\text{K}^{-1}\,\text{kg}^{-1}$
$\boldsymbol{S}$	Source term vector	-
T	Temperature	K

t	Time	s
u	Velocity	$\mathrm{m\,s^{-1}}$
$\boldsymbol{U}$	Vector of conserved variables	-
V_m	Molar volume	$\mathrm{m^3\,mol^{-1}}$
x	Spatial coordinate	m
x_g	Mass fraction of gas	$\mathrm{kg\,kg^{-1}}$
y	Mass fraction of saturated mixture	$\mathrm{m^3\,m^{-3}}$

Greek letters

α_k	Volume fraction of phase k	$\mathrm{m^3/m^3}$
α	Condensation coefficient	–
Γ	Mass-transfer source	$\mathrm{kg\,m^{-3}\,s^{-1}}$
γ	Grüneisen parameter	$\mathrm{Pa\,m^3\,J^{-1}}$
κ	Ratio of specific heats	-
μ	Chemical potential	$\mathrm{J\,kg^{-1}}$
ϕ	Reduction factor	-
ρ	Density	$\mathrm{kg\,m^{-3}}$
$\tilde{\rho}$	Number density	$\mathrm{m^{-3}}$
σ	Surface tension	$\mathrm{N\,m^{-1}}$

Subscripts

bub	Bubble
crit	Critical
evap	Evaporation
g	Gas/vapor
het	Heterogeneous
hom	Homogeneous
int	Interfacial
ℓ	Liquid
m	Metastable
sat	Saturation

Superscripts

*	Critically-sized embryo

Abbreviations

CCS	CO_2 capture and storage
RDF	Running ductile fracture

CERN	Conseil Européen pour la Recherche Nucléaire
CNT	Classical nucleation theory
DEM	Delayed equilibrium model
D-HEM	Delayed homogeneous equilibrium model
ECCSEL	European Carbon Dioxide Capture and Storage Laboratory Infrastructure
ENSTA	École nationale supérieure de techniques avancées
EOS	Equation of state
FVM	Finite-volume method
HEM	Homogeneous equilibrium model
HF	Henry-Fauske
HLLC	Harten-Lax-van Leer Contact
HRM	Homogeneous relaxation model
IEA	International Energy Agency
IPCC	Intergovernmental Panel on Climate Change
LHC	Large hadron collider
NASG	Noble-Abel Stiffened-Gas
NCCS	Norwegian CCS Research Centre
NTNU	Norwegian university of science and technology
PR	Peng-Robinson
SHL	Superheat limit

1 Introduction

1.1 Motivation

1.1.1 CO_2 capture and storage

The Intergovernmental Panel on Climate Change (IPCC) and the International Energy Agency (IEA) point to CO_2 capture and storage (CCS) as a key method to contain global warming within 1.5 °C [1, 2, 3, 4]. In their updated roadmap to net zero emissions by 2050, the IEA [4] finds that several gigatonnes of CO_2 must be captured and stored annually to decarbonize the industry sector. As the CO_2 capture and storage sites are not generally co-located, a large-scale CO_2 transport infrastructure must then be developed.

Norway is at the frontier of the development for large-scale CCS in Europe [5], and partakes in projects involving all parts of the CCS chain; capture, transportation and storage [6]. In particular, the Northern Lights project [7] focuses on the transportation and storage infrastructure needed for CCS in Norway. A goal of the Northern Lights project is to create an infrastructure with excess capacity such that not only Norwegian industry, but also European industry can send captured CO_2 for long-term storage in reservoirs deep below the seabed on the Norwegian continental shelf [6, 7]. The CO_2 will be transported by ships and pipelines [7].

A large fraction of the captured CO_2 will be transported in pipeline networks where the CO_2 is compressed to a dense liquid-like state at high pressures [8, 9, 10]. Even though the CO_2 will be in liquid form during the normal operation of the pipelines, there are several situations where the CO_2 might boil and two-phase flow will occur. This can occur due to fluctuations in the CO_2 supply, or during transient events such as start-up, shut-in, or depressurization of the pipe [11, 12, 13]. The characteristics of two-phase flow is very different from single-phase flow and it is therefore important to predict when it will occur, such that the

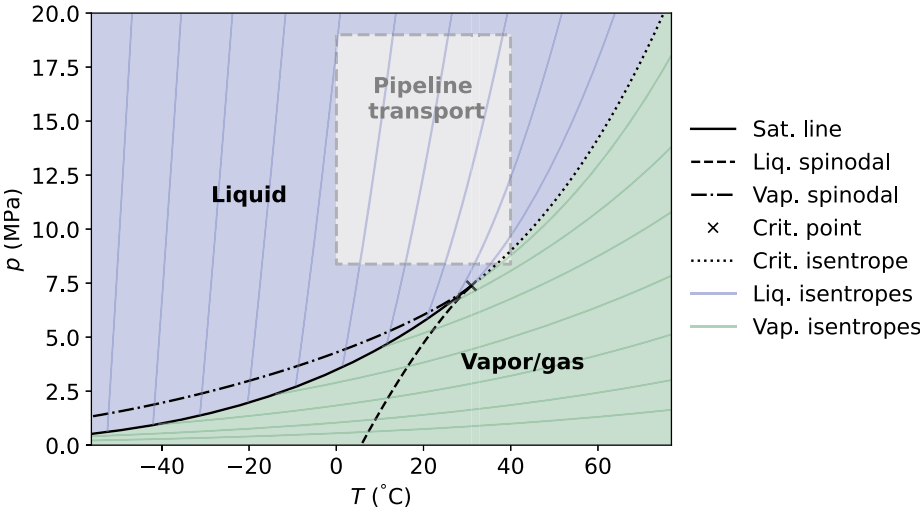

Figure 1.1: Approximate operating region of CO_2 transportation pipelines shown in the phase diagram.

resulting mass-flow, pressure and temperature of the flow will be known. This is relevant both for the operational efficiency of the pipelines and for safety considerations.

1.1.2 Flashing flow during depressurization of CO_2-carrying pipes

The approximate relevant operating region for high-capacity CO_2 transportation pipelines is shown in the phase diagram in Figure 1.1. During the first milliseconds of a depressurization event, the flow will be approximately isentropic. The single-phase isentropes are shown in the phase diagram. The initial state of the CO_2 in the operating region of CO_2 transport pipelines is denoted as a liquid in the present work because it will reach the saturation line from the liquid side and boil during depressurization. Similarly, we denote all the states that will condense due to a depressurization as vapor, as illustrated in Figure 1.1. Boiling caused by a depressurization is referred to as *flashing* or *flash boiling*.

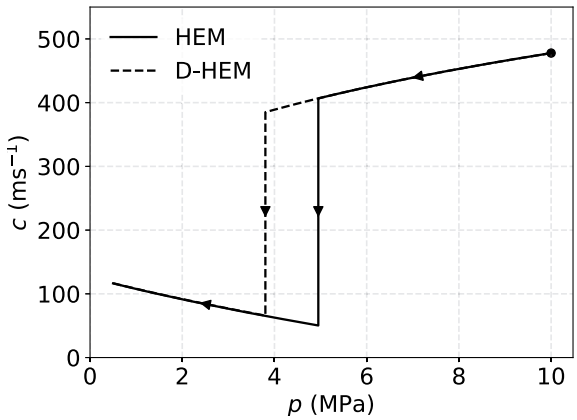

Figure 1.2: Speed of sound along a CO_2 depressurization path with an initial condition of 10 MPa and 20 °C assuming an isentropic process for the homogeneous equilibrium model (HEM) and the delayed homogeneous equilibrium model (D-HEM).

Once flashing begins during depressurization, the flow will choke in most cases, i.e., the speed of the flow becomes equal to the local speed of sound. The choking during flashing is related to an abrupt decrease in the speed of sound for two-phase flow. This is illustrated in Figure 1.2 for the homogeneous equilibrium model (HEM), which is outlined in Section 3.2, and the delayed homogeneous equilibrium model (D-HEM) by Hammer et al. [14]. The occurrence of two-phase flow is highly important to estimate the mass flow of CO_2 as it is depressurized through operational equipment with orifices and nozzles, and to predict the evolution of fractures in the pipe for safety evaluations.

For rapid depressurization events of liquid CO_2, flashing may occur delayed, i.e., at a pressure below the local saturation pressure and above the local boiling point temperature. The liquid is then denoted as *superheated*, and it will be in a metastable state, out of equilibrium. The delayed boiling occurs because a certain amount of energy is required to initiate the phase change, and during a rapid depressurization event, little energy is supplied by the surroundings. Delayed flashing during depressurization has been extensively studied for water in relation to

the safety assessment and operation of water-cooled nuclear reactors [15, 16, 17, 18, 19] and the research is still ongoing today [20, 21]. One of the challenges is to determine the degree of superheat that will be reached. Experiments on flashing water flows show that the attained superheat depends on both the initial temperature, and on the depressurization rate ($\frac{\Delta p}{\Delta t}$) of the fluid [17, 18, 19, 22].

Most flow models studied in the literature for the depressurization of CO_2 assume that phase change occurs at equilibrium [23, 24, 25, 26, 27, 10, 28, 29, 30, 31, 32, 33]. The equilibrium assumption can cause an underestimation of the mass flow through valves and orifices, or a pipe fracture in an accident scenario. De Lorenzo et al. [34] found that the homogeneous equilibrium model underestimated the critical mass flow of flashing water in a short nozzle by an average of 34%, and sometimes by as much as 60%. Some authors have instead tested non-equilibrium models for the depressurization of CO_2 in pipes, where the delayed phase change is accounted for by a relaxation coefficient [35, 36, 37, 38, 39, 40]. In these works, the relaxation coefficient is fitted to individual experiments, and even for the same experiment (Test32A of Botros et al. [41]) authors obtain different "optimal" coefficients that fit the data [37, 38, 39, 40].

Note that some multiphase flow software applied in the oil and gas industry such as LedaFlow [42] include non-equilibrium effects, but the software is typically fitted for slow transients [43] and it is not designed to account for flash boiling. Kjølaas et al. [44] found that the default mass-transfer rate between phases applied in LedaFlow had to be multiplied by a factor of 100 to match experimentally measured pressure and temperature for CO_2 injection in a vertical pipe. Clearly, improvements must be made for such software to be applied in optimizing the operation of CO_2 transportation pipelines. Both from a safety perspective, and for efficient operation of CO_2 flow equipment, it is important to develop and apply new models that correctly account for the observed non-equilibrium phase-change effects.

1.1.3 Designing against running ductile fracture

A key safety element when designing pipelines is to ensure that a running ductile fracture (RDF) cannot occur. A running ductile fracture

(a) CO_2 plume during fracture test (b) Fractured pipe segments

Figure 1.3: CO_2 mixture release plume and pipe after a controlled fracture test, images from DNV/EPCRC/Climit – CO2SafeArrest JIP. Printed with permission from DNV.

is a process where an initial defect in a pipe develops into a fracture which propagates along the pipe, sustained by the pressure forces from the escaping fluid, see, e.g., [45, 46]. If a fracture occurs in a pipeline carrying dense-phase CO_2, the CO_2 will quickly depressurize until flash boiling begins. Once flashing begins, the depressurization slows down as vapor forms and expands. Therefore, a relatively high pressure force will be maintained at the crack tip for a sustained amount of time, which could initiate a running fracture. CO_2-carrying pipes must therefore be designed to withstand stronger forces than pipes carrying other fluids, such as, e.g., natural gas [25, 47].

Figure 1.3 shows pictures from a large-scale pipe fracture test with a CO_2-rich mixture in the dense phase, CO2SafeArrest 2 [48, 49, 50]. A running fracture can propagate along the pipe for several hundred meters [51, 25, 52] and be violent enough to hurl away rock and steel and release vast quantities of CO_2 into the air. As CO_2 is an asphyxiant and heavier than air, the released CO_2 can pose a safety hazard near

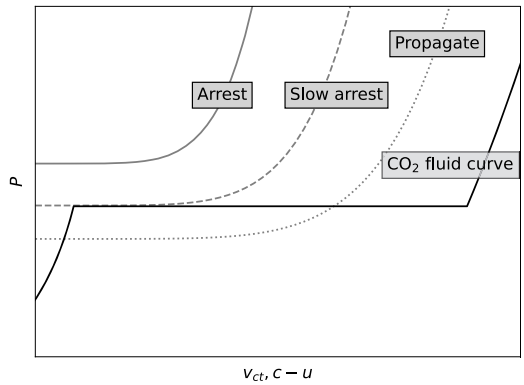

Figure 1.4: Illustration of the BTCM for CO_2, showing an example fluid curve and material curves that would result in propagating and arresting fractures, as well as the limiting case of slow arrest. Made by Hans Langva Skarsvåg [46].

densely populated areas. During a CO_2 pipeline fracture accident in 2020 near Satartia, Mississippi, the high concentration of CO_2 caused issues for combustion engine vehicles, slowing down the evacuation of residents as well [53, 54]. More knowledge on the specific depressurization behavior of CO_2 in accident scenarios is needed to develop appropriate safety guidelines for CO_2 transport pipes. Furthermore, rigorous analysis must be done to assess whether pipelines designed for the transport of other fluids can be repurposed for CO_2 transport.

The most common engineering method applied to design against running fracture in pipes is the Battelle two-curve method (BTCM), which was originally developed for pipes carrying natural gas [46]. In this method, the crack speed and the speed of the depressurization wave in the pipe are assumed to be independent. If the depressurization wave speed is faster than the crack speed, the crack is expected to arrest and if the crack speed is faster than the depressurization wave, the fracture is expected to propagate. Examples of the crack speed curves and the CO_2 fluid curve for the BTCM is shown in Figure 1.4. Here, the fluid curve is calculated using the HEM.

The fluid curve for CO_2 has a pressure plateau which is related to the sudden decrease in the speed of sound when the liquid begins to boil, reducing the depressurization wave speed considerably. The slow depressurization wave means that the pressure will remain relatively high at the crack tip. This reflects the need for stronger materials or a thicker pipe wall to design pipes for dense phase CO_2 transport than for other fluids that do not boil under depressurization. Though the BTCM is a useful tool, it has been found to be non-conservative for CO_2 pipelines [55, 56, 46], due to inaccurate estimates of the crack speed curves. This is the case even though the crack tip pressure is overestimated due to equilibrium assumptions. The model does not capture the fracture and depressurization processes well enough to make accurate predictions. Our hypothesis is that by adding more physics, a better predictive ability can be attained with a reduced need for large-scale tests to fit parameters.

Non-equilibrium flashing is one of the important physical effects that are not accounted for in existing design tools for CO_2 pipelines. For large-scale CO_2 pipe rupture tests, the pressure pushing at the crack tip has been reported to be over 20% lower than expected based on equilibrium assumptions [49]. The plateau is also reported to be sloped [56, 49, 57]. Similar effects are also reproduced in full-bore pipe depressurization experiments with CO_2 and CO_2-rich mixtures by Botros et al. [41, 58] and Munkejord et al. [32, 33]. These effects cannot be captured by equilibrium models. Though overestimating the crack tip pressure can be seen as an advantage for the safety assessment of pipelines, it is key in safety evaluations to know the true forces on the pipe in order to enforce the appropriate safety limits. In addition, if the forces on the pipe are calculated using equilibrium flashing models during safety tests, this could lead to the assumptions that the pipe materials are stronger than they really are.

Another limitation of the BTCM is that it considers RDF an uncoupled fluid-structure problem. In reality, RDF is a coupled problem and this should also be accounted for. By applying a computational fluid dynamics (CFD) model coupled with a pipe structure model, this coupling can be taken into account. Such models are necessarily more computationally heavy than the simpler engineering tools such as BTCM. A visualization

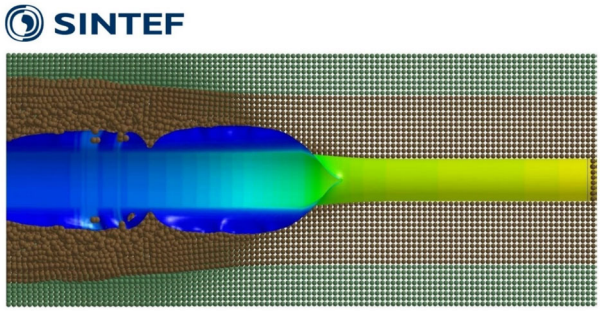

Figure 1.5: Visualization of result from coupled CFD-structure model of SINTEF [45] developed in the research centres BIGCCS [59] and NCCS. Reprinted from [45] with permission from Elsevier.

of the prediction of a coupled CFD-structure model developed at SINTEF is shown in Figure 1.5 [45]. In this model, the HEM was applied for the simulation of the flashing flow, similarly to the approach of other authors evaluating RDF in CO_2-carrying pipes and the resulting CO_2 release [23, 25, 26, 29, 31, 60]. It would be possible to apply the output of these models to tune the simpler engineering tools such as BTCM as well.

One of the main goals of this work has been to develop a two-phase flow model which correctly accounts for the non-equilibrium flashing flow that occurs during rapid depressurizations caused by the full-bore rupture of a pipe based on the physics of boiling. Such a flow model also necessitates the development of robust, accurate and computationally efficient numerical solution methods, and the handling of thermodynamic calculations for non-equilibrium states. In the future, non-equilibrium flow models can be coupled with a structure model to achieve better estimates for whether an RDF will occur in a CO_2-carrying pipe, and what the resulting mass flow of CO_2 would be through a fracture.

1.1.4 Modeling flow across cross-sectional area changes

The main focus in this work is on flow in pipes with constant cross-sectional area, however, while flowing through a pipeline transportation network, the CO_2 will encounter changes in cross-sectional area at multiple locations. Examples include valves, orifices and joints between pipes of different sizing [61, 62, 63]. The effects of cross-sectional area changes can be captured in quasi-one-dimensional flow models where the area change is accounted for by a non-conservative term [64, 65, 66, 67, 68, 69]. For the modeling of long pipe systems, it can be difficult to accurately capture the effects of area changes and the changes from single-phase and two-phase flows due to diffusion in the numerical solution procedure. Numerical diffusion smoothens the predicted CO_2 flow, but can be mitigated by increasing the resolution of the model, see, e.g., Toro [70, Chap. 10]. The down-side of increased resolution is that it increases the computational cost. Numerical schemes that are specifically designed for low numerical diffusion offer a better trade-off between resolution and accuracy. It is therefore desirable to extend low-diffusion numerical schemes originally designed for solving constant cross-sectional area flows to flows with abrupt changes in cross-sectional area.

1.2 Aims of the study

The present thesis is part of the Norwegian CCS Research Centre (NCCS). The goal of NCCS is to fast-track CCS deployment through industry-driven, science-based innovation that addresses the major barriers identified in CCS demonstration and industry projects [71]. The aim of this work is to contribute to the safe design and efficient operation of CO_2-transportation pipelines in the context of CCS. Our hypothesis is that by adding more physics in state-of-the-art flashing flow models, a better predictive ability can be attained. This is mainly aimed towards the modeling of transient flow during the full-bore rupture of CO_2-carrying pipes with constant cross-sectional area. In order to achieve the above aim, and investigate the hypothesis, the work has had the following scope:

- Investigate state-of-the-art non-equilibrium flow models.

- Develop robust and accurate numerical methods for the modeling of the depressurization of CO_2 in pipes.
- Explore and validate physics-based mass-transfer relations for non-equilibrium two-phase flow models.
- Conduct CO_2 pipe depressurization experiments, analyze the results and apply them to validate the flow models and their predictive ability.

1.3 Present contributions

The present thesis work contributed to six journal papers and one conference paper. All of these papers address aspects of the topics motivating this work by the extension of numerical methods, gaining knowledge on non-equilibrium flashing for CO_2 and by developing flow models that account for non-equilibrium flashing. The papers are listed below, and are attached in the Appendix. The contributions of the papers are briefly summarized here:

- In Paper 1, the low-diffusion Harten-Lax-van Leer Contact (HLLC) finite-volume method [72] is extended for the simulation of two-phase flows passing through ducts with abrupt area changes.
- A novel model for the choked flow of CO_2 through nozzles and orifices is provided in Paper 2, in which non-equilibrium flashing is taken into account based on the physics of bubble nucleation.
- In Paper 3, a modified version of the BTCM for CO_2 is introduced where improvements are made for both the material curve, and the fluid curve by accounting for non-equilibrium flashing based on the physics of bubble nucleation.
- One of the important variables in the computation of the modified fluid line is the CO_2 mixture surface tension. A common model for the prediction of mixture surface tension, the parachor model applied in REFPROPv10 [73], is assessed in Paper 4.

- For the validation of new CFD models, and to better understand how the attained superheat varies for different initial conditions, a series of full-bore experiments were conducted. These are introduced in Paper 5, and the pressure measurements are compared to a simple non-equilibrium flashing flow model. A preliminary study of the attained superheat and dependence on initial temperature was conducted in the Conference paper. The data is made openly available.

- A flashing flow model incorporating all the relevant physical effects of flashing flow, including bubble nucleation, coalescence, breakup and growth is introduced in Paper 6. The importance of different bubble nucleation mechanisms is investigated. The present model can also explain the observed effects of how the attained superheat varies with both the initial temperature and the depressurization rate of the fluid.

- For the numerical solution of the non-equilibrium models in Paper 5 and Paper 6, a new numerical integration method was developed for the mass-transfer rate, and a novel outflow boundary condition was proposed.

A detailed summary of the papers is provided in Chapter 7.

Paper 1:
Log, Alexandra Metallinou; Munkejord, Svend Tollak; Hammer, Morten. (2021) HLLC-type methods for compressible two-phase flow in ducts with discontinuous area changes. *Computers & Fluids.* vol 227. doi:10.1016/j.compfluid.2021.105023

Conference paper:
Log, Alexandra Metallinou; Munkejord, Svend Tollak; Hammer, Morten; Hafner, Armin; Deng, Han; Austegard, Anders. (2022) Investigation of non-equilibrium effects during the depressurization of carbon dioxide. *15th IIR-Gustav Lorentzen Conference on Natural Refrigerants - GL2022 - Proceedings - Trondheim, Norway, June 13-15th 2022.*

doi:10.18462/iir.gl2022.0197

Paper 2:
Hammer, Morten; Deng, Han; Austegard, Anders; **Log, Alexandra Metallinou**; Munkejord, Svend Tollak. (2022) Experiments and modelling of choked flow of CO_2 in orifices and nozzles. *International Journal of Multiphase Flow.* vol 156.
doi:10.1016/j.ijmultiphaseflow.2022.104201

Paper 3:
Skarsvåg, Hans Langva; Hammer, Morten; Munkejord, Svend Tollak; **Log, Alexandra Metallinou**; Dumoulin, Stephane; Gruben, Gaute. (2023) Towards an engineering tool for the prediction of running ductile fractures in CO_2 pipelines. *Process Safety and Environmental Protection (PSEP).* vol 171. doi:10.1016/j.psep.2023.01.054

Paper 4:
Log, Alexandra Metallinou; Diky, Vladimir; Huber, Marcia. (2023) Assessment of a Parachor Model for the Surface Tension of Binary Mixtures. *International Journal of Thermophysics.* vol 44 (7).
doi:10.1007/s10765-023-03216-z

Paper 5:
Log, Alexandra Metallinou; Hammer, Morten; Deng, Han; Austegard, Anders; Hafner, Armin; Munkejord, Svend Tollak. (2024) Depressurization of CO_2 in a pipe: Effect of initial state on non-equilibrium two-phase flow. *International Journal of Multiphase Flow.* vol 170.
doi:10.1016/j.ijmultiphaseflow.2023.104624

Paper 6:
Log, Alexandra Metallinou; Hammer, Morten; Munkejord, Svend Tollak. (2024) A flashing flow model for the rapid depressurization of CO_2 in a pipe accounting for bubble nucleation and growth. *International Journal of Multiphase Flow.* vol 171.
doi:10.1016/j.ijmultiphaseflow.2023.104666

The main contributions in this work are the Conference Paper, Paper 5 and Paper 6 concerning experiments and modeling of full-bore depressurization of a pipe filled with CO_2 and the subsequent transient flashing process. In all the papers where flow modeling is included, 1D flow models are applied.

1.4 Open access and data availability

All the publications and experimental data introduced therein are made openly available. The data is shared such that it can be applied for the validation of CFD models for the design and operation of CO_2 flow systems, and to further the field of multiphase flow modeling in general. The available research data is summarized below:

Pipe depressurization data

As part of the present thesis, a series of CO_2 pipe depressurization experiments were conducted and analyzed at the ECCSEL depressurization facility. Furthermore, previous CO_2 depressurization experiments conducted at this facility were also analyzed. All of this data is made openly available at Zenodo. An overview of all available datasets from the ECCSEL depressurization facility, including data from the present work, is presented in Table 1.1. Note that each dataset contain data from several experiments.

Data on the surface tension of binary mixtures

Related to Paper 4 on the parachor method for estimating the surface tension of binary mixtures, Vladimir Diky curated a large dataset on binary mixture surface tension measurements from the NIST database. The dataset can be accessed at:
`https://static-content.springer.com/esm/art%3A10.1007%2Fs10765-023-03216-z/MediaObjects/10765_2023_3216_MOESM2_ESM.txt`

Table 1.1: Overview of available data from ECCSEL pipe depressurization tests.

Open end	Fluids	Access
Full-bore	N_2, CO_2	doi:10.5281/zenodo.3928226
Full-bore	CO_2–N_2, CO_2–He	doi:10.5281/zenodo.3984821
Nozzle/orifice	CO_2	doi:10.1016/j.ijmultiphaseflow.2022.104201
Full-bore*	CO_2	doi:10.5281/zenodo.766953
Full-bore*	CO_2	doi:10.5281/zenodo.8164913

* Present work

1.5 Relevance to and resources from other fields

Though the present work is motivated by the application to CCS, the modeling of flashing flow is relevant in an array of industrial applications. Here, a particular emphasis is put on the relevance to the safety of pressurized water (nuclear) reactors and CO_2 refrigeration systems.

1.5.1 Pressurized water reactor safety

One of the most relevant fields in terms of research on the depressurization of fluids in pipes and flashing flows is that of nuclear safety for pressurized water reactors. Extensive research on this topic has been ongoing since the 1970s. There is a large amount of literature which has been studied in the present work to inform the modeling of flashing flows during the depressurization of pipes, and which may be relevant to other researchers in the field.

Relevant literature on experiments and models for the flashing flow of water is listed below:

Experiments

- The pipe blowdown test of Edwards and O'Brien [15]. Most articles citing this test are also relevant, and provide methods for the modeling of flashing flows.

- The pipe blowdown tests of Lienhard et al. [17] and Alamgir et al. [74].

- The pipe blowdown tests of Barták [19].

- The pipe blowdown tests referred to as the Super Canon experiments. Experimental results can be found in the thesis of Riegel [75].

- The experiments on choked flow in nozzles, short tubes and long tubes, referred to as the Super Moby Dick experiments [76]. Experimental results are listed by Amos and Schrock [77]. They are also plotted against other models by De Lorenzo et al. [34].

- Experiments on flashing flow through slits by Amos and Schrock [77].

Modeling

There are three highly relevant reviews summarizing papers on modeling flashing flows concerning nuclear safety, namely those of Pinhasi et al. [78] and Liao and Lucas [20, 21]. The review of Pinhasi et al. [78] was found particularly relevant to identify the most important mass-transfer models which must be included to capture flashing flows. Even though flashing water flows have been studied for a long time, there are still unanswered questions on how to model the mass-transfer from liquid to vapor appropriately. Some apply a simple relaxation coefficient accounting for the delay in the phase change, while others try to incorporate the effects of bubble formation, or pre-existing bubbles in the boiling process. In addition to the aforementioned reviews, the following papers illustrate different methods to model flashing water flows:

- Models using a simplified relaxation formula:
  Bilicki and Kestin [79], Bilicki et al. [80], Downar-Zapolski et al. [81], Pelanti and Shyue [82], De Lorenzo et al. [83], Helluy et al. [84] and Pelanti [85].

- Models incorporating some form of bubble dynamics:
  Winters and Merte [86] (which also includes experiments on R-12 depressurization), Deligiannis and Cleaver [87], Shin and Jones [88] and Blinkov et al. [89], Ivashnyov et al. [90] and Liao and Lucas [91].

It is further worth noting two simulation codes which have been developed for simulations of fast transients in water, namely WAHA [92] and EUROPLEXUS [93]. Both of these have non-equilibrium models and EUROPLEXUS has a testing and evaluation version openly available for researchers and academics [94].

1.5.2 CO_2 refrigeration

The present research is also highly relevant for the field of CO_2 refrigeration [95]. CO_2 is becoming increasingly popular as a natural refrigerant due to its low global warming potential and known effects on the environment, as compared to synthesized options such as hydro-fluorocarbons HFCs. For trans-critical CO_2 refrigeration cycles, the flashing of CO_2 in ejectors is used to recover lost work, improving the efficiency of the system [95]. For the optimization of CO_2 ejectors, it is necessary to model the non-equilibrium flashing of CO_2 accurately.

The modeling of flashing CO_2 flows is also relevant for the safety analysis of large-scale CO_2 refrigeration systems. For example, a large-scale CO_2 refrigeration system will be applied for the cooling of the ATLAS and CMS particle tracking detectors for future experiments with the Large Hadron Collider (LHC) at CERN [96, 97]. An image of the CMS detector is shown in Figure 1.6, to indicate the scale of the system requiring cooling. The refrigeration system will be located underground, and safety analyses on the outflow of CO_2 through, e.g., faulty valves or cracks in CO_2-carrying pipes are key to develop appropriate evacuation and ventilation procedures of the area and ensure the safety of local personnel. CFD models of flashing flow inside the system can be applied as boundary conditions for outflow and dispersion models for the relevant safety analyses.

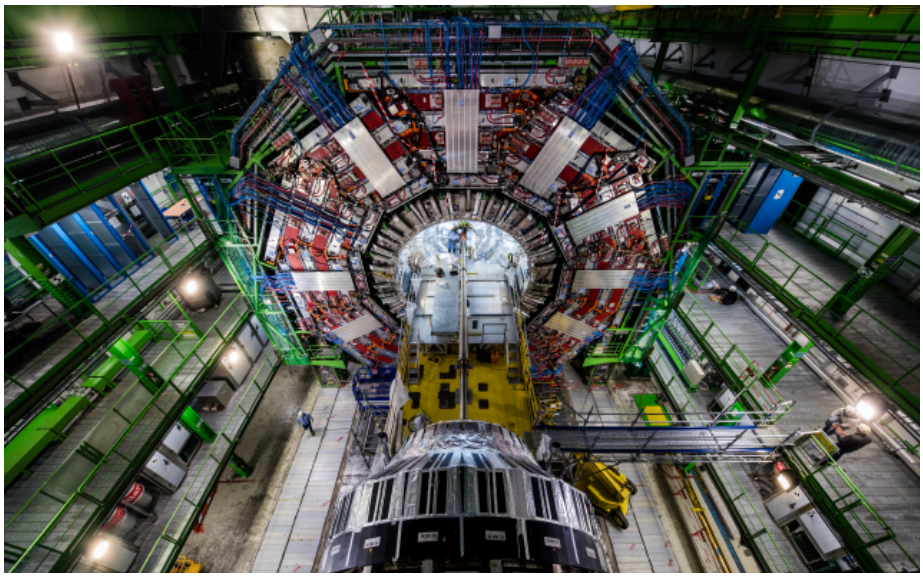

Figure 1.6: The CMS detector at CERN. Photographer: Maximilien Brice. Photo shared by CERN under a CC-BY-4.0 licence.

1.6 Structure of thesis

The present thesis consists of nine chapters, a collection of six journal papers and one conference paper. The content of the remaining chapters is summarized below:

- Chapter 2 disusses the concept of metastability and the attainable superheat in previous experiments. The relation of the attainable superheat to the bubble nucleation mechanism is introduced.
- Chapter 3 summarizes relevant models for two-phase equilibrium and non-equilibrium flow, including common phase change correlations applied in the literature. The choice of the two-phase model applied in Paper 5 and 6 is motivated.
- Chapter 4 describes theory on the kinetics of liquid-vapor phase change and suggests physics-based mass-transfer models which can

be applied in the non-equilibrium two-phase flow models.

- Chapter 5 describes the novel semi-impicit numerical solution method applied to solve the governing equations for flashing flow in Paper 5 and 6.
- Chapter 6 provides details on the experimental work conducted as part of the thesis.
- Chapter 7 summarizes the papers resulting from the present thesis work.
- Chapter 8 provides a summary of the main results and conclusions of the thesis, and suggestions for further work.

2 Thermodynamic metastability

In this chapter, the relation between thermodynamic equations of state, stability and metastability is outlined in Section 2.1, and previous results for the maximum attained metastability in flashing flows and the relation to the bubble nucleation mechanism are presented in Section 2.2.

2.1 Equations of state and metastability

Equations of state (EOS) relate the thermodynamic state variables such as the pressure to, e.g., the density and the specific internal energy, $p = p(\rho, e)$. One of the simplest equations of state, the ideal gas law, assumes that the molecules of the substance act as hard particles with no inter-molecular attraction:

$$p = \rho(\kappa - 1)e, \tag{2.1}$$

where κ is the ratio of specific heats,

$$\kappa = \frac{C_p}{C_v}, \tag{2.2}$$

C_p is the specific heat at constant pressure and C_v is the specific heat at constant volume. As the ideal gas EOS ignores inter-molecular forces, the transition from the gas state to the liquid state is not captured, and the gas phase can also exist for any density and internal energy.

In order to model a liquid-like state, the stiffened gas equation of state can be applied:

$$p = \rho(\kappa - 1)(e - e^*) - \kappa p^0, \tag{2.3}$$

where the term κp^0 models the attractive forces between the molecules, and e^* denotes the zero point for the internal energy. This EOS results from a linearization of the more general Mie-Grüneisen EOS [98]. The stiffened gas EOS does not predict phase change on its own, but it is possible to apply the EOS for liquid and vapor with a different set of

parameters based on a reference state for each phase (essentially modeling each of the phases with their own EOS) and enforce phase change in calculations. Due to the simplicity of the EOS, it has been applied by several authors for numerical simulations of water/steam and water/gas mixtures [99, 100, 101, 102, 103, 104, 105]. A similar, but more accurate EOS denoted the Noble-Abel Stiffened-Gas (NASG) EOS has also been proposed [106].

As both the stiffened-gas EOS and NASG EOS are linearized, they cannot capture the non-linear changes in the thermodynamic state of a fluid near its critical point. This is not a problem when simulating water flows far from the critical point, but for CO_2 simulations the fluid state will often be close to the critical point and these equations of state would provide inaccurate results. Furthermore, similarly to the ideal gas EOS, these equations of state generally provide stable states for the phases at all conditions, which disagrees with both theory and experiments [107, 108, 109, 110, 83].

In real systems, there is a limit to the stable region of the phases, which is denoted the spinodal. At this point a spontaneous phase change will occur [108]. As discussed by Aursand et al. [109], the simplest type of EOS that is able to predict both the presence of the liquid and vapor phases *and* the spinodal are cubic equations of state. These equations of state can be written as a cubic equation of the molar volume V_m. A general form is

$$p(T, V_m) = \frac{RT}{V_m - b} - \frac{a\beta(T)}{(V_m - bm_1)(V_m - bm_2)}, \tag{2.4}$$

where R is the gas constant, T is the temperature, and β, a and b are parameters of the EOS. m_1 and m_2 are constants that characterize various cubic EOS. For example, the Peng-Robinson (PR) EOS has $m_1 = -1+\sqrt{2}$ and $m_2 = -1 - \sqrt{2}$ [109].

The spinodal of a single component phase satisfies

$$\left(\frac{\partial p_k}{\partial \rho_k}\right)_T = 0, \ k \in g, \ell, \tag{2.5}$$

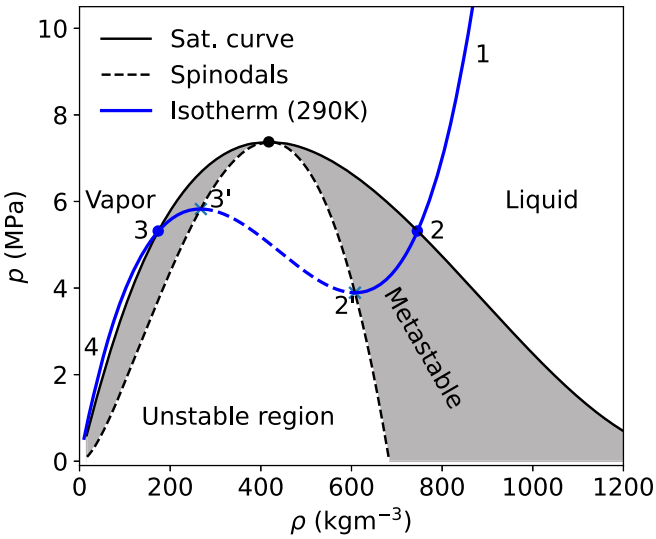

Figure 2.1: The saturation dome, including the metastable region, shown in a p-ρ diagram for CO_2 calculated using the PR EOS. An isotherm (blue) is shown for $T = 290\,\mathrm{K}$.

and the unstable area satisfies

$$\left(\frac{\partial p_k}{\partial \rho_k}\right)_T < 0, \;\; k \in g, \ell, \tag{2.6}$$

where ℓ denotes the liquid phase and g denotes the vapor phase. Note that some authors call the unstable region unphysical because the squared speed of sound becomes negative so the speed of sound would be imaginary, causing issues in flow models [98, 99, 100, 106]. The authors then argue that using the stiffened gas or NASG EOS for each phase is better. Clearly an imaginary speed of sound is unphysical, but that does not mean that the thermodynamically unstable region is unphysical. Rather it is the modeling of fluid flow in this state that breaks down. This is reasonable because the fluid is unstable and any perturbation will initiate phase change (instead of fluid flow). The unstable region is an intrinsic property of the fluid [107, 108, 109, 110].

In Figure 2.1, a p-ρ diagram is shown, illustrating the saturation curve,

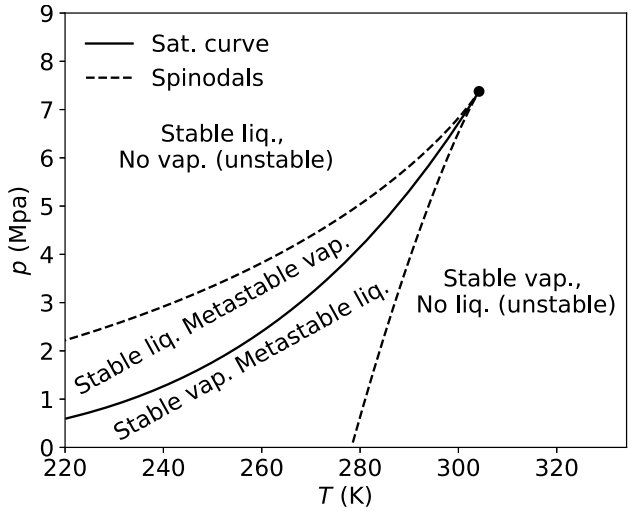

Figure 2.2: The saturation curve and spinodals in the p-T diagram for pure CO_2 calculated using the PR EOS.

metastable region and unstable region of the liquid and vapor phases calculated with the PR EOS fitted for CO_2. The isotherm for $T = 290\,\mathrm{K}$ is also shown. For the liquid and vapor to remain stable and in equilibrium along the isotherm, liquid-vapor phase change must occur when moving from the points 1→2→3→4 that are marked in the figure. Points 2 and 3 mark where the two phases are in equilibrium. For a pure substance, the criterion for equilibrium is that the temperature, pressure and chemical potentials of the phases are equal,

$$\mu_\ell(p, T) = \mu_g(p, T). \tag{2.7}$$

This is explained in detail by, e.g., Hammer et al. [111, Sec. 3.1 and 3.2]. For a rapid process, the phases may become metastable before phase change begins. The maximum degree of metastability that the liquid phase can reach along the isoterm is marked at point 2' and for the vapor phase at point 3'. A metastable liquid is denoted as superheated, and a metastable vapor is denoted as subcooled or supersaturated.

The regions for stable and metastable phases for pure CO_2 are shown in

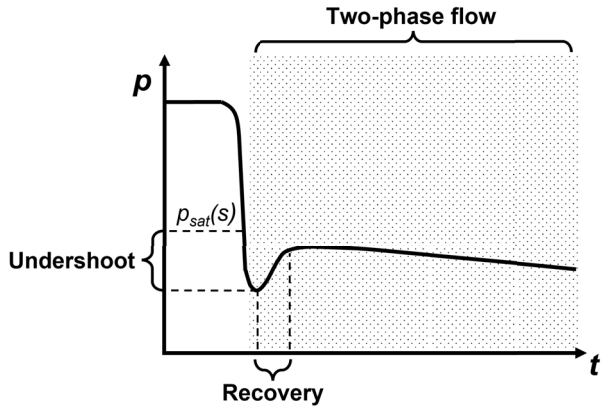

Figure 2.3: Drawing of typical pressure trace near the open end of the pipe during depressurization where flashing occurs.

a p-T diagram in Figure 2.2. It is possible for the liquid state to exist at a pressure below the local saturation pressure, and at a temperature above the local saturation temperature. In relation to pipe depressurization experiments, it is also common to refer to the "pressure undershoot" during which the flow is superheated. Both superheat and the pressure undershoot are measures of non-equilibrium or metastability of the fluid. A typical pressure recording with a pressure undershoot for a depressurization case, and the relation between superheat and the pressure undershoot for a depressurization are illustrated in Figures 2.3 and 2.4, respectively. Note that though the pressure undershoot is shown as $\Delta p = p_{\mathrm{sat}}(s_{\mathrm{init}}) - p$ in the figures, it is more often defined as $\Delta p_{\mathrm{sat}} = p_{\mathrm{sat}}(T) - p$. Though it is theoretically possible to reach the thermodynamic limits of metastability, phase change will generally be initiated before this point is reached.

2.2 Attainable superheat in experiments

As discussed in more detail in Chapter 4, there are two main types of bubble nucleation, homogeneous and heterogeneous. Homogeneous nucleation occurs in the bulk of the superheated liquid due to random density fluctuations creating a vapor-like volume, which – if it is large enough

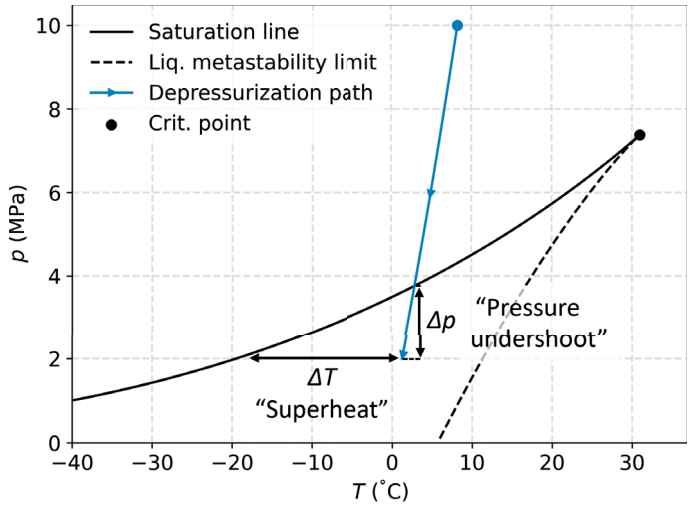

Figure 2.4: Illustration of the relation between the pressure undershoot and the superheat of a flashing liquid, assuming isentropic depressurization.

– will become a stable bubble and grow. The rate of creation of critically-sized bubbles, which will not collapse back to the liquid phase, can be estimated using classical nucleation theory (CNT), which is well described by Debenedetti [108, Chap. 3]. Heterogeneous nucleation instead occurs on a surface or interface. The surface aids the bubble formation process, lowering the required available energy for nucleation to occur.

The superheat limit for different fluids has been extensively studied, and a review of available literature is provided by Debenedetti [108, Chap. 3.1.4]. In several experiments with pure fluids with reduced concentrations of dissolved gases and suspended impurities, where the contact to solid surfaces is eliminated, liquids can be superheated up to 90% of their critical point temperature at atmospheric pressure [112]. This result agrees well with the predictions of CNT. However, the attainable superheat during flashing is often found to be smaller than that predicted by CNT.

The attained pressure undershoot (Δp_{sat}) for water flashing experi-

ments at various initial conditions and depressurization rates ($\frac{\Delta p}{\Delta t}$) was studied by Lienhard et al. [17], and a clear dependence was found on the depressurization rate: higher depressurization rates led to larger pressure undershoots and superheats. In all their experiments except the warmest ones, close to the critical point temperature, Lienhard et al. [17] observed a rapid pressure recovery after the initiation of flashing. Similar trends for the pressure undershoot and recovery with temperature are also observed for different fluids, including CO_2 and CO_2-rich mixtures [41, 113, 32, 33, 114]. Interestingly, Lienhard et al. [17] also captured pressure undershoots with *negative* pressure, i.e., where the water was briefly under tension, for some cold temperature tests [1].

Alamgir and Lienhard [18] later proposed a correlation for the pressure undershoot during hot water depressurization motivated by CNT. The correlation includes a correction factor for the effect of heterogeneous nucleation in CNT and was based on data from a variety of sources including [17, 74, 15, 116]. It was found that the correction factor depends on initial temperature and depressurization rate and reduces exponentially for warmer temperatures, near the critical point, meaning that near the critical point there is good agreement with CNT.

Barták [19] modified the correlation of Alamgir and Lienhard [18], including their own experimental data at different initial conditions. They found that the correlation of Alamgir and Lienhard [18] did not predict the attained superheat as well as their own correlation, but noted that the poor performance was mainly related to the new data which it had not been fitted for. For low depressurization rates, it was later found that the correlation of Alamgir and Lienhard [18] provided inaccurate estimates of the superheat [22]. Elias and Chambré [22] therefore proposed a similar correlation for the maximum attainable superheat for flashing flows that was found to perform well for both low and high depressurization rates.

More recently, Wilhelmsen and Aasen [117] estimated the superheat limit of water and CO_2 based on critical, flashing flow measurements and plotted the result in the phase diagram. The resulting trend in

[1] In fact, water in trees is also shown to be under tension. An interesting educational video on the topic can be found on YouTube under the name: How trees bend the laws of physics [115].

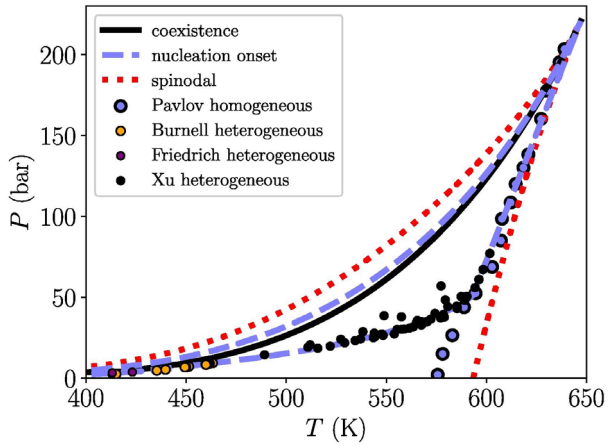

Figure 2.5: The estimated nucleation onset of water for the critical flow tests of Xu et al. [118], Burnell [119] and Friedrich and Vetter [120]. Homogeneous nucleation measurements taken from Pavlov and Skripov [121]. Figure reproduced from Wilhelmsen and Aasen [117].

the superheat limit for water in the phase diagram is very interesting and is therefore reprinted here in Figure 2.5. In this figure, Wilhelmsen and Aasen [117] use circular markers to show the estimated superheat limits and the dashed purple line to show the theoretically calculated homogeneous SHL using CNT, with the exception of the part which agrees with the markers denoted as *heterogeneous* which was fitted to the data using a correlation. Wilhelmsen and Aasen [117] classified the data as heterogeneous or homogeneous based on whether or not it agreed with the homogeneous SHL.

Similarly to the previous work of Alamgir et al. [74], Barták [19] and Elias and Chambré [22], Wilhelmsen and Aasen [117] found that there is a good agreement with the homogeneous superheat limit estimated using CNT for warmer temperatures, and at colder temperatures a heterogeneous superheat limit is encountered. Indeed for temperatures near the triple point temperature, nearly no superheat or pressure undershoot is reached during flashing, even though it is possible to obtain negative pres-

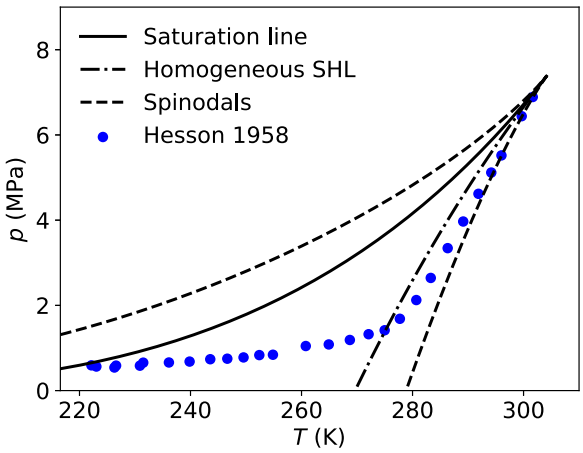

Figure 2.6: Estimated nucleation onset based on the critical flow measurements of Hesson and Peck [122], calculated using the GERG-2008 EOS.

sure undershoots. Based on the data for cold temperatures, Wilhelmsen and Aasen [117, Appendix A] propose a correlation for the heterogeneous superheat limit for water, which was used to plot the part of the purple line in the figure that agrees with the heterogeneous data. Due to a lack of data for CO_2 at colder temperatures, a correlation was not made for the heterogeneous superheat limit of CO_2.

Hesson and Peck [122] conducted a series of critical mass flow tests for CO_2 through nozzles and orifices for cold temperatures. Note that Hendricks et al. [123] questioned the accuracy of the data, as the flow rates were higher than expected. Nevertheless, the estimated resulting nucleation points are shown in Figure 2.6, based on calculations by Hammer et al. [14] as the trend is still interesting. The superheats found using the data of Hesson and Peck [122] are higher than expected, likely due to the inaccuracy of the data noted by Hendricks et al. [123], however, they show the same *qualitative* trend as the measurements for water: a crossover from homogeneous to heterogeneous nucleation with decreasing temperature, and a very small superheat limit at cold temperatures.

The above results raise three questions which are addressed in the present work:

1. Do CO_2 pipe depressurization tests also follow the trend of a crossover in the maximum attained superheat being determined by homogeneous nucleation for warm temperatures, near the critical point, and heterogeneous nucleation for colder temperatures?

2. Is it possible to predict the flashing process of CO_2 using homogeneous nucleation theory alone for warm depressurizations, near the critical point?

3. Why is the superheat limit for flashing flows so small for low reduced temperatures and pressures, close to the triple point of the fluid?

The first question is addressed with the present experimental campaign and analysis of the results in the Conference paper, Paper 5 and Paper 6. The second and third questions are addressed in Paper 6, and they are further expanded upon in Chapter 4 of the thesis, concerning the kinetics of phase change during flashing.

3 Two-phase flow models

In this chapter, an overview of relevant two-phase flow models is provided and the choice of the non-equilibrium flow model applied in Paper 5 and Paper 6 is motivated, namely the four-equation flow model. Other flow models are described as a reference and due to their relevance for further work.

Note that during CO_2 depressurizations, dry-ice will form if the triple point is reached, and the third solid phase must also be accounted for. For the short time-scales relevant for the liquid-vapor phase change considered in the present work, the triple point is not reached. Therefore, only two-phase flow models are considered here. For the interested reader, a method for capturing the formation of solid CO_2 during depressurization is suggested by Hammer et al. [125]. Martynov et al. [126] also investigate the modeling of dry ice in more detail.

Finally, we note that the flow equations provided here are not a closed set of equations for the system, and an equation of state for the fluid must also be provided. Details on the thermodynamic library, equation of state and two-phase thermodynamic solution procedure for the four-equation flow model applied in this work is provided in the Appendix.

3.1 General background on two-phase flow modeling

As mentioned in Section 1.1, there are several scenarios for CO_2 pipe flow where two-phase flow might arise. Generally, two-phase flow can be characterized by the distribution of the phases called flow regimes. An example of different flow regimes encountered in horizontal pipe flow as categorized by Hewitt [124] are shown in Figure 3.1.

The modeling of two-phase flows is complicated by the interfaces between the phases. For simple systems, it is possible to model the flow by capturing all the interfaces directly, such as by the level-set method [127],

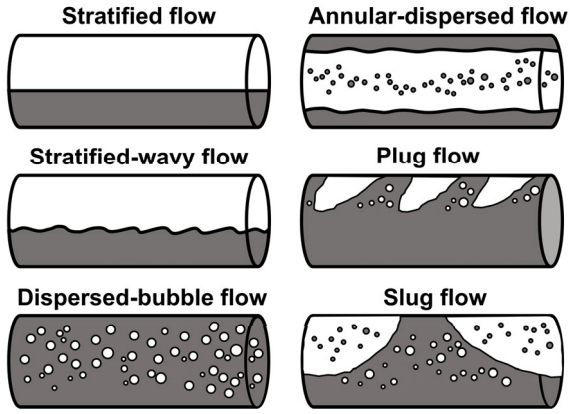

Figure 3.1: Illustration of typical flow regimes encountered in horizontal two-phase liquid-vapor flow in pipes, drawn based on the categories suggested by Hewitt [124].

front-tracking method [128, 129] and volume of fluid method [130]. However, this approach is computationally heavy. The most common modeling approaches for simulating pipe flow instead involve integral averaging such that the need to resolve the interfaces disappears [131]. Information on different averaging approaches can be found in [132, Chap. 9 and 10] and [133, Chap. 2.4]. When the equations are averaged, information on, e.g., the interface mass, momentum and heat exchange is removed, and constitutive relations must be added to account for the effects.

In the present work, we consider models that are averaged across the cross-section of the pipe such that any variation in the radial direction of the flow is ignored. As we assume negligible variations in the radial direction, one-dimensional flow models are considered. These models may be extended to higher dimensions.

We are furthermore interested in rapid depressurization caused by pipe rupture events, due to the relevance for the safety evaluation of CO_2 transport pipelines. Visualization experiments show that during the first instants of rapid depressurization causing flashing due to the full-bore rupture of a pipe, the two phases tend to be dispersed [35]. This is also supported by temperature measurements during CO_2 depressurization

tests conducted by Munkejord et al. [32], where the temperature at the bottom, side and top of the pipe was measured at various locations and found to coincide until around $t = 4\,\mathrm{s}$ after the depressurization started. Therefore, the present thesis focuses on homogeneous flow models, where it is assumed that the phases are well-mixed and travel at the same velocity:

$$u_g = u_\ell = u. \tag{3.1}$$

The governing equations of relevant homogeneous flow models are presented in the following sections.

3.2 Homogeneous equilibrium model

The simplest homogeneous two-phase flow model assumes that the phases are in full thermodynamic equilibrium, i.e.,

- Mechanical equilibrium: $p_g = p_\ell = p$
- Thermal equilibrium: $T_g = T_\ell = T$ and
- Chemical equilibrium: $\mu_g = \mu_\ell$,

and is therefore called the homogeneous equilibrium model (HEM). For this model, all interface transfer between the phases can be calculated using a thermodynamic EOS, where full equilibrium is enforced and the two-phase mixture can be treated as a single fluid in the flow equations. The governing equations take a similar form as the 1D Euler equations for single-phase compressible, inviscid flow, consisting of a mass conservation equation, a momentum balance equation and an energy balance equation:

$$\frac{\partial \rho}{\partial t} + \frac{\partial (\rho u)}{\partial x} = 0, \tag{3.2}$$

$$\frac{\partial (\rho u)}{\partial t} + \frac{\partial (\rho u^2 + p)}{\partial x} = \rho g_x - \mathcal{F}, \tag{3.3}$$

$$\frac{\partial E}{\partial t} + \frac{\partial ((E + p)u)}{\partial x} = \mathcal{Q}, \tag{3.4}$$

where a constant cross-sectional area is assumed for the pipe. Here, $\rho = \alpha_g \rho_g + \alpha_\ell \rho_\ell$ is the density of the liquid-vapor mixture, u is the

common velocity, p the common pressure and E is the total energy of the mixture.

$$E = \rho\left(e + \frac{1}{2}u^2\right), \tag{3.5}$$

where $e = (\alpha_g\rho_g e_g + \alpha_\ell\rho_\ell e_\ell)$ is the internal energy of the mixture and α_k denotes the volume fraction of phase $k \in g, \ell$. In the present set of equations the effect of gravity, friction and heat transfer from the pipe wall is also included. $\mathcal{F}$ is the pipe wall friction and $\mathcal{Q}$ is the heat transferred from the wall of the pipe to the fluid. g_x is the gravitational acceleration in the axial direction of the pipe. The modeling of these terms is discussed by Munkejord and Hammer [10], Munkejord et al. [32].

The eigenvalues of the HEM are:

$$\lambda_1 = u - c_{\text{HEM}}, \quad \lambda_2 = u, \quad \lambda_3 = u + c_{\text{HEM}}, \tag{3.6}$$

where c_{HEM} is the equilibrium mixture speed of sound,

$$c_{\text{HEM}} = \sqrt{\left(\frac{\partial p}{\partial \rho}\right)_s}, \tag{3.7}$$

and $s = (\alpha_g\rho_g s_g + \alpha_\ell\rho_\ell s_\ell)$ is the entropy of the two-phase mixture and s_k is the specific entropy of phase $k \in g, \ell$. The eigenvalues are the characteristic wave speeds which arise in the flow equations. The wave speeds λ_1 and λ_3 are associated with shock and rarefaction waves, and the wave speed $\lambda_2 = u$ is associated with a contact discontinuity. Theory on the types of waves that arise in the compressible Euler equations can be found in, e.g., [70, Chap. 3] and [134, Chap. 14]. During rapid depressurization of a pipe, a rarefaction wave will propagate into the pipe, while a shock and a contact discontinuity will exit the pipe.

If varying or discontinuous changes in cross-sectional area are to be taken into account in the HEM, the flow equations take the following

form:

$$\frac{\partial(\rho A)}{\partial t} + \frac{\partial(\rho u A)}{\partial x} = 0, \tag{3.8}$$

$$\frac{\partial(\rho u A)}{\partial t} + \frac{\partial((\rho u^2 + p)A)}{\partial x} = p\frac{\partial A}{\partial x} + \rho g_x - \mathcal{F}, \tag{3.9}$$

$$\frac{\partial(E A)}{\partial t} + \frac{\partial((E + p)u A)}{\partial x} = \mathcal{Q}. \tag{3.10}$$

Here, A is the cross-sectional area of the flow and $p\dfrac{\partial A}{\partial x}$ is a non-conservative term, which can be difficult to account for appropriately in numerical solution methods. In Paper 1, we propose a numerical solution method for this system of equations, based on the low-dissipation HLLC finite-volume method (FVM). Otherwise, flow equations for constant cross section are applied in this work, as the experimental work was done on a constant cross section pipe.

Though the HEM is able to predict many of the characteristics of compressible two-phase flow, the model is not able to reproduce the non-equilibrium effects observed for flashing flow in pipe depressurization experiments. In order to capture these non-equilibrium effects, models which allow for relaxation towards the equilibrium state are needed.

3.3 Hierarchy of homogeneous non-equilibrium flow models

The following two-phase models belong to the class of Baer and Nunziato [135] type multiphase compressible flow models. The original Baer and Nunziato [135] seven-equation model allows for full non-equilibrium of the phases, such that they have different flow velocities, pressures, temperatures and chemical potentials [85]. The hierarchy of homogeneous non-equilibrium flow models belong to a subset of models where an infinitely fast velocity relaxation between the phases is assumed [136]. By considering various infinitely-fast relaxation processes, increasingly simplified models are reached until the homogeneous equilibrium model is obtained.

As discussed by De Lorenzo [137], the relaxation processes towards equilibrium have different characteristic timescales. It has been found that the characteristic time scale for pressure relaxation tends to be shorter than for temperature relaxation, which again is shorter than for chemical potential relaxation [80, 138, 139]. The subset of models presented here are in agreement with the typical relaxation time-scales, i.e., that pressure relaxation occurs faster than thermal relaxation, and that thermal relaxation occurs faster than chemical potential relaxation. Note that in the governing equations presented below, the effect of friction, gravity and heat transfer from the pipe wall is not included for simplicity.

3.3.1 The six-equation model

The six-equation model is the most complete model of the homogeneous relaxation models considered here. The model allows for differences in pressure, temperature and chemical potentials of the phases. This means that there are no thermodynamic constraints on the phases (with the exception that they must be stable), and all interactions between the phases (mechanical work, heat transfer and mass transfer) must be modeled by constitutive relations. The governing equations are:

$$\frac{\partial \alpha_g}{\partial t} + u\frac{\partial \alpha_g}{\partial x} = \mathcal{I}, \tag{3.11}$$

$$\frac{\partial (\alpha_g \rho_g)}{\partial t} + \frac{\partial (\alpha_g \rho_g u)}{\partial x} = \Gamma, \tag{3.12}$$

$$\frac{\partial (\alpha_\ell \rho_\ell)}{\partial t} + \frac{\partial (\alpha_\ell \rho_\ell u)}{\partial x} = -\Gamma, \tag{3.13}$$

$$\frac{\partial (\rho u)}{\partial t} + \frac{\partial (\rho u^2 + \alpha_g p_g + \alpha_\ell p_\ell)}{\partial x} = 0, \tag{3.14}$$

$$\frac{\partial (\alpha_g E_g)}{\partial t} + \frac{\partial (\alpha_g (E_g + p) u)}{\partial x} + \Sigma = -p_{\text{int}}\mathcal{I} + \mathcal{H} + \left(h_{\text{int}} + \frac{1}{2}u^2\right)\Gamma \tag{3.15}$$

$$\frac{\partial (\alpha_\ell E_\ell)}{\partial t} + \frac{\partial (\alpha_\ell (E_\ell + p) u)}{\partial x} - \Sigma = p_{\text{int}}\mathcal{I} - \mathcal{H} - \left(h_{\text{int}} + \frac{1}{2}u^2\right)\Gamma, \tag{3.16}$$

where the non-conservative term Σ appearing in the energy balance equations is given by

$$\Sigma = -u\left(x_\ell \frac{\partial(\alpha_g p_g)}{\partial x} - x_g \frac{\partial(\alpha_\ell p_\ell)}{\partial x}\right). \tag{3.17}$$

$x_k = \alpha_k \rho_k / \rho$ denotes the mass fraction of phase k. $\mathcal{I}$, Γ and $\mathcal{H}$ denote the volume, mass and heat transfer between the phases, which must be modeled by constitutive relations. The subscript int denotes an interface property. h_{int} denotes the interface specific enthalpy.

The eigenvalues of the six-equation model are:

$$\lambda_1 = u - c_{6\text{eq}}, \quad \lambda_{2,3,4,5} = u, \quad \lambda_6 = u + c_{6\text{eq}}, \tag{3.18}$$

where the additional eigenvalues $\lambda_{3,4,5} = u$ compared to those of HEM are related to the additional discontinuities in pressure, temperature and mass fraction of the phases which propagate with the speed of the flow. The mixture speed of sound for the model assuming no volume, heat or mass transfer between the phases can be shown to be

$$c_{6\text{eq}} = \sqrt{x_g c_g^2 + x_\ell c_\ell^2}, \tag{3.19}$$

where c_g is the speed of sound in the pure vapor phase and c_ℓ is the speed of sound in the pure liquid phase [140].

Note that in some publications, h_{int} is replaced by μ_{int}, an interface chemical potential, in the energy balance equations [140, 141, 136, 85]. However, chemical potential cannot be transferred between phases as this is an intrinsic property of the phase. The choice of an interface enthalpy, as shown here, is in line with the flow equations as derived by Collier and Thome [142, Chap. 2.2].

Examples of publications where the six-equation model has been applied to model flashing flows include [82, 143, 144, 85]. The model has also recently been implemented in the EUROPLEXUS [93] software for the simulation of fast depressurizations in the context of nuclear reactor safety analysis [144].

3.3.2 The five-equation pressure-relaxed model

In line with the assumption that pressure relaxation is faster than thermal and chemical relaxation, the six-equation model can be reduced to the five-equation model by assuming an infinitely fast pressure-relaxation process [140, 141, 145]. For the five-equation model, the pressures of the liquid and vapor phases are assumed equal, but the temperatures and chemical potentials are still allowed to differ. This corresponds to the Kapila et al. [138] model.

The governing equations of the five-equation model are:

$$\frac{\partial \alpha_g}{\partial t} + u\frac{\partial \alpha_g}{\partial x} - \frac{\alpha_g \alpha_\ell}{D}\left(\rho_\ell c_\ell^2 - \rho_g c_g^2\right)\frac{\partial u}{\partial x} = \frac{\alpha_\ell \rho_g \gamma_g + \alpha_g \rho_\ell \gamma_\ell}{D}\mathcal{H} + \\ + \frac{\alpha_\ell \omega_{\mathrm{int},g} + \alpha_g \omega_{\mathrm{int},\ell}}{D}\Gamma, \quad (3.20)$$

$$\frac{\partial(\alpha_g \rho_g)}{\partial t} + \frac{\partial(\alpha_g \rho_g u)}{\partial x} = \Gamma, \quad (3.21)$$

$$\frac{\partial(\alpha_\ell \rho_\ell)}{\partial t} + \frac{\partial(\alpha_\ell \rho_\ell u)}{\partial x} = -\Gamma, \quad (3.22)$$

$$\frac{\partial(\rho u)}{\partial t} + \frac{\partial(\rho u^2 + p)}{\partial x} = 0, \quad (3.23)$$

$$\frac{\partial E}{\partial t} + \frac{\partial((E+p)u)}{\partial x} = 0, \quad (3.24)$$

where

$$D = \alpha_g \rho_\ell c_\ell^2 + \alpha_\ell \rho_g c_g^2 \quad (3.25)$$

and

$$\omega_{\mathrm{int},k} = \rho_k \gamma_k \left(h_{\mathrm{int}} - h_k\right) + c_k^2, \ k = g, \ell. \quad (3.26)$$

Here, γ_k denotes the Grüneisen coefficient for phase $k = g, \ell$, which is defined as

$$\gamma_k = \frac{1}{\rho_k}\left(\frac{\partial p_k}{\partial e_k}\right)_{\rho_k}. \quad (3.27)$$

The eigenvalues associated with the model are

$$\lambda_1 = u - c_{5\mathrm{eq}}, \quad \lambda_{2,3,4} = u, \quad \lambda_5 = u + c_{5\mathrm{eq}}, \quad (3.28)$$

where the additional eigenvalues $\lambda_{3,4} = u$ compared to those of HEM are related to the discontinuities of temperature and mass fraction of the phases which propagate with the speed of the flow. The mixture speed of sound for the model assuming no heat or mass transfer between the phases is given by the well-known Wood's speed of sound [140]

$$c_{5\text{eq}} = \left(\frac{\alpha_g}{\rho_g c_g} + \frac{\alpha_\ell}{\rho_\ell c_\ell} \right)^{-1}. \tag{3.29}$$

The five-equation model involves complicated non-conservative terms in the volume fraction transport equation, which may be difficult to discretize and solve numerically. Instead of discretizing these terms, one may apply the six-equation model and enforce infinitely fast pressure relaxation in the numerical solution approach. This approach is adopted by, e.g., De Lorenzo et al. [144] and Pelanti [85].

3.3.3 The four-equation pressure- and temperature-relaxed model

In the limit of instantaneous thermal relaxation, the five-equation model reduces to the four-equation pressure and temperature relaxed model. Here, both the pressures and temperatures of the phases are assumed to be equal, but a chemical potential difference is allowed. Therefore, only the mass-transfer must be estimated by a constitutive relation. The governing equations of the four-equation model are:

$$\frac{\partial(\alpha_g \rho_g)}{\partial t} + \frac{\partial(\alpha_g \rho_g u)}{\partial x} = \Gamma, \tag{3.30}$$

$$\frac{\partial(\alpha_\ell \rho_\ell)}{\partial t} + \frac{\partial(\alpha_\ell \rho_\ell u)}{\partial x} = -\Gamma, \tag{3.31}$$

$$\frac{\partial(\rho u)}{\partial t} + \frac{\partial(\rho u^2 + p)}{\partial x} = 0, \tag{3.32}$$

$$\frac{\partial E}{\partial t} + \frac{\partial((E + p)u)}{\partial x} = 0. \tag{3.33}$$

The eigenvalues associated with the four-equation model are

$$\lambda_1 = u - c_{4\text{eq}}, \quad \lambda_{2,3} = u, \quad \lambda_5 = u + c_{4\text{eq}}, \tag{3.34}$$

where the additional eigenvalue $\lambda_3 = u$ compared to those of HEM is related to the discontinuity of mass fraction of the phases which propagates with the speed of the flow. The mixture speed of sound for the model assuming no mass transfer between the phases can be shown to be [141, Eq. 6.6]:

$$c_{4eq} = \left[\rho \left(\frac{\alpha_g}{\rho_g c_g^2} + \frac{\alpha_\ell}{\rho_\ell c_\ell^2} + T \frac{\tilde{C}_{p,g} \tilde{C}_{p,\ell}}{\tilde{C}_{p,g} + \tilde{C}_{p,\ell}} \left(\frac{\gamma_g}{\rho_g c_g^2} - \frac{\gamma_\ell}{\rho_\ell c_\ell^2} \right)^2 \right) \right]^{-1/2}, \tag{3.35}$$

where $\tilde{C}_{p,k}$ is the extensive heat capacity

$$\tilde{C}_{p,k} = \alpha_k \rho_k C_{p,k}, \tag{3.36}$$

and $C_{p,k}$ is the specific heat capacity of phase k. Note that if instantaneous mass-transfer relaxation is assumed for the four-equation model, the governing equations of the HEM are retained [140].

The four-equation model has no non-conservative terms, which simplifies the solution approach with numerical methods. It is the simplest model in the hierarchy of homogeneous non-equilibrium flow models which can reproduce the effect of the liquid phase becoming superheated before flashing begins during a rapid depressurization event. Due to these advantages, this model was applied in Papers 5 and 6 to model non-equilibrium flashing flow. A main focus has been on determining an appropriate mass-transfer rate.

Typical models that are applied to estimate the mass-transfer rate are presented in Section 3.5, and theory on the kinetics of liquid-to-vapor phase change in Chapter 4. Note that in Paper 5, the four-equation pressure and temperature relaxed model is denoted as the simplified homogeneous relaxation model and in Paper 6, we denote the model the homogeneous chemical-potential relaxation model. In both cases, the acronym HRM* is applied. This notation was used due to the similarity of the model to the homogeneous relaxation model, HRM, which is discussed in Section 3.4.1.

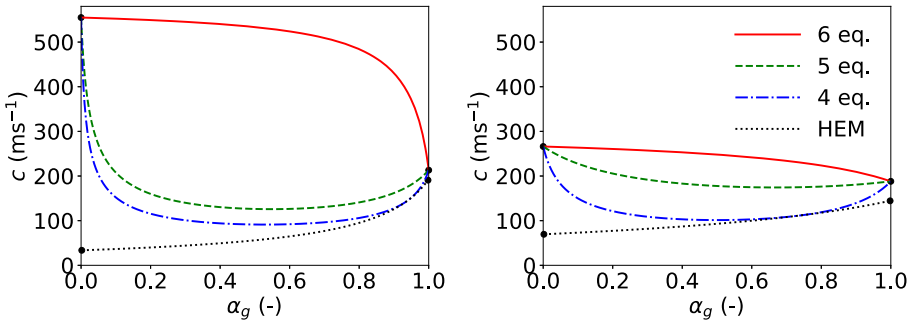

(a) $T = -2\,°\mathrm{C}$ (b) $T = 25.6\,°\mathrm{C}$

Figure 3.2: The variation of the speed of sound with the volume fraction of gas at the saturation line for $T = -2\,°\mathrm{C}$ (a) and $T = 25.6\,°\mathrm{C}$ (b), calculated using the Span and Wagner [146] EOS.

A note on the four-equation model's physical description of non-equilibrium As only chemical non-equilibrium is allowed in this model, the liquid and gas are treated as two different chemical components in a mixture at equal temperature and pressure. With this assumption, a metastable liquid that transitions to the gas phase will become superheated gas (gas at a temperature above the saturation temperature). As more gas forms and brings the two-phase mixture towards equilibrium, its chemical potential will increase, not decrease, i.e., the gas will reach a *less* favorable thermodynamic state. This is unusual, and is considered a limitation of the model. The same issue also arises for the four-equation model in the case of a metastable gas condensing to the liquid phase.

For the case of flashing, it is considered more physically consistent that the metastable liquid will transition to a *saturated* gas. The most common assumption applied for the formation of saturated gas in two-phase flow models, is that the gas phase will be at the saturation temperature at the pressure of the liquid phase. Two models applying this assumption are described in Section 3.4, and may be applied in future works.

3.3.4 Speed of sound in the models

As shown by Flåtten and Lund [140], the models in the hierarchy of homogeneous non-equilibrium flow models follow the subcharacteristic condition. This means that the models allowing for more non-equilibrium obtain a higher speed of sound:

$$c_{\text{HEM}} \leq c_{4\text{eq}} \leq c_{5\text{eq}} \leq c_{6\text{eq}} \tag{3.37}$$

In Figure 3.2, the variation of the speed of sound predicted by the models for a saturated liquid-vapor mixture of CO_2 is shown for a cold temperature, $T = -2\,^{\circ}\text{C}$, and a warm temperature, $T = 25.6\,^{\circ}\text{C}$. Note that the speed of sound of HEM is discontinuous, which is illustrated by the markers in the figure. This is considered unphysical. Experimental measurements of the speed of sound for two-phase flows agree with the qualitative shapes of the four-equation and five-equation models, see, e.g., Brennen [147, Figure 9.2]. Note that at colder temperatures, the decrease in the speed of sound during the transition from single-phase liquid flow to two-phase liquid-vapor flow is generally much stronger. As the pressure evolution during a depressurization is connected to the speed of sound in the fluid, accurately predicting the point where two-phase flow begins is key to obtain accurate pressure predictions.

3.4 Other relevant models

In this section, two other relevant models are mentioned which may be considered for further work in modeling the rapid depressurization in pipes. These models account for a temperature difference between the vapor phase and the metastable liquid phase.

3.4.1 The homogeneous relaxation model

The homogeneous relaxation model (HRM) of Bilicki and Kestin [79][148, 81] is very similar to the four-equation model. The governing equations are the same as for the four-equation model, (3.30)-(3.33), with the mass transfer rate modeled as

$$\Gamma = \rho \frac{x_{g,\text{sat}} - x_g}{\theta}. \tag{3.38}$$

Here, θ is a relaxation time related to the delay in the phase change process. A larger θ provides a slower phase change process, allowing for more superheating of the liquid phase. Correlations for θ have been suggested by Downar-Zapolski et al. [81] for water, based on a large set of experimental data, and Angielczyk et al. [149] for CO_2 based on the experimental data of Nakagawa et al. [150]. The key difference between the HRM and the four-equation model is in the thermodynamic assumptions. In the HRM, the following assumptions are made:

$$p_g = p_\ell = p, \tag{3.39}$$

$$T_g = T_{\text{sat}}(p) \neq T_\ell. \tag{3.40}$$

Thus, the HRM enforces a temperature difference between the phases by forcing the vapor to be at the saturation state corresponding to the common pressure of the phases.

As the flow equations of HRM are the same as for the four-equation model, the model has the same advantages which motivated the application of the four-equation model in the present work. The main reason for the HRM not being tested in the present work is that its thermodynamic assumptions are not in agreement with homogeneous bubble nucleation theory. For homogeneous bubble nucleation, it is assumed that the bubbles form at the following conditions:

$$p_g \approx p_{\text{sat}}(T_\ell) \neq p_\ell, \tag{3.41}$$

$$T_g = T_\ell. \tag{3.42}$$

The four-equation model does not agree with these conditions either, but it is consistent with the temperature equality of the phases.

Though the HRM was not applied in the present work, we note that as the bubbles expand and cool, a temperature non-equilibrium between the liquid and gas similar to that enforced by the HRM is likely established. Furthermore, there is experimental data in support of the assumptions of the HRM, see, e.g., [86], and the model has been applied successfully by several authors to model non-equilibrium effects in flow experiments [81, 83, 151]. It would therefore be natural to apply the HRM and other similar models in further work.

It would be interesting to test the HRM with a different model for the mass-transfer rate, which takes into account bubble nucleation and growth. It could also be interesting to investigate if the six-equation model applied with physics-based terms modeling the mechanical, thermal and chemical relaxation of the phases will reproduce the conditions assumed by the HRM, i.e., that the vapor phase will equilibrate to the saturation temperature at the given pressure.

3.4.2 The delayed equilibrium model

The delayed equilibrium model (DEM) is a flow model specifically made for the prediction of critical, steady flow. It is mentioned here due to its interesting assumptions on the thermodynamic relations between the phases in the flow. As described by De Lorenzo et al. [34], the DEM stems from Lackme [152]'s idea of describing critical flow as composed by three phases: saturated liquid, saturated vapor and metastable liquid. Thus, it is assumed that there will be a two-phase mixture in thermal equilibrium similar to the assumptions of the HEM, but metastable liquid will also be present.

The assumption of three phases in the flow is inspired by the experimental results of Barois [153]. Barois [153] found that local temperature measurements of adiabatic upward flow of water in a duct of uniform cross section oscillated between the stagnation temperature T_0 and the local saturation temperature $T_{\text{sat}}(p)$. To the authors knowledge, the model was first proposed by Feburie et al. [154] for the modelling of choked flow through cracks in steam generators. The model was later revisited by Bartosiewicz et al. [155] and was found to be a good candidate for simulating loss of coolant accidents (LOCA) in nuclear power plants.

The governing equations of the model can be written in the following

form for transient flow in a pipe with constant cross-sectional area:

$$\frac{\partial(\alpha_{\ell,m}\rho_{\ell,m})}{\partial t} + \frac{\partial(\alpha_{\ell,m}\rho_{\ell,m}u)}{\partial x} = \Gamma_{\ell,m}, \tag{3.43}$$

$$\frac{\partial \rho}{\partial t} + \frac{\partial(\rho u)}{\partial x} = 0, \tag{3.44}$$

$$\frac{\partial(\rho u)}{\partial t} + \frac{\partial(\rho u^2 + p)}{\partial x} = 0, \tag{3.45}$$

$$\frac{\partial E}{\partial t} + \frac{\partial((E+p)u)}{\partial x} = 0, \tag{3.46}$$

where the subscript ℓ, m denotes the metastable liquid phase and $\Gamma_{\ell,m}$ denotes the mass transfer rate from the metastable liquid phase to the stable liquid-vapor mixture. To the author's knowledge, the model has not yet been applied to model transient flow.

For the prediction of critical, steady flow in a nozzle, Bartosiewicz and Seynhaeve [156, 157] proposed to model the evolution of the saturated mass fraction, y, as

$$\frac{\mathrm{d}y}{\mathrm{d}x} = \left(C_1 \frac{P_x}{A_x} + C_2\right) \cdot (1-y) \left[\frac{p_{\mathrm{sat}}(T_{\ell,m}) - p}{p_{\mathrm{crit}} - p_{\mathrm{sat}}(T_{\ell,m})}\right]^{C_3}, \tag{3.47}$$

along the channel. Here, P_x is the perimeter of the channel and A_x is the cross-sectional area of the channel. The two relaxation constants C_1 and C_2 are meant to model the contributions of heterogeneous bubble nucleation at the wall and homogeneous nucleation in the bulk of the liquid. The mass-transfer correlation has been fitted to data for critical water flow tests [156, 158]. Angielczyk et al. [159] found that this correlation did not work well for the simulation of CO_2 flow through nozzles when fitting and testing the model for the data of Nakagawa et al. [150]. Angielczyk et al. [160] later proposed the following correlation for the mass-transfer along the channel to fit the data:

$$\frac{\mathrm{d}y}{\mathrm{d}x} = \left[C_1 + C_2 \exp\left(C_3 \frac{\left(\frac{\mathrm{d}A}{\mathrm{d}x}\right)_{\mathrm{div}} - \left(\frac{\mathrm{d}A}{\mathrm{d}x}\right)_{\mathrm{conv}}}{\left(\frac{\mathrm{d}A}{\mathrm{d}x}\right)_{\mathrm{ref}} - \left(\frac{\mathrm{d}A}{\mathrm{d}x}\right)_{\mathrm{conv}}}\right)\right] \cdot (1-y) \left[\frac{p_{\mathrm{sat}}(T_{\ell,m}) - p}{p_{\mathrm{crit}} - p_{\mathrm{sat}}(T_{\ell,m})}\right]^{C_4}, \tag{3.48}$$

where the correlation strongly depends on the nozzle convergence and divergence rates. Similarly to the HRM, it could be interesting to test the DEM with different mass-transfer relations accounting for the nucleation and growth of bubbles in further works.

3.5 Typical mass-transfer correlations

In the flow models where delayed phase change is allowed, i.e., non-instantaneous mass-transfer, the mass-transfer rate from liquid to vapor (Γ) must be modeled. The most common mass-transfer rate models consist of some relaxation parameter multiplied by a measure of the degree of non-equilibrium:

- $\Gamma = K \cdot (\mu_\ell - \mu_g)$ [99, 101, 82, 136, 85]
- $\Gamma = \theta^{-1} \cdot \rho \, (x_{g,\mathrm{sat}} - x_g)$ [79, 81, 149, 35]
- $\Gamma = C \cdot \alpha_\ell \rho_\ell \dfrac{T - T_{\mathrm{sat}}}{T_{\mathrm{sat}}}$ [161, 162, 163, 164]
- $\Gamma = C \cdot \alpha_\ell \rho_\ell \dfrac{p - p_{\mathrm{sat}}}{p_{\mathrm{sat}}}$ [37, 38, 39, 40, 165]

In Paper 6, such mass-transfer correlations are denoted HRM-type mass-transfer models. The correlations for the DEM are also of a similar type, though they take into account two different relaxation parameters for the two different bubble nucleation phenomena (homogeneous and heterogeneous) [156, 160]. The relaxation parameter is either taken to be constant, see, e.g., [163, 37, 38, 39, 40, 165] or a correlation is applied to model it, see, e.g., [81, 149, 85].

The HRM-type mass-transfer rate models are phenomenological, and may not capture all the relevant physical effects. Though much data is available for water flows to fit the correlations, little data is available for CO_2. The CO_2 nozzle flow data of Nakagawa et al. [150] used to fit the correlations of Angielczyk et al. [149, 159] is limited to three depressurization paths passing close to the critical point. Thus, the range of validity for the correlations is likely narrow. Furthermore, for flow systems where the effect of homogeneous and heterogeneous nucleation is different than

those recorded in the experiments, the correlations will most likely not be able to predict the resulting mass-transfer rates.

In the context of CCS, CO_2-transport pipelines will likely contain several impurities from the CO_2 capture process. Even if more data is made available to fit the correlations for pure CO_2 over a range of initial pressures and temperatures, there is no guarantee that the same correlations will fit for the various CO_2-rich mixtures that will be encountered in CCS pipelines. A main focus of the present thesis has therefore been to investigate physics-based mass-transfer models, accounting for the nucleation and growth of bubbles, with the goal of developing a flashing flow model that is fully predictive. The result of this investigation is presented in Paper 6, and relevant background theory on the kinetics of phase change is provided in Chapter 4.

4 Kinetics of liquid-vapor phase change

The mass transfer rate during flashing can be modeled as the sum of contributions from homogeneous and heterogeneous bubble nucleation and the growth of bubbles due to evaporation:

$$\Gamma = \Gamma_{\text{hom}} + \Gamma_{\text{het}} + \Gamma_{\text{evap}}. \tag{4.1}$$

In this chapter, details on the modeling of bubble nucleation and growth are provided. A particular focus is put on heterogeneous nucleation and bubble growth. It is shown how modeling heterogeneous nucleation based on classical nucleation theory cannot explain experimental observations of the attainable superheat, with the aim of preventing others from following this approach. The alternative *crevice model* combined with bubble growth can explain the experimentally observed effects.

4.1 Homogeneous bubble nucleation

Homogeneous nucleation describes the formation of embryos of a new phase within a mother phase through random thermal fluctuations. Classical nucleation theory (CNT) provides a formal estimate on the nucleation rate of critically-sized embryos of a new phase in the mother phase through random density fluctuations. Here, "critically-sized" refers to the size where the embryo is just large enough not to collapse back to the mother phase. The derivation of this rate is thoroughly presented by Debenedetti [108], and are further stated in several of the papers related to this thesis (Conference paper, Paper 2, Paper 3, Paper 5 and Paper 6). The modified equations for mixtures are presented in the appendix of Paper 3. Here, the equations for pure fluids are stated.

The nucleation rate (critically-sized embryos formed per volume and

time) is defined as an Arrhenius-type rate law,

$$J_{\text{hom}} = K \exp\left\{\left(-\frac{\Delta G^*}{k_{\text{B}} T_\ell}\right)\right\}, \tag{4.2}$$

where ΔG is the free-energy barrier of embryo formation, k_{B} is the Boltzmann constant and K is a kinetic prefactor. The superscript $*$ denotes properties of a critically-sized embryo. For the formation of bubbles in a superheated liquid, the free-energy barrier is estimated to be

$$\Delta G^* = \frac{4\pi\sigma r^{*2}}{3}, \tag{4.3}$$

where σ denotes the surface tension and r the radius of the bubble. It is assumed that the surface tension of the bubble, σ, is equal to the macroscopic surface tension of a planar interface between the liquid and vapor at equilibrium [166], sometimes referred to as the capillarity approximation. The radius of the bubbles and the kinetic prefactor can be estimated as

$$r^* = \frac{2\sigma}{p_{\text{sat}}(T_\ell) - p_\ell}, \tag{4.4}$$

and

$$K = \tilde{\rho}_\ell \sqrt{\frac{2\sigma}{\pi m}}, \tag{4.5}$$

where $p_{\text{sat}}(T_\ell)$ is the saturation pressure at the temperature of the liquid, m is the mass of one molecule and $\tilde{\rho}_\ell = \rho_\ell / m$ is the number density of molecules in the liquid.

CNT assumes that the bubbles are at the same temperature as the liquid phase, and with a pressure approximately equal to the saturation pressure. The mass transfer rate from liquid to vapor due to homogeneous bubble nucleation is then:

$$\Gamma_{\text{hom}} = \rho_{g,\text{sat}}(T_\ell) V_{\text{bub}} J_{\text{hom}}, \tag{4.6}$$

where the volume of a critically-sized bubble is

$$V_{\text{bub}} = \frac{4}{3}\pi r^{*3}. \tag{4.7}$$

In many of the related papers for this work, the homogeneous superheat limit (SHL) is estimated. It is assumed that the SHL is reached for a certain bubble nucleation rate $J_{\text{hom, SHL}}(T) = J_{\text{crit}}$. Aursand et al. [167] found that the critical nucleation rate could be taken to be $J_{\text{crit}} = 10^{12}$ bubbles $\text{m}^{-3}\,\text{s}^{-1}$ for CO_2. Wilhelmsen and Aasen [117] chose the critical nucleation rate as $J_{\text{crit}} = 10^{14}$ bubbles $\text{m}^{-3}\,\text{s}^{-1}$. Due to the exponential form of the nucleation rate (4.2), the SHL is not very sensitive to the choice of critical rate. A heat map of the homogeneous nucleation rate is shown in Chapter 6.4, Figure 6.6, with approximate estimates of the maximum superheat reached in the experiments of the present work.

Finally, note that CNT does not account for the spinodal in its estimates. The energy barrier for nucleation only vanishes at the critical point. In reality, the energy barrier should also vanish at the spinodal where spontaneous phase change would occur. Nevertheless, CNT predicts so high nucleation rates near the spinodal that this inconsistency holds no practical effects for the present application.

4.2 Heterogeneous bubble nucleation

Heterogeneous nucleation refers to the formation of an embryo of a new phase within the mother phase helped by a surface such as an impurity or a wall. In the following, the model of heterogeneous nucleation based on classical nucleation theory is presented, and it is shown how the model cannot explain experimental observations of the SHL at low reduced pressures and temperatures. The author considers the crevice model much more promising in the modeling of heterogeneous nucleation.

4.2.1 Model based on classical nucleation theory

Heterogeneous nucleation can be modeled similarly to homogeneous nucleation where the energy barrier required to form a critically-sized bubble is multiplied by a reduction factor, $\phi \in (0, 1)$, and the kinetic prefactor K is modified. Classical models calculate the reduction factor and kinetic prefactor based on geometric considerations for a bubble forming on a surface. For the nucleation of a bubble on an ideally flat surface, the

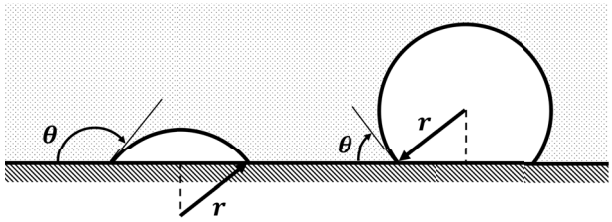

Figure 4.1: Illustration of the contact/wetting angle θ under poorly wetting (left) and highly-wetting (right) conditions, redrawn based on Figure 3.27 in [108].

reduction factor ϕ takes the form [108]:

$$\phi(\theta) = \frac{(1+\cos(\theta))^2(2-\cos(\theta))}{4} \tag{4.8}$$

where θ is the wetting angle of the liquid phase as illustrated in Figure 4.1, and K becomes:

$$K = \tilde{\rho_\ell}^{2/3} a \sqrt{\frac{2\sigma}{\pi m(2-\cos(\theta))}}, \tag{4.9}$$

where a is the surface available for heterogeneous nucleation per bulk volume of the liquid. For a cylindrical pipe, $a = \frac{2}{r}$. As shown by the measurements of [168], liquid CO_2 on stainless steel is found to be highly wetting. The reduction factor for this case is therefore quite small. For the nucleation of a bubble in a conical cavity, the reduction factor becomes [169]:

$$\phi(\theta,\beta) = \frac{2 - 2\sin(\theta-\beta) + \cos(\theta)\cos(\theta-\beta)^2/\sin(\beta)}{4}, \tag{4.10}$$

where β denotes the cone's semi-vertex angle as illustrated in Figure 4.2, and

$$K = \tilde{\rho_\ell}^{2/3} a \frac{1-\sin(\theta-\beta)}{2} \sqrt{\frac{2\sigma}{\pi m \phi(\theta,\beta)}}. \tag{4.11}$$

We show the estimated superheat limit for the cases of nucleation on an ideally flat surface and in a conical cavity for different wetting angles in

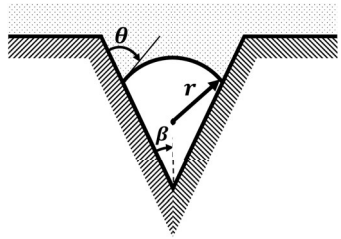

Figure 4.2: Definition of the geometric parameters for the conical cavity model.

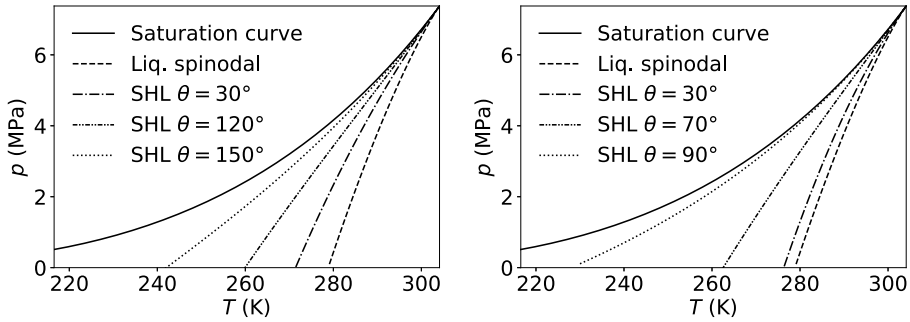

(a) Ideally flat surface.

(b) Conical cavities with $\beta = 5°$.

Figure 4.3: Superheat limits for heterogeneous nucleation on ideally flat surface (a) and conical cavities (b) for different contact/wetting angles.

Figures 4.3. Here, we assume that nucleation takes place in a cylindrical pipe with radius $r = 2\,\mathrm{cm}$. Note that there is no wetting angle in these models that can reproduce the qualitative trend in the maximum attained superheat that are observed in experiments, cf. Section 2.2.

In order to make this model reproduce experimental observations, the reduction factor ϕ is usually fitted to experimental data directly. Banasiak and Hafner [170] applied the delayed equilibrium model, incorporating homogeneous and heterogeneous nucleation with the reduction factor fitted to experimental data to model the critical flow of CO_2 through an ejector. They found that the reduction factor varied from $\phi = 0.03$

to 0.3 for their data in a region of high relative temperatures. Alamgir and Lienhard [18] found good agreement for water depressurization tests with a reduction factor varying from $\phi = 2 \cdot 10^{-7}$ to $\phi = 0.055$, going from lower initial relative temperature to higher initial relative temperatures and varying depressurization rates. They also found a dependence of the reduction factor on the depressurization rate, where slower depressurizations lead to less superheating. Barták [19] found a similar dependency for their tests. Elias and Chambré [22] estimated the maximum limit of superheat at the flashing inception for a series of water flashing experiments and found a reduction factor as low as $\phi = 10^{-8}$ for low reduced temperatures. Wilhelmsen and Aasen [117] obtained similar results when fitting the reduction factor for experiments with critical flow of water through nozzles and found that the factor varied from roughly 10^{-6} to 1 for depressurizations near the triple point to depressurizations near the critical point.

The observed relation between the fluid temperature and the reduction factor found by Elias and Chambré [22] and Wilhelmsen and Aasen [117] is shown in Figure 4.4 and Figure 4.5, respectively. There is no clear reason why bubble nucleation should become more than a million times easier than what is predicted theoretically for depressurizations at low relative temperatures. Thus, the author argues that the present model does not capture the relevant physical effects of heterogeneous nucleation in real (non-ideal) systems.

4.2.2 Crevice model/wall nucleation

The current prevailing theory explaining the observed phenomena for heterogeneous nucleation is the "crevice" model. In the crevice model, it is assumed that there exist several crevices on the surface of the container or on suspended impurities in the bulk of the liquid which are not fully wetted, and which may serve as nucleation sites for bubbles during boiling [171, 172, 173, 142, 174]. In flashing flow models, this is sometimes referred to as wall nucleation [88, 89, 175, 20]. In this model, the nucleation process is not driven by random density fluctuations, but by trapped, pre-existing bubbles providing a surface for the liquid to evaporate into. A certain threshold superheat must be reached to allow the trapped bubble

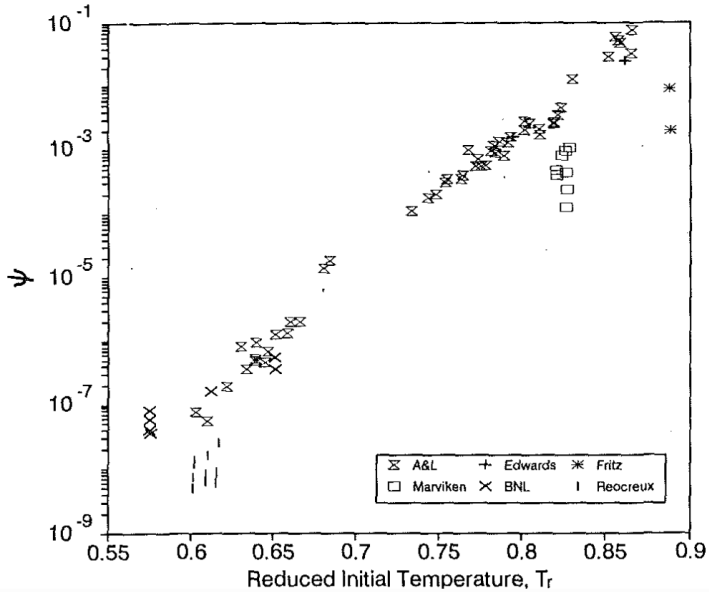

Figure 4.4: The heterogeneous reduction factor, here denoted as ψ, plotted against the reduced initial temperature for a series of flashing flow experiments compiled by Elias and Chambré [22]. Reprinted from [22] with the permission of the original publisher, ASME.

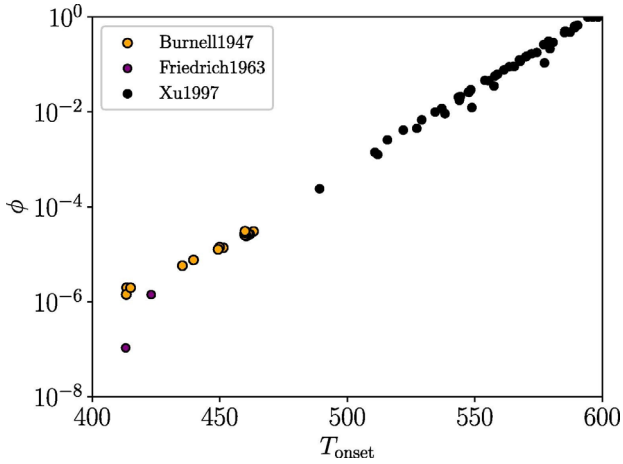

Figure 4.5: The heterogeneous reduction factor for the critical water flow experiments of Burnell [119], Friedrich and Vetter [120] and Xu et al. [118] plotted against the nucleation onset temperature estimated by Wilhelmsen and Aasen [117]. Reprinted from [117] in Elsevier under an open access license.

to keep growing after it has reached the lip of the crevice (though this superheat is generally quite low, on the order of a few Kelvin). When the required superheat is reached, the crevice is referred to as an *activated* nucleation site. The underlying phenomena of this process are well explained by Collier and Thome [142, Chap. 4.3].

For the present application concerning CO_2 transportation in pipes, it is important to note that it is possible for crevices to remain non-wetted at the relevant operation conditions at supercritical pressures – providing nucleation sites once depressurization occurs. As shown in Figure 1.1, the operating region for pipeline transport of CO_2 is outside the spinodal limit for the vapor/gaseous phase. One would therefore expect the vapor to spontaneously condense to the liquid phase. However, the interface at the crevice can be concave such that the vapor pressure is lower than the static liquid pressure, as shown in Figure 4.6. For a low enough pressure, the vapor remains stable and the nucleation sites are preserved.

The number of active nucleation sites depend on the population density

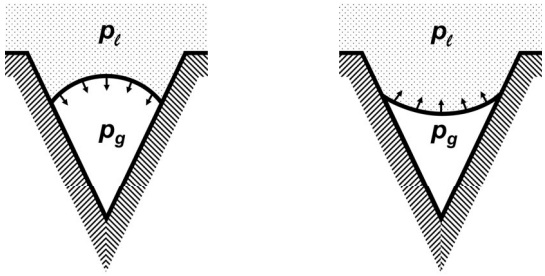

(a) $p_\ell < p_g$ (b) $p_\ell > p_g$

Figure 4.6: Illustration of a non-wetted crevice with a convex interface (a) and a concave interface (b) with the surrounding liquid.

and radii of nucleation sites, and the local superheat. Many correlations have been derived, trying to predict the number of active nucleation sites at the wall or in the bulk of the fluid [176, 177, 88, 89, 178, 20]. Clearly, to estimate the number of microscopic cracks that might trap vapor, and their distribution of radii, requires an array of assumptions and correlations to be made. It is unlikely that these assumptions and correlations should be general for different surface materials and fluids. Most correlations describing wall nucleation are specifically tuned for the application on boiling water, e.g. [177, 175, 88, 89, 178].

As the flow is approximately isentropic for a rapid depressurization event, a small decrease in pressure can lead to a large increase in the system's superheat. Assuming that an array of crevices of various sizes and geometries are available on the containing wall's surface (as one might expect on a non-ideal, real surface), it is reasonable to assume that a large number of nucleation sites will then be activated. In that case, it is possible that the activation of nucleation sites is not the determining factor of the attainable limit of superheat for flashing, but rather how fast the liquid is able to evaporate into the activated sites. If this is the case, it would explain the dependency of the attained superheat on the depressurization rate, as observed by Lienhard et al. [17], Barták [19] and Elias and Chambré [22] – a slower depressurization rate provides more time for the liquid to evaporate into activated nucleation sites, increasing the

pressure and limiting the attained superheat. Indeed, the link between bubble growth due to mass transfer and expansion, and the attainable superheat in flashing flows has already been suggested by Körner and Friedel [179], though this paper has received little attention.

For simplicity it was assumed in Paper 6 that a number of nucleation sites would activate under superheat and contribute to the phase change process by transferring a constant rate of liquid to the vapor phase (K_m), and providing a constant rate of bubble creation (K_b):

$$\Gamma_{\text{het}} = K_{\text{m}},\ J_{\text{het}} = K_{\text{b}}. \tag{4.12}$$

4.3 Bubble growth/evaporation into bubbles

Many models for bubble growth, here meaning mass-transfer into the bubble by evaporation, are described in the reviews of Pinhasi et al. [78] and Liao and Lucas [20]. The most common approach in the literature of modeling bubble growth, is based on the assumption that the evaporation is driven by heat transfer [20, Sec. 2.4.3]. The mass transfer due to evaporation is then:

$$\frac{\Gamma_{\text{evap}}}{a_{\text{int}}} = \frac{q_{\text{int}}}{L}, \tag{4.13}$$

where a_{int} is the interfacial area density between the phases, q_{int} is the heat transfer to the interface and L is the latent heat. The heat transfer is typically modeled as

$$q_{\text{int}} = h_{\text{tc}}^{\ell}(T_\ell - T_{\text{sat}}(p_\ell)), \tag{4.14}$$

where it is assumed that the heat transfer from the vapor to the interface is negligible compared to that of the liquid phase, and that the interface is always at the saturation condition at the local pressure. Here, h_{tc} is the heat transfer coefficient between the surrounding liquid and the interface. This model is not consistent with the assumptions of the four-equation two-phase flow model, but it can be tested for models allowing a temperature difference between the phases, such as HRM, DEM, the five-equation model and the six-equation model.

As the four-equation model only allows for a chemical non-equilibrium between the phases, bubble growth models applied with this flow model must be based on the assumption that evaporation is driven by a chemical potential difference. One such model, which is based on statistical rate theory, is proposed by Lund and Aursand [180]. The evaporation flux is estimated to be:

$$\frac{\Gamma_{\text{evap}}}{a_{\text{int}}} = \rho_g \sqrt{\frac{k_{\text{B}} T}{2\pi m}} \left(\exp\left[m \frac{\mu_\ell - \mu_g}{k_{\text{B}} T} \right] - \exp\left[m \frac{\mu_g - \mu_\ell}{k_{\text{B}} T} \right] \right). \tag{4.15}$$

This model was not tested in the present work, but can be interesting to explore in the future.

Another evaporation model depending on the chemical potential difference is described by Kjelstrup and Bedeaux [181, Chap. 11] based on linear non-equilibrium thermodynamics and kinetic theory. This model was applied in Paper 6. Here, the evaporation or condensation flux is estimated as

$$\frac{\Gamma_{\text{evap}}}{a_{\text{int}}} = \frac{1}{R^{s,\ell}_{\mu\mu} + R^{s,g}_{\mu\mu}} \frac{\mu_\ell - \mu_g}{T}, \tag{4.16}$$

where $R^{s,\ell}_{\mu\mu}$ is the resistivity of mass transfer between the surface and the liquid and $R^{s,g}_{\mu\mu}$ is the resistivity of mass transfer between the surface and the gas phase. Applying simplifying assumptions and the kinetic theory of gases, the sum of the resistivities can be approximated as [181]

$$R^{s,\ell}_{\mu\mu} + R^{s,v}_{\mu\mu} = \frac{2k_B}{u_{\text{mp}}(T^s)\rho_g^{\text{sat}}(T^s)m} \left(\alpha^{-1} + \frac{1}{5\pi} - \frac{31}{32} \right), \tag{4.17}$$

where T^s is the temperature of the interface, $u_{\text{mp}}(T^s) = \sqrt{2k_B T^s/\pi m}$ is the most probable thermal velocity, $\rho_v^{\text{sat}}(T^s)$ is the density of saturated vapor at the surface between liquid and vapor and $\alpha \in [0, 1]$ is the condensation coefficient approximating the fraction of incident particles which are absorbed by the liquid surface after collision. For the four-equation model it is reasonable to assume that $T^s = T$. In Paper 6, α was set to 0.5, i.e., it was assumed that half of the incident particles were absorbed by the liquid surface. Note that Kjelstrup and Bedeaux [181, Fig. 11.6] show with molecular dynamics simulations for a Lennard-Jones fluid that

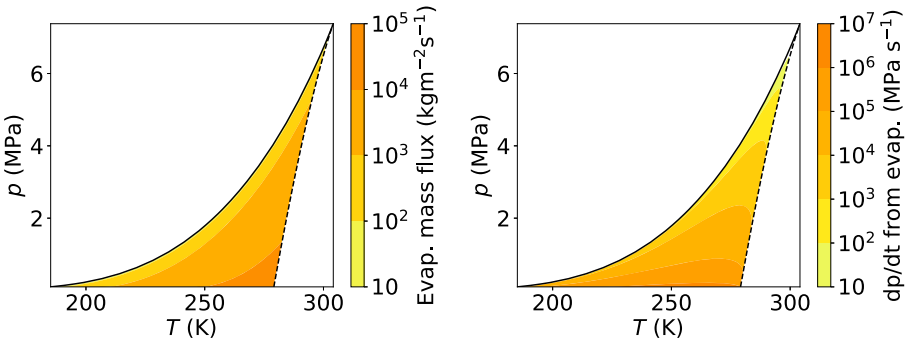

(a) Estimated evaporation mass flux through a liquid-vapor interface based on Equation (4.16).

(b) Rate of change in pressure for a closed volume with the mass flux in Fig (a), for $T_\ell = T_g$ and $p_\ell = p_g$.

Figure 4.7: Calculated evaporation mass flux (a) and the resulting rate of change in pressure in a closed system (b) shown in the CO_2 phase diagram.

the condensation coefficient varies from the triple point to halfway from the critical point from around 0.35 to 0.9.

An interesting observation was made in Paper 6 regarding the rate of change in the pressure of a closed system due to bubble growth in different regions of the phase diagram. In Figure 4.7a, the mass flux predicted by Equation (4.16) is shown in the phase diagram. For a closed system with a volume of $1\,\mathrm{m}^3$, an interface area of $1\,\mathrm{m}^2$ and the thermodynamic constraints of the four-equation model ($T_\ell = T_g$, $p_\ell = p_g$), the resulting rate of change of pressure caused by the evaporation mass flux is illustrated in Figure 4.7b.

The qualitative shape of the isocurves for the rate of change of pressure agree surprisingly well with that of the heterogeneous superheat limit observed in experiments. The rate of increase in pressure caused by evaporation at low relative pressure and temperatures is very high. This is related to the specific volume of the vapor phase increasing and the compressibility of the liquid phase decreasing at low relative temperatures and pressure. The strong "re-pressurization" due to bubble growth at

activated nucleation sites could explain why so small pressure undershoots and superheats are reached for flashing at low reduced temperatures and pressures. Provided that a range of active nucleation sites are available, bubbles growing and being released at these sites increase the pressure, limiting the attained superheat of the liquid phase. This occurs much faster at lower reduced temperatures than higher ones, so the superheat limit becomes smaller.

With the combination of the crevice model and bubble growth, the experimentally observed effects of the attainable superheat during flashing can be explained: both the dependence on depressurization rate and the low superheats reached at low reduced temperatures. Further research would be needed to investigate if the superheat limit can be predicted based on bubble growth models and the assumption that an ample amount of nucleation sites will be activated during flashing.

4.4 Interfacial area density

The bubble growth due to evaporation depends on the interfacial area density, a_{int}. It is therefore necessary to determine the interfacial area density in the flow. This can be done by including an additional transport equation in the two-phase flow model which relates to the geometry of the flow such as a bubble transport equation or a direct transport equation for the interfacial area density. In Paper 6, both of these are applied.

The bubble transport equation is

$$\frac{\partial n_{\text{bub}}}{\partial t} + \frac{\partial (n_{\text{bub}} u)}{\partial x} = J_{\text{bub}} \tag{4.18}$$

where n_{bub} is the number density of bubbles in the flow and J_{bub} is the creation or destruction rate of bubbles in the flow. If one assumes that the bubbles are of equal sizes and spherical, the interfacial area is given by:

$$a_{\text{int}} = (36\pi n_{\text{bub}})^{1/3} \alpha_g^{2/3}. \tag{4.19}$$

The transport equation for interfacial area density is given by

$$\frac{\partial a_{\text{int}}}{\partial t} + \frac{\partial (a_{\text{int}} u)}{\partial x} = S_a, \tag{4.20}$$

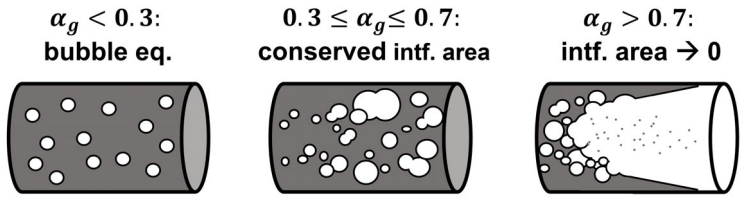

Figure 4.8: Illustration of the interfacial area based on the assumptions provided by Pinhasi et al. [78] for different flow regimes.

where a_{int} is the interfacial area density separating liquid and vapor and S_a denotes the creation or destruction rate of interfacial area.

A suggestion on how to model the creation and destruction rates is presented in Paper 6, based on the assumptions suggested by Pinhasi et al. [78, Sec. 7.1] for different flow regimes, and the assumption that bubble breakup will dominate if a critical Weber number is reached. The assumptions for the interfacial area suggested by Pinhasi et al. [78] are illustrated in Figure 4.8. For this approach, it is assumed that for $\alpha_g < 0.3$, the flow is bubbly and the interfacial area density can be calculated using the bubble number density. For $0.3 \leq \alpha_g \leq 0.7$, the flow is in a transition stage, and it is assumed that the interfacial area density is conserved. For $\alpha_g > 0.7$, the flow is assumed to be in the droplet regime. However, it is not clear how to estimate the number of droplets in the flow. In Paper 6, a simple relation is proposed which ensures that the interfacial area density goes to zero when α_g reaches one.

For more involved approaches in modeling the interfacial area for dispersed bubbly flow, the reader can refer to Liao et al. [182] for bubble breakup and coalescence, and Liao and Lucas [91] for a model accounting for the size distribution of bubbles using the Multiple Size Group (MUSIG) approach. There is still a need for more research to model the transition to droplets flow.

Advanced interfacial area models commonly include several tuneable parameters to enable fitting against experimental data (see, e.g., [182]). The downside of applying many parameters is that they increase the possibility of overfitting. As John von Neumann famously said [183]:

"With four parameters I can fit an elephant, and with five I can make him wiggle his trunk." It is important to follow due diligence regarding the fitting and validation of these models by reserving independent data for model validation, such that the models' predictive capabilities can be evaluated fairly.

5 Novel semi-implicit numerical solution method of the flow equations with mass transfer

This chapter is dedicated to a novel semi-implicit solution method for the four-equation model. The method was introduced and applied in Papers 5 and 6, however as the main focus of these papers is not on the numerical method, further details are given here.

5.1 The two-step solution approach

The governing equations of the four-equation model can be written on the form

$$\frac{\partial \boldsymbol{U}}{\partial t} + \frac{\partial \boldsymbol{F}}{\partial x} = \boldsymbol{S}, \tag{5.1}$$

where $\boldsymbol{U}$ denotes the vector of conserved variables, $\boldsymbol{F}$ denotes the vector of fluxes and $\boldsymbol{S}$ denotes the vector of source terms:

$$\boldsymbol{U} = \begin{pmatrix} \alpha_g \rho_g \\ \alpha_\ell \rho_\ell \\ \rho u \\ E \end{pmatrix}, \ \boldsymbol{F}(\boldsymbol{U}) = \begin{pmatrix} \alpha_g \rho_g u \\ \alpha_\ell \rho_\ell u \\ \rho u^2 + p \\ (E+p)u \end{pmatrix}, \ \boldsymbol{S} = \begin{pmatrix} \Gamma \\ -\Gamma \\ 0 \\ 0 \end{pmatrix}.$$

The relaxation source terms in the hierarchy of relaxation models can be stiff, which can cause instabilities in numerical solvers unless special consideration is taken for them. The system (5.1) is therefore solved using a classical first-order fractional step method known as Godunov splitting [134, Ch. 17], see, e.g., [99, 180, 103, 82, 184, 85]. The present work considers a two-step solution approach:

1. Solution of the homogeneous hyperbolic system

$$\frac{\partial \boldsymbol{U}}{\partial t} + \frac{\partial \boldsymbol{F}}{\partial x} = \boldsymbol{0}. \tag{5.2}$$

We denote the solution from this step using the superscript 0, following the notation of Pelanti [85].

2. Relaxation step, in which the following ODE is solved:

$$\frac{\mathrm{d}\boldsymbol{U}}{\mathrm{d}t} = \boldsymbol{S}(\boldsymbol{U}), \tag{5.3}$$

where the solution state from the homogeneous step $\boldsymbol{U}^0$ is applied as the initial condition.

The homogeneous solution step is solved in the present work using the well-known HLLC finite-volume method [72] in space and the explicit Euler method in time. The equations of the HLLC method for the four-equation model are presented in Paper 5. General information on finite-volume methods are provided in the books of LeVeque [134] and Toro [70], where the HLLC method for the Euler equations is also discussed. Additional, relevant background on the HLLC finite-volume scheme, and how it can be constructed for different flow models, are provided in Log [185].

5.2 The need for an implicit relaxation step

The relaxation step is typically also computed with an explicit solution scheme, though the tendency of the solution towards the equilibrium state is often accounted for [186, 82, 85]. For an explicit solution scheme, the source term must be evaluated at the conditions of $\boldsymbol{U}^0$. Then, the thermodynamic state corresponding to the conserved variables $\boldsymbol{U}^0$ must be determined. However, in certain cases, e.g., for flow close to the critical point, $\boldsymbol{U}^0$ may suggest a liquid state in its thermodynamically unstable area, because phase change has not yet been accounted for.

In the present work, we do not want to evaluate the thermodynamic state, and the resulting mass-transfer in the thermodynamically unstable area. This is due to the following reasons:

- Some multiparameter EOS have unphysical properties in the unstable area, providing pseudostable states [167]. Thermodynamic

evaluation of the fluid's state in this area can provide unphysical results. Both of the high-accuracy equations of state applied in this work to model CO_2, the Span and Wagner [146] EOS and the GERG 2008 [187] EOS, have this problem.

- Mass-transfer terms may provide strange/unexpected results, as they are not developed for the unstable region. A fully physical mass-transfer term would provide no energy-barrier for the phase change in this region.

- In reality, phase change would occur before the unstable region was reached, and at the spinodal at the latest. So it is most reasonable to evaluate the mass-transfer source term in the metastable area instead.

In the semi-implicit solution method, the relaxation step is solved implicitly together with the solution of the thermodynamic state of the fluid. The thermodynamic state of the fluid is solved for at the relaxed state, where phase change is accounted for, so the phases should be in their stable or metastable area (unless too little phase change is predicted). The solution method applied to determine the state of a two-phase mixture using a real gas EOS is denoted a *thermodynamic flash calculation*. The relaxation step is therefore denoted the *implicit flash*. The details of the implicit flash are presented below.

5.3 The implicit flash

After the solution step of the homogeneous hyperbolic system for a given time t^n is computed, the conserved variables will be known: $(\alpha_g\rho_g)^0$, $(\alpha_\ell\rho_\ell)^0$, $(\rho u)^0$, E^0. Based on the known variables, the total density of the fluid in the given grid cell is

$$\rho^0 = (\alpha_g\rho_g)^0 + (\alpha_\ell\rho_\ell)^0, \tag{5.4}$$

the velocity of the flow is

$$u^0 = \frac{(\rho u)^0}{\rho^0} \tag{5.5}$$

and the internal energy of the mixture is

$$(\rho e)^0 = E^0 - \frac{1}{2}\rho^0 (u^0)^2. \tag{5.6}$$

The thermodynamic state for the four-equation model can be defined by the following four variables: α_g, ρ_g, ρ_ℓ and T. These are solved for to satisfy the conservation of mass for the phases, the conservation of energy, and the equality of pressures for the phases during the mass transfer process:

$$\boldsymbol{f} = \begin{pmatrix} \alpha_g \rho_g - \left((\alpha_g \rho_g)^0 + \Delta m_g\right) \\ (1-\alpha_g)\rho_\ell - \left((\alpha_\ell \rho_\ell)^0 + \Delta m_\ell\right) \\ \alpha_g \rho_g e_g(\rho_g, T) + (1-\alpha_g)\rho_\ell e_\ell(\rho_\ell, T) - (\rho e)^0 \\ p_g(\rho_g, T) - p_\ell(\rho_\ell, T) \end{pmatrix} = \mathbf{0}, \tag{5.7}$$

where $e_k(\rho_k, T)$ and $p_k(\rho_k, T)$ are calculated using the thermodynamic library Thermopack [188], as described in the Appendix and Δm_g denotes the mass transfer from liquid to vapor during the time step Δt,

$$\Delta m_g = -\Delta m_\ell = \int_{t^n}^{t^n + \Delta t} \Gamma \, \mathrm{d}t. \tag{5.8}$$

Note that $\Delta m_g = \Delta m_g(\alpha_g, \rho_g, \rho_\ell, T)$, i.e., the mass transfer term is a function of the solution state. In the present work, a backward Euler step is applied:

$$\Delta m_g \approx \Gamma^{t^n + \Delta t} \Delta t. \tag{5.9}$$

The set of equations (5.7) can be solved by an iterative method such as the Newton-Rhapson solver. The Jacobian matrix for the implicit flash is

$$\mathrm{d}\boldsymbol{f} = \begin{bmatrix} \rho_g - \dfrac{\partial(\Delta m_g)}{\partial \alpha_g} & \alpha_g - \dfrac{\partial(\Delta m_g)}{\partial \rho_g} & -\dfrac{\partial(\Delta m_g)}{\partial \rho_\ell} & -\dfrac{\partial(\Delta m_g)}{\partial T} \\ -\rho_\ell + \dfrac{\partial(\Delta m_g)}{\partial \alpha_g} & \dfrac{\partial(\Delta m_g)}{\partial \rho_g} & \alpha_\ell + \dfrac{\partial(\Delta m_g)}{\partial \rho_\ell} & \dfrac{\partial(\Delta m_g)}{\partial T} \\ \rho_g e_g - \rho_\ell e_\ell & \alpha_g \left(h_g - \dfrac{\gamma_g C_{p,g} T}{\kappa_g}\right) & \alpha_\ell \left(h_\ell - \dfrac{\gamma_\ell C_{p,\ell} T}{\kappa_\ell}\right) & \dfrac{\alpha_g \rho_g C_{p,g}}{\kappa_g} + \dfrac{\alpha_\ell \rho_\ell C_{p,\ell}}{\kappa_\ell} \\ 0 & \dfrac{c_g^2}{\kappa_g} & \dfrac{c_\ell^2}{\kappa_\ell} & \dfrac{\gamma_g \rho_g C_{p,g}}{\kappa_g} - \dfrac{\gamma_\ell \rho_\ell C_{p,\ell}}{\kappa_\ell} \end{bmatrix}, \tag{5.10}$$

where $h_k = e_k + \frac{p_k}{\rho_k}$ is the specific enthalpy of phase $k = g, \ell$, γ_k is the Grüneisen coefficient defined by Equation (3.27),

$$C_{p,k} = T_k \left(\frac{\partial s_k}{\partial T_k} \right)_{p_k} \tag{5.11}$$

is the heat capacity at constant pressure,

$$C_{v,k} = T_k \left(\frac{\partial s_k}{\partial T_k} \right)_{\rho_k} \tag{5.12}$$

is the heat capacity at constant volume and

$$\kappa_k = \frac{C_{p,k}}{C_{v,k}} \tag{5.13}$$

is the ratio of specific heats for phase $k \in g, \ell$. Note that applying this iterative method does not add much more complexity to the thermodynamic solution in the given grid cell, as an iterative procedure without the mass-transfer term would be applied to solve the thermodynamic state regardless, as described in the Appendix.

The implicit flash method was applied successfully to simulate depressurizations where the fluid state passes close to the critical point of CO_2 (Test 6 and Test 24) in Paper 5 and Paper 6, highlighting the robustness of the method. With the applied grid of 10,000 grid cells, explicit methods reach the unstable region for these cases.

Note that in addition to this novel numerical solution method, a new outflow boundary condition was also developed, which is detailed in Paper 5.

6 Experiments

This chapter summarizes the experimental activities conducted to provide validation data for the pipe flow simulations, and to provide insight on the role of homogeneous and heterogeneous bubble nucleation for varying initial temperatures. In Section 6.1, the experimental system is described, the experimental procedure is described in Section 6.2, the test campaign is detailed in Section 6.3 and the results are summarized in Section 6.4.

6.1 Description of system

A series of CO_2 pipe depressurization tests were conducted at the ECCSEL [189] depressurization facility. The facility is located at the roof of the Thermal Engineering Laboratories at the campus of NTNU in Trondheim and was designed to provide high-accuracy data for rapid depressurization of CO_2 and CO_2-rich mixtures. The facility is described in detail by Munkejord et al. [32]. For completeness, the setup of the experimental facility is briefly described here.

Figure 6.1 shows a schematic overview of the depressurization facility. The facility consists of a gas supply with mass flow controllers, a two-stage compression with a cooling aggregate and a heater, and a test section with a rupture disk device. The rupture disk opens into a large vent stack which reduces the noise from the experiments and lowers the resulting CO_2 concentration at street level. The maximum operating pressure of the facility is 20 MPa, and the current design allows experiments with initial temperatures in the range from 5 °C to 40 °C.

Gas supply and compression CO_2 and a possible secondary gas are supplied to the system by two separate pipelines. For tests with mixtures, the desired composition is achieved using the two Bronkhorst mass-flow controllers. Two stages of compression and cooling is applied to reach the

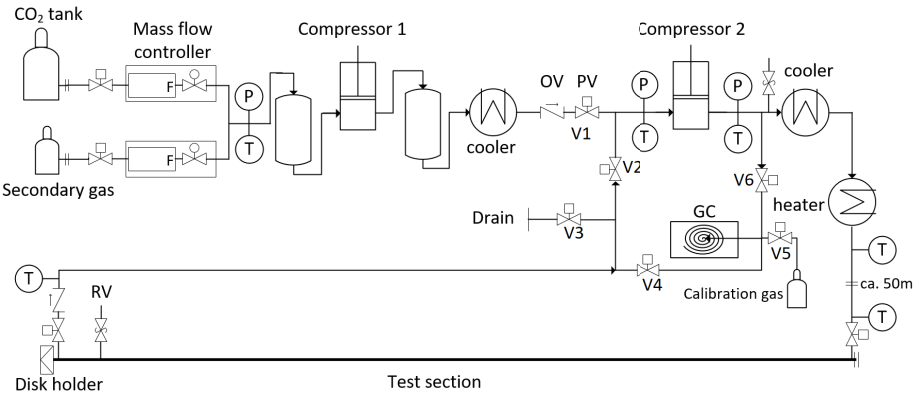

(a) System (RV: relief valve; OV: one-way valve; PV: pneumatic valve)

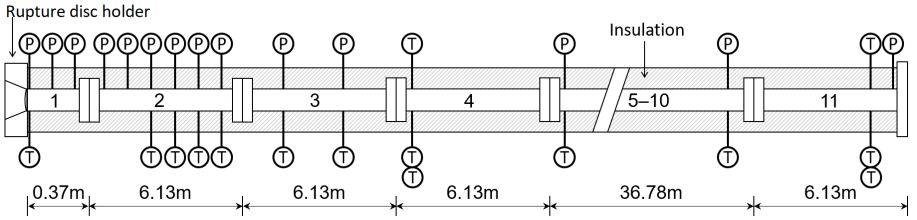

(b) Test section (dimensions are not to scale; pipe no. 5–10 and corresponding sensors are omitted.)

Figure 6.1: Schematic of the ECCSEL depressurization facility drawn by Anders Austegard and Han Deng at SINTEF Energy Research.

Table 6.1: Density and thermal properties of the test section, reproduced from [32].

	Density ($\mathrm{kg\,m^{-3}}$)	Thermal conductivity ($\mathrm{W\,m^{-1}\,K^{-1}}$)	Specific heat ($\mathrm{J\,kg^{-1}\,K^{-1}}$)
Pipe steel	8000	15	500
Insulation layer	75	0.032	840

desired experimental conditions. The CO_2 (or CO_2-mixture) enters at the back end of the test section, shown to the right in Figure 6.1a. A return pipeline near the open end of the test section allows for circulation of the fluid to achieve a uniform temperature and composition for mixture tests. A micro gas chromatograph (GC) is connected to measure the mixture composition. Pressure-relief valves which open at a pressure of 20 MPa are installed after the second compressor and at the test section. The drain lines are used to empty the system after each test. A vacuum pump is installed on the same line to evacuate the system before each test. Note that the experiments conducted in relation to this thesis were all pure CO_2 tests.

Test section and instrumentation The test section is a 61.67 m long stainless steel pipe made of 11 pipes segments. These segments have an inner diameter of 40.8 mm, an outer diameter of 48.3 mm, and were honed to a mean roughness of $R_a = 0.2\,\mu m - 0.3\,\mu m$. The pipe is wrapped in heating cables and covered with a 60 mm thick layer of glass wool. The test section is covered by a stainless-steel mantle with a diameter of 190 mm. The thermal properties of the pipe and insulation layer are provided in Table 6.1. An image of the test section, the depressurization pipe, is shown in Figure 6.2. The test section is anchored horizontally to the railing using an L profile pipe support. The supports have some flexibility, which allow for the pipe to recoil somewhat once the rupture disk opens and the CO_2 is released. We therefore observe a small pressure perturbation near the closed end in our experiments caused by the pipe's recoil.

16 fast-response pressure transducers and 23 type E thermocouples are

Figure 6.2: The ECCSEL depressurization tube. The CO_2 is vented through the stack in the background. Photo taken by Han Deng at SINTEF Energy Research.

flush-mounted to the inner surface of the test section to capture the pressure and temperature transients during depressurization. The pressure sensors are of the type Kulite CTL-190(M). These are high-frequency pressure sensors with a bandwidth up to 200 kHz. 11 of the thermocouples are placed at axial positions coinciding with the location of a pressure sensor. The remaining 12 thermocouples are installed at the top, bottom and side of the pipe at four locations in order to capture any stratification of the flow. The positions of the sensors are reported in Table 6.2. Most of the pressure sensors are densely distributed close to the open end to capture the rapid depressurization wave. The uncertainty of the pressure measurements has been estimated to be around 60 kPa with a confidence interval of 95 % [32] and the uncertainty of the temperature measurements is $\pm 0.22\,^{\circ}\mathrm{C}$ [32]. The calibration procedures for the sensors is described in detail in [32].

The logging frequency of the data from the pressure transducers and thermocouples is 100 kHz and 1 kHz, respectively. The high-frequency data are stored from 0.3 s before disk rupture for a 9 s period. After this period, both pressure and temperature are collected at 50 Hz. The reported initial conditions of the experiments are calculated from the data between 1 ms and 0.5 ms before disk rupture.

For the study of non-equilibrium effects, measurements in the millisecond range are needed as this is the time-scale for the phase-change. For Test 8, the response time of the thermocouples was estimated to be approximately 30 ms [32]. The response time of the pressure measurements is approximately on the scale of the measurement frequency, 10 µs. Thus, in the present work only the recorded pressure data, and the initial temperature, has been applied for the validation of the CFD models. However, the datasets including the complete temperature measurements are available at Zenodo [190, 191, 192].

Rupture disk device A rupture disk with a disk holder is installed at the pipe outlet. The specified burst pressure of the disk is 110 barg for Test 6 and 120 barg for the remaining tests at 22 °C with a burst tolerance of 5%. For Tests 4, 6, 8, and 24, X-scored Fike SCRD BT FSR rupture disks were used, and for Tests 19, 22, 23 and 25 circular-scored triple-layer Fike HOV BT HL rupture disks were used (see Table 6.3 for reference on the test numbers). Images of an X-scored rupture disk and a triple-layer disk after a depressurization test is shown in Figure 6.3. The triple-layered disks were found to open fully more reliably at colder initial temperatures than the X-scored disks, and were therefore applied for cold tests to ensure successful experiments. The open membrane area of the rupture disks has a diameter of 63 mm, ensuring that choking will occur at the end flange of the pipe. Once the disks are fully open, the depressurizations are expected to be the same for both types of disks.

6.2 Experimental procedure

The experiments are conducted as follows. First, the rupture disk is installed and the system is evacuated using a vacuum pump. Then the

Table 6.2: Locations of pressure and temperature sensors at 25 °C, reproduced from Munkejord et al. [32].

Distance from open end (m)	Pressure sensor	Temperature sensor (side)	Temperature sensor (bottom, side, top)
0.080	PT201	TT201	
0.180	PT202		
0.280	PT203		
0.484	PT204		
0.800	PT205		
1.599	PT206	TT206	
3.198	PT207	TT207	
4.798	PT208	TT208	
6.397	PT209	TT209	
7.996	PT210	TT210	
9.595	PT211	TT211	
15.292			TT241, TT242, TT243
19.990	PT212	TT212	
29.986	PT213	TT213	
30.686			TT251, TT252, TT253
39.984	PT214	TT214	
46.085			TT261, TT262, TT263
49.982	PT215	TT215	
61.280			TT271, TT272, TT273
61.479	PT216		

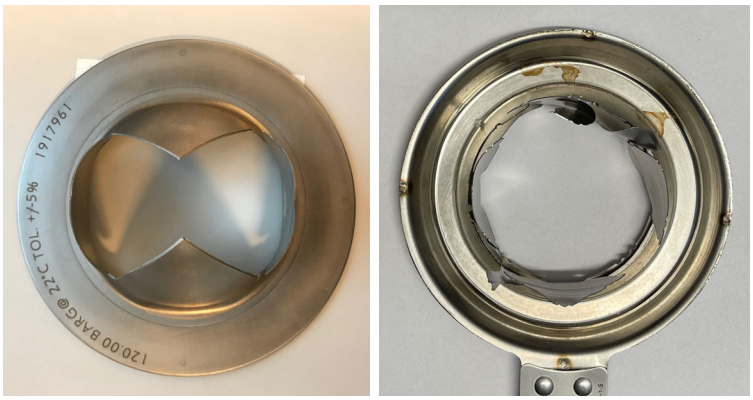

(a) X-scored rupture disk after test.

(b) Triple-layer rupture disk after test.

Figure 6.3: Pictures of X-scored and triple-layer rupture disks.

test section is filled with CO_2 and pressurized. The CO_2 is cooled during the compression to reduce the heating of the fluid. When the pressure reaches about 70% of the desired value, the fluid is circulated to achieve a uniform temperature along the test section. The fluid temperature is controlled using heating elements wrapped around the test section and the cooling and heating circuits in the compression system. The pressure and temperature are then increased at a controlled rate by alternating filling and circulation of CO_2 until the disk ruptures. Upon disk rupture, the valves for filling and circulation are automatically closed and the heating cables are automatically turned off. The CO_2 is released through the vent stack. An image of the CO_2 plume released from Test 4 is shown in Figure 6.4. The vent stack is designed with a large enough flow area that it will not disturb the outflow from the pipe.

In the flow models, it is assumed that the contribution of heat from the heating cables is negligible once they are turned off, and heat is transferred from the ambient air, through the pipe wall and to the fluid. For the short amount of time considered in the simulations, likely only the wall temperature affects the heating of the CO_2. As an initial condition, it is assumed that the temperature at the inside wall is equal to the initial

Figure 6.4: CO_2 plume released during depressurization Test 4, screenshot from video recording by Anders Austegard.

fluid temperature, and that there is steady-state heat conduction through the pipe and insulation to the ambient air, as described in Paper 6. The heat conduction through the pipe steel and the surrounding insulation is then calculated by solving the heat equation in the radial direction in a two-layer domain, as described by Aursand et al. [193].

6.3 Test campaign

During the present work, five full-bore CO_2 pipe depressurization experiments were conducted. The initial conditions for these tests were chosen to investigate the temperature dependence of non-equilibrium effects for CO_2 during depressurization in the relevant region for CO_2 pipeline transport. The tests were further chosen to complement the three full-bore CO_2 depressurization tests already conducted by Munkejord et al. [32] at this facility. The complete set of old and new experiments were conducted with initial temperatures approximately ranging from 5 °C to 40 °C and with an initial pressure of about 12 MPa.

The initial conditions of all the eight full-bore depressurization experiments conducted with pure CO_2 at the facility are reported in Table 6.3. These conditions are representative of the temperatures and pressures which may be encountered for the operation of CO_2 transportation pipelines. In Figure 6.5, the initial conditions and calculated depressur-

Table 6.3: Experimental conditions of the CO_2 depressurization tests, listed in the order of descending initial temperature.

Test no.	Pressure avg. (MPa)	Temperature avg. (°C)
6*	10.40	40.0
24†	11.56	35.8
23†	12.19	31.5
8*	12.22	24.6
4*	12.54	21.1
22†	12.48	14.9
19†	12.47	10.2
25††	12.27	4.6

* Munkejord et al. [32]; † Present work, Log et al. [114]; †† Present work, Log et al. [192].

ization paths for the liquid phase, assuming isentropic conditions, are shown in the phase diagram for CO_2, and in the pressure-entropy diagram. The warmest test crosses the saturation line very close to the critical point.

6.4 Results

Analysis of the experiments show that there is a transition in the type of bubble nucleation determining the maximum superheat reached for these experiments, similarly to that found in earlier work for flashing water flows [18, 22, 117]. The warmer experiments (Test 6, 24, 23, 8 and 4) agree with the homogeneous superheat limit predicted by classical nucleation theory, and the coldest experiments (Test 22, 19 and 25) do not. This is first investigated in the Conference paper [194] and later confirmed in Paper 5 [114] and Paper 6 [195]. The agreement with the homogeneous superheat limit for warm temperatures was leveraged by Morten Hammer to develop the delayed homogeneous equilibrium model, which is applied and studied in Paper 2 and Paper 3.

We show the estimated maximum achieved superheat in Figure 6.6, together with the predicted homogeneous nucleation rate of bubbles based

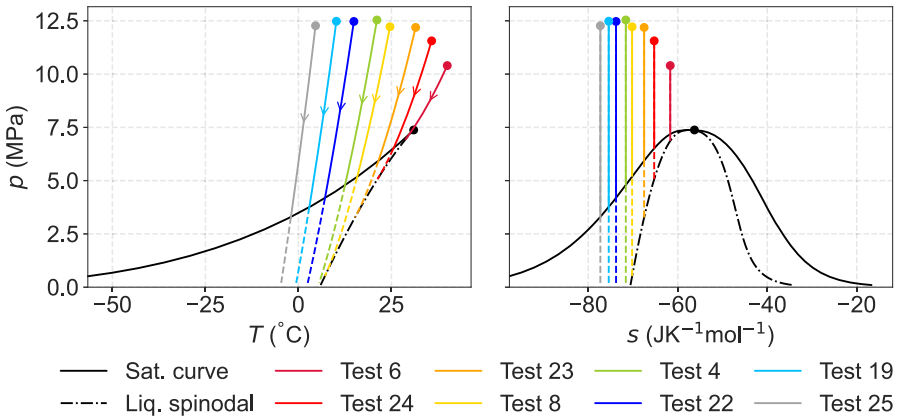

Figure 6.5: Calculated depressurization paths of the dense/liquid phase using the GERG-2008 EOS, assuming isentropic flow in a pressure-temperature (left) and pressure-entropy diagram (right). The metastable path assuming no flashing is shown in dashed lines.

on CNT. The pressure where nucleation begins is estimated based on observed pressure perturbations in the pressure recordings in combination with a significant decrease in the depressurization rate, suggesting that vapor bubbles have started to form. These pressure perturbations are large compared to the experimental measurement uncertainties, and were taken as the main contributor to uncertainty in the estimated maximum superheat. The data from the pressure transducer closest to the open end, PT201, was used for this analysis. The temperature at the point of nucleation was estimated based on the assumption of isentropic flow. Details on this are outlined in the Conference paper.

Though the estimates of the maximum superheat are uncertain, the *trend* in the superheat limit is clear and confirms the transition from homogeneous to heterogeneous nucleation limiting the metastability from warmer to colder relative temperatures. Further inside the pipe, where the depressurization rate is slower, the achieved superheat is also smaller, in agreement with the findings of, e.g., Lienhard et al. [17] that the attained superheat depends on the depressurization rate in addition to the initial temperature. Further discussion on the trends in the recorded pressure evolution and non-equilibrium effects for the experiments is provided in Paper 5.

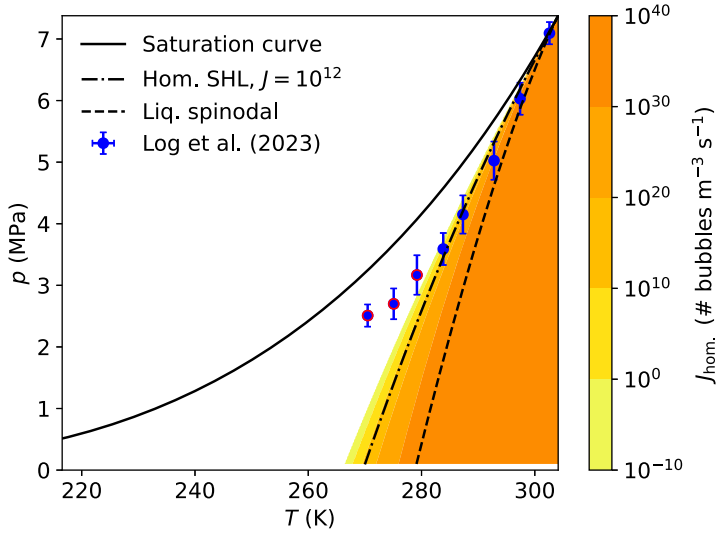

Figure 6.6: The homogeneous nucleation rate of critically-sized bubbles for CO_2 calculated using CNT with the GERG-2008 EOS, compared to the estimated maximum superheat observed in full-bore depressurization experiments [114, 41]. The red edges indicate if the maximum attained superheat is found for a homogeneous nucleation rate less than 10^{-10} bubbles $m^{-3}\,s^{-1}$.

7 Paper summaries

This chapter summarizes the publications related to the present doctoral thesis. The summaries highlight the developed methods and results for each paper, the contributions of the authors following the CRediT (Contributor Roles Taxonomy) classification [196], and a more detailed statement on my contributions. The full papers are attached in the Appendix.

The papers are here presented in chronological order, however the main papers in this work consist of the Conference paper, Paper 5 and Paper 6. These focus on the experiments and modeling of flashing flows during the full-bore depressurization of a pipe. Paper 1 and Paper 4 are exploratory papers which describe the simulation of flows in pipes with variable cross-sectional area, and evaluates the accuracy of a mixture surface tension model, respectively. These studies can later be applied for the extension of the main models to flows with varying cross-sectional area and flows with multicomponent mixtures, both of which are important for application in CCS engineering tools. Finally, Paper 2 and Paper 3 present and extend a method denoted as D-HEM for estimating the delayed nucleation and the choking point for flashing flows without fully resolved simulations.

7.1 Paper 1 – HLLC-type methods for compressible two-phase flow in ducts with discontinuous area changes

Published in Computers & Fluids, vol 227 (2021)
doi:10.1016/j.compfluid.2021.105023
Authors: Alexandra Metallinou Log, Svend Tollak Munkejord and Morten Hammer

7.1.1 Summary of paper

In this paper, we extend the HLLC finite-volume method for computing flows in ducts with discontinuous changes in its cross-sectional area. The HLLC method is applied due to its favorable properties of low numerical diffusion, and the conservation of contact waves. These properties mean that the method can be expected to require fewer computational cells to provide accurate results, and it will be able to resolve the change from single to two-phase flow well.

For the modeling of flow in ducts with discontinuous cross-sections, we consider the quasi one-dimensional flow equations, where changes in the flow area are accounted for by a non-conservative term. We test two approaches in treating the non-conservative term. The first approach, which we denote HLLC+S, treats the non-conservative term as a source term. The source term is discretized and added to the solution of the standard HLLC approach. In the second approach, the HLLC method is extended to include the non-conservative term in its solution. We denote this the HLLCS method. We test these methods for ideal gas shock-tube problems where the exact solution is known, and further with two-phase flow tests using the Peng-Robinson EOS.

The HLLC+S method adopts its discretization of the source term from the approach of Brown et al. [66], which is very easy to implement. We find that HLLC+S often does not converge to the exact solution for simple shock tube tests with the ideal gas EOS. For the two-phase flow test suggested by Brown et al. [66], we further find an unphysical spike in

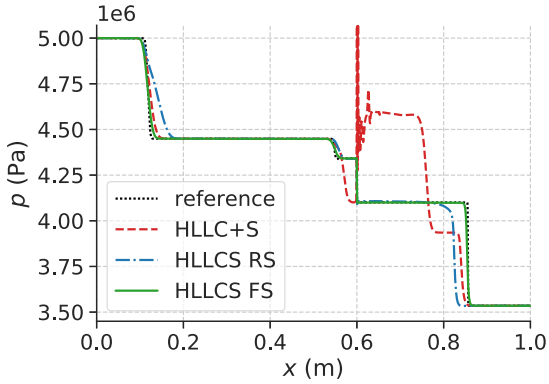

Figure 7.1: Pressure solution for a two-phase flow test case for which the HLLC+S method diverges.

the HLLC+S solution. This suggests that the discretization of the non-conservative term is not well-balanced. We are able to find a similar test case for which the predicted pressure of HLLC+S diverges as shown in Figure 7.1. Thus, though the method is easy to implement, we do not recommend it for engineering purposes.

For the HLLCS method, we assume a four-wave solution as opposed to the typical three-wave solution, where the fourth wave describes the discontinuous area change. We propose two methods of computing the states on either side of the area change. The first method is based on Roe averages as inspired by Murillo and García-Navarro [197] and their solution approach for the shallow-water equations. The second method involves solving a set of nonlinear conservation equations to estimate the flux on either side of the area change which satisfies the assumptions of the HLLC Riemann solver. The FS approach can be considered most accurate. We find that HLLCS with FS can be considered well-balanced in the sense that it preserves the steady state solutions of the governing equations. HLLCS with RS is not well-balanced, but it still performs reasonably well for our benchmark tests with the ideal gas EOS.

We further test HLLCS for two-phase flow problems, assuming equilibrium flow. Though the exact solution is not known for these cases, the models appear to perform well. The HLLCS FS method is also applied

for a water flow test case, and its solution is compared to that of other numerical solvers. We find that HLLCS FS provides reasonable results and shows low numerical diffusion.

Note that the quasi-1D flow equations are resonant, meaning that the waves in the system might interact and can cause extra waves to form. For resonant flow cases, the HLLCS FS method does not compute a solution. One such resonant flow case arises for choked flow at an area increase. The prediction of such flows is relevant for industrial applications, e.g. to model critical, flashing flow through an orifice. It could therefore be relevant to extend the HLLCS FS for this case. Furthermore, it could be interesting to extend the model for non-equilibrium flows.

7.1.2 Author contributions

Alexandra Metallinou Log: Conceptualization, Software, Investigation, Visualization, Writing – original draft. **Svend Tollak Munkejord:** Funding acquisition, Conceptualization, Supervision, Writing – review & editing. **Morten Hammer:** Conceptualization, Software, Supervision, Writing – review & editing.

7.1.3 Personal contribution

I developed the HLLC and HLLCS methods as part of my master's thesis. I extended the models for two-phase flow and wrote the paper on the methods as a part of the present thesis. The flow simulation code was written by me.

7.2 Conference paper – Investigation of non-equilibrium effects during the depressurization of carbon dioxide

Published in the proceedings of the 15th IIR Gustav Lorentzen Conference on Natural Refrigerants, Trondheim, Norway, June 13-15th (2022)
doi:10.18462/iir.gl2022.0197
Authors: Alexandra Metallinou Log, Svend Tollak Munkejord, Morten Hammer, Armin Hafner, Han Deng and Anders Austegard

7.2.1 Summary of paper

In this paper we study the pressure recordings of pipe depressurization tests 4, 6, 8 and 19 conducted at the ECCSEL depressurization facility for pure CO_2. The initial conditions for the tests are reported in Table 6.3. For all the tests, the CO_2 is initially in a dense, liquid-like state at a supercritical pressure. As the rupture disk opens at the pipe's open end, the CO_2's pressure quickly drops below the saturation line and flash boiling begins. Based on the pressure recordings of the sensor closest to the pipe's outlet, we estimated the pressure where bubbles begin to nucleate. We show the point where we assumed nucleation started for Test 19 in Figure 7.2a. Using the assumption of isentropic flow, we calculated the temperature of the fluid at the pressure where nucleation began and thus estimated the local superheat. We compare the calculated superheat with the theoretical superheat limit for homogeneous bubble nucleation based on CNT as shown in Figure 7.2b. The calculated superheat matches the homogeneous superheat limit for the warmest tests, Test 6, 8 and 4. However, Test 19 deviates from the homogeneous superheat limit. This result is in agreement with the findings of Wilhelmsen and Aasen [117], who find a transition in the mode of nucleation determining the superheat limit for flashing flows at a certain temperature. For warm cases the superheat limit was found to be determined by homogeneous nucleation and for colder cases the superheat limit is determined by heterogeneous nucleation. We therefore assume that the superheat limit for Test 19 is determined by heterogeneous bubble nucleation.

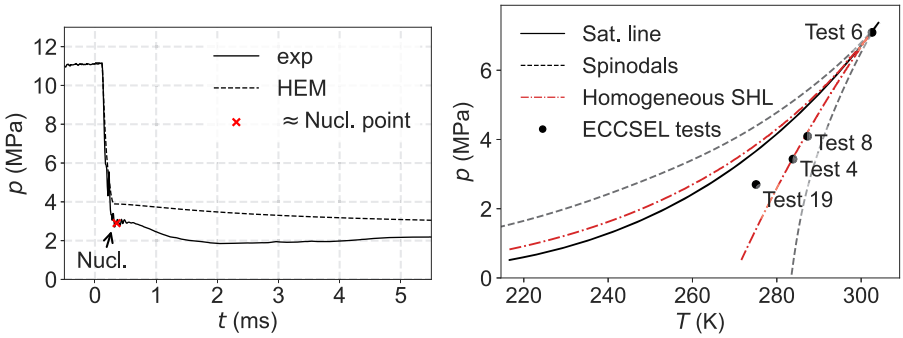

(a) Pressure evolution for the first milliseconds of depressurization for Test 19, 8 cm from the open end.

(b) Estimated nucleation points for the depressurization tests in the CO_2 phase diagram.

Figure 7.2

7.2.2 Author contributions

Alexandra Metallinou Log: Conceptualization, Software, Investigation, Visualization, Writing – original draft. **Svend Tollak Munkejord:** Conceptualization, Supervision, Writing – review & editing, Funding acquisition. **Morten Hammer:** Conceptualization, Software, Supervision, Writing – review & editing. **Armin Hafner:** Supervision, Writing – review & editing. **Han Deng:** Investigation, Writing – review & editing. **Anders Austegard:** Investigation, Writing – review & editing.

7.2.3 Personal contribution

I analyzed the pressure measurements for all the experiments to estimate the point where nucleation began, calculated the corresponding superheats and wrote the code to estimate the superheat limit of CO_2. The paper was written by me.

7.3 Paper 2 – Experiments and modelling of choked flow of CO_2 in orifices and nozzles

Published in the International Journal of Multiphase Flow, vol 156 (2022)
doi:10.1016/j.ijmultiphaseflow.2022.104201
Authors: Morten Hammer, Han Deng, Anders Austegard, Alexandra Metallinou Log and Svend Tollak Munkejord

7.3.1 Summary of paper

In this paper, we report on six pipe-depressurization experiments of pure CO_2 for an initial pressure of 12 MPa and 25 °C with flow through nozzles and orifices of three sizes (4.5, 9.0 and 12.7 mm). The pressure recordings from the first pressure sensor in the pipe, 8 cm from the open end is shared in the supplementary information of the paper [14].

To predict quasi-steady flow in restrictions, the HEM or Henry-Fauske (HF) models are most often applied. These models are considered analytic because they do not require temporal or spatial integration. The HEM often underpredicts the mass flow rate because it does not account for delayed phase transition during flashing. In the present work, we propose a novel analytic model for the prediction of quasi-steady flow in restrictions: the delayed homogeneous equilibrium model, D-HEM. For this model, flashing is assumed to begin at the homogeneous superheat limit calculated using CNT. The flashing is further assumed to be an isenthalpic and isobaric process that instantly brings the flow back to equilibrium. With these assumptions, the corresponding entropy production related to the phase change is retained.

The HEM, HF and D-HEM are employed in 1D CFD pipe simulations to describe the outflow of the depressurization experiments. We find that HF provides the best results and the HEM always underpredicts the mass flow in these simulations. We further compare the HEM, HF and D-HEM models with experimental data for converging-diverging nozzles. Here, D-HEM outperforms the other models, with a relative absolute error of 2.5% for the predicted mass flux.

7.3.2 Author contributions

Morten Hammer: Conceptualization, Methodology, Software, Investigation, Data curation, Visualization, Writing – original draft, Writing – review & editing. **Han Deng:** Software, Formal analysis, Investigation, Data curation, Visualization, Writing – original draft. **Anders Austegard:** Methodology, Software, Investigation, Resources, Writing – review & editing. **Alexandra Metallinou Log:** Software, Investigation, Writing – original draft. **Svend Tollak Munkejord:** Conceptualization, Methodology, Writing – original draft, Supervision, Writing – review & editing, Funding acquisition.

7.3.3 Personal contribution

I conducted the experiments together with Anders Austegard and Han Deng, and wrote the section describing how to calculate the homogeneous superheat limit using CNT.

7.4 Paper 3 – Towards an engineering tool for the prediction of running ductile fractures in CO_2 pipelines

Published in Process Safety and Environmental Protection, vol 171 (2023)
doi:10.1016/j.psep.2023.01.054
Authors: Hans Langva Skarsvåg, Morten Hammer, Svend Tollak Munkejord, Alexandra Metallinou Log, Stephane Dumoulin and Gaute Gruben

7.4.1 Summary of paper

In this paper, we consider the Battelle two-curve method (BTCM) for the prediction of running-ductile fractures in pipes and provide improved model curves for the application on CO_2 transportation pipes. The BTCM is the most common engineering method applied to assess RDF for different pipe designs. However, this method was designed for natural gas pipelines and has been found non-conservative for CO_2.

To improve the method for the application on CO_2 pipeline design, the BTCM is examined for a series of large-scale RDF tests with CO_2-rich mixtures. For the material curve, the change in fluids from natural gas to CO_2 requires a new toughness correlation which is proposed. For the fluid curve, the D-HEM proposed in Paper 2 is extended for mixtures and applied to estimate the depressurization path of the fluid, accounting for the non-equilibrium boiling that occurs for rapid depressurizations. We show the assumed depressurization paths of HEM and D-HEM for the mixture applied in the RDF test COOLTRANS Test 2 [198] in Figure 7.3. The resulting fluid curves for the BTCM are shown in Figure 7.4. With the new material and fluid curves in the BTCM, the RDF predictions are improved. We consider the updated curves for the BTCM as an important step towards a viable engineering tool for the prediction of RDF in CO_2 pipelines.

Note that the calculation of the superheat limit depends on the surface tension of the mixture. In the paper, we calculate the surface tension based on the parachor model as applied in REFPROPv10. We investigate the accuracy of the mixture surface tension in Appendix A and the

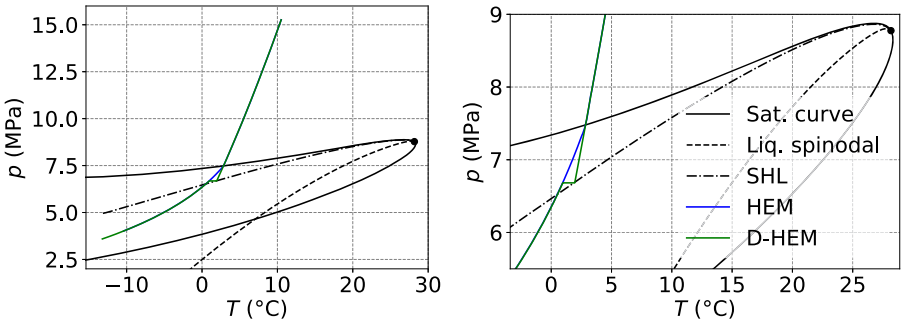

Figure 7.3: Fluid phase diagram for COOLTRANS Test 2 [198] with decompression path calculated using HEM and D-HEM.

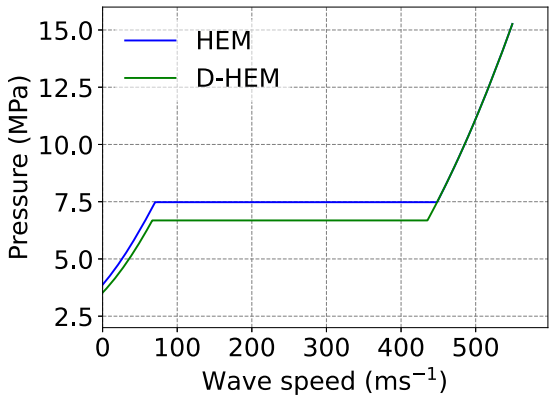

Figure 7.4: The resulting fluid lines in the BTCM estimated by HEM and D-HEM for COOLTRANS Test 2 [198].

sensitivity of the superheat limit to inaccuracies in the estimate of the surface tension in Appendix B of the paper. We find that the estimated superheat limit is sensitive to the uncertainty of the surface tension estimate of the mixture for colder temperatures.

7.4.2 Author contributions

Hans Langva Skarsvåg: Conceptualization, Methodology, Software, Investigation, Visualization, Writing – original draft, Writing – review & editing. **Morten Hammer:** Conceptualization, Methodology, Software, Writing – original draft, Supervision, Writing – review & editing. **Svend Tollak Munkejord:** Conceptualization, Writing – original draft, Supervision, Writing – review & editing, Funding acquisition. **Alexandra Metallinou Log:** Software, Investigation, Visualization, Writing – original draft, Writing – review & editing. **Stephane Dumoulin:** Writing – review & editing. **Gaute Gruben:** Writing – review & editing.

7.4.3 Personal contribution

I extended the D-HEM method developed in Paper 2 [14] for the application on multicomponent fluids, wrote the required code to calculate the homogeneous superheat limit for mixtures and tested the sensitivity of the choice of critical nucleation rate and uncertainty in the surface tension estimate. I wrote the section describing D-HEM and the appendices describing how to calculate the superheat limit for multicomponent fluids and the results of the sensitivity analysis.

7.5 Paper 4 – Assessment of a Parachor Model for the Surface Tension of Binary Mixtures

Published in the International Journal of Thermophysics, vol 44 (2023)
doi:10.1007/s10765-023-03216-z
Authors: Alexandra Metallinou Log, Vladimir Diky and Marcia Huber

7.5.1 Summary of paper

The parachor method is widely used to estimate mixture surface tensions. However, its accuracy for various mixtures has not been extensively tested. In this paper we estimate the performance of the parachor model implemented in REFPROPv10 [73] using a dataset of 154 binary mixtures with a total of 8205 data points. We assess the performance of the parachor method for the following categories of mixtures: mixtures with n-alkanes, mixtures with alcohols, mixtures with water, mixtures with aromatics, mixtures with halocarbons and mixtures with miscellaneous compounds (cryogens with other cryogens, or siloxanes with siloxanes). The model has a single, constant binary interaction parameter δ_{ij} for each pair of components that we fit to the mixture data. We also tested the performance of the method in a predictive mode with the binary interaction parameter set to zero.

Most notably, we find that the parachor method cannot estimate the surface tension of mixtures with water and organic compounds well. There was little data available for CO_2 mixtures, however for CO_2 with n-alkanes we found that a binary interaction parameter should be applied to improve the results. We show the deviation of the parachor method's estimate of the surface tension to the experimentally measured one for a series of n-alkanes in Figure 7.5. Generally, the error of the parachor method increases with the size-difference between the component molecules.

7.5.2 Author contributions

Alexandra Metallinou Log: Conceptualization, Software, Investigation, Visualization, Writing – original draft, Writing – review & editing.

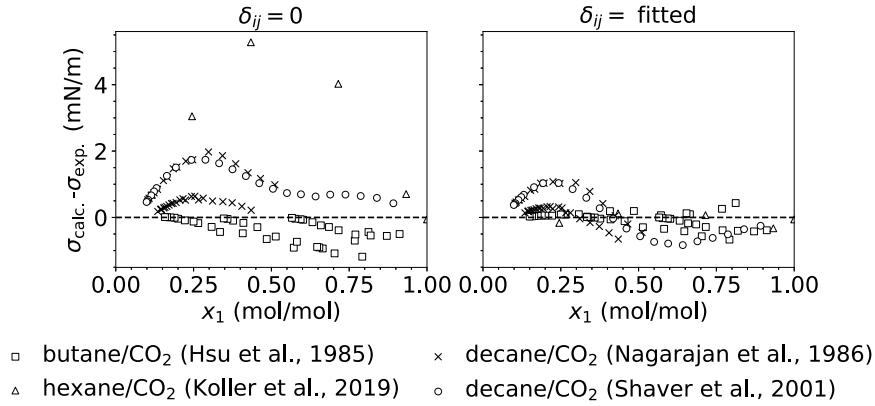

Figure 7.5: Deviations between the model and experimental data for mixtures of a series of n-alkanes with CO_2.

Vladimir Diky: Conceptualization, Investigation, Data curation, Writing – original draft, Writing – review & editing. **Marcia Huber:** Conceptualization, Software, Investigation, Writing – original draft, Writing – review & editing.

7.5.3 Personal contribution

For this paper, I wrote the code needed to parse through the data, sort the mixtures into categories, estimate the mixture surface tension using the parachor method implemented in REFPROPv10, evaluate the deviation from the experimental measurements and create all the figures in the paper. I also wrote the code to fit the binary interaction parameter to the data.

7.6 Paper 5 – Depressurization of CO_2 in a pipe: Effect of initial state on non-equilibrium two-phase flow

Published in the International Journal of Multiphase Flow, vol 170 (2024)
doi:10.1016/j.ijmultiphaseflow.2023.104624
Authors: Alexandra Metallinou Log, Morten Hammer, Han Deng, Anders Austegard, Armin Hafner and Svend Tollak Munkejord

7.6.1 Summary of paper

In this paper, we investigate how the non-equilibrium boiling effects change for CO_2 pipe depressurization tests conducted at various initial temperatures. We conducted four new pipe depressurization tests, and further investigated the results of three previous tests presented by Munkejord et al. [32]. The set of initial temperatures cover most of the relevant temperature range for high-capacity CO_2 transportation in the context of CCS. The data is made openly available at Zenodo [191].

We find interesting trends in the pressure evolution recorded by the sensors closest to the open end of the pipe for the various initial temperatures. For the two warmest tests (see Table 6.3), the pressure recordings suggest that phase change occurs close to the local saturation pressure and the flow chokes shortly afterwards. For the remaining colder experiments, the pressure recordings show a pressure undershoot and recovery. We show the common phenomena observed for the colder tests close to the open end and close to the closed end of the pipe in Figure 7.6. Interestingly, the colder tests also display a pressure hump, where the pressure remains elevated after the pressure recovery for about 50 ms to 150 ms. We believe that this effect is caused by a positive feedback loop, or chain reaction, of bubble-breakup and growth providing enhanced boiling at the pipe's outlet, somewhat restricting the flow at the open end, as proposed by Ivashnyov et al. [90] for the Edwards and O'Brien [15] water pipe blowdown tests.

The experimental results are compared to those of the HRM*, and the HEM. For the relaxation model, we apply the well-known HRM-type

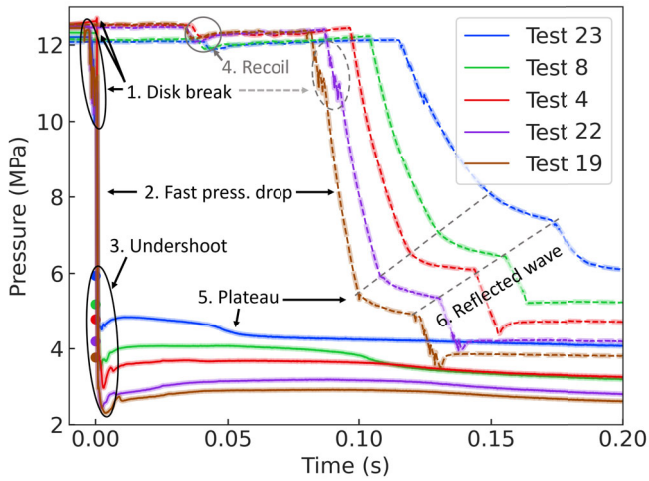

Figure 7.6: Measured pressure at $x = 0.28\,\mathrm{m}$ (solid lines) and $x = 49.98\,\mathrm{m}$ (dashed lines) for Tests 23, 8, 4, 22 and 19. Shaded regions show the 95% confidence interval of the measurements. Circular markers show where the liquid isentrope passes the saturation line for each experiment.

mass transfer model,

$$\Gamma = \rho \frac{x_{g,\mathrm{sat}} - x_g}{\theta}, \tag{7.1}$$

and fit the relaxation time θ for each experiment such that it matches the largest pressure undershoot recorded by one of the three sensors closest to the pipe's open end, PT201-PT203. The governing equations are solved using a two-step solution scheme, where the contribution of mass transfer is solved implicitly.

A novel Bernoulli-choking pressure outflow BC is presented for the HRM*, where a ghost cell is applied. The BC was designed to not restrict the non-equilibrium predicted in the computational domain, by assuming frozen flow at the outlet (i.e. no phase change) and searching for the pressure where the flow would choke. This ensures that the obtained non-equilibrium is determined by the mass-transfer model and not the BC. For warm cases, the state in the boundary ghost cell reaches the

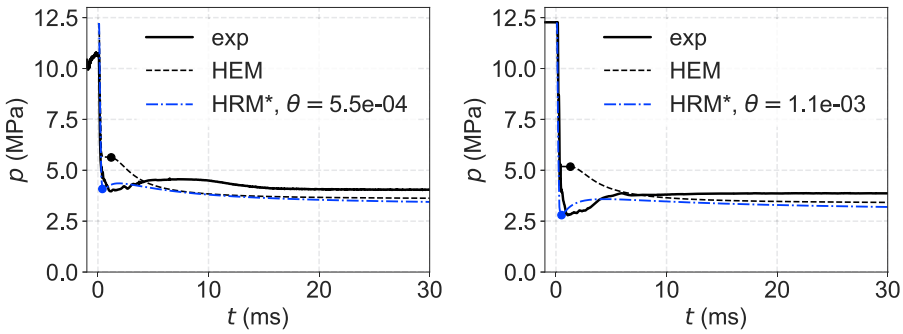

(a) Test 23: $p_0 = 12.19\,\text{MPa}$, $T_0 = 31.5\,°\text{C}$ (b) Test 8: $p_0 = 12.22\,\text{MPa}$, $T_0 = 24.6\,°\text{C}$

Figure 7.7: Measured (full lines) and simulated pressure (dashed lines) at $x = 0.08\,\text{m}$ from open end for Tests 8 and 23. Markers show where $x_g > 0.001$ for the simulations, illustrating where two-phase flow begins.

stability limit before the flow chokes. In this case, the choking pressure is searched for along the stability limit by adding the minimum amount of mass-transfer to keep the thermodynamic state in the ghost cell stable.

We find that the relaxation time for the HRM* increases with decreasing initial temperature and propose a correlation for the relaxation time which can be tested against new data. We show the modeled and measured pressure evolution for Test 8 and Test 23, 8 cm from the open end of the pipe in Figure 7.7. As expected, the HRM* is able to capture the recorded pressure undershoot whereas the HEM is not. However, we find it unlikely that the HRM* captures the correct temperature during the pressure undershoot because it predicts superheats beyond the homogeneous superheat limit. Neither HEM nor HRM* are able to capture the pressure hump.

We finally investigate the flashing inception in the experiments based on the pressure recordings 8 cm from the open end. Similar to our findings in the Conference paper summarized in Section 7.2, and in agreement with the findings of Wilhelmsen and Aasen [117], there is a transition of the maximum superheat being determined by homogeneous nucleation to

heterogeneous nucleation. This occurs for an initial temperature in the region of $14.9\,°C < T_0 < 21.1\,°C$ with an initial pressure around 12 MPa. The HRM* does not capture the flashing inception well. We hypothesize that the flashing inception can be captured if we apply a physics-based mass-transfer rate, where homogeneous and heterogeneous nucleation is accounted for.

7.6.2 Author contributions

Alexandra Metallinou Log: Conceptualization, Methodology, Software, Data curation, Formal analysis, Investigation, Visualization, Writing – original draft, Writing – review & editing. **Morten Hammer:** Conceptualization, Methodology, Software, Writing – review & editing, Supervision. **Han Deng:** Software, Data curation, Investigation, Writing – review & editing. **Anders Austegard:** Software, Investigation, Resources, Writing – review & editing. **Armin Hafner:** Writing – review & editing, Supervision. **Svend Tollak Munkejord:** Conceptualization, Methodology, Writing – review & editing, Supervision, Funding acquisition.

7.6.3 Personal contribution

For this paper, I helped conduct the new experiments and analyzed the experimental results and trends for different initial temperatures. I implemented the HLLC solver and the implicit integration scheme applied for the mass transfer term. I also developed and implemented the novel Bernoulli-choking pressure BC. I ran the test cases, suggested the correlation for the relaxation time and fitted the correlation to the data. Finally, I wrote the paper.

7.7 Paper 6 – A flashing flow model for the rapid depressurization of CO_2 in a pipe accounting for bubble nucleation and growth

Published in the International Journal of Multiphase Flow, vol 171 (2024)
doi:10.1016/j.ijmultiphaseflow.2023.104666
Authors: Alexandra Metallinou Log, Morten Hammer and Svend Tollak Munkejord

7.7.1 Summary of paper

In this paper, we present a flashing flow model with a physics-based model for homogeneous bubble nucleation. A correlation is applied to account for heterogeneous bubble nucleation in the model. The flow model is based on the governing equations of the HRM*, but with additional transport equations for the bubble number density and the interfacial area in the flow. We denote the model the homogeneous flashing model (HFM).

In the HFM, the homogeneous nucleation is modeled using CNT and is thus fully predictive. The heterogeneous nucleation is modeled using constant rates of mass transfer and bubble creation. We choose these constant rates to fit our experiments and apply the same constants for all the tests. Bubble growth is modeled based on the evaporation flux estimated by Kjelstrup and Bedeaux [181] and bubble breakup is modeled based on a critical Weber number chosen to fit all the experiments.

We compare the HFM's results against three CO_2 pipe depressurization tests with very different flashing characteristics: Test 6 with an initial condition of $T = 40.0\,°C$, $p = 10.4\,MPa$, Test 4 with an initial condition of $T = 21.1\,°C$, $p = 12.5\,MPa$ and Test 25 with an initial condition of $T = 4.6\,°C$, $p = 12.3\,MPa$. Test 25 is first reported in this paper, and its data is made openly available at Zenodo [192]. We further provide the results of the HEM and HRM* with the correlation for the relaxation time provided in Paper 5 for comparison. The HFM captures both the pressure evolutions and pressure profile in the pipe well. However, for Test 25 the flashing inception is not captured by HFM, suggesting that

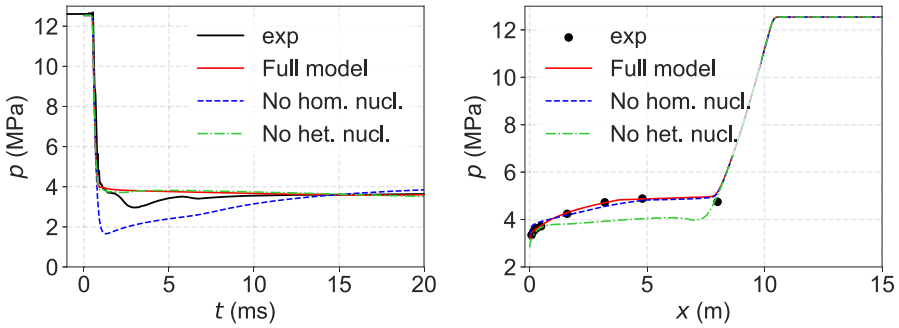

(a) Modeled and measured pressure at 28 cm from the open end of the pipe.

(b) Modeled and measured pressure along the pipe at $t = 20$ ms after disk rupture.

Figure 7.8: Effect on the HFM when the homogeneous nucleation model or the heterogeneous nucleation model is omitted.

the present model for heterogeneous nucleation is too simple.

Finally, we investigate the effect of the models for homogeneous and heterogeneous nucleation for the initial conditions of Test 4. The results are shown in Figure 7.8. We find that the homogeneous nucleation plays a main role in limiting the attained superheat and pressure undershoot near the open end of the pipe as shown in Figure 7.8a. However, heterogeneous nucleation plays a major role in initiating boiling further inside the pipe. When heterogeneous nucleation is ignored, boiling does not initiate further inside the pipe and therefore a much too low pressure plateau is established, as shown in Figure 7.8b. Thus, even for a relatively warm case where homogeneous nucleation is expected to dominate, heterogeneous nucleation is key to capture the full flashing process inside the pipe.

The present findings show the importance of modeling both homogeneous and heterogeneous nucleation in CO_2 pipe transport systems. The model applied for homogeneous nucleation is fully predictive and can be readily incorporated in CCS engineering tools to determine the superheat and pressure undershoot that will be reached during rapid depressurizations of liquid CO_2 near its critical point. The results on the

role of homogeneous and heterogeneous nucleation are also valuable in a broader engineering context as they should hold generally for flashing flows with different fluids and flashing through various geometries such as valves and orifices. More research will be needed to develop accurate mass-transfer models for heterogeneous nucleation.

7.7.2 Author contributions

Alexandra Metallinou Log: Conceptualization, Methodology, Software, Data curation, Formal analysis, Investigation, Visualization, Writing – Original Draft. **Morten Hammer:** Conceptualization, Software, Supervision, Writing – Review & Editing. **Svend Tollak Munkejord:** Conceptualization, Supervision, Writing – Review & Editing, Funding acquisition.

7.7.3 Personal contribution

For this paper, I conducted the related literature study, proposed the mass transfer model and implemented it in our pipe flow code. This includes the homogeneous and heterogeneous bubble nucleation terms, the evaporation term, and the bubble breakup term. I investigated the effect of the bubble growth caused by evaporation in different regions of the phase diagram. I implemented the transport equations for interfacial surface area density and bubble number density. I ran all the test cases, investigated the effects of the homogeneous and heterogeneous nucleation models and wrote the paper. I conducted depressurization Test 25, and curated its data.

8 Conclusions and further work

In this chapter, the main findings, conclusions and suggestions for further work are provided.

8.1 Conclusions

In this work, the depressurization of CO_2 in pipes has been studied with the hypothesis that incorporating more physics in the relevant flow models will improve their predictive ability. A main focus of the work has been to develop physics-based mass transfer models for the phase change during flashing. In this context, it was found that both homogeneous and heterogeneous bubble nucleation must be accounted for.

In order to investigate how the non-equilibrium effects during flashing varies for the depressurization of CO_2 in pipes at different initial conditions, and to provide valuable validation data for flow models, five full-bore depressurization tests were conducted. The initial conditions of the tests were chosen to complement the three full-bore depressurization tests conducted by Munkejord et al. [32], and the full set of experiments have initial temperatures ranging from 5 °C to 40 °C with an initial pressure around 12 MPa. The trend in the maximum attained superheat recorded near the open end of the pipe was analyzed, and it was verified that these tests follow the same trend as has been observed for previous works on flashing flows [18, 19, 22, 117]: there is a crossover from homogeneous nucleation determining the maximum attained superheat at warm temperatures near the critical point, to heterogeneous nucleation at colder temperatures. Further inside the pipe, where the depressurization rate is lower, smaller pressure undershoots and superheats were observed.

Homogeneous bubble nucleation can be modeled by classical nucleation theory (CNT). For heterogeneous nucleation, CNT cannot explain experimentally observed results on how the superheat limit varies with initial temperature and depressurization rate. Instead, the crevice model

should be applied as it is consistent with experimental observations. In the crevice model it is assumed that there are several trapped bubbles in crevices which serve as nucleation sites for bubbles in the flow. The combination of trapped vapor bubbles with models of bubble growth can explain the experimentally observed effects regarding the variation of attainable superheat and pressure undershoot.

A flashing flow model is proposed where homogeneous and heterogeneous nucleation is included, in addition to bubble growth/evaporation into the bubble, coalescence and breakup. This model is denoted the homogeneous flashing model (HFM). As opposed to simpler phenomenological models, the HFM does not require fitting to individual test cases. Thus, by including more physics in the model, the predictive ability of the model is indeed improved.

A key finding when analyzing the HFM is that homogeneous nucleation dominates near the open end of the pipe during depressurization at high temperatures (near the critical point), and heterogeneous nucleation dominates further inside the pipe. Without heterogeneous nucleation activated in HFM, the pressure would become much too low further inside the pipe as boiling would not be activated there. Thus, even though homogeneous nucleation dominates in limiting the superheat during flashing at warm temperatures, heterogeneous nucleation still plays a key role in the flashing process. Simulations which try to capture the pressure evolution along the length of a pipe during depressurization must therefore also include heterogeneous nucleation. However, if the goal is only to simulate the outflow, it may be reasonable to only consider homogeneous nucleation using CNT, as is done in the delayed homogeneous equilibrium model (D-HEM) of Hammer et al. [14].

One of the main parameters in CNT is the surface tension, and thus, to predict the homogeneous superheat limit of CO_2-rich mixtures, the mixture surface tension must be estimated. A common method for estimating mixture surface tensions is the parachor method, however its accuracy had not been tested extensively. To determine the accuracy of the parachor method, the method was tested against experimental data for a series of binary mixtures. Though there was little data available for CO_2 mixtures, it was found that the method generally performed better

for molecules of similar sizes, while a correction factor was needed for molecules with very different lengths.

When studying different flow models, it is important to apply accurate and robust numerical solution methods. During the thesis work, the HLLC finite-volume method has been extended to model equilibrium flow through ducts with discontinuous area changes, and for non-equilibrium flow in pipes with a constant cross-section. For non-equilibrium flow, a semi-implicit numerical solution approach was suggested, where the homogeneous part of the system is solved with the HLLC FVM explicitly, and the relaxation step, where phase change is added, is solved implicitly. This approach is necessary for simulations close to the critical point, where the thermodynamic state of the flow after the homogeneous solution step can be unstable. Furthermore, the Bernoulli-choking-pressure BC suggested by Munkejord and Hammer [10] was extended for non-equilibrium flow, and designed to ensure that it would not restrict the non-equilibrium calculated by the flashing flow model in the computational domain. Special handling was considered for outflows reaching the stability limit, ensuring a stable solution for the boundary ghost cell. The semi-implicit solution scheme and the novel BC were successfully applied for the CO_2 pipe depressurization simulations. These methods may later be applied in coupled CFD-structure models for the prediction of running ductile fractures in CO_2-carrying pipelines.

Though the present work is motivated by the need for accurate estimates of flashing flows in the context of CO_2 transportation for CCS, the results are general and valid for different fluids. As the operating region for CO_2 transportation pipelines will bring the fluid state close to the critical point during depressurization, special considerations have been made both in the numerical methods and mass-transfer models in this work. The results are therefore particularly relevant for other industrial applications where the fluid will be close to its critical point under depressurization, such as transcritical CO_2 refrigeration systems. The results regarding the modeling of heterogeneous nucleation are relevant both close to the critical point and for lower relative temperatures and pressures. Though the crevice model has been identified as the best model for heterogeneous nucleation, as it can explain experimentally observed

effects, there are still many unknowns in this model such as the population density of unwetted crevices on the wall or impurities in the flow. In order to develop fully predictive physics-based models for flashing flows, it will therefore be necessary to investigate heterogeneous nucleation based on the crevice model in more detail.

8.2 Further work

The present work has provided valuable insight on the importance of the physical effects during flashing such as homogeneous and heterogeneous nucleation. However, the most accurate methods to model heterogeneous nucleation, bubble growth and interfacial area in the flow have not yet been determined, and investigating this will be a relevant topic for further work.

It is recommended to investigate heterogeneous nucleation based on the crevice model in more detail. For simplicity, heterogeneous nucleation was modeled by constant rates of mass transfer and bubble creation in this work. However, it is reasonable to assume that the heterogeneous nucleation rate of bubbles depends on the heat transfer from the wall and the liquid phase, and the local superheat at the wall. Furthermore, the mass of the nucleated bubbles depends on how the bubbles grow and detach from the wall. As the population density of nucleation sites (unwetted crevices) is unknown, it will be difficult to determine a fully predictive model for heterogeneous nucleation. As a first step, the correlation of Shin and Jones [88] and Blinkov et al. [89] for water can be investigated and adapted for CO_2 based on the data from the present experimental campaign. It would also be interesting to investigate if a correlation can be made based on fluid-surface properties and the wall roughness.

As heterogeneous nucleation is likely connected to the bubble growth, it is also relevant to study different bubble growth models to improve estimates of heterogeneous nucleation. The bubble growth model applied in HFM is based on linearized non-equilibrium thermodynamics. It could be interesting to test the model by Lund and Aursand [180] based on (non-linear) statistical rate theory, and models based on heat transfer from the wall and the liquid phase to the bubbles. Heat-transfer-based bubble

growth models are most common in the literature. The present work focused on the four-equation two-phase flow model, which does not allow a temperature difference between the phases. To apply a heat-transfer-based bubble growth model, any of the homogeneous flow models that allow for (or enforce) a temperature difference can be applied instead: the six-equation model, the five-equation model, DEM and HRM. Testing one of these models with the HFM mass-transfer model and heat-transfer-based bubble growth would be a natural next step for further work.

Once the most accurate and robust mass-transfer models have been determined, the HFM can be applied in a coupled CFD-structure model to determine the effect of non-equilibrium flashing on a running-ductile fracture. In order to couple these models, it will likely be necessary to improve the suggested boundary condition for non-equilibrium flows. The boundary condition developed in the present work assumes frozen flow at the pipe outlet. However, phase change would occur here as well. The assumption of frozen flow might cause the first grid cells of the computational domain to achieve a too low pressure, thus providing a too low driving force for the fracture in a coupled model. The effect of mass-transfer at the boundary can be included by linearizing the characteristic equations of the flow and using these to estimate the flow at the boundary.

Finally, the heterogeneous superheat limit and the pressure recovery caused by bubble growth appear to be correlated in this work. Thus, it may be possible to determine the heterogeneous superheat limit based on the pressure recovery caused by bubble growth and the depressurization rate of the fluid. Investigating the heterogeneous superheat limit based on bubble growth would be an interesting avenue for future research. If the heterogeneous superheat limit is derived, D-HEM can be extended to determine, e.g., the critical flow in nozzles for all temperatures, and not only near the critical point. To validate a model for the heterogeneous superheat limit, it would be highly useful to conduct a series of critical flow experiments like those conducted by Hesson and Peck [122] from initially saturated states with initial temperatures ranging from the critical point to the triple point of CO_2.

Bibliography

[1] Masson-Delmotte, V., Zhai, P., Pörtner, H.O., Roberts, D., Skea, J., Shukla, P.R., Pirani, A., Moufouma-Okia, W., Péan, C., Pidcock, R., Connors, S., Matthews, J.B.R., Chen, Y., Zhou, X., Gomis, M.I., Lonnoy, E., Maycock, T., Tignor, M., and Waterfield, T. Global Warming of 1.5°C. An IPCC Special Report on the impacts of global warming of 1.5°C above pre-industrial levels and related global greenhouse gas emission pathways, in the context of strengthening the global response to the threat of climate change, sustainable development, and efforts to eradicate poverty. Technical report, IPCC, 2018. URL `https://report.ipcc.ch/sr15/pdf/sr15_spm_final.pdf`.

[2] IPCC. Summary for Policymakers. In *Climate Change 2022: Mitigation of Climate Change. Contribution of Working Group III to the Sixth Assessment Report of the Intergovernmental Panel on Climate Change*. Cambridge University Press, Cambridge, UK and New York, NY, USA, 2022. doi:10.1017/9781009157926.001. URL `https://www.ipcc.ch/report/ar6/wg3/`.

[3] IEA. *Net Zero by 2050 – A Roadmap for the Global Energy Sector*. IEA, Paris, 2021. URL `https://www.iea.org/reports/net-zero-by-2050`. Accessed 2023-08-17.

[4] IEA. *World Energy Outlook 2022*. IEA, Paris, 2022. URL `https://www.iea.org/reports/world-energy-outlook-2022`. Accessed 2023-08-17.

[5] Tosun, J., Biesenbender, S., and Schulze, K., editors. *Energy Policy Making in the EU - Building the Agenda, Chapter 11.4*. Springer, Munich, 2015. ISBN 978-1-4471-6645-0.

[6] The Norwegian Ministry of Petroleum and Energy. Capture, transport and storage of CO_2. URL `https://www.regjeringen.no/e`

n/topics/energy/carbon-capture-and-storage/capture-transport-and-storage-of-co2/id443518/. Accessed 2020-05-31.

[7] Northern lights - A European CO_2 transport and storage network. URL https://northernlightsccs.com/. Accessed 2020-05-30.

[8] Cosham, A. and Eiber, R.J. Fracture control in carbon dioxide pipelines – The effect of impurities. In *7th International Pipeline Conference, IPC2008*, volume 3, pages 229–240, Calgary, Canada, 29 Sep–03 Oct 2008. ASME, IPTI. doi:10.1115/IPC2008-64346.

[9] Roussanaly, S., Bureau-Cauchois, G., and Husebye, J. Costs benchmark of CO_2 transport technologies for a group of various size industries. *Int. J. Greenh. Gas Con.*, 12:341–350, January 2013. doi:10.1016/j.ijggc.2012.05.008.

[10] Munkejord, S.T. and Hammer, M. Depressurization of CO_2-rich mixtures in pipes: Two-phase flow modelling and comparison with experiments. *Int. J. Greenh. Gas Con.*, 37:398–411, June 2015. doi:10.1016/j.ijggc.2015.03.029.

[11] Klinkby, L., Nielsen, C.M., Krogh, E., Smith, I.E., Palm, B., and Bernstone, C. Simulating rapidly fluctuating CO_2 flow into the Vedsted CO_2 pipeline, injection well and reservoir. In Gale, J., Hendriks, C., and Turkenberg, W., editors, *GHGT-10 – 10th International Conference on Greenhouse Gas Control Technologies*, pages 4291–4298, Amsterdam, The Netherlands, 2011. IEAGHGT, Energy Procedia vol. 4. doi:10.1016/j.egypro.2011.02.379.

[12] Munkejord, S.T., Hammer, M., and Løvseth, S.W. CO_2 transport: Data and models – A review. *Appl. Energ.*, 169:499–523, May 2016. doi:10.1016/j.apenergy.2016.01.100.

[13] Pham, L.H.H.P. and Rusli, R. A review of experimental and modelling methods for accidental release behaviour of high-pressurised CO_2 pipelines at atmospheric environment. *Process Saf. Environ.*, 104:48–84, 2016. doi:10.1016/j.psep.2016.08.013.

[14] Hammer, M., Deng, H., Austegard, A., Log, A.M., and Munkejord, S.T. Experiments and modelling of choked flow of CO_2 in orifices and nozzles. *Int. J. Multiphase Flow*, 156:104201, November 2022. doi:10.1016/j.ijmultiphaseflow.2022.104201.

[15] Edwards, A.R. and O'Brien, T.P. Studies of phenomena connected with the depressurization of water reactors. *J. British Nuclear Energy Society*, 9(2):125–135, 1970. URL `https://senior.app.box.com/v/BNES-VOL9-2`.

[16] Reocreux, M. *Contribution to the study of critical flow rates in a water-vapour two-phase flow*. Dr. ing. thesis, Universite Grenoble Alpes, Grenoble, France, 1974. URL `https://inis.iaea.org/search/search.aspx?orig_q=RN:48026127`.

[17] Lienhard, J.H., Alamgir, M., and Trela, M. Early response of hot water to sudden release from high pressure. *J. Heat Trans. – T. ASME*, 100(3):473–479, August 1978. doi:10.1115/1.3450833.

[18] Alamgir, M. and Lienhard, J.H. Correlation of Pressure Undershoot During Hot-Water Depressurization. *J. Heat Transfer*, 103(1):52–55, February 1981. doi:10.1115/1.3244429.

[19] Barták, J. A study of the rapid depressurization of hot water and the dynamics of vapour bubble generation in superheated water. *Int. J. Multiphase Flow*, 16:789–798, September 1990. doi:10.1016/0301-9322(90)90004-3.

[20] Liao, Y. and Lucas, D. Computational modelling of flash boiling flows: A literature survey. *Int. J. Heat Mass Tran.*, 111:246–265, August 2017. doi:10.1016/j.ijheatmasstransfer.2017.03.121.

[21] Liao, Y. and Lucas, D. A review on numerical modelling of flashing flow with application to nuclear safety analysis. *Appl. Therm. Eng.*, 182:116002, 2021. doi:10.1016/j.applthermaleng.2020.116002.

[22] Elias, E. and Chambré, P.L. Flashing Inception in Water During Rapid Decompression. *J. Heat Transfer*, 115(1):231–238, 02 1993. doi:10.1115/1.2910654.

[23] Mahgerefteh, H., Oke, A., and Atti, O. Modelling outflow following rupture in pipeline networks. *Chem. Eng. Sci.*, 61(6):1811–1818, March 2006. doi:10.1016/j.ces.2005.10.013.

[24] Jie, H.E., Xu, B.P., Wen, J.X., Cooper, R., and Barnett, J. Predicting the decompression characteristics of carbon dioxide using computational fluid dynamics. In *9th International Pipeline Conference IPC2012*, pages 585–595, Calgary, Canada, September 2012. ASME, IPTI. doi:10.1115/IPC2012-90649.

[25] Mahgerefteh, H., Brown, S., and Denton, G. Modelling the impact of stream impurities on ductile fractures in CO_2 pipelines. *Chem. Eng. Sci.*, 74:200–210, May 2012. doi:10.1016/j.ces.2012.02.037.

[26] Martynov, S., Brown, S., Mahgerefteh, H., Sundara, V., Chen, S., and Zhang, Y. Modelling three-phase releases of carbon dioxide from high-pressure pipelines. *Process Saf. Environ.*, 92(1):36–46, 2014. doi:10.1016/j.psep.2013.10.004.

[27] Elshahomi, A., Lu, C., Michal, G., Liu, X., Godbole, A., and Venton, P. Decompression wave speed in CO_2 mixtures: CFD modelling with the GERG-2008 equation of state. *Appl. Energ.*, 140: 20–32, 2015. doi:10.1016/j.apenergy.2014.11.054.

[28] Aursand, E., Aursand, P., Hammer, M., and Lund, H. The influence of CO_2 mixture composition and equations of state on simulations of transient pipeline decompression. *Int. J. Greenh. Gas Con.*, 2016. doi:10.1016/j.ijggc.2016.07.004. In Press.

[29] Talemi, R.H., Brown, S., Martynov, S., and Mahgerefteh, H. Hybrid fluid-structure interaction modelling of dynamic brittle fracture in steel pipelines transporting CO_2 streams. *Int. J. Greenh. Gas Con.*, 54(2):702–715, November 2016. doi:10.1016/j.ijggc.2016.08.021.

[30] Gu, S., Li, Y., Teng, L., Hu, Q., Zhang, D., Ye, X., Wang, C., Wang, J., and Iglauer, S. A new model for predicting the decompression behavior of CO_2 mixtures in various phases. *Process Saf. Environ.*, 120:237–247, 2018. doi:10.1016/j.psep.2018.08.034.

[31] Talemi, R.H., Cooreman, S., Mahgerefteh, H., Martynov, S., and Brown, S. A fully coupled fluid-structure interaction simulation of three-dimensional dynamic ductile fracture in a steel pipeline. 101: 224–235, June 2019. doi:10.1016/j.tafmec.2019.02.005.

[32] Munkejord, S.T., Austegard, A., Deng, H., Hammer, M., Stang, H.G.J., and Løvseth, S.W. Depressurization of CO_2 in a pipe: High-resolution pressure and temperature data and comparison with model predictions. *Energy*, 211:118560, November 2020. doi:10.1016/j.energy.2020.118560.

[33] Munkejord, S.T., Deng, H., Austegard, A., Hammer, M., Skarsvåg, H.L., and Aasen, A. Depressurization of CO_2-N_2 and CO_2-He in a pipe: Experiments and modelling of pressure and temperature dynamics. *Int. J. Greenh. Gas Con.*, 109:103361, July 2021. doi:10.1016/j.ijggc.2021.103361.

[34] De Lorenzo, M., Lafon, P., Seynhaeve, J.M., and Bartosiewicz, Y. Benchmark of delayed equilibrium model (DEM) and classic two-phase critical flow models against experimental data. *Int. J. Multiphase Flow*, 92:112–130, 2017. doi:10.1016/j.ijmultiphaseflow.2017.03.004.

[35] Brown, S., Martynov, S., Mahgerefteh, H., and Proust, C. A homogeneous relaxation flow model for the full bore rupture of dense phase CO_2 pipelines. *Int. J. Greenh. Gas Con.*, 17:349–356, 2013. doi:10.1016/j.ijggc.2013.05.020.

[36] Brown, S., Martynov, S., Mahgerefteh, H., Chen, S., and Zhang, Y. Modelling the non-equilibrium two-phase flow during depressurisation of CO_2 pipelines. *Int. J. Greenh. Gas Con.*, 30:9–18, 2014. doi:10.1016/j.ijggc.2014.08.013.

[37] Liu, B., Liu, X., Lu, C., Godbole, A., Michal, G., and Tieu, A.K. Multi-phase decompression modeling of CO_2 pipelines. *Greenh. Gas. Sci. Tech.*, 7(4):665–679, February 2017. doi:10.1002/ghg.1666.

[38] Liu, B., Liu, X., Lu, C., Godbole, A., Michal, G., and Tieu, A.K. A CFD decompression model for CO_2 mixture and the influence of non-equilibrium phase transition. *Appl. Energ.*, 227:516–524, October 2018. doi:10.1016/j.apenergy.2017.09.016.

[39] Flechas, T., Laboureur, D.M., and Glover, C.J. A 2-D CFD model for the decompression of carbon dioxide pipelines using the Peng-Robinson and the Span-Wagner equation of state. *Process Saf. Environ.*, 140:299–313, August 2020. doi:10.1016/j.psep.2020.04.033.

[40] Xiao, C., Lu, Z., Yan, L., and Yao, S. Transient behaviour of liquid CO_2 decompression: CFD modelling and effects of initial state parameters. *Int. J. Greenh. Gas Con.*, 101:103154, 2020. doi:10.1016/j.ijggc.2020.103154.

[41] Botros, K.K., Geerligs, J., Rothwell, B., and Robinson, T. Measurements of decompression wave speed in pure carbon dioxide and comparison with predictions by equation of state. *J. Press. Vess. – T. ASME*, 138(3), June 2016. doi:10.1115/1.4031941.

[42] LedaFlow - Advanced Transient Multiphase Flow Simulator. URL `https://ledaflow.com/`. Accessed 2023-08-11.

[43] Masella, J.M., Tran, Q.H., Ferre, D., and Pauchon, C. Transient simulation of two-phase flows in pipes. *Int. J. Multiphase Flow*, 24 (5):739–755, August 1998. doi:10.1016/S0301-9322(98)00004-4.

[44] Kjølaas, J., Stang, J., Smith, I.E., Dijkhuizen, W., Coutinho, R., Richon, V., Yang, Z., and Stene, M. Adapting the LedaFlow multiphase flow simulator to CCS. In *Trondheim Carbon Capture & Storage Conference (TCCS) 12*, Trondheim, Norway, June 2023. URL `https://az659834.vo.msecnd.net/eventsairwesteuprod/production-ntnu-public/162ce438416648929686ffb8b3ef2a9d`.

[45] Aursand, E., Dumoulin, S., Hammer, M., Lange, H.I., Morin, A., Munkejord, S.T., and Nordhagen, H.O. Fracture propagation control in CO_2 pipelines: Validation of a coupled fluid-structure model. *Eng. Struct.*, 123:192–212, September 2016. doi:10.1016/j.engstruct.2016.05.012.

[46] Skarsvåg, H.L., Hammer, M., Munkejord, S.T., Log, A.M., Dumoulin, S., and Gruben, G. Towards an engineering tool for the prediction of running ductile fractures in CO_2 pipelines. *Process Saf. Environ.*, 171:667–679, March 2023. doi:10.1016/j.psep.2023.01.054.

[47] Aursand, E., Dørum, C., Hammer, M., Morin, A., Munkejord, S.T., and Nordhagen, H.O. CO_2 pipeline integrity: Comparison of a coupled fluid-structure model and uncoupled two-curve methods. In Røkke, N. and Svendsen, H., editors, *7th Trondheim Conference on CO_2 Capture, Transport and Storage (TCCS-7)*, pages 382–391, Trondheim, Norway, June 2014. BIGCCS / SINTEF / NTNU, Energy Procedia, vol. 51. doi:10.1016/j.egypro.2014.07.045.

[48] Michal, G., Davis, B., Østby, E., Lu, C., and Røneid, S. CO2SAFE-ARREST: A full-scale burst test research program for carbon dioxide pipelines – Part 2: Is the BTCM out of touch with dense-phase CO_2? In *12th International Pipeline Conference, IPC 2018*. ASME, September 2018. doi:10.1115/IPC2018-78525.

[49] Michal, G., Østby, E., Davis, B.J., Røneid, S., and Lu, C. An empirical fracture control model for dense-phase CO_2 carrying pipelines. In *13th International Pipeline Conference, IPC 2020*. ASME, September 2020. doi:10.1115/IPC2020-9421.

[50] Illson, T. and Aarnes, J. Building trust in pipeline transportation of CO_2. *Offshore Engineer E-magazine*, May 2021. URL `https://www.maritimemagazines.com/offshore-engineer/202105/building-trust/`. Accessed 2023-07-28.

[51] X. K. Zhu. State-of-the-art review of fracture control technology for modern and vintage gas transmission pipelines. *Eng. Fract. Mech.*, 148:260–280, 11 2015. doi:10.1016/j.engfracmech.2015.05.055.

[52] M. D. Biagio, A. Lucci, E. Mecozzi, and C. M. Spinelli. Fracture Propagation Prevention on CO_2 Pipelines: Full Scale Experimental Testing and Verification Approach, 2017. URL `https://www.eprg`

.net/fileadmin/EPRG_Dokumente/2017_-_3R_-Di_Biagio_et_al_-_Fracture_in_CO2_Pipelines.pdf. Accessed 2023-11-15.

[53] Fowler, S. 'foaming at the mouth': First responders describe scene after pipeline rupture, gas leak. 2020. URL https://eu.clarionledger.com/story/news/local/2020/02/27/yazoo-county-pipe-rupture-co-2-gas-leak-first-responders-rescues/4871726002/. Accessed 2023-07-27.

[54] Mathews, W. and Ruhl, C. Failure investigation report – Denbury Gulf Coast Pipelines LLC – pipeline rupture/natural force damage. Technical report, Pipeline and Hazardous Materials Safety Administration, PHMSA, May 2022. URL https://www.phmsa.dot.gov/sites/phmsa.dot.gov/files/2022-05/Failure%20Investigation%20Report%20-%20Denbury%20Gulf%20Coast%20Pipeline.pdf. Accessed 2023-07-28.

[55] Cosham, A., Jones, D.G., Armstrong, K., Allason, D., and Barnett, J. Ruptures in gas pipelines, liquid pipelines and dense phase carbon dioxide pipelines. In *9th International Pipeline Conference, IPC2012*, volume 3, pages 465–482, Calgary, Canada, 24–28 Sep 2012. ASME, IPTI. doi:10.1115/IPC2012-90463.

[56] Cosham, A., Jones, D.G., Armstrong, K., Allason, D., and Barnett, J. Analysis of two dense phase carbon dioxide full-scale fracture propagation tests. In *10th International Pipeline Conference, IPC2014*, volume 3, Calgary, Canada, 29 Sep–3 Oct 2014. doi:10.1115/IPC2014-33080.

[57] Michal, G., Østby, E., Davis, B.J., Røneid, S., and Lu, C. An empirical fracture control model for dense-phase CO_2 carrying pipelines. volume Volume 3: Operations, Monitoring, and Maintenance; Materials and Joining of *International Pipeline Conference*, page V003T05A005, 09 2020. doi:10.1115/IPC2020-9421.

[58] Botros, K.K., Geerligs, J., Rothwell, B., and Robinson, T. Measurements of decompression wave speed in binary mixtures of carbon

dioxide mixtures and impurities. *J. Press. Vess. – T. ASME*, 139 (2), April 2017. doi:10.1115/1.4034016.

[59] BIGCCS project webpage. URL `https://www.sintef.no/projectweb/bigccs/`. Accessed 2023-08-12.

[60] Keim, V., Paredes, M., Nonn, A., and Münstermann, S. FSI-simulation of ductile fracture propagation and arrest in pipelines: Comparison with existing data of full-scale burst tests. *Int. J. Pres. Ves. Pip.*, 182:104067, May 2020. doi:10.1016/j.ijpvp.2020.104067.

[61] Aursand, P., Hammer, M., Munkejord, S.T., and Wilhelmsen, Ø. Pipeline transport of CO_2 mixtures: Models for transient simulation. *Int. J. Greenh. Gas Con.*, 15:174–185, July 2013. doi:10.1016/j.ijggc.2013.02.012.

[62] Hetland, J., Barnett, J., Read, A., Zapatero, J., and Veltin, J. CO_2 transport systems development: Status of three large European CCS demonstration projects with EEPR funding. In Dixon, T., Herzog, H., and Twinning, S., editors, *GHGT-12 – 12th International Conference on Greenhouse Gas Control Technologies*, pages 2458–2466, Austin, Texas, USA, October 2014. University of Texas at Austin / IEAGHGT, Energy Procedia, vol. 63. doi:10.1016/j.egypro.2014.11.268.

[63] Luo, X., Mistry, K., Okezue, C., Wang, M., Cooper, R., Oko, E., and Field, J. Process simulation and analysis for CO_2 transport pipeline design and operation – case study for the Humber region in the UK. In Klemeš, J.J., Varbanov, P.S., and Liew, P.Y., editors, *24th European Symposium on Computer Aided Process Engineering*, volume 33 of *Comput. Aided Chem. Eng.*, pages 1633–1638. Elsevier, 2014. doi:https://doi.org/10.1016/B978-0-444-63455-9.50107-0.

[64] Helluy, P., Hérard, J.M., and Mathis, H. A well-balanced approximate Riemann solver for compressible flows in variable cross-section ducts. *J. Comput. Appl. Math.*, 236(7):1976–1992, 2012. doi:https://doi.org/10.1016/j.cam.2011.11.008.

[65] Thanh, M.D. and Kröner, D. Numerical treatment of nonconservative terms in resonant regime for fluid flows in a nozzle with variable cross-section. *Comput. Fluids*, 66:130–139, 2012. doi:https://doi.org/10.1016/j.compfluid.2012.06.021.

[66] Brown, S., Martynov, S., and Mahgerefteh, H. Simulation of two-phase flow through ducts with discontinuous cross-section. *Comput. Fluids*, 120:46–56, 2015. doi:10.1016/j.compfluid.2015.07.018.

[67] Cuong, D.H. and Thanh, M.D. Constructing a Godunov-type scheme for the model of a general fluid flow in a nozzle with variable cross-section. *Appl. Math. Comput.*, 305:136–160, 2017. doi:https://doi.org/10.1016/j.amc.2017.01.065.

[68] Daude, F. and Galon, P. A Finite-Volume approach for compressible single- and two-phase flows in flexible pipelines with fluid-structure interaction. *J. Comput. Phys.*, 362:375–408, June 2018. doi:10.1016/j.jcp.2018.01.055.

[69] Daude, F. and Galon, P. Simulations of single- and two-phase shock tubes across abrupt changes of area and branched junctions. *Nucl. Eng. Des.*, 365, August 2020. doi:10.1016/j.nucengdes.2020.110734.

[70] Toro, E.F. *Riemann solvers and numerical methods for fluid dynamics: A practical introduction*. Springer-Verlag, Berlin, third edition, 2009. ISBN 978-3-540-25202-3.

[71] NCCS webpage. URL `https://nccs.no/`. Accessed 2023-07-28.

[72] Toro, E.F., Spruce, M., and Speares, W. Restoration of the contact surface in the HLL-Riemann solver. *Shock Waves*, 4(1):25–34, 1994. doi:10.1007/BF01414629.

[73] Lemmon, E.W., Bell, I.H., Huber, M.L., and McLinden, M.O. REFPROP, NIST Standard Reference Database 23,Version 10.0. 2018. NIST, Standard Reference Data Program, Gaithersburg, Maryland, USA.

[74] Alamgir, M., Kan, C.Y., and Lienhard, J.H. An Experimental Study of the Rapid Depressurization of Hot Water. *J. Heat Transfer*, 102(3):433–438, 08 1980. doi:10.1115/1.3244318.

[75] Riegel, B. *Contribution to the study of the depressurization of a two-phase flow system.* Dr. ing. thesis, L'Institut National Polytechnique de Grenoble, Grenoble, France, 1980. URL `https://inis.iaea.org/search/search.aspx?orig_q=RN:12599658`. Accessed 2023-08-04.

[76] Jeandey, C., D'Aillon, L.G., Bourgine, R., and Barriere, G. Auto vaporisation d'écoulements eau/vapeur. Technical Report TT-163, CEA, Grenoble, 1981.

[77] Amos, C. and Schrock, V. Critical discharge of initially subcooled water through slits. Technical Report NUREG/CR–3475, Lawrence Berkeley Laboratory, September 1983. URL `https://inis.iaea.org/search/search.aspx?orig_q=RN:15014058`. Accessed 2023-08-04.

[78] Pinhasi, G.A., Ullmann, A., and Dayan, A. Modeling of flashing two-phase flow. *Reviews in Chemical Engineering*, 21(3-4):133–264, August 2005. doi:10.1515/REVCE.2005.21.3-4.133.

[79] Bilicki, Z. and Kestin, J. Physical Aspects of the Relaxation Model in Two-Phase Flow. In *Proceedings of the Royal Society of London. Series A, Mathematical and Physical Sciences*, volume 428, pages 379–397. Royal Society, April 1990. URL `https://www.jstor.org/stable/51805`.

[80] Bilicki, Z., Kwidziński, R., and Mohammadein, S.A. Evaluation of the relaxation time of heat and mass exchange in the liquid-vapour bubble flow. *Int. J. Heat Mass Tran.*, 39(4):753–759, 1996. doi:https://doi.org/10.1016/0017-9310(95)00169-7.

[81] Downar-Zapolski, P., Bilicki, Z., Bolle, L., and Franco, J. The non-equilibrium relaxation model for one-dimensional flashing liquid flow. *Int. J. Multiphase Flow*, 22(3):473–483, 1996. doi:10.1016/0301-9322(95)00078-X.

[82] Pelanti, M. and Shyue, K.M. A mixture-energy-consistent six-equation two-phase numerical model for fluids with interfaces, cavitation and evaporation waves. *J. Comput. Phys.*, 259:331–357, 2014. doi:10.1016/j.jcp.2013.12.003.

[83] De Lorenzo, M., Lafon, P., Di Matteo, M., Pelanti, M., Seynhaeve, J.M., and Bartosiewicz, Y. Homogeneous two-phase flow models and accurate steam-water table look-up method for fast transient simulations. *Int. J. Multiphase Flow*, 95:199–219, 2017. doi:10.1016/j.ijmultiphaseflow.2017.06.001.

[84] Helluy, P., Hurisse, O., and Quibel, L. Assessment of numerical schemes for complex two-phase flows with real equations of state. *Comput. Fluids*, 196:104347, 2020. doi:10.1016/j.compfluid.2019.104347.

[85] Pelanti, M. Arbitrary-rate relaxation techniques for the numerical modeling of compressible two-phase flows with heat and mass transfer. *Int. J. Multiphase Flow*, 153:104097, 2022. doi:10.1016/j.ijmultiphaseflow.2022.104097.

[86] Winters, W.S., Jr. and Merte, J.H. Experiments and Nonequilibrium Analysis of Pipe Blowdown. *Nucl. Sci. Eng.*, 69(3):411–429, 1979. doi:10.13182/NSE79-A19959.

[87] Deligiannis, P. and Cleaver, J. The role of nucleation in the initial phases of a rapid depressurization of a subcooled liquid. *Int. J. Multiphase Flow*, 16(6):975–984, 1990. doi:10.1016/0301-9322(90)90102-O.

[88] Shin, T.S. and Jones, O.C. Nucleation and flashing in nozzles – 1. A distributed nucleation model. *Int. J. Multiphase Flow*, 19(6): 943–964, 1993. doi:10.1016/0301-9322(93)90071-2.

[89] Blinkov, V.N., Jones, O.C., and Nigmatulin, B.I. Nucleation and flashing in nozzles – 2. Comparison with experiments using a five-equation model for vapor void development. *Int. J. Multiphase Flow*, 19(6):965–986, 1993. doi:10.1016/0301-9322(93)90072-3.

[90] Ivashnyov, O.E., Ivashneva, M.N., and Smirnov, N.N. Slow waves of boiling under hot water depressurization. *J. Fluid Mech.*, 413: 149–180, 2000. doi:10.1017/S0022112000008417.

[91] Liao, Y. and Lucas, D. Numerical analysis of flashing pipe flow using a population balance approach. *Int. J. Heat Fluid Flow*, 77: 299–313, 2019. doi:10.1016/j.ijheatfluidflow.2019.05.005.

[92] Tiselj, I., Horvat, A., Cerne, G., J., J.G., Parzer, I., Mavko, B., Giot, M., Seynhaeve, J.M., Kucienska, B., and Lemonnier, H. WAHA3 code manual, Final report of the WAHALoads project. Technical report, FIKS-CT-2000-00106, EU 6th program, 2004.

[93] EUROPLEXUS. A computer program for the finite element simulation of fluid-structure systems under transient dynamic loading, 2023. URL `http://www-epx.cea.fr/`. Accessed 2023-30-07.

[94] EUROPLEXUS. EPX education and research light, 2023. URL `http://www-epx.cea.fr/index.php/epx-services/9-epx-education-and-research-light`. Accessed 2023-01-11.

[95] Ringstad, K.E., Allouche, Y., Gullo, P., Ervik, Å., Banasiak, K., and Hafner, A. A detailed review on CO_2 two-phase ejector flow modeling. *Therm. Sci. Eng. Prog.*, 20:100647, December 2020. doi:10.1016/j.tsep.2020.100647.

[96] Barroca, P., Hafner, A., Verlaat, B., Petagna, P., Hulek, W., Zwalinski, L., Hanf, P., Battistin, M., Davoine, L., and Teixeira, D. An ultra-low temperature transcritical R744 refrigeration system for future detectors at CERN LHC. *Applied Sciences*, 11(16), 2021. doi:10.3390/app11167399.

[97] Everitt, N. Large Hadron Collider moves to CO2 refrigeration. *Cooling post*, 2021. URL `https://www.coolingpost.com/world-news/large-hadron-collider-moves-to-co2-refrigeration/`. Accessed 2023-08-04.

[98] Menikoff, R. and Plohr, B.J. The Riemann problem for fluid flow of real materials. *Rev. Mod. Phys.*, 61(1):75–130, January–March 1989. doi:10.1103/RevModPhys.61.75.

[99] Saurel, R., Petitpas, F., and Abgrall, R. Modelling phase transition in metastable liquids: application to cavitating and flashing flows. *J. Fluid Mech.*, 607:313–350, July 2008. doi:10.1017/S0022112008002061.

[100] Saurel, R., Petitpas, F., and Berry, R.A. Simple and efficient relaxation methods for interfaces separating compressible fluids, cavitating flows and shocks in multiphase mixtures. *J. Comput. Phys.*, 228(5):1678–1712, March 2009. doi:10.1016/j.jcp.2008.11.002.

[101] Zein, A., Hantke, M., and Warnecke, G. Modeling phase transition for compressible two-phase flows applied to metastable liquids. *J. Comput. Phys.*, 229(8):2964–2998, April 2010. doi:10.1016/j.jcp.2009.12.026.

[102] Le Métayer, O., Massoni, J., and Saurel, R. Dynamic relaxation processes in compressible multiphase flows. Application to evaporation phenomena. In *Applied Mathematics In Savoie - AMIS 2012: Multiphase flow in industrial and environmental engineering*, volume 40, pages 103–1023, 2013. doi:10.1051/proc/201340007.

[103] Le Martelot, S., Saurel, R., and Nkonga, B. Towards the direct numerical simulation of nucleate boiling flows. *Int. J. Multiphase Flow*, 66:62–78, 2014. doi:10.1016/j.ijmultiphaseflow.2014.06.010.

[104] Lochon, H., Daude, F., Galon, P., and Hérard, J.M. Comparison of two-fluid models on steam-water transients. *ESAIM: M2AN*, 50:1631–1657, October 2016. doi:https://doi.org/10.1051/m2an/2016001.

[105] Daude, F., Berry, R., and Galon, P. A finite-volume method for compressible non-equilibrium two-phase flows in networks of elastic pipelines using the baer–nunziato model. *Comput. Methods Appl. Mech. Eng.*, 354:820–849, 2019. doi:https://doi.org/10.1016/j.cma.2019.06.010.

[106] Le Métayer, O. and Saurel, R. The Noble-Abel Stiffened-Gas equation of state. *Phys. Fluids*, 28(4):046102, April 2016. doi:10.1063/1.4945981.

[107] Lienhard, J.H., Shamsundar, N., and Biney, P.O. Spinodal lines and equations of state: A review. *Nucl. Eng. Design*, 95:297–314, 1986. doi:10.1016/0029-5493(86)90056-7.

[108] Debenedetti, P.G. *Metastable Liquids: Concepts and Principles.* Princeton University Press, 1997. ISBN 9780691213941. doi:10.1515/9780691213941.

[109] Aursand, P., Gjennestad, M.A., Aursand, E., Hammer, M., and Wilhelmsen, Ø. The spinodal of single- and multi-component fluids and its role in the development of modern equations of state. *Fluid Phase Equilib.*, 436:98–112, 2017. doi:10.1016/j.fluid.2016.12.018.

[110] Wilhelmsen, Ø., Aasen, A., Skaugen, G., Aursand, P., Austegard, A., Aursand, E., Gjennestad, M.A., Lund, H., Linga, G., and Hammer, M. Thermodynamic modeling with equations of state: Present challenges with established methods. *Ind. Eng. Chem. Res.*, 56(13): 3503–3515, March 2017. doi:10.1021/acs.iecr.7b00317.

[111] Hammer, M., Skaugen, G., and Aursand, E. Introduction to thermodynamics. `https://thermotools.github.io/thermopack/memo/intro/intro.pdf`, 2020. Accessed 2023-11-09.

[112] Blander, M. and Katz, J.L. Bubble nucleation in liquids. *AIChE Journal*, 21(5):833–848, 1975. doi:10.1002/aic.690210502.

[113] Botros, K.K., Geerligs, J., Rothwell, B., and Robinson, T. Effect of argon as the primary impurity in anthropogenic carbon dioxide mixtures on the decompression wave speed. *Can. J. Chem. Eng.*, 95(3):440–448, March 2017. doi:10.1002/cjce.22689.

[114] Log, A.M., Hammer, M., Deng, H., Austegard, A., Hafner, A., and Munkejord, S.T. Depressurization of CO_2 in pipes: Effect of initial state on non-equilibrium two-phase flow. *Int. J. Multiphase Flow*, 170, 2024. doi:10.1016/j.ijmultiphaseflow.2023.104624.

[115] Muller, D. How trees bend the laws of physics. Youtube video, 2013. URL `https://www.youtube.com/watch?v=BickMFHAZR0`. Accessed 2023-08-15.

[116] Allemann, R.T., McElfresh, A.J., Neuls, A.S., Townsend, W.C., Wilburn, N.P., and Witherspoon, M.E. High-enthalpy-water blowdown tests from a simple vessel through a side outlet. Technical report, Battelle Pacific Northwest Labs., Richland, WA (United States), 1 1971. URL `https://www.osti.gov/biblio/4023509`.

[117] Wilhelmsen, Ø. and Aasen, A. Choked liquid flow in nozzles: Crossover from heterogeneous to homogeneous cavitation and insensitivity to depressurization rate. *Chem. Eng. Sci.*, 248:117176, 2022. doi:10.1016/j.ces.2021.117176.

[118] Xu, J.L., Chen, T.K., and Chen, X.J. Critical flow in convergent-divergent nozzles with cavity nucleation model. *Exp. Therm. Fluid Sci.*, 14:166–173, February 1997. doi:10.1016/S0894-1777(96)00055-6.

[119] Burnell, J. Flow of boiling water through nozzles, orifices and pipes. *Engineering*, 164:572–576, December 1947.

[120] Friedrich, H. and Vetter, G. Influence of nozzle shape on the through flow behavior of jets for water at various thermodynamic states. *Energy*, 14:3, 1962.

[121] Pavlov, P. and Skripov, V. Kinetics of spontaneous nucleation in strongly heated liquids. *High Temperature*, 8(3):540–545, 1970.

[122] Hesson, J.C. and Peck, R.E. Flow of two-phase carbon dioxide through orifices. *AIChE Journal*, 4(2):207–210, 1958. doi:10.1002/aic.690040216.

[123] Hendricks, R.C., Simoneau, R.J., and Ehlers, R.C. Choked flow of fluid nitrogen with emphasis on the thermodynamic critical region. Technical Memorandum TM X-68107, National Aeronautics and Space Administration (NASA), Cleveland, Ohio, USA, August 1972. URL `https://ntrs.nasa.gov/citations/19720020638`.

[124] Hewitt, G.F. *Handbook of Multiphase Systems (Ed. G. Hetsroni), Chapter 2*. Hemisphere Publishing Corporation, 1982. ISBN 978-0070284609.

[125] Hammer, M., Ervik, Å., and Munkejord, S.T. Method using a density-energy state function with a reference equation of state for fluid-dynamics simulation of vapor-liquid-solid carbon dioxide. *Ind. Eng. Chem. Res.*, 52(29):9965–9978, 2013. doi:10.1021/ie303516m.

[126] Martynov, S., Zheng, W., Mahgerefteh, H., Brown, S., Hebrard, J., Jamois, D., and Proust, C. Computational and experimental study of solid-phase formation during the decompression of high-pressure CO_2 pipelines. *Ind. Eng. Chem. Res.*, 57(20):7054–7063, 2018. doi:10.1021/acs.iecr.8b00181.

[127] Osher, S. and Fedkiw, R. *Level set methods and dynamic implicit surfaces*, volume 153 of *Applied Mathematical Sciences*. Springer-Verlag, New York, 2003. ISBN 0-387-95482-1.

[128] Tryggvason, G., Bunner, B., Esmaeli, A., Juric, D., Al-Rawahi, N., Tauber, W., Han, J., Nas, S., and Jan, Y.J. A front-tracking method for the computations of multiphase flow. *J. Comput. Phys.*, 169(2):708–759, May 2001. doi:10.1006/jcph.2001.6726.

[129] She, D., Kaufman, R., Lim, H., Melvin, J., Hsu, A., and Glimm, J. Chapter 15 - front-tracking methods. In Abgrall, R. and Shu, C.W., editors, *Handbook of Numerical Methods for Hyperbolic Problems*, volume 17 of *Handbook of Numerical Analysis*, pages 383–402. Elsevier, 2016. doi:https://doi.org/10.1016/bs.hna.2016.07.004.

[130] Hirt, C. and Nichols, B. Volume of fluid (VOF) method for the dynamics of free boundaries. *J. Comput. Phys.*, 39(1):201–225, 1981. ISSN 0021-9991. doi:https://doi.org/10.1016/0021-9991(81)90145-5.

[131] Ishii, M. and Hibiki, T. *Thermo-fluid Dynamics of Two-Phase Flow*. Springer US, Boston, MA, 2006. ISBN 978-0-387-28321-0. doi:10.1007/978-0-387-29187-1_9.

[132] Drew, D.A. and Passman, S.L. *Theory of Multicomponent Fluids*, volume 135 of *Applied Mathematical Sciences*. Springer-Verlag, New York, 1999. ISBN 0-387-98380-5.

[133] Morin, A. *Mathematical modelling and numerical simulation of two-phase multi-component flows of CO_2 mixtures in pipes*. Doctoral thesis, Norwegian University of Science and Technology, Department of Energy and Process Engineering, Trondheim, August 2012. URL `http://hdl.handle.net/11250/234991`. ISBN 978-82-471-3907-3.

[134] LeVeque, R.J. *Finite Volume Methods for Hyperbolic Problems*. Cambridge University Press, Cambridge, UK, 2002. ISBN 0-521-00924-3.

[135] Baer, M.R. and Nunziato, J.W. A two-phase mixture theory for the deflagration-to-detonation transition (DDT) in reactive granular materials. *Int. J. Multiphase Flow*, 12(6):861–889, 1986. doi:10.1016/0301-9322(86)90033-9.

[136] Linga, G. and Flåtten, T. A hierarchy of non-equilibrium two-phase flow models. *ESAIM: ProcS*, 66:109–143, September 2019. doi:10.1051/proc/201966006.

[137] De Lorenzo, M. *Modelling and numerical simulation of metastable two-phase flows*. PhD thesis, Université Paris-Saclay, Ecole Polytechnique, Palaiseau, 2018. URL `https://pastel.hal.science/tel-01889103`. Accessed 2023-07-10.

[138] Kapila, A.K., Menikoff, R., Bdzil, J.B., Son, S.F., and Stewart, D.S. Two-phase modeling of deflagration-to-detonation transition in granular materials: Reduced equations. *Phys. Fluids*, 13(10): 3002–3024, October 2001. doi:10.1063/1.1398042.

[139] Petitpas, F., Saurel, R., Franquet, E., and Chinnayya, A. Modelling detonation waves in condensed energetic materials: multiphase CJ conditions and multidimensional computations. *Shock Waves*, 19: 377–401, 2009. doi:10.1007/s00193-009-0217-7.

[140] Flåtten, T. and Lund, H. Relaxation two-phase flow models and the subcharacteristic condition. *Math. Mod. Meth. Appl. S.*, 21(12): 2379–2407, December 2011. doi:10.1142/S0218202511005775.

[141] Lund, H. A hierarchy of relaxation models for two-phase flow. *SIAM J. Appl. Math.*, 72(6):1713–1741, December 2012. doi:10.1137/12086368X.

[142] Collier, J.G. and Thome, J.R. *Convective boiling and condensation.* Oxford University Press, Oxford, UK, 3rd edition, 1994. ISBN 0-19-856282-9.

[143] De Lorenzo, M., Pelanti, M., and Lafon, P. HLLC-type and path-conservative schemes for a single-velocity six-equation two-phase flow model: A comparative study. *Appl. Math. Comput.*, 333:95–117, 2018. doi:10.1016/j.amc.2018.03.092.

[144] De Lorenzo, M., Lafon, P., Pelanti, M., Pantano, A., Di Matteo, M., Bartosiewicz, Y., and Seynhaeve, J.M. A hyperbolic phase-transition model coupled to tabulated EoS for two-phase flows in fast depressurizations. *Nucl. Eng. Design*, 371:110954, 2021. doi:10.1016/j.nucengdes.2020.110954.

[145] Pelanti, M. and Shyue, K.M. A numerical model for multiphase liquid–vapor–gas flows with interfaces and cavitation. *Int. J. Multiphase Flow*, 113:208–230, 2019. doi:https://doi.org/10.1016/j.ijmultiphaseflow.2019.01.010.

[146] Span, R. and Wagner, W. A new equation of state for carbon dioxide covering the fluid region from the triple-point temperature to 1100 K at pressures up to 800 MPa. *J. Phys. Chem. Ref. Data*, 25(6):1509–1596, November–December 1996. doi:10.1063/1.555991.

[147] Brennen, C.E. *Fundamentals of Multiphase Flows*, chapter Homogeneous Flows. Cambridge University Press, Pasadena, California, 2005. URL `http://brennen.caltech.edu/INTMult/multbook.pdf`. Accessed 2023-08-03.

[148] Bilicki, Z., Kestin, J., and Pratt, M.M. A reinterpretation of the results of the Moby Dick experiments in terms of the nonequilibrium model. *J. Fluids Eng.*, 112(2):212–217, 06 1990. doi:10.1115/1.2909390.

[149] Angielczyk, W., Bartosiewicz, Y., Butrymowicz, D., and Seynhaeve, J.M. 1-D modeling of supersonic carbon dioxide two-phase flow through ejector motive nozzle. In *International Refrigeration and Air Conditioning Conference*. Purdue University, July 2010. URL `https://docs.lib.purdue.edu/iracc/1102/`.

[150] Nakagawa, M., Berana, M.S., and Kishine, A. Supersonic two-phase flow of CO_2 through converging-diverging nozzles for the ejector refrigeration cycle. *Int. J. Refrig.*, 32(6):1195–1202, 2009. doi:10.1016/j.ijrefrig.2009.01.015.

[151] Haida, M., Smolka, J., Hafner, A., Palacz, M., Banasiak, K., and Nowak, A.J. Modified homogeneous relaxation model for the r744 trans-critical flow in a two-phase ejector. *Int. J. Refrig.*, 85:314–333, 2018. doi:https://doi.org/10.1016/j.ijrefrig.2017.10.010.

[152] Lackme, C. Incompleteness of the flashing of a supersaturated liquid and sonic ejection of the produced phases. *Int. J. Multiphase Flow*, 5(2):131–141, 1979. doi:10.1016/0301-9322(79)90041-7.

[153] Barois, G. *Experimental study of the self-evaporation of an adiabatic upward flow of water in a duct of uniform cross section.* Dr. ing. thesis, Université Scientifique et Médicale de Grenoble, France, 1969. URL `https://inis.iaea.org/collection/NCLCollectionStore/_Public/48/026/48026149.pdf?r=1`. Accessed 2023-07-31.

[154] Feburie, V., Giot, M., Granger, S., and Seynhaeve, J.M. A model for choked flow through cracks with inlet subcooling. *Int. J. Multiphase Flow*, 19(4):541–562, 1993. doi:https://doi.org/10.1016/0301-9322(93)90087-B.

[155] Bartosiewicz, Y., Giot, M., and Seynhaeve, J.M. Revisiting modeling techniques and validation experiments for twophase choked

flows relevant to LOCA. In *Proceedings of The 8th International Topical Meeting on Nuclear Thermal-Hydraulics, Operation and Safety (NUTHOS-8) N8P0317*, page N8P0317, Shanghai, China, October 2010.

[156] Bartosiewicz, Y. and Seynhaeve, J.M. Delayed equilibrium model (DEM) of flashing flows relevant to LOCA. *Multiphase Sci. Technol.*, 25:117–131, September 2013. doi:10.1615/MultScienTechn.v25.i2-4.50.

[157] Bartosiewicz, Y. and Seynhaeve, J.M. Delayed equilibrium model (DEM) of flashing choked flows relevant to LOCA and implementation in system codes. In *Proceedings of the 2014 22nd International Conference on Nuclear Engineering*, volume Volume 2B: Thermal Hydraulics, page V02BT09A040, Prague, Czech Republic, July 2014. doi:10.1115/ICONE22-30957.

[158] Seynhaeve, J.M., Crécy, A.D., and Bartosiewicz, Y. Uncertainty analysis of delayed equilibrium model (DEM) using the CIRCE methodology. In *NURETH16*, Chicago, USA, July 2015. URL `https://glc.ans.org/nureth-16/data/papers/12971.pdf`. Accessed 2023-07-30.

[159] Angielczyk, W., Seynhaeve, J.M., Gagan, J., Bartosiewicz, Y., and Butrymowicz, D. Prediction of critical mass rate of flashing carbon dioxide flow in convergent-divergent nozzle. *Chem. Eng. Process. – Process Intensif.*, 143(4):107599, 2019. doi:10.1016/j.cep.2019.107599.

[160] Angielczyk, W., Bartosiewicz, Y., and Butrymowicz, D. Development of delayed equilibrium model for CO_2 convergent-divergent nozzle transonic flashing flow. *Int. J. Multiphase Flow*, 131:103351, 2020. doi:10.1016/j.ijmultiphaseflow.2020.103351.

[161] Lee, W.H. A pressure iteration scheme for two-phase flow modeling. In Veziroglu, T.N., editor, *Multiphase Transport Fundamentals, Reactor Safety, Applications*. Hemisphere Publishing Corporation, Washington DC, 1980. doi:10.1142/9789814460286_0004.

[162] ANSYS Fluent: 16.7.5 Evaporation-Condensation Model, 2009. URL `https://www.afs.enea.it/project/neptunius/docs/fluent/html/th/node344.htm`. Accessed 2023-08-14.

[163] Wei, J., Pan, L., Chen, D., Zhang, H., Xu, J., and Huang, Y. Numerical simulation of bubble behaviors in subcooled flow boiling under swing motion. *Nucl. Eng. Design*, 241(8):2898–2908, 2011. doi:10.1016/j.nucengdes.2011.05.008.

[164] Giacomelli, F., Mazzelli, F., and Milazzo, A. A novel CFD approach for the computation of R744 flashing nozzles in compressible and metastable conditions. *Energy*, 162:1092–1105, 2018. ISSN 0360-5442. doi:10.1016/j.energy.2018.08.050.

[165] Zhang, Z., Lu, Z., Wang, J., Liu, D., Xiao, C., and Fan, D. Effects of initial flow velocity on decompression behaviours of GLE CO_2 upstream and downstream the pipeline. *Int. J. Greenh. Gas Con.*, 118:103690, 2022. doi:10.1016/j.ijggc.2022.103690.

[166] Aasen, A., Wilhelmsen, Ø., Hammer, M., and Reguera, D. Free energy of critical droplets – from the binodal to the spinodal. *J. Chem. Phys.*, 158(11), 03 2023. doi:10.1063/5.0142533.

[167] Aursand, P., Gjennestad, M.A., Aursand, E., Hammer, M., and Wilhelmsen, Ø. The spinodal of single- and multi-component fluids and its role in the development of modern equations of state. *Fluid Phase Equilib.*, 436:98–112, 2016. doi:10.1016/j.fluid.2016.12.018.

[168] Pei, N.Q., Guo, K.H., Liu, J., and Li, T.X. Measurement of contact angle between stainless steel surface and carbon dioxide by pendant drop method. *Chinese Science Bulletin*, 53:2560–2564, 2008. doi:10.1007/s11434-008-0307-4.

[169] Wilt, P.M. Nucleation rates and bubble stability in water-carbon dioxide solutions. *J. Colloid Interf. Sci.*, 112(2):530–538, 1986. doi:10.1016/0021-9797(86)90122-0.

[170] Banasiak, K. and Hafner, A. Mathematical modelling of supersonic two-phase R744 flows through converging–diverging nozzles: The effects of phase transition models. *Appl. Therm. Eng.*, 51(1):635–643, 2013. ISSN 1359-4311. doi:10.1016/j.applthermaleng.2012.10.005.

[171] Bankoff, S.G. Entrapment of gas in the spreading of a liquid over a rough surface. *AIChE J.*, 4, 1958. doi:10.1002/aic.690040105.

[172] Apfel, R.E. The Role of Impurities in Cavitation-Threshold Determination. *J. Acoust. Soc. Am.*, 48:1179–1186, 1970. doi:10.1121/1.1912258.

[173] Atchley, A.A. and Prosperetti, A. The crevice model of bubble nucleation. *J. Acoust. Soc. Am.*, 86:1065–1084, 1989. doi:10.1121/1.398098.

[174] Chappell, M.A. and Payne, S.J. The effect of cavity geometry on the nucleation of bubbles from cavities . *J. Acoust. Soc. Am.*, 121: 853 – 862, 2007. doi:10.1121/1.2404629.

[175] Riznic, J.R. and Ishii, M. Bubble number density and vapor generation in flashing flow. *Int. J. Heat Mass Tran.*, 32(10):1821–1833, 1989. doi:10.1016/0017-9310(89)90154-3.

[176] Hsu, Y. On the Size Range of Active Nucleation Cavities on a Heating Surface. *J. Heat Transfer*, 84(3):207–213, 1962. doi:10.1115/1.3684339.

[177] Kocamustafaogullari, G. and Ishii, M. Interfacial area and nucleation site density in boiling systems. *Int. J. Heat Mass Tran.*, 26 (9):1377–1387, 1983. doi:10.1016/S0017-9310(83)80069-6.

[178] Hibiki, T. and Ishii, M. Active nucleation site density in boiling systems. *Int. J. Heat Mass Tran.*, 46(14):2587–2601, July 2003. doi:10.1016/S0017-9310(03)00031-0.

[179] Körner, S. and Friedel, L. Assessment of the maximum possible liquid superheat during flashing leak flow. *J. Loss Prev. Process Ind.*, 10(5):345–350, 1997. doi:10.1016/S0950-4230(97)00024-7.

[180] Lund, H. and Aursand, P. Two-phase flow of CO_2 with phase transfer. In Røkke, N.A., Hägg, M.B., and Mazzetti, M.J., editors, *6th Trondheim Conference on CO_2 Capture, Transport and Storage (TCCS-6)*, pages 246–255, Trondheim, Norway, 2012. BIGCCS / SINTEF / NTNU, Energy Procedia vol. 23. doi:10.1016/j.egypro.2012.06.034.

[181] Kjelstrup, S. and Bedeaux, D. *Non-equilibrium thermodynamics of heterogeneous systems*. World Scientific, 2008. doi:10.1142/6672.

[182] Liao, Y., Rzehak, R., Lucas, D., and Krepper, E. Baseline closure model for dispersed bubbly flow: Bubble coalescence and breakup. *Chem. Eng. Sci.*, 122:336–349, January 2015. doi:10.1016/j.ces.2014.09.042.

[183] Dyson, F. A meeting with Enrico Fermi. *Nature*, 427(297), 2004. doi:10.1038/427297a.

[184] Chiapolino, A., Boivin, P., and Saurel, R. A simple and fast phase transition relaxation solver for compressible multicomponent two-phase flows. *Comput. Fluids*, 150:31–45, 2017. doi:https://doi.org/10.1016/j.compfluid.2017.03.022.

[185] Log, A.M. Development and investigation of HLLC-type finite-volume methods for one and two-phase flow in pipes with varying cross-sectional area. Master's thesis, Norwegian University of Science and Technology, June 2020. URL `https://hdl.handle.net/11250/3068095`.

[186] Aursand, P., Evje, S., Flåtten, T., Giljarhus, K.E.T., and Munkejord, S.T. An exponential time-differencing method for monotonic rekaxation systems. *Appl. Numer. Math.*, 80:1–21, 2014. doi:10.1016/j.apnum.2014.01.003.

[187] Kunz, O. and Wagner, W. The GERG-2008 wide-range equation of state for natural gases and other mixtures: An expansion of GERG-2004. *J. Chem. Eng. Data*, 57(11):3032–3091, October 2012. doi:10.1021/je300655b.

[188] Hammer, M., Aasen, A., and Wilhelmsen, Ø. Thermopack. `https://github.com/thermotools/thermopack`, 2023. Accessed 2023-06-14.

[189] ECCSEL. Depressurization facility. `https://www.eccsel.org/catalogue/113`, 2021. Accessed 2023-05-23.

[190] Munkejord, S.T., Austegard, A., Deng, H., Hammer, M., Stang, H.G.J., and Løvseth, S.W. Depressurization of CO_2 in a pipe: High-resolution pressure and temperature data and comparison with model predictions – dataset. Zenodo, 2020. doi:10.5281/zenodo.3928227.

[191] Log, A.M., Hammer, M., Deng, H., Austegard, A., Hafner, A., and Munkejord, S.T. Depressurization of CO_2 in pipes: Effect of initial state on non-equilibrium two-phase flow – dataset. Zenodo, 2023. doi:10.5281/zenodo.7669536.

[192] Log, A.M., Hammer, M., and Munkejord, S.T. A flashing flow model for the rapid depressurization of CO_2 in a pipe accounting for bubble nucleation and growth – dataset. Zenodo, 2023. doi:10.5281/zenodo.8164913.

[193] Aursand, P., Hammer, M., Lavrov, A., Lund, H., Munkejord, S.T., and Torsæter, M. Well integrity for CO_2 injection from ships: Simulation of the effect of flow and material parameters on thermal stresses. *Int. J. Greenh. Gas Con.*, 62:130–141, July 2017. doi:10.1016/j.ijggc.2017.04.007.

[194] Log, A.M., Munkejord, S.T., Hammer, M., Hafner, A., Deng, H., and Austegard, A. Investigation of non-equilibrium effects during the depressurization of carbon dioxide. In *15th IIR-Gustav Lorentzen Conference on Natural Refrigerants (GL2022). Proceedings. Trondheim, Norway, June 13-15th 2022.* International Institute of Refrigeration (IIR), June 2022. doi:10.18462/iir.gl2022.0197.

[195] Log, A.M., Hammer, M., and Munkejord, S.T. A flashing flow model for the rapid depressurization of CO_2 in a pipe accounting

for bubble nucleation and growth. *Int. J. Multiphase Flow*, 171, 2024. doi:10.1016/j.ijmultiphaseflow.2023.104666.

[196] McNutt, M.K., Bradford, M., Drazen, J.M., Hanson, B., Howard, B., Jamieson, K.H., Kiermer, V., Marcus, E., Pope, B.K., Schekman, R., Swaminathan, S., Stang, P.J., and Verma, I.M. Transparency in authors' contributions and responsibilities to promote integrity in scientific publication. *Proceedings of the National Academy of Sciences*, 115(11):2557–2560, 2018. doi:10.1073/pnas.1715374115.

[197] Murillo, J. and García-Navarro. Augmented versions of the HLL and HLLC Riemann solvers including source terms in one and two dimensions for shallow flow applications. *Comput. Fluids*, 231(20): 6861–6906, 2012. doi:10.1016/j.jcp.2012.06.031.

[198] Cosham, A., Jones, D.G., Armstrong, K., Allason, D., and Barnett, J. Analysis of a dense phase carbon dioxide full-scale fracture propagation test. In *11th International Pipeline Conference, IPC2016*, volume 3, Calgary, Canada, 26–30 Sep 2016. doi:10.1115/IPC2016-64456.

[199] Thermotools. Thermopack memos, a thermotools project. `https://thermotools.github.io/thermopack/memo/index.html`, 2023. Accessed 2023-11-09.

[200] Michelsen, M.L. and Mollerup, J.M. *Thermodynamic models: Fundamentals & computational aspects*. Tie-Line Publications, Holte, Denmark, second edition, 2007. ISBN 87-989961-3-4.

Appendix

Thermodynamic library, EOS and two-phase solver in the present work

In the present work, an in-house version of the thermodynamic library Thermopack was applied for thermodynamic calculations. This library has been developed at SINTEF Energy Research and NTNU, Department of Chemistry. An open source version of Thermopack is available at [188], with much of the functionality included from the in-house version. Detailed documentation of the open source version can be found at [199].

Thermopack includes several options for equations of state including cubic EOS, multiparameter EOS and statistical associating fluid theory (SAFT) EOS. In Paper 3, Paper 5, and Paper 6, the highly accurate GERG-2008 [187] multiparameter EOS was applied for thermodynamic calculations for CO_2 and CO_2-rich mixtures. Thermopack is based on a Helmholtz free-energy formulation of the equations of state. From the Helmholtz free energy, other thermodynamic properties are derived based on its partial derivatives as described by Michelsen and Mollerup [200, Chap. 2]. Thermopack evaluates the thermodynamic properties of a given phase based on the temperature and specific volume (T, v) of the fluid. For other sets of thermodynamic variables, e.g., (p, T), (s, p), and (e, v), the properties are solved for iteratively [28].

Thermopack also contains methods to calculate phase equilibrium for different specifications (flash) of a single- or multicomponent mixture. For specified pressure, temperature and overall composition, the Gibbs free energy is minimized, and equilibrium phases are calculated. Similarly, there is an energy-density flash for maximizing the entropy to determine the equilibrium phases [28].

In the present work, where the four-equation model was applied to simulate single-component two-phase (non-equilibrium) flow, the thermodynamic state of the two-phase mixture was solved for using the fol-

lowing variables: $\alpha_g, \rho_g, \rho_\ell, T$. In this case, all thermodynamic variables for the phase $k = g, \ell$ were found using the direct T, v-formulation in Thermopack, where $v = v_k = \frac{M}{\rho_k}$ and M is the molar mass of CO_2. To determine the two-phase thermodynamic state in each grid cell of the flow simulation, the following set of equations (which satisfy the assumptions of the four-equation model) must be satisfied:

$$\boldsymbol{f} = \begin{pmatrix} \alpha_g\rho_g - (\alpha_g\rho_g)^{\text{spec}} \\ (1-\alpha_g)\rho_\ell - (\alpha_\ell\rho_\ell)^{\text{spec}} \\ \alpha_g\rho_g e_g(\rho_g, T) + (1-\alpha_g)\rho_\ell e_\ell(\rho_\ell, T) - (\rho e)^{\text{spec}} \\ p_g(\rho_g, T) - p_\ell(\rho_\ell, T) \end{pmatrix} = \mathbf{0},$$

where the superscript spec denotes known values found based on the flow equations, and the variables $p(\rho_k, T)$ and $e(\rho_k, T)$ are calculated using Thermopack's T, v-formulation. This set of equations was solved using Newton iterations, and constitutes a non-equilibrium flash calculation. As described in Chapter 5, a similar approach was later applied where the mass transfer between the phases was also accounted for in the thermodynamic solution process to ensure thermodynamically stable solutions in the numerical procedure.

As the thermodynamic computations are repeated for all grid cells, and for each time-step in the simulation, the computational time increases significantly with an increase in the number of grid cells. The computational time could be reduced by introducing look-up tables for the EOS for CO_2. The thermodynamic solution steps can also be parallelized in the flow solver to reduce run time. These run time optimizations were not applied in the present work as simulation times were short, on the scale of milliseconds, and main focus was put on modeling the mass-transfer between the phases. However, both look-up tables and parallelization will be useful for longer simulations, e.g., to simulate the complete depressurization experiments lasting for tens of seconds.

Paper 1

Log, Alexandra Metallinou; Munkejord, Svend Tollak; Hammer, Morten. (2021) HLLC-type methods for compressible two-phase flow in ducts with discontinuous area changes. *Computers & Fluids*. vol 227. doi:10.1016/j.compfluid.2021.105023

Computers and Fluids 227 (2021) 105023

Contents lists available at ScienceDirect

Computers and Fluids

journal homepage: www.elsevier.com/locate/compfluid

HLLC-type methods for compressible two-phase flow in ducts with discontinuous area changes

Alexandra Metallinou Log[a,*], Svend Tollak Munkejord[b], Morten Hammer[b]

[a] Norwegian University of Science and Technology, Department of Physics, Department of Energy and Process Engineering, Trondheim NO-7491, Norway
[b] SINTEF Energy Research, P.O. Box 4761 Torgarden, Trondheim NO-7465, Norway

ARTICLE INFO

Article history:
Received 18 December 2020
Revised 16 April 2021
Accepted 26 May 2021
Available online 29 May 2021

Keywords:
Finite-volume method
HLLC solver
Compressible flow
Non-conservative system
Two-phase flow
Variable cross-section
Nozzle flow

ABSTRACT

In this work, the Harten-Lax-van Leer Contact (HLLC) approximate Riemann solver is extended to two-phase flow through ducts with discontinuous cross-sections. Two main strategies are explored regarding the treatment of the non-conservative term arising in the governing equations. In the first, labelled HLLC+S, the non-conservative term is discretized separately. In the second, labelled HLLCS, the non-conservative term is incorporated in the Riemann solver. The methods are assessed by numerical tests for single and two-phase flow of CO_2, the latter employing a homogeneous equilibrium model where the thermodynamic properties are calculated using the Peng–Robinson equation of state. The methods have different strengths, but in general, HLLCS is found to work best. In particular, it is demonstrated to be equally accurate and more robust than existing methods for non-resonant flow. It is also well-balanced for subsonic flow in the sense that it conserves steady-state flow.

1. Introduction

The simulation of two-phase flow through ducts with discontinuous cross-sections is essential in several industrial applications. Such simulations are needed for modelling e.g. two-phase flow in wellbores in the oil and gas industry [1], nuclear reactor coolant flows [2], emergency venting of hydrocarbon pipelines [3] and cavitation in refrigeration systems [4]. Systems like those mentioned above can often be modelled as quasi one-dimensional with discontinuous changes in cross-sectional area of the flow. The system of equations modelling such flow contains a non-conservative term, and this term complicates numerical simulations greatly as it can cause numerical oscillations [5,6] and divergence [5].

Several authors have constructed numerical methods for the compressible nozzle flow equations [1,5,7–9], and systems of similar form [10–16], developing "well-balanced" [17,18] schemes to capture the flow behaviour at discontinuities. Most of the early research has focused on the special case of single-phase flow with the ideal gas equation of state (EOS). Notable schemes include Kröner and Thanh's well-balanced numerical scheme based on the Lax-Friedrichs flux [19], which was extended for resonant cases in [5], Rochette et al.'s VFRoe based scheme [6] and Cuong et al.'s Godunov scheme based on an exact Riemann solver [8]. Brown et al. [20] proposed the first methodology for resolving two-phase CO_2 flow in pipes with discontinuous cross-sectional area changes for the homogeneous equilibrium two-phase flow model (HEM) with the Peng-Robinson (PR) EOS [21] using the AUSM$^+$-up scheme. Recently, Abbasi et al. [1] developed a Godunov-type scheme for the two-phase drift-flux model with variable cross-section, though with simple EOSs for liquid and gas.

A HLLC-type method has yet to be tested on the problem of compressible flow with discontinuous cross-sections. Note, however, that the HLLC-scheme has been extended for the Euler equations in ducts of *smoothly* varying cross sections [22]. HLLC-type schemes apply information about the eigenstructure of the governing equations in their solution [10,11,23], making the schemes less dissipative than general methods such as AUSM$^+$-up [24]. For the application on two-phase flow, the HLLC-scheme's accurate resolution of contact discontinuities [23] is particularly desirable as this also makes the scheme more accurate in resolving transitions between gas, liquid, and mixture flows. As the eigenstructure of the one-dimensional compressible duct flow equations is known, the advantages above motivates the construction of a HLLC solver for this system.

This is further motivated as augmented versions of HLLC have been constructed for similar systems, where abrupt changes are accounted for [10,11]. An augmented version of HLLC for the Baer-Nunziato (BN) equations [25] was developed by Tokareva and Toro

* Corresponding author.
E-mail addresses: Alexandra.Log@hotmail.com, alexandra.m.log@ntnu.no (A.M. Log).

https://doi.org/10.1016/j.compfluid.2021.105023

[10], giving promising results for many test cases. The method involves a nonlinear system which was further linearized by Lochon et al. [26]. Murillo and García-Navarro [11] also developed an augmented version of HLLC for the shallow-water equations. This method produced promising results as well, though the authors note difficulties such as the need for a "source-fix" to avoid unphysical solutions in certain cases.

The contribution of this work is to develop and investigate two modified HLLC solvers for compressible duct flow and assess their strengths and weaknesses. In particular, we will consider two-phase flow of CO_2, due to its use as a natural working fluid in refrigeration engineering, and the importance of safe and efficient CO_2 transportation as part of CO_2 capture and storage (CCS) as a climate-change mitigation technology [27]. We show that the present method is both robust and accurate when solving challenging two-phase Riemann problems.

We will first present the equation system in more detail and briefly discuss the Riemann problem for the system in Section 2. The HEM and the PR EOS are outlined in Section 3. The numerical methods are derived in Section 4, the methods are assessed in Section 5, and finally some concluding remarks and suggestions for further work are given in Section 6.

2. Governing equations and the Riemann problem

The system of equations describing compressible one-dimensional flow of a single fluid in a rigid duct of variable cross-sectional area, A, is

$$\boldsymbol{U}_t + \boldsymbol{F}(\boldsymbol{U})_x = \boldsymbol{S}, \tag{1}$$

where

$$\boldsymbol{U} = \begin{pmatrix} \rho A \\ \rho u A \\ EA \\ A \end{pmatrix}, \quad \boldsymbol{F}(\boldsymbol{U}) = \begin{pmatrix} \rho u A \\ (\rho u^2 + p)A \\ (E+p)uA \\ 0 \end{pmatrix}, \quad \boldsymbol{S} = \begin{pmatrix} 0 \\ p\frac{\partial A}{\partial x} \\ 0 \\ 0 \end{pmatrix}.$$

Here, ρ is the density, u the velocity, $E = \rho(e + \frac{1}{2}u^2)$ the total energy, e the specific internal energy, and p the pressure of the fluid. $\boldsymbol{S}$ is a non-conservative term. The set of Eq. (1) belongs to the class of non-conservative *resonant* systems [5,28] meaning that the waves which arise in this system can interact and "resonate" with each other. For smooth solutions, the system (1) can be rewritten in quasi-linear form,

$$\boldsymbol{U}_t + \boldsymbol{A}(\boldsymbol{U})\boldsymbol{U}_x = \boldsymbol{0}, \tag{2}$$

where $\boldsymbol{A}$ is the Jacobian matrix of the system. Note that the non-conservative term has now been moved to the left-hand side of the equation. A full derivation of $\boldsymbol{A}$ for a general EOS can be found in [29, Appendix D], and we have included the full expression of $\boldsymbol{A}$ in Appendix A.

It can be shown [19,28,29] that the eigenvalues of $\boldsymbol{A}$ are;

$$\lambda_0 = 0, \quad \lambda_1 = u - c, \quad \lambda_2 = u, \quad \lambda_3 = u + c.$$

Note that any of the eigenvalues λ_1, λ_2, λ_3 may coincide with λ_0, giving rise to resonance in the system [28]. The system of equations is hyperbolic away from the points where $\lambda_1 = \lambda_0$ or $\lambda_3 = \lambda_0$ and nonstrictly hyperbolic when $\lambda_2 = \lambda_0$ [28].

2.1. The Riemann problem

Consider the Riemann problem for compressible duct flow,

$$\boldsymbol{U}_t + \boldsymbol{F}(\boldsymbol{U})_x = \boldsymbol{S}, \tag{3}$$

$$\boldsymbol{U}(x,0) = \begin{cases} \boldsymbol{U}_L, & \text{if } x < 0 \\ \boldsymbol{U}_R, & \text{if } x \geq 0 \end{cases}, \tag{4}$$

where $\boldsymbol{U}_L$ and $\boldsymbol{U}_R$ are two different constant states. A thorough analysis on the characteristic fields, Riemann invariants and the solution to this Riemann problem is presented by Andrianov and Warnecke in [28].

When there is no change in A, $A_L = A_R$, the system (1) reduces to the Euler equations. We then have the same characteristics and Riemann invariants as for the Euler equations associated with the eigenvalues $\lambda_1, \lambda_2, \lambda_3$. The Riemann invariants are

$$s, \ u + \frac{2c}{\Gamma} \quad \text{across} \quad \frac{\mathrm{d}x_1}{\mathrm{d}t} = u - c \tag{5}$$

$$u, p \quad \text{across} \quad \frac{\mathrm{d}x_2}{\mathrm{d}t} = u \tag{6}$$

$$s, u - \frac{2c}{\Gamma} \quad \text{across} \quad \frac{\mathrm{d}x_3}{\mathrm{d}t} = u + c, \tag{7}$$

where s is the specific entropy and Γ is the first Grüneisen parameter,

$$\Gamma = \frac{1}{\rho}\left(\frac{\partial p}{\partial e}\right)_\rho = \frac{1}{\rho c_v}\left(\frac{\partial p}{\partial T}\right)_\rho. \tag{8}$$

Here, c_v is the specific heat capacity at constant volume. Admissible waves for the solution to the Riemann problem are then rarefactions and shocks associated with λ_1, λ_3 and a contact discontinuity associated with λ_2.

At points with discontinuous area change, there is a *stationary contact discontinuity* associated with the eigenvalue $\lambda_0 = 0$ [19], the 0-wave. Across the 0-wave we have the following Riemann invariants as shown in [28]

$$A\rho u, \ s, \ h + \frac{1}{2}u^2, \quad \text{across} \quad \frac{\mathrm{d}x_0}{\mathrm{d}t} = \lambda_0 = 0, \tag{9}$$

where $h = e + \frac{p}{\rho}$ is the specific enthalpy of the fluid. The invariants describe the conservation of mass flux, entropy and stagnation enthalpy over the area change. The addition of this wave in the solution to the Riemann problem causes complications such as non-uniqueness [28] and resonance [5,19,30]. In Fig. 1 we provide an example of the structure of a Riemann problem solution in the case of subsonic flow i.e. $|u| < c$ from left to right. The example was created using Andrianov's program [31] (CONSTRUCT).

3. Thermodynamic models

In this work, we model the fluid as an ideal gas for benchmark tests of numerical solvers of the equation system (1), defined by the equation of state (EOS)

$$p = \rho(\gamma - 1)e, \tag{10}$$

where γ is the ratio of specific heats $\gamma = \frac{c_p}{c_v}$. In addition to benchmark testing, it is also relevant to study the system (1) for two-phase flow of liquid and gas. To model this, we apply the *homogeneous equilibrium model* (HEM) with the Peng-Robinson (PR) EOS [21]. The PR EOS is given by

$$p = \frac{RT}{v_m - b} - \frac{\alpha a}{v_m^2 + 2bv_m - b^2}, \tag{11}$$

where v_m is the specific molar volume of the fluid and R is the gas constant. a, b and α are defined as

$$a = 0.45724\frac{R^2T_c^2}{p_c}, \tag{12}$$

$$b = 0.07780\frac{RT_c}{p_c}, \tag{13}$$

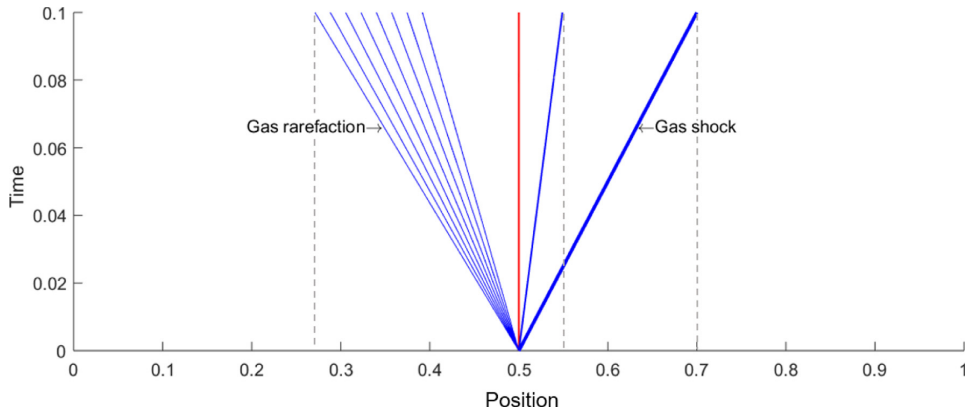

Fig. 1. The characteristics of a Riemann problem for 1D compressible duct flow with subsonic flow where $\rho_L > \rho_R$, $p_L > p_R$ and $A_L > A_R$, giving a rarefaction to the left, a stationary contact discontinuity (red), then a contact discontinuity and a shock to the right. Created using [31]. (For interpretation of the references to colour in this figure legend, the reader is referred to the web version of this article.)

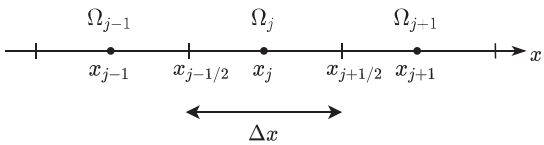

Fig. 2. A one dimensional interval subdivided into grid cells, Ω_j, with cell centers at x_j and faces $x_{j-1/2}$, $x_{j+1/2}$.

and

$$\alpha = \left[1 + \left(0.37464 + 1.54226\omega - 0.26992\omega^2\right)\left(1 - \sqrt{\frac{T}{T_c}}\right)\right]^2, \tag{14}$$

where T_c, p_c and ω are the critical temperature, critical pressure and the acentric factor of the species. For CO_2, these are

$$p_c = 7.3773\text{MPa}, \quad T_c = 304.35\text{K}, \quad \text{and } \omega = 0.2236. \tag{15}$$

The PR EOS only gives residual heat capacities, c_p^{res}, c_v^{res}. In order to compute the total heat capacities $c_p = c_p^{\text{ideal}} + c_p^{\text{res}}$, c_v in $\text{JK}^{-1}\text{kg}^{-1}$ we use the following estimate,

$$c_p^{\text{ideal}} = 479.107 + 1.524318\ T - 1.078176 \cdot 10^{-3}\ T^2 + \\ + 3.38976 \cdot 10^{-7}\ T^3 + 2.8876 \cdot 10^{-11}\ T^4. \tag{16}$$

In the HEM it is assumed that the two phases are in thermal, chemical and mechanical equilibrium, which is valid if the phases are well-mixed. Mixture properties are then used in the flow Eq. (1). In this work, SINTEF's thermodynamic library [32,33] has been applied to provide solutions for the HEM with the PR EOS. Details on the specific methods applied in the library to obtain relevant variables are presented in [34], though we ignore here the presence of any solid.

4. Numerical methods

The computational domain is discretized in finite volumes Ω_j as depicted in Fig. 2. We use two different kinds of finite-volume methods (FVMs) to solve Eq. (1) on this grid. The first FVM is analogous to the spatial discretization that Brown et al. apply in [20], with an Euler time step giving

$$\boldsymbol{U}_j^{n+1} = \boldsymbol{U}_j^n - \frac{\Delta t}{\Delta x}\left(\boldsymbol{\mathcal{F}}_{j+1/2} - \boldsymbol{\mathcal{F}}_{j-1/2}\right) + \Delta t \tilde{\boldsymbol{S}}_j, \tag{17}$$

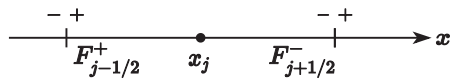

Fig. 3. The flux function $\mathcal{F}^+_{j-1/2}$ approximates the flux $\boldsymbol{F}^+_{j-1/2}$ just to the right of the interface at $x_{j-1/2}$. The flux function $\mathcal{F}^-_{j+1/2}$ approximates the flux $\boldsymbol{F}^-_{j+1/2}$ just to the left of the interface at $x_{j+1/2}$.

where $\boldsymbol{\mathcal{F}} = \boldsymbol{\mathcal{F}}(\boldsymbol{U}_L, \boldsymbol{U}_R)$ is a numerical flux function approximating the average flux $\boldsymbol{F}$ at the cell interfaces $x = x_{j-1/2}, x = x_{j+1/2}$, and $\tilde{\boldsymbol{S}}_j$ approximates the contribution of the non-conservative term in cell j.

The second FVM is a conservative Godunov scheme which includes the non-conservative term in the numerical flux functions [11]. The FVM takes the following form

$$\boldsymbol{U}_j^{n+1} = \boldsymbol{U}_j^n - \frac{\Delta t}{\Delta x}\left(\boldsymbol{\mathcal{F}}^-_{j+1/2} - \boldsymbol{\mathcal{F}}^+_{j-1/2}\right), \tag{18}$$

where again an Euler time step is used for the temporal discretization. Here, $\boldsymbol{\mathcal{F}}^{\pm} = \boldsymbol{\mathcal{F}}^{\pm}(\boldsymbol{U}_L, \boldsymbol{U}_R, \boldsymbol{S})$ are numerical flux functions approximating the average flux, $\boldsymbol{F}$, *right next to* the east, $\boldsymbol{F}^-_{j+1/2}$, and west, $\boldsymbol{F}^+_{j-1/2}$, cell faces as illustrated in Fig. 3.

In the following, we will briefly review the HLLC method and then suggest two modified HLLC-type methods to approximate the fluxes for the compressible duct flow.

4.1. The HLLC approximate Riemann solver

The HLLC method, proposed by Toro, Spruce and Speares [23], approximates the cell interface Riemann problem by a three-wave solution;

$$\tilde{\boldsymbol{U}}(x/t) = \begin{cases} \boldsymbol{U}_L, & \text{if } x < v_L t, \\ \boldsymbol{U}_L^{HLLC}, & \text{if } v_L t \le x < v_C t, \\ \boldsymbol{U}_R^{HLLC}, & \text{if } v_C t \le x < v_R t, \\ \boldsymbol{U}_R, & \text{if } x \ge v_R t, \end{cases} \tag{19}$$

where v_L and v_R are the fastest signal velocities arising from the initial condition of the Riemann problem, and v_C is the speed of the contact wave. The intermediate states $\boldsymbol{U}_L^{HLLC}, \boldsymbol{U}_R^{HLLC}$ are approximated to be constant,

$$\boldsymbol{U}_L^{HLLC} = \frac{1}{\Delta t(v_C - v_L)} \int_{\Delta t v_L}^{\Delta t v_C} \boldsymbol{U}(x, \Delta t)\ \mathrm{d}x \tag{20}$$

and

$$\boldsymbol{U}_R^{HLLC} = \frac{1}{\Delta t(v_R - v_C)} \int_{\Delta t v_C}^{\Delta t v_R} \boldsymbol{U}(x, \Delta t)\ \mathrm{d}x, \tag{21}$$

they are however unknown and must be estimated. HLLC approximates the numerical flux function by

$$\mathcal{F}_{j+1/2} = \begin{cases} \boldsymbol{F}_L, & \text{if } 0 < v_L, \\ \boldsymbol{F}_L^{HLLC}, & \text{if } v_L \le 0 < v_C, \\ \boldsymbol{F}_R^{HLLC}, & \text{if } v_C \le 0 < v_R, \\ \boldsymbol{F}_R, & \text{if } 0 \ge v_R. \end{cases} \tag{22}$$

The intermediate state fluxes, $\boldsymbol{F}_L^{HLLC}$ for positive subsonic flow, and $\boldsymbol{F}_R^{HLLC}$ for negative subsonic flow, are also unknown. In order to determine the fluxes, Rankine-Hugoniot (RH) relations are used across the waves and the additional set of Riemann invariants across the contact discontinuity is applied to close the system. The RH relation states that across a wave

$$\Delta \boldsymbol{F} = v \Delta \boldsymbol{U}, \tag{23}$$

where v is the speed of the wave. For compressible duct flow, we find through some manipulation that the intermediate fluxes $\boldsymbol{F}_K^{HLLC}$, $K = L, R$ can be expressed as

$$\boldsymbol{F}_K^{HLLC} = \boldsymbol{F}_K + v_K(\boldsymbol{U}_K^{HLLC} - \boldsymbol{U}_K), \tag{24}$$

where the intermediate states are approximated by

$$\boldsymbol{U}_K^{HLLC} = \rho_K A_K \left(\frac{v_K - u_K}{v_K - v_C}\right) \begin{pmatrix} 1 \\ v_C \\ \frac{E_K}{\rho_K} + (v_C - u_K)\left(v_C + \frac{p_K}{\rho_K(v_K - u_K)}\right) \end{pmatrix}, \tag{25}$$

$$K = R, L, \tag{25}$$

and

$$v_C = \frac{p_R - p_L + \rho_L u_L(v_L - u_L) - \rho_R u_R(v_R - u_R)}{\rho_L(v_L - u_L) - \rho_R(v_R - u_R)}. \tag{26}$$

4.2. Wave-speed estimates

The HLLC solver needs estimates for the wave speeds v_L and v_R. There are several different approaches to estimate these wave speeds, some of which are outlined in [35], Section 10.5. In this work, the Roe average wave speed estimate [36] is used. Both Davis [37] and Einfeldt [38] suggest using the Roe averaged eigenvalues for the wave speeds;

$$\begin{aligned} v_{L,j+1/2} &= \min\left(\lambda_1(\boldsymbol{U}_j), \lambda_1(\widehat{\boldsymbol{U}}_{j+1/2})\right), \\ v_{R,j+1/2} &= \max\left(\lambda_3(\boldsymbol{U}_{j+1}), \lambda_3(\widehat{\boldsymbol{U}}_{j+1/2})\right), \end{aligned} \tag{27}$$

where $\widehat{\boldsymbol{U}}$ is the Roe average of the conserved variables. The Roe averaged variables can be found by the Roe averaged matrix $\widehat{\boldsymbol{A}}(\boldsymbol{U}_L, \boldsymbol{U}_R)$ [36], which must satisfy certain conditions.

We follow the approach of Evje and Flåtten [39] and Munkejord [40] for the two-fluid model, which also involves a non-conservative term, and search for a Roe averaged matrix $\widehat{\boldsymbol{A}}$ which satisfies the following conditions:

R1 $\widehat{\boldsymbol{A}}(\boldsymbol{U}_L, \boldsymbol{U}_R)(\boldsymbol{U}_R - \boldsymbol{U}_L) = \Delta \boldsymbol{F}(\boldsymbol{U}_L, \boldsymbol{U}_R)$
R2 $\widehat{\boldsymbol{A}}(\boldsymbol{U}_L, \boldsymbol{U}_R)$ has real eigenvalues and is diagonalizable, and
R3 $\widehat{\boldsymbol{A}}(\boldsymbol{U}_L, \boldsymbol{U}_R) \to \boldsymbol{A}(\boldsymbol{U})$ smoothly as $\boldsymbol{U}_L, \boldsymbol{U}_R \to \boldsymbol{U}$,

wherein $\Delta \boldsymbol{F}(\boldsymbol{U}_L, \boldsymbol{U}_R)$ is formulated as

$$\Delta \boldsymbol{F}(\boldsymbol{U}_L, \boldsymbol{U}_R) = \begin{pmatrix} \{\rho u A\} \\ \{(\rho u^2 + p)A\} - \hat{p}\{A\} \\ \{(E + p)uA\} \\ 0 \end{pmatrix}. \tag{28}$$

Here,

$$\{x\} = x_R - x_L, \tag{29}$$

and $\hat{p}$ is a particular average of the pressures from the left and right states $\hat{p} = \hat{p}(\boldsymbol{U}_L, \boldsymbol{U}_R)$, similarly to $\overline{\alpha}_k(\boldsymbol{U}_L, \boldsymbol{U}_R)$ in [39], [40].

$\widehat{\boldsymbol{A}}$ can be determined by finding a special average of the state vectors $\boldsymbol{U}_L$ and $\boldsymbol{U}_R$, $\widehat{\boldsymbol{U}}(\boldsymbol{U}_L, \boldsymbol{U}_R)$, such that $\widehat{\boldsymbol{A}} = \boldsymbol{A}(\widehat{\boldsymbol{U}})$, $\hat{p} = \hat{p}(\widehat{\boldsymbol{U}})$. A set of averages satisfying R1–R3 are:

$$\widehat{\rho A} = \frac{\rho_L A_L + \rho_R A_R}{2}, \tag{30}$$

$$\hat{A} = \frac{A_L + A_R}{2}, \tag{31}$$

$$\hat{u} = \frac{\sqrt{\rho_L A_L}u_L + \sqrt{\rho_R A_R}u_R}{\sqrt{\rho_L A_L} + \sqrt{\rho_R A_R}}, \tag{32}$$

$$\hat{H} = \frac{\sqrt{\rho_L A_L}H_L + \sqrt{\rho_R A_R}H_R}{\sqrt{\rho_L A_L} + \sqrt{\rho_R A_R}}, \tag{33}$$

where $H_k = h_k + \frac{1}{2}u_k^2$, $k = L, R$.

4.3. HLLC with added non-conservative term, HLLC+S

The HLLC scheme assumes a three wave solution, however we can still apply the scheme to compressible duct flow provided that we also account for the fourth, stationary wave. We apply the FVM (17) with the HLLC numerical flux function. This FVM requires a representation of the non-conservative term, $\widetilde{\boldsymbol{S}}_j$. The discretization of this term requires special care to ensure numerical stability. We follow the approach of Brown et al. [20] for their AUSM$^+$-up scheme and apply a discretization of the non-conservative term which satisfies the non-disturbance relation discussed by Liou et al. [41]. The relation states that under steady conditions with $u = 0$ and $p = \text{const}$.

$$\frac{\partial(Ap)}{\partial x} = p\frac{\partial A}{\partial x}. \tag{34}$$

The following discretization, which satisfies the non-disturbance relation, is used:

$$\widetilde{\boldsymbol{S}}_j = \frac{p_j}{\Delta x}\begin{pmatrix} 0 \\ A_j - A_{j-1} \\ 0 \\ 0 \end{pmatrix}, \text{ if } u_j > 0 \text{ and } \widetilde{\boldsymbol{S}}_j = \frac{p_j}{\Delta x}\begin{pmatrix} 0 \\ A_{j+1} - A_j \\ 0 \\ 0 \end{pmatrix}, \text{if } u_j \le 0. \tag{35}$$

4.4. HLLCS approximate Riemann solver

We will here derive an augmented version of HLLC, following in part the approach of Murillo and García-Navarro [11] for the shallow-water equations and the approach of Tokareva and Toro [10] for the Baer-Nunziato equations. We follow the naming convention of Murillo and García-Navarro [11] and call this method "HLLCS", emphasizing that our method is very similar to their discretization of the source term in the shallow-water equations. The HLLCS approximate Riemann solver assumes a four-wave solution instead of a three-wave solution, incorporating the 0-wave. Similarly to HLLC, we will assume that the waves separate constant intermediate states.

For systems in the form of Eq. (1), Murillo and García-Navarro derived the following *consistency condition* which the approximate intermediate states must satisfy:

$$\frac{1}{\Delta t(v_R - v_L)} \int_{\Delta t v_L}^{\Delta t v_R} \boldsymbol{U}(x, \Delta t)\ \mathrm{d}x = \frac{v_R \boldsymbol{U}_R - v_L \boldsymbol{U}_L - (\boldsymbol{F}_R - \boldsymbol{F}_L) + \overline{\boldsymbol{S}}}{v_R - v_L}, \tag{36}$$

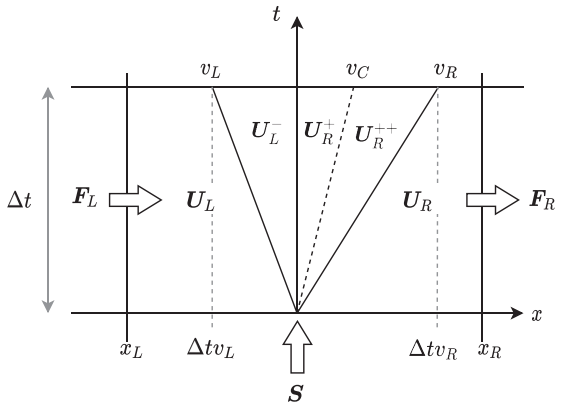

Fig. 4. Integration control volume $[x_L, x_R] \times [0, \Delta t]$ in the $x-t$ plane. The control volume contains the two fastest signal velocities, v_L and v_R from the Riemann problem. The solution consists of three inner states separated by the stationary wave at $x = 0$ and the contact discontinuity of positive speed, v_C.

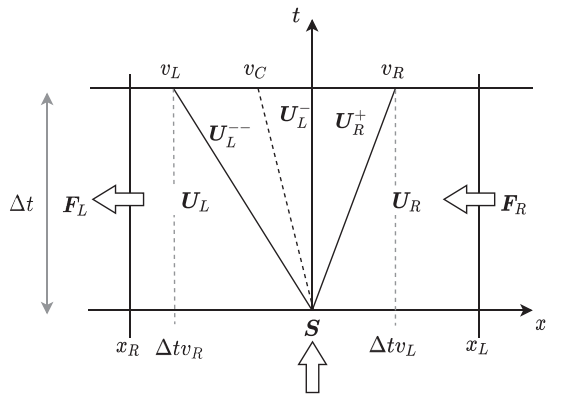

Fig. 5. Integration control volume $[x_L, x_R] \times [0, \Delta t]$ in the $x-t$ plane. The control volume contains the two fastest signal velocities v_L, v_R from the Riemann problem. The solution consists of three inner states separated by the stationary wave at $x = 0$ and the contact discontinuity of negative speed, v_C.

where

$$\bar{\boldsymbol{S}} = \frac{1}{\Delta t}\int_{x_L}^{x_R}\int_0^{\Delta t} \boldsymbol{S}\ \mathrm{d}t\ \mathrm{d}x. \tag{37}$$

Two different estimates of $\bar{\boldsymbol{S}}$ are used in this work and they are presented in Section 4.4.4. HLLCS will be developed to ensure the subsonic case satisfies the condition (36). For supersonic flow, the fluxes are easily found as will be shown below.

4.4.1. Supersonic flow

For positive supersonic flow, the flux just to the left of the interface, $x = 0$, is simply $\boldsymbol{F}_L$, giving

$$\mathcal{F}^-_{j+1/2} = \boldsymbol{F}_L. \tag{38}$$

The flow just to the right of the interface has passed the area change such that

$$\mathcal{F}^+_{j+1/2} = \boldsymbol{F}_L + \bar{\boldsymbol{S}}. \tag{39}$$

Similarly for negative supersonic flow, the numerical fluxes at Δt become:

$$\mathcal{F}^-_{j+1/2} = \boldsymbol{F}_R - \bar{\boldsymbol{S}}, \tag{40}$$

$$\mathcal{F}^+_{j+1/2} = \boldsymbol{F}_R. \tag{41}$$

4.4.2. Subsonic flow

An illustration of a control volume containing the wave structure of a Riemann problem for positive subsonic flow is shown in Fig. 4. In this case there are three unknown intermediate states separated by the stationary wave at $x = 0$ and the contact discontinuity, $\boldsymbol{U}_L^-$, $\boldsymbol{U}_R^+$ and $\boldsymbol{U}_R^{++}$.

We approximate the intermediate states, $\boldsymbol{U}_L^-$, $\boldsymbol{U}_R^+$ and $\boldsymbol{U}_R^{++}$ by

$$\left.\begin{aligned}
\boldsymbol{U}_L^- &= \tfrac{1}{-\Delta t v_L}\int_{\Delta t v_L}^{0} \boldsymbol{U}(x, \Delta t)\ \mathrm{d}x \\
\boldsymbol{U}_R^+ &= \tfrac{1}{\Delta t v_C}\int_{0}^{\Delta t v_C} \boldsymbol{U}(x, \Delta t)\ \mathrm{d}x \\
\boldsymbol{U}_R^{++} &= \tfrac{1}{\Delta t (v_R - v_C)}\int_{\Delta t v_C}^{\Delta t v_R} \boldsymbol{U}(x, \Delta t)\ \mathrm{d}x
\end{aligned}\right\}. \tag{42}$$

In order to estimate the intermediate fluxes, the RH condition is applied across all the waves in the problem. The RH relations are

$$\boldsymbol{F}_L^- - \boldsymbol{F}_L = v_L(\boldsymbol{U}_L^- - \boldsymbol{U}_L), \tag{43}$$

$$\boldsymbol{F}_R^+ - \boldsymbol{F}_L^- - \bar{\boldsymbol{S}} = v(\boldsymbol{U}_R^+ - \boldsymbol{U}_L^-) = \boldsymbol{0}, \tag{44}$$

$$\boldsymbol{F}_R^{++} - \boldsymbol{F}_R^+ = v_C(\boldsymbol{U}_R^{++} - \boldsymbol{U}_R^+), \tag{45}$$

$$\boldsymbol{F}_R - \boldsymbol{F}_R^{++} = v_R(\boldsymbol{U}_R - \boldsymbol{U}_R^{++}). \tag{46}$$

It can be shown that the RH relations (43)-(46) are enough to satisfy the consistency condition (36). To close the system, we impose the Riemann invariants across the stationary wave and the contact discontinuity,

$$\left.\begin{aligned} u_R^{++} &= u_R^+ = v_C \\ p_R^{++} &= p_R^+ \end{aligned}\right\}, \tag{47}$$

$$\left.\begin{aligned} (A\rho u)_L^- &= (A\rho u)_R^+ \\ s_L^- &= s_R^+ \\ (\frac{u^2}{2} + h)_L^- &= (\frac{u^2}{2} + h)_R^+ \end{aligned}\right\}. \tag{48}$$

The RH condition across the wave associated with the wave speed v_L gives

$$\rho_L^- = \rho_L \frac{v_L - u_L}{v_L - u_L^-}, \tag{49}$$

$$p_L^- = p_L + \rho_L(v_L - u_L)(u_L^- - u_L), \tag{50}$$

$$E_L^- = \rho_L\left(\frac{v_L - u_L}{v_L - u_L^-}\right)\left(\frac{E_L}{\rho_L} + (u_L^- - u_L)\left(u_L^- + \frac{p_L}{\rho_L(v_L - u_L)}\right)\right), \tag{51}$$

and the RH condition across the wave associated with the wave speed v_R gives

$$\rho_R^{++} = \rho_R \frac{v_R - u_R}{v_R - u_R^{++}}, \tag{52}$$

$$p_R^{++} = p_R + \rho_R(v_R - u_R)(u_R^{++} - u_R), \tag{53}$$

$$E_R^{++} = \rho_R\left(\frac{v_R - u_R}{v_R - u_R^{++}}\right)\left(\frac{E_R}{\rho_R} + (u_R^{++} - u_R)\left(u_R^{++} + \frac{p_R}{\rho_R(v_R - u_R)}\right)\right). \tag{54}$$

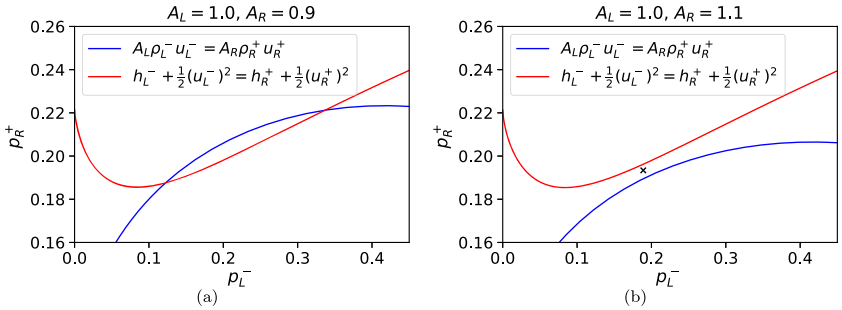

Fig. 6. The graphs show for which values of p_L^-, p_R^+ that $f_1 = 0$ (blue) and $f_2 = 0$ (red) for Mod. A (a) and Mod. B (b). For Mod B, an estimate of the point where $|\boldsymbol{f}|$ is minimized is marked with an x. (For interpretation of the references to colour in this figure legend, the reader is referred to the web version of this article.)

Eqs. (49)-(51) and (52)-(54) with the Riemann invariants constitute a nonlinear system which can be solved iteratively. Tokareva and Toro [10] obtained a similar, but larger system of equations which must be solved for the Baer-Nunziato equations.

Both for compressible duct flow and the Baer-Nunziato equations, either the pressures p_L^-, $p_R^+ = p_R^{++}$ or the velocities u_L^-, $u_R^+ = u_R^{++}$ can be chosen as independent variables to solve the system. As stated in [10], there is no difference between the approaches from a theoretical point of view as the two representations of the system are mathematically equivalent. Following Tokareva et al. [10], we choose p_L^-, p_R^+ as the independent variables to ensure pressure positivity when searching for solutions of the system.

We therefore express u_L^- and $u_R^+ = u_R^{++}$ using p_L^- and p_R^+,

$$u_L^-(p_L^-) = u_L + \frac{p_L^- - p_L}{\rho_L(v_L - u_L)}, \tag{55}$$

$$u_R^+(p_R^+) = u_R + \frac{p_R^+ - p_R}{\rho_R(v_R - u_R)}. \tag{56}$$

We then have that $\boldsymbol{U}_L^- = \boldsymbol{U}_L^-(p_L^-)$, such that $s_L^- = s_L^-(p_L^-)$, and enforcing the Riemann invariant $s_L^- = s_R^+ = s$, we have that $s_R^+ = s_R^+(p_L^-)$. The relation for mass flux and the relation for stagnation enthalpy then give the following:

$$\boldsymbol{f} = \begin{pmatrix} A_L\rho_L^-(p_L^-)u_L^-(p_L^-) - A_R\rho_R^+\left(p_R^+, s(p_L^-)\right)u_R^+(p_R^+) \\ h_R^+\left(p_R^+, s(p_L^-)\right) + \frac{1}{2}\left(u_R^+(p_R^+)\right)^2 - \left[h_L^-\left(p_L^-, s(p_L^-)\right) + \frac{1}{2}\left(u_L^-(p_L^-)\right)^2\right] \end{pmatrix} = \boldsymbol{0}. \tag{57}$$

These are two equations for the two independent variables p_L^-, p_R^+. The system (57) can be solved iteratively by e.g. Newton-Raphson's method and it may have zero or up to three solutions. If the system has multiple solutions, we choose the solution which satisfies the following criteria:

C1 The solution is self-consistent in the sense that the Riemann problem for the states $\boldsymbol{U}_L^-(p_L^-), \boldsymbol{U}_R^+(p_L^-, p_R^+)$ provide wavespeed estimates which suggest *subsonic* flow.

C2 The solution has the highest entropy $s_L^-(p_L^-) = s_R^+ = s$ of the self-consistent solutions.

If there are no solutions, we approximate p_L^-, p_R^+ as the point which minimizes the absolute value $\boldsymbol{f}_1(p_L^-, p_R^+) + \boldsymbol{f}_2(p_L^-, p_R^+)$ of $\boldsymbol{f}$.

Once p_L^- and p_R^+ are determined, the state $\boldsymbol{U}_L^-$ can be calculated using Eqs. (55), (49) and (51). With this we can finally find the unknown fluxes $\boldsymbol{F}_L^-$ and $\boldsymbol{F}_R^+$ from Eq. (43) and Eq. (44), giving

$$\boldsymbol{F}_L^- = \boldsymbol{F}_L + v_L(\boldsymbol{U}_L^- - \boldsymbol{U}_L), \tag{58}$$

$$\boldsymbol{F}_R^+ = \boldsymbol{F}_L^- + \bar{\boldsymbol{S}}. \tag{59}$$

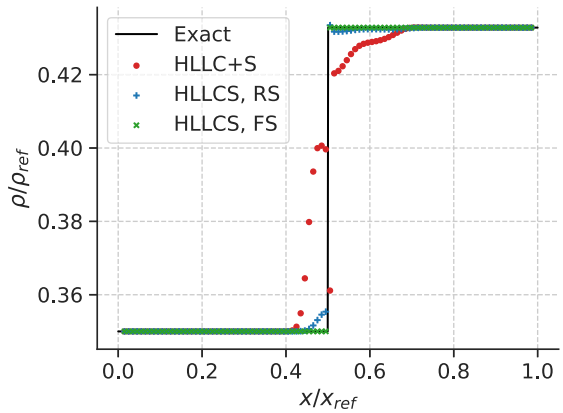

Fig. 7. Comparison of the exact density solution (black line) and the solutions of HLLC+S (red circles), HLLCS with RS (blue plus signs) and HLLCS with FS (green crosses) at $t/t_{ref} = 0.02$ for Test 1. (For interpretation of the references to colour in this figure legend, the reader is referred to the web version of this article.)

The negative subsonic flow case can be seen as simply the mirror image of the positive flow case. We now have the states $\boldsymbol{U}_L^{--}$, $\boldsymbol{U}_L^-$ and $\boldsymbol{U}_R^+$ as illustrated in Fig. 5.

An equivalent system to (57) can be found for this case and the same criteria C1 and C2 can be applied to choose a valid solution.

4.4.3. Solution for stationary waves

Suppose now that we have the states $\boldsymbol{U}_L, \boldsymbol{U}_R$ which satisfy the conditions for a stationary wave across the area change,

$$(A\rho u)_L = (A\rho u)_R, \;\; h_L + \frac{u_L^2}{2} = h_R + \frac{u_R^2}{2}, \;\; s_L = s_R. \tag{60}$$

The exact solution for the Riemann problem (3)–(4) with the two states $\boldsymbol{U}_L, \boldsymbol{U}_R$ is a jump from $\boldsymbol{U}_L$ to $\boldsymbol{U}_R$ at the area change. The solution which satisfies the criteria C1 and C2 is $p_L^- = p_L$ and $p_R^+ = p_R$. The intermediate states then become $\boldsymbol{U}_L^- = \boldsymbol{U}_L$ and $\boldsymbol{U}_R^+ = \boldsymbol{U}_R^{++} = \boldsymbol{U}_R$. This means that for stationary waves, when the correct solution is chosen, the intermediate states found in the HLLCS approximate Riemann solver are exact.

4.4.4. The non-conservative term for HLLCS

In this work, two non-conservative terms are tested to estimate the fluxes based on the HLLCS approximate Riemann solver. The

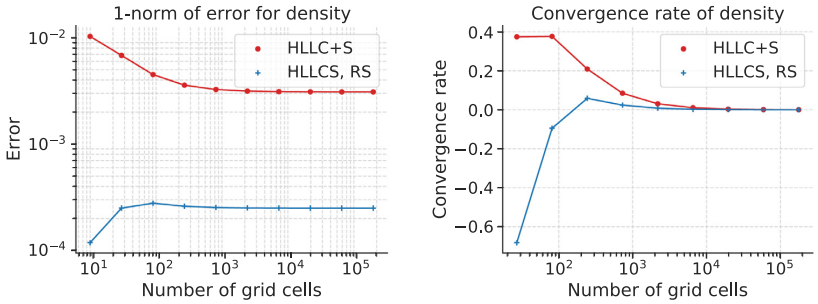

(a) (b)

Fig. 8. Results of the convergence test for HLLC+S (red line with circles) and HLLCS with RS (blue line with plus signs) for Test 1. (For interpretation of the references to colour in this figure legend, the reader is referred to the web version of this article.)

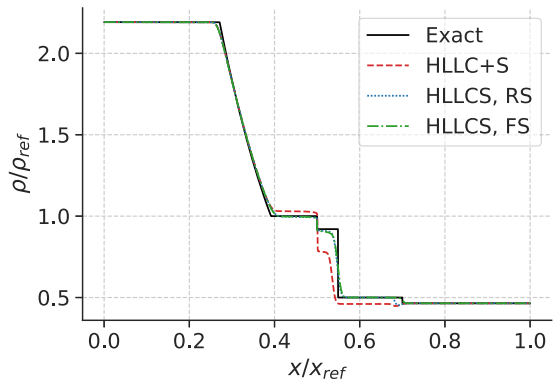

Fig. 9. Density solution of HLLC+S (red dashed line), HLLCS with RS (blue dotted line) and HLLCS with FS (green dash-dotted line) compared to the exact solution (black line) for Test 2 at $t/t_{\text{ref}} = 0.1$, with $N_{\text{cells}} = 1000$. (For interpretation of the references to colour in this figure legend, the reader is referred to the web version of this article.)

first approximate non-conservative term is given by

$$\bar{\boldsymbol{S}}_{\text{RS}} = \begin{pmatrix} 0 \\ \hat{p}(A_R - A_L) \\ 0 \\ 0 \end{pmatrix}, \tag{61}$$

where $\hat{p}$ is the Roe-averaged pressure introduced in Section 4.2. We therefore call this the Roe-average-based term (RS). RS is formulated generally such that it may be applied on subsonic, sonic and supersonic flow.

For subsonic flow, the nonlinear system of equations determining the approximate intermediate states and fluxes is solved. The non-conservative term is then given implicitly by the RH conditions. For positive subsonic flow, we get that the non-conservative term must be

$$\bar{\boldsymbol{S}}_{\text{FS+}} = \boldsymbol{F}_R^{++} - v_C(\boldsymbol{U}_R^{++} - \boldsymbol{U}_R^{+}) - \boldsymbol{F}_L^{-}. \tag{62}$$

Similarly for negative subsonic flow, we get that

$$\bar{\boldsymbol{S}}_{\text{FS-}} = \boldsymbol{F}_R^{+} - \boldsymbol{F}_L^{--} + v_C(\boldsymbol{U}_L^{-} - \boldsymbol{U}_L^{--}). \tag{63}$$

As the non-conservative term includes the approximate fluxes, we call it the flux-based term (FS). Note that this estimate only holds if the HLLCS approximate Riemann solver has a solution. FS is only formulated for subsonic flow and may therefore only be applied for subsonic flow problems.

4.4.5. The HLLCS-based fluxes

The HLLCS method approximates the flux functions $\mathcal{F}^{-}_{j+1/2}$ and $\mathcal{F}^{+}_{j+1/2}$ needed for the FVM (18) as shown in Algorithm 1.

Algorithm 1: The HLLCS solver. If subsonic flow is identified, a solver is called to find a valid solution satisfying C1 and C2 or an optimization method is used to minimize $\boldsymbol{f}$. When a solution is found, v_C and the intermediate states $\boldsymbol{U}_L^{-}$, $\boldsymbol{U}_R^{+}$ and $\boldsymbol{U}_L^{--}$ or $\boldsymbol{U}_R^{++}$ are returned.

Result: Fluxes for the HLLCS solver, $\boldsymbol{F}_R^{+}$ and $\boldsymbol{F}_L^{-}$.
if $v_L > 0$ **then**
  $\boldsymbol{F}_L^{-} = \boldsymbol{F}_L$
  $\boldsymbol{F}_R^{+} = \boldsymbol{F}_L^{-} + \bar{\boldsymbol{S}}$
end
if $v_L \leq 0$ *and* $v_R > 0$ **then**
  call solver, returning v_C and intermediate states;
  if $v_C \geq 0$ **then**
    $\boldsymbol{F}_L^{-} = \boldsymbol{F}_L + v_L(\boldsymbol{U}_L^{-} - \boldsymbol{U}_L)$
    $\boldsymbol{F}_R^{+} = \boldsymbol{F}_L^{-} + \bar{\boldsymbol{S}}$
  else
    $\boldsymbol{F}_R^{+} = \boldsymbol{F}_R - v_R(\boldsymbol{U}_R - \boldsymbol{U}_R^{+})$
    $\boldsymbol{F}_L^{-} = \boldsymbol{F}_R^{+} - \bar{\boldsymbol{S}}$
  end
end
if $v_R \leq 0$ **then**
  $\boldsymbol{F}_R^{+} = \boldsymbol{F}_R$
  $\boldsymbol{F}_L^{-} = \boldsymbol{F}_R^{+} - \bar{\boldsymbol{S}}$
end
Set $\mathcal{F}^{-}_{j+1/2} = \boldsymbol{F}_L^{-}$ and $\mathcal{F}^{+}_{j+1/2} = \boldsymbol{F}_R^{+}$.

Remark: Note that for a (subsonic) steady-state wave across the area change, applying $\bar{\boldsymbol{S}}_{\text{FS}}$ will give that $\mathcal{F}^{-}_{j+1/2} = \boldsymbol{F}_L^{-} = \boldsymbol{F}_L$ and $\mathcal{F}^{+}_{j+1/2} = \boldsymbol{F}_R^{+} = \boldsymbol{F}_R$. Inserting this in the FVM (18), we find that

$$\boldsymbol{U}_j^{n+1} = \boldsymbol{U}_j^{n} \;\forall\; j, \tag{64}$$

i.e. the HLLCS-based FVM with FS conserves the steady-state solution exactly. This means that the FVM is *well-balanced*.

4.5. Summary

In this work, we apply two finite-volume methods HLLC+S and HLLCS. The numerical scheme for the HLLC+S solver is given by

$$\boldsymbol{U}_j^{n+1} = \boldsymbol{U}_j^{n} - \frac{\Delta t}{\Delta x}\left(\boldsymbol{\mathcal{F}}_{j+1/2} - \boldsymbol{\mathcal{F}}_{j-1/2}\right) + \Delta t \tilde{\boldsymbol{S}}_j, \tag{65}$$

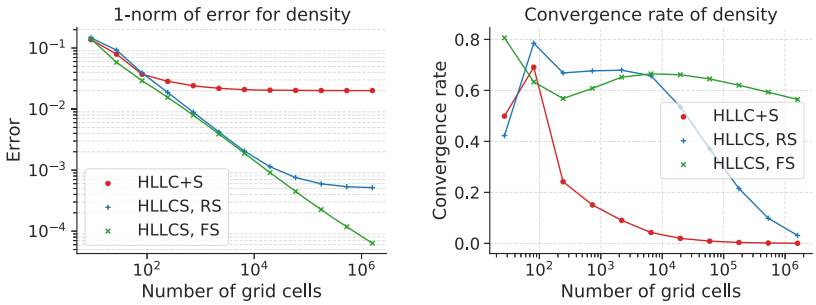

(a) (b)

Fig. 10. Results of the convergence test for HLLC+S (red line with circles), HLLCS with RS (blue line with plus signs) and HLLCS with FS (green line with crosses) for Test 2. (For interpretation of the references to colour in this figure legend, the reader is referred to the web version of this article.)

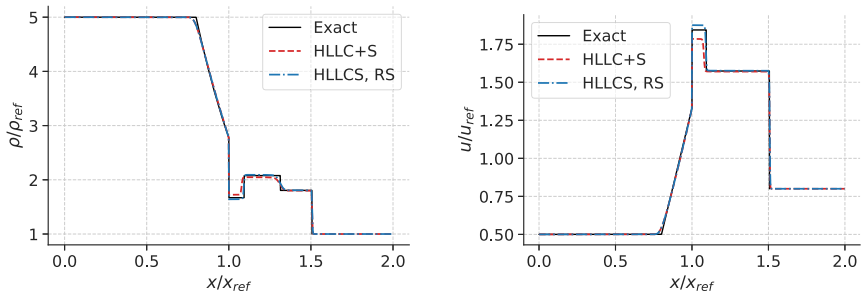

(a) Density (b) Velocity

Fig. 11. Comparison of exact solution (black line) and the density solution (a) and velocity solutions (b) of HLLC+S (red dashed line), and HLLCS with RS (blue dash-dotted line) on Test 3 for velocity at $t/t_{\text{ref}} = 0.2$, $N_{\text{cells}} = 1000$. (For interpretation of the references to colour in this figure legend, the reader is referred to the web version of this article.)

where the flux functions $\mathcal{F}_{j+1/2}, \mathcal{F}_{j-1/2}$ are given by the HLLC solver, and $\widetilde{\boldsymbol{S}}_j$ is given by Eq. (35). The discretization of $\widetilde{\boldsymbol{S}}_j$ is such that the stationary state is conserved.

The HLLCS FVM is given by

$$\boldsymbol{U}_j^{n+1} = \boldsymbol{U}_j^n - \frac{\Delta t}{\Delta x}\left(\mathcal{F}^-_{j+1/2} - \mathcal{F}^+_{j-1/2}\right), \tag{66}$$

where the flux functions $\mathcal{F}^-_{j+1/2}, \mathcal{F}^+_{j-1/2}$ are approximated using the HLLCS approximate Riemann solver as described in Algorithm 1.

5. Assessment of the methods

In this section, we assess the performance of the proposed finite-volume methods, HLLC+S and HLLCS. As the HLLCS FVM is based on a new approximate Riemann solver, we start by testing the HLLCS approximate Riemann solver on local Riemann problems in Section 5.1. We then investigate the performance of the HLLC+S and HLLCS finite-volume methods on benchmark tests for the ideal gas EOS in Section 5.2. The methods are further tested on the HEM with the PR EOS in Section 5.3. We finally compare our methods to the results of different solvers for a water vapour test. Note that for tests with the ideal gas EOS, we use dimensionless variables and denote this by $*/*_{\text{ref}}$, where $*$ is some variable and the subscript ref refers to some reference value.

Table 1
The left and right states for the Sod shock-tube problem with modified left and right areas for Mod. A and Mod. B.

	p/p_{ref}	u/u_{ref}	ρ/ρ_{ref}	Mod. A: A/A_{ref}	Mod. B: A/A_{ref}
Left	1.0	0.0	1.0	1.0	1.0
Right	0.1	0.0	0.125	0.9	1.1

5.1. Behaviour of the HLLCS approximate Riemann solver for local Riemann problems

As shown in Section 4.4.2 we must solve a nonlinear system, $\boldsymbol{f} = (f_1, f_2)^T = \boldsymbol{0}$, to obtain a solution with the HLLCS approximate Riemann solver for subsonic flow. It is therefore of interest to investigate how this nonlinear system behaves for different local Riemann problems inducing subsonic flow. We investigate this using two modified versions of the common Sod shock-tube problem, giving positive subsonic flow, where we include area change. The values of the left and right states in the Sod shock-tube problem and the left and right areas in the modified tests, Mod. A and Mod. B are given in Table 1.

In Fig. 6 we plot for which values of p_L^-, p_R^+ that $f_1 = 0$ and $f_2 = 0$ for the two modified Sod shock-tube tests. When the lines $f_1 = 0$, $f_2 = 0$ cross, $\boldsymbol{f} = \boldsymbol{0}$ has a solution. For Mod. A, there are two possible solutions. We find that the solution to the lower left in Fig. 6(a) is inconsistent as it suggests supersonic flow across the area change even though the Riemann problem is subsonic. The solution to the upper right suggests subsonic flow across the area change and is therefore valid.

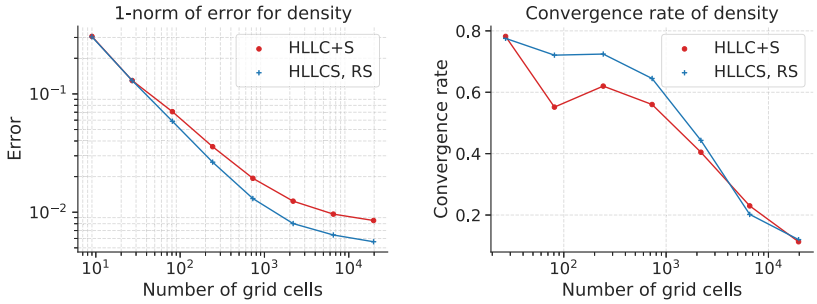

Fig. 12. Results of the convergence test for HLLC+S (red line with circles) and HLLCS with RS (blue line with plus signs) for Test 3. (For interpretation of the references to colour in this figure legend, the reader is referred to the web version of this article.)

Table 2
The left and right states for Test 1.

	p/p_{ref}	u/u_{ref}	ρ/ρ_{ref}	A/A_{ref}
Left	10.0	5.0	0.35	1.0
Right	13.462929846413655	2.695480449295447	0.432823271625514	1.5

For Mod. B there is no solution. Mod. B is a resonant case, where a *fifth* wave is induced in the Riemann solution, so the assumption of a four-wave solution in the HLLCS approximate Riemann solver does not hold here. Strictly speaking, the approximate Riemann solver is invalid for resonant cases. We choose the intermediate pressures p_L^-, p_R^+ to estimate the minimum absolute value of $\boldsymbol{f}$, marked with an x in Fig. 6(b). The resulting intermediate states *approximate* a solution for the HLLCS Riemann solver. These intermediate states do not satisfy the RH relations (43)–(46), however, and the error increases when the area discontinuity or pressure is increased.

5.2. Benchmark tests with the ideal gas EOS

In this section, three selected benchmark tests for compressible duct flow with the ideal gas EOS are used to test the performance of HLLC+S and HLLCS. For all the tests, the CFL number is set to $C = \frac{\max(\lambda)\Delta t}{\Delta x} = 0.9$, extrapolation is used at the boundaries and $\gamma = 1.4$.

5.2.1. Test 1: Steady-state

Test 1 is taken from Cuong and Thanh [8], and includes steady flow which satisfies the conditions for a stationary wave across the area change. The initial condition for Test 1 is given in Table 2. For this test, the solution is computed along the interval $x/x_{\text{ref}} \in [0, 1]$, the discontinuity is at $x/x_{\text{ref}} = 0.5$ and $N_{\text{cells}} = 100$. The solutions for HLLC+S and HLLCS at $t/t_{\text{ref}} = 0.02$ are plotted in Fig. 7.

As expected, HLLCS with FS conserves the steady state because the scheme is well-balanced, as shown in Section 4.4.4. Neither HLLC+S nor HLLCS with RS are well-balanced, however, the solution of HLLCS with RS is not very inaccurate.

We further present a convergence study for HLLC+S and HLLCS with RS for this test. The grids used for the convergence study have tripling numbers of grid cells, N_{cells}, such that cell centres will overlap for all the grids. We calculate the 1-norm of error for the density, the density error, by

$$E_{1,\rho}(\Delta x) = \Delta x \sum_{j=1}^{N_{\text{cells}}} |\rho_j^{\text{exact}} - \rho_j^{\text{approx}}|,$$

Table 3
The left and right states for Test 2 including the intermediate states separating elementary waves of the exact Riemann solution for the test ordered from left to right.

	p/p_{ref}	u/u_{ref}	ρ/ρ_{ref}	A/A_{ref}
Left	3.0	−0.90532425	2.191799866	0.9
State 1	1.0	0.1	1.0	0.9
State 2	0.89002806	0.4890494	0.92015244	0.2
State 3	0.89002806	0.4890494	0.5	0.2
Right	0.80290021	0.37372087	0.46454221	0.2

where Δx is the grid spacing, and the convergence rate, l, for tripling N_{cells} by

$$l = \frac{1}{\log(3)} \log\left(\frac{E_{1,\rho}(\Delta x)}{E_{1,\rho}(\frac{\Delta x}{3})}\right).$$

The density error for HLLC+S and HLLCS with RS is shown in Fig. 8(a) and the convergence rate for their density solution is shown in Fig. 8(b). Though HLLCS with RS has a significantly lower error than HLLC+S, both solvers reach a convergence rate of 0. This means that neither of these solvers is consistent.

5.2.2. Test 2: Strong non-conservative term

We now present Test 2, which includes a strong non-conservative term. In Table 3, the initial conditions and intermediate states separating elementary waves of the exact Riemann solution for Test 2 is given. The interval and discontinuity are the same as for Test 1.

The numerical solvers give significant numerical smearing near the area change due to the strong non-conservative term, so a rather fine grid of $N_{\text{cells}} = 1000$ is used to resolve the problem to see clearly how the solvers perform. The density solution for HLLC+S and HLLCS with both RS and FS are compared to the exact solution at $t/t_{\text{ref}} = 0.1$ in Fig. 9. The exact solution for the test is produced using CONSTRUCT [31].

For this test, HLLC+S produces unsatisfactory results. The behaviour near the area change does not approximate the exact solution. The density after the area change becomes much too low as compared to the exact solution. Both HLLCS with FS and with RS have numerical smearing between the area change and the contact

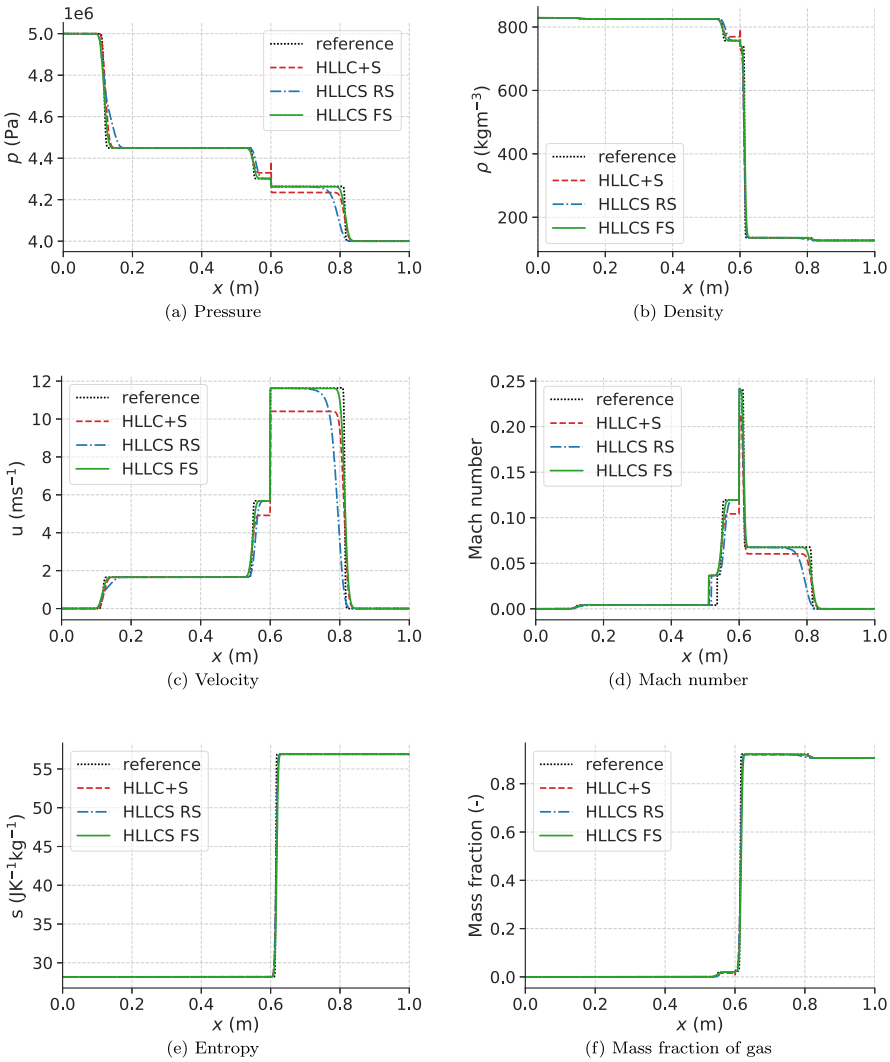

Fig. 13. The solutions of HLLC+S (red, dashed line), HLLCS RS (blue, dash-dotted line) and HLLCS FS (green line) for pressure (a), density (b), velocity(c), Mach number (d), entropy (e) and mass fraction of gas (f) for Test 4 at $t = 1.2$ ms with the initial discontinuity at $x = 0.6$ m. The result is compared to a reference HLLCS FS solution on a finer grid (black dotted line). (For interpretation of the references to colour in this figure legend, the reader is referred to the web version of this article.)

discontinuity, but appear to approximate the solution well otherwise. HLLCS with RS does not approximate the location of the right shock perfectly, but performs similarly to HLLCS with FS otherwise.

We further present a grid refinement study for this test. The density error for the solvers is shown in Fig. 10(a) and the convergence rate for their density solution is shown in Fig. 10(b). It is clear that HLLCS outperforms HLLC+S. HLLC+S' error settles at approximately 0.02, and its convergence rate goes to 0. HLLCS with RS's convergence rate also goes to zero, though at a much lower density error than HLLC+S. The density error for HLLCS with FS keeps falling for increasing numbers of grid cells and its convergence rate stays above 0.5 for very fine grids.

5.2.3. Test 3: Resonance

Test 3, suggested by Thanh and Kröner [5], involves the interaction between a rarefaction to the left and an expansion causing the flow to become choked exactly at the area discontinuity. This leads to resonance which induces an "extra" shock in the wave configuration. In Table 4 the initial condition and the states separating

Table 4
The left and right states for Test 3 and the intermediate states separating elementary waves of the exact Riemann solution ordered from left to right.

	p/p_{ref}	u/u_{ref}	ρ/ρ_{ref}	A/A_{ref}
Left	8.0	0.5	5.0	1.0
State 1	3.5111	1.3306	2.7766	1.0
State 2	1.7227	1.8438	1.6697	1.2
State 3	2.3427	1.5738	2.0779	1.2
State 4	2.3427	1.5738	1.8047	1.2
Right	1.0	0.8	1.0	1.2

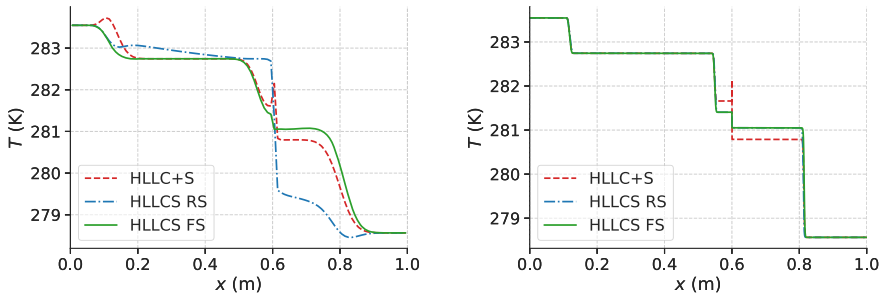

Fig. 14. Temperature results for Test 4 with 100 grid cells (a) and 10,000 grid cells (b).

elementary waves of the exact Riemann solution are given for Test 3. The solution is computed along the interval $x/x_{\text{ref}} \in [0, 2]$ and the discontinuity is at $x/x_{\text{ref}} = 1$. Following Thanh and Kröner [5], Brown et al. [20], we employ $N_{\text{cells}} = 1000$.

For Test 3, HLLCS with FS fails to compute a solution. The nonlinear system in the HLLCS approximate Riemann solver does not have a solution for the local Riemann problem for this test, similarly to Mod. B in Section 5.1. We compute the intermediate states closest to a solution for the HLLCS Riemann solver. However, as they are not a true solution, the states do not satisfy the RH relations (43)–(46). The FS estimate of the non-conservative term (62) is defined implicitly through these relations and the estimate is poor when inconsistent intermediate states are used in its calculation. In this particular case, the error causes HLLCS with FS to obtain negative internal energies during the simulation and crash. HLLCS with RS is less affected by this because the RS discretization does not depend on the intermediate states.

The solutions for density and velocity are given in Figs. 11(a) and 11(b) respectively for HLLC+S and HLLCS with RS at $t/t_{\text{ref}} = 0.2$ together with points of the exact solution. Both HLLC+S and HLLCS with RS resolve the problem well and there is no sign of instability as often occurs for solvers applied on resonant cases [5]. HLLCS RS approximates the solution better than HLLC+S, which is particularly evident for the density between the stationary wave and the additional shock, for $x/x_{\text{ref}} \in [1, 1.1]$ and between the additional shock and the contact discontinuity, $x/x_{\text{ref}} \in [1.1, 1.3]$. HLLCS with RS overestimates the velocity of the fluid in the area between the stationary wave and the additional shock. Thanh and Kröner's LxF scheme with the computational corrector does not obtain such an overshoot [5]. Brown et al., however, get a similar overshoot for their AUSM$^+$-up scheme for this test [20]. We present the results of a grid refinement study in Figs. 12(a) and 12(b). HLLCS with RS obtains a lower density error than HLLC+S. The convergence rates of both solvers tend to zero, confirming once again that HLLC+S and HLLCS with RS are not consistent for the system.

One should note two things here. Firstly, HLLCS with both FS and RS is *not* generally good at solving resonant problems, but the solver shows promising behaviour and might be modified to work well with resonance. Secondly, even though HLLC+S performed poorly for the stationary state and a strong non-conservative term, it still obtained a reasonable result here. One should not be fooled by this as HLLC+S is generally a poor solver for the system (1).

5.3. Two-phase test with the HEM and the PR EOS

We present here two tests with two-phase CO_2 flow modelled by the HEM with the PR EOS. Test 4 is rather similar to "Test 5" presented by Brown et al. for their AUSM$^+$-up scheme [20].

Table 5
Initial conditions for Test 4.

	p (MPa)	u (ms^{-1})	T (K)	A (m^2)	α_g (-)
Left	5	0	283.547	1	0.0
Right	4	0	278.565	0.5	0.986

Our Test 5 includes a stronger non-conservative term than that of Test 4 for which HLLC+S fails to compute a reasonable solution, whereas HLLCS performs well. Note that no exact solution is available for these tests. In order to provide some reference, we compute a solution with our best performing solver, HLLCS FS, with a very fine grid on which the discontinuous area change is smoothed over a few grid cells.

5.3.1. Test 4: Two-phase test similar to that of Brown et al.

Test 4 is similar to "Test 5" presented by Brown et al. [20] for the HEM with the PR EOS and a discontinuous cross-sectional area. The initial conditions for Test 4 is given in Table 5, where α_g is the volume fraction of gas. Here, the temperatures and α_g are chosen to match the initial conditions given for "Test 5" in [20], $p_L = 5$ MPa, $p_R = 4$ MPa, $\rho_L = 829.1$ kg.m^{-3}, $\rho_R = 126.8$kg.m^{-3}. For the initial state to the right, the volume fraction in [20] is set to $\alpha_R = 0.9$, however our calculations with the PR EOS requires $\alpha_R = 0.986$ to get a density of 126.8 kg.m^{-3} at a saturation pressure of 4 MPa for CO_2. We have therefore modified the volume fraction in our initial condition. Furthermore, we choose a CFL number of 0.9 rather than 0.3 as applied by Brown et al. Otherwise, we use the same parameters as Brown et al.: $x \in [0, 1]$ m, the discontinuity is at $x = 0.6m$ and $N_{\text{cells}} = 1000$. For the HLLCS FS reference solution, we apply $N = 9000$ so the area change occurs over 9 grid cells.

The reference solution and the solutions of HLLC+S, HLLCS RS and HLLCS FS for pressure, density, velocity, Mach number, entropy and *mass* fraction of gas are shown in Figs. 13(a), 13(b), 13(c), 13(d), 13(e) and 13(f), respectively, for $t = 1.2$ ms. Similarly to the result in [20], we obtain a rarefaction to the left, a stationary wave at the area change, $x = 0.6$ m, a very slow-moving contact discontinuity just to the right of the area change at $x \approx 0.61$ m and a shock to the right. There is an evaporation jump following the shock and further evaporation to the left of the area change as can be seen in the mass fraction of gas in $x \in [0.52, 0.6]$m, see Fig. 13(f). This causes a "splitting" of the rarefaction wave as observed in Fig. 13(a) because the wave travels quickly in the pure liquid and more slowly in the two-phase area due to different speeds of sound for single and two-phase flow. The entropy increases at the contact discontinuity. These results are as expected.

We note, however, that HLLC+S's solution contains a spike in the pressure and density at the area change, $x = 0.6$ m. Such a

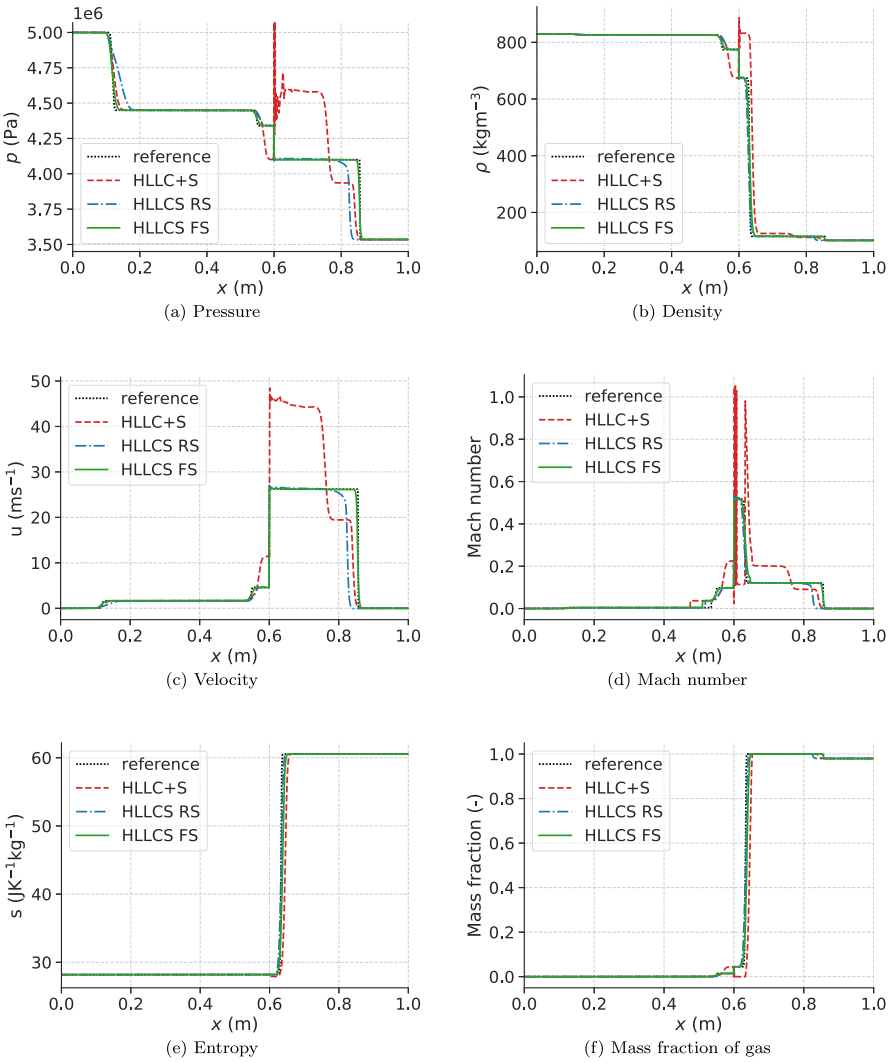

Fig. 15. The solutions of HLLC+S (red, dashed line), HLLCS RS (blue, dash-dotted line) and HLLCS FS (green line) for pressure (a), density (b), velocity(c), Mach number (d), entropy (e) and mass fraction of gas (f) for Test 5 at $t = 1.2$ ms with the initial discontinuity at $x = 0.6$ m. The result is compared to a reference HLLCS FS solution on a finer grid (black dotted line). (For interpretation of the references to colour in this figure legend, the reader is referred to the web version of this article.)

spike is not present for the HLLCS solvers. There is no physical reason for a spike to be present in the pressure and density at the area change so this must be caused by the discretization of the non-conservative term in HLLC+S. The AUSM$^+$-up scheme presented in [20] also gets a spike in its density solution at the area change. Based on our results, it seems likely that the spike for the AUSM$^+$-up scheme in [20] is also caused by the discretization of the non-conservative term, and that the HLLCS methods are more accurate than the AUSM$^+$-up scheme. HLLCS RS approximates the wavespeeds of the rarefaction and shock less accurately than HLLCS FS and HLLC+S, but seems to perform well otherwise. HLLCS FS appears to be the most accurate, which is reasonable based on the results for the ideal gas tests.

We further present the temperature results for a coarse grid with $N_{\text{cells}} = 100$ and a fine grid with $N_{\text{cells}} = 10,000$ in Figs. 14(a) and 14(b). HLLCS with FS performs well, even for the coarse grid. HLLCS with RS performs poorly for the coarse grid, but converges towards HLLCS with FS on the fine grid. HLLC+S converges towards an incorrect solution.

Table 6
Initial conditions for Test 5.

	p (MPa)	u (ms^{-1})	T (K)	A (m^2)	α_g (-)
Left	5	0	283.547	1	0.0
Right	3.5	0	280	0.2	0.986

5.3.2. Test 5: Two-phase test with a large non-conservative term

We have constructed the present case test to provide a challenging test for the discretization of the non-conservative term. The initial condition is given in Table 6. We employ the same domain, position of the discontinuity, grids and CFL number as in Test

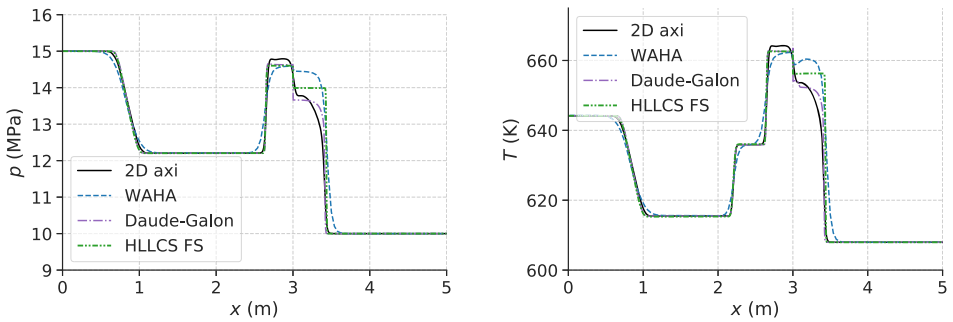

(a) Pressure (b) Temperature

Fig. 16. Test 6: Results of a water vapour shock-tube interaction with an abrupt contraction at $t = 2.5$ ms for HLLCS FS compared with WAHA results from Tiselj et al. [42], the results of Daude and Galon's scheme [45] and a 2D axisymmetric simulation from [46] provided by Daude.

Table 7
Initial conditions for water vapour shock test (Test 6).

	p (MPa)	u (ms^{-1})	T (K)	A (m^2)	α_g (-)
$x \in [0, 2]$	15	0	644.17	0.4	1.0
$x \in [2, 3]$	10	0	607.96	0.4	1.0
$x \in [3, 5]$	10	0	607.96	0.02	1.0

4. We compute a HLLCS FS reference solution on a finer grid for which the area change occurs over 9 grid cells for this test as well.

The reference solution and the solutions of HLLC+S, HLLCS RS and HLLCS FS for pressure, density, velocity, Mach number, entropy and mass fraction of gas are shown in Figs. 15(a), 15(b), 15(c), 15(d), 15(e) and 15(f), respectively, for $t = 1.2$ ms. It is evident in the plots of pressure, density, velocity and Mach number that HLLC+S has failed to compute a reasonable solution and is unstable. In Fig. 15(a), we have cut off the pressure peak at the area change, $x = 0.6$ m which reaches 14 MPa. Based on the results of this test and further on the result of the steady-state test in Section 5.2.1, we see that imposing the non-disturbance relation [41] for compressible duct flow on the discretization of the non-conservative term is not enough to ensure the stability of the solver. As the discretization of the non-conservative term in the AUSM$^+$-up scheme is only based on this principle, similarly to HLLC+S, the scheme will likely also fail for this test.

5.4. Test 6: Single-phase steam shock-tube interaction with an abrupt contraction

We will here apply our best performing method, HLLCS with FS, to a water vapour test originally proposed by Tiselj et al. [42] to compare its results with existing methods. In the present work, the IAPWS-95 equation of state is used for modelling water [43], using the TREND software [44]. We compare our results to those of WAHA [42], a HLLC-based method proposed by Daude and Galon [45] and a 2D axisymmetric simulation of the system provided by Daude and Galon [46]. Note that Daude and Galon model the water differently, using steam-water tables based on the 1984 NBS/NRC formulation [47]. The initial conditions for this test is presented in Table 7. The test is run with 2000 grid cells and a CFL number of 0.8. In WAHA, 125 nodes are applied.

The results for pressure and temperature at $t = 2.5$ ms are plotted in Figs. 16(a) and 16(b) respectively. The schemes perform similarly, except for the calculated plateau between the area change at $x = 3$ m and the transmitted shock wave at $x \approx 3.45$ m. The different thermodynamic modelling of water may contribute to the difference in the results, however, as the results agree well for all the other waves in the solution it seems more likely that the difference is related to the numerical schemes. Daude and Galon's scheme agrees the most with the 2D axisymmetric simulation. However, we note that the 2D result appears to be smeared in this area and the simulation might not be fully converged. Note also that Daude and Galon's scheme obtains a small peak in the temperature at $x = 3.0$ m. None of the other solvers obtain this. HLLCS FS is closer to Daude and Galon's scheme and the 2D axisymmetric result than WAHA. The HLLCS FS scheme provides the least smeared result and has no artefacts such as bumps or peaks in its solution. We therefore find the result reasonable.

6. Conclusion

We have proposed HLLC-type finite-volume methods to simulate transient two-phase flow in pipes with discontinuous cross-sectional area. Such simulations are relevant to describe flow in wellbores, nuclear coolant flows and high-pressure pipeline flow.

HLLC+S is a relatively simple scheme, incorporating the non-conservative term in the governing equations much like a source term with a discretization constructed to conserve the stationary state exactly. This approach is similar to that of Brown et al. [20] for an AUSM$^+$-up scheme. HLLCS is a new approximate Riemann solver, assuming a four-wave solution, which includes the non-conservative term in a more thorough manner. For subsonic flow, HLLCS requires the solution of a nonlinear system. Notably, both HLLC+S and HLLCS can be applied with a *general* equation of state.

The methods are tested on benchmark tests with the ideal gas EOS, including a steady-state test, a Riemann problem with a strong non-conservative term and a resonant case. Though HLLC+S performs well for the resonant case, it performs poorly otherwise. This solution scheme is not consistent for the system. We have tested two discretizations of the non-conservative term for the HLLCS-based FVM which we have called FS and RS. FS is based on the flux-estimates of the HLLCS approximate Riemann solver across cell faces, and RS is based on the Roe-average between neighbouring grid cells. It is found that HLLCS does not have a solution for its nonlinear system for resonant flow, where the assumption of a four-wave solution is incorrect. Despite this, HLLCS with RS computes a more accurate solution than HLLC+S for the resonant case. HLLCS with FS does not reach a solution for this case. Otherwise, HLLCS with FS is superior in accuracy and is found to be well-balanced in the sense that it conserves the steady state exactly.

We have further applied the methods to two Riemann problems with two-phase CO_2 flow, governed by a homogeneous equilibrium model (HEM) together with the Peng–Robinson EOS. In the first test we find that HLLC+S has an unphysical behaviour at the area discontinuity. This is not present for the HLLCS solvers. We show with the second test that it is possible to design a case in which HLLC+S diverges whereas HLLCS does not. Finally, we have tested our best performing method, HLLCS with FS, on a test with water vapour and compared our results to other available solvers for the compressible duct flow equations. The result appears reasonable.

Based on these results, HLLCS with FS holds promise as an accurate and robust method to simulate various challenging transient two-phase flow problems. However, HLLCS cannot be applied in cases of flow towards an expansion where the flow becomes choked at the area discontinuity because such cases are resonant. This is a limitation of HLLCS which should be improved upon if the solver is to be used in general industrial applications. Future work includes the extension of HLLCS to resonant flow, possibly by including a fifth wave in its solution, and the derivation of higher-order HLLCS-based methods.

Declaration of Competing Interest

The authors declare that they have no known competing financial interests or personal relationships that could have appeared to influence the work reported in this paper.

CRediT authorship contribution statement

Alexandra Metallinou Log: Conceptualization, Software, Investigation, Visualization, Writing - original draft. **Svend Tollak Munkejord:** Funding acquisition, Conceptualization, Supervision, Writing - review & editing. **Morten Hammer:** Conceptualization, Software, Supervision, Writing - review & editing.

Acknowledgement

This work received support from the NCCS Research Centre, performed under the Norwegian research program Centres for Environment-friendly Energy Research (FME). The authors acknowledge the following partners for their contributions: Aker Carbon Capture, Allton, Ansaldo Energia, Baker Hughes, CoorsTek Membrane Sciences, Equinor, Fortum Varme Oslo, Gassco, Krohne, Larvik Shipping, Lundin Norway, Norcem, Norwegian Oil and Gas, Quad Geometrics, Stratum Reservoir, Total, Vår Energi, Wintershall DEA and the Research Council of Norway (257579). We are most grateful to Nikolai Andrianov for help with the use of CONSTRUCT, Solomon Brown for a fruitful discussion on Test 4 and Frédéric Daude for providing the results of WAHA, Daude and Galon's solver and the 2D axisymmetric simulation in Test 6. Finally, we would like to thank the reviewers for their detailed feedback which significantly improved the article.

Appendix A. Jacobian matrix of compressible duct flow

For smooth solutions, the compressible duct flow equations can be expressed as

$$\boldsymbol{U}_t + \boldsymbol{A}(\boldsymbol{U})\boldsymbol{U}_x = \boldsymbol{0}, \tag{A.1}$$

where $\boldsymbol{A}$ is the Jacobian matrix of the system. If the pressure is given by some general equation of state (EOS), $p = p(e, \rho)$ a small change in pressure, $\mathrm{d}p$, can be expressed as

$$\mathrm{d}p = \left(\frac{\partial p}{\partial \rho}\right)_e \mathrm{d}\rho + \left(\frac{\partial p}{\partial e}\right)_\rho \mathrm{d}e = (c^2 - \Gamma\frac{p}{\rho})\ \mathrm{d}\rho + \Gamma\rho\ \mathrm{d}e, \tag{A.2}$$

where c is the speed of sound and Γ is the first Grüneisen parameter. Then $\boldsymbol{A}(\boldsymbol{U})$ is given by Eq. (A.3).

$$\boldsymbol{A} = \begin{pmatrix} 0 & 1 & 0 & 0 \\ c^2 - u^2 - \Gamma(e + \frac{p}{\rho} - \frac{1}{2}u^2) & (2-\Gamma)u & \Gamma & p\Gamma - \rho c^2 \\ u\left(c^2 - (\Gamma+1)(e + \frac{1}{2}u^2 + \frac{p}{\rho}) + \Gamma u^2\right) & e + \frac{p}{\rho} + \frac{1}{2}u^2 - \Gamma u^2 & (\Gamma+1)u & u\left(p(\Gamma+1) - \rho c^2\right) \\ 0 & 0 & 0 & 0 \end{pmatrix} \tag{A.3}$$

References

[1] Abbasi M H, Lordejani S N, Velmurugan N, Berg C, Iapichino L, Schilders W H A, et al. A Godunov-type scheme for the drift flux model with variable cross section. J. Pet. Sci. Eng. 2019;179:796–813. doi:10.1016/j.petrol.2019.04.089.
[2] Berry R A, Saurel R, LeMetayer O. The discrete equation method (DEM) for fully compressible, two-phase flows in ducts of spatially varying cross-section. Nucl Eng Des 2010;240:3797–818. doi:10.1016/j.nucengdes.2010.08.003.
[3] Ettouney R S, El-Rifai M A, Elzoubier A A. Emergency venting into redundant pipelines. J Loss Prev Process Ind 2012;25:739–45. doi:10.1016/j.jlp.2012.04.009.
[4] Simões-Moreira J R, Bullard C W. Pressure drop and flashing mechanisms in refrigerant expansion devices. Int J Refrig 2003;26:840–8. doi:10.1016/S0140-7007(03)00070-7.
[5] Thanh M D, Kröner D. Numerical treatment of nonconservative terms in resonant regime for fluid flows in a nozzle with variable cross-section. Comput Fluids 2012;66(15):130–9. doi:10.1016/j.compfluid.2012.06.021.
[6] Rochette D, Clain S, Buffard T. Numerical scheme to complete a compressible gas flow in variable porosity media. Int J Comut Fluid Dyn 2005;19(4):299–309. doi:10.1080/10618560500162702.
[7] Helluy P, Hérard J, Mathis H. A well-balanced approximate Riemann solver for compressible flows in variable cross-section ducts. J Comput and Appl Mathem 2012;236(7):1976–92. doi:10.1016/j.cam.2011.11.008.
[8] Cuong D H, Thanh M D. Constructing a Godunov-type scheme for the model of a general fluid flow in a nozzle with variable cross-section. Appl Mathem and Comput 2017;305(15):136–60. doi:10.1016/j.amc.2017.01.065.
[9] Clain S, Rochette D. First- and second-order finite volume methods for the one-dimensional nonconservative Euler system. J Comput Phys 2009;228(22):8214–48. doi:10.1016/j.jcp.2009.07.038.
[10] Tokareva S A, Toro E F. HLLC-type Riemann solver for the Baer-Nunziato equations of compressible two-phase flow. J Comput Phys 2010;229:3573–604. doi:10.1016/j.jcp.2010.01.016.
[11] Murillo J, García-Navarro P. Augmented versions of the HLL and HLLC Riemann solvers including source terms in one and two dimensions for shallow flow applications. J Comput Phys 2012;231(20):6861–906. doi:10.1016/j.jcp.2012.06.031.
[12] Gallouët T, Hérard J, Seguin N. Some approximate Godunov schemes to compute shallow-water equations with topography. Comput Fluids 2003;32(4):479–513. doi:10.1016/S0045-7930(02)00011-7.
[13] Liang Q, Marche F. Numerical resolution of well-balanced shallow water equations with complex source terms. Adv Water Resour 2009;32(6):873–84. doi:10.1016/j.advwatres.2009.02.010.
[14] Audusse E, Bouchut F, Bristeau M, Klein R, Perthame B. A fast and stable well-balanced scheme with hydrostatic reconstruction for shallow water flows. SIAM J Sci Comput 2006;25(6):2050–65. doi:10.1137/S1064827503431090.
[15] Rochette D, Clain S. Two-dimensional computation of gas flow in a porous bed characterized by a porosity jump. J Comput Phys 2006;219(1):104–19. doi:10.1016/j.jcp.2006.03.013.
[16] Girault L, Hérard J-M. Multidimensional computations of a two-fluid hyperbolic model in a porous medium. Int. J. Finite Vol. 2010;7(1). Publisher: Institut de Mathématiques de Marseille, AMU; https://hal.archives-ouvertes.fr/hal-01114209
[17] Bouchut F. Nonlinear stability of finite volume methods for hyperbolic conservation laws and well-Balanced schemes for sources. Birkhäuser,; 2004. doi:101007/b93802.
[18] Greenberg J M, Leroux A Y. A well-balanced scheme for the numerical processing of source terms in hyperbolic equations. SIAM J Numer Anal 1996;33(1):1–16. doi:10.1137/0733001. Publisher: Society for Industrial and Applied Mathematics
[19] Kröner D, Thanh M D. Numerical solutions to compressible flows in a nozzle with variable cross-section. SIAM J Numer Anal 2005;43(2):796–824. doi:10.1137/040607460.
[20] Brown S, Martynov S, Mahgerefteh H. Simulation of two-phase flow through ducts with discontinuous cross-section. Comput Fluids 2015;120(5):46–56. doi:10.1016/j.compfluid.2015.07.018.
[21] D. Y. Peng, D. B. Robinson. A new two-constant equation of state. Ind Eng Chem Fundam 1976;15:59–64. doi:10.1021/i160057a011.

[22] LeMartelot S, Nkong B, Saurel R. Liquid and liquid–gas flows at all speeds. J Comput Phys 2013;255:53–82. doi:10.1016/j.jcp.2013.08.001.
[23] Toro E F, Spruce M, Speares W. Restoration of the contact surface in the HLL-Riemann solver.. Shock Waves 1994;4(1):25–34. doi:10.1007/BF01414629.
[24] Marzouk O A. The Sod gasdynamics problem as a tool for benchmarking face flux construction in the finite volume method. Sci Afr 2020;10. doi:10.1016/j.sciaf.2020.e00573.
[25] Baer M R, Nunziato J W. A two-phase mixture theory for the deflagration-to-detonation transition (ddt) in reactive granular materials. Int J Multiphase Flow 1986;12:861–89. doi:10.1016/0301-9322(86)90033-9.
[26] Lochon H, Daude F, Galon P, Hérard J-M. HLLC-type Riemann solver with approximated two-phase contact for the computation of the Baer–Nunziato two-fluid model. J Comput Phys 2016;326:733–62. doi:10.1016/j.jcp.2016.09.015.
[27] Munkejord S T, Hammer M, Løvseth SW. CO $_2$transport: data and models–a review. Appl Energy 2016;169:499–523. doi:10.1016/j.apenergy.2016.01.100.
[28] Andrianov N, Warnecke G. On the solution to the Riemann problem for the compressible duct flow. SIAM J Appl Math 2004;64(3):878–901. doi:10.1137/S0036139903424230.
[29] Log A M. Development and investigation of HLLC-type finite-volume methods for one and two-phase flow in pipes with varying cross-sectional area. NTNU; 2020. Master's thesis. https://alexandramlog.files.wordpress.com/2020/12/thesis-5-1.pdf
[30] Goatin P, LeFloch P G. The Riemann problem for a class of resonant hyperbolic systems of balance laws. Annales de l'Institut Henri Poincaré C, Analyse non linéaire 2004;21(6):881–902. doi:10.1016/j.anihpc.2004.02.002.
[31] N. Andrianov. CONSTRUCT, a collection of MATLAB routines for constructing the exact solution to the Riemann problem for the Baer-Nunziato model of two-phase flows. 2004. https://github.com/nikolai-andrianov/CONSTRUCT.
[32] Wilhelmsen Ø, Aasen A, Skaugen G, Aursand P, Austegard A, Aursand E, et al. Thermodynamic modeling with equations of state: present challenges with established methods. Ind. Eng. Chem. Res. 2017;56(13):3503–15. doi:10.1021/acs.iecr.7b00317.
[33] SINTEF Energy Research, Thermopack. 2020. https://github.com/sintef/Thermopack.
[34] Hammer M, Ervik Å, Munkejord S T. Method using a density–energy state function with a reference equation of state for fluid-dynamics simulation of vapor–liquid–solid carbon dioxide. Ind Eng Chem Res 2013;52(29):9965–78. doi:10.1021/ie303516m.
[35] Toro E F. Riemann solvers and numerical methods for fluid mechanics - A practical introduction, 2nd edition.. Springer Dordrecht Heidelberg London New York: Springer; 1999. doi:101007/b79761.
[36] Roe P L. Approximate riemann solvers, parameter vectors, and difference schemes. J Comput Phys 1981;43(2):357–72. doi:10.1016/0021-9991(81)90128-5.
[37] Davis S F. Simplified second-Order Godunov-Type methods.. SIAM J Sci Stat Comput 1988;9(3). doi:10.1137/0909030. 445–437
[38] Einfeldt B. On Godunov-type methods for gas dynamics.. SIAM J Numer Anal 1988;25(2):294–318. doi:10.1137/0725021.
[39] Evje S, Flåtten T. Hybrid flux-splitting schemes for a common two-fluid model. J Comp Phys 2003;192(1):175–210. doi:10.1016/j.jcp.2003.07.001.
[40] Munkejord S T. Comparison of Roe-type methods for solving the two-fluid model with and without pressure relaxation. Comput. Fluids 2007;36(6):1061–80. doi:10.1016/j.compfluid.2007.01.001.
[41] Liou M, Chang C, Nguyen L, Theofanous T G. How to solve compressible multifluid equations: asimple, robust, and accurate method. AIAA J. 2008;46(9):2345–56. doi:10.2514/1.34793.
[42] Tiselj I, Horvat A, Cerne G, J Gale, Parzer I, Mavko B, et al. WAHA3 code manual, Final report of the WAHALoads project Tech. Rep.. FIKS-CT-2000-00106, EU 6th program; 2004.
[43] Wagner W, Pruß A. The IAPWS formulation 1995 for the thermodynamic properties of ordinary water substance for general and scientific use. J Phys Chem Ref Data 2002;31(2):387–535. doi:10.1063/1.1461829. Publisher: American Institute of Physics
[44] SpanR., Eckermann T., Herrig S., Hielscher S., Jäger A., Thol M.. TREND. Thermodynamic reference and engineering data 3.0. 2016. Lehrstuhl für Thermodynamik, Ruhr-Universität Bochum.
[45] Daude F, Galon P. A finite-volume approach for compressible single- and two-phase flows in flexible pipelines with fluid-structure interaction. J Comput Phys 2018;362:375–408. doi:10.1016/j.jcp.2018.01.055.
[46] Daude F, Galon P. Simulations of single- and two-phase shock tubes across abrupt changes of area and branched junctions. Nucl Eng Des 2020;365. doi:10.1016/j.nucengdes.2020.110734.
[47] Haar L, Gallangher J S, Kell G. NBS/NRC Steam tables: thermodynamic and transport properties and computer programs for vapor and liquid states of water in SI units.. Hemisphere Publishing Co; 1984.

Conference paper

Log, Alexandra Metallinou; Munkejord, Svend Tollak; Hammer, Morten; Hafner, Armin; Deng, Han; Austegard, Anders. (2022) Investigation of non-equilibrium effects during the depressurization of carbon dioxide. *15th IIR-Gustav Lorentzen Conference on Natural Refrigerants - GL2022 - Proceedings - Trondheim, Norway, June 13-15th 2022.*
doi:10.18462/iir.gl2022.0197

DOI: 10.18462/iir.gl2022.0197

Investigation of non-equilibrium effects during the depressurization of carbon dioxide

Alexandra M. LOG*[(a)], Svend T. MUNKEJORD [(b)], Morten HAMMER[(b)], Armin HAFNER [(a)], Han DENG[(b)], Anders AUSTEGARD[(b)]

[(a)] NTNU, Department of Energy and Process Engineering
Trondheim, NO-7491, Norway
[(b)] SINTEF Energy Research
Trondheim, NO-7465, Norway
*Corresponding author: alexandra.m.log@ntnu.no

ABSTRACT

Predicting the phase change of liquid CO_2 during depressurization is highly relevant for the application in refrigeration units and for safety analysis in the context of CO_2 capture and storage (CCS). For abrupt depressurization processes, nucleation of gas will not occur at equilibrium and the liquid becomes superheated. In this work, we analyze the experimental results of depressurization tests conducted in the ECCSEL depressurization facility in Trondheim for pure CO_2 and determine the degree of superheat reached in the tests. The experiments include depressurization from 11-12 MPa to atmospheric pressure at different temperatures and the thermodynamic path in one of the cases passes near the critical point. The results agree well with the nucleation rate predicted by classical nucleation theory.

Keywords: Carbon dioxide, expansion, depressurization, phase change, superheat, nucleation.

1. INTRODUCTION

Studying the phase-change behaviour of liquid CO_2 during expansion is relevant in several industrial applications. Examples include the application of CO_2 as a natural refrigerant, and for safety analysis of CO_2-carrying pipelines as part of CO_2 capture and storage (CCS) systems. In various depressurization tests of liquid CO_2, significant degrees of superheat are observed before gas forms and two-phase flow is established. The delayed nucleation leads to two-phase flow occurring at a lower pressure than assumed by equilibrium models. For safety analyses and process optimization, it is key to predict exactly when phase change occurs, as two-phase flow is much slower than single-phase flow and the inception of phase change therefore largely determines the fluid state during depressurization, and, among other things, the resulting flow rates.

In the effort to provide more data on the non-equilibrium phase-change behaviour of liquid CO_2, we study depressurization tests conducted at the ECCSEL depressurization facility, which has dense and accurate instrumentation to dynamically capture pressure and temperature (Munkejord et al., 2020). The tests are conducted with pure CO_2 and include initial conditions from 10 MPa - 12 MPa and 283 K - 313 K. We focus on pressure measurements within a very short timeframe ($\approx$ 5 ms) where gas nucleation can be observed in all the tests. Using pressure measurements to estimate when nucleation occurs contrasts with the more common method of estimating the point of nucleation based on the assumption that it coincides with critical flow. As critical flow and nucleation do not necessarily coincide (though they often do), the present method is thought to better represent the physics. To provide relevant references for the experimental results, we compare the pressure data to the prediction of the homogeneous equilibrium model, and we compare the point of nucleation to the superheat limit predicted by classical nucleation theory.

The paper is structured as follows. In Section 2 the ECCSEL depressurization facility is briefly described, in Section 3, the homogeneous equilibrium model and classical nucleation theory are outlined, in Section 4 the experimental results are presented and analyzed, and finally concluding remarks are given in Section 5.

2. EXPERIMENTAL SETUP AND INSTRUMENTATION

In this section, we briefly describe the experimental setup and instrumentation for the depressurization experiments. A more detailed description is presented by Munkejord et al. (2020).

2.1. Experimental setup and procedure

The ECCSEL depressurization facility consists of a gas supply with mass flow controllers, a compression and cooling system for achieving the desired experimental conditions, and a test section with a rupture disk at the open end. The test section is a tube made of 11 stainless steel pipes providing a total length of 61.67 m. These pipes have an inner diameter of 40.8 mm, an outer diameter of 48.3 mm, and were honed to a mean roughness of $R_a = 0.2\ \mu$m - $0.3\ \mu$m. The tube is wrapped in heating cables and insulated with a 60 mm thick layer of glass wool. In Figure 1, an overview of the setup is shown. The facility is designed for a maximum operating pressure of 20 MPa and initial temperatures within 5 °C to 40 °C.

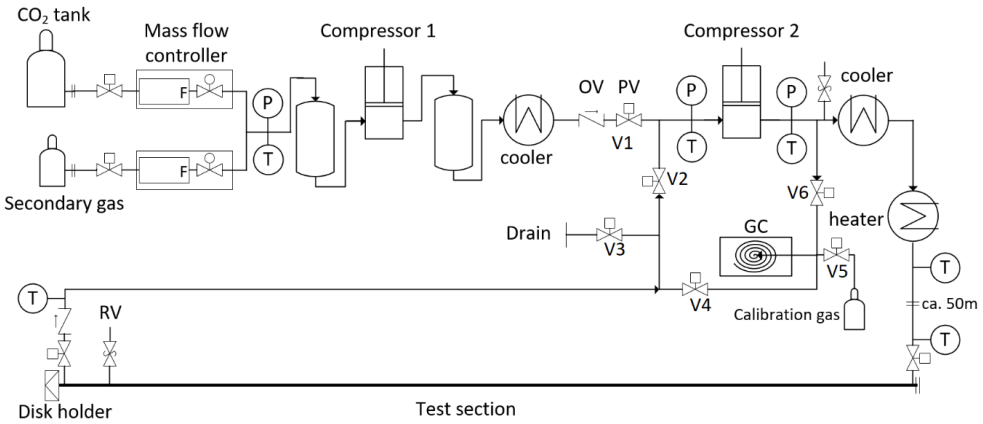

Figure 1: System overview of the ECCSEL depressurization facility (Munkejord et al., 2020). (RV: relief valve; OV: one-way valve; PV: pneumatic valve)

The experimental procedure is as follows. First, the rupture disk is installed and the system is evacuated. Then, the test section is filled with CO_2 and pressurized. When the pressure reaches approximately 70% of the desired pressure, the CO_2 is circulated to achieve a uniform temperature in the test section. The temperature is adjusted using the heating elements wrapped around the test section. The pressure is then increased gradually, with alternating filling and circulation of CO_2, until the disk ruptures. Upon disk rupture, the two pneumatic valves at the ends of the test section are automatically closed to stop circulation. The released CO_2 is vented through an exhaust pipe. An image of the CO_2 plume released from the exhaust pipe in Test 4 is shown in Figure 2.

Figure 2: Image of CO_2 plume released from the exhaust pipe in depressurization test 4.

2.2. Instrumentation

In the experiments studied, two kinds of rupture discs have been applied. Both of which have a specified burst pressure of 120 barg±5% at 22 °C. We study tests 4, 6, 8 and 19 of the ECCSEL depressurization facility. For tests 4, 6 and 8, X-scored discs were used, whereas for Test 19, a circular-scored triple-layer disc was employed. The initial conditions of the tests are presented in Section 4, Table 1. Along the test section of the facility, 16 fast-response pressure transducers and 23 thermocouples are mounted to the inner-surface in order to capture the pressure and temperature transients during depressurization. Most of the pressure sensors are densely distributed close to the open end to capture the expansion wave, as shown in Figure 3.

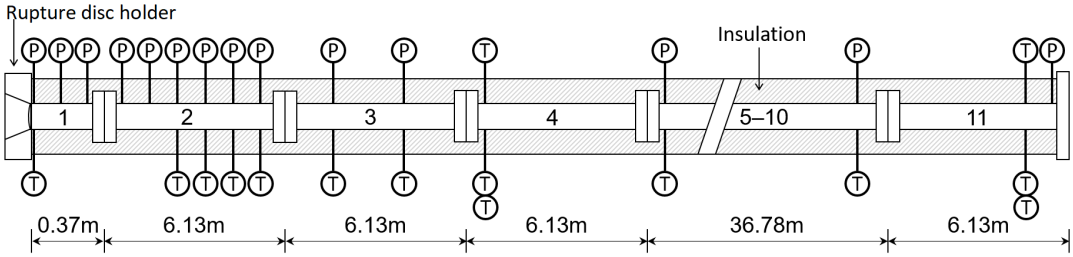

Figure 3: Test section of the ECCSEL depressurization facility (Munkejord et al., 2020). (Dimensions are not to scale, pipes 5-10 and corresponding sensors are omitted)

For our analysis, we will only use data from the first pressure transducer as it is closest to the pipe outlet and therefore experiences the most violent fall in pressure and records a large degree of superheat. This pressure transducer is located at 0.080 m from the rupture disc. The logging frequency of the data from the pressure transducers is 100 kHz for the time frame considered. The uncertainty of the data is 60 kPa with a 95% confidence level. The reported initial conditions of the experiments were estimated from the data between 1 ms and 0.5 ms before disk rupture.

3. THEORY AND MODELLING

3.1. Flow at equilibrium – the homogeneous equilibrium model

In order to analyze the experimental results, 1D CFD simulations of equilibrium flow are provided as a reference. We then apply the homogeneous equilibrium model (HEM) as described by Munkejord and Hammer (2015), with the method of Hammer et al. (2013). HEM is based on two main assumptions for two-phase flow of liquid (l) and gas (g):

1. The flow is well-mixed (homogeneous) such that the two phases are transported at the same velocity, $u_l = u_g = u$, and
2. the liquid and gas are in mechanical, chemical and thermal equilibrium.

For full-bore depressurization, the assumption of homogeneous flow has been found to be fairly accurate (Brown et al., 2013).

The model equations are discretized using the FORCE scheme in space (Toro and Billett, 2000) and forward Euler in time, with a Courant-Friedrichs-Lewy (CFL) number of 0.9. The simulation is conducted over a 12m domain with 800 grid cells. For the calculation of thermodynamic properties, the equation of state (EOS) of Span and Wagner (1996) is applied.

3.2. Nucleation theory and the superheat limit

Energy is required for bubbles to form in a metastable liquid. Boiling due to depressurization is interesting because nearly no energy is added from the outside environment, and large degrees of superheat can be reached before enough energy is available for bubble formation. This can be described by nucleation theory.

During nucleation, random thermal fluctuations cause the formation of small embryos of a new phase within the metastable phase. A certain free-energy barrier must be surpassed by the thermal fluctuations in order to create critically-sized embryos of the new phase. These embryos are just large enough to avoid collapsing back to the mother phase. As this is an activated process, the nucleation rate of critically-sized embryos can be expressed as an Arrhenius-type law,

$$J = K\, exp\left(-\frac{\Delta G^*}{k_B T}\right), \qquad \text{Eq. (1)}$$

where ΔG^* is the free-energy barrier, k_B is the Boltzmann constant, T is the temperature of the mother phase and K is a kinetic prefactor.

There are two main modes of nucleation, homogeneous and heterogeneous. Homogeneous nucleation occurs in the bulk of the liquid and the nucleation rate can be estimated with classical nucleation theory (CNT). Heterogeneous nucleation occurs on some surface or impurity, which lowers the free-energy barrier. The rate of heterogeneous nucleation can be estimated by multiplying the free-energy barrier found in CNT by some reduction factor (Debenedetti, 1996). However, no successful, rigorous model of this reduction factor currently exists for practical purposes, and correlations are often applied.

The following description of CNT is adapted from Debenedetti (1996). The free-energy barrier in CNT is estimated to be

$$\Delta G^* = \frac{4\pi\sigma r^{*2}}{3}, \qquad \text{Eq. (2)}$$

where σ is the surface tension and r^* the critical radius of the embryo. It is assumed that the surface tension of the embryo is equal to the planar surface tension between the phases at equilibrium. For bubble formation in a metastable liquid, the critical radius is approximated as

$$r^* = \frac{2\sigma}{p_{sat}(T_l) - p_l}, \qquad \text{Eq. (3)}$$

where $p_{sat}(T_l)$ is the saturation pressure at the liquid temperature and p_l is the liquid pressure. The kinetic prefactor can be approximated by

$$K = \widetilde{\rho_l}\sqrt{\frac{2\sigma}{\pi m}}, \qquad \text{Eq. (4)}$$

where $\widetilde{\rho_l}$ is the number density of liquid particles and m is the mass of one molecule. For completeness, we also provide the critical radius and kinetic prefactor for the formation of droplets in a metastable gas:

$$r^* = \frac{2\sigma}{\widetilde{\rho_l} k_B T\, ln(p_g/p_{sat})}, \qquad \text{Eq. (5)}$$

$$K = \frac{\widetilde{\rho_g}^2}{\widetilde{\rho_l}}\sqrt{\frac{2\sigma}{\pi m}}, \qquad \text{Eq. (6)}$$

$\widetilde{\rho_g}$ is the number density of gas particles.

In order to estimate the superheat limit (SHL), a critical nucleation rate is set to define the point where sudden phase change is observed. Following Aursand et al. (2017), we choose the critical nucleation rate to be $J_{crit} = 10^{12}\mathrm{m}^{-3}\mathrm{s}^{-1}$. The SHL is then found by solving for the temperature where

$$J(T) = J_{crit}. \qquad \text{Eq. (7)}$$

To determine the SHL, the properties of pure CO_2 in the stable and metastable regions is calculated using the Span and Wagner (1996) EOS and the CO_2 surface tension is approximated using the correlation of Rathjen and Straub (1977).

4. RESULTS AND DISCUSSION

In this section, the depressurization data of selected experiments from Munkejord (2020) and a new experiment from the ECCSEL depressurization facility are analyzed to find the degree of superheat reached. The result is compared to the superheat limit (SHL) predicted by CNT.

4.1. Experimental results

The conditions of the experiments are presented in Table 1. All the experiments were full-bore, meaning that no restriction was present at the outlet. For Test 19, two initial conditions are provided as the layers of the triple-layer rupture disk did not break at the same time, so a different condition was reached before the disk was fully opened. We estimate the temperature before the final layer of the rupture disk broke by assuming that the depressurizations due to other layers breaking were isentropic.

Table 1: Experimental conditions of the depressurization tests. Test 19 has two values provided; initial condition before first layer of rupture disk broke/initial condition before final layer of rupture disk broke.

Test no.	Pressure avg. (MPa)	Temperature avg. (°C)	Ambient temp. (°C)
4*	12.54	21.1	22
6*	10.40	40.0	6
8*	12.22	24.6	9
19	12.47/11.20	10.2/9.0	18

* Munkejord et al. (2020)

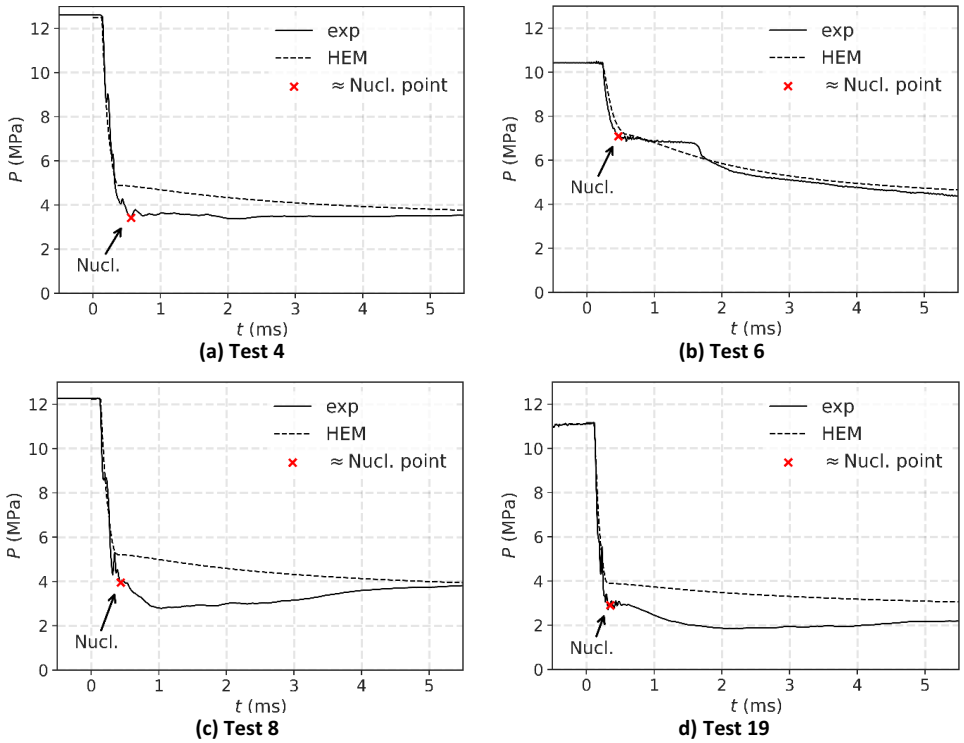

Figure 4: Data from the first pressure transducer over time (exp) for the tests presented in Table 1 compared to the HEM. Arrows and red crosses indicate approximately when bubble nucleation occurred in the experiments.

In Figure 4, the pressure measurements at 0.080 m from the open end is shown for all the tests from 0.5 ms before the rupture disk breaks until 5.5 ms has passed. The results are compared to HEM simulations.

The pressure falls very quickly when the CO_2 is in the liquid phase. As bubbles nucleate, the slope of the pressure time gradient reduces significantly and pressure perturbations can be observed. Based on this, we have marked with arrows the approximate area where nucleation occurred in the experiments. For tests 4, 8 and 19, nucleation of gas occurs at a lower pressure than what is predicted by HEM. For Test 6, nucleation occurs close to the point predicted by HEM, as this is very close to the critical point of CO_2. This is in line with nucleation theory.

4.2. Analysis and comparison to CNT

For further analysis, we choose a particular point for each test, marked with red crosses in Figure 4, to represent the point of nucleation. The exact choice of this point is somewhat uncertain, but it is based on the sudden flattening in the slope of pressure changes over time in combination with pressure perturbations. For such a short timeframe, it is reasonable to assume that the depressurization follows the liquid isentrope until nucleation occurs. We may then estimate the temperature at the point of nucleation. The information on the approximate point of nucleation is summarized in Table 2.

Table 2: Summary on the approximate point where nucleation starts for the ECCSEL depressurization tests and comparison to the homogeneous SHL predicted by CNT.

Test no.	Time (ms)	P (MPa)	T (K)	Exp. superheat (K)	Hom. SHL (K)	Rel. diff. (%)
4	0.56	3.43	283.9	11.3	11.1	2%
6	0.47	7.17	302.9	0.0	0.0	0%
8	0.44	3.95	287.1	9.1	8.2	11%
19	0.32	2.70	274.1	10.3	16.7	-38%

Finally, we plot the approximate points where nucleation first occurred for the ECCSEL depressurization tests in a temperature-pressure diagram and compare this to the homogeneous SHL predicted by CNT. The result is shown in Figure 5.

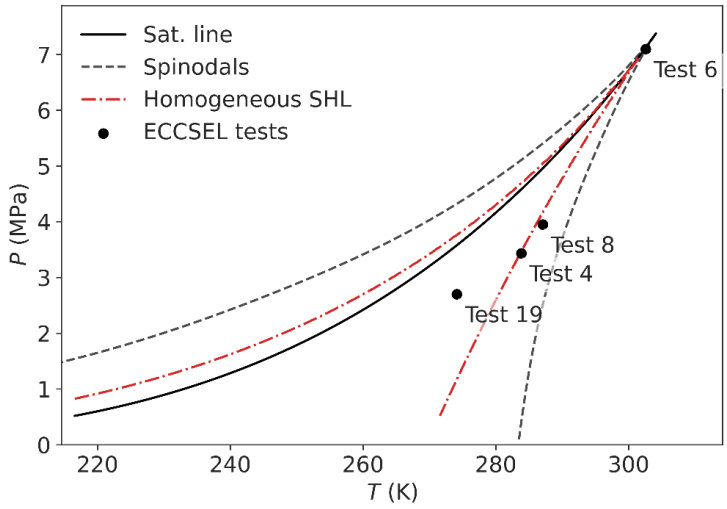

Figure 5: Approximate (p,T)-points of nucleation for the ECCSEL depressurization tests, assuming an isentropic depressurization path. Tests 4, 6, and 8 agree well with the homogeneous SHL predicted by CNT.

The nucleation points of tests 4, 6 and 8 agree very well with the superheat limit predicted by CNT. For Test 19, the superheat reached experimentally is 7.2 K lower than that predicted by CNT. This is likely caused by

heterogeneous nucleation at the wall of the test section. At lower temperatures it is expected that heterogeneous nucleation will dominate over homogeneous nucleation, so the result is reasonable.

The results indicate that the degree of superheat can be predicted quite accurately by the superheat limit derived from CNT for higher temperatures. In turn this can be used to predict mass flow rates in process equipment. At temperatures below about 280 K, heterogeneous nucleation begins to dominate, and more data will be needed in order to create a predictive model or correlation to predict the limit of superheat. However, the available data for this analysis are quite scarce. It would be interesting to see how the effect of heterogeneous nucleation changes both at lower temperatures and with different degrees of wall-roughness in the test section. This could be a fruitful avenue of further research.

5. CONCLUSIONS

In many industrial applications, it is relevant to predict the degree of superheat reached by liquid CO_2 before phase change is initiated during expansion. In the present work, the pressure data of pure CO_2 depressurization tests at the ECCSEL facility has been analyzed and the degree of superheat reached has been determined. The degree of superheat agrees well with the homogeneous superheat limit predicted by CNT for high temperatures, near the critical point. At lower temperatures, a lower degree of superheat is reached in the experiments due to heterogeneous nucleation.

ACKNOWLEDGEMENTS

This paper has been produced with support from the NCCS Centre, performed under the Norwegian research programme Centres for Environment-friendly Energy Research (FME) and the Research Council of Norway (257579).

The construction of the ECCSEL Depressurization Facility was supported by the INFRASTRUKTUR programme of the Research Council of Norway (225868).

NOMENCLATURE

Latin letters

R_a	Mean roughness of pipe (m)	J	Nucleation rate (critical-size embryos $m^{-3}s^{-1}$)
u	Velocity in x-direction (ms^{-1})	K	Kinetic prefactor (embryos $m^{-3}s^{-1}$)
k_B	Boltzmann constant ($1.380649\times 10^{-23} m^2kgs^{-2}K^{-1}$)	T	Temperature (K)
ΔG^*	Free-energy barrier of formation for critical-size embryo (J)	r^*	Radius of critical-size embryo (m)
p	Pressure (Pa)	m	Molecular mass (kg)

Greek letters

$\widetilde{\rho}$	Number density (molecules m^{-3})	σ	Surface tension (Nm^{-1})

Subscripts

l	Liquid phase	g	Gas phase
sat	At saturation	$crit$	At critical nucleation point/ superheat limit

Abbreviations

CCS	CO_2 capture and storage	CFD	Computational fluid dynamics
HEM	Homogeneous equilibrium model	EOS	Equation of state
CNT	Classical nucleation theory	SHL	Superheat limit

REFERENCES

Aursand, P., Gjennestad, M., Aursand, E., Hammer, M., Wilhelmsen, Ø., 2017. The spinodal of single- and multi-component fluids and its role in the development of modern equations of state. Fluid Phase Equilib. 436, 98-112.

Brown, S., Martynov, S., Mahgerefteh, H., Proust, C., 2013. A homogeneous relaxation flow model for the full bore rupture of dense phase CO2 pipelines. Int. J. Greenh. Gas Control. 17, 349-356.

Debenedetti, P.G, 1996. Metastable Liquids: Concepts and Principles. Princeton University Press, Princeton, 412.

ECCSEL, Depressurization facility, http:// eccsel2020.promoscience.com/facilities /transport/no25_sintef_er_depress, Accessed 24 Jan 2022.

Hammer, M., Ervik, Å., Munkejord, S.T., 2013. Method Using a Density-Energy State Function with a Reference Equation of State for Fluid-Dynamics Simulation of Vapor-Liquid-Solid Carbon Dioxide. Ind. Eng. Chem. Res. 52(29), 9965-9978.

Munkejord, S.T., Hammer, M., 2015. Depressurization of CO2-rich mixtures in pipes: Two-phase flow modelling and comparison with experiments. Int. J. Greenh. Gas Control. 37, 398-411.

Munkejord, S.T., Austegard, A., Deng, H., Hammer, M., 2020. Depressurization of CO2 in a pipe: High-resolution pressure and temperature data and comparison with model predictions. Energy. 211, 118560.

Rathjen, W., Straub, J., 1977. Surface tension and refractive index of six refrigerants from triple point up to critical point, 7th Symposium on Thermophysical Properties, American Society of Mechanical Engineers, 839-850.

Span, R., Wagner, W., 1996. A new Equation of State for Carbon Dioxide Covering the Fluid Region from the Triple-Point Temperature to 1100 K at Pressures up to 800 MPa. J. Phys. Chem. Ref. Data. 25(6), 1509-1596.

Toro, E.F., Billett, S.J., 2000. Centred TVD schemes for hyperbolic conservation laws. IMA J. Numer. Anal. 20(1), 47-79.

Paper 2

Hammer, Morten; Deng, Han; Austegard, Anders; **Log, Alexandra Metallinou**; Munkejord, Svend Tollak. (2022) Experiments and modelling of choked flow of CO2 in orifices and nozzles. *International Journal of Multiphase Flow*. vol 156.
doi:10.1016/j.ijmultiphaseflow.2022.104201

International Journal of Multiphase Flow 156 (2022) 104201

Contents lists available at ScienceDirect

International Journal of Multiphase Flow

journal homepage: www.elsevier.com/locate/ijmulflow

Experiments and modelling of choked flow of CO_2 in orifices and nozzles

Morten Hammer [a], Han Deng [a], Anders Austegard [a], Alexandra Metallinou Log [b], Svend Tollak Munkejord [a,*]

[a] SINTEF Energy Research, P.O. Box 4761 Torgarden, NO 7465 Trondheim, Norway
[b] Norwegian University of Science and Technology, Department of Energy and Process Engineering, NO 7491 Trondheim, Norway

ARTICLE INFO

Keywords:
Carbon dioxide
Depressurization
Decompression
Critical flow
Nucleation
Thermodynamics
Fluid dynamics

ABSTRACT

In order to accelerate the deployment of CO_2 capture and storage (CCS), engineers need experimentally validated models, among other things, to predict the mass flow rate in process equipment and flow restrictions like valves, nozzles and orifices. There are few available, relevant data for choked CO_2 flow in such geometries. To amend the situation, in this work, we report on six pipe-depressurization experiments from a pressure of 12 MPa and a temperature of 25 °C through three sizes (4.5, 9.0 and 12.7 mm) of orifices and nozzles. The results indicate that for the present cases, the choke point is at a non-equilibrium state.

In order to predict quasi-steady choked flow in restrictions, the homogeneous equilibrium model (HEM) and the Henry–Fauske (HF) model are commonly used. The HEM often underpredicts the mass flow rate because it does not account for delayed phase transition. Here we develop a delayed HEM (D-HEM) where evaporation starts at the superheat limit described using classical nucleation theory. We then employ the HEM, D-HEM, and HF model in 1D CFD pipe simulations to describe the outflow of depressurization experiments and we also compare with experimental data for converging–diverging nozzles.

In the CFD simulations, HF gave the best results, while HEM consistently underpredicted the mass flux. For the nozzle calculations, we found D-HEM to be the best model with a relative absolute error of 2.5 % for the predicted mass flux.

1. Introduction

There is consensus that in order to mitigate climate change, CO_2 capture and storage (CCS) is one of the necessary tools (Edenhofer et al., 2014). In the IEA (2021) scenario to reach net zero emissions by 2050, 7.6 gigatonnes of CO_2 are captured globally per year, out of which 95 % is permanently stored. Because capture plants and storage sites are in general not colocated, a large-scale CO_2-transportation system needs to be deployed, including pipelines and ships. In designing, optimizing and operating these systems, engineers need to quantify processes and phenomena that are not all covered by standard engineering tools (Munkejord et al., 2016). This includes the tight coupling of fluid and thermodynamics due to the proximity of the operating conditions to both the critical point (above which there is only one phase) and the triple point (at which gas, liquid and solid coexist). One practically important topic is to predict the mass flow rate in flow restrictions like valves, nozzles and orifices, both inside process equipment and in case of leaks to the surroundings.

When a fluid is depressurized through a restriction, the flow will become sonic if the pressure difference is sufficiently large. This is called critical or choked flow (Chapman, 2000). For sonic flow, there are no waves travelling upstream and therefore no feedback from the downstream pressure, so that the flow rate becomes independent of the downstream conditions. The correct prediction of critical flow is relevant not only for CCS systems, but also refrigeration systems (Angielczyk et al., 2010, 2019, 2020; Banasiak and Hafner, 2013; Ringstad et al., 2020), nuclear reactor safety (Downar-Zapolski et al., 1996; Pinhasi et al., 2005; De Lorenzo et al., 2017) and in other industrial facilities involving pressurized fluids.

In ship transportation, the CO_2 will be in a cold liquid state (Rousanaly et al., 2021), whereas in pipelines, it will most often be in a dense liquid phase at supercritical pressures (Munkejord et al., 2016). On depressurization from these states, the liquid will evaporate, and solid CO_2 will be formed at the triple point (see e.g. Hammer et al., 2013). For such systems, valid critical-flow models are needed for correct sizing of valves used for pressure reduction. The discharge mass flow rate influences the depressurization rate of the system and impacts both the time to empty it and the minimum temperature reached during depressurization.

During depressurization of liquids or dense-phase fluids, delayed phase transition and the presence of metastable states is a well known

* Corresponding author.
E-mail address: svend.t.munkejord@sintef.no (S.T. Munkejord).

https://doi.org/10.1016/j.ijmultiphaseflow.2022.104201
Received 17 December 2021; Received in revised form 2 June 2022; Accepted 15 July 2022
Available online 21 July 2022

Nomenclature

Latin letters

A	Area (m^2)
c	Speed of sound (m/s)
C_C	Contraction coefficient (1)
d	Diameter (m)
E	Total energy (J/m^3)
e	Specific internal energy (J/kg)
$\boldsymbol{F}$	Flux vector (-)
$\mathcal{F}$	Friction force (N/m^3)
G	Free energy (J)
H	Enthalpy (J)
h	Specific enthalpy (J/kg)
j	Mass flux ($kg/(m^2\,s)$)
J	Nucleation rate ($1/(m^3\,s)$)
K	Kinetic prefactor ($1/(m^3\,s)$)
k_B	Boltzmann's constant (J/K)
l and L	Length (m)
m	Mass (kg)
$\dot{m}$	Mass flow rate (kg/s)
N	Mol number (mol)
P	Pressure (Pa)
Q	Heat (W/m^3)
r	Radius (m)
S	Entropy (J/K)
s	Specific entropy (J/(K kg))
T	Temperature (K)
t	Time (s)
u	Velocity (m/s)
V	Volume (m^3)
x	Spatial coordinate (m)
z	Mass fraction (kg/kg)

Greek letters

α	Volume fraction (m^3/m^3)
β	Restriction angle parameter, Fig. 3 (°)
δ	Orifice opening length parameter, Fig. 3 (m)
μ	Chemical potential (J/mol)
ρ	Density (kg/m^3)
$\tilde{\rho}$	Number density ($1/m^3$)
σ	Surface tension (N/m)

Subscripts

amb	Ambient
cons	Conserved
crit	Critical
b	Cell at end of inner pipe domain adjacent the restriction
g	Gas
ℓ	Liquid
pipe	Position inside pipe
res	Restriction
sat	Saturation
up	Upstream
vc	Vena contracta
w	Wall

Superscripts

*	Critically-sized embryo

Abbreviations

CCS	CO_2 capture and storage
CFD	Computational fluid dynamics
CNT	Classical nucleation theory
DEM	Delayed equilibrium model
D-HEM	Delayed homogeneous equilibrium model
EOS	Equation of state
HEM	Homogeneous equilibrium model
HF	Henry–Fauske
HRM	Homogeneous relaxation model
RDF	Running ductile fracture
SHL	Superheat limit

phenomenon (Liao and Lucas, 2017), and departure from chemical and thermal equilibrium between the phases must be accounted for. It is known that non-equilibrium flow models predict higher characteristic speeds which in turn gives a higher critical mass flow rate (Flåtten and Lund, 2011). Therefore, models like the often-used homogeneous equilibrium model (HEM) that assume full equilibrium (mechanical, thermal and chemical) are expected to underpredict the critical mass flow rate. Nevertheless, we have obtained good results using the HEM for situations where the characteristic speeds are not determining (Munkejord et al., 2020).

Departure from equilibrium is also relevant for the correct prediction of running ductile fracture (RDF), a phenomenon whereby a defect in the pipeline, caused by e.g. corrosion or external forces, develops into a fracture running along the pipe, sustained by the pressure forces from the escaping fluid, see Aursand et al. (2016a). Assuming full equilibrium will yield higher-than-realistic pressures and therefore a wrong evaluation of the forces impacting the steel, see Munkejord et al. (2020).

In order to model CO_2 flows out of equilibrium, the process of nucleation must be taken into account. Shin and Jones (1993) and Blinkov et al. (1993) modelled the effect of heterogeneous nucleation on the wall and in the bulk of the fluid for water flowing through a converging–diverging nozzle. This work required empirical correlations to describe the heterogeneous nucleation of bubbles on the nozzle surface and impurities present in the bulk liquid. Their approach required an involved integration over time and space and provided promising results. In the present paper, the effect of heterogeneous nucleation is not included as the CO_2 depressurization experiments studied are in the entropy region where spontaneous *homogeneous* nucleation is the dominant mode of nucleation. This kind of nucleation occurs in the bulk of the liquid without the aid of a surface or impurity, and it relates closely to the limit of superheat, i.e., the experimentally attainable limit where a superheated liquid spontaneously starts boiling. This is further discussed in Section 3.3.

Following the approach presented by Debenedetti (1997, Sec. 3.1.5), Aursand et al. (2016b) concluded that the superheat limit (SHL) of a fluid can be accurately predicted by the use of classical nucleation theory (CNT). The CNT predictions depend mainly on the saturation pressure and surface tension of the fluid, and in order to predict the SHL, accurate models for both properties are required. Aursand and Hammer (2018) employed the CNT models to predict rapid phase transition for liquefied natural gas. For liquid and dense-phase specific entropies close to, but below, the critical entropy, Wilhelmsen and Aasen (2022) applied CNT to describe delayed phase transition for flows of water, and CO_2, in converging nozzles. At lower temperatures

(below about 280 K) and entropies, heterogeneous nucleation becomes more important, and this effect was taken into account for water using an empirical correlation.

Elias and Lellouche (1994) reviewed two-phase critical flow models with emphasis on water-steam flows and nuclear reactor safety. The model review comprised 'analytical models' (models not requiring spatial or temporal integration) including the HEM and the models of Moody (1965) and Henry and Fauske (1971) (HF), fitted models, and steady-state two-phase flow models requiring spatial integration. The data review evaluated 42 data sets. Elias and Lellouche found that none of the analytical or fitted models satisfactorily captured the measured mass fluxes for the range of conditions considered.

De Lorenzo et al. (2017) benchmarked the delayed equilibrium model (DEM) and classical two-phase critical flow models against experimental data. In addition to the HEM they evaluated the Moody (1965) and HF models. The DEM originated from Lackme (1979) who assumed two-phase critical flow to be composed of three phases. In addition to saturated vapour, the flow model contained both a saturated and a metastable liquid. Assessing more than 450 experimental data points for three configurations, long tubes, short nozzles and slits, De Lorenzo et al. concluded that the DEM model was superior to the other models, and that HEM predicted the long tube critical flux well while HF overestimated the mass flux in the same geometry. Moody's model had too much slip and overestimated the mass flux for two-phase stagnation conditions.

The homogeneous relaxation model (HRM) takes into account the non-equilibrium evaporation leading to metastable liquid states. In this model, the phases have the same pressure and temperature, but are allowed to have different chemical potential. The model, as formulated by Downar-Zapolski et al. (1996), requires a relaxation time to account for time delay in the phase transition. Angielczyk et al. (2010) adapted the relaxation-time correlation developed for water by Downar-Zapolski et al. to work with CO_2 utilizing experimental data by Nakagawa et al. (2009). These experiments were performed using four different converging–diverging nozzles, with different angles in the diverging part. The fluid used was pure CO_2 that was expanded from a constant upstream pressure. The mass flow rate was estimated assuming a saturated state at the throat, but it was not tabulated by the authors. Brown et al. (2013) used the empirical correlation of Angielczyk et al. to describe the relaxation time in pipe depressurization simulations.

Common formulations of the DEM (De Lorenzo et al., 2017) and HRM (Downar-Zapolski et al., 1996) rely on time-dependent mass transfer between the phases, and require temporal as well as spatial integration over a fully defined geometry. This makes them less generic than the classical methods such as HEM and HF. The steady-state HEM flow can be determined without time integration and HF is a set of analytical equations. Modelling the restriction geometry in detail may be challenging, e.g., for simulations of long pipes, where the spatial resolution of the restriction is not resolved, or for cases where the geometry is partly unknown. Attempts have been made to devise robust numerical methods to simulate transient flow of CO_2 through pipes or ducts with *discontinuous* variation of the cross section (Brown et al., 2015; Log et al., 2021), but so far, these methods have only been applied to equilibrium flow models.

We have only found a limited amount of experimental data of CO_2 flowing through nozzles or orifices that include the mass flow rate and where the decompression path comes from the liquid side of the phase diagram. Hesson and Peck (1958) presented critical flow rates for saturated liquid and saturated vapour CO_2 for a nozzle and an orifice. Henry and Fauske (1971) used the data of Hesson and Peck when developing the HF model. However, Hendricks et al. (1972) questioned the accuracy of the Hesson and Peck data. The measured fluxes were found to be higher than expected, indicating that the liquid states were sub-cooled to some degree.

Martin et al. (2006) performed experiments of supercritical and liquid CO_2 with short tube orifices of length 20 mm and diameter 0.8 mm and 1 mm. The measured mass flow rate increased with increasing upstream pressure and decreasing temperature.

Edlebeck et al. (2014) reported a comprehensive data set for supercritical and two-phase CO_2 flowing through orifices. The orifices were of 1 mm diameter and length-to-diameter ratios of 3.2 and 5. Edlebeck et al. measured the mass flow rates for a wide range of initial conditions, and compared with the isentropic real gas model for fluid expansion through a nozzle. The comparison gave a discharge coefficient for single phase between 0.81 and 0.87.

Banasiak and Hafner (2013) experimentally measured the mass flow rate of dense-phase CO_2 in a converging–diverging nozzle used in ejectors. A nozzle flow model was presented, including delayed equilibrium accounting for both homogeneous and heterogeneous nucleation.

Vree et al. (2015) tested rapid depressurization of CO_2 through 3, 6, and 12 mm nozzles connected to a coil-shaped tube. Mass flow rates were reported, but not as a function of the upstream state. In a somewhat similar study, Li et al. (2016) experimentally investigated the leakage of CO_2 at supercritical pressures through nozzles of different shapes and sizes in the millimetre range. Fan et al. (2018) studied supercritical CO_2 leaking through nozzles with length-diameter ratio (L/D) ranging from 1 to 15. It was found that the choked mass flow rate decreased with increasing length-diameter ratio.

Pipe depressurizations through restrictions have implicit information on the mass flux through the measured pressure as long as the upstream state is single-phase. This can alleviate the lack of experiments with directly measured mass flow rates. The mass flux can be calculated using the Euler compatibility equation, as we will discuss in Section 3.1.

Armstrong and Allason (2014) conducted experiments in which a 200 m long pipe with inner diameter 50 mm was depressurized full-bore or through sharp orifice plates. Two of the experiments had a pipe aperture ratio low enough that the entire initial rarefaction wave remained in the single-phase region. Guo et al. (2016, 2017) and Yan et al. (2018) studied the depressurization of a large pipe of length 257 m and inner diameter 233 mm with full-bore opening and two orifices. They observed pressure transients attributed to phase change as pressure waves were reflected at the pipe ends. Martynov et al. (2018) studied the decompression of a 36.7 mm long pipe with internal diameter 50 mm through orifices of diameter 4 and 6 mm. The focus of the study was the formation of solid CO_2 at the triple point.

To sum up the state of the art, considerable work has been undertaken on critical flow through restrictions, but the main emphasis has been on geometries like converging–diverging nozzles. Among the studies on nozzles that we reviewed, only few could be directly used in the present model evaluation, e.g., reporting the upstream state so that the mass flow rate could be calculated. Further, there is a need to develop and validate models that are generic enough to be implemented in simulation tools for CCS applications such as pipes and vessels.

In this work, the decompression-tube facility described in Munkejord et al. (2020) has been equipped with interchangeable outflow restrictions. We thus present new critical-flow data for CO_2 exiting through sharp-edged orifices and converging nozzles. In addition to modelling the outflow using the classical HEM and HF models, we propose an augmented steady-state HEM (D-HEM) capturing the delayed phase transition and entropy production during mass transfer. These restricted-flow models are discussed both separately and as part of 1D CFD pipe simulations.

The rest of the article is structured as follows: Section 2 briefly describes the experimental setup and procedure. Section 3 presents the theoretical framework for analysing the experimental data, and the models used to predict the mass flux in the nozzle and orifice geometries. Section 4 presents experimental and simulation results, and discusses our observations. Section 5 summarizes the main results and conclusions.

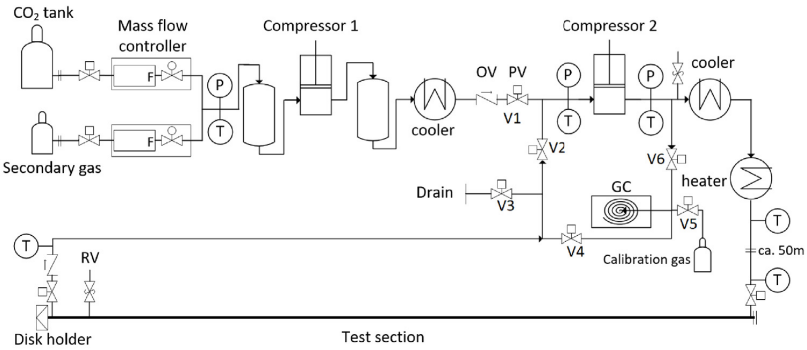

(a) System (RV: relief valve; OV: one-way valve; PV: pneumatic valve)

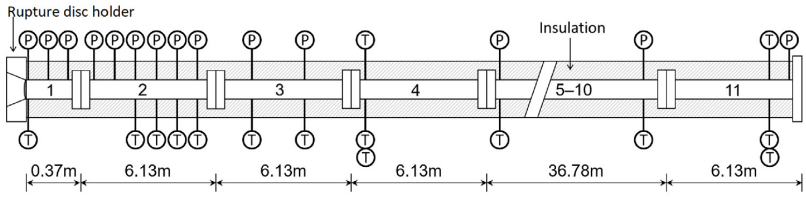

(b) Test section (dimensions are not to scale; pipe no. 5–10 and corresponding sensors are omitted.)

Fig. 1. Schematic of the ECCSEL depressurization facility.

2. Experimental setup

This section gives an overview of the experimental setup. A more detailed description can be found in Munkejord et al. (2020).

2.1. ECCSEL depressurization facility

The test section of the ECCSEL depressurization facility ECCSEL (2021) consists of a pipe equipped with a rupture disk at the open end and instrumented to observe the rapid pressure and temperature transients occurring during depressurization of CO_2 and CO_2-rich mixtures. It is connected to the gas supply with mass flow controllers, and the compression and cooling system for achieving the desired experimental conditions. Fig. 1(a) shows a schematic overview. The maximum operating pressure of the facility is 20 MPa, and the current design allows experiments with initial temperatures in the range of 5 °C to 40 °C.

The test section is made of 11 stainless steel (SS316, EN 1.4401) pipes giving a total length of 61.67 m, as depicted in Fig. 1(b). The pipes have an inner diameter of 40.8 mm and outer diameter of 48.3 mm, and the internal surface of the pipes were honed to a mean roughness, R_a, in a range from 0.2 µm to 0.3 µm. In order to achieve a uniform axial temperature, the pipe is wrapped by self-regulating positive temperature coefficient (PTC) heating cables and insulated with a 60 mm thick glass wool layer. The power output of the heating cables is 1900 W at 20 °C and 950 W at 40 °C.

A rupture disk with a disk holder is installed at the pipe outlet. The specified burst pressure of the disk is 120 barg±5% at 22 °C. The depressurization is triggered once the disk ruptures. Two rupture disk types are employed in this study; X-scored Fike SCRD BT FSR for Tests 8 and 13 and circular-scored triple-layer Fike HOV BT HL for the remaining experiments (Tests 16–18), see Table 2. A fully opened triple-layer disk is shown in Fig. 2(a).

In order to perform depressurization tests with different restrictions at the pipe outlet, we manufactured a series of screw-in tubes with orifice and nozzle profiles, as illustrated in Fig. 3. The dimensions are given in Table 1. In the current work, three restriction diameters, 4.5 mm, 9.0 mm and 12.7 mm, are employed for both the orifice and nozzle geometry. The screw-in tube, depicted in Fig. 2(b) for the 12.7 mm nozzle, is mounted immediately upstream of the rupture disk. The design is such that the flow will choke at the same position as in the full-bore experiments reported in Munkejord et al. (2020, 2021).

Table 1
Geometry of the orifices and nozzles used for our experiments.

	Test no.	d (mm)	l (mm)	β (°)	δ (mm)	L (mm)
Orifice, large	13	12.7	4	45	0.8	–
Orifice, medium	21	9.0	4	45	0.8	–
Orifice, small	16	4.5	4	45	0.8	–
Nozzle, large	18	12.7	5	30	–	22.3
Nozzle, medium	20	9.0	4	35	–	24.5
Nozzle, small	17	4.5	3	45	–	29.3

2.2. Instrumentation and test procedure

Along the test section, 16 fast-response pressure transducers of model Kulite CTL-190(M) are flush-mounted to the internal surface. Most of them are densely distributed close to the rupture disk to capture the decompression wave, as depicted in Fig. 1(b). The fluid temperature is measured by 23 Type E thermocouples. The measurement uncertainty of pressure is ±60 kPa and temperature uncertainty is ±0.22 °C, both with a confidence level of 95 %. In the present work, we focus on investigation of the outflow, thus only the data recorded at the position closest to the outlet, at the location of 0.08 m, will be presented. Details regarding sensor location, calibration, and uncertainty analysis can be found in Munkejord et al. (2020).

The logging frequency of the data from the pressure transducers and thermocouples is 100 kHz and 1 kHz, respectively. The high-frequency data are stored from 0.3 s before disk rupture for a 9 s period. Afterwards, both pressure and temperature data are recorded at 50 Hz. The reported initial conditions of the experiments are calculated from the data between 1 ms and 0.5 ms before disk rupture.

(a) Triple-layer rupture disk after test. (b) Converging nozzle of 12.7 mm diameter.

Fig. 2. Pictures of rupture disk and converging nozzle.

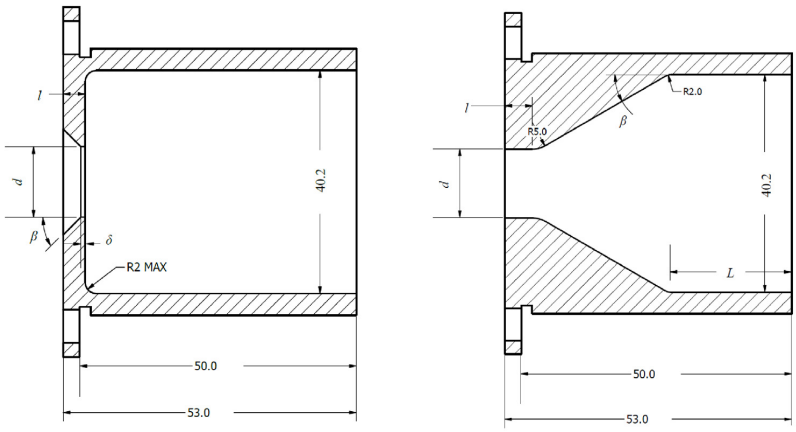

(a) Orifice (b) Converging nozzle

Fig. 3. Schematic of orifice and converging nozzle. The flow direction is from the right to the left.

The experimental procedure involves the following steps. First, the rupture disk is installed and the system is evacuated. Then the test section is filled with CO_2 and pressurized. When the pressure reaches about 70% of the desired pressure, the fluid is circulated to achieve a uniform temperature along the test section. The fluid temperature is controlled using heating elements wrapped around the test section. The desired pressure and temperature are achieved by further heating and addition of CO_2 if needed, both at a controlled rate, until the disk ruptures. Upon disk rupture, the two pneumatic valves at the ends of the test section are automatically closed to stop circulation. After the test, the system is emptied.

3. Models

In this section, we start by describing how the mass flow-rate can be computed from pressure data of a depressurization experiment. Next, we give a short description of the thermophysical models used in this work. We then discuss how classical nucleation theory can be applied to calculate the superheat limit, which is used for delayed phase transition considerations in steady-state critical flow models. Finally, we describe the model used for calculating the vena contracta area reduction of the orifice and we give an outline of the 1D CFD model used for the simulations.

3.1. The Euler compatibility equation for the rarefaction wave

When the rupture disk at the end of the pipe opens, flow is established through the outlet restriction, and a rarefaction wave starts travelling into the pipe. The mass flow rate will depend on the size of the restriction and the fluid state inside the pipe, close to the outlet. After a short initial time, allowing for the fluid to accelerate through the restriction, a quasi-steady state is established, where the flow through the restriction is constant and a pressure plateau (P_1) is established in the pipe with a constant mass flow rate downstream of the rarefaction wave, see Fig. 4. The change in fluid velocity across a rarefaction wave in a single-phase fluid can be described using a compatibility equation of the Euler equations (Picard and Bishnoi, 1988).

The compatibility equations are found when rewriting the original differential equations along the characteristics. The sudden outflow constitutes an event opposite of a hydraulic shock (often referred to as ‘fluid hammer’ or ‘water hammer’), and the compatibility equation is equivalent to the Joukowsky equation used to analyse such events.

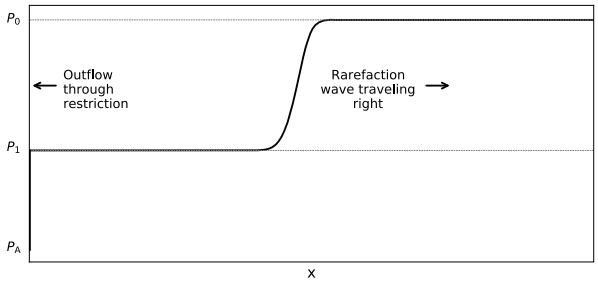

Fig. 4. Example of an adiabatic pipe depressurization trough a restriction on the left side. The pressure in the pipeline is plotted against axial position for a given time. The initial pipe pressure is P_0 and the pressure drops to P_1 due to the outlet flow. P_A is the ambient pressure.

Using only the pressure measurements and an accurate equation of state (EOS) for the fluid properties, we can calculate the constant velocity in the pipe. The Euler compatibility equation for the rarefaction wave states that, at constant entropy,

$$\mathrm{d}P = \rho c \mathrm{d}u. \tag{1}$$

Knowing the initial pressure, P_0, the initial velocity, $u_0 = 0$, and plateau pressure, P_1, from the experiments, we can integrate Eq. (1) to find the velocity behind the rarefaction wave in the pipe as

$$u_1 = \int_{P_0}^{P_1} \frac{\mathrm{d}P}{\rho c}. \tag{2}$$

The mass flow rate corresponding to the change in pressure can then be calculated from the fluid velocity and the fluid properties as $\dot{m} = (u\rho)_1 A_{\mathrm{pipe}}$. For single-phase flow, the density, $\rho(s, P)$, and speed of sound, $c(s, P)$, can be calculated from an equation of state given the entropy (s) and pressure.

3.2. Thermophysical models

For the calculation of thermophysical properties, we employ our in-house framework (Wilhelmsen et al., 2017; Hammer et al., 2020). To describe the thermodynamic properties of pure CO_2, we have utilized the GERG-2008 (Kunz and Wagner, 2012) and the Span and Wagner (1996) EOS, which are highly accurate Helmholtz-type EOSs. GERG-2008 is developed for mixtures, but when employed for pure CO_2, it will give very similar predictions to those of the more accurate Span–Wagner EOS. The main difference will be in the close proximity of the critical point, where the Span–Wagner EOS has some enhancement terms. The EOSs are used to calculate the densities and energies of the existing phases in both the stable and metastable region. The development of the GERG-2008 and Span–Wagner EOS was purely based on experimental measurements of stable thermodynamic states. In addition, these EOSs exhibit an additional unphysical Maxwell-loop in the unstable area (Wilhelmsen et al., 2017).

The accuracy in the metastable liquid region and the accuracy in predicting the spinodal curve is therefore unknown. Alternative equations of state based on statistical thermodynamics are expected to be more physically correct in the metastable region. However, the density and speed-of-sound predictions of GERG-2008 and Span–Wagner EOS are far superior in the stable domain compared to alternative EOSs, and they are therefore used in this work. How far the better predictions will extend into the metastable region is unknown.

To calculate the CO_2 surface tension we employ the correlation of Rathjen and Straub (1977), and the viscosity is modelled using the correlation of Fenghour et al. (1998).

3.3. Estimating the liquid superheat limit using classical nucleation theory

Before describing restricted-flow models accounting for delayed phase transition, it is useful to define what we mean by the SHL. When a liquid reaches its superheat limit, random fluctuations of density will cause the formation of critically-sized gas bubbles that can grow due to evaporation on the gas–liquid interface or by coalescing with other bubbles. The formation of critically-sized embryos in a metastable phase is called nucleation. This is an activated process, meaning that a certain free-energy barrier must be overcome to form embryos of the new phase. If nucleation occurs spontaneously within the bulk of the fluid, it is called *homogeneous*. On the other hand, if nucleation occurs on a surface or an impurity such that the free-energy barrier is lowered, it is called *heterogeneous*. Heterogeneous nucleation dominates at lower temperatures, whereas homogeneous nucleation dominates at higher temperatures.

The data which we will analyse are mostly in the high-temperature region. Therefore, we consider the model presented by Aursand et al. (2016b) to estimate the homogeneous liquid superheat limit. This model is based on CNT, as described by Debenedetti (1997), in which the nucleation rate (critically-sized embryos formed per volume and time) is defined as an Arrhenius-type rate law,

$$J = K \exp\left(-\frac{\Delta G^*}{k_{\mathrm{B}} T_\ell}\right), \tag{3}$$

where ΔG is the free-energy barrier of embryo formation, k_{B} is the Boltzmann constant and K is a kinetic prefactor. The superscript $*$ denotes properties of a critically-sized embryo. Such embryos are just large enough to not spontaneously decompose back to the mother phase. The free-energy barrier is estimated to be

$$\Delta G^* = \frac{4\pi\sigma r^{*2}}{3}, \tag{4}$$

where σ denotes the surface tension and r the radius of the embryo. It is assumed that the surface tension of the embryo, σ, is equal to the macroscopic surface tension of a planar interface between the phases at equilibrium.

For the formation of bubbles in a metastable liquid, the critical radius is approximated as

$$r^* = \frac{2\sigma}{P_{\mathrm{sat}}(T_\ell) - P_\ell}, \tag{5}$$

where $P_{\mathrm{sat}}(T_\ell)$ is the saturation pressure at the temperature of the liquid. The kinetic prefactor can be approximated as

$$K = \tilde{\rho}_\ell \sqrt{\frac{2\sigma}{\pi m}}, \tag{6}$$

where m is the mass of one molecule and $\tilde{\rho}_\ell = \rho_\ell / m$ is the number density of molecules in the liquid. With these relations, the SHL temperature can be estimated by solving

$$J(T_\ell) = J_{\mathrm{crit}} \tag{7}$$

for T_ℓ. Here, J_{crit} is the critical nucleation rate, at which sudden phase change is observed (Aursand et al., 2016b). In this work, we follow Aursand et al. (2016b), employing $J_{\text{crit}} = 1 \times 10^{12}/(\text{m}^3\,\text{s})$. Due to the exponential functional form in (3), the superheat limit is not very sensitive to the critical rate.

The SHL curve for CO_2 is plotted in Fig. 5(a), and it will always lie between the saturation curve and the spinodal curve. The spinodal curve of a pure fluid is the loci of $\frac{\partial P}{\partial \rho}\Big|_T = 0$, which is a property predicted by the GERG-2008 EOS.

3.4. Steady-state flow through restrictions

To model flow through restrictions while avoiding detailed spatial and temporal integration, one must resort to steady-state flow modelling and ignore friction. This is reasonable for many practical applications. The fluid velocity, u, is then calculated from energy conservation under isentropic expansion, i.e., constant stagnation enthalpy,

$$h + \frac{1}{2}u^2 = C, \tag{8}$$

where C is a constant. When the difference between the upstream pressure (P_{up}) and the downstream pressure (P_{amb}) is sufficiently large, the flow will choke when the velocity equals the speed of sound on the calculated path, see the example for HEM in Appendix A. Otherwise, the flow will remain subsonic and the flow rate is determined from (8) and the downstream pressure. In any case, the main output from the restricted-flow model is the mass flux

$$j_{\text{res}} = (\rho u)_{\text{res}} = j_{\text{res}}\left(u_{\text{up}}, s_{\text{up}}, P_{\text{up}}, P_{\text{amb}}\right). \tag{9}$$

The above Eqs. (8) and (9) have been formulated for equilibrium flow for simplicity. It is possible to extend them to non-equilibrium conditions if needed.

In the cases we consider here, at a certain point between the upstream and the ambient conditions, a two-phase state will be encountered. It is straightforward to write the HEM as a steady-state model, only requiring isentropic path calculations. The HEM assumes full equilibrium (mechanical, thermal and chemical) between the gas and the liquid phase. As a consequence, the calculated speed of sound is discontinuous at the saturation curve.

The Henry and Fauske (1971) model incorporates some departure from equilibrium, and the flashing at the throat is correlated against the equilibrium flashing of the liquid. In the HF model, the liquid phase is treated as incompressible, while the gas is approximated as polytropic, with a polytropic exponent calculated assuming thermal equilibrium between the gas and the liquid. For the experiments in this work, the upstream gas fraction is always zero, so we need not discuss the approximate gas properties description in the HF model. To calculate $j_{\text{res}}^{\text{HF}}$, we solve Equation (45) of Henry and Fauske (1971) numerically.

Most models that include some delayed flashing, like the DEM and HRM, require that the flow be integrated over the nozzle geometry. As the geometry in many cases is complex or partly unknown, engineering process and pipe-flow simulators often rely on correlations or models like HEM and HF to describe flow rates in valves and nozzles based only on information of flow area and a discharge or contraction coefficient. If a valve flow coefficient is specified, in order to predict the flow rate, we must convert the flow coefficient to an equivalent flow area. In the following section, we propose a model including delayed flashing that does not require integration over the geometry.

3.5. Delayed homogeneous equilibrium model

In rarefaction-wave measurements from full-bore depressurization experiments of CO_2, one can observe a process where the fluid first experiences delayed phase transition, and then shows an equilibrium-like behaviour after an intermediate transition region (Munkejord et al., 2020, Figs. 14 and 15). The same experimental data are plotted in Fig. 8. In order to model the process, we will as a first approximation ignore the behaviour in this intermediate region (seen for $c-u$ between 280 m/s and 360 m/s in Fig. 8(b)).

We next assume that the fluid experiences some delayed phase transition activated at the SHL and transitions into equilibrium flow at the SHL pressure. We then get a simple model that captures at least some of the observed essential physics. The energy is conserved during this process, and the fluid velocity given by Eq. (8) should be continuous. This leads to a process of constant enthalpy at the SHL pressure. We note that the assumption of a process of constant pressure after the SHL is likely a simplification because the pressure has been observed to increase in pipe experiments when rapid evaporation follows delayed phase transition (Munkejord et al., 2020, Figure 8, Sensor PT203).

The above approach is a steady-state delayed homogeneous equilibrium model, which we label D-HEM. In summary, the process steps of the model are illustrated in Figs. 5(a) and 5(b) for the pressure–temperature and pressure–entropy space, respectively:

- Point 1 is the fluid state upstream of the restriction.
- Point 2 is reached by isentropic expansion to the SHL. The fluid velocity is calculated from (8).
- Point 3 is the equilibrium state resulting from an isenthalpic evaporation process of the metastable liquid state at the SHL pressure.
- Point 4 is the isentropic HEM expansion from Point 3.

In the following we verify that D-HEM is physically sound, and does not violate the second law of thermodynamics. The overall enthalpy, H, differential is given as

$$\mathrm{d}H = T\,\mathrm{d}S + V\,\mathrm{d}P + \mu\,\mathrm{d}N. \tag{10}$$

Here, T is temperature, S is entropy, V is volume, μ is chemical potential and N is the number of moles. Setting the differential to zero, at constant pressure for a pure fluid distributed in two phases, we have,

$$\mathrm{d}H = \mathrm{d}\left(H_{\text{g}} + H_\ell\right) = T_{\text{g}}\mathrm{d}S_{\text{g}} + T_\ell\mathrm{d}S_\ell + \mu_{\text{g}}\mathrm{d}N_{\text{g}} + \mu_\ell\mathrm{d}N_\ell = 0. \tag{11}$$

If we assume temperature equilibrium between the phases, we get $T_{\text{g}}\mathrm{d}S_{\text{g}} + T_\ell\mathrm{d}S_\ell = T\mathrm{d}\left(S_{\text{g}} + S_\ell\right) = T\mathrm{d}S$.

For a process of bubble nucleation, we have $dN = \mathrm{d}N_{\text{g}} = -\mathrm{d}N_\ell$, which gives the following entropy production for the phase transition,

$$\frac{dS}{dN} = \frac{\mu_\ell - \mu_{\text{g}}}{T}. \tag{12}$$

As the liquid fugacity in the metastable region is higher than the gas fugacity, the phase transition will produce entropy. The effect of the entropy production in mass flux predictions is small, and could probably be ignored at the expense of having a discontinuous velocity at the SHL pressure. In this work we include the effect of entropy production.

Even if the fluid velocity is continuous at the SHL pressure, the density is not, giving a discontinuous reduction in mass flux during the isenthalpic evaporation. If the fluid reaches sonic velocities after the SHL, the choke flux is taken as the maximum of the flux at the SHL and the flux where the HEM chokes.

3.6. Flow contraction at orifices

The coefficient of contraction is defined as the ratio between the area of the jet at the vena contracta and the area of the restriction geometry,

$$C_{\text{C}} = \frac{A_{\text{vc}}}{A_{\text{res}}}. \tag{13}$$

See also Fig. B.14 in Appendix B. For a nozzle, the streamlines follow the geometry, except in a thin boundary layer, and the loss is very

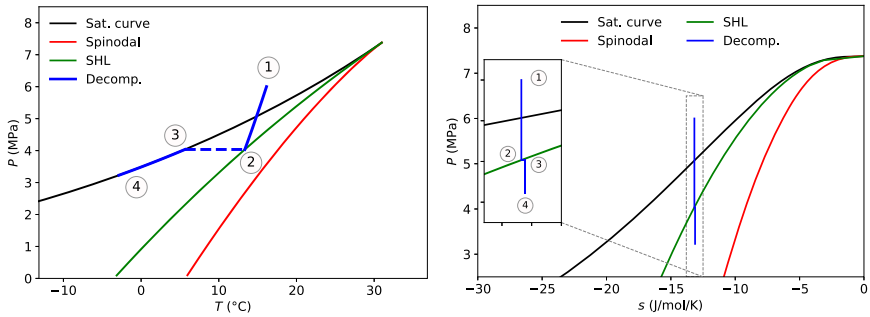

(a) Temperature-pressure space. (b) Entropy-pressure space.

Fig. 5. Expansion path (blue curve) illustrating the D-HEM. The path 1–2 is isentropic with no phase transfer, followed by the isenthalpic and isobaric path 2–3 where the metastable state 2 is transformed to the equilibrium two-phase state 3. If the flow is not critical, the expansion path ends in an isentropic two-phase equilibrium path 3–4. The saturation curve, liquid spinodal and SHL line are shown. All curves are calculated using the GERG-2008 EOS. (For interpretation of the references to colour in this figure legend, the reader is referred to the web version of this article.)

small. By using the method of Tesař (2008) we have estimated the contraction coefficient for our cases to be larger than $C_C = 0.99$. For simplicity, we round off to $C_C = 1$.

On the other hand, for a sharp-edged orifice, $C_C < 1$. For an incompressible, ideal flow in a sharp-edged orifice, the contraction coefficient is known to be (Lienhard and Lienhard, 1984),

$$C_{C,i} = \frac{\pi}{\pi + 2}. \tag{14}$$

By making a simple assumption about the flow pattern at the walls, Bragg (1960) accounted for the compressibility effects on the contraction coefficient. Using a force balance on the fluid from upstream of the flow restriction down to the vena contracta, he derived equations for the contraction coefficient of isentropic ideal gas flow. In this work we use the same assumptions but rigorously solve the GERG-2008 EOS for the properties of the flow. In the calculation of the contraction coefficient we assume frozen flow, i.e., no phase transfer. The incompressible contraction coefficient in (14) is used as input to the model of Bragg (1960). Further details on the calculation of the contraction coefficient can be found in Appendix B.

3.7. Pipe-flow model

We have implemented the quasi-steady-state HEM, D-HEM and HF models for flow through restrictions discussed above in our numerical workbench for 1D, transient, multiphase, multicomponent flow in pipes. In the inner domain of that model, the fluid flow is modelled using the HEM including source terms for wall friction and heat transfer through the pipe wall. The model has been presented previously (Munkejord and Hammer, 2015; Munkejord et al., 2016), and we briefly review it here for completeness. We remark that it is common to use separate outflow models to provide the boundary conditions to transient pipe-flow models (see Elias and Lellouche, 1994, Sec. 4).

The governing equations have the same form as the Euler equations for single-phase, compressible, inviscid flow, and consist of a mass-conservation equation,

$$\frac{\partial}{\partial t}(\rho) + \frac{\partial}{\partial x}(\rho u) = 0, \tag{15}$$

a momentum-balance equation,

$$\frac{\partial}{\partial t}(\rho u) + \frac{\partial}{\partial x}(\rho u^2 + P) = -\mathcal{F}, \tag{16}$$

and a balance equation for the total energy,

$$\frac{\partial}{\partial t}(E) + \frac{\partial}{\partial x}u(E + P) = \mathcal{Q}. \tag{17}$$

Herein, $\rho = \alpha_g\rho_g + \alpha_\ell\rho_\ell$ is the density of the gas (g) and liquid (ℓ) mixture. u is the common velocity and P is the pressure. $E = \rho(e + 1/2u^2)$ is the total energy density of the mixture, while $e = \left(e_g\alpha_g\rho_g + e_\ell\alpha_\ell\rho_\ell\right)/\rho$ is the mixture specific internal energy. α_k denotes the volume fraction of phase $k \in g, \ell$. $\mathcal{F}$ is the wall friction and $\mathcal{Q}$ is the heat transferred through the pipe wall to the fluid. The wall friction is calculated by the Friedel (1979) correlation. The heat conduction through the pipe steel and the surrounding insulation is calculated by solving the heat equation in the radial direction in a two-layer domain, as described by Aursand et al. (2017). The in-pipe heat-transfer coefficient is calculated based on the Dittus–Boelter correlation, see e.g. Bejan (1993, Chap. 6). The outside heat-transfer coefficient is estimated to be $4\,\mathrm{W/(m^2\,K)}$. For more details on the friction and heat-transfer modelling, see Munkejord et al. (2021).

At the outflow boundary, a flux, $\boldsymbol{F}$, is enforced for the governing Eqs. (15)–(17). Given the mass flux per cell cross-sectional area,

$$j_{\mathrm{pipe}} = j_{\mathrm{res}}\frac{A_{\mathrm{res}}}{A_{\mathrm{pipe}}}, \tag{18}$$

calculated from the restricted-flow model, and the state of the boundary cell, the following flux vector is used,

$$\boldsymbol{F} = \begin{bmatrix} j_{\mathrm{pipe}} \\ j_{\mathrm{pipe}}u_{\mathrm{b}} + P_{\mathrm{b}} \\ j_{\mathrm{pipe}}\left(h_{\mathrm{b}} + \frac{1}{2}u_{\mathrm{b}}^2\right) \end{bmatrix}. \tag{19}$$

Here, the subscript b refers to the cell at the end of the inner pipe domain adjacent to the outflow restriction. In the case when $j_{\mathrm{pipe}} = (\rho u)_{\mathrm{b}}$, the flux will extract mass from the pipe isentropically. However, numerically, we see a small entropy production at the boundary.

We solve the system (15)–(17) using the finite-volume method, where the numerical fluxes are calculated using the first-order centred (FORCE) scheme (Toro and Billett, 2000). As described in Hammer et al. (2013), we obtain a second-order method by employing a semi-discrete monotone upwind-centred scheme for conservation laws (MUSCL) along with a second-order strong-stability-preserving Runge–Kutta method. For the simulations performed in this work, we employed a Courant–Friedrichs–Lewy (CFL) number of 0.85, and a spatial grid of 4800 cells. The Span–Wagner EOS is used to calculate the CO_2 fluid properties.

4. Results and discussion

In this section, we present new pipe-depressurization data taken at the same nominal conditions (12 MPa, 25 °C) for same-size nozzles and orifices. Next, we compare measured pressure traces with transient 1D CFD simulations and discuss the performance of the different restricted-flow models. Finally, we expand the analysis of the restricted-flow models by including published data on flow through nozzles.

Table 2
Experimental conditions of the depressurization tests of CO_2 with orifices and nozzles.

Test no.	Type	Diameter (mm)	Aperture ratio (%)	Pressure avg. (MPa)	Temperature avg. (°C)	Ambient temp. (°C)	Figures
8[b]	Full-bore	40.8	100	12.22	24.6	9	6, 8(b)
13[a]	Orifice	12.7	9.7	12.75	24.6	12	6, 10(a)
16[a]	Orifice	4.5	1.2	12.18	24.7	7	6, 10(c)
17[a]	Nozzle	4.5	1.2	12.43	25.2	7	6, 9(c)
18[a]	Nozzle	12.7	9.7	12.41	25.4	9	6, 9(a)
20[a]	Nozzle	9.0	4.9	11.42	23.4	7	6, 9(b)
21[a]	Orifice	9.0	4.9	11.51	23.2	0	6, 10(b)

[a]Present work.
[b]Munkejord et al. (2020).

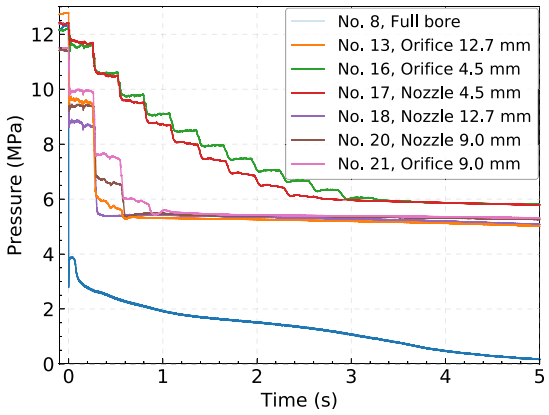

Fig. 6. Measured pressure at $x = 0.08$ m for the tests in Table 2.

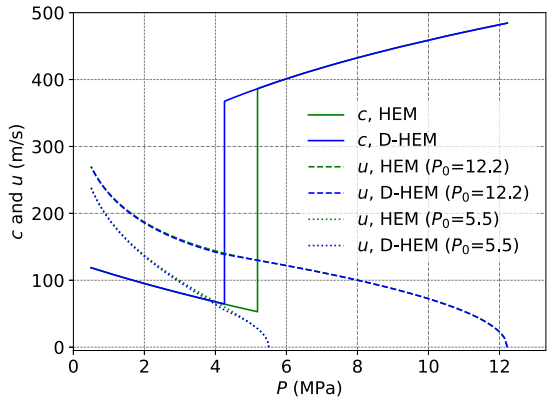

Fig. 7. Comparison of D-HEM and HEM for a decompression process. Speed of sound (full lines) and fluid velocity (dashed and dotted lines) as a function of pressure. The initial state of Test 8 (12.2 MPa, 24.6 °C) defines the stagnant state for the dashed lines, whereas that of the dotted lines is (5.5 MPa,16.3 °C), on the same isentrope. The GERG-2008 EOS is used for the property predictions. The fluid velocity curves for the different models are very similar and might be difficult to distinguish.

4.1. Pipe depressurization

The initial conditions of the depressurization experiments and the restrictions are listed in Table 2. We report on six experiments with three sizes of orifices and nozzles. A previous full-bore experiment (Test 8) is included as a reference.

4.1.1. Pressure response to different outlet restrictions

Fig. 6 shows the pressure measured at $x = 0.08$ m from the outlet in the seven tests 8, 13, 16, 17, 18, 20 and 21 defined in Table 2. Following a single pressure trace, e.g. Test 13, we observe that the pressure drops fast from the initial level to a plateau of 9.5 MPa upon arrival of the first rarefaction wave. The pressure remains at the plateau for about 0.3 s, the time required for the wave to travel to the closed end and be reflected back, after which the pressure again drops to a lower plateau value. When the wave enters the two-phase region, the evaporated gas will maintain the pipe pressure while the mass flux drops.

The effect of the outlet restriction sizes can be seen by comparing the full-bore test (no. 8) and the nozzle tests (nos. 17, 18 and 20) in Fig. 6. One can observe that for the full-bore test, there is only one pressure plateau and it lasts for very short time. The pressure continues to drop afterwards and enters the two-phase region. For the tests with a restricted outlet, the number of pressure plateaux increases as the diameter decreases, and it takes longer to reach a two-phase state.

The difference between nozzles and orifices of the same diameter can also be observed in Fig. 6. When comparing Tests 16 (orifice) and 17 (nozzle), fewer pressure plateaux are observed for the nozzle, and the pressure levels are lower. This is caused by the vena contracta area reduction of the orifice. In the end, both cases reach a similar two-phase pressure state.

4.1.2. Comparison of HEM and D-HEM

Before discussing results obtained using our transient pipe-flow model, we want to consider some of the differences between HEM and D-HEM presented in Section 3.5. Fig. 7 compares HEM and D-HEM for a decompression process, plotting speed of sound and fluid velocity as a function of pressure for pure CO_2. The effect of the delayed phase transition is seen to be small for the fluid velocity, but the impact on the speed of sound is large, due to the difference in the equilibrium speed of sound compared to the metastable liquid speed of sound. The effect on fluid velocity of reducing the pressure along the same isentrope is also illustrated. For sufficiently low pressures, 5.5 MPa in the example, the flow will no longer choke at the SHL but in the following delayed HEM flow region.

We now consider two full-bore depressurization tests (Tests 6 and 8) reported in Munkejord et al. (2020). In Fig. 8, we have plotted experimentally observed decompression-wave speeds along with model predictions by HEM and D-HEM. The modelled decompression-wave speed curves are found by integrating (1). Such curves are valuable for assessing running ductile fracture in pipelines, and are often plotted together with the fracture speed in the Battelle two-curve method (see Aursand et al., 2016a). For Test 6, we observe in Fig. 8(a) that the decompression path enters the two-phase region close to the critical pressure. In this case, the HEM and D-HEM have the same performance, and they are both in good agreement with the experiment. For Test 8, shown in Fig. 8(b), the decompression path enters the two-phase region at a lower pressure. Here, the HEM predicts phase transition at about 5.2 MPa, whereas the D-HEM gives phase transition at about 4.2 MPa. This level agrees well with the experiment, which indicates

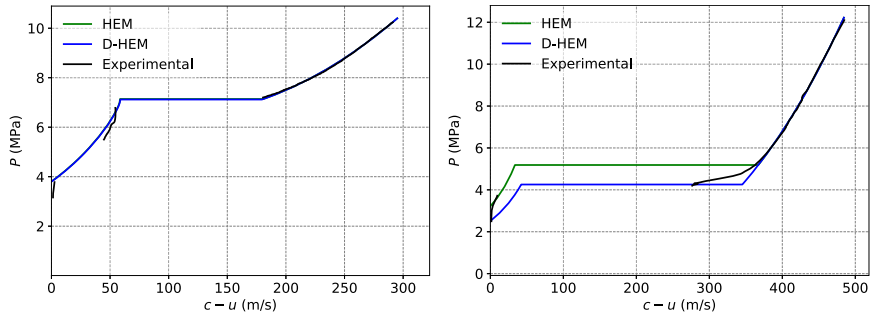

(a) Test 6: $T_0 = 39.5\,^{\circ}\mathrm{C}$, $P_0 = 10.4\,\mathrm{MPa}$. (b) Test 8: $T_0 = 24.6\,^{\circ}\mathrm{C}$, $P_0 = 12.22\,\mathrm{MPa}$.

Fig. 8. Experimentally observed and calculated decompression-wave velocities for full-bore depressurizations of pure CO_2 (Munkejord et al., 2020, Figs. 14 and 15). The GERG-2008 EOS is used for the property predictions.

departure from thermodynamic equilibrium in the flow path. However, in the experiment, we observe a more gradual transition between a metastable state and a more homogeneous equilibrium state, indicating less entropy production than calculated by the D-HEM.

The difference between Tests 6 and 8 can be further illuminated by considering Fig. 5(a). Close the critical point, there is little difference between the superheat limit and the saturation curve. Therefore, for Test 6, there is little difference between HEM and D-HEM, as opposed to the case for Test 8.

4.1.3. Comparison of nozzle experiments and 1D CFD simulations

We have simulated the above cases employing our transient pipe-flow model described in Section 3.7 together with the restricted-flow models in Section 3.4. Fig. 9 displays the measured and simulated pressure for Tests 17, 18 and 20 with nozzles, at $x = 0.08\,\mathrm{m}$ from the outlet.

In Fig. 9(a) for Test 18 with a 12.7 mm nozzle, we observe a fast pressure drop to a plateau pressure of 8.8 MPa, and the plateau remains for about 0.26 s. Upon arrival of the decompression wave reflected from the closed end of the pipe, the pressure further decreases. As already shown in Fig. 6, there are several plateaux before the two-phase region is reached. The pressures simulated using the three restricted-flow models, HEM, HF, and D-HEM, are similar and agree well with the measurements. The HEM predicts the highest pressure plateau (about 8.9 MPa) and smallest mass outflow rate while the D-HEM predicts the lowest pressure plateau (about 8.6 MPa) and largest mass outflow rate. The HEM tends to overestimate the plateau pressure due to the underestimation of mass outflow rate. In the present case, the HF model appears to match the measurement best.

Fig. 9(b) shows the results for Test 20 with a 9.0 mm nozzle. The experimentally observed pressure plateau is increased to about 9.4 MPa, otherwise the trends are very similar to those in Fig. 9(a).

In Fig. 9(c) for Test 17 with a 4.5 mm nozzle, the simulated pressure plateau matches well with the measured values for the first 0.06 s. Later, the measured pressure is affected by pressure waves present in the pipe before the disk rupture. Since the pressure drop is smaller for a smaller-diameter nozzle, the disturbance is relatively more significant in this case.

In Figs. 9(a)–9(c), we observe a small intermediate pressure plateau between the initial pressure and the main plateau. This is related to the gradual opening of the triple-layer rupture disk. The effect is most pronounced for the small-diameter nozzle, most likely due to the smaller flow rate. To account for the reduced flow area in Tests 17 and 20, the mass flux at the intermediate plateau is calculated using (1), and an area scaling is calculated as the fraction of the intermediate mass flux and the main plateau mass flux. For Test 17, a reduced area fraction of 0.371 is applied for the initial 9.8 ms of the simulation. For Test 20, a reduced area fraction of 0.295 is applied for the initial 6.7 ms of the simulation. For Test 18, the effect of the gradual opening is ignored.

4.1.4. Comparison of orifice experiments and 1D CFD simulations

For the simulations of the tests with orifices, we employ contraction coefficients as described in Section 3.6. The employed coefficients are given in Table 4. In addition, for Test 16, a reduced area fraction of 0.43 is applied for the initial 18.09 ms. For Test 21, a reduced area fraction of 0.35 is applied for the initial 7.51 ms. Test 13 was conducted using a single-layer rupture disk not prone to the gradual opening of the triple-layer disks.

Fig. 10(a) shows the measured and calculated pressure for Test 13 with a 12.7 mm orifice. In this case, the calculated contraction coefficient, C_C, has a value of 0.75. It can be seen that all the three restricted-flow models show good agreement with the measured pressure. The HF model matches the measurement best, while the HEM predicts a slightly higher pressure plateau and the D-HEM predicts a slightly lower one. As can be seen in Fig. 10(b), the trends are similar for Test 21 with a 9.0 mm orifice.

In Fig. 10(c), we compare the measured and simulated pressure for Test 16 with a 4.5 mm orifice. In this case, the procedure in Section 3.6 to estimate the contraction coefficient, C_C, yields a value of 0.74. One can see that all the models overestimate the plateau pressure, and that the HF and D-HEM give almost the same results.

4.1.5. Analysis of restricted-flow models

We will now further analyse the models presented in Section 3.4. In doing so, we consider the pressure jump in the decompression (rarefaction) wave between the initial pressure and the first pressure plateau. The flow resulting from this pressure drop is regarded as steady. The initial temperature and pressure at the outlet, as well as the observed pressure-plateau value are given in Table 3. (The values given in Table 2 are averages for the whole pipe.) Using the GERG-2008 EOS and the Euler compatibility Eq. (1), we calculate the mass flow rate in the pipe integrating (2) isentropically using an adaptive Gauss–Legendre quadrature, and convert it to an equivalent mass flux through the nozzle or orifice. This will be used as the experimental value in the following discussion. Further details on the calculation of the mass flow rate and the experimental uncertainty are given in Appendix C.

In order to illustrate the state where the flow chokes in the orifice or nozzle at the outlet, Fig. 11 shows the isentropic path from the pressure plateau after the first decompression wave down into the metastable region for frozen flow. The initial state is given by the plateau pressure and the initial entropy (P_1, s_0). The isentrope is mapped down to the pressure where the single-phase (stable or metastable) flux, calculated using (8) and the local density, equals the flux calculated across the

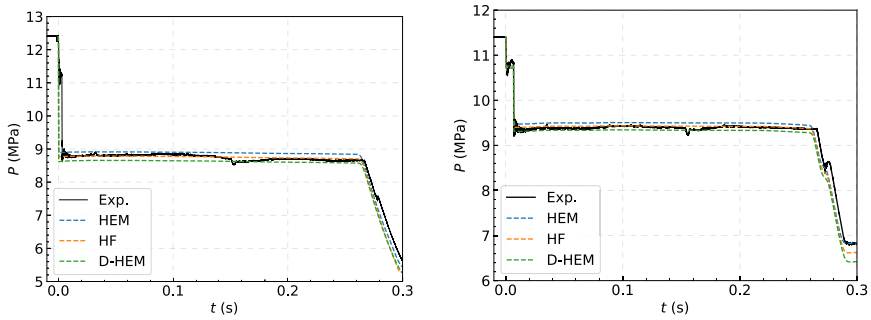

(a) Test 18, nozzle diameter 12.7 mm.

(b) Test 20, nozzle diameter 9.0 mm.

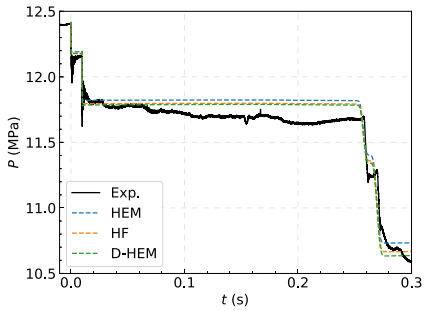

(c) Test 17, nozzle diameter 4.5 mm.

Fig. 9. Measured (full lines) and simulated pressure (dashed lines) at $x = 0.08$ m for Tests 18, 20 and 17 with nozzles.

Table 3
Mass flow estimated from experimental pressure drop using the $x = 0.08$ m sensor. The mass flux is $j = \dot{m}/A_{\text{res}}$.

Test no.	T_0 (°C)	P_0 (MPa)	P_1 (MPa)	$\dot{m}$ (kg/s)	j (t/(s m^2))
13 (orifice)	24.6	12.77	9.61	8.592	67.8
16 (orifice)	24.4	12.17	11.58	1.600	100.6
17 (nozzle)	25.2	12.40	11.74	1.807	113.6
18 (nozzle)	25.1	12.41	8.81	10.072	79.5
20 (nozzle)	22.7	11.40	9.40	5.515	86.7
21 (orifice)	22.0	11.50	9.94	4.208	66.2

Table 4
Calculated contraction coefficient and predicted mass flux (tonnes per square metre and second). Relative deviation to experimental data in parenthesis.

Test no.	C_C (–)	j_{HEM} (t/(s m^2))	$j_{\text{D-HEM}}$ (t/(s m^2))	j_{HF} (t/(s m^2))
13 (orifice)	0.75	63.9 (−6 %)	70.1 (3 %)	66.8 (−1 %)
16 (orifice)	0.74	74.8 (−26 %)	79.6 (−21 %)	78.1(−22 %)
17 (nozzle)	1.0	101.6 (−11 %)	107.7 (−5 %)	106.1 (−7 %)
18 (nozzle)	1.0	76.1 (−4 %)	84.5 (6 %)	80.3 (1 %)
20 (nozzle)	1.0	83.7 (−3 %)	92.5 (7 %)	87.6 (1 %)
21 (orifice)	0.74	66.4 (0 %)	73.0 (10 %)	69.3 (5 %)

decompression wave and given in Table 3. For the two largest nozzles, Test 18 and 20, the process ends at a pressure between the saturation curve and the SHL curve. This indicates that the process departs from thermodynamic equilibrium.

For Test 17, however, the flow predicted to choke below the SHL curve, which is lower than expected. The most likely explanation for this result is the uncertainty in the calculated flow rate, due to the small pressure difference between P_0 and P_1. As little as a 0.035 MPa increase in P_1 is enough for Test 17 to terminate at the SHL.

For the orifice geometry, the contraction coefficient is calculated using the method outlined in Section 3.6, and it is listed along with the mass fluxes predicted using the HEM, D-HEM and HF models in Table 4. The relative deviation to the experimental values are shown in parenthesis.

As the flow apparently chokes below the SHL curve for Test 17, D-HEM agrees best with that experiment, with an underprediction of the mass flux of 5 %. For the largest nozzles, Test 18 and 20, the HF model gives the best prediction of the mass flux, with an overprediction of 1 %. D-HEM overpredicts by 6 % for Test 18 and 7 % for Test 20, while HEM underpredicts by 4 % and 3 %, respectively.

For the small orifice (Test 16), the predicted mass fluxes are off by more than −20 % for all models. For the largest orifice, the HF model gives the best result, only underpredicting the mass flux by 1 %. For the medium orifice (Test 21), the HEM model agrees well with the experimental flux (less than 0.5 % deviation), while the HF and the D-HEM model overpredict the flux by 5 % and 10 %, respectively.

4.2. Mass flux through a nozzle

We now consider the mass flux of dense-phase CO_2 through a converging–diverging nozzle, using the data of Banasiak and Hafner (2013) as reference. Fig. 12 shows a comparison between the experimental data and values calculated using the HEM, D-HEM and HF models. The experimental data are taken at different temperatures and pressures, and are not straightforward to plot two-dimensionally. To get most of the information into one graph, we have plotted mass flux indirectly against the inlet entropy. The x-axis variable is calculated as the saturation pressure corresponding to the stagnant inlet entropy, $P = P_{\text{sat}}\left(s\left(T_0, P_0\right)\right)$. Banasiak and Hafner estimated the experimental

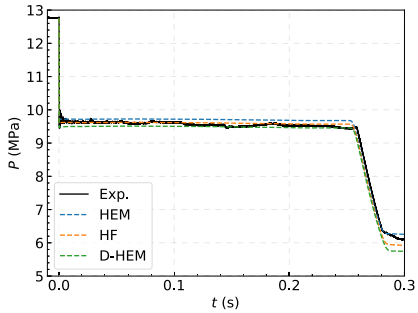

(a) Test 13, orifice diameter 12.7 mm, contraction coefficient $C_C = 0.75$.

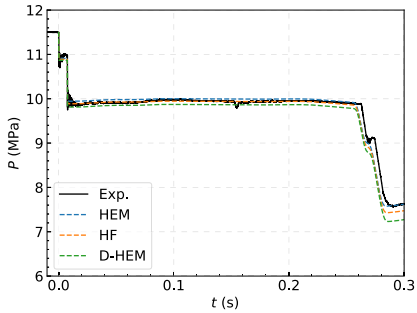

(b) Test 21, orifice diameter 9.0 mm, contraction coefficient $C_C = 0.74$.

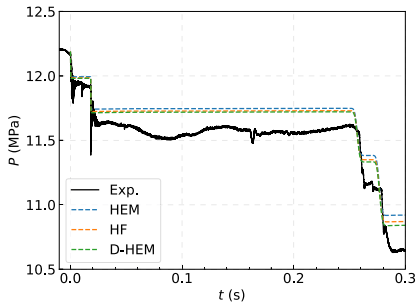

(c) Test 16, orifice diameter 4.5 mm, contraction coefficient $C_C = 0.74$.

Fig. 10. Measured (full lines) and simulated pressure (dashed lines) at $x = 0.08$ m For Tests 13, 21 and 16 with orifices.

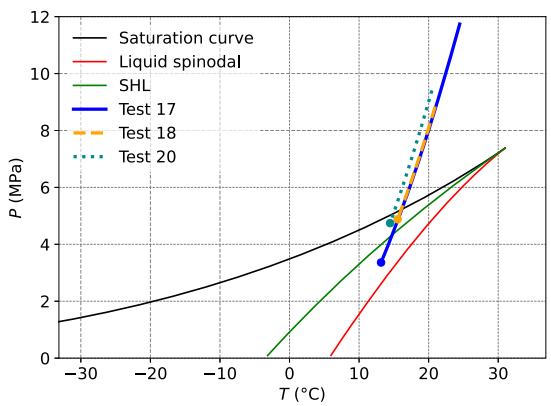

Fig. 11. Restricted-flow calculation for Tests 17, 18 and 20: Isentropic path assuming frozen flow. The choke point (dot) calculated from observed mass flux for each experiment. GERG-2008 spinodal and superheat limit calculated from CNT are included.

uncertainty to be ±0.5 K for the inlet temperature, ±30 kPa for the pressure and $\pm 0.5 \times 10^3$ kg/s for the mass flow rate. With these estimates, error bars have been calculated for the saturation pressure and the mass flux. In Fig. 12, the dashed line separates data with an inlet pressure above or below 8.2 MPa.

Table 5
Relative absolute errors for model predictions compared to Banasiak and Hafner (2013) experimental data.

Model	Rel. Abs. Err. (All data) (%)	Rel. Abs. Err. (Low press data) (%)
HEM	7.8	17
D-HEM	2.5	5.8
HF	5.4	8.2

We observe that the HF model is in good agreement with the experimental data, with the exception of some points with low inlet pressure and low inlet entropy where the mass flux is underpredicted. The HEM is seen to predict the mass flux well for entropies close to the critical point. However, elsewhere, the model underpredicts the mass flux. This is expected because the distance between the saturation curve and the SHL is small in this region, and the delay before onset of nucleation is short. The D-HEM is in very good agreement with the experimental data points above the grey dashed line. From Table 5 we see that D-HEM outperforms HF both for the low-pressure data and when all data are taken into account. For the latter case the mean absolute deviation is 2.5 % for D-HEM versus 5.4 % for HF.

Finally, we consider the experimental data of Hesson and Peck (1958) for saturated liquid flowing through a converging nozzle. Fig. 13 shows a comparison between the experimentally determined mass-flux data and values calculated using the HEM, D-HEM and HF models, plotted as a function of the reported saturation pressure of the experiments. Both HEM and D-HEM are seen to consistently underpredict

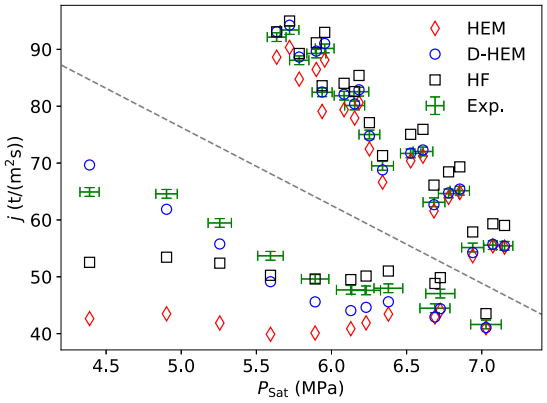

Fig. 12. Model predictions using HF, HEM and D-HEM, plotted together with the Banasiak and Hafner (2013) experimental data (Exp.). The experimental data include error bars calculated using the uncertainties reported by Banasiak and Hafner. The mass flux is plotted as a function of the saturation pressure calculated from the stagnant inlet conditions, $P = P_{sat}\left(s\left(T_0, P_0\right)\right)$. The GERG-2008 EOS is used for the property predictions. The dashed grey line separates data based on inlet pressure, below it, all data have an inlet pressure below 8.2 MPa.

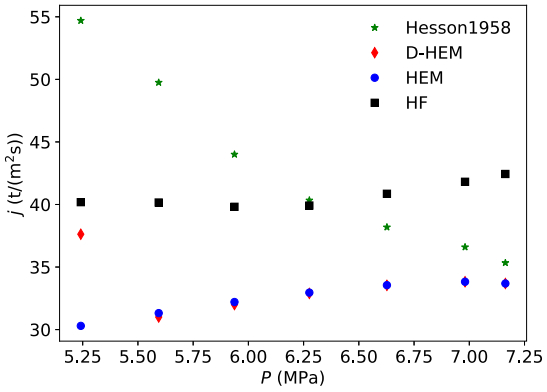

Fig. 13. Model predictions using HF, HEM and D-HEM, plotted together with the Hesson and Peck (1958) experimental data for saturated liquid states. The GERG-2008 EOS is used for the property predictions.

the data. With the exception of the data point with the lowest saturation pressure, HEM and D-HEM give almost the same result, the only difference being the small entropy production in D-HEM. For the experiment starting at 5.25 MPa, D-HEM predicts choking before the SHL line, leading to a larger mass flux than for HEM. For the other points, D-HEM chokes after the SHL and the mass flux is slightly lower than for HEM due to the entropy production.

The HF model overpredicts the mass flux close to the critical pressure. However, for saturation pressures below 6.25 MPa, it underpredicts the experimental mass flux. As reported by Hendricks et al. (1972), the mass fluxes in Hesson and Peck (1958) are higher than expected and there might be systematic errors in the data.

5. Conclusion

In CO_2 processing, transportation and injection systems, compressed CO_2 will, during normal operation or exceptional venting, flow through valves or other restrictions. In order to calculate the flow rates and fluid states needed for operational or safety considerations, there is a need for validated models providing realistic results without the need for detailed geometry input.

We have experimentally investigated the effect of outlet restriction geometry type and size on the depressurization of a 41 mm inner-diameter pipe. From an initial state of 12 MPa and 25 °C, the pipe was depressurized through six sharp orifices and converging nozzles, made in pairs with 90 %, 95 % and 99 % area reduction.

In our previous full-bore experiment, the pressure in the pipe rapidly decreased to a two-phase state. The introduction in this work of flow restrictions at the outlet yielded pressure traces displaying intermediate plateaux at single-phase states, the number of plateaux and time to empty the pipe increasing for decreasing restriction diameter. For a given diameter, flow through an orifice yielded higher pressure-plateau levels than for flow through a nozzle. This is consistent with the orifice resulting in a smaller practical cross-sectional area (vena contracta), which in turn gives a smaller mass flow rate.

Our current setup does not allow the direct measurement of the mass flow rate. However, by exploiting the fact that the state in the pipe was single-phase, and by assuming a quasi-steady state for each pressure plateau, we could calculate the mass flow rate based on the measured pressure. Here, we employed the Euler compatibility equation, which is commonly used for hydraulic-shock calculations, and the GERG-2008 EOS.

Three different models were used to calculate the flow through the restrictions. All the models were formulated in a manner not requiring integration over the actual geometry, but only using the upstream state and the minimum cross section of the restriction. The models are therefore valid when the influence by friction on the flow rate can be assumed to be small. This is useful in simulations where the spatial dimension of the restriction is not resolved (long pipes) or for cases where the geometry is partly unknown.

In addition to the classical HEM and HF model, we propose an augmented HEM, allowing for delayed phase transition, labelled D-HEM. The model assumes a process where there are no bubble nuclei before reaching the SHL calculated by classical nucleation theory. After reaching the SHL, the state is transitioned to full equilibrium at constant pressure, including entropy production during phase transfer.

We compared the three models to experimental data for flow through nozzles by Hesson and Peck (1958) and Banasiak and Hafner (2013). The mass fluxes reported by Hesson and Peck are significantly larger than those predicted by the models. This is an inconsistency that has also been noted by other authors. For the Banasiak and Hafner experiments we found the D-HEM to be the best model among those tested, with a relative absolute error of 2.5 % for the predicted mass flux. This indicates that the approach behind D-HEM is viable and should be considered in the further development of simulation tools for compressed CO_2.

Another promising avenue for further research is to apply the D-HEM in the assessment of running ductile fracture in CO_2-transportation pipelines. We gave examples of typical plots of pressure as a function of decompression-wave speed used in such assessments, showing that D-HEM is applicable and gives lower pressures than HEM, which is known to give too high pressures and therefore the wrong load on the steel structure.

In the sharp-orifice geometry, the actual flow throat area will be smaller than the minimum physical area. We accounted for this by calculating a contraction coefficient employing a steady-state force balance, an approach generalized from that of Bragg (1960).

The above models for flow through restrictions were implemented in our numerical workbench for 1D, transient, multiphase flow, and we compared simulated and measured pressures. Good results were obtained for all models, with the best agreement obtained using the HF model. For the pressure-plateau, the HEM gave the highest level, consistent with the lowest mass flow rate, followed by the HF model and D-HEM. Our results for the decompression through orifices indicate that

the calculated contraction coefficient is uncertain. Further experimental and modelling efforts are needed here.

A subject for future work would be to study cases with different initial fluid states, so that the isentropic decompression path hits the two-phase region at a low pressure and temperature, where heterogeneous nucleation needs to be accounted for.

Another topic for further work would be to modify the experimental setup and procedure in order to have a more uniform initial condition.

CRediT authorship contribution statement

Morten Hammer: Conceptualization, Methodology, Software, Investigation, Data curation, Writing – original draft, Writing – review & editing, Visualization. **Han Deng:** Software, Formal analysis, Investigation, Data curation, Writing – original draft, Visualization. **Anders Austegard:** Methodology, Software, Investigation, Resources, Writing – review & editing. **Alexandra Metallinou Log:** Software, Investigation, Writing – original draft. **Svend Tollak Munkejord:** Conceptualization, Methodology, Writing – original draft, Writing – review & editing, Supervision, Funding acquisition.

Declaration of competing interest

The authors declare that they have no known competing financial interests or personal relationships that could have appeared to influence the work reported in this paper.

Acknowledgements

This publication has been produced with support from the NCCS Centre, performed under the Norwegian research programme Centres for Environment-friendly Energy Research (FME). The authors acknowledge the following partners for their contributions: Aker Carbon Capture, Allton, Ansaldo Energia, Baker Hughes, CoorsTek Membrane Sciences, Equinor, Fortum Oslo Varme, Gassco, Krohne, Larvik Shipping, Lundin Energy Norway, Norcem, Norwegian Oil and Gas, Quad Geometrics, Stratum Reservoir, TotalEnergies, Vår Energi, Wintershall Dea and the Research Council of Norway (257579).

The construction of the ECCSEL Depressurization Facility was supported by the INFRASTRUKTUR programme of the Research Council of Norway (225868).

Appendix A. Calculation of choking conditions for steady-state HEM

This section outlines the calculation of the choking condition of the HEM model under a steady-state assumption. The case of the HF model is given in the original article (Henry and Fauske, 1971). How to solve the D-HEM model is indicated in Section 3.5.

In steady state, the HEM without source terms reduces to three flow constants:

- constant mass flow rate: $\dot{m}$,
- constant entropy: s,
- constant energy: $h + \frac{1}{2}u^2$.

The energy equation, subject to constant entropy, will give $u = u(p)$. Under the same conditions, the speed of sound will be a function of pressure, $c = c(p)$, and solving for $u = c$ is a single-variable problem in pressure. One complication is the discontinuity in speed of sound at the phase boundaries. This is seen in Fig. 7 where u and c are plotted as functions of p for one test condition. Due to the discontinuity, the flow will often choke on the saturation curve.

The speed of sound is given by

$$c = \sqrt{\left.\frac{\partial p}{\partial \rho}\right|_s}. \tag{A.1}$$

Under the HEM assumption of chemical equilibrium ($\mu_g = \mu_\ell$), this equation becomes constrained. This can be accounted for by defining the following equation system where entropy (s_{cons}) and mass density (ρ_{cons}) are known,

$$\boldsymbol{G}\left(s_{\text{cons}}, \rho_{\text{cons}}, \boldsymbol{X}\right) = \boldsymbol{0}, \tag{A.2}$$

where

$$\boldsymbol{G} = \begin{bmatrix} \mu_g - \mu_\ell \\ \dfrac{1}{\frac{z}{\rho_g} + \frac{1-z}{\rho_\ell}} - \rho_{\text{cons}} \\ s - s_{\text{cons}} \end{bmatrix} \tag{A.3}$$

and

$$\boldsymbol{X} = \begin{bmatrix} T \\ P \\ z \end{bmatrix}, \tag{A.4}$$

with the overall entropy given as $s = zs_g + (1-z)s_\ell$.

Differentiating Eq. (A.2) with respect to ρ_{cons} we get

$$\nabla_{\boldsymbol{X}}\boldsymbol{G}\frac{\partial \boldsymbol{X}}{\partial \rho_{\text{cons}}} + \frac{\partial \boldsymbol{G}}{\partial \rho_{\text{cons}}} = \boldsymbol{0}, \tag{A.5}$$

where $\nabla_{\boldsymbol{X}}\boldsymbol{G}$ is the Jacobian matrix of $\boldsymbol{G}$ with respect to $\boldsymbol{X}$ and $\partial \boldsymbol{G}/\partial \rho_{\text{cons}} = [0, -1, 0]^\intercal$. Solving for $\partial \boldsymbol{X}/\rho_{\text{cons}} = [\partial T/\partial \rho_{\text{cons}}, \partial P/\partial \rho_{\text{cons}}, \partial z/\partial \rho_{\text{cons}}]^\intercal$, we obtain $\partial P/\partial \rho$, and the speed of sound can be calculated. The speed of sound is calculated using an analytical Jacobian matrix and the discontinuity when entering the two-phase region is illustrated in Fig. 7.

Appendix B. Calculation of the flow contraction coefficient at orifices

The coefficient of contraction, defined in Section 3.6, establishes the actual flow area and must be known when calculating the outflow through a nozzle or orifice. In this work we have utilized an isentropic force balance as described by Bragg (1960, Eq. (5)) and Benedict (1971, Eq. (2)). The area and the forces acting on the fluid are illustrated in Fig. B.14.

The force balance accounting for inlet momentum and back pressure is

$$\begin{aligned} F + A_{\text{pipe}}p_{\text{pipe}} - \left(A_{\text{pipe}} - A_{\text{res}}\right)p_{\text{pipe}} \\ = A_{\text{vc}}p_{\text{vc}} + \left(A_{\text{res}} - A_{\text{vc}}\right)p_{\text{amb}} + \dot{m}\left(u_{\text{vc}} - u_{\text{pipe}}\right), \end{aligned} \tag{B.1}$$

where F is the force defect described by the integral

$$F = \int_{A_{\text{res}}}^{A_{\text{pipe}}} \left(p_{\text{pipe}} - p_w\right) \mathrm{d}A_w, \tag{B.2}$$

where the subscript w refers to the wall, and F can be integrated using a Gauss–Legendre quadrature with error control. Dividing (B.1) by A_{res}, and setting $F^* = F/A_{\text{res}}$ we get,

$$F^* + p_{\text{pipe}} - p_{\text{amb}} + \left(p_{\text{vc}} - p_{\text{amb}}\right)C_{\text{C}} = C_{\text{C}}\rho_{\text{vc}}u_{\text{vc}}\left(u_{\text{vc}} - u_{\text{pipe}}\right), \tag{B.3}$$

which yields

$$C_{\text{C}} = \frac{F^* + p_{\text{pipe}} - p_{\text{amb}}}{p_{\text{vc}} - p_{\text{amb}} + \rho_{\text{vc}}u_{\text{vc}}\left(u_{\text{vc}} - u_{\text{pipe}}\right)}. \tag{B.4}$$

Bragg (1960, Eq. (15)) proposed that the mass velocity distribution on the stream tube boundary upstream of the orifice could be described as

$$j_w = kC_{\text{C}}j_{\text{vc}}A_{\text{res}}/A_w, \tag{B.5}$$

where

$$k = \sqrt{\frac{2}{C_{\text{C,i}}} - \frac{1}{C_{\text{C,i}}^2}}, \tag{B.6}$$

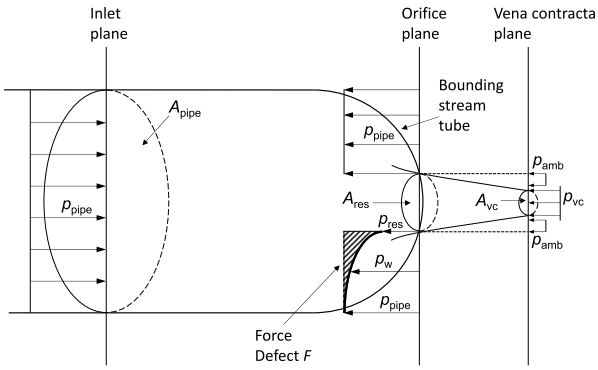

Fig. B.14. Generalized orifice flow with notation and forces on the fluid.
Source: Adapted from Benedict (1971).

and

$$C_{C,i} = \frac{\pi}{\pi + 2}. \tag{B.7}$$

p_w can then be found implicitly by solving

$$j_w = \rho\left(s_{pipe}, p_w\right) u\left(s_{pipe}, p_w\right), \tag{B.8}$$

where the steady-state energy equation (Bernoulli) for isentropic flow is used to determine the velocity u_w:

$$h_{pipe} + \frac{1}{2}u_{pipe}^2 = h_w\left(s_{pipe}, p_w\right) + \frac{1}{2}u_w^2. \tag{B.9}$$

We use a bracketing solver to solve Eq. (B.8).

To solve for the contraction coefficient we use a successive substitution approach as follows.

- Guess $C_C = 1.1 C_{C,i}$
- Set $C_{C,old} = 1$
- Calculate critical state based on upstream conditions. Output: p_{vc}, u_{vc}, ρ_{vc}
- Iterate until $\|C_C - C_{C,old}\|/C_C < 10^{-10}$:
  - Set $C_{C,old} = C_C$
  - Find F^* by integrating (B.2)
  - Calculate C_C from (B.4)

Appendix C. Experimental uncertainty of mass flow rate

The mass flow is calculated as

$$\dot{m} = (u\rho)_{P_1} A_{Pipe} \tag{C.1}$$

with

$$u(P) = \int_{P=P_0}^{P=P_1} \frac{\mathrm{d}P}{\rho c}. \tag{C.2}$$

The pressure measured at the position closest to the outlet, at $x = 0.08$ m, by the sensor PT201 is used to determine the initial pressure, P_0, and first pressure plateau, P_1. The temperature measured at the position $x = 1.6$ m is used for T_0.

The value of P_1 is obtained by averaging the measurement between the time when the pressure plateau stabilizes and the time when a dip reaches about the middle of the pressure plateau, as indicated in Fig. C.15. This dip is a result of the recoil of the pipe: When depressurization occurs, a wave travels in both the fluid and the stainless-steel pipe towards the closed end. The wave travelling in the steel has a speed of about 5800 m/s. After it reaches the end, the wave is reflected and travels back in the fluid, as seen by the dip.

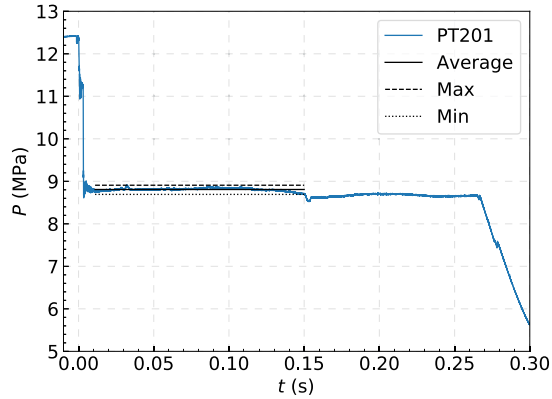

Fig. C.15. Averaged plateau pressure P_1 for the calculation of mass flow rate in Test 18.

Table C.6
Initial pressure P_0, temperature T_0, and pressure plateau P_1 with differences to the maximum and minimum values.

Test no.	T_0 (°C)	P_0 (MPa)	P_1 (MPa)	$\delta P_{1,max}$ (MPa)	$\delta P_{1,min}$ (MPa)
13	24.6	12.77	9.61	0.14	0.09
16	24.4	12.17	11.58	0.07	0.07
17	25.2	12.40	11.74	0.09	0.06
18	25.1	12.41	8.81	0.10	0.12
20	22.7	11.40	9.40	0.06	0.10
21	22.0	11.50	9.94	0.06	0.10

The values of P_0 and T_0 are stable, thus we focus on the measurement uncertainty caused by the value of P_1. We employ the min–max method to estimate the uncertainty of the mass flow rate $\dot{m}$. The values of P_0, T_0, and P_1 are listed in Table C.6, with the differences to the maximum and minimum values $\delta P_{1,max} = P_{1,max} - P_1$ and $\delta P_{1,min} = P_1 - P_{1,min}$.

The mass flow rate for the maximum and minimum values of the pressure plateau can be expressed as

$$\dot{m}_{min} = u\left(P_0, P_1 + \delta P_{1,max}\right) \rho\left(P_0, P_1 + \delta P_{1,max}\right) A_{Pipe}, \tag{C.3}$$

$$\dot{m}_{max} = u\left(P_0, P_1 - \delta P_{1,min}\right) \rho\left(P_0, P_1 - \delta P_{1,min}\right) A_{Pipe}. \tag{C.4}$$

Table C.7
Measured mass flow rate and the absolute and relative uncertainties.

Test no.	$\dot{m}$ (kg/s)	$\dot{m}_{max}$ (kg/s)	$\dot{m}_{min}$ (kg/s)	$\delta\dot{m}$ (kg/s)	$\frac{\delta\dot{m}}{\dot{m}}$ (%)
13	8.592	8.850	8.203	0.389	4.5
16	1.600	1.799	1.400	0.201	12.5
17	1.807	1.972	1.567	0.241	13.3
18	10.072	10.408	9.781	0.336	3.3
20	5.515	5.788	5.339	0.273	4.9
21	4.208	4.489	4.037	0.280	6.7

The measured mass flow rate can be expressed with the absolute uncertainty, $\dot{m} \pm \delta\dot{m}$, as

$$\delta\dot{m} = \max\left(\dot{m}_{max} - \dot{m}, \dot{m} - \dot{m}_{min}\right). \quad (C.5)$$

Since the data are not normally distributed, we use the maximum difference to $\dot{m}$ to be conservative. The relative uncertainty can be then expressed as $\frac{\delta\dot{m}}{\dot{m}}$. The absolute and relative uncertainties of the mass flow rates are listed in Table C.7.

Appendix D. Supplementary data

The experimental data used in this study is available online at https://doi.org/10.1016/j.ijmultiphaseflow.2022.104201.

References

Angielczyk, W., Bartosiewicz, Y., Butrymowicz, D., 2020. Development of delayed equilibrium model for CO_2 convergent-divergent nozzle transonic flashing flow. Int. J. Multiph. Flow. 131, 103351. http://dx.doi.org/10.1016/j.ijmultiphaseflow.2020.103351.

Angielczyk, W., Bartosiewicz, Y., Butrymowicz, D., Seynhaeve, J.-M., 2010. 1-d modeling of supersonic carbon dioxide two-phase flow through ejector motive nozzle. In: International Refrigeration and Air Conditioning Conference. Purdue University, URL https://docs.lib.purdue.edu/iracc/1102/.

Angielczyk, W., Seynhaeve, J.M., Gagan, J., Bartosiewicz, Y., Butrymowicz, D., 2019. Prediction of critical mass rate of flashing carbon dioxide flow in convergent-divergent nozzle. Chem. Eng. Process. – Process Intensif. 143 (4), 107599. http://dx.doi.org/10.1016/j.cep.2019.107599.

Armstrong, K., Allason, D., 2014. 2 NB Shocktube Releases of Dense Phase CO_2. Tech. rep., GL Noble Denton, Gilsland Cumbria, UK, Available from URL https://www.dnvgl.com/oilgas/innovation-development/joint-industry-projects/co2pipetrans.html.

Aursand, E., Dumoulin, S., Hammer, M., Lange, H.I., Morin, A., Munkejord, S.T., Nordhagen, H.O., 2016a. Fracture propagation control in CO_2 pipelines: Validation of a coupled fluid–structure model. Eng. Struct. 123, 192–212. http://dx.doi.org/10.1016/j.engstruct.2016.05.012.

Aursand, P., Gjennestad, M.A., Aursand, E., Hammer, M., Wilhelmsen, Ø., 2016b. The spinodal of single- and multi-component fluids and its role in the development of modern equations of state. Fluid Phase Equilib. 436, 98–112. http://dx.doi.org/10.1016/j.fluid.2016.12.018.

Aursand, E., Hammer, M., 2018. Predicting triggering and consequence of delayed LNG RPT. J. Loss Prevent. Proc. 55, 124–133. http://dx.doi.org/10.1016/j.jlp.2018.06.001.

Aursand, P., Hammer, M., Lavrov, A., Lund, H., Munkejord, S.T., Torsæter, M., 2017. Well integrity for CO_2 injection from ships: Simulation of the effect of flow and material parameters on thermal stresses. Int. J. Greenh. Gas Con 62, 130–141. http://dx.doi.org/10.1016/j.ijggc.2017.04.007.

Banasiak, K., Hafner, A., 2013. Mathematical modelling of supersonic two-phase r744 flows through converging–diverging nozzles: The effects of phase transition models. Appl. Therm. Eng. (ISSN: 1359-4311) 51 (1), 635–643. http://dx.doi.org/10.1016/j.applthermaleng.2012.10.005.

Bejan, A., 1993. Heat Transfer. John Wiley & Sons, Inc., New York, ISBN: 0-471-50290-1.

Benedict, R.P., 1971. Generalized contraction coefficient of an orifice for subsonic and supercritical flows. J. Basic Eng. 93 (2), 99–120. http://dx.doi.org/10.1115/1.3425245.

Blinkov, V.N., Jones, O.C., Nigmatulin, B.I., 1993. Nucleation and flashing in nozzles – 2. comparison with experiments using a five-equation model for vapor void development. Int. J. Multiph. Flow. 19 (6), 965–986. http://dx.doi.org/10.1016/0301-9322(93)90072-3.

Bragg, S.L., 1960. Effect of compressibility on the discharge coefficient of orifices and convergent nozzles. J. Mech. Eng. Sci. 2 (1), 35–44. http://dx.doi.org/10.1243/JMES_JOUR_1960_002_007_02.

Brown, S., Martynov, S., Mahgerefteh, H., 2015. Simulation of two-phase flow through ducts with discontinuous cross-section. Comput. Fluids 120, 46–56. http://dx.doi.org/10.1016/j.compfluid.2015.07.018.

Brown, S., Martynov, S., Mahgerefteh, H., Proust, C., 2013. A homogeneous relaxation flow model for the full bore rupture of dense phase CO_2 pipelines. Int. J. Greenh. Gas Con 17, 349–356. http://dx.doi.org/10.1016/j.ijggc.2013.05.020.

Chapman, C.J., 2000. High Speed Flow. Cambridge University Press, Cambridge, UK, ISBN: 0-521-66647-3.

De Lorenzo, M., Lafon, P., Seynhaeve, J.-M., Bartosiewicz, Y., 2017. Benchmark of delayed equilibrium model (DEM) and classic two-phase critical flow models against experimental data. Int. J. Multiph. Flow. 92, 112–130. http://dx.doi.org/10.1016/j.ijmultiphaseflow.2017.03.004.

Debenedetti, P.G., 1997. Metastable Liquids: Concepts and Principles. Princeton University Press, ISBN: 9780691213941, http://dx.doi.org/10.1515/9780691213941.

Downar-Zapolski, P., Bilicki, Z., Bolle, L., Franco, J., 1996. The non-equilibrium relaxation model for one-dimensional flashing liquid flow. Int. J. Multiph. Flow. 22 (3), 473–483. http://dx.doi.org/10.1016/0301-9322(95)00078-X.

ECCSEL, 2021. Depressurization facility. URL https://www.eccsel.org/catalogue/113. (Accessed 07 December 2021).

Edenhofer, O., Pichs-Madruga, R., Sokona, Y., Farahani, E., Kadner, S., Seyboth, K., Adler, A., Baum, I., Brunner, S., Eickemeier, P., Kriemann, B., Savolainen, J., Schlømer, S., Stechow, C.von., Zwickel, T., J.M, 2014. Climate Change 2014: Mitigation of Climate Change. Tech. rep. Working Group III Contribution to the Fifth Assessment Report of the Intergovernmental Panel on Climate Change, Summary for Policymakers, IPCC., URL http://mitigation2014.org/.

Edlebeck, J., Nellis, G.F., Klein, S.A., Anderson, M.H., Wolf, M., 2014. Measurements of the flow of supercritical carbon dioxide through short orifices. J. Supercrit. Fluid 88, 17–25. http://dx.doi.org/10.1016/j.supflu.2014.01.008.

Elias, E., Lellouche, G.S., 1994. Two-phase critical flow. Int. J. Multiph. Flow. 20 (suppl.), 91–168. http://dx.doi.org/10.1016/0301-9322(94)90071-X.

Fan, X., Wang, Y., Zhou, Y., Chen, J., Huang, Y., Wang, J., 2018. Experimental study of supercritical CO_2 leakage behavior from pressurized vessels. Energy 150, 342–350. http://dx.doi.org/10.1016/j.energy.2018.02.147.

Fenghour, A., Wakeman, W.A., Vesovic, V., 1998. The viscosity of carbon dioxide. J. Phys. Chem. Ref. Data 27 (1), 31–44. http://dx.doi.org/10.1063/1.556013.

Flåtten, T., Lund, H., 2011. Relaxation two-phase flow models and the subcharacteristic condition. Math. Mod. Meth. Appl. S 21 (12), 2379–2407. http://dx.doi.org/10.1142/S0218202511005775.

Friedel, L., 1979. Improved friction pressure drop correlations for horizontal and vertical two phase pipe flow. In: Proceedings, European Two Phase Flow Group Meeting. Ispra, Italy. Paper E2.

Guo, X., Yan, X., Yu, J., Yang, Y., Zhang, Y., Chen, S., Mahgerefteh, H., Martynov, S., Collard, A., 2017. Pressure responses and phase transitions during the release of high pressure CO_2 from a large-scale pipeline. Energy 118, 1066–1078. http://dx.doi.org/10.1016/j.energy.2016.10.133.

Guo, X., Yan, X., Yu, J., Zhang, Y., Chen, S., Mahgerefteh, H., Martynov, S., Collard, A., Proust, C., 2016. Pressure response and phase transition in supercritical CO_2 releases from a large-scale pipeline. Appl. Energy 178, 189–197. http://dx.doi.org/10.1016/j.apenergy.2016.06.026.

Hammer, M., Aasen, A., Wilhelmsen, Ø., 2020. Thermopack. URL https://github.com/SINTEF/thermopack/. (Accessed 15 December 2020).

Hammer, M., Ervik, Å., Munkejord, S.T., 2013. Method using a density-energy state function with a reference equation of state for fluid-dynamics simulation of vapor–liquid–solid carbon dioxide. Ind. Eng. Chem. Res. 52 (29), 9965–9978. http://dx.doi.org/10.1021/ie303516m.

Hendricks, R.C., Simoneau, R.J., Ehlers, R.C., 1972. Choked Flow of Fluid Nitrogen with Emphasis on the Thermodynamic Critical Region. Technical Memorandum TM X-68107, National Aeronautics and Space Administration (NASA), Cleveland, Ohio, USA, URL https://ntrs.nasa.gov/citations/19720020638.

Henry, R.E., Fauske, H.K., 1971. The two-phase critical flow of one-component mixtures in nozzles, orifices, and short tubes. J. Heat Transf. 93, 179.

Hesson, J.C., Peck, R.E., 1958. Flow of two-phase carbon dioxide through orifices. AIChE J. 4 (2), 207–210. http://dx.doi.org/10.1002/aic.690040216.

IEA, 2021. Net zero by 2050 – A roadmap for the global energy sector. IEA, Paris. URL https://www.iea.org/reports/net-zero-by-2050.

Kunz, O., Wagner, W., 2012. The GERG-2008 wide-range equation of state for natural gases and other mixtures: An expansion of GERG-2004. J. Chem. Eng. Data 57 (11), 3032–3091. http://dx.doi.org/10.1021/je300655b.

Lackme, C., 1979. Incompleteness of the flashing of a supersaturated liquid and sonic ejection of the produced phases. Int. J. Multiph. Flow. 5 (2), 131–141. http://dx.doi.org/10.1016/0301-9322(79)90041-7.

Li, K., Zhou, X., Tu, R., Xie, Q., Yi, J., Jiang, X., 2016. An experimental investigation of supercritical CO_2 accidental release from a pressurized pipeline. J. Supercrit. Fluid 107, 298–306. http://dx.doi.org/10.1016/j.supflu.2015.09.024.

Liao, Y., Lucas, D., 2017. Computational modelling of flash boiling flows: A literature survey. Int. J. Heat Mass. Transf. 111, 246–265. http://dx.doi.org/10.1016/j.ijheatmasstransfer.2017.03.121.

Lienhard, J.H.V., Lienhard, J.H., 1984. Velocity coefficients for free jets from sharp-edged orifices. J. Fluids Eng. 106 (1), 13–17. http://dx.doi.org/10.1115/1.3242391.

Log, A.M., Munkejord, S.T., Hammer, M., 2021. HLLC-type methods for compressible two-phase flow in ducts with discontinuous area changes. Comput. Fluids 227, http://dx.doi.org/10.1016/j.compfluid.2021.105023.

Martin, K., Rieberer, R., Hager, J., 2006. Modeling of short tube orifices for CO_2. In: International Refrigeration and Air Conditioning Conference. Purdue University, Paper 781.

Martynov, S., Zheng, W., Mahgerefteh, H., Brown, S., Hebrard, J., Jamois, D., Proust, C., 2018. Computational and experimental study of solid-phase formation during the decompression of high-pressure CO_2 pipelines. Ind. Eng. Chem. Res. 57 (20), 7054–7063. http://dx.doi.org/10.1021/acs.iecr.8b00181.

Moody, F.J., 1965. Maximum flow rate of a single component, two-phase mixture. J. Heat Transf. 87 (1), 134–141. http://dx.doi.org/10.1115/1.3689029.

Munkejord, S.T., Austegard, A., Deng, H., Hammer, M., Stang, H.G.J., Løvseth, S.W., 2020. Depressurization of CO_2 in a pipe: High-resolution pressure and temperature data and comparison with model predictions. Energy 211, 118560. http://dx.doi.org/10.1016/j.energy.2020.118560.

Munkejord, S.T., Deng, H., Austegard, A., Hammer, M., Skarsvåg, H.L., Aasen, A., 2021. Depressurization of CO_2- and CO_2-he in a pipe: Experiments and modelling of pressure and temperature dynamics. Int. J. Greenh. Gas Con. 109, 103361. http://dx.doi.org/10.1016/j.ijggc.2021.103361.

Munkejord, S.T., Hammer, M., 2015. Depressurization of CO_2-rich mixtures in pipes: Two-phase flow modelling and comparison with experiments. Int. J. Greenh. Gas Con. 37, 398–411. http://dx.doi.org/10.1016/j.ijggc.2015.03.029.

Munkejord, S.T., Hammer, M., Løvseth, S.W., 2016. CO_2 transport: Data and models – A review. Appl. Energ 169, 499–523. http://dx.doi.org/10.1016/j.apenergy.2016.01.100.

Nakagawa, M., Berana, M.S., Kishine, A., 2009. Supersonic two-phase flow of CO_2 through converging-diverging nozzles for the ejector refrigeration cycle. Int. J. Refrig. 32 (6), 1195–1202. http://dx.doi.org/10.1016/j.ijrefrig.2009.01.015.

Picard, D.J., Bishnoi, P.R., 1988. The importance of real-fluid behavior and non-isentropic effects in modeling decompression characteristics of pipeline fluids for application in ductile fracture propagation analysis. Can. J. Chem. Eng. 66 (1), 3–12. http://dx.doi.org/10.1002/cjce.5450660101.

Pinhasi, G.A., Ullmann, A., Dayan, A., 2005. Modeling of flashing two-phase flow. Rev. Chem. Eng. 21 (3–4), 133–264. http://dx.doi.org/10.1515/REVCE.2005.21.3-4.133.

Rathjen, W., Straub, J., 1977. Temperature dependence of surface tension, coexisting curve, and vapor pressure of CO_2, $CClF_3$, $CBrF_3$, and SF_6. In: Hahne, E., Grigull, U. (Eds.), Heat Transfer in Boiling. Taylor & Francis Inc., ISBN: 0-123-14450-7, chap. 18.

Ringstad, K.E., Allouche, Y., Gullo, P., Ervik, Å., Banasiak, K., Hafner, A., 2020. A detailed review on CO_2 two-phase ejector flow modeling. Therm. Sci. Eng. Prog. 20, 100647. http://dx.doi.org/10.1016/j.tsep.2020.100647.

Roussanaly, S., Deng, H., Skaugen, G., Gundersen, T., 2021. At what pressure shall CO_2 be transported by ship? An in-depth cost comparison of 7 and 15 barg shipping. Energies 14 (18), 271–280. http://dx.doi.org/10.3390/en14185635.

Shin, T.S., Jones, O.C., 1993. Nucleation and flashing in nozzles – 1. A distributed nucleation model. Int. J. Multiph. Flow. 19 (6), 943–964. http://dx.doi.org/10.1016/0301-9322(93)90071-2.

Span, R., Wagner, W., 1996. A new equation of state for carbon dioxide covering the fluid region from the triple-point temperature to 1100 K at pressures up to 800 MPa. J. Phys. Chem. Ref. Data 25 (6), 1509–1596. http://dx.doi.org/10.1063/1.555991.

Tesař, V., 2008. Characterisation of subsonic axisymmetric nozzles. Chem. Eng. Res. Des. 8 (11), 1253–1262. http://dx.doi.org/10.1016/j.cherd.2008.04.012.

Toro, E.F., Billett, S.J., 2000. Centred TVD schemes for hyperbolic conservation laws. IMA J. Numer. Anal. 20 (1), 47–79. http://dx.doi.org/10.1093/imanum/20.1.47.

Vree, B., Ahmad, M., Buit, L., Florisson, O., 2015. Rapid depressurization of a CO_2 pipeline – experimental study. Int. J. Greenh. Gas Con. 41, 41–49. http://dx.doi.org/10.1016/j.ijggc.2015.06.011.

Wilhelmsen, Ø., Aasen, A., 2022. Choked liquid flow in nozzles: Crossover from heterogeneous to homogeneous cavitation and insensitivity to depressurization rate. Chem. Eng. Sci. 248, 117176. http://dx.doi.org/10.1016/j.ces.2021.117176.

Wilhelmsen, Ø., Aasen, A., Skaugen, G., Aursand, P., Austegard, A., Aursand, E., Gjennestad, M.A., Lund, H., Linga, G., Hammer, M., 2017. Thermodynamic modeling with equations of state: Present challenges with established methods. Ind. Eng. Chem. Res. 56 (13), 3503–3515. http://dx.doi.org/10.1021/acs.iecr.7b00317.

Yan, X., Guo, X., Yu, J., Chen, S., Zhang, Y., Mahgerefteh, H., Martynov, S., Brown, S., 2018. Flow characteristics and dispersion during the vertical anthropogenic venting of supercritical CO_2 from an industrial scale pipeline. In: Yan, J., Feitz, A., Li, X., Zhang, X. (Eds.), Applied Energy Symposium and Forum, Carbon Capture, Utilization and Storage. CCUS 2018, Perth, Australia, In: Energy Procedia, vol. 154, pp. 66–72. http://dx.doi.org/10.1016/j.egypro.2018.11.012.

Paper 3

Skarsvåg, Hans Langva; Hammer, Morten; Munkejord, Svend Tollak; **Log, Alexandra Metallinou**; Dumoulin, Stephane; Gruben, Gaute. (2023) Towards an engineering tool for the prediction of running ductile fractures in CO2 pipelines. *Process Safety and Environmental Protection (PSEP)*. vol 171.
doi:10.1016/j.psep.2023.01.054

Process Safety and Environmental Protection 171 (2023) 667–679

Contents lists available at ScienceDirect

Process Safety and Environmental Protection

journal homepage: www.journals.elsevier.com/process-safety-and-environmental-protection

Towards an engineering tool for the prediction of running ductile fractures in CO_2 pipelines

Hans Langva Skarsvåg [a], Morten Hammer [a], Svend Tollak Munkejord [a,*], Alexandra Metallinou Log [c], Stéphane Dumoulin [b], Gaute Gruben [b]

[a] SINTEF Energy Research, P.O. Box 4761 Torgarden, NO-7465 Trondheim, Norway
[b] SINTEF Industry, P.O. Box 4760 Torgarden, NO-7465 Trondheim, Norway
[c] Norwegian University of Science and Technology, Department of Energy and Process Engineering, NO-7491 Trondheim, Norway

ARTICLE INFO

Keywords:
CO_2 pipelines
Running ductile fracture
Carbon dioxide
Decompression
Non-equilibrium
Pipeline integrity

ABSTRACT

A prerequisite for the deployment of CO_2 capture and storage (CCS) is to establish a large network of high-pressure transport pipelines. It is then vital to assess new and existing pipeline designs for running ductile fracture (RDF). RDF is a phenomenon in which a defect develops into a crack propagating along the pipeline, sustained by the pressure forces from the escaping fluid. The most common engineering method for RDF, the Battelle two-curve method (BTCM), was originally developed for natural gas (NG) and has proved non-conservative for CO_2. In this work we examine the BTCM in the light of available RDF experiments with CO_2-rich mixtures. We present an improved material curve, in which the change in fluid properties when replacing NG with CO_2 results in a new effective toughness correlation. Furthermore, we present an improved method for calculating the crack-tip pressure. This delayed homogeneous equilibrium model (D-HEM) accounts for the non-equilibrium thermodynamics due to the rapid depressurization, resulting in boiling pressures below the saturation pressure. Together, the adaptation of the material and fluid treatment yields improved results, and is a step towards a viable engineering tool for the prediction of RDF in CO_2 pipelines.

1. Introduction

CO_2 capture and storage (CCS) is regarded as one of the technologies needed in order to mitigate climate change (Edenhofer et al., 2014). In the IEA (2021) scenario to reach net zero emissions by 2050, 7.6 gigatonnes of CO_2 are captured globally per year, out of which 95% is permanently stored. By mass, this is more than the global production of natural gas (NG), which was about 4000 billion standard cubic metres in 2020 (IEA, 2021), corresponding to about 2.8 gigatonnes.

Because capture plants and storage sites are in general not colocated, a large-scale CO_2-transportation system needs to be deployed, including pipelines and ships. Due to the sheer size of the system, optimized and safe design and operation will be crucial, taking the properties of CO_2 and CO_2-rich mixtures into account (Bilio et al., 2009; Zhao and Li, 2014; Martynov et al., 2014; Munkejord et al., 2016; d'Amore et al., 2018; Gu et al., 2018,2019; Vitali et al., 2022). The impurities present in CO_2 streams can roughly be divided into two categories, (i) 'non-condensable gases' such as N_2, Ar, H_2 and CH_4, which can be present in the range of percent, and which can therefore significantly affect the thermophysical properties (Munkejord et al., 2016), and (ii) potentially reactive impurities such as NOx and SOx, which must be limited to the ppmv range in order to avoid corrosion in carbon steel pipelines (Morland et al., 2022).

The deployment of CO_2 pipelines requires safety assessments, including, among other things, the dispersion of CO_2 in the terrain in the event of an accidental release. Such a release could be caused by equipment failure, corrosion, maintenance errors, external impacts and operator errors (Pham and Rusli, 2016). With the aim of estimating safety distances to CO_2 transportation pipelines, quantitative risk assessments (QRA) have been proposed (Teng et al., 2021).

In order to limit the consequences of a failure or rupture, pipelines transporting highly pressurized compressible fluids need to be designed to avoid running ductile fracture (RDF) for more than 1–2 pipe sections (DNV, 2012). RDF is a phenomenon whereby a defect in the pipeline, caused by e.g. corrosion or accidental loads, develops into a fracture running along the pipe, sustained by the pressure forces from the escaping fluid. The most commonly used design method to assess RDF, the Battelle two-curve method (BTCM) (Maxey, 1974) is semi-empirical and was developed for NG pipelines in the 1970s. It relies on the

* Corresponding author.
E-mail address: svend.t.munkejord@sintef.no (S.T. Munkejord).

https://doi.org/10.1016/j.psep.2023.01.054
Received 1 November 2022; Received in revised form 6 January 2023; Accepted 20 January 2023
Available online 24 January 2023

Nomenclature

Latin letters

A	Charpy specimen cross-section area ($m^{2)}$
a_c	Half-length of through-wall flaw (m)
c	Speed of sound (m/s)
C_{VN}	Charpy V-notch value (J)
E	Young's modulus (Pa)
G	Bubble work of formation (J)
h	Enthalpy (J/kg)
J	Nucleation rate ($1/(m^3\ s)$)
k_B	Boltzmann constant (J/K)
K	Kinetic prefactor ($1/(m^3\ s)$)
K_{BF}	Backfill parameter ($kg^2\ m^{0.5}$)
K_{mat}	Fracture resistance parameter (J^2/m^4)
m	Mass of one molecule (kg)
M_T	Folias factor (1)
$\tilde{N}$	Total number density ($1/m^3$)
P	Pressure (Pa)
R	Pipe outer radius (m)
r	Radius (m)
R_f	Fracture resistance parameter (1)
R_σ	Stress-ratio parameter (1)
T	Temperature (K)
t	Pipe wall thickness (m)
u	Fluid velocity (m/s)
V	Volume (m^3)
v	Velocity (m/s)
Y	Vapour molar fraction (mol/mol)

Greek letters

ε	Relative difference (%)
ρ	Mass density (kg/m^3)
$\overline{\sigma}$	Flow stress (Pa)
σ	Surface tension (N/m)

Subscripts

0	Initial
a	Arrest
bub	Bubble point
choke	Choke
C	Component
cr	Critical
ct	Crack tip
eq	Equilibrium
exp	Experiment
f	Fracture
ℓ	Liquid
sat	Saturation
tot	Total

Superscripts

*	Critically-sized
′	Integrated quantity
eff	Effective
W	Wilkowski

Abbreviations

BTCM	Battelle two-curve method
CCS	CO_2 Capture and storage
CFD	Computational fluid dynamics
CNT	Classical nucleation theory
D-HEM	Delayed homogeneous equilibrium model
EoS	Equation of state
FEM	Finite-element method
HEM	Homogeneous equilibrium model
NG	Natural gas
RDF	Running ductile fracture
SHL	Superheat limit
SI	International System of Units

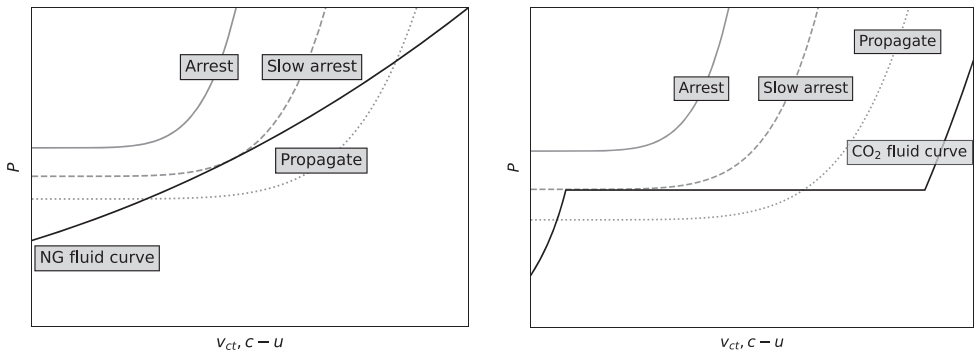

(a) BTCM for (dry) NG. (b) BTCM for CO_2.

Fig. 1. Illustration of the Battelle two-curve method (BTCM) for CO_2 and (dry) natural gas (NG) showing an example fluid curve and material curves that would result in propagating and arresting fractures, as well as the limiting case of slow arrest.

assumption that the crack-propagation speed in the steel and the decompression-wave speed in the fluid are independent. These quantities are drawn as a function of pressure level (hence the name, see Fig. 1) and the resulting method has had considerable practical impact. A major difference between CO_2 and NG during RDF is that for typical conditions, CO_2 boils while NG does not. Therefore, the fluid curve for CO_2 in Fig. 1a has a plateau as opposed to the curve for NG in Fig. 1b.

The BTCM gives a good indication of the arrest/propagation boundary for steel pipes with yield strength less than 450 MPa and Charpy V-notch values (C_{VN}) less than 100 J. However, most modern steels have C_{VN} values larger than 150 J, and it has been demonstrated that the original BTCM had to be modified to capture the arrest/

propagate boundary for such steels (Wilkowski et al., 1977; Leis et al., 1998). Recent studies have shown that these toughness-modified versions of the BTCM do not provide conservative results for CO_2 pipelines (Cosham et al., 2012,2014), presumably since they do not include enough relevant physics (Aursand et al., 2016a).

Maxey (1986) addressed the differences between NG pipelines and CO_2 pipelines with respect to RDF. He proposed that fracture arrest will occur if the CO_2 boiling pressure is lower than the pipe's 'arrest pressure' which is a function of pipe geometry and material properties. This approach is mentioned in ISO (2016) where a safety factor for the calculated arrest pressure is recommended for cases where C_{VN} is less than 330 J.

Michal et al. (2020) and DNVGL (2021) proposed a modification of the BTCM based on available full-scale fracture arrest tests for CO_2. It defines a region of likely propagation, a region of likely arrest, and a transition region between these two, where the boundary resides. In DNVGL (2021), a relatively large area is labelled 'evaluation based on assessments'. This indicates the scarcity of experiments for certain pipe configurations. In addition, for some conditions, an increase of the pipe-wall thickness could lead to a more strict evaluation.

Recently, efforts have been made to develop coupled fluid-structure models that can predict RDF in CO_2 pipelines (Aursand et al., 2016a; Nakai et al., 2016; Nordhagen et al., 2017; Gruben et al., 2019; Talemi et al., 2019; Keim et al., 2019,2020). While there is good reason to believe that such models can incorporate more physics and therefore help providing better predictions, they remain highly specialized tools requiring long computational times.

For practical engineering purposes, therefore, there is a need to develop a tool of similar ease of use as the Battelle two-curve method, and with increased predictive capability for CO_2 pipelines. Our hypothesis is that this is possible, by drawing more appropriate fluid and material curves. Furthermore, it should be possible to do this by taking more of the governing physics into account, rather than using purely empirical correlations. Thus, the aim of the current work is to improve both the material and fluid curves.

(i) Material curve: The original Battelle two-curve method was developed for NG, assuming that the crack-tip pressure alone sufficiently describes the forces acting on the pipe. However, for liquid or dense-phase operating conditions, CO_2 will boil during depressurization, leading to a different pressure distribution, especially behind the crack-tip on the flaps, see e.g. Aursand et al. (2016a). It is likely that this would lead to a different functional form of the material curve.

(ii) Fluid curve: When employing the BTCM for CO_2 pipelines, it is customary to assume that the crack-tip pressure is equal to the gas-liquid equilibrium pressure calculated by an isentropic expansion from the operational state (Cosham et al., 2012; Gu et al., 2018). However, the importance of considering non-equilibrium for CO_2 expansion was emphasized by Benintendi (2014). Lopes et al. (2018) presented an outflow model taking non-equilibrium into account, but did not discuss the resulting pressure level. It has been experimentally observed during crack-propagation tests that the pressure is lower than that predicted assuming equilibrium (Cosham et al., 2012; Michal et al., 2020). It is reasonable to assume that thermodynamic equilibrium does not have time to establish itself during the few milliseconds the depressurization process lasts, and this will affect the observed pressure levels (Flechas et al., 2020). Furthermore, the degree of pressure 'undershoot' with respect to the equilibrium value is dependent on the initial state, see Munkejord et al. (2020). It should also be noted that an accurate equation of state (EoS) is of primary importance in order to obtain an accurate fluid curve. See, e.g., the discussion of the effect of density and speed of sound in Munkejord et al. (2021).

In the present work, we investigate both of the above topics. First, we modify the material curve by changing the arrest-pressure functional form. Next, we modify the fluid curve by employing the recent 'delayed homogeneous equilibrium model' (D-HEM) (Hammer et al., 2022) taking non-equilibrium into account. While the resulting model is not intended to be the 'final' answer, and further work is needed, we show that the present approach holds significant promise, by comparing with experimental data (Cosham et al., 2016) and obtaining significantly better match than with the original two-curve method. Finally, the present approach is relatively easy to implement as an engineering tool that can be used by pipeline engineers – not requiring specialists within finite-element methods (FEM) or computational fluid dynamics (CFD) in order to provide predictions.

The rest of this paper is organized as follows. Section 2 introduces and briefly discusses the BTCM. In Section 3, we present a modified two-curve method and evaluate it using full-scale fracture propagation test data. Section 4 concludes the work.

2. The Battelle two-curve method

This section briefly discusses the Battelle two-curve method (BTCM) in the context of CO_2 pipelines. The acceleration or deceleration of a running ductile fracture (RDF) is dependent on the balance between energy dissipation and the work done by high-pressure fluid that is exposed as the crack propagates. The driving force, determined by the pressure profile in the vicinity of the crack tip, will be lowered if the decompression-wave speed is faster than the crack-tip velocity. In the opposite case, if the crack-tip velocity is faster than the decompression-wave speed, the pressure-determined driving force will increase. Steady-state propagation occurs when these two velocities are equal, see Fig. 1. If the crack-tip velocity as a function of the crack-tip pressure, $v_{ct}(P_{ct})$ (material curve), and the decompression-wave speed as a function of fluid properties (fluid curve) are known, one can analyse the evolution from fracture initiation. The fluid and material curves are the *two curves* of the BTCM. An intersection of these two curves indicates that a steady state will form provided that the initial fluid pressure inside the pipe is higher than the pressure at the intersection. Fig. 1b illustrates the BTCM for three scenarios, (i) arrest, (ii) slow arrest, (iii) propagate, with a fluid curve resembling that of (dry) NG. In the following, we will present the fluid curve for CO_2 and the material curve as illustrated in Fig. 1a, and how the latter can be influenced by the fluid dynamics.

2.1. Material curve

The material curve correlates the fluid pressure at the crack tip to the crack-tip velocity, $P_{ct}(v_{ct})$. From full-scale fracture-propagation tests with NG, this relation has empirically been found to be (Maxey, 1974)

$$P_{ct} = P_a\left[1 + \left(v_{ct}\frac{\sqrt{C_{VN}/A}}{K_{BF}\bar{\sigma}}\right)^6\right], \tag{1}$$

where C_{VN}/A is the Charpy V-notch value divided by the Charpy specimen cross-section, K_{BF} is a parameter that accounts for the backfill, and the flow stress, $\bar{\sigma}$, is found from the yield stress, σ_{ys}, as $\bar{\sigma} \equiv \sigma_{ys} + 68.95$ MPa. The arrest pressure, P_a, is the threshold pressure, below which a crack will not propagate. According to the strip-yield model (Kiefner et al., 1973) it is

$$P_a = \frac{2\bar{\sigma}t}{M_T \pi R}\arccos\left[\exp\left(-\frac{K_{mat}^2\pi}{8a_c\bar{\sigma}^2}\right)\right]. \tag{2}$$

Here t, is the pipe thickness, R is the radius and $M_T(a_c/\sqrt{Rt})$ is the Folias function which accounts for stress amplification at the crack tip in pressurized pipes, resulting from the outward radial deflection along the crack (Folias, 1970):

$$M_T = \left(1 + 1.255\frac{a_c^2}{Rt} - 0.0135\frac{a_c^4}{R^2t^2}\right)^{1/2}, \tag{3}$$

where a_c is the half-length of the through-wall flaw. For a propagating crack, a_c must be replaced by an effective value empirically found to be

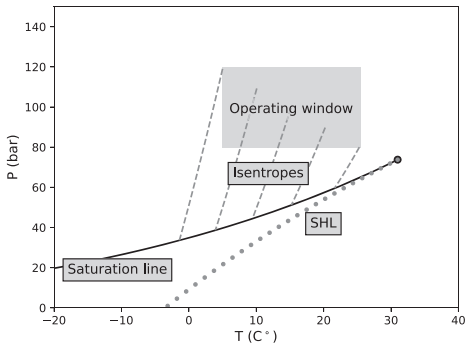

Fig. 2. Illustration of typical operating window and decompression paths (isentropes) in a temperature–pressure phase diagram.

$a_c^{\text{eff}} = 3\sqrt{Rt}$, which then yields $M_T \approx 3.33$. The material toughness parameter K_{mat} is a material dependent parameter related to the material's resistance to fracture (Maxey et al., 1972).

The material toughness is usually inferred from small-scale tests. It has been found that there is a 1:1 relation between the Charpy V-notch value and the material toughness squared

$$K_{\text{mat}}^2 = E\frac{C_{VN}}{A}, \tag{4}$$

where E is the Young's modulus of the material. This relation has been developed by correlating full-scale burst data to small-scale experiments (Maxey et al., 1972).

A capability to acquire the relevant material parameters to a sufficient accuracy, without the need for full-scale tests, is essential for the usefulness of the BTCM. Since the BTCM was developed for NG pipelines, the correlations and effective parameters have been verified by and correlated from NG pipeline experiments. The material curve is set up to correlate the pressure at the crack tip to the crack-tip velocity. Because the fluid properties influence the pressure and hence force distribution, it appears reasonable that they have an impact on this correlation. That is, it is unlikely that two identical pipes carrying NG and CO_2 will have the same steady-state crack-tip velocity, v_{ct}, at the same crack-tip pressure, P_{ct} (P_{ct} can in theory be adjusted by tuning the initial pressure and temperature). A more sophisticated model could include calculations of the pressure profile, and correlate the velocity to the pressure decay function. Because of the simplicity required to make a useful engineering tool, we here keep the method of pressure-point-value correlation of the original BTCM. The effect of a changed pressure profile due to different fluid properties when replacing NG with CO_2 must therefore be captured by other parameters, such as the toughness correlation given by Eq. (4) or a_c^{eff}.

2.2. Fluid curve for CO_2

The typical operating pressure of a CO_2 pipeline is well above the critical pressure ($P_{\text{cr}} = 73.8$ bar). The CO_2 is thus in a liquid-like state. Rapid decompression is close to isentropic, and follows the isentrope into the two-phase region, where CO_2 starts boiling. Fig. 2 illustrates decompression curves originating in a typical pipeline operating window and hitting the gas-liquid two-phase saturation line (for pure CO_2). One can observe that, perhaps counter-intuitively, a higher operating pressure leads to a lower saturation pressure upon decompression.

The phase change observed for CO_2 is in contrast to the case for dry NG, which follows the relevant isentrope through the gas region. The liquid-to-gas phase change is associated with significant volume increase and a larger amount of available work. This can be demonstrated by calculating the pressure (force) and available work ($\int pdV$) along two isentropes for CO_2 and pure methane. In Fig. 3 this has been done for the isentropes that correspond to a crack-tip pressure of $P_{\text{ct}} = 70$ bar. The qualitative picture does not change by changing the reference pressure, and 70 bar is chosen because it is close to the worst-case scenario where P_{ct} is at critical pressure of CO_2. By plotting pressure as a function of the change in relative volume, we get an indication of how the pressure is reduced behind the crack tip, see Fig. 3a. For methane, a 50% reduction in pressure occurs at 65% volume increase, while for CO_2, the same pressure reduction occurs at approximately three times that volume increase (180%). This results in a significantly larger available work for CO_2, e.g., 60% larger available work for a 300% volume increase, see Fig. 3b. The estimated pressure decay is also in line with full-scale experimental results for NG (Ives et al., 1974) and CO_2 (Aursand et al., 2016a).

The decompression-wave speed, $c - u$, is determined by the speed of sound of the rarefaction wave, c, relative to the flow velocity, u. This speed is found by analysis of the Euler equations, assuming one-dimensional isentropic quasi-steady flow. The result is

$$c(P) - \left|\mathbf{u}(P)\right| = c(P) - \int_P^{P_0} \frac{dP'}{\rho(P')c(P')}, \tag{5}$$

where ρ is the fluid density and P_0 is the initial pressure. When deriving the above expression, full thermodynamic equilibrium is assumed, i.e., for a two-phase state, the phases have the same pressure, temperature and chemical potential. This assumption leads to a discontinuous speed of sound at the phase boundary, see Linga and Flåtten (2019), and

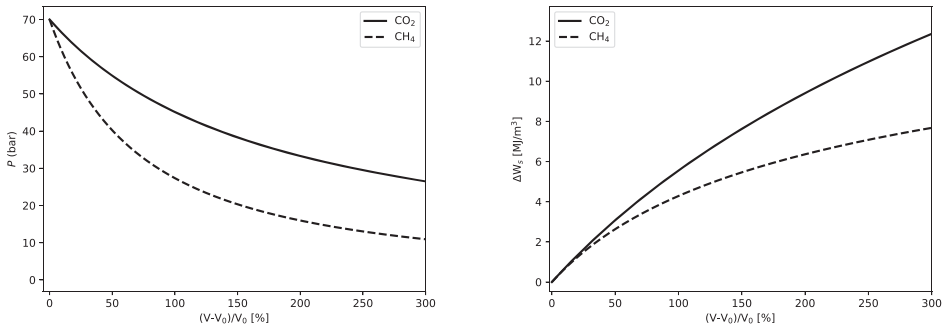

(a) Pressure along isentropes vs relative volume change. (b) Available work along isentropes vs relative volume change.

Fig. 3. A comparison of the pressure and available work for methane and pure CO_2 along the isentropes corresponding to a crack-tip pressure of 70 bar. The volume is normalized by the initial volume, V_0.

Table 1
Initial temperature (T_0) and pressure (P_0), and crack-tip pressure (P_{ct}) interpreted by Michal et al. (2020), for various fracture-propagation tests, and plateau pressure calculated using the HEM and D-HEM models, along with the deviation (ε) from the experimental value.

Test	T_0 (°C)	P_0 (bar)	P_{ct} (bar)	P_{HEM} (bar)	ε (%)	$P_{D\text{-}HEM}$ (bar)	ε (%)
CO2PIPETRANS 1 (Aursand et al., 2016a)	30.0	89.5	54	63.7	18	61.6	14
CO2PIPETRANS 2 (Aursand et al., 2016a)	8.6	92.5	26	38.5	48	12.1*	53*
COOLTRANS-1 (Cosham et al., 2016,2014)	13.1	150.3	73.5	81.0	10	77.1	5
COOLTRANS-2 (Cosham et al., 2016,2014)	10.5	152.6	66.4	74.8	13	66.8	1
COOLTRANS-3 (Cosham et al., 2016)	15.0	152.2	82	90.0	10	88.0	7
SARCO2-B (Di Biagio et al., 2017)	17.8	128.0	68	73	7	70.0	3
CO2SAFE-ARREST 1 (Michal et al., 2018,2020)	11.6	151.4	65	79.5	22	76.1	17
CO2SAFE-ARREST 2 (Michal et al., 2020)	12.8	149.7	74.5	84.9	14	83.0	11

*T, P lower than the range of validity of D-HEM.

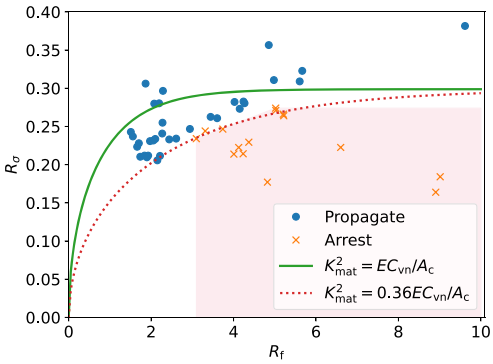

Fig. 4. Experimental data on CO_2 RDF and arrest curves. The arrest curve in Eq. (2) with both the conventional toughness correlation (green) and adapted correlation (red dashed) is included. The shaded pink region denotes expected arrest according to Eq. (6).

further, to a jump in the decompression-wave speed as a function of pressure. This has significant implications for the BTCM, since it creates a plateau in the fluid curve in the region where one would expect intersection of the two curves. Typically the plateau pressure will be in the range from 40 bar up to the maximum two-phase pressure, which can be more than 80 bar for CO_2-rich mixtures, see Section 3.2.

When the decompression process is rapid, the nucleation of vapour bubbles is too slow to keep the fluid in thermodynamic equilibrium. In crack-propagation experiments, the plateau pressure has therefore been observed to be lower than the saturation pressure (Cosham et al., 2012; Michal et al., 2020). Munkejord et al. (2020) observed that for tube-depressurization experiments, the experimentally recorded plateau pressure lay between that calculated assuming equilibrium and that calculated with no phase transfer. Analysis with the crack-tip pressure as input therefore requires a non-equilibrium thermodynamic model for the estimation of the pressure. One such model is presented in Sec. 3.2.

3. Improved model for predicting running ductile fractures in CO_2 transportation pipelines

This section describes an approach to obtain improved RDF predictions for CO_2 pipelines using the BTCM framework. We first consider the material curve, next the fluid curve, and then we illustrate the performance of the model by applying it to experimental data from COOLTRANS Tests 1 and 2.

3.1. Crack-tip propagation model adapted to running ductile fracture experimental results

Several experiments on RDF in CO_2 pipelines have been conducted (Aursand et al., 2016a; Cosham et al., 2014; Michal et al., 2018; Cosham et al., 2016; Di Biagio et al., 2017), see Table 1. The data from these experiments have been extracted and listed by Michal et al. (2020). Based on these data, Michal et al. mapped values of the arrest-curve parameters to the regions of expected arrest

$$\begin{aligned} R_f &\geq 3.1, \\ R_\sigma &\leq 0.0208R_f + 0.1696, \\ R_\sigma &\leq 0.2739. \end{aligned} \tag{6}$$

Herein,

$$R_f = \frac{\pi C_{VN} E}{24 A \bar{\sigma}^2 \sqrt{Rt}} \tag{7}$$

is the fracture resistance parameter, and

$$R_\sigma = \frac{P_{ct} R}{t\bar{\sigma}} \tag{8}$$

is the stress-ratio parameter. Note that there is an additional factor 1000 appearing in R_f in Michal et al. (2020) because the units MPa and mm are used instead of SI units, and slightly different coefficients since they employed gauge pressure (MPag). The sparse experimental data makes the region of uncertain propagate/arrest quite large.

We now revisit the crack-arrest parameters appearing in Eq. (2). We hypothesize that because of the difference in forces acting at the crack tip when NG is replaced by CO_2, parameters such as the effective crack length, a_c^{eff}, flow stress or material toughness parameter should be scaled. The steel properties themselves are not altered, but the apparent properties appearing in the simplified correlation in Eq. (2) could be different due to the different fluid-structure interaction when NG has been replaced by CO_2. Using the toughness parameter K_{mat} in the tuning is the simplest way of getting a good fit to the data. Inserting

$$K^2_{mat,eff} = 0.36EC_{VN}/A \tag{9}$$

in Eq. (2) gives a reasonable fit. The result is shown in Fig. 4, where we have also shaded the safe region defined by Eq. (6). We believe that this new curve can be a useful step in adapting the BTCM to CO_2. This also emphasizes the need for more experiments, both in the flow-stress-dependent region (high R_f), where the curve reaches a plateau, and far into the toughness-dependent region ($R_f < 3$). In both of these regions the lack of data imply a large degree of uncertainty (Michal et al., 2018). In these regions, the material curve, Eq. (2), will be correct only to the extent that the relevant physics are captured.

Cosham et al. (2022) recently modified the material curve by tuning the empirical relation between the effective crack length, a_c^{eff}, and $\sqrt{Rt}$. It should be noted that employing the toughness parameter, K_{mat}, is different, because a_c^{eff} also appears implicitly in the prefactor of the arccos function in Eq. (1) through the Folias factor in Eq. (3). We found that Eq. (9) gave the best result, reducing the need for conservatism.

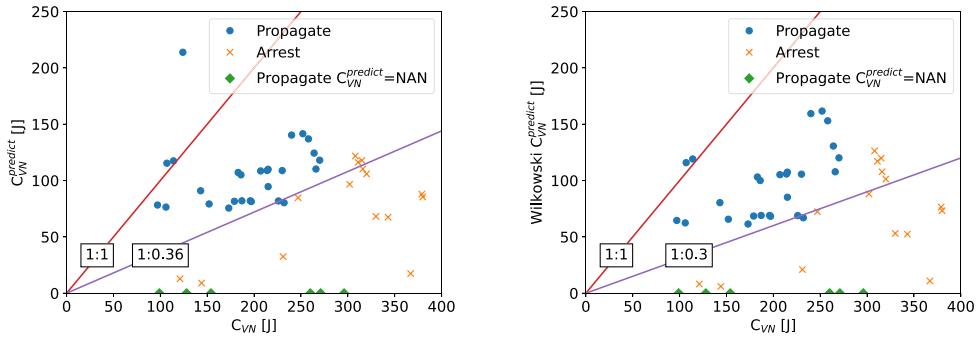

(a) Actual and predicted C_{VN}

(b) Actual and predicted C_{VN} with Wilkowski correction.

Fig. 5. Actual versus predicted Charpy V-notch values with and without the Wilkowski correction predicted by the BTCM. C_{VN} NAN indicates that the crack will propagate for arbitrarily high C_{VN}.

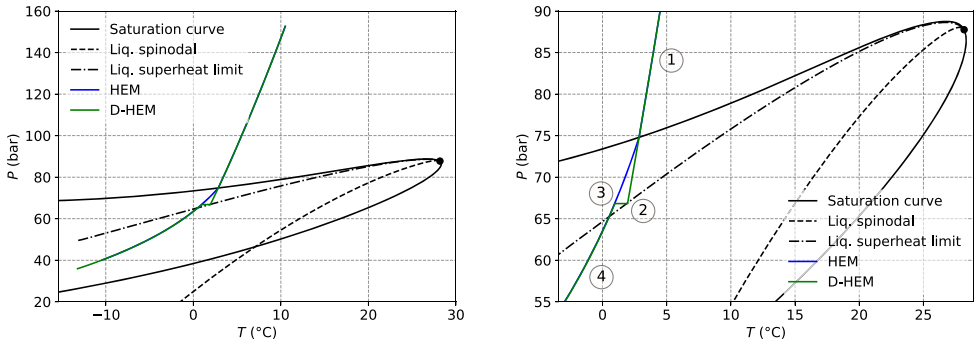

(a) Overview.

(b) The steps in the D-HEM calculation (zoom-in).

Fig. 6. Fluid phase diagram for COOLTRANS Test 2 (Cosham et al., 2016) with decompression path calculated using HEM and D-HEM.

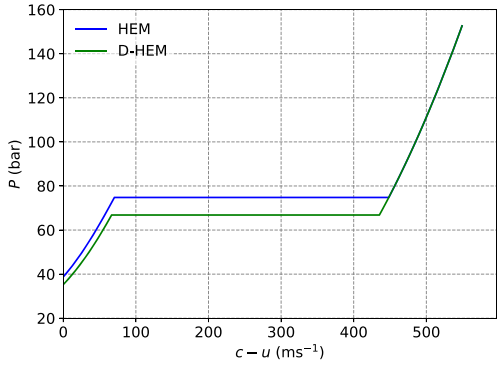

Fig. 7. Fluid decompression curves in the BTCM method for COOLTRANS Test 2 (Cosham et al., 2016) calculated using HEM and D-HEM.

Some interesting observations can be made from this adaptation of the BTCM. Firstly, the toughness-dependent region, where the arrest behaviour depends on C_{VN}, becomes much larger (dashed red curve in the figure) as it is a straight vertical line ($R_f = 3.1$) in the approach suggested by Michal et al. (2020) . The implication for design is that an increase in steel toughness still pays off for relatively high-toughness steel. Secondly, a reasonably good fit could be made without special treatment of high-toughness steels such as the Wilkowski correction of the C_{VN} used for NG-carrying pipelines (Wilkowski et al., 2000):

$$C_{VN}^{W} = 0.043(0.102C_{VN} + 10.29)^{2.597} - 16.81 \text{ for B to X70 steel.} \quad (10)$$

This becomes even more apparent when plotting the actual C_{VN} versus the C_{VN} predicted from Eq. (2), see Fig. 5. Here, Eq. (2) has been solved for C_{VN} employing the standard toughness correlation in Eq. (4). One possible cause for this behaviour could be the fluid-pressure profile for CO_2, with a larger high-pressure region than for NG. It is also interesting to note that when the original BTCM was developed, only low-toughness steels ($C_{VN} \lesssim 100$ J) were used. When tougher steel types became available, moving the fracture dynamics into the flow-stress dominated

Table 2
CO_2 mixture composition (mole%) in fracture-propagation tests.

Test	CO_2	N_2	H_2	O_2	CH_4
CO2PIPETRANS 1	100.0	–	–	–	–
CO2PIPETRANS 2	100.0	–	–	–	–
COOLTRANS-1	90.9	4.0	1.0	1.8	2.2
COOLTRANS-2	93.7	3.4	1.1	1.8	–
COOLTRANS-3	90.3	6.6	1.1	2.0	–
SARCO2-B	94.0	6.0	–	–	–
CO2SAFE-ARREST 1	91.1	8.9	–	–	–
CO2SAFE-ARREST 2	89.8	10.2	–	–	–

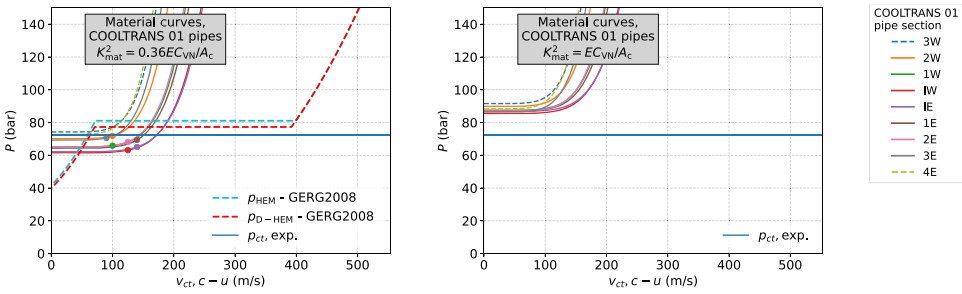

(a) With modified toughness correlation and decompression curves.

(b) With original toughness correlation.

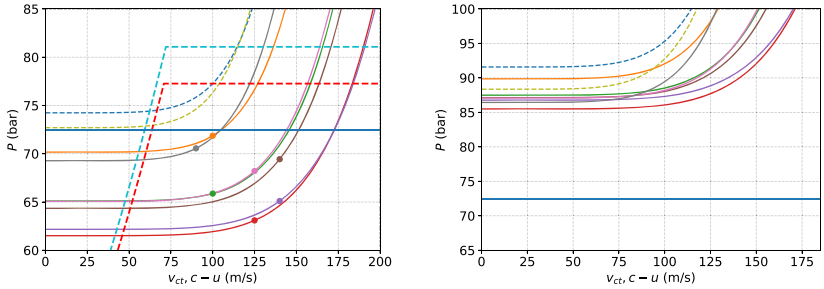

(c) With modified toughness correlation and decompression curves (zoom-in).

(d) With original toughness correlation (zoom-in).

Fig. 8. Two-curve plots for COOLTRANS Test 1 with and without updated toughness correlation. For the dashed material curves, arrest was observed experimentally. Fluid decompression curves for HEM and D-HEM are included in addition to the crack-tip pressure inferred from the experiment (Michal et al., 2020).

regime, corrections had to made, such as the one by Wilkowski et al. (2000). For CO_2 it seems that the toughness-dominated regime is increased, and at the same time there is less need for a C_{VN}-dependent correction factor. That is, corrections such as the Wilkowski correction do not improve the results here.

3.2. Fluid decompression model taking non-equilibrium into account

Usually the calculation of the fluid decompression-wave speed in BTCM is conducted using the homogeneous equilibrium model (HEM). In HEM it is assumed that the phases, usually liquid (ℓ) and vapour (v), are in mechanical, chemical and thermal equilibrium. These assumptions lead to the pressure plateau in the fluid curve forming at the pressure where the liquid isentrope intersects the two-phase saturation curve, P_{sat}. However, full-scale RDF experiments (Aursand et al., 2016a; Cosham et al., 2014; Michal et al., 2018; Cosham et al., 2016; Di Biagio et al., 2017) suggest that the observed pressure is generally lower than the saturation pressure. In addition, it has been observed that the pressure plateau is not really a plateau, but rather a slope. This is due to friction, heat transfer, pressure recovery due to phase transition, and possibly other factors, see Munkejord et al. (2020, Fig. 10). In the following, we will disregard the slope and concentrate on the pressure level.

3.2.1. Delayed nucleation

There are many complex phenomena in the fluid flow that may contribute to the reduced pressure level during RDF. However, obtaining a pressure-undershoot below the saturation pressure is a well-known phenomenon also for 'normal' full-bore pipe depressurizations, both for CO_2 and other fluids (Munkejord et al., 2020, 2021; Botros et al., 2016; Bartak, 1990; Borkar et al., 1977; Lienhard et al., 1978). This phenomenon is generally understood to be caused by delayed phase change, which is a non-equilibrium effect. The creation of gas bubbles requires energy, and the decompression is too fast for the energy to be supplied by the fluid's surroundings. Therefore, the phase change is delayed until the liquid has enough energy within itself to create bubbles through random thermal fluctuations (Debenedetti, 1997). This process is called nucleation. Before nucleation starts, the liquid is at a temperature above its boiling-point temperature and its state is denoted as 'superheated'.

The experimentally attainable limit of superheat, the largest superheat possible before phase change is observed, can be estimated using classical nucleation theory (CNT). CNT describes the homogeneous nucleation, which dominates at high temperatures. In contrast, heterogeneous nucleation occurs on a surface or impurity which lowers the energy barrier of bubble formation, and it therefore dominates at lower temperatures. Aursand et al. (2016b) found good agreement with experiments of the superheat limit (SHL) for pure CO_2 and the SHL obtained using CNT. Wilhelmsen and Aasen (2022) applied the SHL found using CNT to estimate choked CO_2 and water flows through nozzles by accounting for delayed phase change in the high-temperature range. It was found that heterogeneous nucleation started to dominate at a temperature of approximately 12°C at the SHL for CO_2. The transition from one mode of nucleation to the other was observed to be gradual and the homogeneous nucleation model is therefore also expected to give reasonable results somewhat below $T = 12$°C. However, for a complete model description down to the triple point, a heterogeneous nucleation model is required, and this is left to future work.

3.2.2. Delayed homogeneous equilibrium model

Most models that account for delayed phase change require a full computational fluid dynamics (CFD) simulation. A simplified delayed

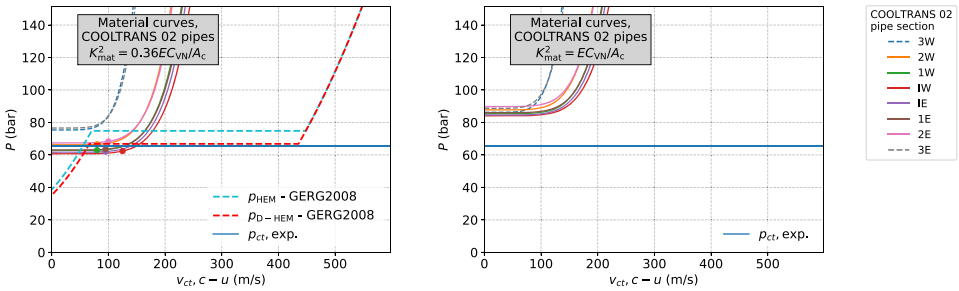

(a) With modified toughness correlation and decompression curves.

(b) With original toughness correlation.

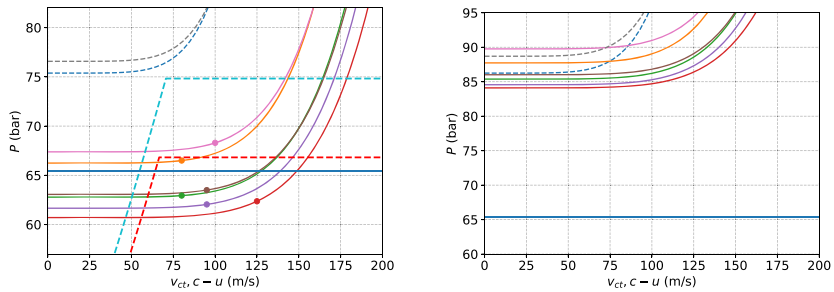

(c) With modified toughness correlation and decompression curves (zoom-in).

(d) With original toughness correlation (zoom-in).

Fig. 9. Two-curve plots for COOLTRANS Test 2 with and without updated toughness correlation. For the dashed material curves, arrest was observed experimentally. Fluid decompression curves for HEM and D-HEM are included in addition to the crack-tip pressure inferred from the experiment (Michal et al., 2020).

Table A.1
Comparison of the mixture surface tension measured experimentally (Schenk et al., 2020) and estimated by the REFPROP parachor method (Huber et al., 2022) for a CO_2-CH_4 mixture.

T (°C)	P (bar)	σ_{exp} (mN/m)	$\sigma_{REFPROP}$ (mN/m)	ε (%)	Within exp. uncertainty?
− 50	30	8.7 ± 1.0	9.5	9.2	yes
− 50	39	6.0 ± 0.4	7.2	20.0	no
− 50	55	3.0 ± 0.7	2.8	– 6.7	yes
− 40	30	9.4 ± 1.1	8.5	– 9.6	yes
− 40	41	6.1 ± 0.7	6.2	1.6	yes
− 40	50	4.6 ± 0.5	4.3	– 6.5	yes
− 40	51	3.6 ± 0.1	4.1	13.9	no

homogeneous equilibrium model, D-HEM, avoiding detailed spatial and temporal resolution, was developed by Hammer et al. (2022). They applied D-HEM to pure CO_2 and steady-state flow in nozzles and orifices. In the present work, the D-HEM formalism has been applied to the rarefaction wave of the decompressing pipeline, and it has also been extended to fluid mixtures. The main difference between the pure fluid and mixture model lies in how the SHL is calculated, and this is detailed in Appendix B.1. In addition, Appendix B.2 quantifies the SHL sensitivity to two main parameters, namely, the critical nucleation rate and the surface tension.

It should be noted that CNT applied to mixtures is less accurate than when applied to pure fluids, especially for strongly interacting molecules (Aasen et al., 2020). However, because the CO_2 mixtures considered in this work consist of relatively simple molecules without strong interactions, without self or cross association, we expect CNT to give reasonable results.

Figs. 6 and 7 illustrate the fluid behaviour calculated using HEM and D-HEM for COOLTRANS Test 2. In Fig. 6 we have plotted the phase diagram of the CO_2 mixture (see Table 2) including the saturation curve, the liquid SHL and the liquid limit of stability, also called the spinodal. The decompression paths calculated using HEM and D-HEM are the same, except at the important stage between the saturation curve and the SHL. This is highlighted in Fig. 6b, showing the effect of the different steps of the D-HEM calculation. Fig. 7 shows the pressure level plotted as a function of decompression-wave speed, to be employed in the BTCM. We observe that in this case, D-HEM yielded a plateau pressure 8 bar lower than HEM.

The following steps are taken when calculating the fluid decompression curve using D-HEM. The numbers refer to the process steps indicated in Fig. 6b.

1. Beginning at the initial pressure of the pipe, integrate towards lower pressures using Eq. (5) with single-phase liquid properties at constant entropy.
2. Instead of assuming that nucleation begins at the pressure where the liquid isentrope crosses the bubble line, continue calculating the integral along the liquid isentrope until P_{SHL} is reached, i.e., where the isentrope crosses the liquid SHL. This accounts for the delayed nucleation of bubbles.
3. At the SHL, assume that all phase transfer occurs instantaneously from the SHL point to a two-phase equilibrium state denoted with the subscript eq. It is assumed that the phase change is isenthalpic and isobaric, and the fluid velocity stays constant, such that

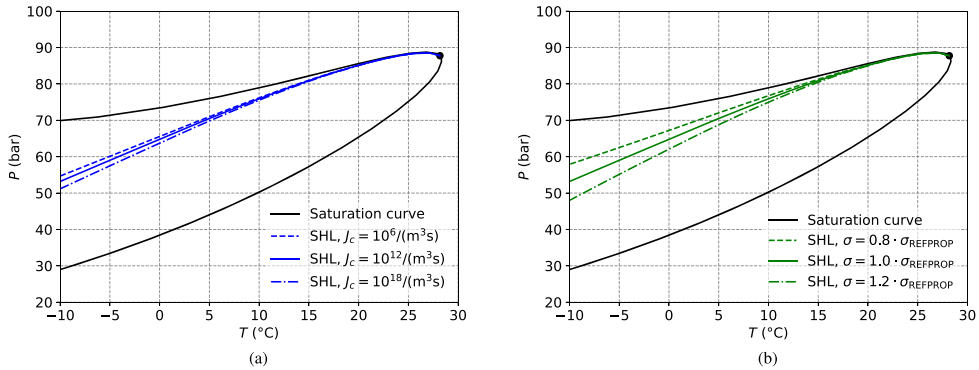

Fig. B.1. The effect on the estimated superheat limit (SHL) when varying the critical nucleation rate J_{cr} (a) and the surface tension σ (b). The critical point is marked as a black dot.

Table B.1
Sensitivity of the superheat-limit pressure, P_{SHL}, in the D-HEM approach for the different CO_2-mixture RDF tests for different choices of critical nucleation rate, J_{cr}. The crack-tip pressure, P_{ct}, evaluated by Michal et al. (2020) is also provided for reference.

Test	P_{SHL} (bar)				P_{ct} (bar)
	$J_{cr} = 10^6/(m^3s)$	$J_{cr} = 10^{12}/(m^3s)$	$J_{cr} = 10^{18}/(m^3s)$	$J_{cr} = 10^{24}/(m^3s)$	
COOLTRANS-1	77.5	77.1	76.6	75.7	73.5
COOLTRANS-2	67.6	66.8	65.7	63.8	66.4
COOLTRANS-3	88.2	88.0	87.7	87.2	82
SARCO2-B	70.4	70.0	69.6	66.9	68
CO2SAFE-ARREST 1	76.4	76.1	75.6	74.8	65
CO2SAFE-ARREST 2	83.2	83.0	82.7	82.3	74.5

Table B.2
Sensitivity of the superheat-limit pressure, P_{SHL}, in the D-HEM approach for the different CO_2-mixture RDF tests due to a ± 20% variation in the surface tension estimate. The crack-tip pressure, P_{ct}, evaluated by Michal et al. (2020) is also provided for reference.

Test	P_{SHL} (bar)			P_{ct} (bar)
	$\sigma = 0.8 \cdot \sigma_{REFPROP}$	$\sigma = \sigma_{REFPROP}$	$\sigma = 1.2 \cdot \sigma_{REFPROP}$	
COOLTRANS-1	78.3	77.1	75.8	73.5
COOLTRANS-2	69.2	66.8	64.0	66.4
COOLTRANS-3	88.6	88.0	87.3	82
SARCO2-B	71.0	70.0	69.0	68
CO2SAFE-ARREST 1	77.1	76.1	74.9	65
CO2SAFE-ARREST 2	83.6	83.0	82.4	74.5

$$P_{SHL} = P_{eq}, \quad h_{SHL} = h_{eq}, \quad u_{SHL} = u_{eq}. \tag{11}$$

With these assumptions, the instantaneous phase change provides a slight entropy production. This means that the model is in agreement with the second law of thermodynamics.

4. Continue calculating the fluid curve properties using Eq. (5) with HEM from P_{eq} until the choke pressure, P_{choke}, is reached when $c - u = 0$.

For the calculation of thermophysical properties, we employ our in-house framework (Wilhelmsen et al., 2017; Hammer et al.) using the GERG2008 EoS (Kunz and Wagner, 2012). The development of the GERG-2008 EoS was purely based on experimental measurements of stable thermodynamic states. In addition, the EoS exhibits an additional unphysical Maxwell-loop in the unstable area. The accuracy in the metastable liquid region and the accuracy in predicting the spinodal curve is therefore unknown. Alternative EoSs based on statistical thermodynamics are expected to be more physically correct in the metastable region. However, the density and speed-of-sound prediction of the GERG-2008 EoS are far superior in the stable domain compared to alternative EoSs, and they are therefore used in this work. How far the better predictions will extend into the metastable region is unknown, but the use of a highly accurate EoS ensures that most of the deviation in the calculation of the thermodynamic properties will stem from the D-HEM approach. In the present work, the mixture surface tension is predicted using the parachor method applied in REFPROPv10 (Huber et al., 2022). The accuracy of the the parachor method is discussed in Appendix A.

In Table 1, we compare plateau pressures calculated using HEM and D-HEM with the crack-tip pressure evaluated by Michal et al. (2020) for several relevant full-scale RDF experiments. For reference, the CO_2 mixture compositions are given in Table 2. It can be seen that the deviation between the experiments and calculations are significantly reduced for all experiments when employing D-HEM instead of HEM. One exception is CO2PIPETRANS Test 2. This result is expected, because the isentrope crosses the SHL at a temperature about 11°C below the point where heterogeneous nucleation begins to dominate. As the SHL only accounts for homogeneous nucleation, D-HEM cannot provide a good estimate of the plateau pressure for this test. Furthermore, the pipes used in the CO2PIPETRANS tests were short, which could mean the propagating crack had not reached a steady state by the time the relevant sensor was reached. This is particularly true for Test 2, in which the fracture arrested after roughly 1 m.

3.3. Evaluation of the modified two-curve method applied to COOLTRANS Tests 1 and 2

We now evaluate our modified two-curve method by studying COOLTRANS Tests 1 and 2 (Cosham et al., 2016) in more detail. These tests are chosen because they both produced several data points and the crack-tip pressure was high enough to make D-HEM applicable. In COOLTRANS Test 1, the fracture propagated from initiation at the centre of the pipe length, through three sections on the east side and four sections on the west side. The crack arrested in the last of these sections. With the initiation segments this gives a total of nine data points with

the same initial conditions (see Table 1) for the same fluid mixture (see Table 2). COOLTRANS Test 2 similarly gave eight data points, with a different fluid mixture and initial condition. In Fig. 8 and Fig. 9 we have plotted the crack-tip pressure, P_{ct}, from Eq. (1) with $K_{BF} = 0.6 \times 10^{-3}\mathrm{m}^2\mathrm{kg}^{-0.5}$, for Test 1 and 2, respectively. Figs. 8a and 9a show the result with the modified toughness correlation Eq. (9), and Figs. 8b and 9b shows the results with the original correlation Eq. (4).

In the zoomed-in Figs. 8c and 9c we also see the improved splitting of arrest and propagate data by our proposed method. The two propagate curves in Test 2 that do not intersect with the P_{ct} curve (2E and 2W) are the same propagate points that appear on the wrong side of the arrest correlation in Figs. 4 and 5. The dots on the velocity curves are the observed velocities. Ideally, the velocities should have appeared at the intersection with P_{ct}. This is sensitive to uncertainties, both on the modelling side and the experimental side. E.g., a shift in P_{ct} of just a few bars can move the point of intersection 10–100 m/s. Here we have simply used the P_{ct} extracted by Michal et al. (2020), see Table 1.

From Figs. 8b and 9b, we see that the original BTCM would predict 'arrest' in all pipe sections. The modified method in Figs. 8a and 9a comes much closer to correctly separating 'arrest' from 'propagate'. Regarding the fluid curves (green (HEM), cyan (D-HEM), blue (experiment)), we observe that HEM yielded a plateau pressure about 8 bar above the experimentally observed crack-tip pressure for both tests. We also observe that D-HEM yielded a lower value; 4 bar above the experimental value for Test 1 and 0.5 bar above the experimental value for Test 2. Given the uncertainties, we regard both results as very good.

Finally, we note that the results are highly sensitive to the crack-tip pressure. This means, e.g., that a small change in crack-tip pressure could move the crack arrest to a different pipe section.

4. Conclusion

The deployment of CCS as a climate change mitigation technology relies on establishing a massive CO_2 transportation system by the mid century, capable of transporting several gigatonnes per year. A large fraction of this CO_2 is expected to be transported in high-pressure pipelines. For the reuse of existing pipelines, or the design of new pipelines, it is vital to assess the design with respect to running ductile fracture.

For fluids such as natural gas, the Battelle two-curve method is the most commonly used engineering method for such assessments. In that method, the fracture-propagation speed in the steel and the decompression-wave speed in the fluid are drawn as a function of pressure level. It has been shown that the method is non-conservative for CO_2 pipelines. This, combined with the limited number of available full-scale fracture-propagation experiments, has led current practice to rely on special assessments.

In this work, we have suggested ways to modify the Battelle two-curve method for CO_2 pipelines. First, motivated by the different pressure distribution during fracture propagation, the material curve was modified by changing the fracture toughness dependence on the Charpy V-notch value. Second, we have drawn the fluid curve using the D-HEM method, taking thermodynamic non-equilibrium into account. This gives a lower crack-tip pressure than the current common practice of employing the two-phase saturation pressure. The practical implication of this is two-fold, as it can avoid overdesign, and also the possible overestimation of material strength.

We have applied our method to the full-scale crack-propagation test data from COOLTRANS Tests 1 and 2 and obtained significantly improved predictions with respect to the original Battelle two-curve method. This indicates that our approach is viable and should be further developed. It also confirms that both fluid and material properties need to be correctly predicted when studying running ductile fracture.

We emphasize that more work is needed in order to arrive at an engineering method. In particular, the D-HEM method needs to be extended to a wider range of initial fluid conditions in order to cover heterogeneous nucleation.

Declaration of Competing Interest

The authors declare that they have no known competing financial interests or personal relationships that could have appeared to influence the work reported in this paper.

Acknowledgement

This publication has been produced with support from the NCCS Research Centre, performed under the Norwegian research program Centres for Environment-friendly Energy Research (FME). The authors acknowledge the following partners for their contributions: Aker Carbon Capture, Allton, Ansaldo Energia, Baker Hughes, CoorsTek Membrane Sciences, Equinor, Fortum Oslo Varme, Gassco, Krohne, Larvik Shipping, Lundin Energy Norway, Norcem, Norwegian Oil and Gas, Quad Geometrics, Stratum Reservoir, TotalEnergies, Vår Energi, Wintershall Dea and the Research Council of Norway (257579).

Appendix A. Assessment of the accuracy of the REFPROP parachor method

In the delayed homogeneous equilibrium model (D-HEM) method for mixtures, we employ the REFPROP (Huber et al., 2022) parachor method to estimate mixture surface tension. The accuracy of the method is not documented. In order to quantify this some extent for CO_2-mixtures, we compare model predictions to measured surface tensions of a CO_2-CH_4 mixture (Schenk et al., 2020). The relative difference was computed as follows:

$$\varepsilon = \frac{\sigma_{\mathrm{REFPROP}} - \sigma_{\mathrm{exp}}}{\sigma_{\mathrm{exp}}} \cdot 100\%. \tag{A.1}$$

Some of the experimental measurements reported by Schenk et al. (2020) have quite large uncertainty. We therefore report whether the relative difference between the REFPROP estimate and the experiment is within the experimental uncertainty. The results are summarized in Table A.1. For five out of seven experimental points, the model predictions match the experiments within the uncertainty. Therefore we conclude that the parachor method can be expected to yield reasonable results for CO_2-rich mixtures.

B. Effect of the superheat limit

B.1. Calculation of the superheat limit

The superheat limit (SHL) can be estimated using classical nucleation theory. This is done by correlating the SHL to the rate of nucleation of bubbles large enough to grow as predicted by CNT. Such bubbles are just large enough not to collapse back into the liquid, and are called *critically-*

sized. In the following, the properties of these bubbles are denoted by an asterisk, *. As described by Debenedetti (1997), the rate of nucleation of such bubbles per volume and time can be expressed as

$$J = K\exp\left(-\frac{\Delta G^*}{k_B T_\ell}\right), \tag{B.1}$$

where ΔG is the free-energy barrier of bubble formation, k_B is the Boltzmann constant and K is a kinetic prefactor. The free-energy barrier is estimated to be

$$\Delta G^* = \frac{4\pi\sigma r^{*2}}{3}, \tag{B.2}$$

where σ denotes the surface tension and r the radius of the bubble. It is assumed that the surface tension of the bubble, σ, is equal to the macroscopic surface tension of a planar interface between the phases at the bubble curve. In the present work, the mixture surface tension is approximated using the parachor method applied in REFPROPv10 (Huber et al., 2022). A main advantage of the parachor method is that the surface tension goes to zero at the critical point of the mixture. This provides consistent results near the critical point, where the energy barrier of bubble formation should vanish.

The threshold radius for bubble formation is approximated as

$$r^* = \frac{2\sigma}{P_{bub}(T_\ell) - P_\ell}, \tag{B.3}$$

where $P_{bub}(T_\ell)$ is the bubble curve pressure at the liquid temperature. Debenedetti (1997) states that results for mixtures are in many cases well-correlated by approximating the kinetic prefactor as

$$K = \widetilde{N}_{tot}\sqrt{\frac{2\sigma}{\pi}}m^{1/2}, \tag{B.4}$$

where the total number density, $\widetilde{N}_{tot}$, is written as the sum of component number densities in the liquid:

$$\widetilde{N}_{tot} = \sum_{i=1}^{N_C}\frac{\rho_{i,\ell}}{m_i}. \tag{B.5}$$

Here, N_C is the number of components in the liquid and m_i is the mass of one molecule of component i. Furthermore, $m^{1/2}$ can be approximated by

$$m^{1/2} = \sum_{i=1}^{N_C}\frac{Y_i}{\sqrt{m_i}}, \tag{B.6}$$

where Y_i is component i's vapour-phase mole fraction at $T = T_\ell$, $P = P_{bub}(T_\ell)$.

The SHL temperature can be estimated by solving

$$J(T_\ell) = J_{cr} \tag{B.7}$$

for T_ℓ. Here, J_{cr} is the critical nucleation rate, at which sudden phase change is observed (Aursand et al., 2016b). In this work, we follow Aursand et al. (2016b), employing $J_{cr} = 1 \times 10^{12}/(m^3 s)$.

B.2. Sensitivity of the superheat limit and the superheat-limit pressure, P_{SHL}

The effect of different choices of the critical rate on the SHL is shown in Fig. B.1a for the mixture studied in COOLTRANS Test 2 (Cosham et al., 2016). The effect is limited even for a variation of ± six orders of magnitude. As the critical temperature is approached, the effect diminishes. At $T = -10$°C, the difference in the SHL pressures for the different J_{cr}s is approximately ± 2 bar. Table B.1 shows the superheat-limit pressure, P_{SHL}, calculated using the D-HEM method for varying critical nucleation rate, J_{cr}. It can be seen that the sensitivity is low, even for a huge span in J_{cr}.

In addition to the critical nucleation rate, J_{cr}, the surface tension, σ, is a key parameter in determining the SHL. No data are available to assess the accuracy of the parachor surface tension model for the mixtures in the various RDF tests considered here (Cosham et al., 2014; Michal et al., 2018; Cosham et al., 2016; Di Biagio et al., 2017). To find an estimate of the accuracy of the parachor method, the results of the method were compared to experimental measurements of the surface tension for a CO_2-CH_4 mixture conducted by Schenk et al. (2020). The relative deviations for the six data points are presented in Table A.1 and the largest relative deviation was 20%. In the following discussion, we therefore make the assumption that the uncertainty is ± 20%.

In Fig. B.1b, we show the effect of a 20% error in the surface tension on the predicted SHL for COOLTRANS Test 2 (Cosham et al., 2016). As can be seen, the effect is largest at cold temperatures. At $T = -10$°C, the difference in the SHL pressure for a 20% offset in σ is approximately ± 5 bar.

Increasing or decreasing the surface tension will affect where the superheat limit lies in the temperature-pressure space. The liquid isentrope will therefore cross the superheat limit at different pressures, P_{SHL}, giving different plateau pressures in the D-HEM method for calculating the fluid decompression curve in BTCM. A summary of the variation in P_{SHL} for the different CO_2-mixture RDF tests due to a ± 20% variation in the surface tension estimate is provided in Table B.2. The largest sensitivity due to a ± 20% variation in the surface tension is for the COOLTRANS-2 test. Here, the difference in P_{SHL} is approximately ± 2.8 bar. The sensitivity increases for tests conducted at lower temperatures, i.e., further away from the critical temperature.

References

Aasen, A., Reguera, D., Wilhelmsen, Ø., 2020. Curvature corrections remove the inconsistencies of binary classical nucleation theory. Phys. Rev. Lett. 124, 045701 https://doi.org/10.1103/PhysRevLett.124.045701.

Aursand, E., Dumoulin, S., Hammer, M., Lange, H.I., Morin, A., Munkejord, S.T., Nordhagen, H.O., 2016a. Fracture propagation control in CO_2 pipelines: validation of a coupled fluid-structure model. Eng. Struct. 123, 192–212. https://doi.org/10.1016/j.engstruct.2016.05.012.

Aursand, P., Gjennestad, M.A., Aursand, E., Hammer, M., Wilhelmsen, Ø., 2016b. The spinodal of single- and multi-component fluids and its role in the development of modern equations of state. Fluid Phase Equilib 436, 98–112. https://doi.org/10.1016/j.fluid.2016.12.018.

Barták, J., 1990. A study of the rapid depressurization of hot water and the dynaics of vapour bubble generation in superheated water. Int. J. Multiphase Flow 16, 789–798. https://doi.org/10.1016/0301-9322(90)90004-3.

Benintendi, R., 2014. Non-equilibrium phenomena in carbon dioxide expansion. Process Saf. Environ. 92 (1), 47–59. https://doi.org/10.1016/j.psep.2013.11.001.

Bilio, M., Brown, S., Fairweather, M., Mahgerefteh, H., 2009.CO_2 pipelines material and safety considerations. In: Hazards XXI. vol. 155 of Institution of Chemical Engineers Symposium Series pp. 423-429.

Borkar, G.S., Lienhard, J.H., Trela, M., 1977. Rapid hot-water depressurization experiment. Interim report, University of Kentucky Research Foundation.10.2172/5053323.

Botros, K.K., Geerligs, J., Rothwell, B., Robinson, T., 2016. Measurements of decompression wave speed in pure carbon dioxide and comparison with predictions by equation of state. J. Press. Vess. – T. ASME 138 (3). https://doi.org/10.1115/1.4031941.

Cosham, A., Jones, D.G., Armstrong, K., Allason, D., Barnett, J., 2012. Ruptures in gas pipelines, liquid pipelines and dense phase carbon dioxide pipelines. In: 9th International Pipeline Conference, IPC2012. ASME, IPTI, Calgary, Canada, vol. 3, pp. 465-482.10.1115/IPC2012-90463.

Cosham, A., Jones, D.G., Armstrong, K., Allason, D., Barnett, J., 2014. Analysis of two dense phase carbon dioxide full-scale fracture propagation tests. In: 10th International Pipeline Conference, IPC2014. Calgary, Canada.10.1115/IPC2014-33080.

Cosham, A., Jones, D.G., Armstrong, K., Allason, D., Barnett, J., 2016. Analysis of a dense phase carbon dioxide full-scale fracture propagation test in 24 inch diameter pipe. In: 11th International Pipeline Conference, IPC2016. American Society of Mechanical Engineers, Calgary, Canada.10.1115/IPC2016-64456.

Cosham, A., Michal, G., Østby, E., Barnett, J., 2022. The decompressed stress level in dense phase carbon dioxide full-scale fracture propagation tests. In: 14th International Pipeline Conference, IPC2022. ASME, IPTI, Calgary, Canada, vol. 3.10.1115/IPC2022-86855.

d'Amore, F., Mocellin, P., Vianello, C., Maschio, G., Bezzo, F., 2018. Economic optimisation of European supply chains for CO_2 capture, transport and sequestration, including societal risk analysis and risk mitigation measures. Appl. Energ. 223, 401–415. https://doi.org/10.1016/j.apenergy.2018.04.043.

Debenedetti, P.G., 1997. Metastable Liquids: Concepts and Principles. Princeton University Press. https://doi.org/10.1515/9780691213941.

Di Biagio, M., Lucci, A., Mecozzi, E., Spinelli, C.M., 2017. Fracture propagation prevention on CO_2 pipelines: Full scale experimental testing and verification approach. In: 12th Pipeline Technology Conference. Lab. Soete and Tiratsoo Technical, Berlin, Germany. Paper no. S06-02.

DNV, 2012.Submarine pipeline systems.Offshore standard DNV-OS-F-101.

DNVGL, 2021. Design and operation of carbon dioxide pipelines. Recommended practice DNVGL-RP-F104.

Edenhofer, O., Pichs-Madruga, R., Sokona, Y., Farahani, E., Kadner, S., Seyboth, K., Adler, A., Baum, I., Brunner, S., Eickemeier, P., Kriemann, B., Savolainen, J., Schlømer, S., vonStechow, C., Zwickel, T., 2014. Climate Change 2014: Mitigation of Climate Change. Tech. rep., Working Group III Contribution to the Fifth Assessment Report of the Intergovernmental Panel on Climate Change, Summary for Policymakers (eds.), J. M.. IPCC ⟨http://mitigation2014.org/⟩.

Flechas, T., Laboureur, D.M., Glover, J. Charles, 2020. A 2-D CFD model for the decompression of carbon dioxide pipelines using the Peng-Robinson and the Span-Wagner equation of state. Process Saf. Environ. 140, 299–313. https://doi.org/10.1016/j.psep.2020.04.033.

Folias, E.S., 1970. On the theory of fracture of curved sheets. Eng. Fract. Mech. 2 (2), 151–164. https://doi.org/10.1016/0013-7944(70)90019-6.

Gruben, G., Dumoulin, S., Nordhagen, H., Hammer, M., Munkejord, S. T., 2019. Calibration of pipeline steel model for computational running ductile fracture assessment. In: ISOPE 2019 – 29th International Ocean and Polar Engineering Conference. Honolulu, Hawaii, USA. Paper ISOPE-I-19-347.

Gu, S., Li, Y., Teng, L., Hu, Q., Zhang, D., Ye, X., Wang, C., Wang, J., Iglauer, S., 2018. A new model for predicting the decompression behavior of CO_2 mixtures in various phases. Process Saf. Environ. 120, 237–247. https://doi.org/10.1016/j.psep.2018.08.034.

Gu, S., Li, Y., Teng, L., Wang, C., Hu, Q., Zhang, D., Ye, X., Wang, J., Iglauer, S., 2019. An experimental study on the flow characteristics during the leakage of high pressure CO_2 pipelines. Process Saf. Environ. 125, 92–101. https://doi.org/10.1016/j.psep.2019.03.010.

Hammer, M., Aasen, A., Wilhelmsen, Ø., 2020. Thermopack.⟨https://github.com/SINTEF/thermopack/⟩. Accessed 2020-12-15.

Hammer, M., Deng, H., Austegard, A., Log, A.M., Munkejord, S.T., 2022. Experiments and modelling of choked flow of CO_2 in orifices and nozzles. Int. J. Multiphase Flow 156, 104201. https://doi.org/10.1016/j.ijmultiphaseflow.2022.104201.

Huber, M.L., Lemmon, E.W., Bell, I.H., McLinden, M.O., 2022. The NIST REFPROP database for highly accurate properties of industrially important fluids. Ind. Eng. Chem. Res. https://doi.org/10.1021/acs.iecr.2c01427.

IEA, 2021. Net Zero by 2050 – A Roadmap for the Global Energy Sector. IEA, Paris.10.1787/c8328405-en, ⟨https://www.iea.org/reports/net-zero-by-2050⟩.

ISO, 2016. Carbon dioxide capture, transportation and geological storage – pipeline transportation systems. Standard 27913.

Ives, K.D., Shoemaker, A.K., McCartney, R.F., 1974. Pipe deformation during a running shear fracture in line pipe. J. Eng. Mater. – T. ASME 96 (4), 309–317. https://doi.org/10.1115/1.3443246.

Keim, V., Marx, P., Nonn, A., Münstermann, S., 2019. Fluid-structure-interaction modeling of dynamic fracture propagation in pipelines transporting natural gases and CO_2-mixtures. Int. J. Pres. Ves. Pip. 175, 103934 https://doi.org/10.1016/j.ijpvp.2019.103934.

Keim, V., Paredes, M., Nonn, A., Münstermann, S., 2020. FSI-simulation of ductile fracture propagation and arrest in pipelines: comparison with existing data of full-scale burst tests. Int. J. Pres. Ves. Pip. 182, 104067 https://doi.org/10.1016/j.ijpvp.2020.104067.

Kiefner, J.F., Maxey, W.A., Eiber, R.J., Duffy, A.R., 1973. Failure stress levels of flaws in pressurized cylinders. In: Kaufman, J.G. (Ed.), Progress in flaw growth and fracture toughness testing, American Society for Testing and Materials. ASTM Special Technical Publication, pp. 461–481. https://doi.org/10.1520/STP49657S.

Kunz, O., Wagner, W., 2012. The GERG-2008 wide-range equation of state for natural gases and other mixtures: an expansion of GERG-2004. J. Chem. Eng. Data 57 (11), 3032–3091. https://doi.org/10.1021/je300655b.

Leis, B. N., Eiber, R. J., Carlson, L., Gilroy-Scott, A., 1998. Relationship between apparent (total) Charpy vee-notch toughness and the corresponding dynamic crack-propagation resistance. In: 2nd International Pipeline Conference, IPC1998. ASME, Calgary, Canada, vol. 2.10.1115/ipc1998-2084.

Lienhard, J.H., Alamgir, M., Trela, M., 1978. Early response of hot water to sudden release from high pressure. J. Heat Transfer 100 (3), 473–479. https://doi.org/10.1115/1.3450833.

Linga, G., Flåtten, T., 2019. A hierarchy of non-equilibrium two-phase flow models. ESAIM: Proceedings and Surveys 66, 109–143. https://doi.org/10.1051/proc/201966006.

Lopes, J.T., Francesconi, A.Z., Vianna, S.S.V., 2018. Modelling of source term from accidental release of pressurised CO_2. Process Saf. Environ. 113, 88–96. https://doi.org/10.1016/j.psep.2017.08.046.

Martynov, S., Brown, S., Mahgerefteh, H., Sundara, V., Chen, S., Zhang, Y., 2014. Modelling three-phase releases of carbon dioxide from high-pressure pipelines. Process Saf. Environ. 92 (1), 36–46. https://doi.org/10.1016/j.psep.2013.10.004.

Maxey, W. A., 1974. Fracture initiation, propagation and arrest. In: Fifth Symposium on Line Pipe Research. American Gas Association, Houston, Texas, USA, pp. J1-J31.

Maxey, W.A., 1986. Long shear fractures in CO_2 lines controlled by regulating saturation, arrest pressures. Oil Gas J. 84 (31), 44–46.

Maxey, W.A., Kiefner, J.F., Eiber, R.J., Duffy, A.R., 1972. Ductile fracture initiation, propagation, and arrest in cylindrical vessels. Fracture Toughness: Part II. ASTM International. https://doi.org/10.1520/stp38819s.

Michal, G., Davis, B., Østby, E., Lu, C., Røneid, S., 2018.CO2SAFE-ARREST: A full-scale burst test research program for carbon dioxide pipelines – Part 2: Is the BTCM out of touch with dense-phase co2? In: 12th International Pipeline Conference, IPC 2018. ASME.10.1115/IPC2018-78525.

Michal, G., Østby, E., Davis, B. J., Røneid, S., Lu, C., 2020. An empirical fracture control model for dense-phase CO2 carrying pipelines. In: 13th International Pipeline Conference, IPC 2020. ASME.10.1115/IPC2020-9421.

Morland, B.H., Dugstad, A., Svenningsen, G., 2022. Experimental based CO_2 transport specification ensuring material integrity. Int. J. Greenh. Gas Con. 119, 103697 https://doi.org/10.1016/j.ijggc.2022.103697.

Munkejord, S.T., Austegard, A., Deng, H., Hammer, M., Stang, H.G.J., Løvseth, S.W., 2020. Depressurization of CO_2 in a pipe: High-resolution pressure and temperature data and comparison with model predictions. Energy 211, 118560. https://doi.org/10.1016/j.energy.2020.118560.

Munkejord, S.T., Deng, H., Austegard, A., Hammer, M., Skarsvåg, H.L., Aasen, A., 2021. Depressurization of CO_2-N_2 and CO_2-He in a pipe: experiments and modelling of pressure and temperature dynamics. Int. J. Greenh. Gas Con. 109, 103361 https://doi.org/10.1016/j.ijggc.2021.103361.

Munkejord, S.T., Hammer, M., Løvseth, S.W., 2016. CO_2 transport: data and models – a review. Appl. Energ. 169, 499–523. https://doi.org/10.1016/j.apenergy.2016.01.100.

Nakai, H., Shibanuma, K., Aihara, S., 2016. Numerical model for unstable ductile crack propagation and arrest in pipelines using finite difference method. Eng. Fract. Mech. 162, 179–195. https://doi.org/10.1016/j.engfracmech.2016.03.048.

Nordhagen, H.O., Munkejord, S.T., Hammer, M., Gruben, G., Fourmeau, M., Dumoulin, S., 2017. A fracture-propagation-control model for pipelines transporting CO_2-rich mixtures including a new method for material-model calibration. Eng. Struct. 143, 245–260. https://doi.org/10.1016/j.engstruct.2017.04.015.

Pham, L.H.H.P., Rusli, R., 2016. A review of experimental and modelling methods for accidental release behaviour of high-pressurised CO_2 pipelines at atmospheric environment. Process Saf. Environ. 104, 48–84. https://doi.org/10.1016/j.psep.2016.08.013.

Schenk, M.R., Köddermann, T., Kirschner, K.N., Knauer, S., Reith, D., 2020. Molecular dynamics in the energy sector: experiment and modeling of the CO_2/CH_4 mixture. J. Chem. Eng. Data 65, 1117–1123. https://doi.org/10.1021/acs.jced.9b00503.

Talemi, R.H., Cooreman, S., Mahgerefteh, H., Martynov, S., Brown, S., 2019. A fully coupled fluid-structure interaction simulation of three-dimensional dynamic ductile

fracture in a steel pipeline. Theor. Appl. Fract. Mec. 101, 224–235. https://doi.org/10.1016/j.tafmec.2019.02.005.
Teng, L., Liu, X., Li, Y., Lu, C., 2021. An approach of quantitative risk assessment for release of supercritical CO_2 pipelines. J. Nat. Gas Sci. Eng. 94, 104131 https://doi.org/10.1016/j.jngse.2021.104131.
Vitali, M., Corvaro, F., Marchetti, B., Terenzi, A., 2022. Thermodynamic challenges for CO_2 pipelines design: a critical review on the effects of impurities, water content, and low temperature. Int. J. Greenh. Gas Con. 114, 103605. https://doi.org/10.1016/j.ijggc.2022.103605.
Wilhelmsen, Ø., Aasen, A., 2022. Choked liquid flow in nozzles: crossover from heterogeneous to homogeneous cavitation and insensitivity to depressurization rate. Chem. Eng. Sci. 248, 117176 https://doi.org/10.1016/j.ces.2021.117176.
Wilhelmsen, Ø., Aasen, A., Skaugen, G., Aursand, P., Austegard, A., Aursand, E., Gjennestad, M.A., Lund, H., Linga, G., Hammer, M., 2017. Thermodynamic modeling with equations of state: present challenges with established methods. Ind. Eng. Chem. Res. 56 (13), 3503–3515. https://doi.org/10.1021/acs.iecr.7b00317.
Wilkowski, G., Wang, Y. Y., Rudland, D., 2000. Recent efforts on characterizing propagating ductile fracture resistance of linepipe steels. In: Proceedings of the 3rd Pipeline Technology Conference.pp.359-386.
Wilkowski, G. M., Maxey, W. A., Eiber, R. J., 1977. Use of a brittle notch DWTT specimen to predict fracture characteristics of line pipe steels. In: ASME 1977 Energy Technology Conference, Houston, Texas.pp.18-22.
Zhao, Q., Li, Y.-X., 2014. The influence of impurities on the transportation safety of an anthropogenic CO_2 pipeline. Process Saf. Environ. 92 (1), 80–92. https://doi.org/10.1016/j.psep.2013.10.007.

Paper 4

Log, Alexandra Metallinou; Diky, Vladimir; Huber, Marcia. (2023) Assessment of a Parachor Model for the Surface Tension of Binary Mixtures. *International journal of thermophysics.* vol 44 (7). doi:10.1007/s10765-023-03216-z

International Journal of Thermophysics (2023) 44:110
https://doi.org/10.1007/s10765-023-03216-z

Assessment of a Parachor Model for the Surface Tension of Binary Mixtures

Alexandra Metallinou Log[1] · Vladimir Diky[2] · Marcia L. Huber[2]

Received: 25 April 2023 / Accepted: 12 May 2023 / Published online: 7 June 2023

Abstract

We compiled an experimental database for the surface tension of binary mixtures containing a wide variety of fluids, from the chemical classes (water, alcohols, amines, ketones, linear and branched alkanes, naphthenes, aromatics, refrigerants, and cryogens). The resulting data set includes 65 pure fluids and 154 binary pairs with a total of 8205 points. We used this database to test the performance of a parachor model for the surface tension of binary mixtures. The model uses published correlations to determine the parachors of the pure fluids. The model has a single, constant binary interaction parameter for each pair that was found by fitting experimental mixture data. It can be also used in a predictive mode when the interaction parameters are set to zero. We present detailed comparisons on the performance of the model for both cases. In general, the parachor model in a predictive mode without fitted interaction parameters can predict the surface tension of binary mixtures of non-polar mixtures such as linear and branched alkanes, linear and branched alkanes with naphthenes, aromatics with aromatics, aromatics with naphthenes, and mixtures of linear alkanes of similar sizes with an average absolute percentage deviation of about 3 % or less. Polar mixtures of halocarbons with other halocarbons and also polar/nonpolar mixtures of alkanes with halocarbons could be modeled with an average absolute deviation of less than 0.35 $mN \cdot m^{-1}$ with the use of a binary interaction parameter. The parachor model even with a fitted binary interaction parameter performs poorly for mixtures of water and organic compounds and is not recommended.

Keywords Binary mixtures · Parachor · Surface tension

✉ Alexandra Metallinou Log
alexandra.m.log@ntnu.no; Alexandra.Log@hotmail.com

[1] Department of Energy and Process Engineering, Faculty of Engineering, Norwegian University of Science and Technology, 7491 Trondheim, Norway

[2] Applied Chemicals and Materials Division, National Institute of Standards and Technology, 325 Broadway, Boulder, CO 80305, USA

1 Introduction

Surface tension is an important physical property that has long had significance in the oil and gas industry, and is also of interest in applications as varied as pharmaceuticals [1, 2], heat transfer in low-global warming potential (GWP) refrigerants [3], ink-jet printing [4, 5] and diesel engine design [6]. Specific examples in the pharmaceutical industry include [2] the importance of controlling the surface tension of coating solutions of tablets to improve product appearance and control the rate of drug release, the effect of surface tension on the size of droplets in a nebulizer, and control of the size of eye drops. In addition, fluorocarbon based fluids with low surface tension are being investigated as blood substitutes for oxygen delivery [1]. In the refrigeration industry, new low-GWP refrigerant blends are being proposed. In order to evaluate the performance of heat exchangers, accurate knowledge of the surface tension is needed to model the bubble behavior in pool boiling [3]. In ink-jet printing, From [5] analyzed the fluid flow behavior of impulsively driven laminar jet flow in terms of dimensionless parameters involving the surface tension, density, viscosity, and a characteristic dimension, and made recommendations for when the fluid has stable drop formation. In order to optimize engine performance to reduce soot emissions, there is a need for surface tension data at high pressures and high temperatures [6]. Accurate property values for surface tension are necessary for successful analysis of all these processes.

In 1923, Macleod proposed a simple empirical relationship between surface tension σ and the density of the liquid and vapor phases ρ_L and ρ_V

$$P = \frac{\sigma^{1/4}}{\rho_L - \rho_V}, \tag{1}$$

where P is a temperature-independent parameter called the parachor by Sugden [7]. Other practical engineering methods for predicting surface tension can be found in handbooks such as Ref. [8]. In addition, there are numerous theoretically based approaches to predicting the surface tension such as density gradient theory [9, 10], density functional theory [11], hard-sphere fluid scaled particle theory [12], perturbation theory [13] and friction theory [14].

The parachor approach can also be applied to mixtures, as was demonstrated by Weinaug and Katz [15] and Hugill *et al.* [16]. Although the parachor method has been used for many years in the petrochemical industry, is in active use now [17], is the recommended approach in the API Technical Databook [18], and is discussed in reference books for engineers [8] there has not been a comprehensive evaluation of the performance of this type of model with respect to mixtures using a large database of binary data in the open literature. It is the goal of this work to provide an evaluation of the parachor model to a wide variety of binary mixtures, including not only common hydrocarbons involved in the petrochemical industry, but also recent low-GWP fluids of interest to the refrigeration industry and to indicate expected performance and limitations of this model for a wide variety of mixtures.

2 The Parachor Model

The parachor model that we will apply to mixtures was originally presented by Weinaug and Katz [15] and later modified by Hugill *et al.* [16] to allow for the use of binary interaction parameters. For a mixture,

$$\sigma_{\mathrm{mix}} = \left(\mathrm{P_L}\rho_{\mathrm{L}} - \mathrm{P_V}\rho_{\mathrm{V}}\right)^m \tag{2}$$

with mixing and combining rules

$$\mathrm{P_L} = \sum_{i=1}^{n}\sum_{j=1}^{n} x_i x_j \mathrm{P}_{ij} \quad \text{and} \quad \mathrm{P_V} = \sum_{i=1}^{n}\sum_{j=1}^{n} y_i y_j \mathrm{P}_{ij} \tag{3}$$

$$\mathrm{P}_{ij} = (1-\delta_{ij})\frac{\mathrm{P}_i + \mathrm{P}_j}{2}, \tag{4}$$

where δ_{ij} is an optional binary interaction parameter, and x_i and y_i are the molar compositions of the liquid and gas phases, respectively. Historically [15, 16, 19] the exponent m has been set to 4, but here we use $m = 3.87$ based on theoretical considerations as presented by Garrabos *et al.* [20]. In addition, it also is common to use a fixed value of the parachor obtained from compilations such as that of Quayle [21]. Zhelezny *et al.* [22] has studied the temperature dependence of the parachor. Mulero and coworkers [23–31] developed an extensive body of work on correlations for the surface tension of many important industrial fluids that can be used to compute the pure fluid parachors P_i as a function of temperature. These correlations are very accurate and can represent the data to within experimental uncertainty. We primarily use these correlations as implemented in the computer program REFPROP v10 [32] for pure fluid surface tension σ_i. The parachors are evaluated at the temperature of interest for the binary mixture, however for temperatures greater than or equal to $0.9T_{\mathrm{c,i}}$, where $T_{\mathrm{c,i}}$ is the pure fluid critical temperature, the parachor is calculated at $0.9T_{\mathrm{c,i}}$. It also is necessary to have the saturation densities and compositions x_i and y_i of the liquid and vapor phases. If the compositions and densities from the VLE calculations are inaccurate this will increase the uncertainty in the surface tension calculations, so care should be used in the selection of the VLE model. We obtain these compositions and densities from the default equations of state and models implemented in REFPROP v10 [32]; a description of these can be found in [33]. A few changes were made in the models of REFPROP v10 that enabled calculation for some mixtures not permitted in the original version, as well as some changes in mixture parameters that are summarized in the Supplementary Information in Appendix A.

3 Experimental Data

We extracted experimental data for the surface tension of binary mixtures for liquid–gas interfaces from the NIST TDE database [34] for which the pure fluid components are available, the composition of the liquid is explicitly specified, and also for which there are reliable models for the vapor–liquid equilibrium and thermodynamic properties in the REFPROP database [32]. We excluded HCl/water and benzene/water due to the lack of a good mixture model for thermodynamic properties in REFPROP. The resulting data set includes 65 pure fluids and 154 binary pairs with a total of 8205 points. Table 1 provides a list of the pure components along with information for compound identification, along with a reference for the pure fluid surface tension correlation implemented in REFPROP v10 [32] used to evaluate pure fluid surface tension in this work. A summary of the binary mixture data is given in Table 2 including a reference code (starting with the publication year), the experimental method, an uncertainty estimate, the fluids in the binary mixture, the number of data points, temperature range, and composition in terms of the mole fraction of the first component. The full data set is available in the supplementary information in the file InputData.txt. A discussion of experimental methods for obtaining surface tension can be found in Ref. [35]. The estimated uncertainties (at a $k=2$ level) are those as assessed by the NIST TDE database and may not be the same as those stated by the original authors. As part of the data capture process, software [36] is used that assesses the uncertainty of the data taking into account factors such as the experimental method, the sample purity, property precision, precision of independent variables. However, the reader should consult the original data reference for complete details of the measurement technique and uncertainty analysis for assessment of the quality of an individual data set.

4 Results

Evaluations were first made with the interaction parameter in Eq. 4 set to zero ($\delta_{ij}=0$) for all the mixtures. All properties such as the pure fluid surface tensions and the mixture densities and compositions required in Eqs. 1–4 were obtained using the REFPROP v10 [32] computer program, with additional changes that are detailed in the supplementary information, Appendix A. A second set of evaluations was made after fitting the binary interaction parameter δ_{ij} to the experimental data with a trust-region reflective least squares algorithm in Python, scipy.optimize.curve_fit [198].[1] A single binary interaction parameter was fit for each fluid mixture pair, including all data sets for any given pair. For discussion of the results, we define AAPD as the average absolute percentage deviation, where $\mathrm{PCTDEV}=100(\sigma_{\mathrm{calc}}-\sigma_{\mathrm{exp}})/\sigma_{\mathrm{exp}}$, and $\mathrm{AAPD}=(\sum\left|\mathrm{PCTDEV}\right|)/n$, and the summation is over all n points. AAD is

[1] Certain equipment, instruments, software, or materials, commercial or non-commercial, are identified in this paper to specify the experimental procedure adequately. Such identification is not intended to imply recommendation or endorsement of any product or service by NIST, nor is it intended to imply that the materials or equipment identified are necessarily the best available for the purpose.

Table 1 List of fluids

Name	Full name	Formula	Family	CAS no.	Standard InChI key	References
Acetone	Propanone	C_3H_6O	Ketone	67-64-1	CSCPPACGZOOCGX-UHFFFAOYSA-N	[26]
Argon	Argon	Ar	Cryogen	7440-37-1	XKRFYHLGVUSROY-UHFFFAOYSA-N	[26]
Benzene	Benzene	C_6H_6	Aromatic	71-43-2	UHOVQNZJYSORNB-UHFFFAOYSA-N	[26]
Butane	*n*-Butane	C_4H_{10}	*n*-Alkane	106-97-8	IJDNQMDRQITEOD-UHFFFAOYSA-N	[26]
Carbon dioxide	Carbon dioxide	CO_2	Other	124-38-9	CURLTUGMZLYLDI-UHFFFAOYSA-N	[26]
Carbon monoxide	Carbon monoxide	CO	Cryogen	630-08-0	UGFAIRIUMAVXCW-UHFFFAOYSA-N	[26]
Chlorobenzene	Chlorobenzene	C_6H_5Cl	Halocb	108-90-7	MVPPADPHJFYWMZ-UHFFFAOYSA-N	[37]
Cyclohexane	Cyclohexane	C_6H_{12}	Naphthene	110-82-7	XDTMQSROBMDMFD-UHFFFAOYSA-N	[26]
Cyclopentane	Cyclopentane	C_5H_{10}	Naphthene	287-92-3	RGSFGYAAUTVSQA-UHFFFAOYSA-N	[24]
D4	Octamethylcyclotetrasiloxane	$C_8H_{24}O_4Si_4$	Siloxane	556-67-2	HMMGMWAXVFQUOA-UHFFFAOYSA-N	[24]
D5	Decamethylcyclopentasiloxane	$C_{10}H_{30}O_5Si_5$	Siloxane	541-02-6	XMSXQFUHVRWGNA-UHFFFAOYSA-N	[24]
DEA	Diethanolamine	$C_4H_{11}NO_2$	Amine	111-42-2	ZBCBWPMODOFKDW-UHFFFAOYSA-N	[37]
Decane	*n*-Decane	$C_{10}H_{22}$	*n*-Alkane	124-18-5	DIOQZVSQGTUSAI-UHFFFAOYSA-N	[26]
Deuterium	Deuterium	D_2	Cryogen	7782-39-0	UFHFLCQGNIYNRP-VVKOMZTBSA-N	[26]
Dichloroethane	1,2-Dichloroethane	$C_2H_4Cl_2$	Halocb	107-06-2	WSLDOOZREJYCGB-UHFFFAOYSA-N	[37]
Diethyl ether	Diethyl ether	$C_4H_{10}O$	Ether	60-29-7	RTZKZFJDLAIYFH-UHFFFAOYSA-N	[24]
Dimethyl carbonate (DMC)	Dimethyl ester carbonic acid	$C_3H_6O_3$	Other	616-38-6	IEJIGPNLZYLLBP-UHFFFAOYSA-N	[24]
Dimethyl ether	Methoxymethane	C_2H_6O	Ether	115-10-6	LCGLNKUTAGEVQW-UHFFFAOYSA-N	[26]
Docosane	*n*-Docosane	$C_{22}H_{46}$	*n*-Alkane	629-97-0	HOWGUJZVBDQJKV-UHFFFAOYSA-N	[37]
Dodecane	*n*-Dodecane	$C_{12}H_{26}$	*n*-Alkane	112-40-3	SNRUBQQJIBEYMU-UHFFFAOYSA-N	[26]
Ethane	Ethane	C_2H_6	*n*-Alkane	74-84-0	OTMSDBZUPAUEDD-UHFFFAOYSA-N	[26]
Ethanol	Ethyl alcohol	C_2H_6O	Alcohol	64-17-5	LFQSCWFLJHTTHZ-UHFFFAOYSA-N	[27]
Ethylene glycol	1,2-Ethandiol	$C_2H_6O_2$	Glycol	107-21-1	LYCAIKOWRPUZTN-UHFFFAOYSA-N	[37]
Ethylbenzene	Phenylethane	C_8H_{10}	Aromatic	100-41-4	YNQLUTRBYVCPMQ-UHFFFAOYSA-N	[24]
Heavy water	Deuterium oxide	D_2O	Water	7789-20-0	XLYOFNOQVPJJNP-ZSJDYOACSA-N	[38]
Helium	Helium-4	He	Cryogen	7440-59-7	SWQJXJOGLNCZEY-UHFFFAOYSA-N	[26]

Table 1 (continued)

Name	Full name	Formula	Family	CAS no.	Standard InChI key	References
Heptane	*n*-Heptane	C_7H_{16}	*n*-Alkane	142-82-5	IMNFDUFMRHMDMM-UHFFFAOYSA-N	[26]
Hexadecane	*n*-Hexadecane	$C_{16}H_{34}$	*n*-Alkane	544-76-3	DCAYPVUWAIABOU-UHFFFAOYSA-N	[37]
Hexane	*n*-Hexane	C_6H_{14}	*n*-Alkane	110-54-3	VLKZOEOYAKHREP-UHFFFAOYSA-N	[26]
Hydrogen (normal)	Hydrogen (normal)	H_2	Cryogen	1333-74-0	UFHFLCQGNIYNRP-UHFFFAOYSA-N	[26]
Isooctane	2,2,4-Trimethylpentane	C_8H_{18}	*br*-Alkane	540-84-1	NHTMVDHEPJAVLT-UHFFFAOYSA-N	[24]
Krypton	Krypton	Kr	Cryogen	7439-90-9	DNNSSWSSYDEUBZ-UHFFFAOYSA-N	[26]
MD2M	Decamethyltetrasiloxane	$C_{10}H_{30}Si_4O_3$	Siloxane	141-62-8	YFCGDEUVHLPRCZ-UHFFFAOYSA-N	[24]
MD3M	Dodecamethylpentasiloxane	$C_{12}H_{36}Si_5O_4$	Siloxane	141-63-9	FBZANXDWQAVSTQ-UHFFFAOYSA-N	[24]
MD4M	Tetradecamethylhexasiloxane	$C_{14}H_{42}O_5Si_6$	Siloxane	107-52-8	ADANNTOYRVPQLJ-UHFFFAOYSA-N	[24]
Monoethanolamine (MEA)	Ethanolamine	C_2H_7NO	Amine	141-43-5	HZAXFHJVJLSVMW-UHFFFAOYSA-N	[37]
Methane	Methane	CH_4	*n*-Alkane	74-82-8	VNWKTOKETHGBQD-UHFFFAOYSA-N	[26]
Methanol	Methanol	CH_4O	Alcohol	67-56-1	OKKJLVBELUTLKV-UHFFFAOYSA-N	[26]
Methyl palmitate	Methyl hexadecanoate	$C_{17}H_{34}O_2$	FAME	112-39-0	FLIACVVOZYBSBS-UHFFFAOYSA-N	[24]
Methylcyclohexane	Methylcyclohexane	C_7H_{14}	Naphthene	108-87-2	UAEPNZWRGJTJPN-UHFFFAOYSA-N	[24]
m-Xylene	1,3-Dimethylbenzene	C_8H_{10}	Aromatic	108-38-3	IVSZLXZYQVIEFR-UHFFFAOYSA-N	[24]
Neon	Neon	Ne	Cryogen	7440-01-9	GKAOGPIIYCISHV-UHFFFAOYSA-N	[26]
Nitrogen	Nitrogen	N_2	Cryogen	7727-37-9	IJGRMHOSHXDMSA-UHFFFAOYSA-N	[26]
Nonane	*n*-Nonane	C_9H_{20}	*n*-Alkane	111-84-2	BKIMMITUMNQMOS-UHFFFAOYSA-N	[26]
Octane	*n*-Octane	C_8H_{18}	*n*-Alkane	111-65-9	TVMXDCGIABBOFY-UHFFFAOYSA-N	[26]
Oxygen	Oxygen	O_2	Cryogen	7782-44-7	MYMOFIZGZYHOMD-UHFFFAOYSA-N	[26]
o-Xylene	1,2-Dimethylbenzene	C_8H_{10}	Aromatic	95-47-6	CTQNGGLPUBDAKN-UHFFFAOYSA-N	[24]
Pentane	*n*-Pentane	C_5H_{12}	*n*-Alkane	109-66-0	OFBQJSOFQDEBGM-UHFFFAOYSA-N	[26]
Propane	Propane	C_3H_8	*n*-Alkane	74-98-6	ATUOYWHBWRKTHZ-UHFFFAOYSA-N	[26]
Propylene	Propene	C_3H_6	*n*-Alkene	115-07-1	QQONPFPTGQHPMA-UHFFFAOYSA-N	[26]
p-Xylene	1,4-Dimethylbenzene	C_8H_{10}	Aromatic	106-42-3	URLKBWYHVLBVBO-UHFFFAOYSA-N	[24]
R1123	Trifluoroethylene	C_2HF_3	Halocb	359-11-5	MIZLGWKEZAPEFJ-UHFFFAOYSA-N	[37]

Table 1 (continued)

Name	Full name	Formula	Family	CAS no.	Standard InChI key	References
R115	Chloropentafluoroethane	C_2ClF_5	Halocb	76-15-3	RFCAUADVODFSLZ-UHFFFAOYSA-N	[26]
R1234yf	2,3,3,3-Tetrafluoroprop-1-ene	$C_3F_4H_2$	Halocb	754-12-1	FXRLMCRCYDHQFW-UHFFFAOYSA-N	[26]
R1234ze(E)	*trans*-1,3,3,3-Tetrafluoropropene	$C_3F_4H_2$	Halocb	29,118-24-9	CDOOAUSHHFGWSA-OWOJBTEDSA-N	[24]
R125	Pentafluoroethane	C_2HF_5	Halocb	354-33-6	GTLACDSXYULKMZ-UHFFFAOYSA-N	[26]
R134a	1,1,1,2-Tetrafluoroethane	$C_2H_2F_4$	Halocb	811-97-2	LVGUZGTVOIAKKC-UHFFFAOYSA-N	[26]
R143a	1,1,1-Trifluoroethane	$C_2H_3F_3$	Halocb	420-46-2	UJPMYEOUBPIPHQ-UHFFFAOYSA-N	[24]
R152a	1,1-Difluoroethane	$C_2H_4F_2$	Halocb	75-37-6	NPNPZTNLOVBDOC-UHFFFAOYSA-N	[26]
R22	Chlorodifluoromethane	$CHClF_2$	Halocb	75-45-6	VOPWNXZWBYDODV-UHFFFAOYSA-N	[26]
R227ea	1,1,1,2,3,3,3-Heptafluoropropane	C_3HF_7	Halocb	431-89-0	YFMFNYKEUDLDTL-UHFFFAOYSA-N	[26]
R32	Difluoromethane	CH_2F_2	Halocb	75-10-5	RWRIWBAIICGTTQ-UHFFFAOYSA-N	[26]
RC318	Octafluorocyclobutane	C_4F_8	Halocb	115-25-3	BCCOBQSFUDVTJQ-UHFFFAOYSA-N	[26]
Toluene	Methylbenzene	C_7H_8	Aromatic	108-88-3	YXFVVABEGXRONW-UHFFFAOYSA-N	[26]
Water	Water	H_2O	Water	7732-18-5	XLYOFNOQVPJJNP-UHFFFAOYSA-N	[39]

Table 2 Summary of surface tension binary mixture data

Reference code	Method	Unc. ($mN \cdot m^{-1}$)	Fluid 1	Fluid 2	Npts	T range (K)	x_1 range
1974 jai sin 0 [40]	DROPW	0.6–0.7	Ethylbenzene	Cyclohexane	28	298–308	0.0–1.0
2014 pra cow 0 [41]	DROPSH	0.4	Ethylbenzene	Hexadecane	9	294	0.0–1.0
1978 dhi mah 0 [42]	CAPRISE	0.7–0.8	*p*-Xylene	Chlorobenzene	18	293–303	0.1–0.9
1972 mah cho 0 [43]	CAPRISE	0.1–0.2	*p*-Xylene	Pentane	7	288	0.14–0.82
2010 dom ril 0 [44]	DROPV	0.1–0.2	*p*-Xylene	Hexane	16	298	0.12–0.95
1974 jai sin 0 [40]	DROPW	0.6–0.7	*p*-Xylene	Cyclohexane	28	298–308	0.0–1.0
2013 gay cas 0 [45]	DROPV	0.2–0.3	*p*-Xylene	Octane	12	308	0.05–0.95
2009 mos cas 0 [46]	DROPV	0.3	*p*-Xylene	Decane	11	298	0.10–0.95
2013 gay cas 0 [45]	DROPV	0.3	*p*-Xylene	Decane	11	308	0.10–0.95
2004 ouy lu 3 [47]	DROPSH	0.3	*p*-Xylene	Ethanol	11	298	0.0–1.0
1992 wan nar 1 [48]	CAPRISE	0.6–0.7	*p*-Xylene	Methanol	44	293–318	0.0–1.0
2004 ouy yan 0 [49]	DROPSH	0.3	*p*-Xylene	Acetone	9	298	0.10–0.90
2013 gay cas 0 [45]	DROPV	0.3	*p*-Xylene	DMC	10	308	0.06–0.95
1978 cal mcl 0 [50]	CAPRISE	0.1	Butane	RC318	24	234–254	0.0–1.0
1985 hsu nag 0 [51]	DROPSH	0.1–0.2	Butane	Carbon dioxide	42	319–378	0.15–0.91
2005 goz dan 0 [52]	OTHER	0.02	Butane	methane	1	311	0.49
1914 wor & 1 [53]	UNKN	0.5–0.6	Dichloroethane	Benzene	13	286–343	0.0–1.0
1978 dhi mah 0 [42]	CAPRISE	0.7–0.8	*m*-Xylene	Chlorobenzene	18	293–303	0.1–0.9
1972 mah cho 0 [43]	CAPRISE	0.1–0.2	*m*-Xylene	Pentane	9	288	0.12–0.89
2017 tah & 0 [54]	DROPSH	0.3–0.4	*m*-Xylene	Pentane	11	293	0.0–1.0
2006 dom seg 0 [55]	DROPV	0.1–0.2	*m*-Xylene	Hexane	18	298	0.04–0.95
2017 tah & 0 [54]	DROPSH	0.3–0.4	*m*-Xylene	Hexane	11	293	0.0–1.0
1974 jai sin 0 [40]	DROPW	0.6–0.7	*m*-Xylene	Cyclohexane	28	298–308	0.0–1.0
2017 tah & 0 [54]	DROPSH	0.3–0.4	*m*-Xylene	Octane	11	293	0.0–1.0
2017 tah & 0 [54]	DROPSH	0.3–0.4	*m*-Xylene	Heptane	11	293	0.0–1.0
2004 ouy lu 3 [47]	DROPSH	0.3	*m*-Xylene	Ethanol	11	298	0.0–1.0
2004 ouy yan 0 [49]	DROPSH	0.3	*M*-Xylene	Acetone	9	298	0.10–0.90

Table 2 (continued)

Reference code	Method	Unc. ($mN \cdot m^{-1}$)	Fluid 1	Fluid 2	Npts	T range (K)	x_1 range
1929 ham and 0 [56]	CAPRISE	0.2	*m*-Xylene	Benzene	5	298	0.40–1.0
1917 mor gri 0 [57]	DROPW	0.2	Toluene	Chlorobenzene	6	283–313	0.26–0.81
1972 mah cho 0 [43]	CAPRISE	0.1	Toluene	Pentane	8	288	0.18–0.79
1970 lam ben 0 [58]	BUBBLEP	0.7	Toluene	Cyclohexane	11	298	0.11–0.90
1958 lin van 1 [59]	OTHER	8–10	Toluene	Octane	17	303–398	0.0–1.0
2021 vak alw 0 [60]	RINGTE	0.5	Toluene	Nonane	44	298–313	0.0–1.0
2003 kah wad 0 [61]	DROPSH	0.2–0.3	Toluene	Heptane	34	288–328	0.0–1.0
1970 lam ben 0 [58]	BUBBLEP	0.6–0.7	Toluene	Cyclopentane	10	298	0.10–0.89
2014 pra cow 0 [41]	DROPSH	0.4	Toluene	Hexadecane	8	294	0.0–1.0
2021 vak alw 0 [60]	RINGTE	0.5	Toluene	Hexadecane	44	298–313	0.0–1.0
1974 mye cle 0 [62]	BUBBLEP	0.3	Toluene	Ethanol	10	303	0.0–1.0
1993 sha muk 0 [63]	DROPW	0.8–1.1	Toluene	Ethanol	5	298	0.1–0.9
1982 sin lar 0 [64]	CAPRISE	0.1	Toluene	Methanol	11	308	0.0–1.0
1992 wan nar 1 [48]	CAPRISE	0.5–0.7	Toluene	Methanol	44	293–318	0.0–1.0
2003 kah wad 1 [65]	DROPSH	0.2–0.3	Toluene	Acetone	55	288–328	0.0–1.0
2007 end kah 0 [66]	DROPSH	0.5–0.6	Toluene	Acetone	55	288–328	0.0–1.0
1917 mor gri 0 [57]	DROPW	0.3–0.6	Toluene	Benzene	6	284–313	0.22–0.72
1970 kon lya 1 [67]	BUBBLEP	0.3–0.4	Toluene	Benzene	21	293–333	0.0–1.0
1972 mah cho 0 [43]	CAPRISE	0.1–0.2	Chlorobenzene	Pentane	7	288	0.18–0.84
1978 dhi mah 0 [42]	CAPRISE	0.6–0.8	Chlorobenzene	Cyclohexane	18	293–303	0.1–0.9
1917 mor gri 0 [57]	DROPW	0.2	Chlorobenzene	Acetone	1	288	0.34
1917 mor gri 0 [57]	DROPW	0.4–0.6	Chlorobenzene	Benzene	6	283–313	0.21–0.62
1978 dhi mah 0 [42]	CAPRISE	0.7–0.8	Chlorobenzene	Benzene	17	293–303	0.1–0.9
1978 dhi mah 0 [42]	CAPRISE	0.7–0.8	Chlorobenzene	*o*-Xylene	18	293–303	0.1–0.9
1972 mah cho 0 [43]	CAPRISE	0.1–0.2	Pentane	Cyclohexane	7	288	0.15–0.81
1992 abd ada 0 [68]	CAPRISE	0.1–1.2	Pentane	Heptane	61	303–538	0.0–1.0

Table 2 (continued)

Reference code	Method	Unc. ($mN \cdot m^{-1}$)	Fluid 1	Fluid 2	Npts	T range (K)	x_1 range
2010 moh ras 0 [69]	BUBBLEP	0.2	Pentane	Heptane	38	293–323	0.17–0.97
2011 moh & 0 [70]	CAPRISE	0.1–0.2	Pentane	Hexadecane	35	293–323	0.2–0.9
1972 mah cho 0 [43]	CAPRISE	0.1–0.2	Pentane	Benzene	7	288	0.09–0.81
2018 sat coo 0 [71]	DROPSH	0.1–0.2	Pentane	Methane	7	313	0.50–0.95
1963 cle cha 0 [72]	BUBBLEP	0.2–0.3	Hexane	Cyclohexane	19	298–308	0.0–1.0
1967 rid but 0 [73]	RINGTE	0.6–0.7	Hexane	Cyclohexane	8	293	0.0–1.0
1968 sch cle 1 [74]	BUBBLEP	0.5–0.7	Hexane	Dodecane	21	298–313	0.0–1.0
2019 kol yan 0 [75]	SLS	0.1–0.2	Hexane	Carbon dioxide	5	303	0.25–1.0
1994 pap pan 1 [76]	CAPRISE	0.1	Hexane	Ethanol	20	298	0.0–1.0
2000 jim cas 0 [77]	DROPV	0.1	Hexane	Ethanol	17	298	0.04–0.93
2007 gin vil 1 [78]	DROPV	0.3	Hexane	Ethanol	77	283–313	0.07–0.91
1935 tri & 0 [79]	UNKN	0.1	Hexane	Methanol	4	295	0.0–1.0
1970 ram pat 0 [80]	UNKN	0.5–0.7	Hexane	Methanol	22	303–318	0.0–1.0
1966 sch ran 0 [81]	BUBBLEP	0.5–0.6	Hexane	Benzene	23	298–313	0.0–1.0
1967 rid but 0 [73]	RINGTE	0.6–0.8	Hexane	Benzene	8	293	0.0–1.0
2002 gom mej 0 [82]	DROPW	0.6	Cyclohexane	Decane	6	298	0.0–1.0
2003 kah wad 1 [65]	DROPSH	0.2–0.3	Cyclohexane	Heptane	55	288–328	0.0–1.0
2001 gom mej 0 [83]	RINGTE	0.4–0.5	Cyclohexane	Isooctane	126	298–323	0.0–1.0
1935 tri & 0 [79]	UNKN	0.1	Cyclohexane	Ethanol	6	295	0.0–1.0
1974 mye cle 0 [62]	BUBBLEP	0.3	Cyclohexane	Ethanol	11	303	0.0–1.0
2003 kah wad 1 [65]	DROPSH	0.2–0.3	Cyclohexane	Acetone	44	288–318	0.0–1.0
2008 mej seg 1 [84]	BUBBLEP	0.3	Cyclohexane	Acetone	10	303	0.06–0.95
1929 ham and 0 [56]	CAPRISE	0.2	Cyclohexane	Benzene	5	298	0.30–0.62
1967 rid but 0 [73]	RINGTE	0.7–0.8	Cyclohexane	Benzene	9	293	0.0–1.0
1968 sur ram 0 [85]	CAPRISE	0.1	Cyclohexane	Benzene	15	293–303	0.09–0.87
1970 kon lya 1 [67]	BUBBLEP	0.3–0.4	Cyclohexane	Benzene	39	293–333	0.0–1.0

Table 2 (continued)

Reference code	Method	Unc. ($mN \cdot m^{-1}$)	Fluid 1	Fluid 2	Npts	T range (K)	x_1 range
1970 lam ben 0 [58]	BUBBLEP	0.6–0.8	Cyclohexane	Benzene	28	293–303	0.10–0.89
1974 jai sin 0 [40]	DROPW	0.6–0.8	Cyclohexane	*o*-Xylene	28	298–308	0.0–1.0
2019 abr bag 0 [86]	RINGTE	0.5–0.7	DEA	Ethanol	13	313	0.0–1.0
2019 abr bag 0 [86]	RINGTE	0.5–0.7	DEA	Methanol	14	313	0.0–1.0
1994 rin oel 0 [87]	RINGTE	1.5–1.7	DEA	Water	12	293–353	0.02–0.07
1996 vaz alv 0 [88]	OTHER	0.3–0.5	DEA	Water	66	298–323	0.0–1.0
1998 alv ren 0 [89]	DROPW	0.8	DEA	Water	6	298–323	0.15
2001 agu tre 0 [90]	DROPSH	1.3–1.5	DEA	Water	21	293–363	0.02–0.07
2003 alv can 0 [91]	DROPSH	0.5	DEA	Water	6	298–323	0.15
2014 fu du 0 [92]	OTHER	2.0	DEA	Water	12	293–323	0.04–0.07
2018 dey das 0 [93]	DROPSH	0.8	DEA	Water	9	313–333	0.02–0.07
2018 fu xie 0 [94]	OTHER	0.6	DEA	Water	15	303–323	0.0–1.0
2018 sho & 0 [95]	RINGTE	0.6–0.9	DEA	Water	65	298–348	0.0–1.0
2015 lop igl 0 [96]	DROPV	0.1	Octane	Isooctane	55	293–313	0.0–1.0
2003 seg del 0 [97]	DROPV	0.2	Octane	Ethanol	17	298	0.07–0.92
2011 mej car 0 [98]	BUBBLEP	0.3	Octane	Ethanol	31	298–318	0.04–0.90
2016 and mar 0 [99]	DROPSH	0.3	Octane	*o*-Xylene	11	298	0.05–0.95
2013 gay cas 0 [45]	DROPV	0.2–0.3	Octane	DMC	12	308	0.05–0.95
2021 vak alw 0 [60]	RINGTE	0.4–0.5	Nonane	Benzene	44	298–313	0.0–1.0
2016 and mar 0 [99]	DROPSH	0.3–0.4	Nonane	*o*-Xylene	11	298	0.05–0.95
2020 ond sar 0 [100]	DROPV	0.3	Methyl palmitate	Ethanol	1	298	0.04
1964 eva cle 0 [101]	BUBBLEP	0.2–0.3	Dodecane	Isooctane	9	303	0.0–1.0
2022 yan wu 0 [102]	DROPSH	0.2–0.4	Dodecane	Hexadecane	36	298–573	0.31–0.80
2011 mej car 0 [98]	BUBBLEP	0.3	Dodecane	Ethanol	22	298–303	0.05–0.95
1966 sch ran 0 [81]	BUBBLEP	0.5–0.6	Dodecane	Benzene	23	298–313	0.0–1.0
2018 pra mun 0 [103]	DROPSH	0.3	Dodecane	Methylcyclohexane	9	293	0.1–0.9

Table 2 (continued)

Reference code	Method	Unc. ($mN \cdot m^{-1}$)	Fluid 1	Fluid 2	Npts	T range (K)	x_1 range
2010 bi li 0 [104]	CAPRISE	0.4	Dimethyl ether	Propane	114	243–333	0.29–0.69
1986 nag rob 0 [105]	DROPW	0.1–0.7	Decane	Carbon dioxide	41	344–378	0.10–0.51
2001 sha rob 0 [106]	DROPSH	0.1–0.7	Decane	Carbon dioxide	23	344	0.10–0.89
2002 rol cac 0 [107]	RINGTE	0.3–0.4	Decane	Heptane	25	293–333	0.0–1.0
2002 gom mej 0 [82]	DROPW	0.6	Decane	Isooctane	6	298	0.0–1.0
2002 rol cac 0 [107]	RINGTE	0.4	Decane	Hexadecane	25	293–333	0.0–1.0
2005 que cac 0 [108]	OTHER	0.3–0.4	Decane	Docosane	19	313–343	0.2–0.8
2011 mej car 0 [98]	BUBBLEP	0.3	Decane	Ethanol	32	303–318	0.02–0.97
2016 and mar 0 [99]	DROPSH	0.4	Decane	*o*-Xylene	11	298	0.05–0.95
2013 gay cas 0 [45]	DROPV	0.3	Decane	DMC	11	308	0.05–0.95
1964 gri rud 0 [109]	CAPRISE	0.1	Hydrogen	Deuterium	67	16–20	0.30–0.96
1967 bla kro 0 [110]	CAPRISE	0.1	Hydrogen	Argon	21	87–140	0.0–0.05
2019 abr bag 0 [86]	RINGTE	0.5–0.7	MEA	Ethanol	14	313	0.0–1.0
2020 abr bag 0 [111]	RINGTE	0.5–0.7	MEA	Ethanol	12	303	0.27–0.98
2019 abr bag 0 [86]	RINGTE	0.5–0.7	MEA	Methanol	12	313	0.0–1.0
2020 abr bag 0 [111]	RINGTE	0.5–0.7	MEA	Methanol	10	303	0.28–0.99
1981 ano & 5 [112]	CAPRISE	0.9–1.1	MEA	Water	20	303–393	0.03–0.05
1997 vaz alv 0 [113]	OTHER	0.4–0.6	MEA	Water	83	298–323	0.0–1.0
1998 alv ren 0 [89]	DROPW	1.5–1.6	MEA	Water	5	298–323	0.23
2012 han jin 0 [114]	DROPSH	0.6–0.8	MEA	Water	44	303–333	0.0–1.0
2013 jay jay 0 [115]	DROPV	1.8	MEA	Water	4	313–343	0.54
2013 jay wee 0 [116]	DROPV	2.5–2.9	MEA	Water	24	303–333	0.07–0.41
2014 fu du 0 [92]	OTHER	2.0	MEA	Water	12	293–323	0.07–0.11
2018 fu xie 0 [94]	OTHER	0.6	MEA	Water	15	303–323	0.0–1.0
2018 sho & 0 [95]	RINGTE	0.6–0.9	MEA	Water	66	298–348	0.0–1.0
2014 lun cow 0 [117]	DROPSH	0.3–0.4	Heptane	Isooctane	4	294	0.0–1.0

Table 2 (continued)

Reference code	Method	Unc. ($mN \cdot m^{-1}$)	Fluid 1	Fluid 2	Npts	T range (K)	x_1 range
2015 lop igl 0 [96]	DROPV	0.1	Heptane	Isooctane	55	293–313	0.0–1.0
1958 koe vil 0 [118]	CAPRISE	0.1–0.7	Heptane	Hexadecane	6	293–303	0.0–1.0
2002 rol cac 0 [107]	RINGTE	0.3–0.4	Heptane	Hexadecane	25	293–333	0.0–1.0
2011 moh & 0 [70]	CAPRISE	0.2	Heptane	Hexadecane	35	293–323	0.2–0.9
2003 que sil 0 [119]	RINGTE	0.6–0.8	Heptane	Docosane	12	313–343	0.25–0.75
1994 pap pan 1 [76]	CAPRISE	0.1	Heptane	Ethanol	22	298	0.0–1.0
2016 yue liu 0 [120]	OTHER	0.2	Heptane	Ethanol	66	293–318	0.0–1.0
1970 kon lya 1 [67]	BUBBLEP	0.3–0.4	Heptane	Benzene	27	293–333	0.0–1.0
1993 zho zhu 0 [121]	BUBBLEP	0.5–0.7	Heptane	Benzene	20	293–303	0.08–0.90
1970 lam ben 0 [58]	BUBBLEP	0.6–0.7	Cyclopentane	Benzene	9	298	0.11–0.90
1996 hei sch 0 [122]	CAPRISE	0.-0.2	R125	R143a	21	223–333	0.28–0.79
1999 oka shi 0 [123]	CAPRISE	0.2	R125	R143a	7	273–303	0.41
2001 fro wil 1 [124]	OTHER	0.2	R125	R143a	10	243–333	0.41
1996 hei sch 0 [122]	CAPRISE	0–0.2	R125	R32	8	223–333	0.27–0.77
1999 oka shi 0 [123]	CAPRISE	0.2	R125	R32	18	273–313	0.31–0.35
2003 dua lin 0 [125]	CAPRISE	0.2	R125	R32	236	253–333	0.18–0.58
1996 hei sch 0 [122]	CAPRISE	0.1–0.2	R125	R152a	21	223–333	0.16–0.69
2009 bi zha 1 [126]	CAPRISE	0.4	R125	R152a	54	243–328	0.06–0.19
1996 hei sch 0 [122]	CAPRISE	0–0.2	R125	R134a	21	223–333	0.24–0.75
1996 hei sch 0 [122]	CAPRISE	0.1–0.2	R143a	R134a	21	223–333	0.23–0.72
2004 lin dua 0 [127]	CAPRISE	0.2	R143a	R134a	105	257–329	0.29–0.79
2003 lin dua 2 [128]	CAPRISE	0.1	R143a	R227ea	241	253–333	0.39–0.85
2016 yue liu 0 [120]	OTHER	0.2	Isooctane	Ethanol	44	288–318	0.0–1.0
1964 eva cle 0 [101]	BUBBLEP	0.2–0.3	Isooctane	Benzene	9	303	0.0–1.0
2015 zha li 3 [129]	DROPV	0.2	Isooctane	Methylcyclohexane	44	293–308	0.0–1.0
2021 vak alw 0 [60]	RINGTE	0.5	Hexadecane	Benzene	44	298–313	0.0–1.0

Table 2 (continued)

Reference code	Method	Unc. ($mN \cdot m^{-1}$)	Fluid 1	Fluid 2	Npts	T range (K)	x_1 range
2018 pra mun 0 [103]	DROPSH	0.3	Hexadecane	Methylcyclohexane	9	293	0.1–0.90
1969 mye cle 0 [130]	BUBBLEP	0.2–0.3	Hexadecane	D4	9	303	0.0–1.0
1929 ham and 0 [56]	CAPRISE	0.1–0.2	Diethyl ether	Benzene	4	298	0.24–1.0
1965 spr pra 1 [131]	CAPRISE	0.2	Carbon monoxide	Nitrogen	10	84	0.0–1.0
1970 kon lya 1 [67]	BUBBLEP	0.3	Ethanol	Methanol	39	293–333	0.0–1.0
1929 ham and 0 [56]	CAPRISE	0.1	Ethanol	Acetone	5	298	0.0–1.0
1902 ram ast 0 [132]	CAPRISE	0.2–0.8	Ethanol	Benzene	39	283–351	0.0–1.0
1907 rit & 0 [133]	UNKN	0.1	Ethanol	Benzene	5	298	0.0–1.0
1917 mor sca 0 [134]	UNKN	0.1–0.2	Ethanol	Benzene	13	298–318	0.0–1.0
1929 ham and 0 [56]	CAPRISE	0.1–0.2	Ethanol	Benzene	4	298	0.42–1.0
1935 tri & 0 [79]	UNKN	0.1	Ethanol	Benzene	8	295	0.0–1.0
1974 mye cle 0 [62]	BUBBLEP	0.3	Ethanol	Benzene	7	303	0.0–1.0
1885 tra & 0 [135]	UNKN	0.1	Ethanol	Water	7	288	0.01–1.0
1903 des & 0 [136]	UNKN	0.2–0.7	Ethanol	Water	11	288	0.0–1.0
1913 mor nei 0 [137]	DROPW	0.1–0.5	Ethanol	Water	36	273–303	0.0–1.0
1922 bir & 0 [138]	DROPW	0.3–0.6	Ethanol	Water	15	298	0.0–1.0
1936 ern wat 0 [139]	CAPRISE	0.1–0.2	Ethanol	Water	9	298	0.04–0.78
1937 val hoh 0 [140]	UNKN	0.1–0.5	Ethanol	Water	44	293–323	0.0–0.88
1940 bon bym [141]	CAPRISE	0.2–0.5	Ethanol	Water	42	293–362	0.01–0.83
1950 sta guy 0 [142]	RINGTE	1	Ethanol	Water	11	298	0.0–0.85
1951 tei gor 0 [143]	BUBBLEP	0.2–0.8	Ethanol	Water	200	263–333	0.0–1.0
1968 efr & 1 [144]	BUBBLEP	0.5–1.4	Ethanol	Water	54	283–333	0.02–1.0
1986 wan jey 0 [145]	RINGTE	0.5–1.2	Ethanol	Water	5	303	0.0–1.0
1988 kal bid 0 [146]	BUBBLEP	0.2–0.4	Ethanol	Water	12	351–369	0.01–0.90
1995 vaz alv 0 [147]	RINGTE	0.3–0.9	Ethanol	Water	98	293–323	0.0–1.0
2005 bel her 0 [148]	DROPW	0.2–0.3	Ethanol	Water	11	298	0.0–1.0

Table 2 (continued)

Reference code	Method	Unc. ($mN \cdot m^{-1}$)	Fluid 1	Fluid 2	Npts	T range (K)	x_1 range
2009 max & 0 [149]	DROPV	0.2–0.3	Ethanol	Water	13	298	0.0–1.0
2016 lud kus 0 [150]	BUBBLEP	0.3	Ethanol	Water	1	293	0.04
2018 gon pal 0 [151]	RINGTE	2	Ethanol	Water	6	298	0.27–0.60
2019 raz hal 0 [152]	RINGTE	0.5–0.9	Ethanol	Water	10	298–313	0.0–0.09
2020 gon pan 0 [153]	OTHER	0.4	Ethanol	Water	4	298	0.28–0.61
2020 kho rah 0 [154]	DROPSH	0.8	Ethanol	Water	10	298	0.0–0.002
2021 gom nav [155]	OTHER	0.3	Ethanol	Water	16	293–323	0.04–0.16
2012 bag ami 0 [156]	RINGTE	0.5–1.0	Ethanol	Heavy water	84	288–318	0.001–0.86
2004 ouy lu 3 [47]	DROPSH	0.3	Ethanol	*o*-Xylene	11	298	0.0–1.0
1974 mye cle 0 [62]	BUBBLEP	0.3	Ethanol	Methylcyclohexane	10	303	0.0–1.0
2003 azi hem 0 [157]	RINGTE	0.3–0.7	Ethanol	Ethylene glycol	56	293–323	0.0–1.0
1973 cam kar 0 [158]	UNKN	0.7	Methanol	Acetone	12	298	0.0–1.0
1982 sin lar 0 [64]	CAPRISE	0.1	Methanol	Acetone	8	308	0.0–1.0
1917 mor sca 0 [134]	UNKN	0.2	Methanol	Benzene	14	273–303	0.0–1.0
1933 sha muk 0 [63]	DROPW	0.9–1.1	Methanol	Benzene	5	298	0.1–0.9
1885 tra & 0 [135]	UNKN	0.1	Methanol	Water	6	288	0.01–1.0
1913 mor nei 0 [137]	DROPW	0.5–0.6	Methanol	Water	26	273–303	0.0–1.0
1937 val hoh 0 [140]	UNKN	0.1–0.4	Methanol	Water	31	291–323	0.05–1.0
1951 tei gor 0 [143]	BUBBLEP	0.2–0.7	Methanol	Water	110	263–323	0.0–1.0
1958 uch mat 0 [159]	OTHER	0.5–1.8	Methanol	Water	76	303–363	0.0–1.0
1968 efr & 1 [144]	CAPRISE	0.5–1.0	Methanol	Water	30	283–333	0.17–1.0
1988 kal bid 0 [146]	BUBBLEP	0.3–0.5	Methanol	Water	11	339–356	0.17–0.95
1995 vaz alv 0 [147]	RINGTE	0.3–0.9	Methanol	Water	98	293–323	0.0–1.0
2009 max & 0 [149]	DROPV	0.2–0.3	Methanol	Water	13	298	0.0–1.0
2012 bag ami 0 [156]	RINGTE	0.5–0.9	Methanol	Heavy water	64	288–318	0.00–0.82
1929 ham and 0 [56]	CAPRISE	0.1–0.2	Acetone	Benzene	5	298	0.30–1.0

Table 2 (continued)

Reference code	Method	Unc. ($mN \cdot m^{-1}$)	Fluid 1	Fluid 2	Npts	T range (K)	x_1 range
1970 shi & 1 [160]	CAPRISE	4.7–5.7	Acetone	Benzene	10	298	0.0–1.0
1988 ron lu 0 [161]	BUBBLEP	0.6–0.7	Acetone	Benzene	18	303	0.0–1.0
1917 mor sca 0 [134]	UNKN	0.2–0.3	Acetone	Water	78	273–318	0.0–1.0
1932 ern lit 0 [162]	CAPRISE	0.2	Acetone	Water	9	298	0.03–0.74
1951 tei gan 0 [163]	BUBBLEP	0.2–0.6	Acetone	Water	81	273–313	0.0–1.0
1957 how mca [164]	CAPRISE	0.1–0.4	Acetone	Water	81	288–343	0.0–1.0
1970 kon lya 1 [67]	BUBBLEP	0.3–0.9	Acetone	Water	17	293	0.0–1.0
1976 tor pog 0 [165]	BUBBLEP	0.2–0.5	Acetone	Water	48	298–343	0.0–1.0
1988 ron lu 0 [161]	BUBBLEP	0.6–1.9	Acetone	Water	19	303	0.0–1.0
2007 end kah 0 [66]	DROPSH	0.3–0.7	Acetone	Water	70	288–328	0.0–1.0
2004 ouy yan 0 [49]	DROPSH	0.3	Acetone	*o*-Xylene	8	298	0.10–0.80
1970 lam ben 0 [58]	BUBBLEP	0.8	Benzene	*o*-Xylene	8	298	0.10–0.79
2013 bai kav 0 [166]	CAPRISE	0.1–1.7	Methane	Ethane	70	93–283	0.0–1.0
2017 sen hug 0 [167]	CAPRISE	0.7	Methane	Propane	27	272–303	0.0–0.55
1960 bla & 0 [168]	CAPRISE	0.3–0.5	Methane	Nitrogen	33	76–90	0.29–0.91
1965 spr pra 1 [131]	CAPRISE	0.2–0.5	Methane	Nitrogen	12	91	0.0–1.0
1966 fuk bel 0 [169]	CAPRISE	0.1–0.6	Methane	Krypton	35	110–118	0.18–0.67
1960 bla & 0 [168]	CAPRISE	0.4–0.6	Methane	Argon	28	84–111	0.29–1.0
2009 tan hig 2 [170]	CAPRISE	0.4	Propane	R32	99	280–300	0.00–1.00
2010 zha bi 0 [171]	CAPRISE	0.2	Propane	R152a	51	248–328	0.27–0.59
1996 hei sch 0 [122]	CAPRISE	0.1–0.2	R32	R134a	17	223–333	0.23–0.72
2003 yua hon 0 [172]	CAPRISE	0.2	R32	R134a	300	254–334	0.35–0.86
2021 liu kon 0 [173]	CAPRISE	0.2–0.3	R32	R1123	37	266–307	0.48–0.87
2005 lin dua 0 [174]	CAPRISE	0.3	R32	R227ea	412	252–334	0.54–0.90
2016 cui bi 0 [175]	SLS	0.1	R32	R1234yf	24	293–348	0.52–1.0
2021 liu kon 0 [173]	CAPRISE	0.1–0.2	R32	R1234yf	36	267–333	0.27–0.89

Table 2 (continued)

Reference code	Method	Unc. ($mN \cdot m^{-1}$)	Fluid 1	Fluid 2	Npts	T range (K)	x_1 range
2013 tan hig 0 [176]	CAPRISE	0.6	R32	R1234ze(E)	26	273–323	0.69
2016 cui bi 0 [175]	SLS	0.1	R32	R1234ze(E)	26	293–348	0.30–1.0
1996 hei sch 0 [122]	CAPRISE	0.1–0.2	R152a	R134a	21	223–333	0.24–0.71
1969 ano & 2 [177]	OTHER	1.0	R22	R115	1	298	0.63
1959 bla rud 0 [178]	CAPRISE	0.3–0.6	Nitrogen	Oxygen	34	61–88	0.1–0.9
1994 ost ost 1 [179]	CAPRISE	0.3–0.5	Nitrogen	Oxygen	88	55–78	0.0–1.0
2008 bai kav 0 [180]	CAPRISE	0.1–0.2	Nitrogen	Oxygen	61	80–132	0.0–1.0
2006 kav and 0 [181]	CAPRISE	0.05–1.3	Helium	Argon	33	108–140	0.0–0.01
2006 kav and 0 [181]	CAPRISE	0.05–0.2	Neon	Argon	27	111–140	0.0–0.04
2004 bai kav 0 [182]	CAPRISE	0.1–0.3	Nitrogen	Helium	38	90–118	0.97–1.0
1960 bla & 0 [168]	CAPRISE	0.3–0.4	Nitrogen	Argon	21	69–86	0.02–0.7
1965 spr pra 1 [131]	CAPRISE	0.2–0.3	Nitrogen	Argon	19	84	0.0–1.0
1946 cle & 0 [183]	RINGTE	1	Water	Ethylene glycol	2	298	0.0–1.0
1971 nak mat 0 [184]	CAPRISE	0.3	Water	Ethylene glycol	18	303	0.0–1.0
1981 won chu [185]	RINGTE	1–1.2	Water	Ethylene glycol	4	298	0.8–1.0
1991 hok che 0 [186]	BUBBLEP	0.4–0.6	Water	Ethylene glycol	174	295–471	0.0–0.95
1996 hor fuk 0 [187]	CAPRISE	0.5–0.8	Water	Ethylene glycol	44	253–298	0.0–1.0
1998 tsi mol 0 [188]	RINGTE	1.6–2.4	Water	Ethylene glycol	64	283–323	0.0–1.0
2004 hab hov 0 [189]	RINGTE	1.4–2.0	Water	Ethylene glycol	15	298	0.80–0.99
2008 zha zha 2 [190]	DROPV	1.1–1.4	Water	Ethylene glycol	48	308–323	0.0–1.0
2011 raf bag 0 [191]	RINGTE	0.6–0.9	Water	Ethylene glycol	54	283–308	0.10–0.99
2014 tiw son 0 [192]	OTHER	0.4	Water	Ethylene glycol	4	298	0.88–1.0
1959 bla rud 0 [178]	BUBBLEP	0.4–1.0	Oxygen	Argon	28	69–88	0.19–0.9
1965 saj oku 0 [193]	RINGTE	0.3	Oxygen	Argon	36	79–88	0.0–1.0
2016 bi cui 0 [194]	SLS	0.1	R134a	R1234yf	23	293–363	0.32–0.81
2016 bi cui 0 [194]	SLS	0.1	R134a	R1234ze(E)	9	293–369	0.44

Table 2 (continued)

Reference code	Method	Unc. ($mN \cdot m^{-1}$)	Fluid 1	Fluid 2	Npts	T range (K)	x_1 range
1958 wat van 0 [195]	RINGTE	0.5	D4	MD4M	2	293	0.39–0.78
1958 wat van 0 [195]	RINGTE	0.5	D4	MD2M	3	293	0.3–0.7
1987 nad & 0 [196]	UNKN	0–0.4	Krypton	Argon	60	120–200	0.0–1.0
1994 sul bai 0 [197]	CAPRISE	0.1–0.8	Krypton	Argon	40	120–193	0.0–1.0
1958 wat van 0 [195]	RINGTE	0.5	MD4M	D5	3	293	0.26–0.66
1958 wat van 0 [195]	RINGTE	0.5	MD3M	D5	1	293	0.5
2021 liu kon 0 [173]	CAPRISE	0.2	R1123	R1234yf	39	234–312	0.11–0.73

BUBBLEP maximum bubble pressure; *CAPRISE* capillary rise; *DROPSH* pendant drop shape; *DROPV* drop volume; *DROPW* drop weight; *OTHER* other; *RINGTE* ring tensiometer; *SLS* surface light scattering; *UNKN* unknown

the average absolute deviation, AAD = $(\sum | \sigma_{calc} - \sigma_{exp} |)/n$, expressed in mN·m^{-1}, and AADMAX is the maximum value of the AAD. We do not include in the statistics any points where the REFPROP program had convergence errors. Since the surface tension is zero at the critical point, some points near the critical region may have unusually large percentage deviations and it is more informative to examine the absolute deviation instead. Detailed results for each data set listed in Table 2 are presented in the supplemental information in Appendix B, Table B1. The data are also provided in the supplemental information. Here we will discuss the results in terms of chemical families.

4.1 Mixtures with *n*-Alkanes

Table 3 summarizes the results for mixtures with *n*-alkanes, presenting results both for binary interaction parameters set to zero and for fitted binary interaction parameters. Figure 1 displays these results graphically. The mixtures considered in this section contain *n*-alkanes mixed only with nonpolar fluids (branched alkanes, naphthenes, cryogens, and CO_2) except for four mixtures with polar aprotic fluids dimethyl ether, acetone, dimethyl carbonate, and octamethylcyclotetrasiloxane (D4). Excluded from these results are mixtures of *n*-alkanes with hydrogen bonding fluids, aromatics, or halocarbons; these mixtures are treated separately in later sections. The results in Table 3 are arranged by mixture classes.

Overall, Fig. 1 and Table 3 show that without the use of binary interaction parameters, non-polar mixtures such as linear and branched alkanes, and linear and branched alkanes with naphthenes have average absolute percentage deviations of about 3 % or less. The propane/dimethyl ether mixture and the cyclohexane/acetone mixture also are represented very well without an interaction parameter. Mixtures of linear alkanes show increasing deviations as the mixtures become more asymmetric with respect to size, as has been discussed previously [199]. Figure 2 shows that the deviations of the parachor model for a series of mixtures of components of varying chain lengths (pentane, heptane, decane, and dodecane). Note that the full citations for the reference codes used in the figures are given in Table 2. The pentane/hexadecane mixture has the largest size difference, and the largest deviation, reaching 2.5 mN·m^{-1}, and this deviation can be reduced with the use of a fitted binary interaction parameter to 1 mN·m^{-1} indicating that even mixtures of linear alkanes that only have size differences can benefit from the use of a binary interaction parameter. The temperatures of the data covered 293 K to 598 K, the details for each data set are given in Table 2. Although we used a simple constant binary interaction parameter, Hugill and Van Welsenes [16] and Gasem *et al.* [200] pointed out that the binary interaction parameters are temperature dependent, and introducing temperature dependence in the interaction parameters could further reduce the deviations.

Mixtures of n-alkanes with dimethyl carbonate and hexadecane with a siloxane have larger deviations with the maximum absolute deviation of approximately 2 mN·m^{-1}, and although the use of an interaction parameter can reduce the deviations, the parachor model does not perform quite as well for these systems (with a max AD of ~ 1 mN·m^{-1}) as it does for the *n*-alkane/*n*-alkane systems that often have max

Table 3 Summary of results for alkane mixtures

Mixture class	Fluids	Npts	$\delta_{ij}=0$			Fitted results			
			AAPD (%)	AAD (mN·m^{-1})	max AD (mN·m^{-1})	AAPD (%)	AAD (mN·m^{-1})	max AD (mN·m^{-1})	δ_{ij}
n-Alkane/*br*-alkane	Decane/isooctane	6	3.68	0.79	0.96	1.37	0.29	0.65	− 0.026
n-Alkane/*br*-alkane	Dodecane/isooctane	9	1.22	0.26	0.47	0.16	0.03	0.08	− 0.010
n-Alkane/*br*-alkane	Heptane/isooctane	59	1.32	0.24	0.41	0.53	0.10	0.33	− 0.010
n-Alkane/*br*-alkane	Octane/isooctane	55	1.41	0.27	0.38	0.46	0.09	0.33	− 0.010
n-Alkane/cryogen	Methane/argon	28	2.72	0.42	1.22	2.34	0.36	0.85	0.017
n-Alkane/cryogen	Methane/krypton	35	1.30	0.19	0.31	0.35	0.05	0.18	0.008
n-Alkane/cryogen	Methane/nitrogen	45	9.71	1.08	2.24	3.68	0.42	0.88	0.067
n-Alkane/ether	Propane/dimethyl ether	114	1.37	0.11	0.36	1.38	0.11	0.37	0.001
n-Alkane/*n*-alkane	Butane/methane	1	18.18	0.15	0.15	0.00	0.00	0.00	− 0.089
n-Alkane/*n*-alkane	Decane/docosane	19	6.23	1.51	2.00	0.68	0.17	0.46	0.036
n-Alkane/*n*-alkane	Decane/heptane	25	1.86	0.39	0.61	0.90	0.19	0.61	− 0.012
n-Alkane/*n*-alkane	Decane/hexadecane	25	1.10	0.27	0.61	0.86	0.21	0.61	0.005
n-Alkane/*n*-alkane	Dodecane/hexadecane	36	3.04	0.40	0.92	2.86	0.28	0.74	0.011
n-Alkane/*n*-alkane	Heptane/docosane	12	5.72	1.27	2.13	2.03	0.49	1.70	0.030
n-Alkane/*n*-alkane	Heptane/hexadecane	66	2.22	0.50	0.91	0.98	0.22	0.91	0.015
n-Alkane/*n*-alkane	Hexane/dodecane	21	0.82	0.18	0.42	0.56	0.12	0.28	0.006
n-Alkane/*n*-alkane	Methane/ethane	70	8.05	0.56	2.47	3.29	0.19	1.70	0.074
n-Alkane/*n*-alkane	Methane/propane	27	5.69	0.12	0.24	5.67	0.12	0.24	− 0.001
n-Alkane/*n*-alkane	Pentane/heptane	99[a]	8.80	0.11	0.67	8.80	0.11	0.67	0.000
n-Alkane/*n*-alkane	Pentane/hexadecane	35	8.07	1.58	2.45	1.67	0.31	1.05	0.045
n-Alkane/*n*-alkane	Pentane/methane	7	54.34	1.35	1.70	10.43	0.16	0.36	0.227
n-Alkane/naphthene	Decane/cyclohexane	6	2.68	0.66	0.70	1.14	0.28	0.68	− 0.017
n-Alkane/naphthene	Dodecane/methylcyclohexane	9	2.52	0.62	0.88	0.46	0.11	0.37	− 0.018
n-Alkane/naphthene	Heptane/cyclohexane	55	1.44	0.30	0.64	0.56	0.12	0.35	0.011

Table 3 (continued)

Mixture class	Fluids	Npts	$\delta_{ij}=0$			Fitted results			
			AAPD (%)	AAD ($mN \cdot m^{-1}$)	max AD ($mN \cdot m^{-1}$)	AAPD (%)	AAD ($mN \cdot m^{-1}$)	max AD ($mN \cdot m^{-1}$)	δ_{ij}
n-Alkane/naphthene	Hexadecane/methylcyclohexane	9	0.67	0.18	0.57	0.72	0.19	0.54	0.002
n-Alkane/naphthene	Hexane/cyclohexane	27	0.96	0.20	0.54	0.75	0.16	0.54	0.007
n-Alkane/naphthene	Pentane/cyclohexane	7	2.02	0.42	0.62	0.45	0.09	0.16	0.013
n-Alkane/other	Butane/carbon dioxide	42[b]	28.99	0.38	1.18	20.98	0.17	0.67	− 0.178
n-Alkane/other	Hexane/carbon dioxide	5	28.23	2.62	5.28	1.37	0.15	0.33	0.186
n-Alkane/other	Decane/carbon dioxide	64	468.69	0.82	1.97	358.68	0.49	1.08	0.081
n-Alkane/other	Decane/DMC	11	3.40	0.78	1.62	2.04	0.47	0.91	0.023
n-Alkane/other	Octane/DMC	12	5.22	1.11	2.22	2.41	0.52	1.23	0.036
n-Alkane/siloxane	Hexadecane/D4	9	5.39	1.13	2.12	1.90	0.39	0.72	0.045
Naphthene/*br*-alkane	Cyclohexane/isooctane	126	1.38	0.27	0.68	0.60	0.12	0.68	0.010
Naphthene/*br*-alkane	Methylcyclohexane/isooctane	44	0.56	0.12	0.25	0.53	0.11	0.25	0.001
Naphthene/ketone	Cyclohexane/acetone	54	0.94	0.21	0.48	0.83	0.19	0.51	0.002

[a]Six points omitted from statistics due to REFPROP calculation problems

[b]Three points omitted from statistics due to REFPROP calculation problems

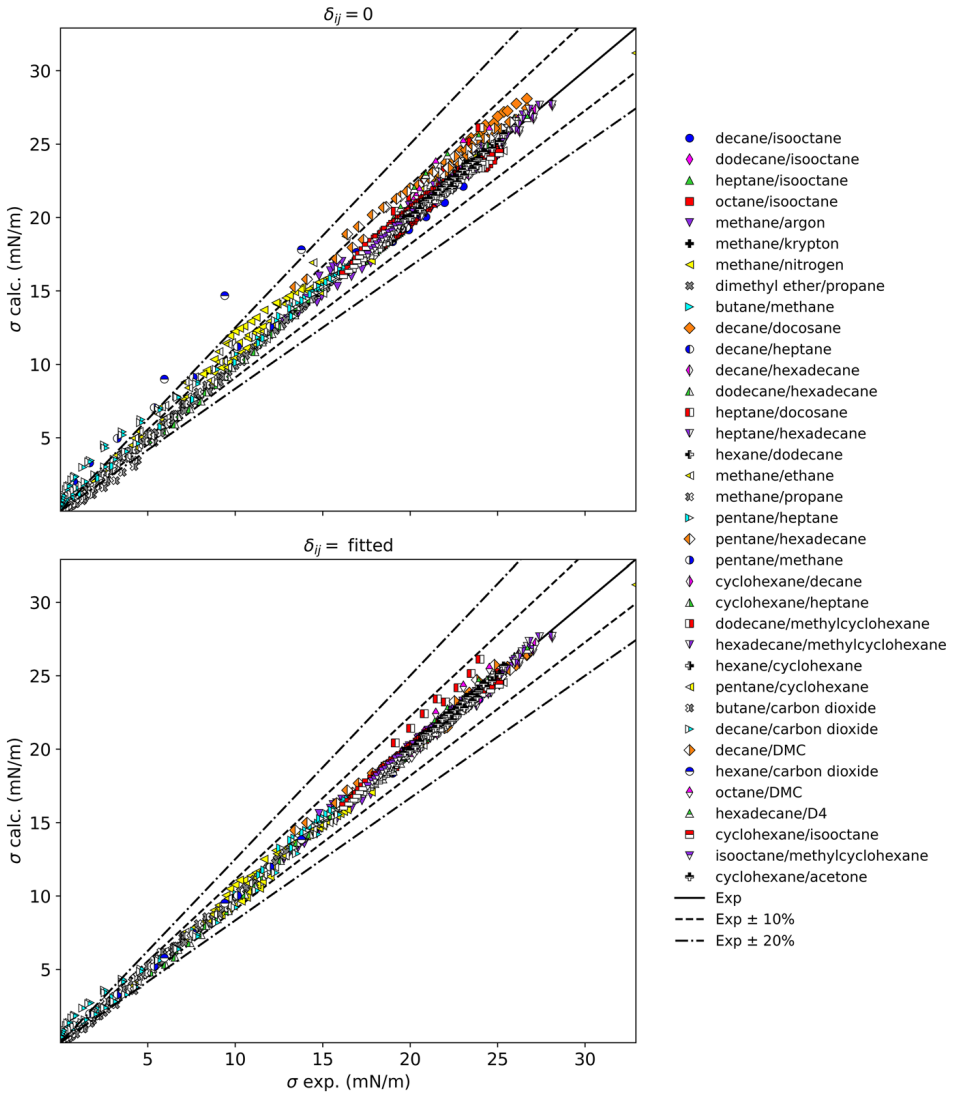

Fig. 1 Summary of results for mixtures with alkanes

AD of 0.7 mN·m^{-1} or less with an interaction parameter. There are three mixtures of methane with cryogens; methane/argon and methane/krypton were represented to within 3 % without an interaction parameter, but methane/nitrogen required a binary interaction parameter to achieve an AAPD of less than 4 %.

Finally, the parachor model without interaction parameters does not adequately capture the mixture composition behavior of *n*-alkanes with carbon dioxide, and an interaction parameter is needed. This is illustrated in Fig. 3. The temperatures of the data covered 303 K to 378 K, the details for each data set are given in Table 2. Similar to what is indicated in Fig. 2, Fig. 3 shows the largest deviations occur for systems with the largest size differences, with decane/CO_2 showing larger deviations

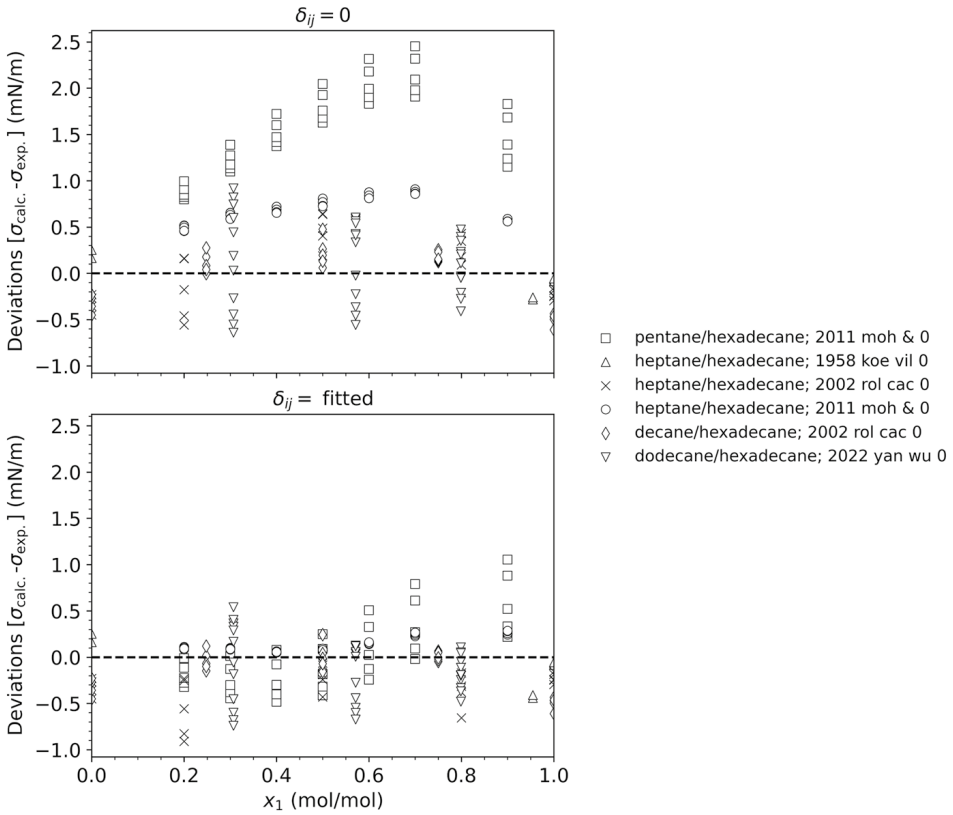

Fig. 2 Deviations between the model and experimental data for mixtures of a series of *n*-alkanes with hexadecane

than hexane/CO_2 and butane/CO_2. For the hexane/CO_2 mixture without interaction parameters, the AAPD is near 30 % but can be reduced to less than 2 % (0.3 $mN{\cdot}m^{-1}$) with a binary interaction parameter. Note that the percentage deviations for decane/CO_2 and butane/CO_2 are still large even with a binary interaction parameter, but this is because the data sets contain points approaching the critical region where the values of the surface tensions are small and the resulting percentage deviations are very large.

4.2 Mixtures with Alcohols

Table 4 summarizes the results for mixtures with alcohols, and Fig. 4 displays these results graphically. We include only mixtures with methanol and ethanol; larger alcohols are not presently available in REFPROP. This group of mixtures includes alcohols with a variety of fluid types [alcohols, *n*-alkanes, branched alkanes, amines, aromatics, glycols, ketones, naphthenes, and a fatty acid methyl ester (FAME)]. Mixtures with water are excluded and treated in Sect. 4.3. For the binary mixture of methanol and ethanol, the parachor method represents the

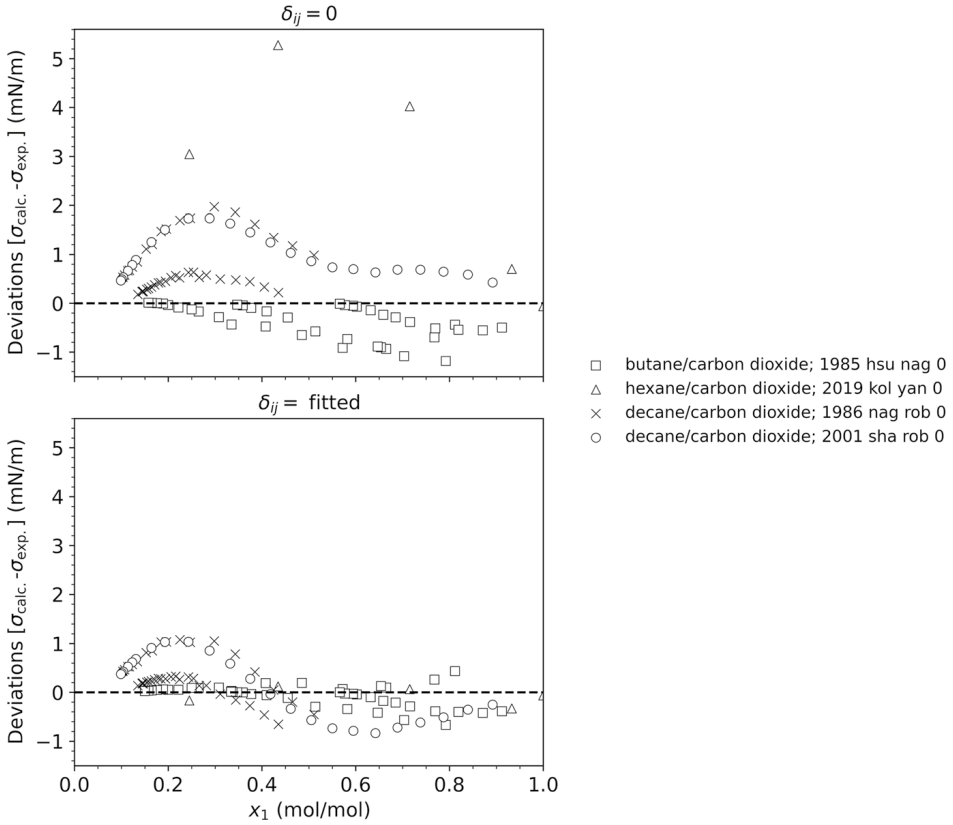

Fig. 3 Deviations between the model and experimental data for mixtures of a series of *n*-alkanes with carbon dioxide

surface tension to essentially within experimental uncertainty, and an interaction parameter is unnecessary. Similarly, mixtures of methanol and ethanol with acetone are represented very well without an interaction parameter. Mixtures of alcohols with aromatics and alcohols with linear alkanes have AAPD's without binary interaction parameters ranging from roughly 1 % to 5 %, which can be reduced to less than 3 % with binary interaction parameters. In Fig. 4, for mixtures without binary interaction parameters, mixtures of alcohols with the amines MEA and DEA, and with ethylene glycol show large deviations. Of the components in mixtures with methanol and ethanol, pure MEA, DEA, and ethylene glycol have the largest values of surface tension (approximately 45 $mN{\cdot}m^{-1}$ at 313 K) compared to less than about 27 $mN{\cdot}m^{-1}$ for the other fluids in Table 4, and approximately 21 $mN{\cdot}m^{-1}$ for pure methanol and ethanol. Maximum deviations can be as large as 7 $mN{\cdot}m^{-1}$ for the mixtures with these three fluids and the parachor model is not recommended without a binary interaction parameter. With a binary interaction parameter, the maximum deviations can be reduced to 1–2 $mN{\cdot}m^{-1}$.

Table 4 Summary of results for alcohol mixtures

Mixture class	Fluids	Npts	$\delta_{ij}=0$			Fitted results			
			AAPD (%)	AAD (mN·m^{-1})	max AD (mN·m^{-1})	AAPD (%)	AAD (mN·m^{-1})	max AD (mN·m^{-1})	δ_{ij}
Alcohol/alcohol	Ethanol/methanol	39	0.37	0.08	0.18	0.21	0.04	0.18	− 0.002
Alcohol/amine	Ethanol/DEA	13	4.78	1.47	3.67	1.83	0.64	1.44	0.046
Alcohol/amine	Ethanol/MEA	26	10.65	3.55	5.45	1.47	0.52	1.17	0.089
Alcohol/amine	Methanol/DEA	14	1.97	0.66	2.68	1.80	0.63	2.00	0.013
Alcohol/amine	Methanol/MEA	22	7.43	2.62	4.84	1.23	0.47	1.06	0.063
Alcohol/aromatic	Ethanol/benzene	76	2.71	0.64	1.59	1.53	0.36	1.16	0.020
Alcohol/aromatic	Ethanol/*m*-xylene	11	1.07	0.27	0.52	0.79	0.20	0.32	0.006
Alcohol/aromatic	Ethanol/*o*-xylene	11	0.83	0.21	0.45	0.56	0.15	0.21	0.005
Alcohol/aromatic	Ethanol/*p*-xylene	11	0.99	0.24	0.55	0.79	0.20	0.33	0.006
Alcohol/aromatic	Ethanol/toluene	15	2.60	0.60	2.25	2.95	0.69	1.90	0.015
Alcohol/aromatic	Methanol/benzene	19[a]	5.00	1.25	2.04	1.42	0.35	0.92	0.033
Alcohol/aromatic	Methanol/*p*-xylene	44	5.42	1.30	2.58	1.42	0.35	1.39	0.040
Alcohol/aromatic	Methanol/toluene	55	2.32	0.55	1.17	2.06	0.50	1.38	0.007
Alcohol/*br*-alkane	Ethanol/isooctane	44	0.86	0.16	0.45	0.66	0.13	0.32	− 0.005
Alcohol/FAME	Ethanol/methyl palmitate	1	8.08	1.80	1.80	0.00	0.00	0.00	0.089
Alcohol/glycol	Ethanol/ethylene glycol	56	11.44	3.26	7.09	1.67	0.47	1.40	0.100
Alcohol/ketone	Ethanol/acetone	5	1.08	0.25	0.56	0.82	0.19	0.36	− 0.008
Alcohol/ketone	Methanol/acetone	20	0.52	0.12	0.32	0.44	0.10	0.32	0.001
Alcohol/*n*-alkane	Ethanol/decane	32	0.88	0.19	0.53	0.76	0.16	0.40	0.004
Alcohol/*n*-alkane	Ethanol/dodecane	22	1.43	0.33	0.85	0.92	0.21	0.42	0.010
Alcohol/*n*-alkane	Ethanol/heptane	88	5.81	1.14	2.15	1.82	0.36	0.66	0.045
Alcohol/*n*-alkane	Ethanol/hexane	114	1.80	0.34	0.79	0.99	0.19	0.41	0.013
Alcohol/*n*-alkane	Ethanol/octane	48	1.14	0.23	0.77	0.78	0.16	0.61	0.008

Table 4 (continued)

Mixture class	Fluids	Npts	$\delta_{ij}=0$			Fitted results			
			AAPD (%)	AAD ($mN \cdot m^{-1}$)	max AD ($mN \cdot m^{-1}$)	AAPD (%)	AAD ($mN \cdot m^{-1}$)	max AD ($mN \cdot m^{-1}$)	δ_{ij}
Alcohol/*n*-alkane	Methanol/hexane	26	8.21	1.47	3.89	3.16	0.56	1.51	0.073
Alcohol/naphthene	Ethanol/cyclohexane	17	1.98	0.44	0.83	0.82	0.18	0.43	0.015
Alcohol/naphthene	Ethanol/methylcyclohexane	10	1.82	0.39	0.83	1.07	0.23	0.41	0.015

[a]One point omitted from statistics due to REFPROP calculation problems

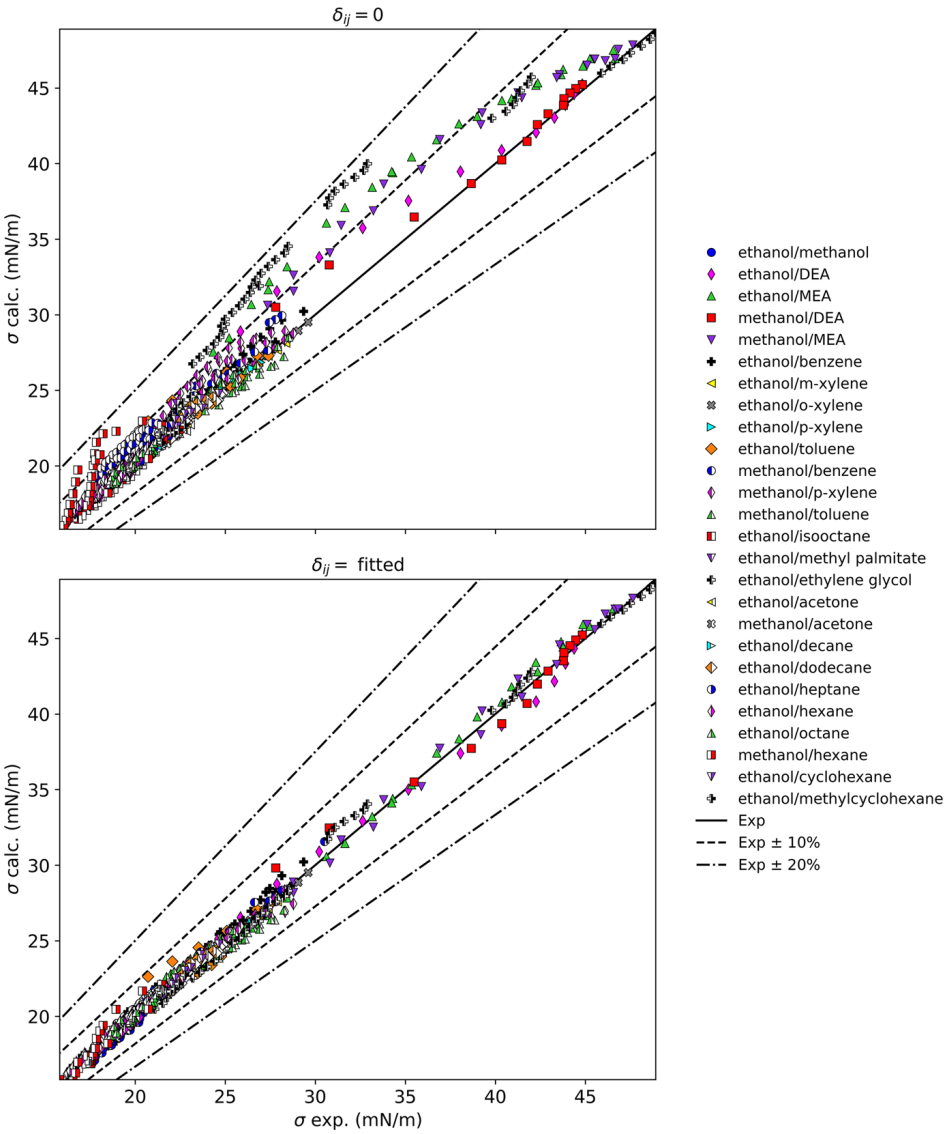

Fig. 4 Summary of results for mixtures with alcohols

4.3 Mixtures with Water

Table 5 summarizes the results for mixtures with water, and Fig. 5 displays these results graphically. The mixtures of water and heavy water with methanol and ethanol, and those with water and acetone show extremely large deviations, with a maximum AAD reaching 15–41 $mN \cdot m^{-1}$. The parachor model completely fails to represent the surface tension of these mixtures. The use of a single, constant binary interaction parameter somewhat reduces the magnitude of the deviations, but the model is still not very good with maximum deviations on the order of 5–13 $mN \cdot m^{-1}$.

Table 5 Summary of results for aqueous mixtures

Mixture class	Fluids	Npts	$\delta_{ij}=0$			Fitted results			
			AAPD (%)	AAD ($mN \cdot m^{-1}$)	max AD ($mN \cdot m^{-1}$)	AAPD (%)	AAD ($mN \cdot m^{-1}$)	max AD ($mN \cdot m^{-1}$)	δ_{ij}
Water/alcohol	Heavy water/ethanol	84	40.53	13.18	27.65	15.06	5.14	12.25	0.353
Water/alcohol	Heavy water/methanol	64	23.30	9.19	14.99	7.22	2.85	5.58	0.184
Water/alcohol	Water/ethanol	615	32.34	11.24	25.27	15.23	5.07	12.90	0.304
Water/alcohol	Water/methanol	401	18.62	7.14	16.73	5.48	2.04	5.42	0.164
Water/amine	Water/DEA	212	4.93	2.67	6.74	1.84	1.03	5.79	0.037
Water/amine	Water/MEA	273	5.41	3.05	7.10	2.30	1.32	4.13	0.041
Water/glycol	Water/ethylene glycol	427	4.91	2.77	7.18	2.03	1.11	4.40	0.041
Water/ketone	Water/acetone	403	55.44	18.90	40.51	14.90	5.33	12.96	0.433

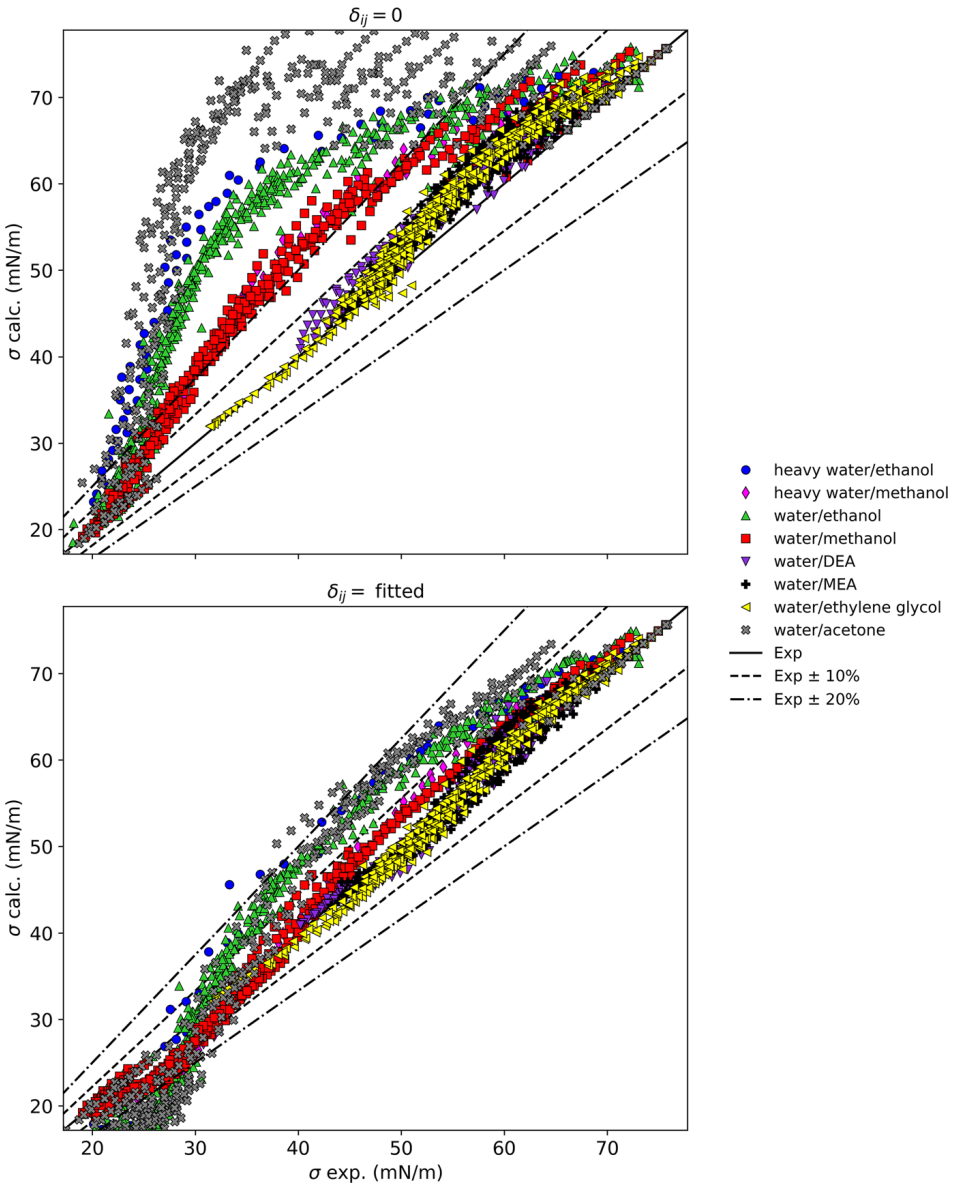

Fig. 5 Summary of results for aqueous mixtures

Without interaction parameters, all organic/aqueous mixtures investigated here show a common deviation pattern, where the deviations have an asymmetric shape with respect to composition, with a very rapid change as one nears the pure water end [8]. Water also has a very high surface tension (~70 mM·m^{-1} at 313 K) compared to other fluids. Figure 6, showing the percentage deviations of the acetone/water mixture as a function of composition, illustrates this pattern. The temperatures of the data covered 273 K to 343 K, the details for each data set are given in Table 2. One can see that although the use of an interaction parameter can somewhat reduce

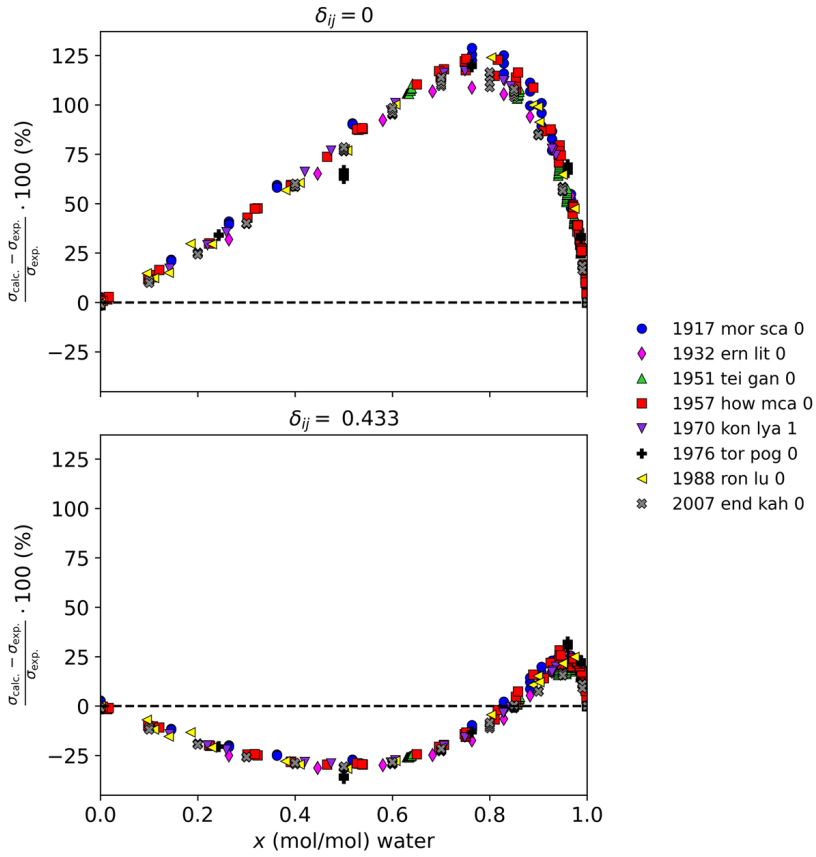

Fig. 6 Relative deviations as a function of composition of water for acetone/water mixture

the size of the deviations, it cannot properly reproduce the composition behavior. A small amount of the organic can greatly change the surface tension, and the parachor model does not have the ability to model this composition behavior. It is possible that a more complex, composition and temperature dependent interaction parameter could capture this behavior, but it is beyond the scope of this work.

4.4 Mixtures with Aromatics

Table 6 summarizes the results for mixtures with aromatics, and Fig. 7 displays these results graphically. With a fitted binary interaction parameter all mixtures show an AAPD below 5 % except for the mixture toluene/octane that has an AAPD of 5 %. Without interaction parameters some of the points exceed 10 % deviation. However, these points occur at relatively high temperatures (380 K to 400 K) where the magnitude of the deviation is not excessively large (AAD of less than 0.82 $mN \cdot m^{-1}$) but the percentage deviations are larger due to the smaller value of the surface tension at higher temperatures. Other systems with deviations of approximately 10 % without interaction parameters are *o*-xylene/acetone, and

Table 6 Summary of results for aromatic mixtures

Mixture class	Fluids	Npts	$\delta_{ij}=0$			Fitted results			
			AAPD (%)	AAD (mN·m^{-1})	max AD (mN·m^{-1})	AAPD (%)	AAD (mN·m^{-1})	max AD (mN·m^{-1})	δ_{ij}
Aromatic/aromatic	Benzene/*o*-xylene	8	1.33	0.38	0.52	0.32	0.09	0.15	0.008
Aromatic/aromatic	*m*-Xylene/benzene	5	2.80	0.82	2.33	1.80	0.54	2.33	0.010
Aromatic/aromatic	Toluene/benzene	27	1.05	0.28	0.99	1.30	0.34	0.76	0.005
Aromatic/*br*-alkane	Benzene/isooctane	9	5.39	1.13	1.81	0.48	0.10	0.35	0.041
Aromatic/ether	Benzene/diethyl ether	4	2.48	0.52	0.90	0.42	0.09	0.15	0.020
Aromatic/halocb	Benzene/chlorobenzene	23	1.22	0.36	1.04	1.06	0.31	0.73	0.008
Aromatic/halocb	Benzene/dichloroethane	13	3.85	1.05	1.74	2.09	0.57	1.74	0.021
Aromatic/halocb	*m*-Xylene/chlorobenzene	18	0.62	0.18	0.61	0.62	0.18	0.63	0.001
Aromatic/halocb	*o*-Xylene/chlorobenzene	18	0.73	0.22	0.42	0.23	0.07	0.15	0.005
Aromatic/halocb	*p*-Xylene/chlorobenzene	18	0.80	0.24	0.67	0.87	0.26	0.53	0.004
Aromatic/halocb	Toluene/chlorobenzene	6	3.35	0.97	1.16	0.59	0.17	0.28	0.021
Aromatic/ketone	Benzene/acetone	33	0.94	0.24	0.77	0.85	0.21	0.77	0.003
Aromatic/ketone	*m*-Xylene/acetone	9	2.14	0.56	1.02	0.76	0.20	0.74	− 0.013
Aromatic/ketone	*o*-Xylene/acetone	8	8.78	2.39	3.16	1.06	0.29	0.62	− 0.062
Aromatic/ketone	*p*-Xylene/acetone	9	1.36	0.35	0.91	0.85	0.22	0.75	− 0.008
Aromatic/ketone	Toluene/acetone	110	1.10	0.27	0.83	0.84	0.20	0.71	0.007
Aromatic/*n*-alkane	Benzene/dodecane	23	6.71	1.65	3.15	0.95	0.24	0.64	0.060
Aromatic/*n*-alkane	Benzene/heptane	47	1.57	0.35	1.16	1.02	0.22	0.87	0.012
Aromatic/*n*-alkane	Benzene/hexadecane	44	1.08	0.28	0.69	1.01	0.26	0.55	0.005
Aromatic/*n*-alkane	Benzene/hexane	31	1.86	0.41	1.08	1.20	0.26	0.73	0.015
Aromatic/*n*-alkane	Benzene/nonane	44	1.52	0.35	0.77	0.57	0.14	0.34	0.012
Aromatic/*n*-alkane	Benzene/pentane	7	7.62	1.61	2.33	2.04	0.44	0.81	0.051
Aromatic/*n*-alkane	Ethylbenzene/hexadecane	9	3.63	1.01	1.58	0.45	0.12	0.27	0.026

Table 6 (continued)

Mixture class	Fluids	Npts	$\delta_{ij}=0$			Fitted results			
			AAPD (%)	AAD ($mN \cdot m^{-1}$)	max AD ($mN \cdot m^{-1}$)	AAPD (%)	AAD ($mN \cdot m^{-1}$)	max AD ($mN \cdot m^{-1}$)	δ_{ij}
Aromatic/*n*-alkane	*m*-Xylene/heptane	11	2.31	0.54	0.89	0.13	0.03	0.11	0.019
Aromatic/*n*-alkane	*m*-Xylene/hexane	29	3.00	0.68	1.30	0.87	0.19	0.35	0.024
Aromatic/*n*-alkane	*m*-Xylene/octane	11	2.33	0.57	0.98	0.16	0.04	0.07	0.020
Aromatic/*n*-alkane	*m*-Xylene/pentane	20	1.46	0.32	0.84	0.91	0.20	0.36	0.012
Aromatic/*n*-alkane	*o*-Xylene/decane	11	5.26	1.33	1.86	0.81	0.21	0.58	0.039
Aromatic/*n*-alkane	*o*-Xylene/nonane	11	4.59	1.14	1.68	0.92	0.23	0.52	0.034
Aromatic/*n*-alkane	*o*-Xylene/octane	11	4.83	1.17	1.73	1.09	0.27	0.84	0.037
Aromatic/*n*-alkane	*p*-Xylene/decane	22	4.68	1.12	1.51	0.67	0.17	0.49	0.031
Aromatic/*n*-alkane	*p*-Xylene/hexane	16	3.42	0.76	1.13	0.51	0.11	0.21	0.024
Aromatic/*n*-alkane	*p*-Xylene/octane	12	3.90	0.88	1.19	0.83	0.19	0.53	0.027
Aromatic/*n*-alkane	*p*-Xylene/pentane	7	3.30	0.68	0.89	0.97	0.20	0.51	0.019
Aromatic/*n*-alkane	Toluene/heptane	34	2.88	0.62	1.28	0.55	0.12	0.32	0.024
Aromatic/*n*-alkane	Toluene/hexadecane	52	1.80	0.47	1.06	0.84	0.22	0.82	0.013
Aromatic/*n*-alkane	Toluene/nonane	44	2.37	0.55	0.99	0.34	0.08	0.29	0.019
Aromatic/*n*-alkane	Toluene/octane	17	6.06	0.82	1.73	5.03	0.77	1.15	0.027
Aromatic/*n*-alkane	Toluene/pentane	8	8.31	1.72	2.24	0.91	0.18	0.30	0.050
Aromatic/naphthene	Benzene/cyclohexane	96	0.53	0.13	0.37	0.50	0.13	0.41	0.001
Aromatic/naphthene	Benzene/cyclopentane	9	1.63	0.40	0.54	0.22	0.06	0.14	0.011
Aromatic/naphthene	Ethylbenzene/cyclohexane	28	1.56	0.40	0.82	0.50	0.13	0.24	0.013
Aromatic/naphthene	*m*-Xylene/cyclohexane	28	1.38	0.35	0.70	0.36	0.09	0.31	0.011
Aromatic/naphthene	*o*-Xylene/cyclohexane	28	1.31	0.34	0.76	0.45	0.11	0.26	0.010
Aromatic/naphthene	*p*-Xylene/cyclohexane	28	1.13	0.29	0.56	0.31	0.08	0.23	0.009
Aromatic/naphthene	Toluene/cyclohexane	11	4.40	1.12	1.55	0.11	0.03	0.07	0.031

Table 6 (continued)

Mixture class	Fluids	Npts	$\delta_{ij} = 0$			Fitted results			
			AAPD (%)	AAD (mN·m^{-1})	max AD (mN·m^{-1})	AAPD (%)	AAD (mN·m^{-1})	max AD (mN·m^{-1})	δ_{ij}
Aromatic/naphthene	Toluene/cyclopentane	10	0.20	0.05	0.07	0.07	0.02	0.03	− 0.001
Aromatic/other	*p*-Xylene/dimethyl carbonate	10	2.39	0.62	1.09	0.72	0.19	0.42	− 0.019

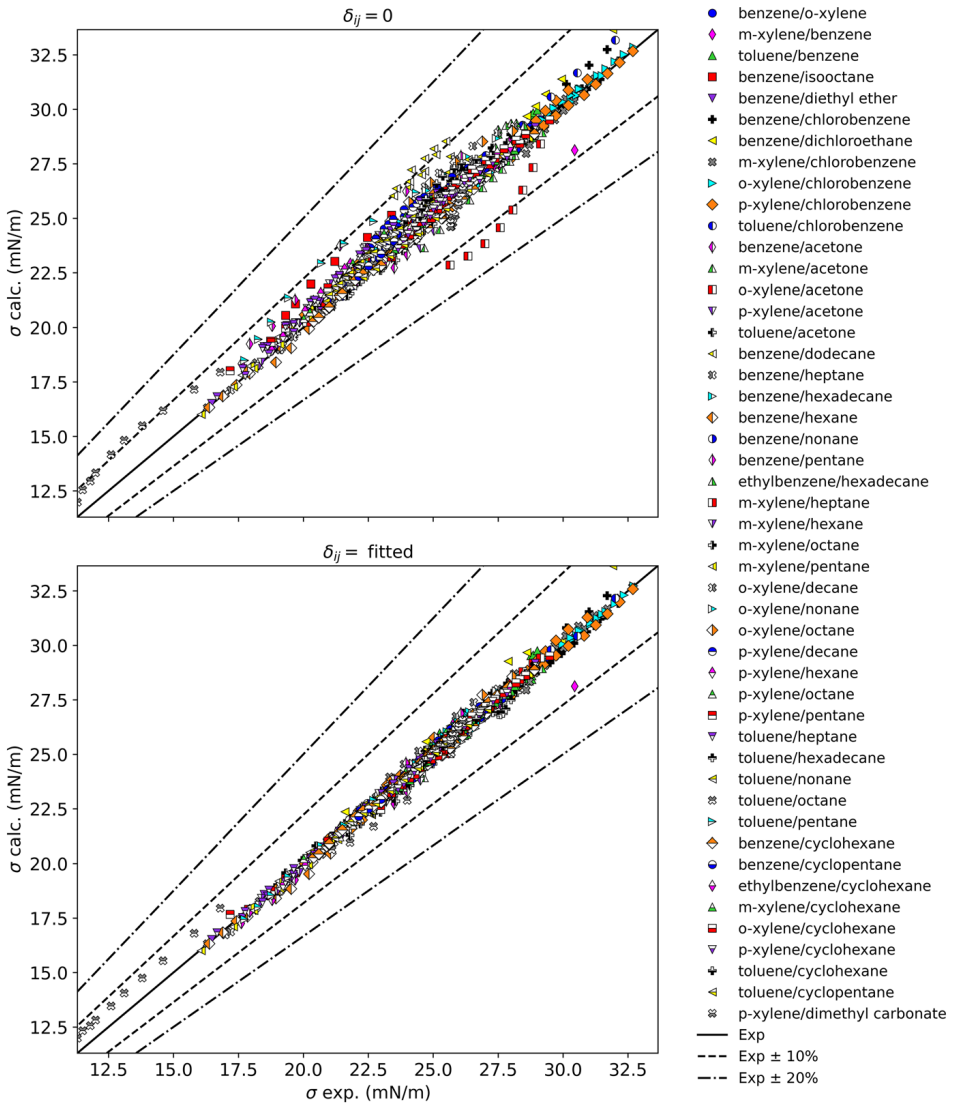

Fig. 7 Summary of results for mixtures with aromatics

some points in benzene/dodecane, toluene/pentane, and *m*-xylene/benzene. With interactions parameters the AADP in these systems, except *m*-xylene/benzene, can be reduced to 1 %. The *m*-xylene/benzene point with near 10 % deviation (for both fitted and non-fitted cases) is due to a pure fluid point for *m*-xylene (that we believe is flawed) from the 1929 data set of Hammick and Andrew [56]. In summary, when a fitted binary interaction parameter is used, the aromatic/alkane and aromatic/napthene mixtures have an AAPD of no greater than 1 %, however the deviations are a function of composition. With the use of a binary interaction parameter these mixtures can generally be represented to within 3 % over the entire composition range.

Table 7 Summary of results for halocarbon mixtures

Mixture class	Fluids	Npts	$\delta_{ij}=0$			Fitted results			
			AAPD (%)	AAD ($mN{\cdot}m^{-1}$)	max AD ($mN{\cdot}m^{-1}$)	AAPD (%)	AAD ($mN{\cdot}m^{-1}$)	max AD ($mN{\cdot}m^{-1}$)	δ_{ij}
Halocb/halocb	R1123/R1234yf	39	4.37	0.32	1.11	4.43	0.31	1.09	0.002
Halocb/halocb	R125/R134a	21	1.13	0.07	0.25	0.99	0.06	0.18	0.004
Halocb/halocb	R125/R143a	38	2.07	0.09	0.28	1.65	0.05	0.16	0.008
Halocb/halocb	R125/R152a	75	3.24	0.25	0.68	1.66	0.11	0.31	0.020
Halocb/halocb	R125/R32	262	1.87	0.07	0.38	1.81	0.05	0.50	0.004
Halocb/halocb	R134a/R1234yf	23	8.05	0.19	0.37	4.88	0.09	0.22	− 0.025
Halocb/halocb	R134a/R1234ze(E)	9	2.71	0.10	0.25	2.43	0.04	0.06	0.012
Halocb/halocb	R143a/R134a	126	1.73	0.11	0.69	1.96	0.12	0.61	0.002
Halocb/halocb	R143a/R227ea	241	3.57	0.17	0.31	1.89	0.08	0.21	− 0.013
Halocb/halocb	R152a/R134a	21	1.50	0.15	0.38	1.06	0.12	0.33	− 0.006
Halocb/halocb	R22/R115	1	29.91	2.39	2.39	0.00	0.00	0.00	− 0.196
Halocb/halocb	R32/R1123	37	4.24	0.27	0.56	2.29	0.14	0.41	− 0.021
Halocb/halocb	R32/R1234yf	60	7.65	0.23	0.47	6.24	0.18	0.43	− 0.017
Halocb/halocb	R32/R1234ze(E)	52	4.14	0.28	0.97	3.07	0.15	0.41	0.026
Halocb/halocb	R32/R134a	317	1.08	0.07	0.47	1.11	0.07	0.47	0.001
Halocb/halocb	R32/R227ea	412	3.90	0.19	0.43	2.58	0.12	0.36	− 0.012
Halocb/ketone	Chlorobenzene/acetone	1	6.36	1.69	1.69	0.00	0.00	0.00	− 0.036
Halocb/*n*-alkane	Chlorobenzene/pentane	7	3.04	0.63	0.91	1.20	0.27	0.42	0.017
Halocb/*n*-alkane	R152a/propane	51	10.61	0.87	1.09	3.54	0.25	0.60	− 0.050
Halocb/*n*-alkane	R32/propane	99	2.60	0.16	0.51	2.53	0.15	0.45	− 0.010
Halocb/*n*-alkane	RC318/butane	24	5.89	0.88	1.68	2.27	0.34	0.79	0.044
Halocb/naphthene	Chlorobenzene/cyclohexane	18	0.89	0.24	0.64	0.49	0.13	0.54	− 0.005

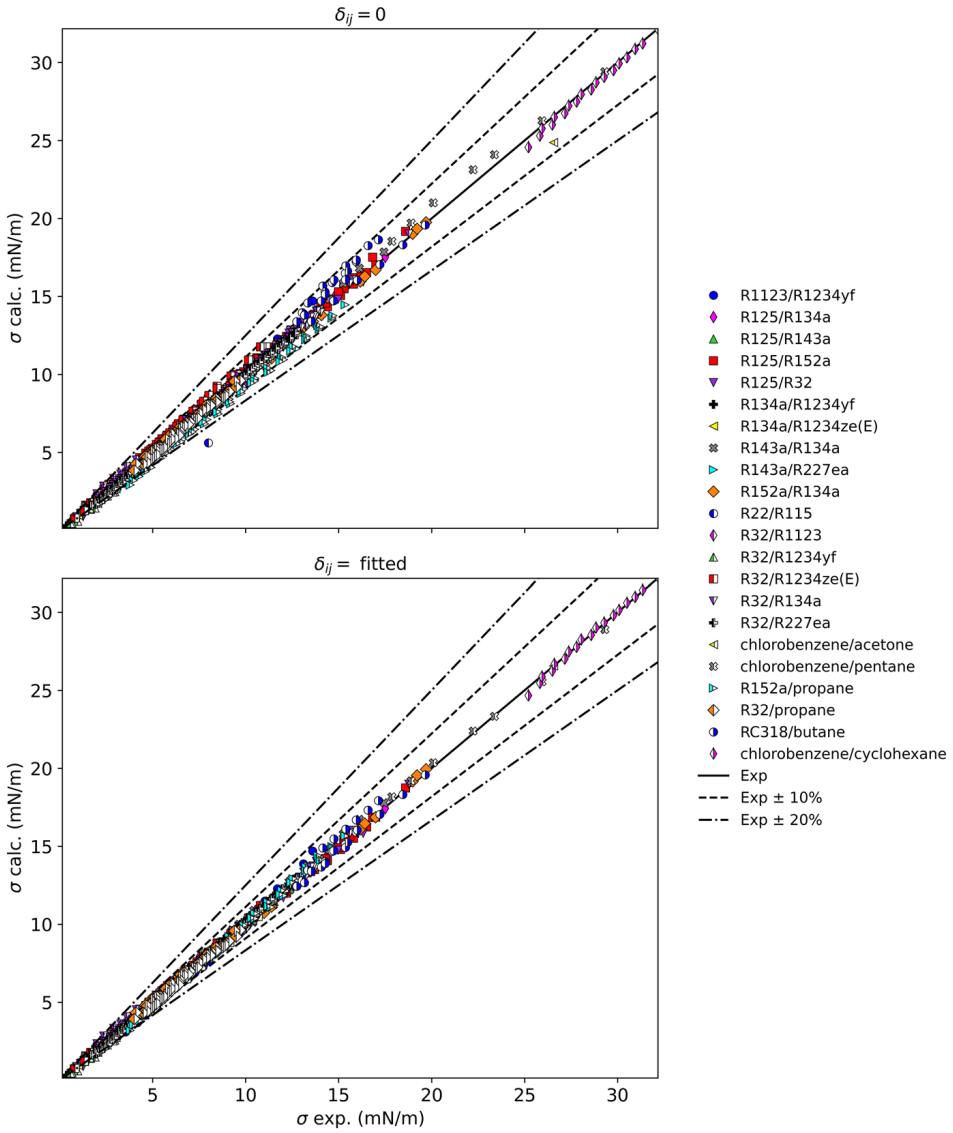

Fig. 8 Summary of results for halocarbon mixtures

4.5 Mixtures with Halocarbons

Table 7 summarizes the results for mixtures with halocarbons, and Fig. 8 displays these results graphically. Included are mixtures containing some of the new low-GWP fluids such as R1234yf and R1234ze(E) in addition to HFC's such as R32, R134a, R143a, R152a, and R125, and mixtures of polar halocarbons with nonpolar alkanes such as propane and butane. Without using an interaction parameter, almost all results are within 10 %, the AAPD's are generally less than 5 %. Exceptions are visible in Fig. 8; the single point for R22/R115 has

Table 8 Summary of results for miscellaneous mixtures

Mixture class	Fluids	Npts	$\delta_{ij}=0$			Fitted results			
			AAPD (%)	AAD (mN·m^{-1})	max AD (mN·m^{-1})	AAPD (%)	AAD (mN·m^{-1})	max AD (mN·m^{-1})	δ_{ij}
Cryogen/cryogen	Carbon monoxide/nitrogen	10	1.28	0.10	0.18	0.21	0.02	0.04	0.012
Cryogen/cryogen	Helium/argon	33[a]	13.08	0.25	0.69	13.08	0.25	0.69	0.000
Cryogen/cryogen	Hydrogen/argon	21	6.42	0.44	0.96	2.92	0.15	0.54	− 0.678
Cryogen/cryogen	Hydrogen/deuterium	67	4.98	0.13	0.30	2.65	0.07	0.19	− 0.033
Cryogen/cryogen	Krypton/argon	100[b]	4.92	0.24	1.35	4.92	0.24	1.35	0.000
Cryogen/cryogen	Neon/argon	27	7.82	0.22	1.47	8.13	0.23	1.46	0.048
Cryogen/cryogen	Nitrogen/argon	40	1.96	0.21	0.50	1.15	0.13	0.41	0.012
Cryogen/cryogen	Nitrogen/helium	38[c]	4.94	0.16	1.67	4.94	0.16	1.67	0.000
Cryogen/cryogen	Nitrogen/oxygen	183	5.41	0.68	2.41	3.31	0.33	1.26	0.055
Cryogen/cryogen	Oxygen/argon	64	0.48	0.07	0.19	0.48	0.07	0.19	0.001
Siloxane/siloxane	D4/MD2M	3	3.26	0.60	0.66	0.43	0.08	0.12	− 0.019
Siloxane/siloxane	D4/MD4M	2	7.35	1.40	1.43	0.28	0.05	0.06	− 0.047
Siloxane/siloxane	MD3M/D5	1	4.56	0.86	0.86	0.00	0.00	0.00	− 0.024
Siloxane/siloxane	MD4M/D5	3	6.55	1.25	1.39	0.02	0.00	0.01	− 0.039

[a] 14 points omitted from statistics due to REFPROP calculation problems

[b] 3 points omitted from statistics due to REFPROP calculation problems

[c] 15 points omitted from statistics due to REFPROP calculation problems

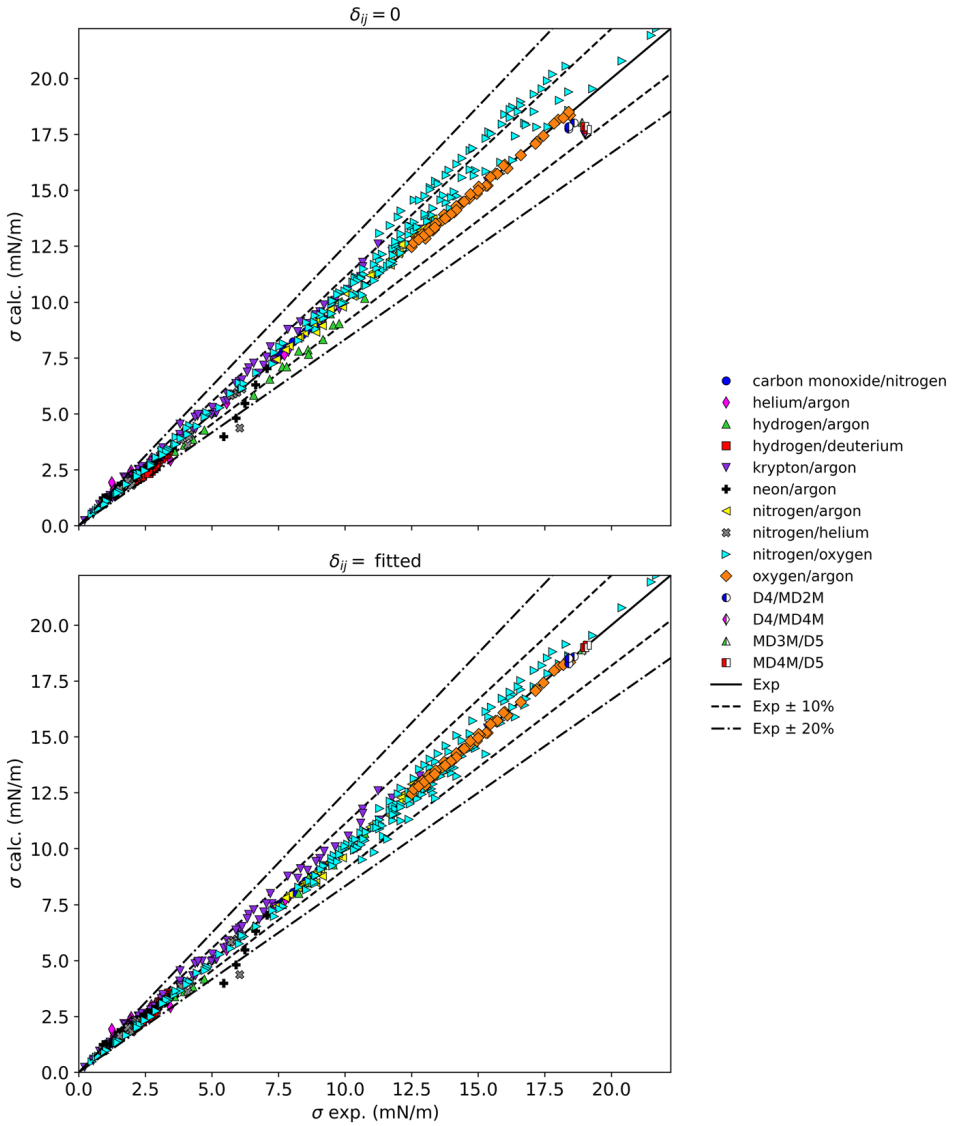

Fig. 9 Summary of results for mixtures with miscellaneous compounds

very large deviations; it is unclear why this mixture should deviate from the others. The mixture of R152a/propane also has deviations slightly greater than 10 % without an interaction parameter. It is unclear why R152a/propane should show this magnitude of deviation (AAPD 10.6 %), as a similar polar/nonpolar mixture of R32/propane displays smaller deviations (AAPD 2.6 %) without the use of an interaction parameter. The mixtures of halocarbons with other halocarbons without an interaction parameter have AAD of about 0.3 $mN \cdot m^{-1}$, while the mixtures of polar halocarbons with nonpolar alkanes have a higher AAD of up to 0.9

$mN \cdot m^{-1}$. The use of an interaction parameter improves the results, providing an AAD less than 0.35 $mN \cdot m^{-1}$ for both types of mixtures.

4.6 Mixtures with Miscellaneous Compounds

Table 8 summarizes the results for mixtures with miscellaneous compounds, and Fig. 9 displays these results graphically. The mixtures are either of cryogens with other cryogens, or siloxanes with siloxanes. All mixtures without interaction parameters except helium/argon show an AAPD of less than 10 %. As shown in Table 2, the helium/argon mixture data were obtained only for extremely dilute solutions of helium less than about a helium mole fraction of 0.01. Without more data over a larger composition range, it is difficult to assess the performance of the parachor model for the helium/argon system. In addition, there were convergence failures in REFPROP for the systems helium/argon, krypton/argon, and nitrogen/helium; points without convergence were not included in the statistics and binary interaction parameters were not determined for these systems. There also was an extremely limited composition range for neon/argon, hydrogen/argon, and nitrogen/helium so we cannot fully assess these systems either. The data for siloxane mixtures are very limited in the number of points, so it also is premature to assess these systems. For the cryogen/cryogen mixtures where there are a wide range of data, the parachor model appears to represent the data to within 10 % without interaction parameters, with AAPD's of less than 5 %.

5 Conclusions

We compiled a database for the surface tension of binary mixtures by extracting data from the NIST TDE database [34]. It contains a wide variety of fluids, covering the chemical classes water, alcohols, amines, ketones, linear and branched alkanes, naphthenes, aromatics, refrigerants, and cryogens. The data set includes 65 pure fluids and 154 binary pairs with a total of 8205 points. We used this database to test the performance of a parachor model for mixtures, in both a predictive mode (no mixture data used) and with a single, constant binary interaction parameter found by fitting the mixture data. The parachor model is not new and variants of it have been used for many years, but a comprehensive summary of its performance on a wide variety of mixtures has not been available until now. The data are available in the supporting information to enable model comparisons for future research on binary mixtures with new models. In general, the parachor model in a predictive mode without fitted interaction parameters can predict the surface tension of binary mixtures of non-polar fluids such as linear and branched alkanes, linear and branched alkanes with naphthenes, aromatics with aromatics, aromatics with naphthenes, and mixtures of linear alkanes of similar sizes with an AAPD of about 3 % or less. For mixtures of linear alkanes of differing sizes, as the size difference increases it is necessary to use a fitted binary interaction

parameter to reduce deviations. Similarly, in a predictive mode the model has large deviations for mixtures of *n*-alkanes with CO_2, and an interaction parameter should be used. Mixtures of methanol and ethanol did not require an interaction parameter. Polar mixtures of halocarbons with other halocarbons and also polar/nonpolar mixtures of alkanes with halocarbons could be modeled with an AAD of less than 0.35 $mN{\cdot}m^{-1}$ with the use of a binary interaction parameter for each pair of fluids. Future work on developing a predictive scheme for binary interaction parameters for classes of mixtures would make the parachor model more useful. Finally, the parachor model even with a fitted binary interaction parameter is not suitable for mixtures of water with organic compounds.

Supplementary Information The online version contains supplementary material available at https://doi.org/10.1007/s10765-023-03216-z.

Acknowledgements We thank Dr. Allan Harvey for helpful discussions.

Author contributions All authors participated in the writing and review of the manuscript. AML developed the python code used to perform the analysis and generate figures. VD provided the data.

Funding Open access funding provided by NTNU Norwegian University of Science and Technology (incl St. Olavs Hospital - Trondheim University Hospital). This work was partially funded by the National Institute of Standards and Technology. Additional support was provided by the NCCS Centre, performed under the Norwegian research programme Centres for Environment-friendly Energy Research (FME), funded by industry partners and the Research Council of Norway (257579).

Declarations

Conflict of interest The authors have no conflicts to declare.

References

1. M.P. Krafft, Adv. Drug Deliv. Rev. **47**, 209 (2001). https://doi.org/10.1016/S0169-409X(01)00107-7
2. A. Fathi Azarbayjani, A. Jouyban, S.Y. Chan, J. Pharm. Pharm. Sci. **12**, 218 (2009). https://doi.org/10.18433/j32p40
3. R. Nagata, C. Kondou, S. Koyama, Int. J. Refrig. **63**, 157 (2016). https://doi.org/10.1016/j.ijrefrig.2015.11.002
4. D. Jang, D. Kim, J. Moon, Langmuir **25**, 2629 (2009). https://doi.org/10.1021/la900059m
5. J.E. Fromm, IBM J. Res. Dev. **28**, 322 (1984). https://doi.org/10.1147/rd.283.0322
6. R.R. Mallepally, B.A. Bamgbade, A.J. Rowane, H.B. Rokni, M.S. Newkirk, M.A. McHugh, J. Supercrit. Fluids **134**, 33 (2018). https://doi.org/10.1016/j.supflu.2017.12.003
7. S. Sugden, J. Chem. Soc. **125**, 1177 (1924). https://doi.org/10.1039/ct9242501177

8. B.E. Poling, J.M. Prausnitz, J.P. O'Connell, *The Properties of Gases and Liquids*, 5th edn. (McGraw-HIll, New York, 2001)
9. J.W. Cahn, J.E. Hilliard, J. Chem. Phys. **28**, 258 (1958). https://doi.org/10.1063/1.1744102
10. X.D. Liang, M.L. Michelsen, G.M. Kontogeorgis, Fluid Phase Equilib. **428**, 153 (2016). https://doi.org/10.1016/j.fluid.2016.06.017
11. J.Z. Wu, AlChE J. **52**, 1169 (2006). https://doi.org/10.1002/aic.10713
12. J.L. Li, J. Ma, C.J. Peng, H.L. Liu, Y. Hu, J. Jiang, Ind. Eng. Chem. Res. **46**, 7267 (2007). https://doi.org/10.1021/ie070341m
13. S. Toxvaerd, J. Chem. Phys. **55**, 3116 (1971). https://doi.org/10.1063/1.1676556
14. S.E. Quinones-Cisneros, U.K. Deiters, R.E. Rozas, T. Kraska, J. Phys. Chem. B **113**, 3504 (2009). https://doi.org/10.1021/jp8073255
15. C.F. Weinaug, D.L. Katz, Ind. Eng. Chem. **35**, 239 (1943). https://doi.org/10.1021/ie50398a028
16. J.A. Hugill, A.J. Van Welsenes, Fluid Phase Equilib. **29**, 383 (1986). https://doi.org/10.1016/0378-3812(86)85038-5
17. T. Fechter, R. Villablanca, V. Leontijevic, A. Martin, P. Jaeger, M.J. Cocero, J. Supercrit. Fluids **196**, 105899 (2023). https://doi.org/10.1016/j.supflu.2023.105899
18. T.E. Daubert, *API Technical Databook* (American Petroleum Institute, Washington, DC, 1997)
19. D.B. Macleod, Trans. Faraday Soc. **19**, 38 (1923). https://doi.org/10.1039/TF9231900038
20. Y. Garrabos, F. Palencia, C. Lecioutre, D. Broseta, B. Le Neindre, Phys. Rev. E **76**, 061109 (2007). https://doi.org/10.1103/PhysRevE.76.061109
21. O.R. Quayle, Chem. Rev. **53**, 439 (1953). https://doi.org/10.1021/cr60166a003
22. V.P. Zhelezny, Y.V. Semenyuk, S.N. Ancherbak, N.V. Emel'yanenko, Russ. J. Phys. Chem. A **83**, 182 (2009). https://doi.org/10.1134/s0036024409020071
23. I. Cachadiña, A. Mulero, J. Tian, J. Phys. Chem. Ref. Data **44**, 023104 (2015). https://doi.org/10.1063/1.4921749
24. A. Mulero, I. Cachadiña, J. Phys. Chem. Ref. Data **43**, 023104 (2014). https://doi.org/10.1063/1.4878755
25. A. Mulero, I. Cachadiña, D. Bautista, J. Phys. Chem. Ref. Data **50**, 023104 (2021). https://doi.org/10.1063/5.0048675
26. A. Mulero, I. Cachadiña, M.I. Parra, J. Phys. Chem. Ref. Data **41**, 043105 (2012). https://doi.org/10.1063/1.4768782
27. A. Mulero, I. Cachadiña, E.L. Sanjuán, J. Phys. Chem. Ref. Data **44**, 033104 (2015). https://doi.org/10.1063/1.4927858
28. A. Mulero, I. Cachadiña, E.L. Sanjuán, J. Phys. Chem. Ref. Data **45**, 033105 (2016). https://doi.org/10.1063/1.4959989
29. A. Mulero, I. Cachadiña, A. Vegas, J. Phys. Chem. Ref. Data **50**, 033106 (2021). https://doi.org/10.1063/5.0061617
30. A. Mulero, I. Cachadiña, A. Vegas, J. Phys. Chem. Ref. Data **51**, 023102 (2022). https://doi.org/10.1063/5.0092546
31. A. Mulero, I. Cachadiña, A. Becerra, J. Phys. Chem. Ref. Data **52**, 013103 (2023). https://doi.org/10.1063/5.0139446
32. E.W. Lemmon, I.H. Bell, M.L. Huber, M.O. McLinden, *REFPROP, NIST Standard Reference Database 23,Version 10.0* (NIST, Standard Reference Data Program, Gaithersburg, 2018). https://doi.org/10.18434/T4/1502528
33. M.L. Huber, E.W. Lemmon, I.H. Bell, M.O. McLinden, Ind. Eng. Chem. Res. **61**, 15449 (2022). https://doi.org/10.1021/acs.iecr.2c01427
34. V. Diky, R.D. Chirico, M. Frenkel, A. Bazyleva, J.W. Magee, E. Paulechka, A. Kazakov, E.W. Lemmon, C.D. Muzny, A.Y. Smolyanitsky, S. Townsend, K. Kroenlein, *NIST ThermoData Engine, NIST Standard Reference Database 103a/103b, Version 10.4* (NIST, Standard Reference Data Program, Gaithersburg, 2019). https://www.nist.gov/mml/acmd/trc/thermodata-engine/srd-nist-tde-103b
35. C. Tropea, A.L. Yarin, J.F. Foss, *Springer Handbook of Experimental Fluid Mechanics* (Springer, Berlin, 2007)
36. V. Diky, R.D. Chirico, R.C. Wilhoit, Q. Dong, M. Frenkel, J. Chem. Inf. Comput. Sci. **43**, 15 (2003). https://doi.org/10.1021/ci025534t
37. M.L. Huber, *Models for Viscosity, Thermal Conductivity, and Surface Tension of Selected Pure Fluids as Implemented in REFPROP v10.0* (National Institute of Standards and Technology, NISTIR 8209, 2018). https://nvlpubs.nist.gov/nistpubs/ir/2018/NIST.IR.8209.pdf

38. International Association for the Properties of Water and Steam, Release on Surface Tension of Heavy Water Substance, IAPWS R5-85 (1994). http://www.iapws.org/relguide/surfd2o.pdf
39. International Association for the Properties of Water and Steam, Revised Release on Surface Tension of Ordinary Water Substance, IAPWS R1-76 (2014). http://www.iapws.org/relguide/Surf-H2O.html
40. D.V.S. Jain, S. Singh, Indian J. Chem. **12**, 714 (1974)
41. D.J.L. Prak, J.S. Cowart, A.M. McDaniel, P.C. Trulove, J. Chem. Eng. Data **59**, 3571 (2014). https://doi.org/10.1021/je500498m
42. M.S. Dhillon, B.S. Mahl, Z. Phys. Chem. (Leipzig) **259**, 249 (1978). https://doi.org/10.1515/zpch-1978-25933
43. B.S. Mahl, S.L. Chopra, P.P. Singh, Z. Phys. Chem. (Leipzig) **249**, 337 (1972)
44. M. Domínguez-Peréz, E. Rilo, L. Segade, C. Franjo, O. Cabeza, J. Chem. Eng. Data **55**, 1317 (2010). https://doi.org/10.1021/je900643r
45. A. Gayol, L.M. Casas, A.E. Andreatta, R.E. Martini, J.L. Legido, J. Chem. Eng. Data **58**, 758 (2013). https://doi.org/10.1021/je301282p
46. L. Mosteiro, L.M. Casás, J.L. Legido, J. Chem. Thermodyn. **41**, 695 (2009). https://doi.org/10.1016/j.jct.2008.12.010
47. G. Ouyang, G. Lu, Y. Yang, Z.Q. Huang, Acta Sci. Nat. Univ. Sunyatseni **43**, 44 (2004)
48. R.K. Wanchoo, J. Narayan, Phys. Chem. Liq. **25**, 15 (1992). https://doi.org/10.1080/00319109208027283
49. G. Ouyang, Y. Yang, S.S. Lu, Z.Q. Huang, B. Kang, J. Chem. Eng. Data **49**, 330 (2004). https://doi.org/10.1021/je0341763
50. J.C.G. Calado, I.A. McLure, V.A.M. Soares, Fluid Phase Equilib. **2**, 199 (1978). https://doi.org/10.1016/0378-3812(78)80009-0
51. J.J.-C. Hsu, N. Nagarajan, R.L. Robinson Jr., J. Chem. Eng. Data **30**, 485 (1985). https://doi.org/10.1021/je00042a036
52. F. Gozalpour, A. Danesh, A.C. Todd, B. Tohidi, Fluid Phase Equilib. **233**, 144 (2005). https://doi.org/10.1016/j.fluid.2005.03.032
53. R.P. Worley, J. Chem. Soc. **105**, 273 (1914). https://doi.org/10.1039/CT9140500273
54. R. Tahery, J. Chem. Thermodyn. **106**, 95 (2017). https://doi.org/10.1016/j.jct.2016.11.018
55. M. Dominguez-Perez, L. Segade, O. Cabeza, C. Franjo, E. Jimenez, J. Chem. Eng. Data **51**, 294 (2006). https://doi.org/10.1021/je0504111
56. D.L. Hammick, L.W. Andrew, J. Chem. Soc. (1929). https://doi.org/10.1039/JR9290000754
57. J.L.R. Morgan, M.A. Griggs, J. Am. Chem. Soc. **39**, 2261 (1917). https://doi.org/10.1021/ja02256a002
58. V.T. Lam, G.C. Benson, Can. J. Chem. **48**, 3773 (1970). https://doi.org/10.1139/v70-637
59. T.D. Ling, M. Van Winkle, Ind. Eng. Chem. Chem. Eng. Data Ser. **3**, 82 (1958). https://doi.org/10.1021/i460003a017
60. G.R. Vakili-Nezhaad, M. Al-Wadhahi, S. Al-Haddabi, A. Vakilinejad, W.E. Acree, J. Chem. Thermodyn. **152**, 106292 (2021). https://doi.org/10.1016/j.jct.2020.106292
61. H. Kahl, T. Wadewitz, J. Winkelmann, J. Chem. Eng. Data **48**, 580 (2003). https://doi.org/10.1021/je0201323
62. R.S. Myers, H.L. Clever, J. Chem. Thermodyn. **6**, 949 (1974). https://doi.org/10.1016/0021-9614(74)90216-x
63. S.S. Shastri, A.K. Mukherjee, T.R. Das, J. Chem. Eng. Data **38**, 399 (1993). https://doi.org/10.1021/je00011a017
64. S. Singh, B.S. Lark, S.K. Aggarwal, Indian J. Chem. Sect. A: Inorg. Phys. Theor. Anal. **21**, 1116 (1982)
65. H. Kahl, T. Wadewitz, J. Winkelmann, J. Chem. Eng. Data **48**, 1500 (2003). https://doi.org/10.1021/je034062r
66. S. Enders, H. Kahl, J. Winkelmann, J. Chem. Eng. Data **52**, 1072 (2007). https://doi.org/10.1021/je7000182
67. B.I. Konobeev, V.V. Lyapin, Zh. Prikl. Khim. **43**, 803 (1970)
68. I.M. Abdulagatov, A.P. Adamov, I.M. Abdurakhmanov, J. Eng. Phys. Thermophys. **63**, 1193 (1992). https://doi.org/10.1007/BF00853519
69. M. Mohsen-Nia, H. Rasa, S.F. Naghibi, J. Chem. Thermodyn. **42**, 110 (2010). https://doi.org/10.1016/j.jct.2009.07.018
70. M. Mohsen-Nia, Phys. Chem. Liq. **49**, 608 (2011). https://doi.org/10.1080/00319104.2010.489189

71. J. Satherley, D.L. Cooper, D.J. Schiffrin, Fluid Phase Equilib. **456**, 193 (2018). https://doi.org/10.1016/j.fluid.2017.10.023
72. H.L. Clever, W.E. Chase, J. Chem. Eng. Data **8**, 291 (1963). https://doi.org/10.1021/je60018a004
73. K. Ridgway, P.A. Butler, J. Chem. Eng. Data **12**, 509 (1967). https://doi.org/10.1021/je60035a012
74. R.L. Schmidt, H.L. Clever, J. Colloid Interface Sci. **26**, 19 (1968). https://doi.org/10.1016/0021-9797(68)90266-X
75. T.M. Koller, S. Yan, C. Steininger, T. Klein, A.P. Fröba, Int. J. Thermophys. **40**, 79 (2019). https://doi.org/10.1007/s10765-019-2544-y
76. D. Papaioannou, C.G. Panayiotou, J. Chem. Eng. Data **39**, 457 (1994). https://doi.org/10.1021/je00015a012
77. E. Jimenez Cuesta, H. Casad, L. Segade, C. Franjo, J. Chem. Eng. Data **45**, 862 (2000). https://doi.org/10.1021/je000060k
78. B. Giner, A. Villares, S. Martin, H. Artigas, C. Lafuente, J. Chem. Eng. Data **52**, 1904 (2007). https://doi.org/10.1021/je700215z
79. H.G. Trieschmann, Z. Phys. Chem. Abt. B **29**, 328 (1935)
80. V. Ramakrishna, M. Patel, Indian J. Chem. **8**, 256 (1970)
81. R.L. Schmidt, J.C. Randall, H.L. Clever, J. Phys. Chem. **70**, 3912 (1966). https://doi.org/10.1021/j100884a027
82. D. Gomez-Diaz, J.C. Mejuto, J.M. Navaza, A. Rodriguez-Alvarez, J. Chem. Eng. Data **47**, 872 (2002). https://doi.org/10.1021/je010288n
83. D. Gomez-Diaz, J.C. Mejuto, J.M. Navaza, J. Chem. Eng. Data **46**, 720 (2001). https://doi.org/10.1021/je000310x
84. A. Mejia, H. Segura, M. Cartes, C. Calvo, Fluid Phase Equilib. **270**, 75 (2008). https://doi.org/10.1016/j.fluid.2008.06.006
85. S.K. Suri, V. Ramakrishna, J. Phys. Chem. **72**, 3073 (1968). https://doi.org/10.1021/j100855a001
86. M. Abroodi, A. Bagheri, B.M. Razavizadeh, J. Mol. Liq. **287**, 110924 (2019). https://doi.org/10.1016/j.molliq.2019.110924
87. E.B. Rinker, D.W. Oelschlager, A.T. Colussi, K.R. Henry, O.C. Sandall, J. Chem. Eng. Data **39**, 392 (1994). https://doi.org/10.1021/je00014a046
88. G. Vazquez, E. Alvarez, R. Rendo, E. Romero, J.M. Navaza, J. Chem. Eng. Data **41**, 806 (1996). https://doi.org/10.1021/je960012t
89. E. Alvarez, R. Rendo, B. Sanjurjo, M. Sanchez-Vilas, J.M. Navaza, J. Chem. Eng. Data **43**, 1027 (1998). https://doi.org/10.1021/je980106y
90. J. Aguila-Hernandez, A. Trejo Rodriguez, J. Gracia-Fadrique, Fluid Phase Equilib. **185**, 165 (2001). https://doi.org/10.1016/s0378-3812(01)00467-8
91. E. Alvarez, A. Cancela, R. Maceiras, J.M. Navaza, R. Taboas, J. Chem. Eng. Data **48**, 32 (2003). https://doi.org/10.1021/je020048n
92. D. Fu, L. Du, H. Wang, J. Chem. Thermodyn. **69**, 132 (2014). https://doi.org/10.1016/j.jct.2013.10.016
93. A. Dey, S.K. Dash, B. Mandal, Fluid Phase Equilib. **463**, 91 (2018). https://doi.org/10.1016/j.fluid.2018.01.030
94. D. Fu, J. Xie, F. Wang, S. Wang, J. Chem. Thermodyn. **116**, 197 (2018). https://doi.org/10.1016/j.jct.2017.08.024
95. A. Shojaeian, J. Mol. Liq. **254**, 26 (2018). https://doi.org/10.1016/j.molliq.2018.01.077
96. J. de los S. López-Lázaro, G.A. Iglesias-Silva, A. Estrada-Baltazar, J. Baraja-Fernandez, J. Chem. Eng. Data **60**, 1823 (2015). https://doi.org/10.1021/acs.jced.5b00009
97. L. Segade, J.J. de Llano, M. Dominguez-Perez, O. Cabeza, M. Cabanas, E. Jimenez, J. Chem. Eng. Data **48**, 1251 (2003). https://doi.org/10.1021/je034053i
98. A. Mejia, M. Cartes, H. Segura, J. Chem. Thermodyn. **43**, 1395 (2011). https://doi.org/10.1016/j.jct.2011.04.005
99. A.E. Andreatta, R.E. Martini, J.L. Legido, L. Casas, Int. J. Eng. Res. Sci. **2**, 51 (2016)
100. E. Onder, N. Sarier, Thermochim. Acta **690**, 178698 (2020). https://doi.org/10.1016/j.tca.2020.178698
101. H.B. Evans, H.L. Clever, J. Phys. Chem. **68**, 3433 (1964). https://doi.org/10.1021/j100793a507
102. J. Yang, J. Wu, J. Chem. Thermodyn. **170**, 106782 (2022). https://doi.org/10.1016/j.jct.2022.106782
103. D.J.L. Prak, A.L. Mungan, J.S. Cowart, P.C. Trulove, J. Chem. Eng. Data **63**, 1642 (2018). https://doi.org/10.1021/acs.jced.8b00008

104. S. Bi, X. Li, G. Zhao, J. Wu, Fluid Phase Equilib. **298**, 150 (2010). https://doi.org/10.1016/j.fluid.2010.07.026
105. N. Nagarajan, R.L. Robinson Jr., J. Chem. Eng. Data **31**, 168 (1986). https://doi.org/10.1021/je00044a012
106. R.D. Shaver, R.L. Robinson Jr., K.A.M. Gasem, Fluid Phase Equilib. **179**, 43 (2001). https://doi.org/10.1016/s0378-3812(00)00475-1
107. L.I. Rolo, A.I. Caco, A.J. Queimada, I.M. Marrucho, J.A.P. Coutinho, J. Chem. Eng. Data **47**, 1442 (2002). https://doi.org/10.1021/je025536+
108. A.J. Queimada, A.I. Caco, I.M. Marrucho, J.A.P. Coutinho, J. Chem. Eng. Data **50**, 1043 (2005). https://doi.org/10.1021/je050024r
109. V.N. Grigor'ev, N.S. Rudenko, Zh. Eksp. Teor. Fiz. **47**, 92 (1964)
110. Y.P. Blagoi, G.P. Kropachev, V.V. Pashkov, Ukr. Fiz. Zh. **12**, 1300 (1967)
111. M. Abroodi, A. Bagheri, B.M. Razavizadeh, J. Chem. Eng. Data **65**, 3173 (2020). https://doi.org/10.1021/acs.jced.0c00192
112. Anonymous, Chem. Eng. Oil Gas **3**, 1 (1981). https://oversea.cnki.net/kcms/detail/detail.aspx?dbcode=CJFD&filename=STQG198103000&dbname=CJFD7984
113. G. Vazquez, E. Alvarez, J.M. Navaza, R. Rendo, E. Romero, J. Chem. Eng. Data **42**, 57 (1997). https://doi.org/10.1021/je960238w
114. J. Han, J. Jin, D.A. Eimer, M.C. Melaaen, J. Chem. Eng. Data **57**, 1095 (2012). https://doi.org/10.1021/je2010038
115. S.A. Jayarathna, C.K. Jayarathna, D.A. Kottage, S. Dayarathna, D.A. Eimer, M.C. Melaaen, J. Chem. Eng. Data **58**, 343 (2013). https://doi.org/10.1021/je300920t
116. S.A. Jayarathna, A. Weerasooriya, S. Dayarathna, D.A. Eimer, M.C. Melaaen, J. Chem. Eng. Data **58**, 986 (2013). https://doi.org/10.1021/je301279x
117. D.J. Luning Prak, J.S. Cowart, P.C. Trulove, J. Chem. Eng. Data **59**, 3842 (2014). https://doi.org/10.1021/je5007532
118. J. Koefoed, J.V. Villadsen, Acta Chem. Scand. **12**, 1124 (1958)
119. A.J. Queimada, F.A.E. Silva, A.I. Caco, I.M. Marrucho, J.A.P. Coutinho, Fluid Phase Equilib. **214**, 211 (2003). https://doi.org/10.1016/s0378-3812(03)00354-6
120. H. Yue, Z. Liu, J. Chem. Eng. Data **61**, 1270 (2016). https://doi.org/10.1021/acs.jced.5b00903
121. H. Zhou, W. Zhu, Huaxue Gongcheng **21**, 61 (1993)
122. R. Heide, J. Schenk, in *Bestimmung der der Transportgrößen von HFKW, Bericht zum AiF-Forschungsvorhaben Nr. 10044B, Heft 1: Viskosität und Oberflächenspannung* (Forschungsrat Kältetechnik e.V., Frankfurt am Main, 1996)
123. M. Okada, T. Shibata, Y. Sato, Y. Higashi, Int. J. Thermophys. **20**, 119 (1999). https://doi.org/10.1023/a:1021482231102
124. A.P. Fröba, S. Will, A. Leipertz, Int. J. Thermophys. **22**, 1349 (2001). https://doi.org/10.1023/a:1012832701996
125. Y.Y. Duan, H. Lin, Fluid Phase Equilib. **213**, 89 (2003). https://doi.org/10.1016/s0378-3812(03)00236-x
126. S. Bi, G. Zhao, J. Wu, Fluid Phase Equilib. **287**, 23 (2009). https://doi.org/10.1016/j.fluid.2009.09.005
127. H. Lin, Y.Y. Duan, J. Chem. Eng. Data **49**, 372 (2004). https://doi.org/10.1021/je0342163
128. H. Lin, Y.Y. Duan, Int. J. Thermophys. **24**, 1495 (2003). https://doi.org/10.1023/b:ijot.0000004090.64922.63
129. C. Zhang, G. Li, L. Yue, Y. Guo, W. Fang, J. Chem. Eng. Data **60**, 2541 (2015). https://doi.org/10.1021/acs.jced.5b00105
130. R.S. Myers, H.L. Clever, J. Chem. Eng. Data **14**, 161 (1969). https://doi.org/10.1021/je60041a014
131. F.B. Sprow, J.M. Prausnitz, Trans. Am. Inst. Chem. Eng. **62**, 1105 (1965). https://doi.org/10.1039/TF9666201105
132. W. Ramsay, E. Aston, Trans. R. Ir. Acad. **32**, 93 (1902)
133. A. Ritzel, Z. Phys. Chem. Stoechiom. Verwandschaftsl. **60**, 319 (1907)
134. J.L.R. Morgan, A.J. Scarlett, J. Am. Chem. Soc. **39**, 2275 (1917). https://doi.org/10.1021/ja02256a003
135. J. Traube, J. Prakt. Chem. **31**, 77 (1885)
136. M. Descude, J. Phys. Paris **2**, 348 (1903)
137. J.L.R. Morgan, M. Neidle, J. Am. Chem. Soc. **35**, 1856 (1913). https://doi.org/10.1021/ja02201a006

138. L.L. Bircumshaw, J. Chem. Soc. Trans. **121**, 887 (1922). https://doi.org/10.1039/CT9222100887
139. R.C. Ernst, C.H. Watkins, H.H. Ruwe, J. Phys. Chem. **40**, 627 (1936). https://doi.org/10.1021/j150374a008
140. S. Valentiner, H.W. Hohls, Z. Phys. **108**, 101 (1937)
141. W.S. Bonnell, L. Byman, D.B. Keyes, Ind. Eng. Chem. **32**, 532 (1940). https://doi.org/10.1021/ie50364a019
142. B. Stahlberger, A. Guyer, Helv. Chim. Acta **33**, 243 (1950)
143. B.Y. Teitel'baum, T.A. Gortalova, E.E. Sidorova, Zh. Fiz. Khim. **25**, 911 (1951)
144. Y.V. Efremov, Zh. Fiz. Khim. **42**, 1906 (1968)
145. L.S.C. Wan, T. Jeyabalan, Chem. Pharm. Bull. **34**, 4744 (1986). https://doi.org/10.1248/cpb.34.4744
146. M.A. Kalbassl, M.W. Biddulph, J. Chem. Eng. Data **33**, 473 (1988). https://doi.org/10.1021/je00054a024
147. G. Vazquez, E. Alvarez, J.M. Navaza, J. Chem. Eng. Data **40**, 611 (1995). https://doi.org/10.1021/je00019a016
148. R. Belda, J.V. Herraez, O. Diez, Phys. Chem. Liq. **43**, 91 (2005). https://doi.org/10.1080/00319100512331327342
149. R.B. Maximino, Phys. Chem. Liq. **47**, 475 (2009). https://doi.org/10.1080/00319100802241657
150. K. Ludzik, K. Kustrzepa, H. Piekarski, M. Jozwiak, J. Chem. Eng. Data **61**, 1047 (2016). https://doi.org/10.1021/acs.jced.5b00485
151. D. Gonçalves, M.F. Paludetti, P.M. Florido, C. Tonetti, C.B. Gonçalves, C.E.C. Rodrigues, J. Chem. Eng. Data **63**, 2718 (2018). https://doi.org/10.1021/acs.jced.8b00086
152. M.A. Raza, P.D. Hallett, X. Liu, M. He, W. Afzal, J. Chem. Eng. Data **64**, 5049 (2019). https://doi.org/10.1021/acs.jced.9b00026
153. D. Gonçalves, C. Panzarin, C.B. Gonçalves, C.E.C. Rodrigues, Fluid Phase Equilib. **521**, 112730 (2020). https://doi.org/10.1016/j.fluid.2020.112730
154. S. Khosharay, M. Rahmanzadeh, B. ZareNezhad, Int. J. Thermophys. **41**, 166 (2020). https://doi.org/10.1007/s10765-020-02738-0
155. D. Gomez-Diaz, J.M. Navaza, J. Chem. Eng. Data **66**, 2160 (2021). https://doi.org/10.1021/acs.jced.1c00061
156. A. Bagheri, A.H. Amiri-Majed, J. Chem. Thermodyn. **51**, 45 (2012). https://doi.org/10.1016/j.jct.2012.02.017
157. S. Azizian, M. Hemmati, J. Chem. Eng. Data **48**, 662 (2003). https://doi.org/10.1021/je025639s
158. R.H. Campbell, E.M. Kartzmark, J. Chem. Thermodyn. **5**, 163 (1973). https://doi.org/10.1016/s0021-9614(73)80076-x
159. S.I. Uchida, K. Matsumoto, Kagaku Kogaku **22**, 570 (1958)
160. W.E. Shipp, J. Chem. Eng. Data **15**, 308 (1970). https://doi.org/10.1021/je60045a020
161. Z.M. Rong, Y. Lu, Huaxue Gongcheng **16**, 56 (1988)
162. R.C. Ernst, E.E. Litkenhous, J.W. Spanyer, J. Phys. Chem. **36**, 842 (1932). https://doi.org/10.1021/j150333a006
163. B.Y. Teitel'baum, S.G. Ganelina, T.A. Gortalova, Zh. Fiz. Khim. **25**, 1043 (1951)
164. K.S. Howard, R.A. McAllister, AIChE J. **3**, 325 (1957). https://doi.org/10.1002/aic.690030308
165. A.I. Toryanik, V.G. Pogrebnik, J. Struct. Chem. **17**, 464 (1976). https://doi.org/10.1007/BF00746671
166. V.G. Baidakov, A.M. Kaverin, M.N. Khotienkova, Fluid Phase Equilib. **356**, 90 (2013). https://doi.org/10.1016/j.fluid.2013.07.008
167. K.N. Seneviratne, T.J. Hughes, M.L. Johns, K.N. Marsh, E.F. May, J. Chem. Thermodyn. **111**, 173 (2017). https://doi.org/10.1016/j.jct.2017.03.002
168. Y.P. Blagoi, Ukr. Fiz. Zh. **5**, 109 (1960)
169. S. Fuks, A. Bellemans, Physica **32**, 594 (1966). https://doi.org/10.1016/0031-8914(66)90049-8
170. K. Tanaka, Y. Higashi, J. Chem. Eng. Data **54**, 1656 (2009). https://doi.org/10.1021/je800756r
171. G. Zhao, S. Bi, J. Wu, Z. Liu, J. Chem. Eng. Data **55**, 3077 (2010). https://doi.org/10.1021/je901085t
172. Y.Y. Duan, L. Hong, J. Chem. Eng. Data **48**, 1068 (2003). https://doi.org/10.1021/je030137f
173. Y. Liu, C. Kondou, C. Coquelet, C. Houriez, Int. J. Refrig. **132**, 276 (2021). https://doi.org/10.1016/j.ijrefrig.2021.09.021
174. H. Lin, Y.Y. Duan, J. Chem. Eng. Data **50**, 182 (2005). https://doi.org/10.1021/je049743g

175. J. Cui, S. Bi, X. Meng, J. Wu, J. Chem. Eng. Data **61**, 950 (2016). https://doi.org/10.1021/acs.jced.5b00798
176. K. Tanaka, Y. Higashi, J. Chem. Eng. Jpn. **46**, 371 (2013). https://doi.org/10.1252/jcej.13we021
177. Anonymous, *Freon Fluorocarbons – Properties and Applications* (E.I. Du Pont De Nemours & Co. (INC.), Wilmington, 1969)
178. Y.P. Blagoi, N.S. Rudenko, Izv. Vyssh. Uchebn. Zaved. Fiz. **2**, 22 (1959)
179. V.B. Ostromukhov, M.G. Ostronov, Zh. Fiz. Khim. **68**, 39 (1994)
180. V.G. Baidakov, A.M. Kaverin, V.N. Andbaeva, Fluid Phase Equilib. **270**, 116 (2008). https://doi.org/10.1016/j.fluid.2008.06.016
181. A.M. Kaverin, V.N. Andbaeva, V.G. Baidakov, Zh. Fiz. Khim. **80**, 495 (2006). https://doi.org/10.1134/s0036024406030174
182. V.G. Baidakov, A.M. Kaverin, Zh. Fiz. Khim. **78**, 1150 (2004)
183. K.A. Clendenning, Can. J. Res. Sect. F **24**, 249 (1946)
184. K. Nakanishi, T. Matsumoto, M. Hayatsu, J. Chem. Eng. Data **16**, 44 (1971). https://doi.org/10.1021/je60048a010
185. Y.S. Won, D.K. Chung, A.F. Mills, J. Chem. Eng. Data **26**, 140 (1981). https://doi.org/10.1021/je00024a011
186. B.C. Hoke, J.C. Chen, J. Chem. Eng. Data **36**, 322 (1991). https://doi.org/10.1021/je00003a019
187. A. Horibe, S. Fukusako, M. Yamada, Int. J. Thermophys. **17**, 483 (1996). https://doi.org/10.1007/bf01443405
188. N.G. Tsierkezos, I.E. Molinou, J. Chem. Eng. Data **43**, 989 (1998). https://doi.org/10.1021/je9800914
189. K. Habrdova, S. Hovorka, L. Bartovska, J. Chem. Eng. Data **49**, 1003 (2004). https://doi.org/10.1021/je049955d
190. J. Zhang, P. Zhang, F. Han, G. Chen, R. Deng, X.H. Wei, J. Chem. Eng. Data **53**, 2372 (2008). https://doi.org/10.1021/je800271e
191. A.A. Rafati, A. Bagheri, M. Najafi, J. Chem. Thermodyn. **43**, 248 (2011). https://doi.org/10.1016/j.jct.2010.09.003
192. A.K. Tiwari, Sonu, S.K. Saha, J. Chem. Thermodyn. **70**, 24 (2014). https://doi.org/10.1016/j.jct.2013.10.010
193. Y. Saji, T. Okuda, Adv. Cryog. Eng. **10**, 209 (1965)
194. S. Bi, J. Cui, G. Zhao, J. Wu, Fluid Phase Equilib. **414**, 60 (2016). https://doi.org/10.1016/j.fluid.2016.01.013
195. H.I. Waterman, W.R.E. van Herwijnen, H.W. den Hartog, J. Appl. Chem. (Lond.) **8**, 625 (1958). https://doi.org/10.1002/jctb.5010081001
196. K.C. Nadler, Ph.D. Thesis, Cornell University, 1987
197. I.I. Sulla, V.G. Baidakov, Zh. Fiz. Khim. **68**, 63 (1994)
198. P. Virtanen, R. Gommers, T.E. Oliphant et al., Nat. Methods **17**, 261 (2020). https://doi.org/10.1038/s41592-019-0686-2
199. A.S. Bezera, J.M.T. Santos, M.L.L. Paredes, Fluid Phase Equilib. **288**, 55 (2010). https://doi.org/10.1016/j.fluid.2009.10.011
200. K.A.M. Gasem, P.B. Dulcamara, K.B. Dickson, R.L. Robinson, Fluid Phase Equilib. **53**, 39 (1989). https://doi.org/10.1016/0378-3812(89)80071-8

Paper 5

Log, Alexandra Metallinou; Hammer, Morten; Deng, Han; Austegard, Anders; Hafner, Armin; Munkejord, Svend Tollak. (2024) Depressurization of CO2 in a pipe: Effect of initial state on non-equilibrium two-phase flow. *International Journal of Multiphase Flow.* vol 170. doi:10.1016/j.ijmultiphaseflow.2023.104624

International Journal of Multiphase Flow 170 (2024) 104624

Contents lists available at ScienceDirect

International Journal of Multiphase Flow

journal homepage: www.elsevier.com/locate/ijmulflow

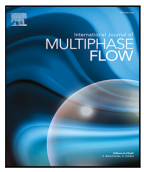

Depressurization of CO_2 in a pipe: Effect of initial state on non-equilibrium two-phase flow

Alexandra Metallinou Log [b,*], Morten Hammer [a], Han Deng [a], Anders Austegard [a], Armin Hafner [b], Svend Tollak Munkejord [a]

[a] SINTEF Energy Research, P.O. Box 4761, Torgarden, NO-7465, Trondheim, Norway
[b] Norwegian University of Science and Technology, Department of Energy and Process Engineering, NO-7491, Trondheim, Norway

ARTICLE INFO

Keywords:
Carbon dioxide
Decompression
Flashing flow
Non-equilibrium
Experiment
Boiling flow

ABSTRACT

It is key in several industrial applications to accurately describe rapid depressurization of liquid and dense phase states. Examples include refrigeration systems, nuclear reactor cooling and CO_2 capture and storage (CCS). It is expected that large-scale CO_2 pipeline transportation must be deployed as a vital part of reaching net zero emissions by 2050. During rapid depressurization of liquid-like CO_2, boiling will in many cases occur out of equilibrium, at a lower pressure than the local saturation pressure. Capturing the non-equilibrium effects is necessary to predict outflow rates and the resulting pressure and temperature inside the pipe. In the present work, we quantify the non-equilibrium effects by studying a series of CO_2 pipe depressurization experiments from liquid-like states at initial temperatures from 10 °C to 40 °C. We compare the experimental results to predictions of the homogeneous equilibrium model (HEM) and a homogeneous relaxation-type non-equilibrium model (HRM*) where the mass-transfer rate from liquid to gas is tuned by a relaxation time. The relaxation time was found to decrease for increasing temperatures, and it was observed to be approximately 60 times longer for the coldest experiment than for the warmest one.

1. Introduction

CO_2 capture and storage (CCS) has been identified as one of the necessary tools to mitigate climate change (IPCC, 2022; IEA, 2021, 2022). IEA (2022) describes a global pathway to reach net zero global emissions by 2050. In this pathway, several gigatonnes of CO_2 must be captured and stored annually. As the CO_2 capture plants and storage sites will generally not be co-located, CO_2 will need to be transported by pipelines, ships or other means. For pipeline transportation, the CO_2 will mostly be in the liquid phase at supercritical pressures (Cosham and Eiber, 2008; Roussanaly et al., 2013). Should the CO_2 be depressurized from this state, it will start boiling. Boiling due to depressurization is often called *flashing*. A depressurization event may occur during planned operations, e.g., when releasing some CO_2 through a pressure relief valve, or as an accident, e.g., due to a pipe fracture. The resulting pressure, temperature, sound speed and mass flow of the CO_2 during the depressurization will be strongly affected by the flashing process. Current engineering tools commonly assume that flashing occurs at equilibrium. However, experimental data indicate that flashing often happens at a lower pressure than expected for an equilibrium process (Pinhasi et al., 2005). These effects need to be accounted for in new engineering tools for the safe and economical design and operation of CO_2-transport pipelines. Similar non-equilibrium considerations are also relevant for, e.g., nuclear reactor cooling systems (Edwards and O'Brien, 1970), refrigeration systems (Banasiak and Hafner, 2013), and other industrial systems operating with compressible fluids that will boil if they are depressurized (Liao and Lucas, 2017).

One of the key safety elements for the design and operation of pipelines with compressible fluids is the prediction of running ductile fracture (RDF). A running ductile fracture is a process where an initial defect in the pipe develops into a fracture which runs along the pipe, sustained by the pressure forces from the escaping fluid, see Aursand et al. (2016a). When the depressurization through the fracture causes flashing, the reduction in pressure is abruptly slowed down as vapor is produced and expands. During two-phase flow, a relatively high pressure is maintained and large forces will be available to sustain an RDF. For large-scale CO_2 pipe rupture tests, the crack-tip pressure has been reported to be over 20% lower than expected based on equilibrium assumptions (Michal et al., 2020). Recent work by Skarsvåg et al. (2023) shows that estimates of the crack-tip pressure can be significantly improved by taking into account non-equilibrium flashing. At bends and valves of the pipeline, dry-ice will also form which can

* Corresponding author.
E-mail addresses: alexandra.log@hotmail.com, alexandra.log@sintef.no (A.M. Log).

https://doi.org/10.1016/j.ijmultiphaseflow.2023.104624
Received 6 March 2023; Received in revised form 17 July 2023; Accepted 25 September 2023
Available online 27 September 2023

Nomenclature

Latin letters

c	Speed of sound ($m\,s^{-1}$)
$\tilde{C}_p$	Heat capacity ($J\,K^{-1}$)
C_p	Specific heat capacity ($J\,K^{-1}\,kg^{-1}$)
E	Total energy ($J\,m^{-3}$)
e	Specific internal energy ($J\,kg^{-1}$)
$\boldsymbol{F}$	Flux vector (–)
F	Friction force ($N\,m^{-3}$)
G	Free energy (J)
h	Specific enthalpy ($J\,kg^{-1}$)
J	Nucleation rate ($m^{-3}\,s^{-1}$)
K	Kinetic prefactor ($m^{-3}\,s^{-1}$)
k_B	Boltzmann's constant ($J\,K^{-1}$)
m	Mass (kg)
p	Pressure (MPa)
Q	Heat ($W\,m^{-3}$)
r	Radius (m)
s	Specific entropy ($J\,K^{-1}\,kg^{-1}$)
$\boldsymbol{S}$	Source term vector (–)
S	Wave speed estimate for HLLC solver ($m\,s^{-1}$)
T	Temperature (°C)
t	Time (s)
u	Velocity ($m\,s^{-1}$)
$\boldsymbol{U}$	Vector of conserved variables (–)
x	Spatial coordinate (m)
x_g	Mass fraction of gas ($kg\,kg^{-1}$)

Greek letters

α	Volume fraction ($m^3\,m^{-3}$)
Γ	Mass-transfer source ($kg\,m^{-3}\,s^{-1}$)
γ	Grüneisen parameter ($Pa\,m^3\,J^{-1}$)
ρ	Density ($kg\,m^{-3}$)
$\tilde{\rho}$	Number density (m^{-3})
σ	Surface tension ($N\,m^{-1}$)
θ	Relaxation time (s)

Subscripts

C	Contact discontinuity
crit	Critical
g	Gas/vapor
i	Index of grid cell/finite volume in finite-volume method
L	Left (of cell boundary)
ℓ	Liquid
R	Right (of cell boundary)
sat	Saturation

Superscripts

n	Time step index in finite-volume method
$*$	Critically-sized embryo of new phase

Abbreviations

BBC	Bernoulli-choking-pressure boundary condition
BC	Boundary condition
CCS	CO_2 capture and storage
RDF	Running ductile fracture
CNT	Classical nucleation theory
ECCSEL	European Carbon Dioxide Capture and Storage Laboratory Infrastructure
EOS	Equation of state
FVM	Finite-volume method
HEM	Homogeneous equilibrium model
HLLC	Harten–Lax–van Leer Contact
HRM	Homogeneous relaxation model
SHL	Superheat limit

cause blockage of the flow and may pose a safety risk. Martynov et al. (2018) present experiments and models on the solid formation of CO_2 during depressurization. In the present work, we focus on the first instants of depressurization where the pressure remains above the triple point and dry-ice has not yet formed.

It has been observed in several depressurization experiments with various fluids that flashing occurs out of equilibrium (Pinhasi et al., 2005). Such experiments are also called flashing experiments or blow-down experiments. In such experiments, it is observed that the pressure becomes lower than the local saturation pressure before flashing begins. This is referred to as a "pressure undershoot". Equivalently, the temperature becomes higher than the local boiling-point temperature, and the fluid is denoted as "superheated". Both of these terms, pressure undershoot and superheat, quantify the degree of non-equilibrium reached during the depressurization. In Fig. 1, we show an example of a depressurization path where a pressure undershoot is attained and the liquid becomes superheated before flashing begins. Such "delayed" flashing is also observed for CO_2 depressurization experiments and large-scale CO_2 pipe-rupture tests (Botros et al., 2016; Munkejord et al., 2020; Michal et al., 2020).

In order to incorporate delayed flashing in depressurization simulations, non-equilibrium models must be applied. This requires determining appropriate closure relations describing the mass-transfer rates between liquid and gas, which has been shown to be challenging (Pinhasi et al., 2005; Liao and Lucas, 2017). The flashing is governed by an array of complex processes including bubble nucleation, bubble coalescence and break-up and bubble growth. A thorough review on the current challenges in modeling these terms was conducted by Liao and Lucas (2017). In particular the bubble nucleation process, or the onset of flashing, is not fully understood. Though much effort has been made to model the mass-transfer rates, generally some correlation is applied in the end. Furthermore, the correlations tend to be specific to the particular case and fluid for which they were fitted.

Research efforts on the simulation of transient CO_2 depressurization have focused on non-equilibrium models with fairly simple correlations for the mass-transfer rates between the phases that are fitted on a case-to-case basis. Brown et al. (2013) tested the homogeneous relaxation model (HRM) and later a two-fluid model (Brown et al., 2014), with simple mass-transfer correlations. The correlations were tuned to individual experiments using "relaxation times". Downar-Zapolski et al. (1996) made a correlation for the relaxation time based on water depressurization through nozzles. De Lorenzo et al. (2017) slightly modified this correlation to better represents measured pressure undershoots for steam-water depressurization tests. The correlation has also been adapted by Angielczyk et al. (2010) for CO_2 based on nozzle-flow measurements of Nakagawa et al. (2009). However, the relaxation time correlation requires vapor to be present in the flow, and the data of Nakagawa et al. (2009) is limited to three depressurization paths passing close to the critical point such that the correlation is only valid near the critical point of CO_2.

Later work on the simulation of transient CO_2 depressurization has focused on two-fluid models with a new mass-transfer correlation

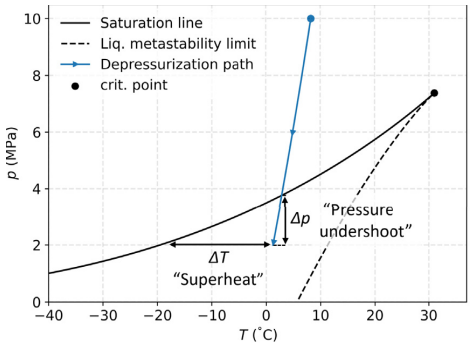

Fig. 1. Illustration of a possible depressurization path in the liquid/dense liquid phase before boiling begins in a $p-T$ diagram.

suggested by Liu et al. (2017). This correlation also requires the tuning of a relaxation coefficient to individual cases. Variations of this model have been tested by different authors and validated against data from Test32A of Botros et al. (2016), and optimal relaxation coefficients have been found in the range $7\,s^{-1}$ to $15\,s^{-1}$ (Liu et al., 2017, 2018; Flechas et al., 2020; Xiao et al., 2020). There is no clear agreement on the choice of relaxation coefficient even for this single depressurization case. Furthermore, as the degree of superheat reached in experiments can vary significantly for different initial conditions (Botros et al., 2016; Munkejord et al., 2020; Quinn et al., 2022), it cannot be expected that the same coefficient value can be applied for different cases. Without a more general correlation or otherwise improved closure relation for the mass-transfer rate between liquid and gas during flashing, the model cannot be applied to make general predictions on the flashing of CO_2 during depressurization.

Hammer et al. (2022) applied the theoretical homogeneous superheat limit to predict the outflow of CO_2 through orifices and nozzles, and reached good agreement with experiments. In a study of nozzle flow data for both CO_2 and water, Wilhelmsen and Aasen (2022) found a transition in the mechanism determining the limit of superheat reached (from homogeneous to heterogeneous nucleation) at temperatures a certain distance below the critical point of the fluid. An initial study by Log et al. (2022) on some of the experimental data which will be presented in the present paper indicates that this is also the case for CO_2 pipe depressurizations. For depressurization cases with the warmest initial conditions, the maximum degree of superheat reached agreed well with the theoretical homogeneous superheat limit (SHL) estimated by classical nucleation theory. For lower temperatures, the maximum degree of superheat reached was lower than that predicted by the homogeneous SHL. In order to develop models that account for this effect, more depressurization data are needed for a range of initial temperatures, or rather: initial entropies. Note that this effect is relevant for other fluids in addition to CO_2. Pipe depressurization experiments have been conducted for both water (Barták, 1990) and R-12 (Winters and Merte, 1979) at different initial entropies, but they were all conducted at much colder initial temperatures than the critical point temperature of the fluid, such that the transition in the mechanism determining the limit of superheat was not captured.

As summarized by Munkejord et al. (2016, 2020), many rupture and pipe depressurization tests for CO_2 and CO_2-rich mixtures have been conducted and studied (Armstrong and Allason, 2014; Botros et al., 2013; Brown et al., 2014; Clausen et al., 2012; Cosham et al., 2012; Drescher et al., 2014; Jie et al., 2012; Guo et al., 2017; Teng et al., 2016; Gu et al., 2019). More recently, visualization experiments have been conducted to gain further understanding on the non-equilibrium bubble nucleation process during the depressurization of pure CO_2 in vertical (Hansen et al., 2019; Ibrahim et al., 2021) and horizontal ducts (Quinn et al., 2022). For the validation of depressurization simulations, the data of Botros et al. (2016, 2017) and Munkejord et al. (2020, 2021) are of highest relevance due to the availability of high resolution, high-frequency pressure data. The experimental data of Botros et al. (2016) and Munkejord et al. (2020) for pure CO_2 cover a sizable range of initial entropies, with three published experiments each. However, the spread in initial entropies for the experiments is quite large. The available data may therefore miss important information on the different boiling processes occurring for different initial entropies, and more data are needed to fully capture how the non-equilibrium phenomena vary in different areas of pressure–temperature space.

In the present work, we present four new pure-CO_2 depressurization experiments conducted at the ECCSEL depressurization facility (ECCSEL, 2021) at a range of initial temperatures complementing our previous experiments (Munkejord et al., 2020). The experiments are intended to provide more knowledge on depressurization events specifically, but they may also help to bring more understanding on flashing flows in general including steady state flows through nozzles and orifices, for which there are large uncertainties related to critical flow during flashing. We study how the non-equilibrium effects change from colder to higher initial temperatures and compare the results to simulations with a simple non-equilibrium model tuned with relaxation times. To provide a reference for the pressure undershoot and degree of superheat observed in the experiments, we also compare the experimental results to simulations using the homogeneous equilibrium model (HEM). The experimental data presented in this paper are openly available and can be downloaded from Zenodo (Log et al., 2023).

The rest of this article is structured as follows: Section 2 provides an overview of the scope of the experimental campaign, the experimental setup and the experimental procedure. Section 3 describes the homogeneous equilibrium and non-equilibrium models. Section 4 presents the numerical solution method of the governing equations. Notably, in Section 4.2 a novel boundary method is suggested which allows for numerical simulations of depressurization cases where the fluid state passes very close to the critical point of the fluid. Section 5 presents experimental and model results, these are analyzed with respect to non-equilibrium effects. Section 6 summarizes the main results and provides concluding remarks.

2. Scope of test program and experimental setup

In this section, we describe the scope of the test program and provide an overview of the experimental setup. A more detailed description of the experimental setup can be found in Munkejord et al. (2020).

2.1. Scope of the test program

In Table 1, we present the experimental conditions of all the depressurization tests studied in the present work. We present four new experiments (Tests 19, 22, 23, 24), and also study three experiments that were introduced by Munkejord et al. (2020) (Tests 4, 6 and 8). The complete set of old and new experiments were conducted with initial temperatures approximately ranging from 10 °C to 40 °C and with an initial pressure of about 12 MPa. An initial study on the data from Tests 19, 4, 8 and 6 showed that there is a transition in the type of bubble nucleation determining the maximum superheat reached for these experiments, where the warmer experiments (Test 4, 8 and 6) agree with the homogeneous superheat limit predicted by classical nucleation theory, and the coldest experiment (Test 19) does not (Log et al., 2022). Details on how the homogeneous superheat limit can be estimated are provided in Appendix A.

An overview of the expected depressurization paths of the tests before boiling begins is plotted with a solid line in a pressure–temperature diagram in Fig. 2. We also show in dashed lines the depressurization paths for the metastable liquid states. At temperatures away from the critical point, it is possible to reach further into the metastable liquid area.

Table 1
Experimental conditions of the CO_2 depressurization tests.

Test no.	Pressure avg. (MPa)	Temperature avg. (°C)	Ambient temp. (°C)	Figures
4[b]	12.54	21.1	22	9, 10, 15(c), 16(c), 19(e)
6[b]	10.40	40.0	6	8, 13(a), 14(a), 19(a)
8[b]	12.22	24.6	9	9, 10, 15(b), 16(b), 19(d)
19[a]	12.47	10.2	18	9, 10, 15(e), 16(e), 20(b)
22[a]	12.48	14.9	14	9, 10, 15(d), 16(d), 20(a)
23[a]	12.19	31.5	15	9, 10, 15(a), 16(a), 19(c)
24[a]	11.56	35.8	10	8, 13(b), 14(b), 19(b)

[a] Present work.
[b] Munkejord et al. (2020).

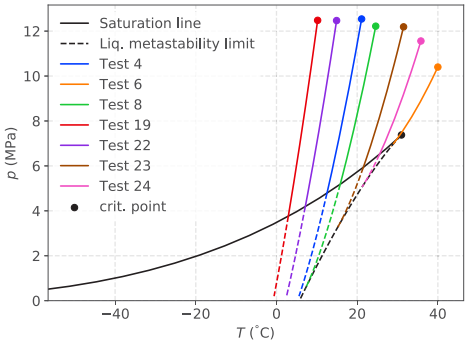

Fig. 2. Calculated depressurization paths for the liquid or supercritical state for all the tests presented in Table 1, assuming isentropic flow. The possible metastable parts of the depressurization paths are marked with dashed lines.

2.2. ECCSEL depressurization facility and test procedure

The ECCSEL depressurization facility (ECCSEL, 2021) consists of a gas supply with mass flow controllers, a compression and cooling system for achieving the desired experimental conditions, and a test section with a rupture disk at the open end. The gas supply allows for a secondary gas to be added to the CO_2, but in the present experiments, only pure CO_2 was used. See Munkejord et al. (2021) for results for CO_2-rich mixtures. The test section is a tube made of 11 stainless steel pipes providing a total length of 61.67 m. These pipes have an inner diameter of 40.8 mm, an outer diameter of 48.3 mm, and were honed to a mean roughness of $R_a = 0.2\ \mu m - 0.3\ \mu m$. The tube is wrapped in heating cables and covered with a 60 mm thick layer of glass wool. The thermal properties of the pipe and insulation layer are provided in Munkejord et al. (2020). A P&ID diagram is shown in Fig. 3(a), providing a schematic overview of the setup. The P&ID is described in detail in Munkejord et al. (2020) and we here only provide a brief overview, focusing on the test section and the experimental procedure. The maximum operating pressure of the facility is 20 MPa, and the current design allows experiments with initial temperatures in the range from 5 °C to 40 °C.

A rupture disk with a disk holder is installed at the pipe outlet. The specified burst pressure of the disk is 120 barg ± 5% at 22 °C. For Tests 4, 6, 8, and 24, X-scored Fike SCRD BT FSR rupture disks were used and for Tests 19, 22, and 23 circular-scored triple-layer Fike HOV BT HL rupture disks were used (see Table 1 for reference on the test numbers). Images of an X-scored rupture disk and a triple-layer disk after a depressurization test is shown in Fig. 4. The triple-layered disks were found to open fully more reliably at colder initial temperatures than the X-scored disks, and were therefore applied for later tests to ensure successful experiments. The open membrane area of the rupture disks have a diameter of 63 mm, ensuring that choking will occur at the open end of the pipe. Once the disks are fully open, the depressurizations are expected to be the same for both types of rupture disks.

The experimental procedure is as follows. First, the rupture disk is installed and the system is evacuated. Then the test section is filled with CO_2 and pressurized. When the pressure reaches about 70% of the desired value, the fluid is circulated to achieve a uniform temperature along the test section. The fluid temperature is controlled using heating elements wrapped around the test section. The pressure and temperature are then increased at a controlled rate by alternating filling and circulation of CO_2 until the disk ruptures. Upon disk rupture, the inlet valves at the closed end of the pipe, and outlet valve at the open end of the pipe are automatically closed to stop the circulation/filling. The heating cables are also automatically turned off at this point. The released CO_2 is vented through an exhaust pipe. An image of the CO_2 plume released from Test 4 is shown in Fig. 5. The exhaust pipe is designed with a large enough flow area that it will not disturb the flow from the pipe.

2.3. Instrumentation

Along the test section of the facility, 16 fast-response pressure transducers and 23 thermocouples are flush-mounted to the inner surface to capture the pressure and temperature transients during depressurization. The pressure sensors are of the type Kulite CTL-190(M) and the uncertainty of the pressure measurements has been estimated to be around 60 kPa with a confidence interval of 95% (Munkejord et al., 2020). Most of the pressure sensors are densely distributed close to the open end to capture the depressurization wave, as shown in Fig. 3(b). Further details regarding the sensors, including a table reporting their locations, can be found in Munkejord et al. (2020). In the present work we only report data from three sensors located 8 cm, 28 cm and 49.98 m from the pipe's open end.

The logging frequency of the data from the pressure transducers and thermocouples is 100 kHz and 1 kHz, respectively. The high-frequency data are stored from 0.3 s before disk rupture for a 9 s period. After this period, both pressure and temperature are collected at 50 Hz. The reported initial conditions of the experiments are calculated from the data between 1 ms and 0.5 ms before disk rupture.

For the study of non-equilibrium phase change, the first milliseconds of depressurization are of high importance, as this is the time scale where phase change occurs. For Test 8, the response time of the thermocouples was estimated to be approximately 30 ms (Munkejord et al., 2020). Therefore, only the pressure data are studied in the present work. The complete dataset is made available at Log et al. (2023), and will be relevant to validate flow models accounting for the complete depressurization process; capturing the temperature in the pipe, the formation of dry-ice at the closed end of the pipe and dry-out of the liquid. It is beyond the scope of the present work to study these effects.

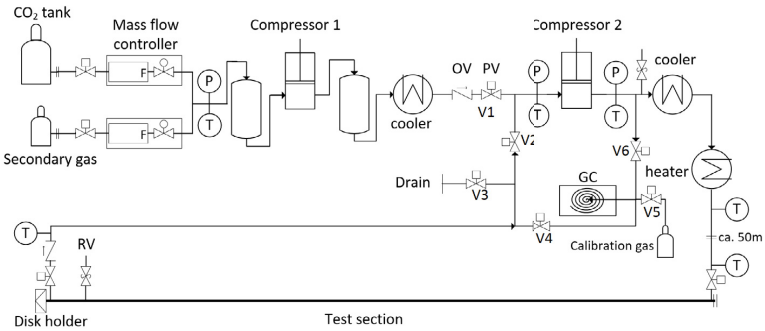

(a) System (RV: relief valve; OV: one-way valve; PV: pneumatic valve)

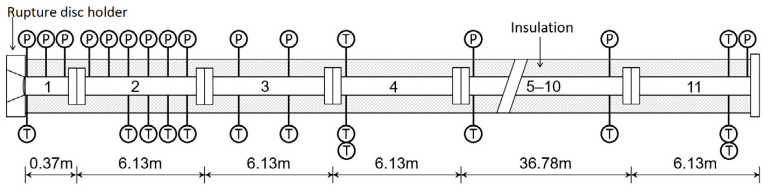

(b) Test section (dimensions are not to scale; pipe no. 5–10 and corresponding sensors are omitted.)

Fig. 3. Schematic of the ECCSEL depressurization facility.

(a) X-scored rupture disk after test. (b) Triple-layer rupture disk after test.

Fig. 4. Pictures of X-scored and circular-scored triple-layer rupture disks.

Fig. 5. CO_2 plume released during depressurization test 4.

3. Models

We apply two flow models to analyze the experimental results — a homogeneous equilibrium model (HEM) and a simple homogeneous non-equilibrium model, denoted HRM*. Based on flow visualization experiments (Brown et al., 2013, 2014; Quinn et al., 2022) the flow is likely well-dispersed during the time-scale considered here, so it is reasonable to apply models assuming homogeneously dispersed flow. In the following sections the models are described in more detail.

3.1. Governing equations

3.1.1. The homogeneous equilibrium model

In the homogeneous equilibrium model (HEM) it is assumed that the phases present in the flow travel at the same velocity and are in mechanical, thermal and chemical equilibrium. The governing equations then take the form of the 1D Euler equations for single-phase compressible inviscid flow, with a mass conservation equation, a momentum balance equation and an energy balance equation:

$$\frac{\partial \rho}{\partial t} + \frac{\partial (\rho u)}{\partial x} = 0, \tag{1}$$

$$\frac{\partial (\rho u)}{\partial t} + \frac{\partial (\rho u^2 + p)}{\partial x} = \rho g_x - \mathcal{F}, \tag{2}$$

$$\frac{\partial E}{\partial t} + \frac{\partial ((E + p)u)}{\partial x} = \mathcal{Q}. \tag{3}$$

Here, $\rho = \alpha_g\rho_g + \alpha_\ell\rho_\ell$ is the density of the gas (g) and liquid (ℓ) mixture, u is the common velocity, p the pressure and E the total energy of the mixture.

$$E = \rho\left(e + \frac{1}{2}u^2\right), \tag{4}$$

where $e = (\alpha_g\rho_g e_g + \alpha_\ell\rho_\ell e_\ell)$ is the specific internal energy of the mixture and α_k denotes the volume fraction of phase $k \in g, \ell$. $\mathcal{F}$ is the pipe wall friction and $\mathcal{Q}$ is the heat transferred from the wall of the pipe to the fluid. g_x is the gravitational acceleration in the axial direction of the pipe. We assume that the pipe is completely horizontal such that $g_x = 0$.

The wall friction is calculated using the Friedel (1979) correlation and the heat transferred from the pipe wall to the fluid is calculated by solving the heat equation in the radial direction in a two-layer domain, as described by Aursand et al. (2017). The in-pipe heat-transfer coefficient is estimated based on the Dittus–Boelter correlation, see, e.g., Bejan (1993, Chap. 6) and the outside heat-transfer coefficient is estimated to $4\,\mathrm{W\,m^{-2}\,K^{-1}}$. The main heat transfer effect for the time intervals considered in the present work is directly from the pipe steel to the fluid. To account for the enhanced heat transfer due to boiling, the correlation of Gungor and Winterton (1987) is applied due to its simplicity. For more details on the friction and heat-transfer modeling, see Munkejord et al. (2021).

In the numerical solution of the governing equations, the two-phase mixture speed of sound will be needed. The speed of sound is also closely connected to the depressurization wave speed, $u - c$. The two-phase mixture speed of sound of the HEM can be calculated analytically to be

$$c_{\mathrm{HEM}} = \left[\rho\left(\frac{\alpha_g}{\rho_g c_g^2} + \frac{\alpha_\ell}{\rho_\ell c_\ell^2} + T\tilde{C}_{p,g}\left(\frac{\frac{1}{\rho_\ell} - \frac{1}{\rho_g}}{h_g - h_\ell} + \frac{\gamma_g}{\rho_g c_g^2}\right)^2 + T\tilde{C}_{p,\ell}\left(\frac{\frac{1}{\rho_\ell} - \frac{1}{\rho_g}}{h_g - h_\ell} - \frac{\gamma_\ell}{\rho_\ell c_\ell^2}\right)^2\right)\right]^{-1/2}, \tag{5}$$

where $c_k = \left(\frac{\partial p_k}{\partial \rho_k}\right)_{s_k}$ is the speed of sound, γ_k the Grüneisen parameter,

$$\gamma_k = \frac{1}{\rho_k}\left(\frac{\partial p_k}{\partial e_k}\right)_{\rho_k}, \tag{6}$$

$\tilde{C}_{p,k}$ the extensive heat capacity

$$\tilde{C}_{p,k} = \alpha_k\rho_k C_{p,k}, \tag{7}$$

and $C_{p,k}$ is the specific heat capacity of phase k (Flåtten and Lund, 2011, Sec. 6) for a general equation of state.

3.1.2. The simplified homogeneous relaxation model

In the HEM, full equilibrium is assumed between the phases. However, during rapid depressurization, the finite mass-transfer rate between the phases is not always fast enough for equilibrium to be maintained. This can be accounted for by allowing for some non-equilibrium between the phases. We choose here to apply a simplified homogeneous relaxation model, which we denote HRM*, where chemical non-equilibrium is allowed between the phases. Otherwise, we apply the same assumptions as in the HEM. For the standard HRM, it is assumed that $T_g = T_{\mathrm{sat}}(p) \neq T_\ell$. For the HRM*, we apply the simpler assumption that $T_g = T_\ell$. With this simpler assumption, the HRM* belongs in a hierarchy of relaxation models studied by, e.g., Flåtten and Lund (2011), Lund (2012) and Linga and Flåtten (2019), where the HRM* is referred to as the pT-relaxed model. The model has been applied by, e.g., Lund and Aursand (2012), Le Martelot et al. (2014), Saurel et al. (2016) and Pelanti (2022) to simulate boiling flows out of equilibrium.

The HRM* consists of four equations describing the mass balance of gas, mass balance of liquid, the conservation of momentum for the two-phase mixture and the conservation of total energy for the mixture:

$$\frac{\partial(\alpha_g\rho_g)}{\partial t} + \frac{\partial(\alpha_g\rho_g u)}{\partial x} = \Gamma, \tag{8}$$

$$\frac{\partial(\alpha_\ell\rho_\ell)}{\partial t} + \frac{\partial(\alpha_\ell\rho_\ell u)}{\partial x} = -\Gamma, \tag{9}$$

$$\frac{\partial(\rho u)}{\partial t} + \frac{\partial(\rho u^2 + p)}{\partial x} = \rho g_x - \mathcal{F}, \tag{10}$$

$$\frac{\partial E}{\partial t} + \frac{\partial((E + p)u)}{\partial x} = \mathcal{Q}, \tag{11}$$

where Γ is the mass-transfer rate between the phases. For an infinitely fast mass-transfer rate, the HRM* relaxes to the HEM. The frozen two-phase mixture speed of sound of the HRM* can be calculated analytically as

$$c_{\mathrm{HRM^*}} = \left[\rho\left(\frac{\alpha_g}{\rho_g c_g^2} + \frac{\alpha_l}{\rho_l c_l^2} + T\frac{\tilde{C}_{p,g}\tilde{C}_{p,l}}{\tilde{C}_{p,g} + \tilde{C}_{p,l}}\left(\frac{\gamma_g}{\rho_g c_g^2} - \frac{\gamma_l}{\rho_l c_l^2}\right)^2\right)\right]^{-1/2}, \tag{12}$$

Lund (2012, Eq. 6.6) for a general equation of state. Here, frozen refers to the mass fraction of gas being assumed constant. As the HRM* relaxes towards the HEM, the speed of sound of the model will always be greater than or equal to the speed of sound in the HEM (Flåtten and Lund, 2011; Lund, 2012). This is referred to as the subcharacteristic condition.

The mass-transfer source, Γ, is modeled as

$$\Gamma = \rho\frac{x_{g,\mathrm{sat}} - x_g}{\theta}, \tag{13}$$

where $x_g = \frac{\alpha_g\rho_g}{\rho}$ is the mass fraction of gas, $x_{g,\mathrm{sat}}$ is the saturated mass fraction of gas and θ is a relaxation time > 0. In this work, θ is modeled as a constant value, fitted for each experiment.

This formulation of the mass-transfer source is general for any relaxation process and has been applied by several researchers to model systems relaxing towards an equilibrium state, including Einstein (1920) as noted by Bilicki and Kestin (1990). The formulation assumes a linear approximation of the relaxation evolution. As shown by Bilicki and Kestin (1990), the mass-transfer source (13) provides a local and instantaneous exponential tendency towards equilibrium from some initial mass fraction $x_{g,0}$,

$$x = x_{g,\mathrm{sat}} - (x_{g,\mathrm{sat}} - x_{g,0})\exp(t/\theta). \tag{14}$$

3.2. Thermophysical property models

The thermodynamic properties of the two-phase mixture are obtained with our in-house framework (Wilhelmsen et al., 2017; Hammer et al., 2020) using the GERG-2008 (Kunz and Wagner, 2012) equation of state (EOS). A version of this framework which includes the GERG-2008 EOS has been made openly available (Hammer et al., 2023). The EOS is used to calculate the densities and energies of the existing phases in both the stable and metastable region. The stability limits of the phases, the spinodals, are also calculated using the GERG-2008 EOS and are defined by

$$\left(\frac{\partial p_k}{\partial \rho_k}\right)_{T_k} = 0, \quad k \in g, \ell. \tag{15}$$

The unstable region is never reached for any of the phases.

Due to numerical issues near the critical point for the HEM simulations of Test 6 with the GERG-2008 EOS, we instead employed the Span and Wagner (1996) EOS. We note that the difference between the GERG-2008 EOS and the Span-Wagner EOS on the predicted pressures was in the order of 0.01 MPa and can be considered negligible for our analysis.

4. Numerical methods

4.1. Numerical discretization

We now consider the numerical solution of the models, focusing on the HRM*. The governing equations, (8)–(11), can be written in the vectorial form

$$\frac{\partial \boldsymbol{U}}{\partial t} + \frac{\partial \boldsymbol{F}}{\partial x} = \boldsymbol{S}, \tag{16}$$

where

$$\boldsymbol{U} = \begin{pmatrix} \alpha_g \rho_g \\ \alpha_\ell \rho_\ell \\ \rho u \\ E \end{pmatrix}, \quad \boldsymbol{F}(\boldsymbol{U}) = \begin{pmatrix} \alpha_g \rho_g u \\ \alpha_\ell \rho_\ell u \\ \rho u^2 + p \\ (E+p)u \end{pmatrix}, \quad \boldsymbol{S} = \begin{pmatrix} \Gamma \\ -\Gamma \\ \rho g_x - \mathcal{F} \\ \mathcal{Q} \end{pmatrix}.$$

The mass-transfer source term, Γ, can be stiff, which can cause instabilities in numerical solvers unless special consideration is taken in the solution of the system. The system (16) is therefore solved using a classical first-order fractional step method known as Godunov splitting (LeVeque, 2002, Ch. 17), which is often applied for stiff source terms. In Godunov splitting, two steps are applied to reach the solution. First the homogeneous part of the system is solved without the source term,

$$\frac{\partial \boldsymbol{U}}{\partial t} + \frac{\partial \boldsymbol{F}}{\partial x} = \boldsymbol{0}. \tag{17}$$

The solution of the first step is then applied in the second "relaxation" step, where the following ODE is solved

$$\frac{\mathrm{d}\boldsymbol{U}}{\mathrm{d}t} = \boldsymbol{S}(\boldsymbol{U}). \tag{18}$$

The homogeneous part of the system is solved using the Harten–Lax–van Leer Contact (HLLC) finite-volume method (FVM) (Toro et al., 1994) in space and explicit Euler in time. For the FVM, the 1D computational domain is split into equidistant grid cells of length $\Delta x = \frac{L}{N}$, where L is the length of the pipe and N is the number of grid cells. At each time-step n, the variables in grid cell i are updated by

$$\boldsymbol{U}_i^{n+1} = \boldsymbol{U}_i^n - \frac{\Delta t}{\Delta x}(\boldsymbol{\mathcal{F}}_{i+1/2}^n - \boldsymbol{\mathcal{F}}_{i-1/2}^n) \tag{19}$$

where $\boldsymbol{\mathcal{F}}_{i\pm1/2}$ are fluxes through the left and right edges of the grid cells, estimated using HLLC.

The HLLC FVM takes the following form for the HRM*:

$$\boldsymbol{\mathcal{F}}_{i+1/2} = \begin{cases} \boldsymbol{F}_L, & \text{if } 0 < S_L, \\ \boldsymbol{F}_L^{\mathrm{HLLC}}, & \text{if } S_L \le 0 < S_C, \\ \boldsymbol{F}_R^{\mathrm{HLLC}}, & \text{if } S_C \le 0 < S_R, \\ \boldsymbol{F}_R, & \text{if } 0 \ge S_R, \end{cases} \tag{20}$$

where

$$\boldsymbol{F}_K^{\mathrm{HLLC}} = \boldsymbol{F}_K + S_K(\boldsymbol{U}_K^{\mathrm{HLLC}} - \boldsymbol{U}_K), \tag{21}$$

$$\boldsymbol{U}_K^{\mathrm{HLLC}} = \left(\frac{S_K - u_K}{S_K - S_C}\right) \begin{pmatrix} (\alpha_g \rho_g)_K \\ (\alpha_\ell \rho_\ell)_K \\ \rho_K S_C \\ E_K + (S_C - u_K)\left(\rho_K S_C + \dfrac{p_K}{(S_K - u_K)}\right) \end{pmatrix},$$

$$K = R, L, \tag{22}$$

and

$$S_C = \frac{p_R - p_L + \rho_L u_L(S_L - u_L) - \rho_R u_R(S_R - u_R)}{\rho_L(S_L - u_L) - \rho_R(S_R - u_R)}. \tag{23}$$

The subscripts L and R refer to the grid cells with index i and $i+1$ respectively, i.e. they refer to the grid cell to the left or to the right of the cell face at $i+1/2$. The left and right wave speeds S_L and S_R must be estimated. In the present work, the simple estimate of Davis (1988) is applied,

$$S_L = \min(u_L - c_L, u_R - c_R), \quad S_R = \max(u_L + c_L, u_R + c_R), \tag{24}$$

where c_L and c_R denote the two-phase mixture speed of sound to the left and to the right of the cell boundary. Finally, the remaining ODE (18) is solved with backward Euler using Newton–Raphson iterations.

For the HEM, the HLLC scheme is applied as proposed by Toro et al. (1994) for the Euler equations. The solution is integrated in time using the explicit Euler method. Aside from the special consideration made to discretize the mass-transfer source term for HRM*, the numerical solution method for the HRM* and HEM are equivalent. For both models, the numerical solution method is first order accurate in time and space.

4.2. Boundary conditions

At the closed end of the pipe, the boundary condition $u = 0$ is set. This is enabled by a mirror ghost cell.

At the open end, a Bernoulli-choking-pressure boundary condition (BBC) is applied using a ghost cell. We here take the open end to be at the left end of the computational domain. The BBC is described by Munkejord and Hammer (2015) for HEM where it was found to provide overlapping results with a characteristics-based pressure BC at reduced computational cost (see their Fig. 8). For HEM, the BBC is based on the assumption that the flow will be in equilibrium.

For the HRM* we instead assume that the minimum amount of flashing occurs, i.e., either frozen flow with no phase change or the minimum amount of flashing to keep the fluid state within the spinodals of the phases. This provides the minimum possible choking pressure in the ghost cell. With this assumption, the pressure in the ghost cell will always be lower or equal to the pressure in the computational domain and thus it cannot restrain the obtained non-equilibrium in the computational domain. This is an advantage because any relaxation time can be tested in the mass transfer model for HRM* with the certainty that the BC will not restrain the non-equilibrium effects. We denote this BC as the "minimum BBC".

The minimum BBC is set in the following way: we extrapolate the specific entropy, mass fraction and flow speed from the first cell in the computational domain to the ghost cell:

$$x_{g,0} = x_{g,1} = x_g, \tag{25}$$

$$s_0 = s_1 = s, \tag{26}$$

$$u_0 = u_1 \tag{27}$$

where the subscript 1 denotes the index of the first cell in the computational domain and the subscript 0 denotes the index of the ghost cell, to the left of cell 1. The maximum of the Bernoulli-choking pressure and the atmospheric pressure is then set in the ghost cell:

$$p_0 = \max(p_{\mathrm{BBC}}, p_{\mathrm{atm}}). \tag{28}$$

Munkejord and Hammer (2015) and Log (2020) (see Fig. 4.42, Naive BC) showed that setting the atmospheric pressure in the ghost cell directly can cause the numerical solver to overestimate the fluid's acceleration at the open end of the pipe, leading to too low temperature estimates and a flow with a Mach number u/c higher than 1. For the steady state assumption, the flow cannot accelerate further than to its choking pressure, so it is reasonable to set the choking pressure in the ghost cell, provided that the flow chokes above the atmospheric pressure.

The Bernoulli choking pressure can be estimated using a steady-state flow assumption and applying the Bernoulli equation for compressible flow,

$$\frac{1}{2}u(p, s_1, x_{g,1})^2 + h(p, s_1, x_{g,1}) = \frac{1}{2}u_1^2 + h_1 \tag{29}$$

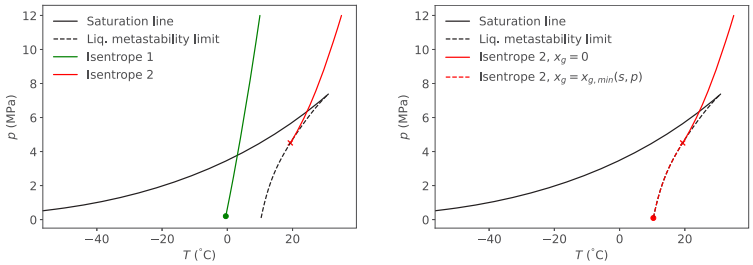

Fig. 6. Illustration of a case where special consideration must be taken to search for the choking pressure in the BBC approach (Isentrope 2). For the minimum BBC, we add a minimum amount of gas, $x_{g,\min}(s,p)$, "walking along" the metastability limit to find the choking point.

which defines u as a function of pressure, where h denotes the specific enthalpy of the mixture. The Bernoulli choking pressure is found by solving

$$u(p_{\text{BBC}}, s_1, x_{g,1}) - c(p_{\text{BBC}}, s_1, x_{g,1}) = 0 \tag{30}$$

for p_{BBC} using the bisection method, where $u(p_{\text{BBC}}, s_1, x_{g,1})$ is given by Equation 29. In some cases, choking does not occur for pressures above the spinodal, where the liquid phase becomes thermodynamically unstable. This is particularly an issue for depressurization simulations where the depressurization path passes close to the critical point. In such a case, no solution exists for p_{BBC}. No stable state exists for the frozen flow at atmospheric pressure either, so atmospheric pressure cannot be set directly.

We avoid the above problem as follows: At the liquid spinodal, liquid would flash instantaneously. We then assume that the minimum amount of flashing will occur if the liquid spinodal is reached. We further assume that the entropy will stay constant:

$$x_{g,0} = x_{g,\min}(p, s_1). \tag{31}$$

An illustration of the problem and our solution is shown in Fig. 6. With this method, we will "walk" along the liquid spinodal when searching for the choking pressure, providing the lowest possible Bernoulli choking pressure for nearly frozen flow. We emphasize that this "walk" along the spinodal does not occur *at* the outflow boundary where the HLLC method estimates the resulting flow, it is simply a means to search for the minimum Bernoulli-choking pressure in the ghost cell while avoiding the unstable region of the phases.

We finally note that an increase in the mass fraction of gas would also involve a small increase in the entropy of the fluid. For simplicity, we ignore this entropy increase. The effect of a too low entropy in the outflow ghost cell is negligible inside the computational domain, as analysis of the flow equations shows that entropy is carried with the flow out of the pipe (and not into it).

5. Results and discussion

In this section, we will present the results of the new full-bore depressurization tests and compare the results to previous full-bore depressurization tests (Munkejord et al., 2020). We will then analyze the effect of the initial temperature of the depressurization experiments by comparing the experimental data to computations employing the HRM* and HEM models.

5.1. Experimental results

We first compare the experimental results, focusing on how the different initial temperatures affects the depressurization and non-equilibrium phase change. As explained in Section 2.3, we will only focus on the pressure measurements and on the millisecond time-frame, as this is most relevant to study the flashing out of equilibrium. The initial conditions of the depressurization experiments are listed in Table 1.

We observe a clear difference between the pressure measurements near the pipe outlet for the two warmest experiments compared to the colder experiments, due to how choking occurs. Therefore, the results of the warmest experiments and the colder experiments are shown and discussed separately.

The pressure recordings over time at the different positions in the pipe provide information on the local wave speed $u + c$ of the depressurization wave traveling into the pipe. We generally observe a strong decrease in the wave speed once two-phase flow begins, due to a decrease in the speed of sound. In Fig. 7, we show an example of how the pressure and wave speed are related using a HEM simulation with the initial conditions for Test 6. Though the HEM is a simplification, the figure illustrates relevant effects which we will discuss in relation to the pressure recordings from the experiments in the following section.

We note the following: the pressure drops closest to the open end first. The depressurization is fast in the single-phase state and there is a discontinuous decrease in wave speed once two-phase flow begins. After this, the flow chokes near the open end, slowing the depressurization down significantly. The decrease of the wave speed once two-phase flow begins causes a short pressure-plateau to form for the positions further inside the pipe (similar to traffic backing up on a highway), a second long-lasting pressure-plateau forms near the open end when the flow has choked.

5.1.1. Warm experiments, $T_0 \geq 35.8\,°\text{C}$

In Fig. 8, we present a comparison between the pressure measurements near the open end and the closed end of the pipe for the first 400 ms of depressurization for Test 24 and Test 6. The depressurization paths of these tests pass close to the critical point, with Test 6 passing the closest. We note six events/phenomena which are common to both experiments, and which are marked in Fig. 8.

First the rupture disk breaks (1) and a fast pressure drop is recorded. A short pressure plateau is recorded as CO_2 vapor starts forming (2). This is caused by the speed of sound decreasing for two-phase flow, an effect which can be reproduced by flow simulations as shown above. After this short plateau, the fast pressure drop continues until the flow chokes at the pipe outlet (3) and a long-lasting pressure plateau is established inside the pipe. Due to the recoil of the pipe[1] at the initial disk rupture, a small pressure perturbation is recorded traveling inwards from the pipe's closed end (4). After approximately 140 ms for Test 24 and 170 ms for Test 6, the rarefaction wave from the disk opening approaches the closed end of the pipe. The rarefaction wave stretches when traveling into the pipe due to the acceleration of the fluid.[2] A pressure plateau is established also here (5). The pressure

[1] Due to some elasticity in the pipe supports

[2] Theory on rarefaction waves in compressible fluids can be found in, e.g., Toro (2009), Chap. 4.

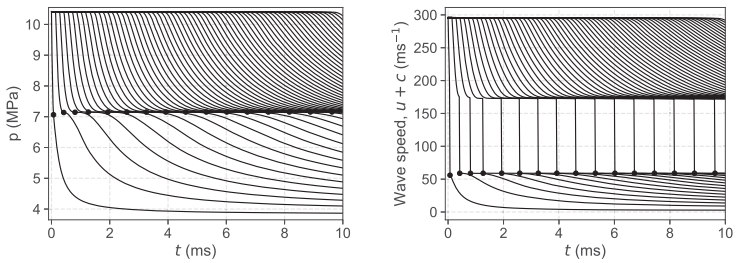

(a) Pressure evolution (b) Wave speed

Fig. 7. Pressure and wave speed over time for a HEM simulation of Test 6 for positions from 0.03 m (leftmost) to 3.20 m (rightmost) from the open end. A marker illustrates where flashing begins in each grid cell.

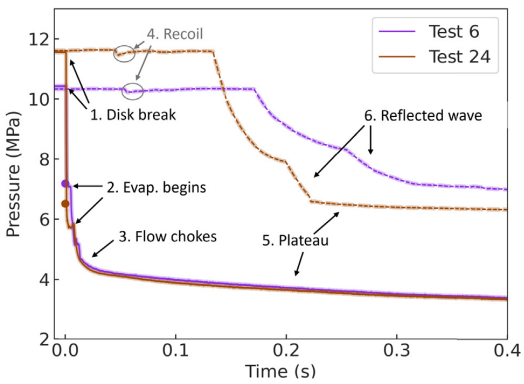

Fig. 8. Measured pressure at $x = 0.28$ m (solid lines) and $x = 49.98$ m (dashed lines) for Test 6 and Test 24 presented in Table 1. Shaded regions show the 95% confidence interval of the measurements. Circular markers show where the liquid isentrope passes the saturation line for each experiment.

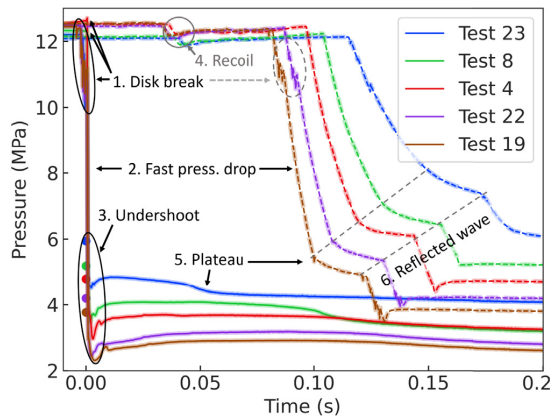

Fig. 9. Measured pressure at $x = 0.28$ m (solid lines) and $x = 49.98$ m (dashed lines) for Tests 23, 8, 4, 22 and 19 presented in Table 1. Shaded regions show the 95% confidence interval of the measurements. Circular markers show where the liquid isentrope passes the saturation line for each experiment.

plateau is reached at a higher pressure near the closed end due to heat transfer and friction in the pipe as shown by Munkejord et al. (2020, Fig. 10) using HEM simulations. Finally, the rarefaction wave reaches the closed end of the pipe and is reflected (6).

In addition to these phenomena, Fig. 8 shows the points where the liquid depressurization path crosses the saturation line. For Test 6, flashing occurs exactly at the point where the saturation line is crossed, as indicated by the pressure level of the short pressure plateau caused by flashing initiation. Test 6 passes very close to the critical point, as shown in Fig. 8. At the critical point, the activation energy for bubble formation vanishes and bubbles form immediately as the saturation line is crossed. For Test 24, there is a pressure undershoot before flashing begins. This is also shown in later simulation results.

5.1.2. Cold experiments, $10.2\,^{\circ}\text{C} \leq T_0 \leq 31.5\,^{\circ}\text{C}$

In Fig. 9, we present a comparison between the resulting pressure measurements near the open end and the closed end of the pipe for the first 200 ms of depressurization for Tests 4, 8, 19, 22 and 23. Six phenomena that are common to all these tests are marked in the figure. These are nearly all the same as for the warm experiments, with the exception of a clear pressure undershoot and recovery.

First, the rupture disk breaks (1). For the multilayered rupture disk, there are several rapid pressure drops as each layer breaks, creating jagged pressure waves. The disk break is followed by a fast pressure drop (2). For all the tests presented in Fig. 9, the CO_2 is in a liquid state initially and the pressure waves travel very fast. After the initial pressure drop, there is a pressure undershoot (3) and a recovery when gas bubbles suddenly form. Due to the recoil of the pipe at the initial disk rupture, a pressure perturbation is recorded traveling from the closed end of the pipe (4). At the open end, the flow chokes at the pipe outlet shortly after the pressure recovery and a pressure plateau is formed inside the pipe (5).

After 70 ms to 120 ms, the rarefaction wave from the disk opening approaches the end of the pipe. The pressure wave has stretched when traveling into the pipe. A pressure plateau is established also here (5). Finally, the rarefaction wave reaches the closed end of the pipe and is reflected (6). For Tests 19 and 22, pressure disturbances from the opening of the multilayered disk can be seen in the reflected wave. A slight pressure-undershoot is observed after the reflected wave and a somewhat lower plateau pressure is established.

The comparison of the cold experiments in Fig. 9 show many interesting trends. We will here focus on three main observations: how the initial temperature affects the pressure waves and plateaus, the non-equilibrium effects and finally the presence of "humps" in the pressure paths.

Pressure wave and plateau. Fig. 9 shows clear trends regarding how the initial temperature affects the pressure paths of the experiments. The plateau pressure decreases for the depressurization tests with lower initial temperature. This is reasonable as the saturation pressure of CO_2 decreases with temperature. We can also observe that the single-phase

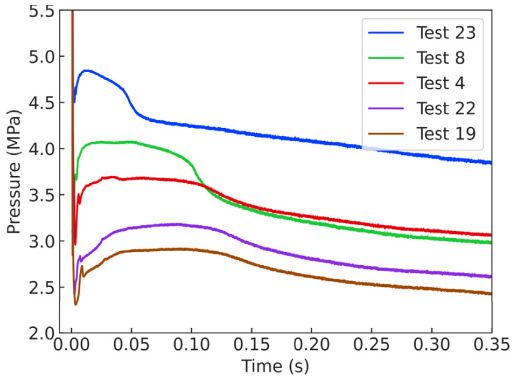

Fig. 10. Measured pressure at $x = 0.28\,\text{m}$ for Tests 4, 8, 19, 22 and 23, zoomed in to show the pressure "hump" which follows the pressure undershoot and recovery.

wave speed in the CO_2 is slower for the warm experiments and faster for the colder ones as the rarefaction wave arrives later at the position $x = 49.98\,\text{m}$ for the warmer experiments. This is also in agreement with theory as pressure waves travel faster in denser fluids and the initial density of the colder experiments is higher than for the warmer experiments.

Non-equilibrium effects. The cold tests show a clear pressure undershoot and recovery, which are signs of non-equilibrium phase change in the flow. It has been shown by several authors that the pressure undershoot and recovery cannot be described by equilibrium flow models, e.g., Winters and Merte (1979), Deligiannis and Cleaver (1990), Barták (1990), Ivashnyov et al. (2000) and Munkejord et al. (2020). We also demonstrate this in Section 5.2.1. For the cold tests, there is a significant distance between the pressure where the depressurization path passes the saturation line and where it reaches the liquid limit of metastability, as shown in Fig. 2. This allows for delayed gas formation. The delayed phase change causes the pressure recovery as bubbles are suddenly formed and grow violently. Once phase change is initiated, the speed of sound decreases and the flow chokes shortly afterwards, causing the long-lasting pressure plateau to form.

Pressure humps. An interesting phenomenon, which can be better observed in Fig. 10, is the presence of a pressure "hump" in the pressure traces measured near the open end of the pipe. Following the pressure undershoot, the pressure rebounds and stays high for a few ms before the pressure again begins to decrease, though much slower than before. For the higher-temperature experiments, the pressure hump is more pronounced and lasts for a shorter amount of time. This phenomenon is observed for all the cold experiments, despite varying initial temperatures and the application of different rupture disks. The same effect can also be observed in the results of Botros et al. (2016) and the water depressurization experiments of Edwards and O'Brien (1970).

Ivashnyov et al. (2000) were able to reproduce similar pressure traces for the Edwards and O'Brien (1970) pipe blowdown experiments by accounting for bubble transport, growth, and bubble breakup near the open end of the pipe. They argue that the breakup of bubbles near the open end of the pipe provides more available surface area for bubble growth to occur, and the violent bubble growth causes an elevated pressure to be sustained for a short amount of time. Provided that bubble growth and breakup causes the pressure hump, the hump likely ends once the flow transitions away from the bubbly flow regime.

In order to gain a better understanding of the non-equilibrium effects observed in the experimental campaign, and to evaluate the accuracy of the HRM*, we compare the experimental results to computational fluid dynamics simulations using the HRM* and the HEM as described in Sections 3 and 4.

5.2. Analysis of 1D CFD models and comparison to experiments

In this section, the results of the numerical simulations are presented and compared to the experimental results. For all the numerical simulations, a Courant–Friedrichs–Lewy (CFL) number of 0.9 is applied.[3] The 1D simulation domain is 61.7 m long. Based on a grid-refinement study presented in Appendix B, 10,000 grid cells are employed in all the simulations.

The section is structured as follows. First a study on the effect of the relaxation time in the simulations is presented and appropriate relaxation times are chosen for the conditions of each depressurization test. Next, we compare the simulated and measured pressure in the pipe for all the experiments. Finally, more detailed analysis is conducted to study the speed of the flashing front and how the flow deviates from the saturation line. Here, we refer to the flashing front as the location in the pipe where the flow transitions from single-phase liquid flow to two-phase gas–liquid flow due to flashing.

5.2.1. The relaxation time in the HRM*

For the HRM*, a relaxation time, θ, must be chosen in order to estimate the mass-transfer rate between the phases. Here, we study how the choice of this relaxation time, θ, affects the simulated pressure evolution during depressurization. The effect of θ is studied for initial conditions corresponding to Test 19 up to $t_{\text{end}} = 40\,\text{ms}$. Test 19 was chosen as the liquid depressurization path does not cross the liquid spinodal, such that the effect of long relaxation times can be tested without the simulation reaching thermodynamically unstable states. Based on the findings, we choose appropriate relaxation times for the experiments studied.

Fig. 11 shows the pressure evolution 8 cm from the open end of the pipe for the HRM* with three different relaxation times in the range from 0.1 ms to 3 ms. The results are compared to those of the HEM. We also illustrate how the HRM* relaxes towards HEM by enforcing the HEM BBC and setting $\theta = 10\,\text{ns}$. The relaxation time has a clear effect on the pressure undershoot and recovery, and the pressure undershoot is larger for longer relaxation times. However, after approximately 20 ms, the pressure predicted by HRM* converges to a value somewhat below that calculated using HEM. For $\theta = 0.1\,\text{ms}$, this pressure is closer to the HEM pressure than for the longer relaxation times. However, the difference is small, only 0.1 MPa–0.2 MPa.

When the HEM BC is enforced and $\theta = 10\,\text{ns}$, the pressure prediction of the HRM* nearly overlaps with the HEM's pressure, though some numerical dissipation is present from the calculation of the strong mass transfer. With the present mass-transfer model, the boundary condition must be changed in order to obtain larger differences in the resulting pressure plateau near the open end of the pipe. The present BC for HRM* assumes the lowest possible choking pressure for a given entropy and mass fraction to not disturb the predicted non-equilibrium effects. Enforcing a higher choking pressure in the BC would lead to a higher plateau pressure, but it may also limit the predicted pressure undershoot.

We note three findings from this initial study:

1. Longer relaxation times provide larger pressure undershoots.
2. Before approximately 20 ms, the choice of relaxation time for the HRM* has a large effect on the simulated pressure near the pipe outlet.
3. After approximately 20 ms, the pressure calculated by HRM* near the pipe outlet converges towards a value below that calculated by HEM. This plateau pressure could be increased by applying a different BC, but a different BC may also limit the obtained pressure undershoot.

[3] For the present numerical solver, the CFL number must be between 0 and 1 to ensure stability (LeVeque, 2002, Ch. 4.4).

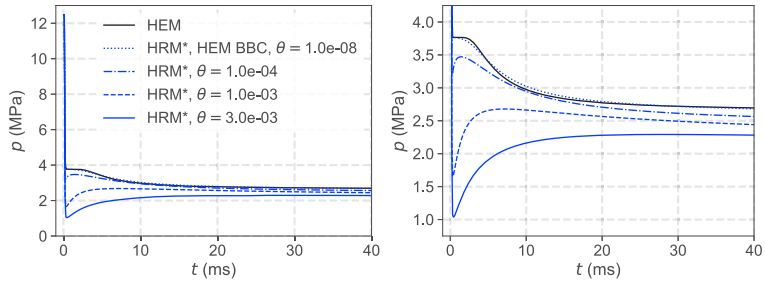

(a) Full pressure evolution (b) Zoomed pressure evolution

Fig. 11. Comparison between HRM* with various relaxation times θ and HEM at $x = 0.08$ m for the initial conditions of Test 19.

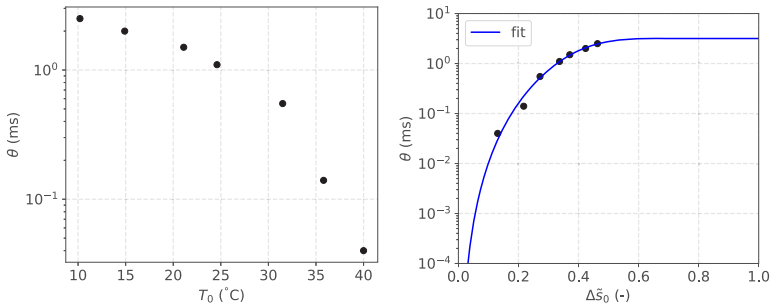

(a) The relaxation time as a function of initial temperature, T_0.

(b) The relaxation time as a function of the scaled, relative initial entropy, $\Delta\tilde{s}_0 = \frac{s_0 - s_c}{s_{\text{tr.}} - s_c}$.

Fig. 12. The chosen relaxation times for HRM* plotted with the proposed relaxation time correlation.

Table 2
Chosen relaxation time for HRM* for each experiment, listed in the order of descending initial temperature.

Test no.	p_0 (MPa)	T_0 (°C)	θ (ms)
6	10.40	40.0	0.04
24	11.56	35.8	0.14
23	12.19	31.5	0.55
8	12.22	24.6	1.10
4	12.54	21.1	1.50
22	12.48	14.9	2.00
19	12.47	10.2	2.50

Based on these findings, θ was chosen by visual inspection to provide the best possible fit of the calculated pressure evolution to the pressure dip measured by the sensors near the open end of the pipe (PT201–PT203), 8 cm to 28 cm from the open end. Relaxation times in the range from 0.01 ms to 4 ms were tested. The chosen relaxation time for each experiment is displayed in Table 2.

It is clear that the higher-temperature experiments have a much shorter relaxation time than the colder ones. The relaxation time of the coldest experiment is approximately 60 times longer than for the warmest experiment. In Fig. 12(a), the chosen relaxation time is plotted as a function of the initial temperature for each depressurization test. For the higher temperatures, $T_0 \geq 31.5$ °C, there is a logarithmic decrease in the relaxation time for increasing temperatures. For the colder tests, the relaxation time increases linearly for increasing temperatures. Obviously, there is no "optimal" relaxation time which can be applied for all the different cases as the phase-change process varies drastically for the different initial temperatures.

At the critical point, the energy barrier for creating a bubble vanishes, so the relaxation time should be zero. Our chosen relaxation times fitting the experimentally measured pressure undershoot further appears to approach a constant value at colder temperatures, or lower entropies. Based on this information, we propose the following correlation for the relaxation time for different depressurization paths:

$$\theta = a\left[1 - \exp\left(-b\Delta\tilde{s}_0^c\right)\right], \tag{32}$$

where

$$\Delta\tilde{s}_0 = \frac{s_0 - s_c}{s_{\text{tr.}} - s_c}, \tag{33}$$

is the scaled, relative initial entropy and s_0 is the initial entropy before the depressurization begins, s_c is the critical point entropy and $s_{\text{tr.}}$ is the triple point entropy. Note that $\Delta\tilde{s}_0 = 0$ when $s_0 = s_c$ and $\Delta\tilde{s}_0 = 1$ when $s_0 = s_{\text{tr.}}$. As the depressurization path is expected to be nearly isentropic before phase change begins, the scaled, relative initial entropy provides information on whether the depressurization path will cross the saturation line closer to the triple point or the critical point. We find the best fit for our chosen relaxation times with $a = 3.165$ ms, $b = 33.283$ and $c = 4.014$. The resulting correlation is shown in Fig. 12(b). Near $\Delta\tilde{s}_0 = 0$, the relaxation time goes to zero and for $\Delta\tilde{s}_0 \lesssim 0.5$ the relaxation time becomes constant, equal to 3.165 ms. More experimental data are needed to determine whether this functional form is appropriate for the relaxation time. The correlation may also be tested for different fluids.

5.2.2. Comparison to experiments

In this section, we compare HEM and HRM* simulations to experimental data. The simulations are run up to $t_{\text{end}} = 100$ ms. As the non-equilibrium effects are most pronounced near the pipe outlet, we present the results for the simulated and measured pressure at

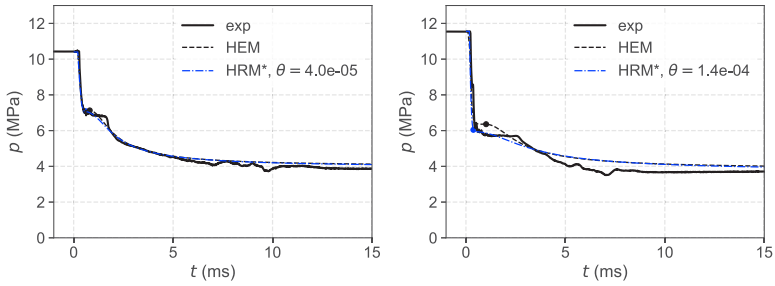

(a) Test 6: $p_0 = 10.40$ MPa, $T_0 = 40.0$ °C (b) Test 24: $p_0 = 11.56$ MPa, $T_0 = 35.8$ °C

Fig. 13. Measured (full lines) and simulated pressure (dashed lines) at $x = 0.08$ m from the open end for Tests 6 and 24. Markers show where $x_g > 0.001$ for the simulations, illustrating where two-phase flow begins.

the sensor closest to the pipe outlet, PT201, which is situated 8 cm from the open end. For plots over time, the plotted line width of the experimental measurement is chosen to match the 95% confidence interval of the data. Thus if the model predictions do not overlap with the line, they are outside of the experimental uncertainty. We also study the pressure wave along the length of the pipe. Once again, we separate the warm (6 and 24) and cold (4, 8, 19, 22, 23) tests and discuss them separately.

Warm experiments, $T_0 \geq 35.8$ °C. In Fig. 13, the modeled and measured pressure traces at 8 cm from the open end of the pipe are shown for Test 6 and Test 24 up to $t = 15$ ms. The flashing begins for both tests at a very short-lasting pressure plateau after about 1 ms and the flow chokes at the pipe outlet after approximately 10 ms. The difference between HEM and HRM* is small for Test 6, and more pronounced for Test 24.

For Test 24, flashing begins at a lower pressure than what is predicted by HEM. The HEM predicts flashing at approximately 6.5 MPa, at the point where the single-phase isentrope crosses the saturation line. However, at 1 ms to 3 ms, the experimental measurements show a pressure plateau around $p = 5.8$ MPa, indicating boiling. The HRM* agrees with the delayed boiling, but it does not obtain a pronounced pressure plateau as observed in the experimental measurement. The HEM obtains a sharper pressure plateau than HRM*. As shown in Fig. 7, the plateau is related to the decrease in speed of sound once flashing begins. Though HRM* is fitted to the approximate flashing onset, the mass-transfer rate is too low to provide the abrupt decrease in the speed of sound that causes the plateau. However, the prediction of the pressure plateau may also be affected by numerical dissipation, causing an unwanted smoothing effect. After the onset of flashing, the models obtain a too slow pressure drop. Finally, both HEM and HRM* overestimate the pressure plateau after choking occurs.

In Fig. 14, we show the measured and simulated pressure wave along the pipe at $t = 100$ ms. The predictions of the HEM and HRM* models are overlapping and they agree well with the experimental data. The rarefaction wave is split into two waves along the pipe. Closest to the open end of the pipe, there is a slow-moving two-phase rarefaction wave, and further inside the pipe there is a fast-moving single-phase rarefaction wave. In-between these two waves is a plateau where the CO_2 is in the single phase. If no friction or heat transfer was present, this plateau would be at a constant pressure, at the pressure where flashing begins. The heat transfer from the steel wall of the pipe to the fluid and the friction in the pipe cause a slope in the pressure plateau so that the pressure stays above the boiling pressure.

Cold experiments, $10.2\,°C \leq T_0 \leq 31.5\,°C$. In Fig. 15, the simulated and measured pressures at 8 cm from the open end of the pipe are shown for Tests 4, 8, 19, 22 and 23. For these tests, the difference between HEM and HRM* is substantial, particularly during the first 10 ms of the flow. As expected, HEM reaches two-phase flow too early, and does not capture the pressure undershoot and recovery. At $t \approx 1$ ms, the difference between the pressure calculated using the HEM and the recorded pressure is in the order of 2 MPa for Tests 8, 19, 22 and 23. After the first few ms of the simulations, there is a transition from HEM overestimating the pressure to HEM *under*estimating the pressure for Tests 4, 8 and 23. This also occurs for Tests 19 and 22 for a longer t_{end}.

HRM* clearly outperforms HEM for the first ms as it captures a pressure undershoot and recovery recorded 8 cm from the open end. Fig. 15(c) shows that Test 4 does not obtain a clear pressure undershoot and recovery at this position, causing a discrepancy between the HRM* pressure and the experimental measurements. However, as shown in Fig. 9, a pressure undershoot and recovery is observed for Test 4 at 28 cm from the open end. The difference between the recorded pressure behaviors 8 cm and 28 cm from the open end for this case is larger than the measurement uncertainty. The result may simply reflect the chaotic nature of the flow during the first few ms of the depressurization and it might not be possible to fully capture this with a 1D model. The pressure recovery calculated by the HRM* is a bit more abrupt than the experimental measurements. This is particularly evident for Test 8. After the pressure recovery, HRM* also underestimates the pressure for Tests 4, 8 and 23, and a pressure plateau is established somewhat below that of HEM.

As discussed in Section 5.1, the presence of pressure humps for the colder experiments suggests a violent bubble breakup and growth process (Ivashnyov et al., 2000). It is the elevated pressure hump that neither HEM nor HRM* can capture, causing an underestimation of the pressure over time. The underestimation of the HEM can be very clearly seen in Munkejord et al. (2020, Fig. 11), where longer simulations were conducted. In order to capture the boiling process fully, a physics-based model for the mass-transfer rate would be needed, where bubble growth and breakup is accounted for.

We now consider the depressurization wave along the pipe. In Fig. 16 we show the simulated and measured pressure wave along the pipe at $t = 100$ ms for all the cold experiments. Generally, the models provide quite similar predictions and agree well with the measured pressure data along the pipe. The clearest difference in the model predictions is at the beginning of the two-phase rarefaction wave at around $x = 5$ m, where HEM predicts a sharper change in the pressure than HRM* where two-phase flow begins. This difference is caused by the relaxation time in HRM* giving a more gradual flashing process. The experimental data agree more with the HRM* prediction in this region of the pipe. For the two warmer tests, Test 23 with $T_0 = 31.5$ °C and Test 8 with $T_0 = 24.6$ °C, the predictions of HEM and HRM* are nearly overlapping otherwise.

For the three coldest tests, HRM* predicts a slightly lower pressure than HEM in-between the single-phase and two-phase rarefaction

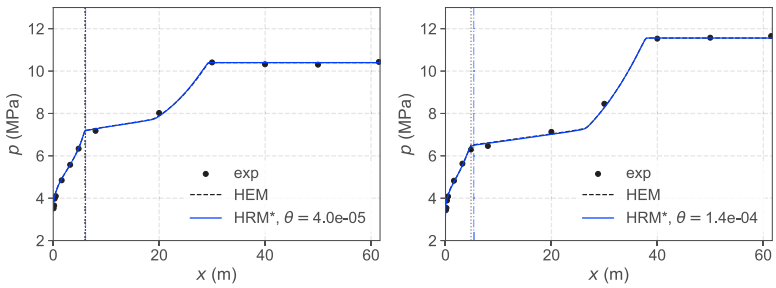

(a) Test 6: p_0 = 10.40 MPa, T_0 = 40.0 °C (b) Test 24: p_0 = 11.56 MPa, T_0 = 35.8 °C

Fig. 14. Measured and simulated pressure along the pipe at t = 100 ms. The vertical lines mark where two-phase flow begins near the open end for HEM (dotted line) and HRM* (dash dotted line).

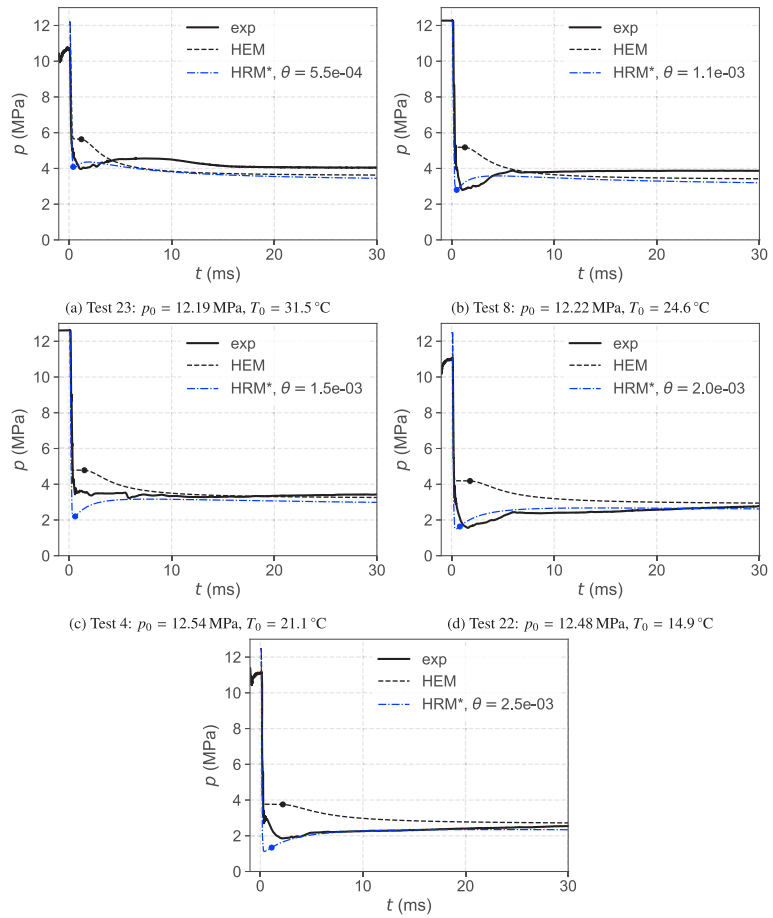

(a) Test 23: p_0 = 12.19 MPa, T_0 = 31.5 °C (b) Test 8: p_0 = 12.22 MPa, T_0 = 24.6 °C

(c) Test 4: p_0 = 12.54 MPa, T_0 = 21.1 °C (d) Test 22: p_0 = 12.48 MPa, T_0 = 14.9 °C

(e) Test 19: p_0 = 12.47 MPa, T_0 = 10.2 °C

Fig. 15. Measured (full lines) and simulated pressure (dashed lines) at x = 0.08 m from the open end for Tests 4, 8, 19, 22 and 23. Markers show where $x_g > 0.001$ for the simulations, illustrating where two-phase flow begins.

waves. Around 10 m to 40 m from the open end of the pipe, the experimental measurements seem to agree more with the prediction of HRM*, whereas further inside the pipe behind the single-phase rarefaction wave, the experimental measurements seem to agree more with HEM. It is possible that the friction and/or the heat transfer models should be slightly stronger, providing a larger slope in the pressure along the pipe

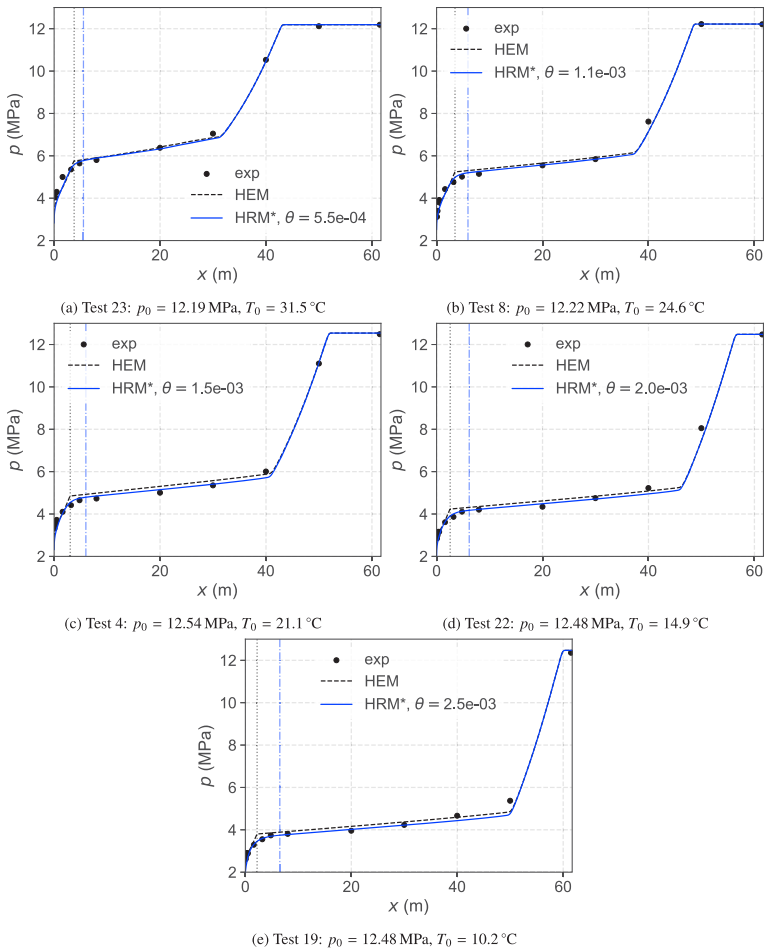

(a) Test 23: p_0 = 12.19 MPa, T_0 = 31.5 °C

(b) Test 8: p_0 = 12.22 MPa, T_0 = 24.6 °C

(c) Test 4: p_0 = 12.54 MPa, T_0 = 21.1 °C

(d) Test 22: p_0 = 12.48 MPa, T_0 = 14.9 °C

(e) Test 19: p_0 = 12.48 MPa, T_0 = 10.2 °C

Fig. 16. Measured and simulated pressure along the pipe at t = 100 ms. The vertical lines mark where two-phase flow begins near the open end for HEM (dotted line) and HRM* (dash dotted line).

between the two-phase and single-phase rarefaction waves. The HRM* would then agree better with the measured data.

5.3. Analysis of model predictions and experimental non-equilibrium effects

5.3.1. Flashing front

Recent visualization experiments for the depressurization of CO_2 conducted by Quinn et al. (2022) show that the flashing front travels faster than what is predicted by HEM. We study the simulated flashing front by plotting the volume fraction of gas along the pipe at various times. In Fig. 17, we show the simulated volume fraction of gas along the pipe at times t = 2 ms, t = 4 ms and t = 6 ms for Test 8. The plots show that the flashing front predicted by HRM* moves faster into the pipe than that of HEM. This is also the case for the other depressurization tests. HRM* predicts a slightly lower pressure plateau than HEM and a more gradual transition from single-phase to two-phase flow due to the relaxation time in the flashing process. As flashing begins in all grid cells where the pressure is below the saturation pressure, flashing is initiated faster, further inside the computational domain for HRM*. Furthermore, following the subcharacteristic condition (see, e.g., Flåtten and Lund (2011)), the two-phase mixture speed of sound is higher for HRM* than for HEM, such that the pressure drops faster in the two-phase region, also bringing more grid cells to a low enough pressure to initiate flashing. These two effects cause the flashing front to move faster into the pipe for HRM*, providing qualitative agreement with the experimental observations of Quinn et al. (2022).

5.3.2. Superheat and pressure undershoot

In order to gain further understanding on the non-equilibrium effects observed in the experiments, we plot the predicted depressurization path of the HRM* in a $p - T$ diagram for all the experiments 8 cm from the open end, as shown in Fig. 18. We cannot compare these $p - T$ paths directly to experimental data due to the response time of the temperature sensors. The homogeneous superheat limit (SHL) predicted by classical nucleation theory is also included in the plot. This illustrates the line where a rate of 10^{12} bubbles $m^{-3}\,s^{-1}$ are predicted to nucleate homogeneously in the fluid, i.e. through random density fluctuations in the fluid. It has been shown by Wilhelmsen and Aasen (2022) that the maximum superheat attained in nozzle flow can be predicted by the homogeneous SHL for warm temperatures. Preliminary studies of the presented data shows a similar trend for pipe depressurizations (Log et al., 2022). Details on how the homogeneous SHL can be computed are provided in Appendix A. Note that even though the homogeneous SHL can predict the maximum degree of

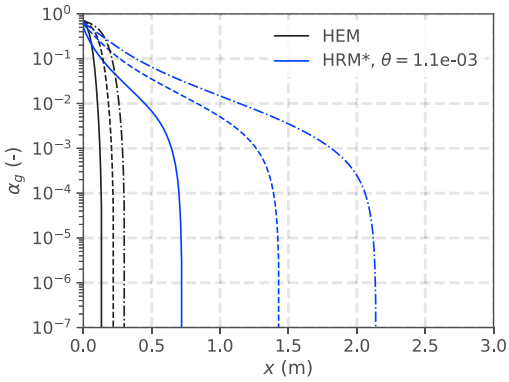

Fig. 17. Evolution of the gas volume fraction along the pipe for Test 8 calculated using the HEM (black lines) and HRM* (blue lines) for $t = 2$ ms (full lines), 4 ms (dashed lines) and 6 ms (dash dotted lines). (For interpretation of the references to color in this figure legend, the reader is referred to the web version of this article.)

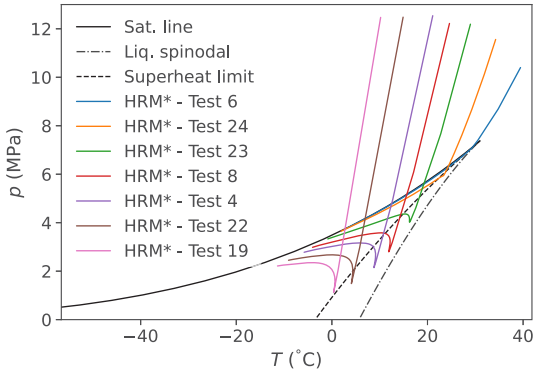

Fig. 18. The $p-T$ paths simulated by the HRM* at $x = 8$ cm from the open end of the pipe.

superheat observed in warm experiments, this does not mean that heterogeneous nucleation, i.e., nucleation occurring on a surface such as the wall of the pipe, is not present.

The HRM* simulations indicate strong non-equilibrium. Nevertheless, we would not expect the state of the CO_2 in the pipe to pass beyond the homogeneous SHL. For the colder experiments, the HRM* yields large pressure undershoots and strong superheating, indicating strong non-equilibrium effects. The $p-T$ paths of Tests 23, 8, 4 and 22 calculated by the HRM* pass beyond the homogeneous SHL and approach the liquid spinodal. It is possible to reach such degrees of superheat, but we find it unlikely that they should be reached in pipe depressurization experiments. Instead the temperature is most likely colder at the lowest point of the pressure dip than what is predicted by the HRM*, reducing the degree of superheat reached. In other words, we hypothesize that the depressurization paths will move further to the left in the phase diagram than what is predicted by HRM*. Such a cooling effect occurs when two-phase liquid–gas flow begins.

The above analysis suggests that the HRM* mass-transfer rate should be somewhat higher, producing more vapor once the saturation line is passed — and in particular when the superheat limit is passed. This could be achieved by reducing the relaxation time for increasing superheat. After all, the relaxation time is likely not constant. More physics should be incorporated in the mass-transfer rate model to account for this effect.

In Appendix C we test whether the high superheat predicted by the HRM* is caused by our minimum BBC. The minimum BBC intentionally allows for large superheat and pressure undershoots. However, we find that applying a BC with earlier choking does not change the superheat reached in the model, provided that the relaxation time is re-fitted to match the observed pressure undershoot. Thus, the problem lies with the mass-transfer model: it cannot fit the pressure undershoot without providing a too strong superheat. For the interested reader, the simulated $p-T$-path in the first grid cell in the computational domain, and in the outflow boundary cell for the HRM* is shown in Appendix D.

5.3.3. Onset of flashing

Based on the depressurization paths of our non-equilibrium simulations, we assume that in the HRM*, more vapor should be produced before the bottom of the pressure dip is reached. We here present an analysis of the vapor production in the experiments and for the HRM*. This is done by studying the experimental and simulated pressure over a short time-frame of 10 ms and observing signs of bubble nucleation, namely:

- pressure disturbances, and
- reduction in the depressurization rate.

In Fig. 19, we show the recorded and simulated pressure path at 8 cm from the open end of the pipe for the five warmest experiments, Test 4, 6, 8, 23 and 24. The pressure where the liquid isentrope crosses the homogeneous superheat limit (SHL) is marked by a red cross. The pressure where a significant mass fraction of gas is detected for the HRM* simulation, $x_g > 0.001$, is marked with a circle. For all these experiments, we observe the signs of bubble nucleation for the experimental measurement near the point where the superheat limit is crossed. For the warmest experiments, Tests 6, 23 and 24, bubble nucleation appears to occur at a pressure slightly below the superheat limit. For Test 8, bubble nucleation appears to occur slightly above the superheat limit. Interestingly, the pressure plateau recorded for Test 4 matches exactly with the superheat limit. For the HRM*, significant vapor production occurs at a lower pressure. Though the lowest point of the pressure dip matches well with the experiments, the details of the phase change is not fully captured by the HRM*.

In Fig. 20, we show the recorded and simulated pressure path at 8 cm from the open end of the pipe for the two coldest experiments, Test 19 and Test 22. We once again observe signs of significant vapor production in the recorded pressure at a higher pressure than what is predicted by the HRM*. In contrast to the warmer experiments, bubble nucleation for Test 19 and Test 22 occurs far above the homogeneous superheat limit. In fact, the pressure of Test 19 never reaches the expected homogeneous superheat limit, and therefore no red cross is marked in Fig. 20(b). For these cold initial temperatures, the maximum degree of superheat is likely determined by heterogeneous nucleation instead of homogeneous nucleation. This transition occurs somewhere between the initial conditions of Test 4 and Test 22, i.e., $14.9\,°C \leq T_0 \leq 21.1\,°C$ and $p_0 \approx 12$ MPa.

6. Conclusion

In the present work, we have presented a series of CO_2 depressurization experiments and compared the pressure measurements of the first 100 ms with model predictions of a simple non-equilibrium relaxation model (HRM*) and the homogeneous equilibrium model (HEM). This is done in order to better understand and quantify non-equilibrium effects during the flashing process (boiling caused by the depressurization). The non-equilibrium phase-transition is characterized by a pressure undershoot and recovery. This is important to take into account in engineering tools to accurately estimate mass flow rates through valves and orifices, and for safety assessments such as the prediction of running ductile fracture in CO_2-carrying pipelines.

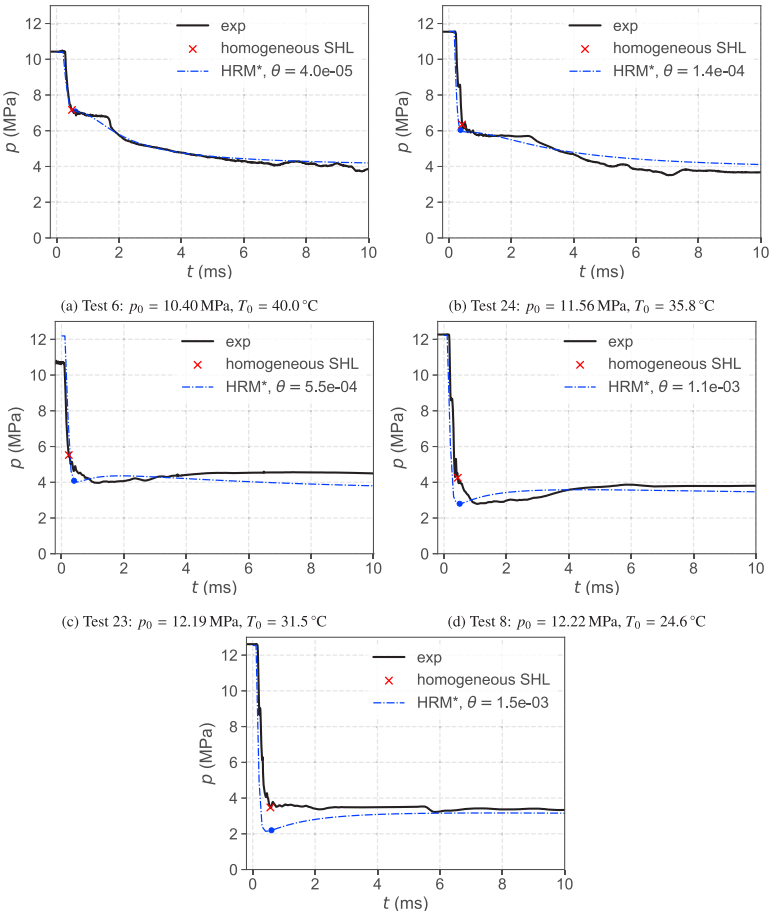

(a) Test 6: p_0 = 10.40 MPa, T_0 = 40.0 °C

(b) Test 24: p_0 = 11.56 MPa, T_0 = 35.8 °C

(c) Test 23: p_0 = 12.19 MPa, T_0 = 31.5 °C

(d) Test 8: p_0 = 12.22 MPa, T_0 = 24.6 °C

(e) Test 4: p_0 = 12.54 MPa, T_0 = 21.1 °C

Fig. 19. Measured and simulated pressure at $x = 0.08$ m from the open end for Tests 4, 6, 8, 23, and 24. The pressure at which the liquid isentrope crosses the homogeneous superheat limit (SHL) is marked as a red cross. A circular markers shows where $x_g > 0.001$ for the HRM* simulations.

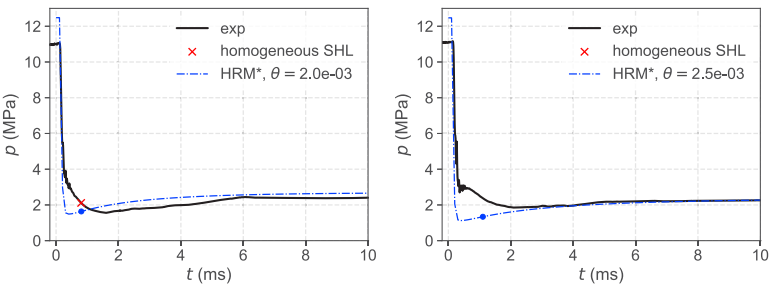

(a) Test 22: p_0 = 12.48 MPa, T_0 = 14.9 °C

(b) Test 19: p_0 = 12.47 MPa, T_0 = 10.2 °C

Fig. 20. Measured and simulated pressure at $x = 0.08$ m from open end for Test 19 and Test 22. The pressure at which the liquid isentrope crosses the homogeneous superheat limit (SHL) is marked as a red cross. A circular markers shows where $x_g > 0.001$ for the HRM* simulations. For Test 19, the measured pressure always stays above the SHL pressure, so there is no cross marked.

The CO_2 depressurization tests are conducted at seven different initial temperatures for an initial pressure of approximately 12 MPa. For the two warmest experiments, where the depressurization paths pass very close to the critical point of CO_2, no pressure recovery was observed. Our simulations indicate that the phase change occurred slightly out of equilibrium. For the lower temperature experiments, a

clear pressure undershoot and recovery was observed near the pipe outlet. The models suggest strong non-equilibrium effects.

The HRM* was fitted to the experimentally measured pressure dip by tuning a relaxation time. The relaxation time decreases for increasing initial temperatures, with the relaxation time for the coldest test at $T_0 = 10.2\,°C$ being approximately 60 times longer than that for the warmest test at $T_0 = 40.0\,°C$. We suggest a correlation for the relaxation time based on the initial entropy of the fluid in the pipe, where the relaxation time goes to zero at the critical point entropy. This is in agreement with bubble nucleation theory. More experimental data are needed to determine the accuracy of the correlation at colder temperatures, with $T_0 \leq 10\,°C$, and different initial pressures. The pressure–temperature paths simulated by the HRM* near the open end of the pipe approach the liquid stability limit (spinodal). Though it is possible to reach the liquid stability limit under extreme conditions, it is unlikely that it is reached in a pipe depressurization experiment. We therefore conclude that the HRM* with the present mass-transfer correlation overestimates the fluid temperature during the first ms of the flow.

Upon closer inspection of the pressure traces near the open end of the pipe, we observe that the onset of significant vapor production predicted by the HRM* occurs at a lower pressure than the point where bubble nucleation is observed in the experiments. The five warmest depressurization tests studied show signs of bubble nucleation near the predicted homogeneous superheat limit. In contrast, the two coldest tests show signs of bubble nucleation at a higher pressure than the homogeneous superheat limit. This is in agreement with the findings of Wilhelmsen and Aasen (2022), showing that the maximum superheat reached becomes determined by heterogeneous nucleation instead of homogeneous nucleation at colder temperatures.

The experimental results show that the pressure remained elevated around 50 ms to 150 ms after the pressure recovery near the pipe outlet for the colder tests, providing a "hump" in the pressure recordings. It is hypothesized that this is caused by bubble breakup and growth enhancing the boiling process and elevating the pressure near the pipe's open end, as suggested by Ivashnyov et al. (2000) for water depressurization tests. Both the HEM and the HRM* underestimate the pressure during this time. Finally, the HRM* simulations predict a flashing front that moves faster into the pipe than the HEM simulations. This is in agreement with recent visualization experiments conducted by Quinn et al. (2022).

In order to capture the complex non-equilibrium effects during depressurization, a more refined model will be needed for the mass-transfer rate from liquid to gas, incorporating nucleation and bubble growth. A first step in this direction can be to design a relaxation time correlation where the relaxation time decreases as the homogeneous superheat limit is approached. Further work may include the conduction of experiments at different initial pressures and colder initial temperatures. Experiments at colder initial temperatures are relevant to capture how the non-equilibrium effects change for depressurization paths crossing the saturation line closer to the triple point of CO_2, and to determine the effect of heterogeneous nucleation.

CRediT authorship contribution statement

Alexandra Metallinou Log: Conceptualization, Methodology, Software, Data curation, Formal analysis, Investigation, Writing – original draft, Visualization. **Morten Hammer:** Conceptualization, Methodology, Software, Investigation, Writing – review & editing. **Han Deng:** Investigation, Software, Data curation, Writing – review & editing. **Anders Austegard:** Investigation, Methodology, Software, Resources, Writing – review & editing. **Armin Hafner:** Writing – review & editing, Supervision. **Svend Tollak Munkejord:** Conceptualization, Methodology, Writing – review & editing, Supervision, Funding acquisition.

Declaration of competing interest

The authors declare that they have no known competing financial interests or personal relationships that could have appeared to influence the work reported in this paper.

Data availability

The experimental data recorded in this study can be downloaded from Zenodo (Log et al., 2023). (The DOI will be activated at publication.)

Acknowledgments

This publication has been produced with support from the NCCS Centre, performed under the Norwegian research programme Centres for Environment-friendly Energy Research (FME). The authors acknowledge the following partners for their contributions: Aker BP, Aker Carbon Capture, Allton, Ansaldo Energia, Baker Hughes, CoorsTek Membrane Sciences, Elkem, Eramet, Equinor, Gassco, Hafslund Oslo Celsio, KROHNE, Larvik Shipping, Norcem Heidelberg Cement, Offshore Norge, Quad Geometrics, Stratum Reservoir, TotalEnergies, Vår Energi, Wintershall Dea and the Research Council of Norway (257579).

The construction of the ECCSEL Depressurization Facility was supported by the INFRASTRUKTUR programme of the Research Council of Norway (225868).

Appendix A. The homogeneous superheat limit

We here present details on how the homogeneous superheat limit can be estimated using classical nucleation theory. The superheat limit can be considered the experimentally obtainable superheat achieved before sudden phase change is observed. This limit is assumed to be connected to the rate of bubble formation, or "nucleation" rate.

Generally, nucleation is divided into two categories: homogeneous and heterogeneous nucleation. Homogeneous nucleation occurs in the bulk of the liquid and is caused by random density fluctuations in the liquid creating bubbles large enough to grow and not collapse back into the liquid phase. In order to create a stable bubble, an activation energy must be reached. Heterogeneous nucleation occurs on a surface like a wall or an impurity, lowering the activation energy of nucleation.

The experimentally achievable superheat limit can be estimated using classical nucleation theory (CNT), which models homogeneous nucleation. CNT provides a formal estimate on the nucleation rate of critically-sized embryos of a new phase in the mother phase. Here, critically-sized is defined as the size where the embryo is just large enough not to collapse back to the mother phase. The derivation of this rate is presented by Debenedetti (1997), and we here simply state the resulting equations.

The nucleation rate (critically-sized embryos formed per volume and time) is defined as an Arrhenius-type rate law,

$$J = K \exp\left(-\frac{\Delta G^*}{k_B T_\ell}\right), \tag{A.1}$$

where ΔG is the free-energy barrier of embryo formation, k_B is the Boltzmann constant and K is a kinetic prefactor. The superscript $*$ denotes properties of a critically-sized embryo. For the formation of bubbles in a superheated liquid, the free-energy barrier is estimated to be

$$\Delta G^* = \frac{4\pi\sigma r^{*2}}{3}, \tag{A.2}$$

where σ denotes the surface tension and r the radius of the bubble. It is assumed that the surface tension of the bubble, σ, is equal to the macroscopic surface tension of a planar interface between the liquid and vapor at equilibrium.

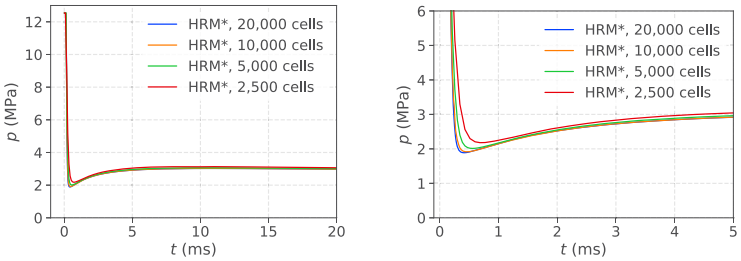

(a) Full pressure path. (b) Differences in the pressure dip (zoom).

Fig. B.21. Simulated pressure trace (HRM*) at $x = 0.08$ m for 2500, 5000, 10,000 and 20,000 grid cells for the initial condition of Test 4.

The critical radius of the bubble is approximated as

$$r^* = \frac{2\sigma}{p_{\text{sat}}(T_\ell) - p_\ell}, \tag{A.3}$$

where $p_{\text{sat}}(T_\ell)$ is the saturation pressure at the temperature of the liquid. The kinetic prefactor can be approximated as

$$K = \tilde{\rho}_\ell \sqrt{\frac{2\sigma}{\pi m}}, \tag{A.4}$$

where m is the mass of one molecule and $\tilde{\rho}_\ell = \rho_\ell / m$ is the number density of molecules in the liquid. With these relations, the superheat limit temperature can be estimated by solving

$$J(T_\ell) = J_{\text{crit}} \tag{A.5}$$

for T_ℓ. Here, J_{crit} is the critical nucleation rate, at which sudden phase change is observed. In this work, we follow (Aursand et al., 2016b), employing $J_{\text{crit}} = 1 \times 10^{12}\,\text{m}^{-3}\,\text{s}^{-1}$. Due to the exponential functional form in (A.1), the superheat limit is not very sensitive to the critical rate.

Appendix B. Grid-refinement study

In order to determine an appropriate number of grid cells applied in the simulations, a grid refinement study is conducted. With the assumption that the results will hold for all the initial conditions studied in this work, the grid-refinement is conducted for the conditions of Test 4. We test grids with 2500, 5000, 10,000 and 20,000 grid cells. The simulations are conducted up to $t_{\text{end}} = 20$ ms and the relaxation time for the mass-transfer source term is set to $\theta = 2$ ms. The results are presented in Figs. B.21 and B.22.

Fig. B.21 shows the pressure traces simulated using the HRM* for the different grids at $x = 0.08$ m. The result of the different grids nearly overlap, but the lowest point of the pressure undershoot becomes lower for finer grids and occurs earlier in time. This effect is smaller further inside the pipe. In Fig. B.22, we show that the pressure waves become sharper for finer grids, as expected. The sharper pressure drop is likely causing the change in the pressure undershoot as a faster pressure drop allows for further penetration into the metastable region before delayed gas nucleation begins.

The simulation with 2500 grid cells predicts the lowest point in the pressure dip to be approximately 0.3 MPa higher than that with 20,000 grid cells. For 5000 grid cells, this difference is 0.13 MPa and the difference is around 0.03 MPa for 10,000 grid cells. Based on these results, we choose to apply 10,000 grid cells for the simulations in the present paper.

Appendix C. $p - T$ Path of the HRM* with the HEM outflow boundary condition

The pressures predicted by HRM* matches experimentally measured pressure undershoots well, but the calculated superheats are quite high.

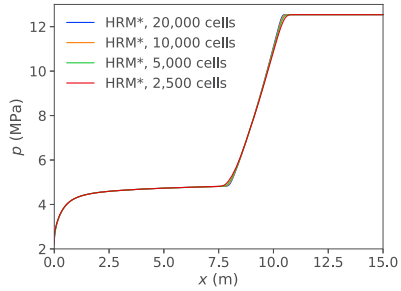

Fig. B.22. Simulated pressure (HRM*) along the pipe at $t = 20$ ms for 2500, 5000, 10,000 and 20,000 grid cells for the initial condition of Test 4.

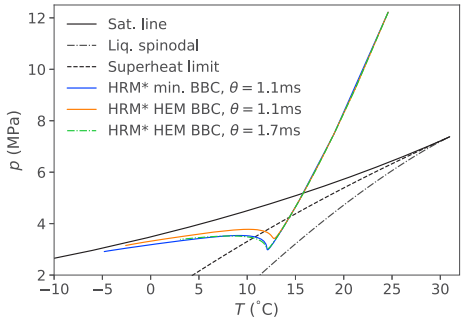

Fig. C.23. Effect of different settings for the outflow BC for Test 8. p–T paths simulated by the HRM* $x = 3$ mm from the open end of the pipe.

In this section, we investigate whether the HRM* predicts a smaller superheat if we apply the HEM BBC instead of the minimum BBC as the outflow BC. The HEM BBC assumes that the flow occurs in equilibrium, such that the fluid state is locked to the saturation line for two-phase flow. Generally, this will lead to a higher choking pressure at the boundary than what is predicted by the minimum BBC.

In Fig. C.23, we compare the $p-T$-paths predicted by the HRM* for Test 8 applying the minimum BBC with $\theta = 1.1$ ms, and the HEM BBC with $\theta = 1.1$ ms and $\theta = 1.7$ ms at $x = 3$ mm from the open end. As the HEM BBC enforces a higher choking pressure, the pressure undershoot becomes smaller with this BBC than for the minimum BBC with the same relaxation time in the mass-transfer rate. If the relaxation time in the HRM* is increased for the HEM BBC to $\theta = 1.7$ ms, the same pressure undershoot can be reached as for the minimum BBC with $\theta = 1.1$ ms.

The relaxation time is chosen to fit the pressure undershoot measured in the experiments i.e. $\theta = 1.7$ ms for the HEM BBC. Though

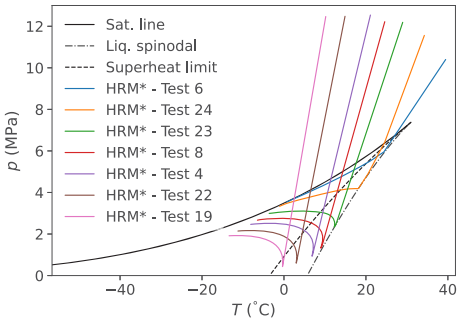

Fig. D.24. Effect of initial condition on the depressurization process: The $p-T$ paths simulated by the HRM* in the first grid cell of the computational domain, at $x = 3$ mm from the open end of the pipe.

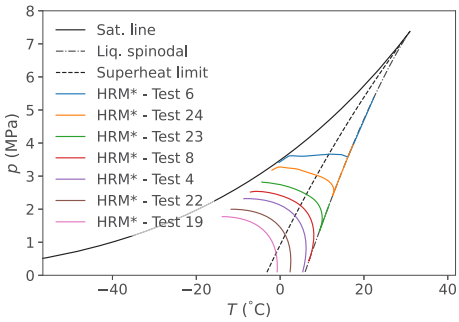

Fig. D.25. The $p-T$ paths simulated by the HRM* in the outflow ghost cell, at $x = -3$ mm from the open end of the pipe.

the pressure recovery becomes slightly different for the HEM BBC, the degree of superheat reached is the same for the HRM* with both BCs. This means that the large superheat predicted by the HRM* is not caused by the minimum BBC, but by the mass-transfer model. To reduce computational costs, these simulations were run with 1000 grid cells, but the results apply for finer grids as well.

Appendix D. $p-T$ path in the first grid cell and the outflow ghost cell

In Fig. D.24, we show the simulated $p-T$ paths for all the tests in the first grid cell of the computational domain, which has its cell center at 3 mm from the open end. For this grid cell, the simulated depressurization path of Tests 6, 8, 23 and 24 reaches the liquid spinodal. For these tests, the relaxation times are at their maximum value. If a longer relaxation time is chosen, the simulations will crash as the liquid phase will pass into the unstable domain.

In Fig. D.25, we show the simulated $p-T$-paths for all the experiments in the outflow ghost cell. It is clear that the method where the choking pressure for the BC is searched for by "walking" along the spinodal (see Section 4.2) is needed for the four warmest experiments, Tests 6, 8, 23 and 24.

References

Angielczyk, W., Bartosiewicz, Y., Butrymowicz, D., Seynhaeve, J.-M., 2010. 1-D modeling of supersonic carbon dioxide two-phase flow through ejector motive nozzle. In: International Refrigeration and Air Conditioning Conference. Purdue University, URL https://docs.lib.purdue.edu/iracc/1102/.

Armstrong, K., Allason, D., 2014. 2" NB Shocktube Releases of Dense Phase CO_2. Tech. rep., GL Noble Denton, Gilsland Cumbria, UK, Available from https://www.dnvgl.com/oilgas/innovation-development/joint-industry-projects/co2pipetrans.html.

Aursand, E., Dumoulin, S., Hammer, M., Lange, H.I., Morin, A., Munkejord, S.T., Nordhagen, H.O., 2016a. Fracture propagation control in CO_2 pipelines: Validation of a coupled fluid–structure model. Eng. Struct. 123, 192–212. http://dx.doi.org/10.1016/j.engstruct.2016.05.012.

Aursand, P., Gjennestad, M.A., Aursand, E., Hammer, M., Wilhelmsen, Ø., 2016b. The spinodal of single- and multi-component fluids and its role in the development of modern equations of state. Fluid Phase Equilib. 436, 98–112. http://dx.doi.org/10.1016/j.fluid.2016.12.018.

Aursand, P., Hammer, M., Lavrov, A., Lund, H., Munkejord, S.T., Torsæter, M., 2017. Well integrity for CO_2 injection from ships: Simulation of the effect of flow and material parameters on thermal stresses. Int. J. Greenh. Gas Control 62, 130–141. http://dx.doi.org/10.1016/j.ijggc.2017.04.007.

Banasiak, K., Hafner, A., 2013. Mathematical modelling of supersonic two-phase R744 flows through converging–diverging nozzles: The effects of phase transition models. Appl. Therm. Eng. (ISSN: 1359-4311) 51 (1), 635–643. http://dx.doi.org/10.1016/j.applthermaleng.2012.10.005.

Barták, J., 1990. A study of the rapid depressurization of hot water and the dynamics of vapour bubble generation in superheated water. Int. J. Multiph. Flow. 16, 789–798. http://dx.doi.org/10.1016/0301-9322(90)90004-3.

Bejan, A., 1993. Heat Transfer. John Wiley & Sons, Inc, New York, ISBN: 0-471-50290-1.

Bilicki, Z., Kestin, J., 1990. Physical Aspects of the Relaxation Model in Two-Phase Flow. In: Proceedings of the Royal Society of London. Series A, Mathematical and Physical Sciences, Vol. 428. Royal Society, pp. 379–397.

Botros, K.K., Geerligs, J., Rothwell, B., Robinson, T., 2016. Measurements of decompression wave speed in pure carbon dioxide and comparison with predictions by equation of state. J. Press. Vess. – Trans. ASME 138 (3), http://dx.doi.org/10.1115/1.4031941.

Botros, K.K., Geerligs, J., Rothwell, B., Robinson, T., 2017. Effect of argon as the primary impurity in anthropogenic carbon dioxide mixtures on the decompression wave speed. Can. J. Chem. Eng. 95 (3), 440–448. http://dx.doi.org/10.1002/cjce.22689.

Botros, K.K., Hippert, Jr., E., Craidy, P., 2013. Measuring decompression wave speed in CO_2 mixtures by a shock tube. Pipelines Int. 16, 22–28.

Brown, S., Beck, J., Mahgerefteh, H., Fraga, E.S., 2013. Global sensitivity analysis of the impact of impurities on CO_2 pipeline failure. Reliab. Eng. Syst. Safe 115, 43–54. http://dx.doi.org/10.1016/j.ress.2013.02.006.

Brown, S., Martynov, S., Mahgerefteh, H., Chen, S., Zhang, Y., 2014. Modelling the non-equilibrium two-phase flow during depressurisation of CO_2 pipelines. Int. J. Greenh. Gas Control 30, 9–18. http://dx.doi.org/10.1016/j.ijggc.2014.08.013.

Clausen, S., Oosterkamp, A., Strøm, K.L., 2012. Depressurization of a 50 km long 24 inches CO_2 pipeline. In: Røkke, N.A., Hägg, M.-B., Mazzetti, M.J. (Eds.), 6th Trondheim Conference on CO_2 Capture, Transport and Storage (TCCS-6). In: BIGCCS / SINTEF / NTNU, Energy Procedia, vol. 23, Trondheim, Norway, pp. 256–265. http://dx.doi.org/10.1016/j.egypro.2012.06.044.

Cosham, A., Eiber, R.J., 2008. Fracture control in carbon dioxide pipelines – The effect of impurities. In: 7th International Pipeline Conference, IPC2008, Vol. 3. ASME, IPTI, Calgary, Canada, pp. 229–240.

Cosham, A., Jones, D.G., Armstrong, K., Allason, D., Barnett, J., 2012. Ruptures in Gas Pipelines, Liquid Pipelines and Dense Phase Carbon Dioxide Pipelines. ASME, IPTI, Calgary, Canada, pp. 465–482. http://dx.doi.org/10.1115/IPC2012-90463.

Davis, S.F., 1988. Simplified second-order godunov-type methods. SIAM J. Sci. Stat. Comput. 9, 445–473. http://dx.doi.org/10.1137/0909030.

De Lorenzo, M., Lafon, P., Di Matteo, M., Pelanti, M., Seynhaeve, J.-M., Bartosiewicz, Y., 2017. Homogeneous two-phase flow models and accurate steam-water table look-up method for fast transient simulations. Int. J. Multiph. Flow. 95, 199–219. http://dx.doi.org/10.1016/j.ijmultiphaseflow.2017.06.001.

Debenedetti, P.G., 1997. Metastable Liquids: Concepts and Principles. Princeton University Press, ISBN: 9780691213941, http://dx.doi.org/10.1515/9780691213941.

Deligiannis, P., Cleaver, J., 1990. The role of nucleation in the initial phases of a rapid depressurization of a subcooled liquid. Int. J. Multiph. Flow. 16 (6), 975–984. http://dx.doi.org/10.1016/0301-9322(90)90102-O.

Downar-Zapolski, P., Bilicki, Z., Bolle, L., Franco, J., 1996. The non-equilibrium relaxation model for one-dimensional flashing liquid flow. Int. J. Multiph. Flow. 22 (3), 473–483. http://dx.doi.org/10.1016/0301-9322(95)00078-X.

Drescher, M., Varholm, K., Munkejord, S.T., Hammer, M., Held, R., de Koeijer, G., 2014. Experiments and modelling of two-phase transient flow during pipeline depressurization of CO_2 with various N_2 compositions. In: Dixon, T., Herzog, H., Twinning, S. (Eds.), GHGT-12–12th International Conference on Greenhouse Gas Control Technologies. In: University of Texas at Austin / IEAGHGT, Energy Procedia, vol. 63, Austin, Texas, USA, pp. 2448–2457. http://dx.doi.org/10.1016/j.egypro.2014.11.267.

ECCSEL, 2021. Depressurization facility. https://www.eccsel.org/catalogue/113, Accessed 2023-05-23.

Edwards, A.R., O'Brien, T.P., 1970. Studies of phenomena connected with the depressurization of water reactors. J. Br. Nucl. Energy Soc. 9 (2), 125–135.

Einstein, A., 1920. Propagation of Sound in Partly Dissociated Gases. In: Sitzungsberichte. Berlin, pp. 380–385, URL https://einsteinpapers.press.princeton.edu/vol7-doc/373.

Flåtten, T., Lund, H., 2011. Relaxation two-phase flow models and the subcharacteristic condition. Math. Mod. Methods Appl. Syst. 21 (12), 2379–2407. http://dx.doi.org/10.1142/S0218202511005775.

Flechas, T., Laboureur, D.M., Glover, C.J., 2020. A 2-D CFD model for the decompression of carbon dioxide pipelines using the Peng-Robinson and the Span-Wagner equation of state. Process Saf. Environ. 140, 299–313. http://dx.doi.org/10.1016/j.psep.2020.04.033.

Friedel, L., 1979. Improved friction pressure drop correlations for horizontal and vertical two phase pipe flow. In: Proceedings, European Two Phase Flow Group Meeting. Ispra, Italy, Paper E2.

Gu, S., Li, Y., Teng, L., Wang, C., Hu, Q., Zhang, D., Ye, X., Wang, J., Iglauer, S., 2019. An experimental study on the flow characteristics during the leakage of high pressure CO_2 pipelines. Process Saf. Environ. 125, 92–101. http://dx.doi.org/10.1016/j.psep.2019.03.010.

Gungor, K.E., Winterton, R.H.S., 1987. Simplified general correlation for saturated flow boiling and comparisons of correlations with data. Chem. Eng. Res. Des. 65 (2), 148–156.

Guo, X., Yan, X., Yu, J., Yang, Y., Zhang, Y., Chen, S., Mahgerefteh, H., Martynov, S., Collard, A., 2017. Pressure responses and phase transitions during the release of high pressure CO_2 from a large-scale pipeline. Energy 118, 1066–1078. http://dx.doi.org/10.1016/j.energy.2016.10.133.

Hammer, M., Aasen, A., Wilhelmsen, Ø., 2020. Thermopack. https://github.com/SINTEF/thermopack/, Accessed 2020-12-15.

Hammer, M., Aasen, A., Wilhelmsen, Ø., 2023. Thermopack. https://github.com/thermotools/thermopack, Accessed 2023-06-14.

Hammer, M., Deng, H., Austegard, A., Log, A.M., Munkejord, S.T., 2022. Experiments and modelling of choked flow of CO_2 in orifices and nozzles. Int. J. Multiph. Flow. 156, 104201. http://dx.doi.org/10.1016/j.ijmultiphaseflow.2022.104201.

Hansen, P.M., Gåthaug, A.V., Bjerketvedt, D., Vågsæther, K., 2019. Rapid depressurization and phase transition of CO_2 in vertical ducts – small-scale experiments and rankine-hugoniot analyses. J. Hazard. Mater 365, 16–25. http://dx.doi.org/10.1016/j.jhazmat.2018.10.092.

Ibrahim, O.M., Hansen, P.M., Bjerketvedt, D., Vågsæther, K., 2021. Evaporation characteristics during decompression of liquified CO_2 from a conical-shaped vessel. Results Eng. 12. http://dx.doi.org/10.1016/j.rineng.2021.100304.

IEA, 2021. Net Zero By 2050 – A Roadmap for the Global Energy Sector. IEA, Paris, URL https://www.iea.org/reports/net-zero-by-2050.

IEA, 2022. World Energy Outlook 2022. IEA, Paris, URL https://www.iea.org/reports/net-zero-by-2050.

IPCC, 2022. Summary for Policymakers. In: Climate Change 2022: Mitigation of Climate Change. Contribution of Working Group III To the Sixth Assessment Report of the Intergovernmental Panel on Climate Change. Cambridge University Press, Cambridge, UK and New York, NY, USA, http://dx.doi.org/10.1017/9781009157926.001, URL https://www.ipcc.ch/report/ar6/wg3/.

Ivashnyov, O.E., Ivashneva, M.N., Smirnov, N.N., 2000. Slow waves of boiling under hot water depressurization. J. Fluid Mech. 413, 149–180. http://dx.doi.org/10.1017/S0022112000008417.

Jie, H.E., Xu, B.P., Wen, J.X., Cooper, R., Barnett, J., 2012. Predicting the decompression characteristics of carbon dioxide using computational fluid dynamics. In: 9th International Pipeline Conference IPC2012. ASME, IPTI, Calgary, Canada, pp. 585–595. http://dx.doi.org/10.1115/IPC2012-90649.

Kunz, O., Wagner, W., 2012. The GERG-2008 wide-range equation of state for natural gases and other mixtures: An expansion of GERG-2004. J. Chem. Eng. Data 57 (11), 3032–3091. http://dx.doi.org/10.1021/je300655b.

Le Martelot, S., Saurel, R., Nkonga, B., 2014. Towards the direct numerical simulation of nucleate boiling flows. Int. J. Multiph. Flow. 66, 62–78. http://dx.doi.org/10.1016/j.ijmultiphaseflow.2014.06.010.

LeVeque, R.J., 2002. Finite Volume Methods for Hyperbolic Problems. Cambridge University Press, Cambridge, UK, ISBN: 0-521-00924-3.

Liao, Y., Lucas, D., 2017. Computational modelling of flash boiling flows: A literature survey. Int. J. Heat Mass Transf. 111, 246–265. http://dx.doi.org/10.1016/j.ijheatmasstransfer.2017.03.121.

Linga, G., Flåtten, T., 2019. A hierarchy of non-equilibrium two-phase flow models. ESAIM: ProcS 66, 109–143. http://dx.doi.org/10.1051/proc/201966006.

Liu, B., Liu, X., Lu, C., Godbole, A., Michal, G., Tieu, A.K., 2017. Multi-phase decompression modeling of CO_2 pipelines. Greenh. Gas. Sci. Technol. 7 (4), 665–679. http://dx.doi.org/10.1002/ghg.1666.

Liu, B., Liu, X., Lu, C., Godbole, A., Michal, G., Tieu, A.K., 2018. A CFD decompression model for CO_2 mixture and the influence of non-equilibrium phase transition. Appl. Energy 227, 516–524. http://dx.doi.org/10.1016/j.apenergy.2017.09.016.

Log, A.M., 2020. Development and Investigation of HLLC-Type Finite-Volume Methods for One and Two-Phase Flow in Pipes with Varying Cross-Sectional Area (Master's thesis). Norwegian University of Science and Technology, URL https://alex{and}ramlog.wordpress.com/2020/12/14/masters-thesis/.

Log, A.M., Hammer, M., Deng, H., Austegard, A., Hafner, A., Munkejord, S.T., 2023. Depressurization of CO_2 in Pipes: Effect of Initial State on Non-Equilibrium Two-Phase Flow – Dataset. Zenodo, http://dx.doi.org/10.5281/zenodo.7669536.

Log, A.M., Munkejord, S.T., Hammer, M., Hafner, A., Deng, H., Austegard, A., 2022. Investigation of non-equilibrium effects during the depressurization of carbon dioxide. In: 15th IIR-Gustav Lorentzen Conference on Natural Refrigerants (GL2022). Proceedings. Trondheim, Norway, June 13-15th 2022. International Institute of Refrigeration (IIR), http://dx.doi.org/10.18462/iir.gl2022.0197.

Lund, H., 2012. A hierarchy of relaxation models for two-phase flow. SIAM J. Appl. Math. 72 (6), 1713–1741. http://dx.doi.org/10.1137/12086368X.

Lund, H., Aursand, P., 2012. Two-phase flow of CO_2 with phase transfer. In: Røkke, N.A., Hägg, M.-B., Mazzetti, M.J. (Eds.), 6th Trondheim Conference on CO_2 Capture, Transport and Storage (TCCS-6). In: BIGCCS / SINTEF / NTNU, Energy Procedia, vol. 23, Trondheim, Norway, pp. 246–255. http://dx.doi.org/10.1016/j.egypro.2012.06.034.

Martynov, S., Zheng, W., Mahgerefteh, H., Brown, S., Hebrard, J., Jamois, D., Proust, C., 2018. Computational and experimental study of solid-phase formation during the decompression of high-pressure CO_2 pipelines. Ind. Eng. Chem. Res. 57 (20), 7054–7063. http://dx.doi.org/10.1021/acs.iecr.8b00181.

Michal, G., Østby, E., Davis, B.J., Røneid, S., Lu, C., 2020. An empirical fracture control model for dense-phase CO2 carrying pipelines. In: 13th International Pipeline Conference, IPC 2020. ASME, http://dx.doi.org/10.1115/IPC2020-9421.

Munkejord, S.T., Austegard, A., Deng, H., Hammer, M., Stang, H.G.J., Løvseth, S.W., 2020. Depressurization of CO_2 in a pipe: High-resolution pressure and temperature data and comparison with model predictions. Energy 211, 118560. http://dx.doi.org/10.1016/j.energy.2020.118560.

Munkejord, S.T., Deng, H., Austegard, A., Hammer, M., Skarsvåg, H.L., Aasen, A., 2021. Depressurization of CO_2-N_2 and CO_2-He in a pipe: Experiments and modelling of pressure and temperature dynamics. Int. J. Greenh. Gas Control 109, 103361. http://dx.doi.org/10.1016/j.ijggc.2021.103361.

Munkejord, S.T., Hammer, M., 2015. Depressurization of CO_2-rich mixtures in pipes: Two-phase flow modelling and comparison with experiments. Int. J. Greenh. Gas Con 37, 398–411. http://dx.doi.org/10.1016/j.ijggc.2015.03.029.

Munkejord, S.T., Hammer, M., Løvseth, S.W., 2016. CO_2 Transport: Data and models – A review. Appl. Energy 169, 499–523. http://dx.doi.org/10.1016/j.apenergy.2016.01.100.

Nakagawa, M., Berana, M.S., Kishine, A., 2009. Supersonic two-phase flow of CO_2 through converging-diverging nozzles for the ejector refrigeration cycle. Int. J. Refrig. 32 (6), 1195–1202. http://dx.doi.org/10.1016/j.ijrefrig.2009.01.015.

Pelanti, M., 2022. Arbitrary-rate relaxation techniques for the numerical modeling of compressible two-phase flows with heat and mass transfer. Int. J. Multiph. Flow. 153, 104097. http://dx.doi.org/10.1016/j.ijmultiphaseflow.2022.104097.

Pinhasi, G.A., Ullmann, A., Dayan, A., 2005. Modeling of flashing two-phase flow. Rev. Chem. Eng. 21 (3–4), 133–264. http://dx.doi.org/10.1515/REVCE.2005.21.3-4.133.

Quinn, D., Stannard, D., Edwards, J., Botros, K.K., Johansen, C., 2022. Experimental visualization and characteristics of bubble nucleation during rapid decompression of supercritical and subcooled carbon dioxide. Int. J. Pres. Ves. Pip. 195, 104569. http://dx.doi.org/10.1016/j.ijpvp.2021.104569.

Roussanaly, S., Bureau-Cauchois, G., Husebye, J., 2013. Costs benchmark of CO_2 transport technologies for a group of various size industries. Int. J. Greenh. Gas Control 12, 341–350. http://dx.doi.org/10.1016/j.ijggc.2012.05.008.

Saurel, R., Boivin, P., Le Métayer, O., 2016. A general formulation for cavitating, boiling and evaporating flows. Comput. & Fluids 128, 53–64. http://dx.doi.org/10.1016/j.compfluid.2016.01.004.

Skarsvåg, H.L., Hammer, M., Munkejord, S.T., Log, A.M., Dumoulin, S., Gruben, G., 2023. Towards an engineering tool for the prediction of running ductile fractures in CO_2 pipelines. Process Saf. Environ. 171, 667–679. http://dx.doi.org/10.1016/j.psep.2023.01.054.

Span, R., Wagner, W., 1996. A new equation of state for carbon dioxide covering the fluid region from the triple-point temperature to 1100 k at pressures up to 800 MPa. J. Phys. Chem. Ref. Data 25 (6), 1509–1596. http://dx.doi.org/10.1063/1.555991.

Teng, L., Li, Y., Zhao, Q., Wang, W., Hu, Q., Ye, X., Zhang, D., 2016. Decompression characteristics of CO_2 pipelines following rupture. J. Nat. Gas Sci. Eng. 36 (A), 213–223. http://dx.doi.org/10.1016/j.jngse.2016.10.026.

Toro, E.F., 2009. Riemann solvers and numerical methods for fluid dynamics: A practical introduction, Third Springer-Verlag, Berlin, ISBN: 978-3-540-25202-3.

Toro, E.F., Spruce, M., Speares, W., 1994. Restoration of the contact surface in the HLL-Riemann solver. Shock Waves 4 (1), 25–34.

Wilhelmsen, Ø., Aasen, A., 2022. Choked liquid flow in nozzles: Crossover from heterogeneous to homogeneous cavitation and insensitivity to depressurization rate. Chem. Eng. Sci. 248, 117176. http://dx.doi.org/10.1016/j.ces.2021.117176.

Wilhelmsen, Ø., Aasen, A., Skaugen, G., Aursand, P., Austegard, A., Aursand, E., Gjennestad, M.A., Lund, H., Linga, G., Hammer, M., 2017. Thermodynamic modeling with equations of state: Present challenges with established methods. Ind. Eng. Chem. Res. 56 (13), 3503–3515. http://dx.doi.org/10.1021/acs.iecr.7b00317.

Winters, Jr., W.S., Merte, J.H., 1979. Experiments and Nonequilibrium Analysis of Pipe Blowdown. Nucl. Sci. Eng. 69 (3), 411–429. http://dx.doi.org/10.13182/NSE79-A19959.

Xiao, C., Lu, Z., Yan, L., Yao, S., 2020. Transient behaviour of liquid CO_2 decompression: CFD modelling and effects of initial state parameters. Int. J. Greenh. Gas Control 101, 103154. http://dx.doi.org/10.1016/j.ijggc.2020.103154.

Paper 6

Log, Alexandra Metallinou; Hammer, Morten; Munkejord, Svend Tollak. (2024) A flashing flow model for the rapid depressurization of CO_2 in a pipe accounting for bubble nucleation and growth. *International Journal of Multiphase Flow.* vol 171.

International Journal of Multiphase Flow 171 (2024) 104666

Contents lists available at ScienceDirect

International Journal of Multiphase Flow

journal homepage: www.elsevier.com/locate/ijmulflow

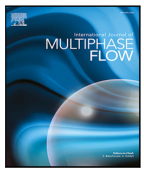

A flashing flow model for the rapid depressurization of CO_2 in a pipe accounting for bubble nucleation and growth

Alexandra Metallinou Log [b,*], Morten Hammer [a], Svend Tollak Munkejord [a]

[a] SINTEF Energy Research, P.O. Box 4761 Torgarden, NO-7465 Trondheim, Norway
[b] Norwegian University of Science and Technology, Department of Energy and Process Engineering, NO-7491 Trondheim, Norway

ARTICLE INFO

Keywords:
Carbon dioxide
Decompression
Flashing
Non-equilibrium
Nucleation
Vapor–liquid flows

ABSTRACT

Flashing flow is encountered in many industrial systems involving nozzles, valves and decompression of vessels and pipes. In the context of CO_2 capture and storage (CCS), the design of safe and efficient CO_2 transportation systems requires accurate flashing models, e.g., for safety analysis of pipe fractures and to predict the mass flow through relief valves. We propose a homogeneous flashing model (HFM) for flashing flow accounting for the underlying physical phenomena of the phase change: bubble nucleation, coalescence, break-up and growth. Homogeneous nucleation is modeled using classical nucleation theory and heterogeneous nucleation is approximated with constant rates of bubble creation and mass transfer from liquid to vapor. The flashing flow model is fitted for CO_2 pipe depressurization data at various initial conditions. We find that the same, constant model parameters can be applied for the whole set of depressurization cases considered, as opposed to the conventional homogeneous relaxation model which typically is tuned on a case-by-case basis. For depressurization paths where the fluid state passes close to the critical point, we demonstrate that an accurate description of the flashing process along the length of the pipe can only be achieved when both homogeneous and heterogeneous nucleation are accounted for.

1. Introduction

1.1. Motivation

Flash boiling (flashing) is a phase change phenomenon that is triggered by the depressurization of a liquid below its saturation pressure. This phenomenon affects the operation and safety assessment of several industrial systems including pressurized water (nuclear) reactors, refrigeration systems and of main interest for the present work: CO_2 transportation pipelines in the context of CO_2 capture and storage (CCS). Scenarios where flashing may occur includes the opening of a pressure relief valve or accidents such as a pipe rupture (Klinkby et al., 2011; Munkejord et al., 2016; Pham and Rusli, 2016; Liao and Lucas, 2017b). In such scenarios, the flashing process determines the resulting pressure, temperature, speed of sound and outflow rate of the fluid. It is therefore important to model flashing flows accurately.

During a rapid depressurization event, the liquid state can pass far into its thermodynamically metastable region before significant flashing begins, producing a *pressure undershoot* and the liquid becomes *superheated* as illustrated in Fig. 1. These are both measures of non-equilibrium. The non-equilibrium effects are strongly dependent on how bubbles nucleate and grow in the liquid. A better understanding of the underlying phenomena during flashing, such as bubble nucleation and growth, can benefit industrial applications both in terms of optimizing their efficiency and ensuring their safe operation.

The present work is particularly motivated by the need to develop accurate models to ensure that an initial puncture or crack in a CO_2-carrying pipeline will not develop into a *running ductile fracture* (RDF). RDF is a phenomenon where a defect in a pipe develops into a crack that propagates along the pipe, driven by the pressure forces of the escaping fluid (Cosham et al., 2014; Aursand et al., 2016a; DNV, 2021; Skarsvåg et al., 2023). Thus, accurate modeling of the pressure evolution during depressurization is required to design RDF-resistant pipes. The pressure evolution during depressurization is in turn strongly affected by the flashing process. In large-scale fracture tests with CO_2 and CO_2-rich mixtures, the crack-tip pressure is found to be up to 20% lower than the saturation pressure, see, e.g., Michal et al. (2020). In previous work, we have shown that predictions of the crack-tip pressure can be improved by taking into account non-equilibrium flashing as compared to the homogeneous equilibrium model (HEM), which assumes equilibrium between the phases (Skarsvåg et al., 2023).

For high-capacity CO_2-carrying pipelines, the CO_2 will typically be transported at supercritical pressures, and with an entropy below

* Corresponding author.
E-mail addresses: alexandra.m.log@ntnu.no, alexandra.log@sintef.no (A.M. Log).

https://doi.org/10.1016/j.ijmultiphaseflow.2023.104666
Received 1 August 2023; Received in revised form 30 October 2023; Accepted 5 November 2023
Available online 7 November 2023

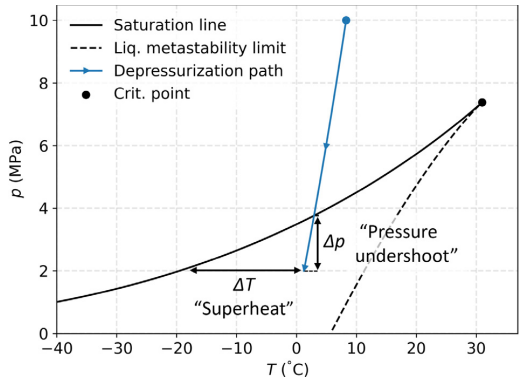

Fig. 1. Illustration of a depressurization path in the liquid/dense liquid phase before flashing begins in a *p-T* diagram for CO_2. The superheat and pressure undershoot reached before flashing begins are indicated.

that of the critical point, providing a liquid-like behavior of the fluid. This state is often referred to as "dense phase", although the definition of the term varies somewhat, see, e.g., IPCC (2005, Chap. 4), Brownsort (2019) and Committee on Carbon Capture, Use, and Storage (2019). For simplicity, we will call these states *liquid* if an isentropic depressurization will bring them to flash boil as a liquid. Our present definition of the liquid phase is shown in Fig. 2. In the figure we also show the (approximate) relevant operating range for high-capacity CO_2 pipelines. A part of the transcritical CO_2 refrigeration cycle will also be in this region, see, e.g., Ringstad et al. (2020). For transcritical CO_2 refrigeration cycles, flashing through an ejector device can be applied to regain lost work, making accurate modeling of flashing CO_2 valuable in order to optimize the system.

We have run a series of pipe depressurization tests for pure CO_2 in the relevant operating range for CO_2 pipelines, with initial temperatures from 10 °C to 40 °C and an initial pressure around 12 MPa (Munkejord et al., 2020b; Log et al., 2024). Note that for the warmer cases, an isentropic depressurization path will pass very close to the critical point of CO_2, whereas the colder cases pass further away. In this region of the phase diagram, the distance from the saturation curve to the metastability limit increases significantly as the temperature decreases, see Fig. 1. Therefore, the non-equilibrium effects during flashing vary considerably. To optimize the operation of and provide safety analyses for CO_2-carrying pipes, flow models should be able to predict these effects.

1.2. Typical depressurization results: importance of mass transfer during flashing

In Fig. 3, we show a typical pressure profile in a pipe filled with a liquid, initially at rest, during depressurization. As the pipe is depressurized, a rarefaction wave propagates into the pipe at the local speed of sound. When the pressure becomes low enough, the liquid starts flashing at the open end of the pipe. In Fig. 4, we show how the speed of sound in a liquid–vapor mixture changes with the vapor volume fraction for the homogeneous chemical potential-relaxation model, which is described in Section 2.2. As vapor is added to the flow, the mixture speed of sound decreases significantly. Therefore, the rarefaction wave splits into a slow-moving wave in the two-phase mixture and a fast-moving wave in the single-phase fluid, with a single-phase pressure plateau in-between.

The pressure evolution near the open end of the pipe is different for warmer and colder depressurization tests. As discussed in Log et al. (2024), if the depressurization path passes sufficiently close to the critical point of the fluid (i.e., within a few K/°C), we observe nearly no pressure undershoot or superheat before significant flashing begins. A typical pressure trace near the open end of the pipe for such a case is shown in Fig. 5(a). The pressure decreases quickly in the single-phase region until flashing begins nearly at the local saturation pressure. The depressurization continues at near saturation conditions until the flow chokes, i.e., the flow speed is equal to the local speed of sound. After this, the pressure decreases very slowly as the maximum flow rate has been reached. Such pressure evolutions have been observed in high-temperature depressurization experiments with pure CO_2, e.g., Test #31 of Botros et al. (2016), Test 6 of Munkejord et al. (2020b) and Test 24 of Log et al. (2024).

For colder depressurization cases, we observe a clear pressure undershoot and recovery, as illustrated in Fig. 5(b). The pressure decreases quickly below the local saturation pressure, providing a pressure undershoot. The pressure then rebounds as flashing is initiated, the flow chokes abruptly and a slow pressure reduction follows while the fluid is in a two-phase mixture state. This kind of pressure evolution has been observed in several experiments for a variety of fluids including water (Edwards and O'Brien, 1970; Lienhard et al., 1978; Barták, 1990), R-12 (Winters and Merte, 1979), pure CO_2 Botros et al. (2016), Munkejord et al. (2020b), Log et al. (2024) and CO_2-rich mixtures (Botros et al., 2017,b,c; Munkejord et al., 2021). As illustrated in Fig. 4, the speed of sound decreases more abruptly for colder depressurization cases when the flow transitions from pure liquid to a two-phase mixture. The pressure evolution in the pipe is therefore significantly affected once flashing begins. In order to capture the pressure evolution during depressurization in engineering tools, the mass-transfer rate from liquid to vapor must therefore be accurately modeled.

1.3. Background on mass-transfer models for flashing flows

A number of models have been developed to model flashing during depressurization. For detailed reviews, we refer the readers to Pinhasi et al. (2005), Liao and Lucas (2017a) and Liao and Lucas (2021). The mass-transfer models can be categorized into two types: the simpler HRM-type models and the more complex models which account for bubble nucleation. We provide a brief overview of the two types of mass-transfer models below.

1.3.1. HRM-type mass-transfer models

One of the more widely used and simple models which can reproduce the effect of a pressure undershoot is the homogeneous relaxation model (HRM) discussed by Bilicki and Kestin (1990). Here, the mass-transfer rate is modeled phenomenologically using a relaxation parameter multiplied by a driving force for the phase change. We will call this kind of mass-transfer model *HRM-type* models. Examples of other HRM-type mass-transfer models include those of Lee (1980), Saurel et al. (2008) and Liu et al. (2017).

Various correlations have been suggested for the relaxation parameter in HRM-type models for different initial conditions, e.g., the correlations of Downar-Zapolski et al. (1996) for water and Angielczyk et al. (2010), Log et al. (2024) for CO_2. These correlations usually do not provide accurate results for other cases than the ones they are fitted to, and for low temperatures the correlation of Downar-Zapolski et al. (1996) has been found to predict non-physically large relaxation times (Liao and Lucas, 2021; Saha et al., 2017). As we pointed out in Log et al. (2024), the mass-transfer model suggested by Liu et al. (2017) has been applied by several authors (Liu et al., 2017, 2018; Flechas et al., 2020; Xiao et al., 2020) to test their flow models for CO_2 depressurization cases. This model is a modified version of the HRM-type mass-transfer model of Lee (1980) where the driving force of the mass transfer is based on the pressure undershoot as opposed to the liquid superheat. The Liu et al. (2017) model's relaxation parameter has been fitted to the pressure recordings of Test #32A of Botros et al.

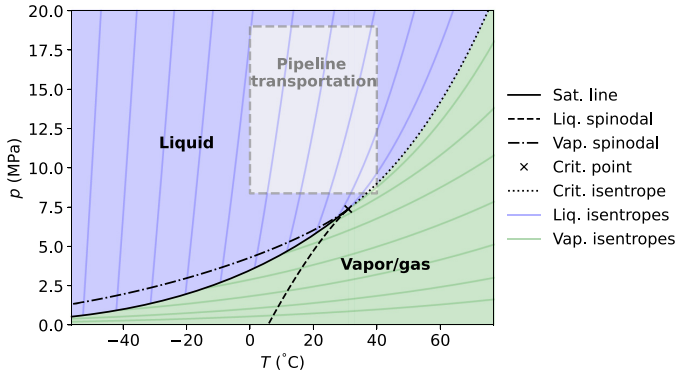

Fig. 2. Phase diagram for CO_2 illustrating the present definition of liquid and vapor, and the relevant operating range for CO_2 pipeline transportation. Note that the liquid phase may exist in a metastable state up to the liquid metastability limit and vice versa for the vapor phase.

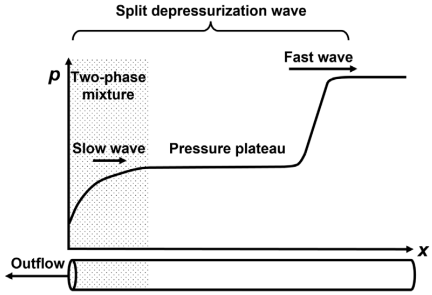

Fig. 3. Illustration of a typical pressure profile for a depressurization wave in a pipe where flashing occurs. The flashing slows down the pressure wave significantly and causes the wave to split into a fast-moving part in the single-phase region and a slow-moving part in the two-phase region with a pressure plateau in-between.

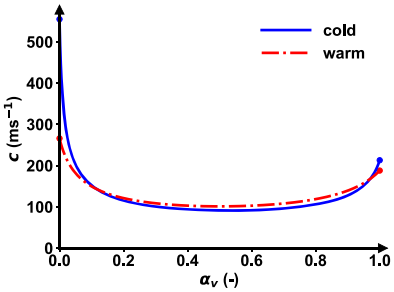

Fig. 4. Computed variation in speed of sound with the vapor volume fraction for a saturated mixture of liquid–vapor CO_2 for a warm temperature ($T = 25.6\,°C$), relatively near the critical point, and for a colder temperature ($T = -2\,°C$). HRM* was used, see Section 2.2.

(2016), and the various authors have found an optimal value in the range $7\,s^{-1}$ to $15\,s^{-1}$. Even for a single depressurization test, there is no agreement on the value of the relaxation parameter.

More complex HRM-type mass-transfer correlations have also been developed. An example is the mass-transfer relation applied in the delayed equilibrium model (DEM) to predict critical flow in nozzles (Bartosiewicz and Seynhaeve, 2013, 2014; Seynhaeve et al., 2015; De Lorenzo et al., 2017). In this mass-transfer relation, two relaxation parameters are applied: one accounting for the time-scale of heterogeneous bubble nucleation and another accounting for the time-scale of bubble nucleation in the bulk of the fluid. The correlation has been fitted for water flashing flow tests (Bartosiewicz and Seynhaeve, 2013; Seynhaeve et al., 2015). However, the correlation was found to be unsuited for CO_2 flow in nozzles (Angielczyk et al., 2019) when tested against the CO_2 nozzle flow data of Nakagawa et al. (2009). This was the case even with updated relaxation parameters fitted to the data. Angielczyk et al. (2020) later proposed a more complex correlation for CO_2, including an exponential term related to the convergence and divergence rates of the nozzle and an additional parameter for model tuning. With this model, they were able to fit the data better.

Though the HRM-type models are practical due to their simplicity, they generally lack predictive abilities and must be fitted to experimental data, typically on a case-by-case basis. For the safety evaluation of pipelines, it is necessary to make *predictive* estimates for various pipe configurations and flow compositions. To this end, mass-transfer models which account for the physical processes that occur during flashing are needed. These processes include bubble nucleation, bubble breakup, coalescence and growth. The reviews of Pinhasi et al. (2005), Liao and Lucas (2017a) and Liao and Lucas (2021) provide details on the challenges and progress in modeling these terms. A main challenge remains in predicting the nucleation of bubbles in the flow.

1.3.2. Models accounting for bubble nucleation

There are two main types of bubble nucleation: homogeneous and heterogeneous. Homogeneous nucleation occurs in the bulk of the fluid and is caused by random density fluctuations creating vapor-like volumes that – if they are large enough – become their own stable phase and grow (Debenedetti, 1997). In order for bubbles to form in this manner, a certain energy barrier must be overcome. This energy barrier decreases near the critical point of the fluid, and larger bubble nucleation rates are expected. The nucleation rate and mass-transfer caused by homogeneous nucleation can be estimated using classical nucleation theory (CNT). CNT has been found to work well in estimating the superheat limit of CO_2 Aursand et al. (2016b), Wilhelmsen and Aasen (2022) and water (Wilhelmsen and Aasen, 2022) for temperatures near the critical point.

Heterogeneous nucleation occurs on surfaces of, e.g., suspended impurities or confining walls. There are two main methods currently being applied to model heterogeneous nucleation. The first method involves the assumption that the mechanism of nucleation is still governed by random density fluctuations, but with a decreased energy-barrier for the bubble formation (Alamgir and Lienhard, 1981; Barták, 1990; Deligiannis and Cleaver, 1990, 1992; Elias and Chambré, 1993; Banasiak

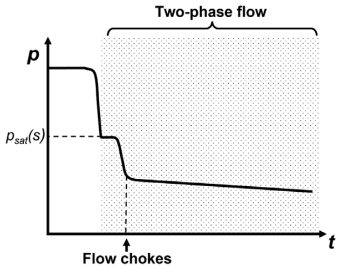

(a) Depressurization path passing close to the critical point.

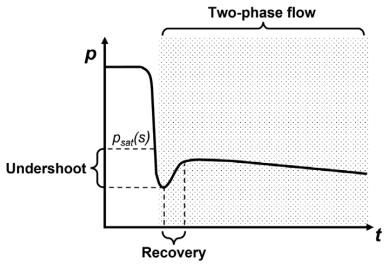

(b) Depressurization path passing further away from the critical point.

Fig. 5. Illustrations of typical pressure traces near the open end of the pipe for depressurization cases where the depressurization path passes (a) close to or (b) further away from the critical point of the fluid.

and Hafner, 2013; Wilhelmsen and Aasen, 2022). The second method is based on the assumption that the nucleation occurs on trapped vapor seeds on these surfaces, see, e.g., the *crevice model* (Bankoff, 1958; Apfel, 1970; Atchley and Prosperetti, 1989; Chappell and Payne, 2007). Some authors refer to the latter form of nucleation as *wall nucleation* (Liao and Lucas, 2017a).

Although investigations have been made for heterogeneous nucleation on ideally flat surfaces (Debenedetti, 1997; Gallo et al., 2021) and conical crevices (Wilt, 1986), to our knowledge, an accurate, predictive model for heterogeneous bubble nucleation in real systems does not yet exist. Models for heterogeneous nucleation in real systems are therefore typically correlated to experimental data. See, e.g., Alamgir and Lienhard (1981), Barták (1990), Deligiannis and Cleaver (1990, 1992), Elias and Chambré (1993), Banasiak and Hafner (2013), Wilhelmsen and Aasen (2022) for correlations of the reduction factor for the energy of bubble formation and Kocamustafaogullari and Ishii (1983), Shin and Jones (1993), Blinkov et al. (1993), Hibiki and Ishii (2003) for correlations for wall nucleation. Most correlations based on a reduction factor for the energy of bubble formation are fitted to match a chosen critical nucleation rate to the recorded superheat limit or maximum pressure undershoot observed in experiments. Consequently, the reduction factor based nucleation models tend to predict the superheat limit and expected maximum pressure undershoots well. However, these models are rarely used in flow models to predict the mass transfer during flashing.

An example of a reduction factor based nucleation model being applied to model the mass transfer during the depressurization of a pipe can be found in Riznic and Ishii (1989). With this mass-transfer model, the predicted pressure became much too low over time after the pressure undershoot had occurred as compared to experimental results. Riznic and Ishii (1989) therefore suggested that some other nucleation process was keeping the pressure elevated over time.

Heterogeneous nucleation models based on the assumption of wall nucleation tend to perform better in flashing flow models, see, e.g., Shin and Jones (1993), Blinkov et al. (1993). Models assuming a constant number of bubble seeds in the flow also tend to match experimental data quite well, see, e.g., Winters and Merte (1979) for the simulation of R-12 depressurization tests and Ivashnyov et al. (2000) for the simulation of the Edwards and O'Brien (1970) water depressurization tests. Winters and Merte (1979) applied a discharge coefficient $C_d < 1$ at the open end to match the experimental results, but Ivashnyov et al. (2000) found that this was not needed when bubble breakup was accounted for in the flow. The models assuming that vapor seeds initiate the flashing typically ignore the effect of homogeneous bubble nucleation. In fact, homogeneous nucleation is often deemed irrelevant when modeling flashing flows, see, e.g., Liao and Lucas (2017a), though this is likely based on the assumption that the depressurization will occur far away from the critical point of the fluid.

1.4. Present contribution and overview of paper

For the relevant operating region of CO_2 pipelines and refrigeration systems, homogeneous nucleation will be non-negligible. Wilhelmsen and Aasen (2022) showed that for flashing flows near the critical point there is a transition from the maximum attainable superheat being determined by homogeneous nucleation for warmer cases and heterogeneous nucleation for colder cases. The same trend can be found for our pipe depressurization tests (Log et al., 2022, 2024). Flow visualization experiments of CO_2 depressurizations show that bubbles tend to form on the wall of the test section as well, suggesting that heterogeneous nucleation plays an important role in the flashing process (Hansen et al., 2019). It is not clear how homogeneous and heterogeneous nucleation affect the resulting flow during depressurization. We further hypothesize that including the effect of homogeneous nucleation in flashing flow models will improve their predictive ability.

The purpose of the present work is therefore to develop and study a flashing flow model where both homogeneous and heterogeneous bubble nucleation is accounted for. We also include simple models for bubble growth, coalescence and breakup. The model fit to experiments with pure CO_2 (Munkejord et al., 2020b; Log et al., 2024) is assessed and the effect of the two nucleation modes on the flashing process is studied. The results are further compared to predictions of a non-equilibrium flow model with a HRM-type mass-transfer model, and the homogeneous equilibrium model, to illustrate the deviation from equilibrium of the experiments and non-equilibrium models.

The remainder of the article is structured as follows. Section 2 presents the flow models and Section 3 presents the main mass-transfer model studied in the present work. Then, we describe the numerical solution method for the governing equations in Section 4. In Section 5, we assess the model fit to the experimental pressure recordings, and discuss the effect of homogeneous and heterogeneous nucleation. We finally provide a summary and concluding remarks in Section 6.

2. Flow models

In this section, we outline the flow models applied in the present work: the homogeneous equilibrium model, the homogeneous chemical-potential relaxation model with HRM-type mass-transfer and the novel homogeneous flashing model. In Section 2.4, we outline our models for wall friction and heat transfer through the pipe wall. In Section 2.5, the initial and boundary conditions are described, and in Section 2.6 the thermophysical modeling of the fluid is described. Details on our mass-transfer model for the homogeneous flashing model are provided in the next section, Section 3.

All the flow models employed in this work are based on the assumption that the flow is homogeneous, i.e., that all phases are advected with the same velocity. This is a reasonable assumption if the phases are

dispersed. Flow visualization experiments show that this assumption is reasonable for the time-scales considered here (0 ms to 20 ms) (Brown et al., 2013, 2014; Quinn et al., 2022).

2.1. The homogeneous equilibrium model

In the HEM it is assumed that all phases are advected at the same velocity and are in mechanical, thermal and chemical equilibrium. The model is therefore mainly applicable for multiphase dispersed flow where the time-scale of pressure exchange, heat transfer and mass transfer between the phases is much shorter than the characteristic time-scales of the flow. The governing equations of the HEM take the form of the 1D Euler equations for single-phase compressible inviscid flow, with a mass conservation equation, a momentum balance equation and an energy balance equation:

$$\frac{\partial \rho}{\partial t} + \frac{\partial(\rho u)}{\partial x} = 0, \tag{1}$$

$$\frac{\partial(\rho u)}{\partial t} + \frac{\partial(\rho u^2 + p)}{\partial x} = \rho g_x - \mathcal{F}, \tag{2}$$

$$\frac{\partial E}{\partial t} + \frac{\partial((E + p)u)}{\partial x} = \mathcal{Q}. \tag{3}$$

Here, $\rho = \alpha_v \rho_v + \alpha_\ell \rho_\ell$ is the density of the vapor (v) and liquid (ℓ) mixture, u is the mixture velocity, p the pressure and E the total energy of the mixture.

$$E = \rho\left(e + \frac{1}{2}u^2\right), \tag{4}$$

where $e = (\alpha_v \rho_v e_v + \alpha_\ell \rho_\ell e_\ell)$ is the specific internal energy of the mixture and α_k denotes the volume fraction of phase $k \in v, \ell$. $\mathcal{F}$ is the pipe wall friction and $\mathcal{Q}$ is the heat transferred through the pipe wall. g_x is the gravitational acceleration in the axial direction of the pipe. We assume that the pipe is completely horizontal such that $g_x = 0$.

2.2. The homogeneous chemical potential-relaxation model

For certain transient flow processes, such as depressurization, the time-scale of mass transfer from liquid to vapor is too slow to maintain equilibrium between the phases. In order to model the flow accurately for such cases, the equilibrium assumptions must be relaxed. The homogeneous chemical potential-relaxation model, HRM*, keeps the assumptions of the HEM with the exception that chemical non-equilibrium between the phases is allowed. Note that other authors denote this model differently, such as the "temperature equilibrium model" (Le Martelot et al., 2014), the "pressure-temperature relaxation model" (Lund, 2012) and the "four-equation pT-relaxed model" (Pelanti, 2022).

The HRM* consists of four equations describing the mass balance of vapor, mass balance of liquid, the conservation of momentum for the two-phase mixture and the conservation of total energy for the mixture:

$$\frac{\partial(\alpha_v \rho_v)}{\partial t} + \frac{\partial(\alpha_v \rho_v u)}{\partial x} = \Gamma, \tag{5}$$

$$\frac{\partial(\alpha_\ell \rho_\ell)}{\partial t} + \frac{\partial(\alpha_\ell \rho_\ell u)}{\partial x} = -\Gamma, \tag{6}$$

$$\frac{\partial(\rho u)}{\partial t} + \frac{\partial(\rho u^2 + p)}{\partial x} = \rho g_x - \mathcal{F}, \tag{7}$$

$$\frac{\partial E}{\partial t} + \frac{\partial((E + p)u)}{\partial x} = \mathcal{Q}, \tag{8}$$

where Γ is the mass-transfer rate between the phases. For an infinitely fast mass-transfer rate, the HRM* relaxes to the HEM.

The mass-transfer rate, Γ, is modeled with the standard HRM-term (Bilicki and Kestin, 1990):

$$\Gamma = \rho \frac{y_{g,\mathrm{eq}} - y_v}{\theta}, \tag{9}$$

where $y_v = \dfrac{\alpha_v \rho_v}{\rho}$ is the mass fraction of vapor, $y_{v,\mathrm{eq}}$ is the equilibrium mass fraction of vapor and θ is a relaxation time > 0. In our previous work (Log et al., 2024), we derived a correlation for the relaxation time fitting the maximum pressure undershoots observed for a series of pipe depressurization experiments with CO_2 (Munkejord et al., 2020b; Log et al., 2024) listed in Table 1, with the exception of Test 25:

$$\theta = 3.165\ \mathrm{ms}\left[1 - \exp\left(-33.283 \Delta \tilde{s}_0^{4.014}\right)\right]. \tag{10}$$

Here,

$$\Delta \tilde{s}_0 = \frac{s_0 - s_c}{s_{\mathrm{tr}} - s_c} \tag{11}$$

is the scaled, relative initial entropy and s_0 is the initial entropy before the depressurization begins, s_c is the critical point entropy and s_{tr} is the triple point entropy.

Though the relaxation time can be fitted to experiments, it does not account for all the complex processes which occur during flashing.

2.3. The homogeneous flashing model

In this section, we summarize the flow equations of the homogeneous flashing model (HFM). The HFM is based on the governing equations of the HRM*, (5)–(8), however, the term describing the mass-transfer between the liquid and vapor phase, Γ, is modeled taking into account different kinds of bubble nucleation in addition to bubble growth through evaporation, bubble breakup and coalescence. The details of the mass-transfer model in the HFM are presented in Section 3.

Evaporation causes a flux of mass transfer through a liquid–vapor surface. In order to model the mass transfer due to evaporation, it is necessary to recover information on the interfacial area density between the liquid and vapor phases. We therefore include additional transport equations for the bubble number density in the flow and interfacial area separating the liquid and vapor. The bubble transport equation is

$$\frac{\partial n_{\mathrm{bub}}}{\partial t} + \frac{\partial(n_{\mathrm{bub}} u)}{\partial x} = J_{\mathrm{bub}}, \tag{12}$$

where n_{bub} is the number density of bubbles in the flow and J_{bub} is the creation or destruction rate of bubbles in the flow. The transport of interfacial area density is given by

$$\frac{\partial a_{\mathrm{int}}}{\partial t} + \frac{\partial(a_{\mathrm{int}} u)}{\partial x} = S_a, \tag{13}$$

where a_{int} is the interfacial area density separating liquid and vapor and S_a denotes the creation or destruction rate of interfacial area. S_a is either provided implicitly based on the creation rate of bubbles, or conservation is assumed, such that $S_a = 0$. Details on the estimate of the interfacial area density are given in Section 3.4.

2.4. Heat transfer and friction

For all the flow models above, the wall friction is calculated using the Friedel (1979) correlation and the heat transferred through the pipe wall is calculated by solving the heat equation in the radial direction in a two-layer domain, as described by Aursand et al. (2017). The in-pipe heat-transfer coefficient is estimated based on the Dittus–Boelter correlation, see, e.g. Bejan (1993, Chap. 6) and the outside heat-transfer coefficient is estimated to be $4\ \mathrm{W\,m^{-2}\,K^{-1}}$. To account for the enhanced heat transfer due to boiling/flashing at the wall, the correlation of Gungor and Winterton (1987) is applied for its simplicity. For more details on the friction and heat-transfer modeling, see Munkejord et al. (2021).

2.5. Initial and boundary conditions

The flow models were applied to simulate pipe depressurization experiments. For these experiments, we assume that the fluid is initially stationary, $u = 0$, and that it has a uniform pressure distribution, $p = p_{\text{init}}$. The initial temperature profile along the pipe is set based on recorded initial temperatures in the pipe using linear interpolation. As the initial condition for all cases considered here are fully in the liquid phase, $\alpha_{v,\text{init}} = 0$. For the initial condition of the pipe wall temperature, the steady state temperature is calculated based on the initial fluid temperature and the ambient temperature outside the pipe. The governing equations for the heat transfer are described by Aursand et al. (2017).

At the left end of the pipe, $x = 0$, the pipe is assumed to be fully open to the outside where $p = p_{\text{atm}}$. The numerical method applied to estimate the flow at the open end of the pipe is briefly summarized in Section 4, and details can be found in Log et al. (2024). At the right end of the pipe, the pipe has a closed wall. However, in the present work, the simulation times are too short for pressure waves to reach this region.

2.6. Thermophysical property models

The thermodynamic properties of the two-phase mixture are obtained with our in-house framework (Wilhelmsen et al., 2017) using the GERG-2008 (Kunz and Wagner, 2012) equation of state (EOS). An open source version of the thermodynamic library can be found at GitHub (Hammer et al., 2023). The EOS is used to calculate the densities and energies of the existing phases in both the stable and metastable region. The metastability limit or *spinodal* curve of the liquid phase is calculated based on

$$\left(\frac{\partial p_\ell}{\partial \rho_\ell}\right)_{T_\ell} = 0, \tag{14}$$

which is defined by the EOS.

3. Mass transfer in the homogeneous flashing model

In the present work, we model the mass-transfer rate, Γ, for the HFM as the sum of three terms: homogeneous nucleation, heterogeneous nucleation and evaporation through the liquid–vapor interface of bubbles in the flow:

$$\Gamma = \Gamma_{\text{hom}} + \Gamma_{\text{het}} + \Gamma_{\text{evap}}. \tag{15}$$

The bubble source term in the transport equation for bubbles (12), J_{bub}, is modeled in a similar way

$$J_{\text{bub}} = J_{\text{hom}} + J_{\text{het}} + J_{\text{break}} + J_{\text{coal}}, \tag{16}$$

where subscript 'break' denotes bubble breakup and subscript 'coal' stands for coalescence of bubbles. J_{coal} is modeled implicitly by limiting the bubble surface area in a control volume when a certain threshold for α_v is reached, as suggested by Pinhasi et al. (2005). We present the details on the modeling of each of the terms in the following sections.

3.1. Homogeneous nucleation

Homogeneous nucleation describes the formation of embryos of a new phase within a mother phase through random thermal fluctuations. Classical nucleation theory provides a formal estimate on the nucleation rate of critically-sized embryos through random density fluctuations. Here, *critically-sized* refers to the size where the embryo is just large enough not to collapse back to the mother phase. The derivation of this rate is thoroughly presented by Debenedetti (1997), and we here simply state the resulting equations. Note that we have presented similar descriptions of CNT in Hammer et al. (2022) and Skarsvåg et al. (2023), and it is re-stated here for completeness.

The nucleation rate (critically-sized embryos formed per volume and time) is defined as an Arrhenius-type rate law,

$$J_{\text{hom}} = K \exp\left(-\frac{\Delta G^*}{k_{\text{B}} T_\ell}\right), \tag{17}$$

where ΔG is the free-energy barrier of embryo formation, k_{B} is the Boltzmann constant and K is a kinetic prefactor. The superscript $*$ denotes properties of a critically-sized embryo. For the formation of bubbles in a superheated liquid, the free-energy barrier is estimated to be

$$\Delta G^* = \frac{4\pi\sigma r^{*2}}{3}, \tag{18}$$

where σ denotes the surface tension and r the radius of the bubble. It is assumed that the surface tension of the bubble, σ, is equal to the macroscopic surface tension of a planar interface between the liquid and vapor at equilibrium (Aasen et al., 2023). We use the correlation of Rathjen and Straub (1977) to model the surface tension of CO_2.

The critical radius of the bubble is approximated as

$$r^* = \frac{2\sigma}{p_{\text{sat}}(T_\ell) - p_\ell}, \tag{19}$$

where $p_{\text{sat}}(T_\ell)$ is the saturation pressure at the temperature of the liquid. The kinetic prefactor can be approximated as

$$K = \bar{\rho}_\ell \sqrt{\frac{2\sigma}{\pi m}}, \tag{20}$$

where m is the mass of one molecule and $\bar{\rho}_\ell = \rho_\ell / m$ is the number density of molecules in the liquid. The mass-transfer rate from liquid to vapor due to homogeneous nucleation of bubbles is then estimated to be

$$\Gamma_{\text{hom}} = \rho_{g,\text{sat}}(T_\ell) V_{\text{bub}} J_{\text{hom}}, \tag{21}$$

where the volume of a critically-sized bubble is

$$V_{\text{bub}} = \frac{4}{3}\pi r^{*3}. \tag{22}$$

Assuming that the depressurization path in the liquid phase is isentropic, we can estimate the maximum attained superheat in pipe depressurization tests with pure CO_2. See, e.g., Log et al. (2022). In Fig. 6, we compare the maximum attained superheat for CO_2 pipe depressurization experiments (Botros et al., 2016; Log et al., 2024), with a heat map of bubble nucleation rates predicted by CNT. For high temperatures, the maximum attainable superheat coincides with regions where significant amounts of bubbles are nucleated as predicted by CNT. However, for colder depressurization cases, we observe five experiments where the maximum superheat is reached in a region where lower nucleation rates than $J_{\text{hom}} = 10^{-10}$ bubbles m^{-3} s^{-1} are predicted. This means that it should take over 316 years for a single, critically-sized bubble to form in a cubic meter of liquid CO_2, yet the experimental results suggest that flashing occurred. This deviation from CNT is observed for a variety of systems and fluids, and it is generally understood to be caused by *heterogeneous* bubble nucleation.

3.2. Heterogeneous nucleation

Heterogeneous nucleation refers to the formation of an embryo of a new phase within the mother phase on a surface, such as suspended impurities or a confining wall. As described in the introduction, there are currently two main methods being applied to estimate heterogeneous nucleation for flashing or boiling liquids. One method is based on the assumption that the bubbles form through density fluctuations with a reduced activation energy. The nucleation rate then becomes similar to CNT, but with the activation energy multiplied by a reduction factor between 0 and 1.

Expressions for the reduction factor has been derived for ideally flat surfaces and conical cavities, depending on knowledge of the contact

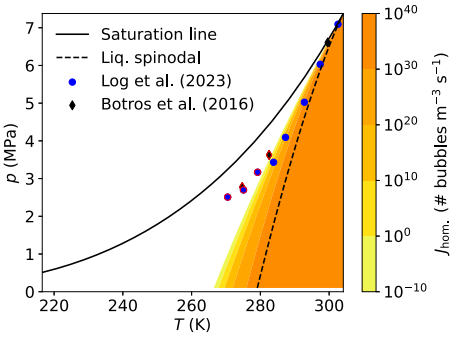

Fig. 6. The homogeneous nucleation rate of critically-sized bubbles for CO_2 calculated using CNT with the GERG-2008 EOS, compared to the estimated maximum superheat observed in full-bore depressurization experiments (Log et al., 2024; Botros et al., 2016). The markers with red edges show points where the maximum superheat was reached in the experiments despite the homogeneous bubble nucleation rate calculated by CNT being lower than 10^{-10} bubbles m^{-3} s^{-1}. (For interpretation of the references to color in this figure legend, the reader is referred to the web version of this article.)

angle of the fluid on the surface (Debenedetti, 1997; Wilt, 1986). However, these estimates fail to reproduce the superheat limits obtained during flashing in real (non-ideal) systems, see, e.g., Deligiannis and Cleaver (1990), Elias and Chambré (1993). To fit experimental data at low reduced temperatures, the reduction factor for the activation energy must be as small as 10^{-7} and 10^{-6} (Deligiannis and Cleaver, 1990; Elias and Chambré, 1993; Wilhelmsen and Aasen, 2022). The other method, denoted the crevice model or wall nucleation, assumes that the nucleation is aided by trapped bubbles in crevices providing a surface for the liquid to evaporate into (Bankoff, 1958; Apfel, 1970; Atchley and Prosperetti, 1989; Chappell and Payne, 2007). The trapped vapor seeds are denoted as *nucleation sites*.

We base our present model on the assumptions of the crevice model. However, we do not wish to derive complex correlations of the kind that have been developed for water, e.g., Kocamustafaogullari and Ishii (1983), Shin and Jones (1993), Blinkov et al. (1993), Hibiki and Ishii (2003). For simplicity, we assume that there exist a number of "perfect" nucleation sites in the pipe and that these nucleation sites provide a constant rate of mass transfer from liquid to vapor if the liquid is superheated. Similarly we also assume a constant rate of bubbles being produced due to the heterogeneous nucleation. The mass-transfer rate and bubble creation rate are then simply modeled as:

$$\Gamma_{\text{het}} = K_m, \text{ and } J_{\text{het}} = K_b. \tag{23}$$

We choose K_m and K_b as constant values fitted as well as possible to our CO_2 depressurization experiments, as reported in Section 5.2. This model for heterogeneous nucleation is not predictive, as opposed to the model for homogeneous nucleation.

3.3. Evaporation through bubble growth

Once bubbles have formed through nucleation, we assume that rapid evaporation will take place at the bubble surface. Most authors assume that the evaporation through the bubble surface is governed by heat transfer between the phases, see, e.g., Winters and Merte (1979), Blinkov et al. (1993), Ivashnyov et al. (2000), Liao and Lucas (2017a). In the present work, we assume that evaporation is driven by the difference in chemical potential between the liquid and vapor phases, and estimate the evaporation flux using linear non-equilibrium thermodynamics coupled with kinetic theory as described in Kjelstrup and Bedeaux (2008), Chapter 11.

Consider a partially filled funnel with a liquid–vapor interface, where liquid is continuously supplied from the bottom as evaporation

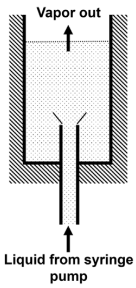

Fig. 7. Illustration of evaporation system where vapor is withdrawn from the cell at the same rate as liquid is being supplied. The interface between the phases is assumed to be perfectly flat.

takes place such that the interface remains stationary, as illustrated in Fig. 7. We ignore viscous effects and assume a constant pressure in the system. Furthermore, the surface is regarded as flat on a molecular scale. As described in more detail in Chapter 11 of Kjelstrup and Bedeaux (2008), the mass-transfer rate through the interface during evaporation or condensation can be estimated as

$$\frac{\Gamma_{\text{evap}}}{a_{\text{int}}} = \frac{1}{R^{s,\ell}_{\mu\mu} + R^{s,v}_{\mu\mu}} \frac{\mu_\ell - \mu_v}{T}, \tag{24}$$

where μ_k denotes the chemical potential of phase $k \in \{\ell, v\}$, $R^{s,\ell}_{\mu\mu}$ is the resistivity of mass transfer between the surface and the liquid and $R^{s,v}_{\mu\mu}$ is the resistivity of mass transfer between the surface and the vapor phase. Applying simplifying assumptions and the kinetic theory of gases, the sum of the resistivities can be approximated as (Kjelstrup and Bedeaux, 2008)

$$R^{s,\ell}_{\mu\mu} + R^{s,v}_{\mu\mu} = \frac{2k_B}{u_{\text{mp}}(T^s)\rho_v^{\text{sat}}(T^s)m} \left(\alpha^{-1} + \frac{1}{5\pi} - \frac{31}{32}\right), \tag{25}$$

where T^s is the temperature of the interface, $u_{\text{mp}}(T^s) = \sqrt{2k_B T^s/\pi m}$ is the most probable thermal velocity, $\rho_v^{\text{sat}}(T^s)$ is the density of saturated vapor at the surface between liquid and vapor and α is the condensation coefficient approximating the fraction of incident particles which are absorbed by the liquid surface after collision. In the present work, we take $T^s = T$ due to the temperature equilibrium condition of the pipe flow model. We further assume that $\alpha = 0.5$, i.e., that half of the incident particles on the liquid surface will pass through it.

In Fig. 8(a), we show how the mass flux predicted by this evaporation model varies for different regions in the phase diagram. For a closed system with a volume of 1 m^3, a surface area of 1 m^2, and the thermodynamic constraints of our flow model ($T_\ell = T_v$, $p_\ell = p_v$), the resulting rate of change in pressure caused by the predicted evaporation mass flux is illustrated in Fig. 8(b). We note that these plots seem to better agree with the maximum superheat observed for colder temperatures in depressurization experiments.

3.4. Interfacial area density

In order to determine the total mass-transfer rate caused by evaporation at the bubble surface, the interfacial area density between liquid and vapor must be determined, cf. Eq. (24). Similarly to the approach described by Pinhasi et al. (2005), our estimates depend on assumed flow regimes based on the volume fraction of vapor in the flow.

We assume that the bubbles stay separate up until $\alpha_v = 0.3$. With the assumption that the bubbles are perfectly spherical, we can then apply the transport equation for the number density of bubbles to estimate the interfacial area density in the flow.

At volume fractions of $0.3 \leq \alpha_v \leq 0.7$, it is assumed that the bubbles will coalesce and break apart. For simplicity, we generally assume that

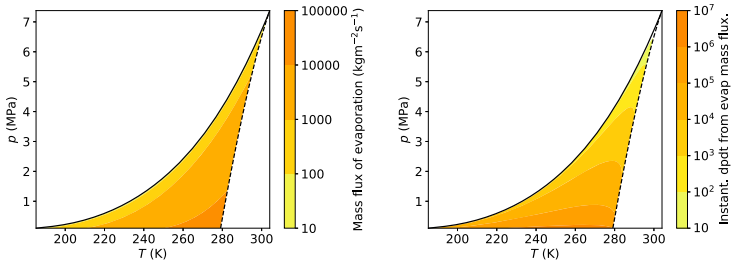

(a) Estimated evaporation mass flux through a liquid-vapor interface based on Equations (24) and (25).

(b) Rate of change in pressure for a closed volume with the evaporation mass flux shown in Fig (a), assuming that $T_\ell = T_v$ and $p_\ell = p_v$.

Fig. 8. Calculated evaporation mass flux (a) and the resulting rate of change in pressure in a closed system (b) shown in the CO_2 phase diagram.

the coalescence and break-up of bubbles keeps the total interfacial area density conserved. We then apply the transport Eq. (13) for the interfacial area density with $S_a = 0$ to find $a_{\text{int,cons}}$. However, if we are approaching conditions where bubble breakup should dominate, we calculate the surface area density based on the number density of bubbles after break up has occurred. The model for bubble breakup is provided in the next section.

At $\alpha_v = 0.7$, we assume that the flow has transitioned to droplet flow. As we lack a model to predict the number of droplets that will be present at this stage, the interfacial area density is currently modeled with a simple correlation to ensure that a_{int} vanishes for single-phase flow when $\alpha_v = 1$.

Our estimate can be summarized as follows for different volume fractions of vapor:

$$a_{\text{int}} = \begin{cases} (36\pi n_b)^{1/3}\alpha_v^{2/3} & \text{if } 0 \le \alpha_v \le 0.3 \text{ or } \Delta n_{\text{bub,break}} > 0 \text{ and } \alpha_v \le 0.7 \\ a_{\text{int,cons}} & \text{if } 0.3 < \alpha_v \le 0.7 \\ \dfrac{a_{\text{int,cons}}}{0.3}(1-\alpha_v) & \text{if } 0.7 < \alpha_v \le 1, \end{cases} \tag{26}$$

where the subscript "cons" denotes that the interfacial area density is taken from the interfacial area conservation and $\Delta n_{\text{bub,break}}$ denotes the change in bubble number density due to bubble breakup as described in the following section.

3.5. Bubble breakup

We model the bubble breakup process inspired by the approach outlined by Ivashnyov et al. (2000). It is assumed that bubble breakup will occur once a critical Weber number is approached. We estimate the Weber number based on the expression of Levich (1962) as suggested by Hesketh et al. (1987) for the application on turbulent flow in horizontal pipes:

$$We = \left[\frac{2r}{1.38} \frac{\rho_\ell^{0.3}\rho_v^{0.3}\eta_\ell^{0.1}}{\sigma^{0.6}} \frac{|u_\ell|^{1.1}}{D_{\text{pipe}}^{0.5}} \right]^{1/0.6}, \tag{27}$$

where r is the bubble radius, η_ℓ is the dynamic viscosity of the liquid phase and D_{pipe} is the inner diameter of the pipe. To avoid division by zero at the critical point, we limit the surface tension such that $\sigma \approx \sigma(0.95T_{\text{crit}})$ if $T > 0.95T_{\text{crit}}$. The current radius of the bubbles is calculated using the volume fraction and number density of bubbles:

$$r = \left(\frac{3}{4\pi} \frac{\alpha_v}{n_{\text{bub}}} \right)^{1/3}, \tag{28}$$

where we have assumed that the bubbles are spherical.

We assume that the maximum possible bubble radius is the one where the critical Weber number is reached:

$$r_{\max} = \frac{1.38We_{\text{crit}}^{0.6}}{2} \frac{\sigma^{0.6}}{\rho_\ell^{0.3}\rho_v^{0.2}\nu_\ell^{0.1}} \frac{D_{\text{pipe}}^{0.5}}{|u_\ell|^{1.1}}. \tag{29}$$

$r_{\max}$ then defines the minimum, or critical, number of bubbles in the flow:

$$n_{\text{crit,break}} = \frac{\alpha_v}{\frac{4}{3}\pi r_{\max}^3}. \tag{30}$$

In Ivashnyov et al. (2000), if the Weber number in the flow is found to be greater than the critical Weber number, the corresponding minimum number density of bubbles is enforced in the flow. Here, we instead apply a logistic function which continuously increases from the present number of bubbles to the critical number of bubbles as a function of the Weber number.

$$\Delta n_{\text{bub,break}} = \frac{n_{\text{crit, break}} - n_{\text{bub}}}{1 + \exp\left(-k\left(We - We_{\text{crit}}\right)\right)} \tag{31}$$

where k is the growth rate of the function. We find that setting $k = 30$ and $We_{\text{crit}} = 2.1$ works reasonably well for our test cases. We limit the calculated radius to be smaller than or equal to $r = 10^{-5}$ m. The choice of this threshold radius is connected to the choice of the critical Weber number and can therefore not be considered an independent parameter.

For the pipe depressurization cases studied in the present work, the resulting pressure near the open end of the pipe is very sensitive to the choice of the critical Weber number. There is no guarantee that the present model will extend to other test cases nor to longer time-frames for the cases that are considered in the present study. The main role of the bubble breakup model is to elevate the pressure near the open end of the pipe over time, accounting for a pressure hump effect observed in experiments (Log et al., 2024; Ivashnyov et al., 2000). We expect the sensitivity to the critical Weber number to reduce for more refined models, e.g., allowing for a temperature difference in the phases such that heat-transfer governed bubble growth can be applied.

3.6. Summary

This section provides a concise overview of the relevant equations for the mass-transfer model in the HFM. The mass-transfer rate in the HFM consists of the sum of contributions from homogeneous nucleation, heterogeneous nucleation and bubble growth through evaporation:

$$\Gamma = \Gamma_{\text{hom}} + \Gamma_{\text{het}} + \Gamma_{\text{evap}}, \tag{32}$$

where Γ_{hom} is calculated using CNT and is given by Eq. (21), $\Gamma_{\text{het}} = K_m$ where K_m is a constant chosen to fit experimental data and $\frac{\Gamma_{\text{evap}}}{a_{\text{int}}}$ is estimated using Eq. (24).

To determine the mass transfer due to evaporation, Γ_{evap}, we must estimate the interfacial area density between the liquid and vapor phases, a_{int}. The interfacial area density a_{int} is approximated by Eq. (26), where different flow regimes are assumed based on the volume fraction of vapor.

When $\alpha_v < 0.3$, or $\alpha_v < 0.7$ and bubble breakup is found to dominate, a_{int} is estimated based on the bubble number density in the flow. The bubble source term in the transport Eq. (12) for bubbles, J_{bub}, is modeled by

$$J_{\text{bub}} = J_{\text{hom}} + J_{\text{het}} + J_{\text{break}} + J_{\text{coal}}, \tag{33}$$

where J_{hom} is calculated using CNT and is given by Eq. (17) and $J_{\text{het}} = K_b$ where K_b is a constant fitted to experimental data. The bubble number density added due to bubble breakup is described in Section 3.5. Provided that bubble breakup is not dominating the flow, coalescence of bubbles is emulated by enforcing the conservation of interfacial area density for $0.3 \leq \alpha_v \leq 0.7$. Finally, for $\alpha_v > 0.7$ a simple function is applied to ensure that $a_{\text{int}} \to 0$ as $\alpha_v \to 1$.

4. Numerical methods

4.1. Numerical discretization

We now consider the numerical solution of the HFM. The governing equations, (5)–(8) with the additional flow topology Eqs. (12)–(13), can be written in the vectorial form

$$\frac{\partial \boldsymbol{U}}{\partial t} + \frac{\partial \boldsymbol{F}}{\partial x} = \boldsymbol{S}, \tag{34}$$

where

$$\boldsymbol{U} = \begin{pmatrix} \alpha_v\rho_v \\ \alpha_\ell\rho_\ell \\ \rho u \\ E \\ n_{\text{bub}} \\ a_{\text{int}} \end{pmatrix}, \quad \boldsymbol{F}(\boldsymbol{U}) = \begin{pmatrix} \alpha_v\rho_v u \\ \alpha_\ell\rho_\ell u \\ \rho u^2 + p \\ (E+p)u \\ n_{\text{bub}} u \\ a_{\text{int}} u \end{pmatrix}, \quad \boldsymbol{S} = \begin{pmatrix} \Gamma \\ -\Gamma \\ \rho g_x - \mathcal{F} \\ \mathcal{Q} \\ J_{\text{bub}} \\ S_a \end{pmatrix},$$

and where we include both the bubble transport equation and the transport equation for interfacial area density. Depending on the resulting local volume fraction, the rate of change of interfacial area, S_a, is set to zero or determined based on the bubble transport equation, in consistency with Section 3.4. The flow topology equations are linearly independent and contribute to the eigenstructure of the system with two characteristic waves overlapping the contact discontinuity, having eigenvalues of u.

The system (34) is solved using a classical first-order fractional step method known as Godunov splitting (LeVeque, 2002, Ch. 17). In Godunov splitting, two steps are applied to reach the solution. First, the homogeneous part of the system is solved without the source term,

$$\frac{\partial \boldsymbol{U}}{\partial t} + \frac{\partial \boldsymbol{F}}{\partial x} = \boldsymbol{0}. \tag{35}$$

The solution of the first step is then applied in the second relaxation step, where the following ODE is solved

$$\frac{\mathrm{d}\boldsymbol{U}}{\mathrm{d}t} = \boldsymbol{S}(\boldsymbol{U}). \tag{36}$$

The homogeneous part of the system is solved using the Harten–Lax–van Leer-Contact (HLLC) finite-volume method (FVM) (Toro et al., 1994) in space and the explicit Euler method in time. Details on the HLLC FVM for the HRM* can be found in Log et al. (2024). The transport equations for the bubble number density and the interfacial area density are discretized equivalently to the mass balance equations in Log et al. (2024). Finally, the ODE (36) is solved with the implicit Euler method using Newton–Raphson iterations. The ODE is solved simultaneously with the thermodynamic variables, as described in the following section.

At the open end of the pipe, a Bernoulli-choking-pressure boundary condition (BBC) is applied using a single ghost cell outside the computational domain of the pipe. Details on the BBC for the HRM* can be found in Log et al. (2024), and the method is equivalent for the HFM. Briefly summarized, the flow velocity, entropy and mass fraction are extrapolated from the first cell in the computational domain and the pressure in the ghost cell is set as the approximate choking pressure based on a steady flow assumption. If the liquid spinodal is reached along the flow isentrope, the minimum amount of vapor required to keep the liquid stable is added to avoid issues with the thermodynamic calculations. The assumption of frozen or minimal flashing ensures that the pressure set in the ghost cell is always equal to or lower than the pressure in the computational domain. Thus, the BC cannot restrict the predicted pressure undershoot or superheat in the computational domain.

4.2. Evaluation of the thermodynamic state and mass transfer in each grid cell

The thermodynamic state and mass transfer is evaluated in each grid cell in the domain to satisfy the governing equations of the flow. After the conservative part of the flow equations is solved using the HLLC FVM, the resulting conserved variables will be known in each grid cell: $(\alpha_v\rho_v)_{\text{spec}}$, $(\alpha_\ell\rho_\ell)_{\text{spec}}$, $(\rho u)_{\text{spec}}$, E_{spec}, $n_{\text{bub, spec}}$ and $a_{\text{int, spec}}$, where the subscript spec denotes *specified* variables. Based on the known variables, the total density of the fluid in the given grid cell is

$$\rho_{\text{spec}} = (\alpha_v\rho_v)_{\text{spec}} + (\alpha_\ell\rho_\ell)_{\text{spec}}, \tag{37}$$

the velocity of the flow is

$$u_{\text{spec}} = \frac{(\rho u)_{\text{spec}}}{\rho_{\text{spec}}} \tag{38}$$

and the internal energy of the mixture becomes

$$(\rho e)_{\text{spec}} = E_{\text{spec}} - \frac{1}{2}\rho_{\text{spec}} u^2_{\text{spec}}. \tag{39}$$

In order to define the thermodynamic state of the two phases in the HFM, four thermodynamic variables are needed. We choose to solve for α_v, ρ_v, ρ_ℓ and T. Additionally, we solve for the number of bubbles in the flow. These variables must satisfy the mass balances for the two phases, the conservation of internal energy during the mass-transfer process, the equality of pressures for the two phases and the balance of bubbles:

$$\boldsymbol{f} = \begin{pmatrix} \alpha_v\rho_v - \left((\alpha_v\rho_v)_{\text{spec}} + \Delta m_v\right) \\ (1-\alpha_v)\rho_\ell - \left((\alpha_\ell\rho_\ell)_{\text{spec}} + \Delta m_\ell\right) \\ \alpha_v\rho_v e_v(\rho_v, T) + (1-\alpha_v)\rho_\ell e_\ell(\rho_\ell, T) - (\rho e)_{\text{spec}} \\ p_v(\rho_v, T) - p_\ell(\rho_\ell, T) \\ n_{\text{bub}} - \left(n_{\text{bub,spec}} + \Delta n_{\text{bub}}\right) \end{pmatrix} = \boldsymbol{0}, \tag{40}$$

where Δm_v denotes the mass transfer from liquid to vapor during the time step Δt,

$$\Delta m_v = -\Delta m_\ell = \int_t^{t+\Delta t} \Gamma \, dt. \tag{41}$$

We presently apply a simple Euler step in the time integration:

$$\Delta m_v \approx \Gamma \Delta t. \tag{42}$$

Similarly, Δn_{bub} denotes the nucleation of bubbles during this time step:

$$\Delta n_{\text{bub}} = (J_{\text{hom}} + J_{\text{het}})\Delta t. \tag{43}$$

Note that $\Delta m_v = \Delta m_v(\alpha_v, \rho_v, \rho_\ell, T)$ and $\Delta n_{\text{bub}} = \Delta n_{\text{bub}}(\alpha_v, \rho_v, \rho_\ell, T)$, i.e., the mass-transfer term Γ and bubble creation rates $J_{\text{hom}}, J_{\text{het}}$ are functions of the solution state. The method is therefore implicit, so the mass transfer is solved using the implicit Euler method. Note that the complete two-step solution procedure with the HLLC FVM and the

Table 1
Initial conditions of the full-bore CO_2 depressurization tests.

Test no.	Pressure avg. (MPa)	Temperature avg. (°C)	Ambient temp. (°C)
4[a]	12.54	21.1	22
6[a]	10.40	40.0	6
8[a]	12.22	24.6	9
19[b]	12.47	10.2	18
22[b]	12.48	14.9	14
23[b]	12.19	31.5	15
24[b]	11.56	35.8	10
25[c]	12.27	4.6	−8.5

[a] Munkejord et al. (2020b).
[b] Log et al. (2024).
[c] Present work.

subsequent implicit solution of the ODE (36) using Eq. (40) ensures mixture-energy-consistency as defined by Pelanti and Shyue (2014).

The set of Eqs. (40) can be solved by an iterative method. In the present work, we apply a Newton–Raphson solver. For numerical reasons we found it best to add the contribution of bubble breakup directly in the calculation of the interfacial area density during the iteration process. The contribution of bubble breakup is therefore always included in the mass-transfer calculation, but the number of bubbles is only updated with the bubbles generated due to breakup after the iterations have converged.

In certain areas of the phase diagram, CNT predicts extremely small values for the rate of bubbles and mass being added to the flow. In order to avoid numerical issues with vanishingly small masses and numbers of bubbles being produced, we enforce the following threshold: If the iterations converge to a solution with $\alpha_v \rho_v < 10^{-100}$, we set $\rho_\ell = \rho_{\text{spec}}$, $n_{\text{bub}} = 0$ and $\alpha_v = 0$.

5. Results and discussion

In this section, we briefly introduce the experimental data used to fit the parameters for heterogeneous nucleation in the HFM in Section 5.1 and evaluate the model fit in Section 5.2. We then compare the modeled pressure estimates to experimental values for different initial conditions with very different flashing characteristics in Section 5.3. Finally, we investigate the contributions of the homogeneous and heterogeneous bubble nucleation models of the HFM in more detail in Section 5.4.

5.1. Depressurization experiments

To show the range of applicability of the present model, we compare calculations with data from the ECCSEL depressurization facility (ECCSEL, 2021). The test section consists of a 61.67 m long pipe with an inner diameter of 40.8 mm. The pipe is densely instrumented with high-frequency pressure and temperature sensors. The pressure measurements are logged at 100 kHz and the measurement uncertainty has been estimated to be 60 kPa with a 95% confidence level. Details on the experimental setup, procedure and equipment, including the heat transfer properties of the test section and surface roughness of the pipe can be found in Munkejord et al. (2020b).

As discussed in further detail by Log et al. (2024), a series of full-bore depressurization tests with pure CO_2 have been conducted at this facility for a range of initial temperatures. The data from these experiments are available at Zenodo (Munkejord et al., 2020a; Log et al., 2023a). The initial conditions for these tests, including one new test (Test 25), are presented in Table 1. Test 25 is the coldest test conducted at the facility to date and its results are first presented here. The data from this experiment is available at Log et al. (2023b).

We show the depressurization paths of the warmest (Test 6), coldest (Test 25) and the intermediate-temperature test (Test 4) in the CO_2 phase diagram in Fig. 9. We also show the homogeneous superheat limit ($J_{\text{hom}}(T) = 10^{12}$ bubbles m^{-3} s^{-1}) in the phase diagram. The warmest test has a depressurization path which crosses the saturation curve at a temperature 1.2 K below the critical temperature. The intermediate-temperature experiment crosses the saturation curve at a temperature 18.5 K below the critical temperature while that temperature difference is 32.5 K for the coldest experiment. As shown in Fig. 9, the depressurization path of the coldest test, Test 25, does not cross the superheat limit estimated from homogeneous nucleation, so this test is only affected by heterogeneous nucleation.

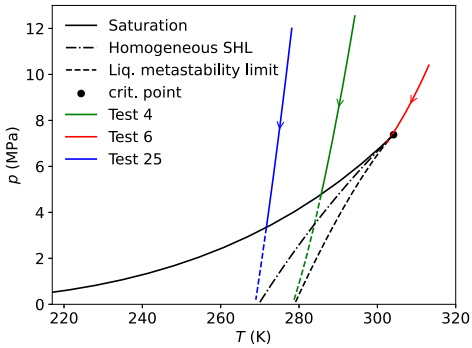

Fig. 9. Calculated single-phase isentropic depressurization paths of the warmest (Test 6), coldest (Test 25) and an intermediate temperature (Test 4) depressurization test conducted at the ECCSEL depressurization facility. The dashed part of the depressurization paths illustrate the possible metastable path before flashing begins.

5.2. Choice of coefficients in the heterogeneous nucleation model

In this section, we demonstrate how the choice of the mass-transfer rate (K_m) and bubble nucleation rate (K_b) modeling heterogeneous nucleation (23) affects the resulting depressurization wave inside the pipe. This investigation was done for all the full-bore depressurization tests reported in Table 1, with similar results for all the tests. In the following, we take Test 4 as an example to be discussed in detail. We model the flow in 15 m of the pipe using $N = 250$ grid cells. The grid was found to be sufficiently fine while providing a low computational time for model fitting.

In Fig. 10(a) we show the resulting pressure profile in the pipe at $t = 20$ ms when we vary K_b while keeping $K_m = 400$ kg m^{-3} s^{-1} constant. When $K_b = 0$ we get a linear increase in pressure from the pipe outlet until the equilibrium pressure is reached approximately 4 m inside the pipe. When the bubble nucleation rate is increased, the pressure rises faster near the outlet, creating a more curved pressure profile in the region before the equilibrium pressure is met, 4 m inside the pipe. For higher bubble nucleation rates, the pressure profile approaches the profile predicted by the HEM.

In Fig. 10(b), we show the resulting pressure profile in the pipe at $t = 20$ ms when we vary K_m while keeping $K_b = 10$ bubbles m^{-3} s^{-1} constant. Varying K_m affects the resulting pressure level. For $K_m = 100$ kg m^{-3} s^{-1}, the pressure remains lower than the equilibrium pressure in the region behind the single-phase portion of the depressurization wave, i.e., for $x < 7.5$ m. For $K_m = 400$ kg m^{-3} s^{-1}, the equilibrium pressure is met around 4 m inside the pipe, and for $K_m = 1000$ kg m^{-3} s^{-1} the equilibrium pressure is met around 2.5 m inside the pipe.

The parameter values for K_b and K_m were fitted by visual inspection to capture the recorded pressure profile at $t = 20$ ms and the recorded pressure traces for the first 20 ms of the depressurization, for all of the experiments listed in Table 1. We found that applying $K_b = 10$ bubbles m^{-3} s^{-1} and $K_m = 400$ kg m^{-3} s^{-1} gave the best agreement with the experimental results for all cases. The resulting pressure profiles

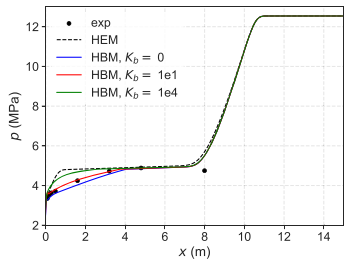

(a) Pressure profile along the pipe for varying heterogeneous bubble nucleation rates, K_b and a constant mass-transfer rate, $K_m = 400\,\mathrm{kg\,m^{-3}\,s^{-1}}$.

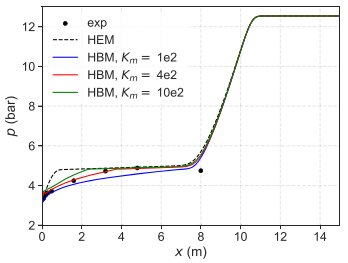

(b) Pressure profile along the pipe for varying heterogeneous mass-transfer rates, K_m, with a constant bubble nucleation rate, $K_b = 10$ bubbles $\mathrm{m^{-3}\,s^{-1}}$.

Fig. 10. Investigation of the effect of varying the bubble formation rate and the mass-transfer rate caused by heterogeneous nucleation for Test 4 (with initial conditions given in Table 1). The results are plotted at time $t = 20\,\mathrm{ms}$.

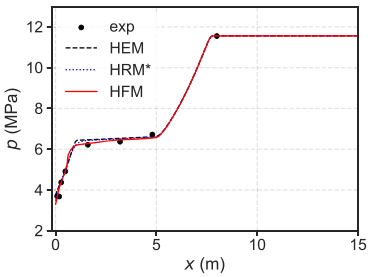

(a) Test 24: $p_0 = 11.6\,\mathrm{MPa}$, $T_0 = 35.8\,^\circ\mathrm{C}$

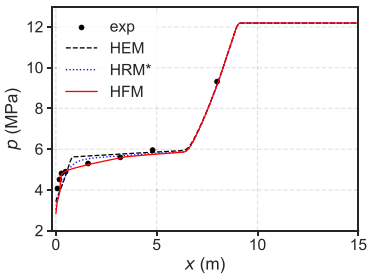

(b) Test 23: $p_0 = 12.2\,\mathrm{MPa}$, $T_0 = 31.5\,^\circ\mathrm{C}$

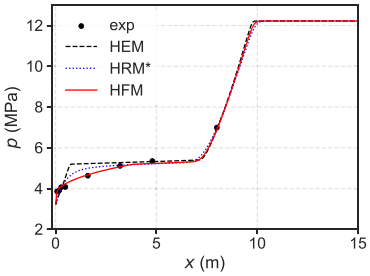

(c) Test 8: $p_0 = 12.2\,\mathrm{MPa}$, $T_0 = 24.6\,^\circ\mathrm{C}$

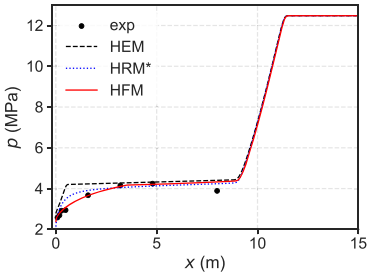

(d) Test 22: $p_0 = 12.5\,\mathrm{MPa}$, $T_0 = 14.9\,^\circ\mathrm{C}$

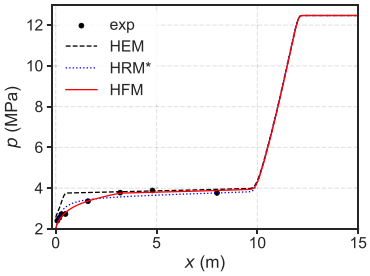

(e) Test 19: $p_0 = 12.5\,\mathrm{MPa}$, $T_0 = 10.2\,^\circ\mathrm{C}$

Fig. 11. Comparison of experimentally measured and modeled pressure profiles along the pipe at $t = 20\,\mathrm{ms}$ for depressurization tests conducted at various initial temperatures. For the HFM, setting the parameters for heterogeneous nucleation to $K_b = 10$ bubbles $\mathrm{m^{-3}\,s^{-1}}$ and $K_m = 400\,\mathrm{kg\,m^{-3}\,s^{-1}}$ worked well for all the tests.

Table 2
The mean absolute percentage error for the model fit of the HRM* and HFM pressure predictions to the experimental measurements at 8 cm, 28 cm, 48.4 cm and 1.6 m from the open end of the pipe over $t = 20$ ms after disk rupture.

Test no.	Temperature avg. (°C)	MAPE HRM* (%)	MAPE HFM (%)
6	40.0	2.2	1.7
24	35.8	4.2	3.2
23	31.5	7.4	5.8
8	24.6	7.8	6.3
4	21.1	8.3	3.5
22	14.9	12.7	6.8
19	10.2	7.6	9.0
25	4.6	10.8	11.5

for the remaining depressurization tests conducted at different initial conditions are shown in Fig. 11, and Figs. 13 and 18.

We now assess and compare the model fit of the HRM* and HFM models to the experimental data using the average mean absolute percentage error (MAPE) at four sensor locations close to the open end of the pipe over the first $t = 20$ ms after the disk rupture at 0.1 ms intervals. For these simulations, a fine grid was applied with $N = 2500$ cells. The sensor locations were 8 cm, 28 cm, 48.4 cm and 1.6 m from the open end of the pipe, and the result is reported in Table 2. The average MAPE was 7.6% for the HRM* and 6.0% for the HFM. The HFM gave a lower MAPE for all tests, except the two coldest ones. The mass transfer for the HRM* is determined by the relaxation time which varies significantly for each depressurization case using the correlation (10) to fit the data (Log et al., 2024). The HFM achieved a similar accuracy while applying constant parameter values. This supports our hypothesis that including homogeneous nucleation in flashing flow models improves their predictive ability.

5.2.1. A note on the chosen value for K_b

The fitted value of the heterogeneous bubble nucleation rate, K_b, in the HFM suggests that only 10 bubbles nucleate heterogeneously in one cubic meter of CO_2 per second. This number is very low, and likely not physical. In practice, such a low value of K_b leads to a limited surface area for evaporation to occur, thus limiting the evaporation/bubble growth in the model. Therefore, the present bubble growth model described in Section 3.3 may be too strong, for the following reasons:

- One of the model assumptions for the bubble growth is that the evaporation occurs through a stationary surface. However, there is a limited quantity of liquid available to be supplied towards the liquid–vapor interface and evaporate at any given moment to keep the surface stationary. The process is instead likely limited by the heat transfer between the bubble and the surrounding liquid, and/or the wall of the pipe.
- The present model assumes that the process of bubble growth is driven by a difference in chemical potentials between the phases. Our flow model further assumes equal temperatures and pressures of the phases. This causes a thermodynamic state of the liquid–vapor mixture which may exaggerate the difference in chemical potentials between the phases, causing a too high driving force for bubble growth.
- The present formulation of the resistivities in the bubble growth model is based on kinetic gas theory and several simplifying assumptions and relations which may not be representative in the relevant area of the phase diagram. Furthermore, the accommodation coefficient for evaporation through the surface of the bubble is unknown and may not be constant.

Based on the limitations of the bubble growth (and flow) model currently applied, it may be advantageous to test the HFM mass-transfer terms for a flow model which allows the phases to be at different temperatures, and apply a bubble growth model driven by heat transfer, such as the ones in Shin and Jones (1993), Blinkov et al. (1993), Ivashnyov et al. (2000) and Liao and Lucas (2017a).

5.3. Comparison to experimental measurements

We now study in more detail how the flow models presented in Section 2 fit the experimental measurements for the warm (Test 6), intermediate temperature (Test 4) and cold (Test 25) pipe depressurization experiments. For all the tests, we model 15 m of the pipe using a fine grid with $N = 2500$ grid cells and applying a CFL number of 0.9. The simulations end at $t_{\text{end}} = 20$ ms. For the heterogeneous nucleation in the HFM, we set $K_b = 10$ bubbles $\text{m}^{-3}\,\text{s}^{-1}$ and $K_m = 400\,\text{kg}\,\text{m}^{-3}\,\text{s}^{-1}$ for all cases, as discussed in the previous section. For the HRM*, the relaxation time is found using the correlation (10), which gave $\theta = 0.04$ ms for Test 6, $\theta = 1.50$ ms for Test 4 and $\theta = 2.82$ ms for Test 25.

5.3.1. Test 6 — warmest case

In Fig. 12, we show the experimental and modeled pressure traces for Test 6 at the positions $x = 28$ cm and $x = 160$ cm from the open end of the pipe. We compare the results to the HEM and the HRM*. As discussed in detail in Log et al. (2024), nearly no non-equilibrium effects are present for this test due to the depressurization path crossing the saturation curve so close to the critical point of CO_2. The HEM's predicted pressure is in excellent agreement with the recorded pressure trace, both at $x = 28$ cm as shown in Fig. 12(a) and $x = 160$ cm as shown in Fig. 12(b). The HRM* pressure overlaps with that of HEM, as it is explicitly fitted with a short relaxation time. The HFM pressure prediction mostly overlaps with that of HEM and is also in excellent agreement with the recorded pressure traces. After $t = 10$ ms, the HFM predicts a few bar lower pressure than the recorded pressure at $x = 28$ cm from the open end of the pipe.

Note that the HEM and HRM* predictions for this case are forced to be at or close to equilibrium. This is not the case for the HFM. The near-equilibrium result of the HFM is due to the accurate flashing model and in particular the homogeneous nucleation term, which is very strong near the critical point. Also note that for the present case, a small error in the numerical solution procedure can bring the liquid phase into its thermodynamically unstable region, causing thermodynamic solution routines to fail. Thus, the present case demonstrates the robustness of the numerical solution method for the HRM* and HFM as well.

We further compare the model predictions with the recorded pressure profile along the pipe at $t = 20$ ms as shown in Fig. 13. In Fig. 13(a) we show the measured and modeled pressure profile along 15 m of the pipe. As observed earlier, the pressure predictions of both HEM and HRM* agree well with the experimental recordings. The HFM provides nearly overlapping predictions with the HEM, with the exception of a somewhat lower predicted pressure near the open end of the pipe. This can be seen more easily in Fig. 13(b), where we have zoomed in on the pressure plateau and the slow-moving part of the depressurization wave in the two-phase mixture. We note that a similar trend is observed in the experimental data near the open end. The lower pressure occurs in a region where the HFM predicts $\alpha_v > 0.7$.

For $\alpha_v > 0.7$, we assume that the interfacial area between liquid and vapor starts to decrease, cf. Eq. (26) which gives an exponential decrease in the interfacial area density. For $\alpha_v = 0.74$, at $x = 0.455$ m the interfacial area has reduced significantly enough that evaporation/bubble growth cannot keep the pressure elevated to the saturation

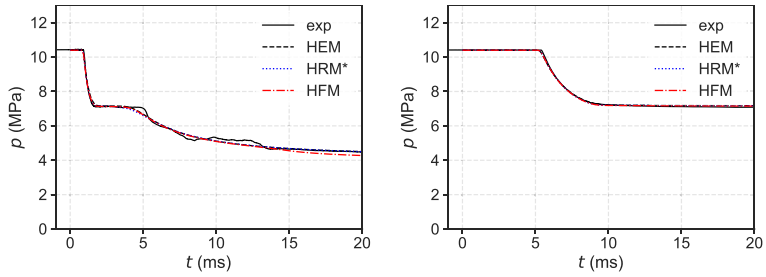

(a) 28 cm from open end. (b) 160 cm from open end.

Fig. 12. Comparison of experimentally measured pressure at $x = 28$ cm and $x = 160$ cm from open end with model predictions of the HEM, HRM* and the HFM for the warm depressurization test, Test 6.

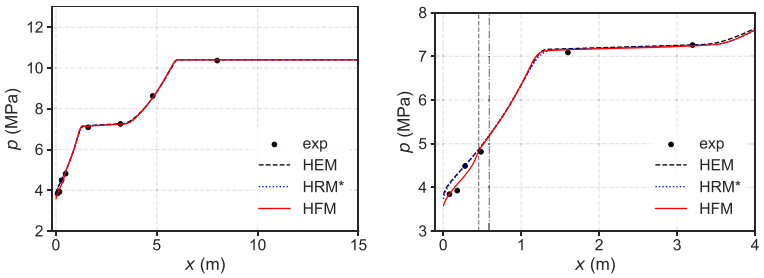

(a) $t = 20$ ms (b) $t = 20$ ms (zoomed). The vertical lines indicate the points where $\alpha_g = 0.7$ (dash dotted) and $\alpha_g = 0.74$ (dashed).

Fig. 13. Comparison of experimentally measured pressure along the pipe with model predictions of the HEM, HRM* and the HFM for the warm depressurization test, Test 6.

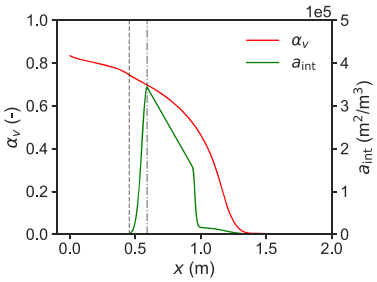

Fig. 14. HFM prediction of volume fraction (red, left y axis) and interfacial area density (green, right y axis) along the pipe for the warm depressurization test, Test 6. The vertical lines indicate the points where $\alpha_g = 0.7$ (dash dotted) and $\alpha_g = 0.74$ (dashed). $t = 20$ ms. (For interpretation of the references to color in this figure legend, the reader is referred to the web version of this article.)

pressure. The volume fraction and estimated interfacial area density along the pipe are shown in Fig. 14 . The experimental data is consistent with a reduction in the interfacial area density near the open end, though it seems to occur slightly closer to the open end than what is predicted by the HFM.

5.3.2. Test 4 — intermediate-temperature case

In Fig. 15, we show the experimental and modeled pressure traces for Test 4 at the positions $x = 28$ cm and $x = 160$ cm from the open end of the pipe. For this test, the recorded pressure traces and pressure prediction of the non-equilibrium models clearly deviate from the pressure modeled by HEM. The HEM overpredicts the pressure, especially for the first 10 ms near the open end of the pipe, as shown in Fig. 15(a). Further inside the pipe, the HEM pressure prediction is still too high, but the deviation is smaller. The HFM pressure agrees well with the recorded pressure traces, both at $x = 28$ cm and $x = 160$ cm, though the model fails to capture an increased pressure undershoot occurring at $x = 28$ cm for t =2.5 ms to 5 ms. At $x = 160$ cm, the HFM pressure overlaps nearly perfectly with the recorded pressure. In this region the HRM* slightly overpredicts the pressure.

In Fig. 16, we compare model predictions with the recorded pressure profile along the pipe at $t = 20$ ms. As shown in Fig. 16(a), the HEM overpredicts the pressure near the open end for $x < 4$ m, and gives a too slow-moving two-phase wave. The HRM* predicts a too low pressure at the pipe outlet and then predicts a too fast increase in the pressure along the x-axis. The HFM pressure agrees very well with the recorded pressure profile in the pipe. The difference in the pressure predictions of the models is most pronounced near the pipe outlet and can be more clearly seen in Fig. 16(b), where we zoom in on the first 5 m of the pipe. The elevated pressure near the open end for HFM is caused by the bubble breakup model. The bubble breakup provides extra available interfacial area for bubble growth, enhancing the flashing. This is in agreement with the results of Ivashnyov et al. (2000).

5.3.3. Test 25 — coldest case

In Fig. 17, we show the experimental and modeled pressure traces for Test 25 at the positions $x = 28$ cm and $x = 160$ cm from the open end of the pipe. As discussed earlier, this test has such a cold initial condition that only the heterogeneous nucleation term contributes in the HFM. For this test, a triple-layered rupture disk was used. As the different layers did not all open exactly at the same time, we see some jagged pressure traces from the disk opening for $t \lesssim 3$ ms in Fig. 17(b). In the fluid simulations, the opening process of the rupture

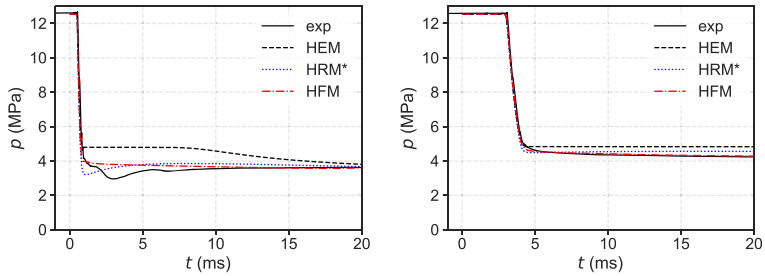

(a) 28 cm from open end. (b) 160 cm from open end.

Fig. 15. Comparison of experimentally measured pressure at $x = 28\,\text{cm}$ and $x = 160\,\text{cm}$ from open end with model predictions of the HEM, HRM* and the HFM for the intermediate-temperature depressurization test, Test 4.

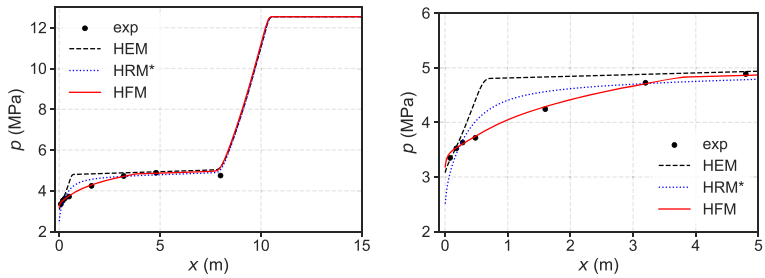

(a) $t = 20\,\text{ms}$ (b) $t = 20\,\text{ms}$ (zoomed)

Fig. 16. Comparison of experimentally measured pressure along the pipe with model predictions of the HEM, HRM* and the HFM for the intermediate-temperature depressurization test, Test 4.

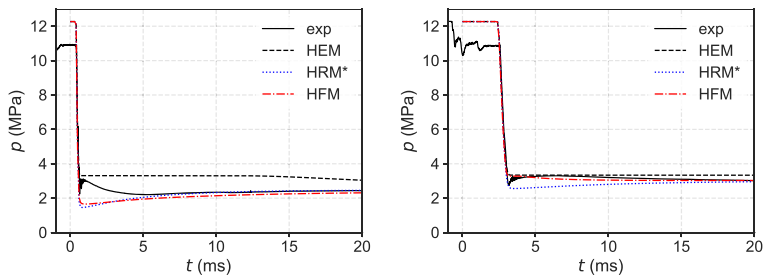

(a) 28 cm from open end. (b) 160 cm from open end.

Fig. 17. Comparison of experimentally measured pressure at $x = 28\,\text{cm}$ and $x = 160\,\text{cm}$ from open end with model predictions of the HEM, HRM* and the HFM for the cold depressurization test, Test 25.

disk was assumed to be instantaneous, causing a discrepancy between the simulated and recorded pressure wave. As this inaccuracy is equal for all the models, their results can still be directly compared.

Similarly to the intermediate-temperature test, the experimentally recorded pressure traces deviate from the HEM for Test 25. This is most evident in Fig. 17(a), showing the pressure evolution at $x = 28\,\text{cm}$ from the open end of the pipe. Here, the HEM again overestimates the pressure significantly after approximately $t = 2\,\text{ms}$. Both the HRM* and the HFM underpredict the pressure at $x = 28\,\text{cm}$ for the first $t = 5\,\text{ms}$. The recorded pressure trace suggests that chaotic bubble nucleation is occurring just after the fast pressure drop, where we see a series of small pressure oscillations. Due to the simplicity of the model for the heterogeneous nucleation, it is reasonable that this process is not captured well by the HFM. After the initial nucleation process, the recorded pressure remains quite high for the first 3 ms to 4 ms before it falls to a similar level as the pressure predicted by HRM* and HFM. The HRM* and HFM pressure evolutions agree well with the recorded pressure trace for $t > 5\,\text{ms}$, though the pressure of the HFM remains slightly below the experimental measurement. At $x = 160\,\text{cm}$, the recorded pressure agrees fairly well with all the models, though the HFM appears to capture the pressure evolution best.

In Fig. 18(a), we show the measured and modeled pressure 15 m along the pipe at $t = 20\,\text{ms}$ for Test 25. We observe the same general trends as for the intermediate-temperature test with HEM overpredicting the pressure near the open end and HFM pressure agreeing well with the recorded depressurization wave. However, when we

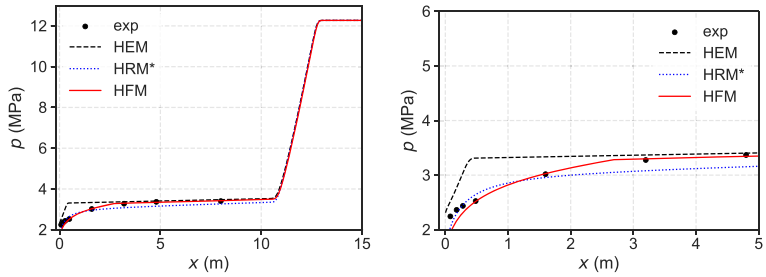

(a) $t = 20$ ms (b) $t = 20$ ms (zoomed)

Fig. 18. Comparison of experimentally measured pressure along the pipe with model predictions of the HEM, HRM* and the HFM for the cold depressurization test, Test 25.

zoom in near the open end of the pipe, we see that the pressure is underpredicted by HFM at positions closer than 0.5 m from the open end. In this region, the mass-transfer rate and bubble nucleation rate should likely be higher than the constant values we have set to model heterogeneous nucleation. The HRM* predicts a similar pressure estimate as the HFM close to the open end. However, further inside the pipe, behind the fast-moving rarefaction wave, the pressure is somewhat underpredicted. This suggests that the relaxation time in the HRM* should be shorter further inside the pipe in order to bring the pressure closer to equilibrium.

5.3.4. Discussion

In the present section, we have tested the HFM against CO_2 depressurization data for three different initial conditions, with very different flash boiling characteristics. For the warmest test with $p_0 = 10.4$ MPa and $T_0 = 40.0$ °C, flashing occurs very close to the critical point. Nearly no metastability occurs before flashing begins and the homogeneous nucleation term is very strong. For the intermediate-temperature test with $p_0 = 12.6$ MPa and $T_0 = 21.1$ °C, there is a significant pressure undershoot before flashing occurs, and both homogeneous and heterogeneous nucleation are present. For the coldest test with $p_0 = 12.3$ MPa and $T_0 = 4.6$ °C, only heterogeneous nucleation contributes to the flashing.

For all the tests, the HFM pressure predictions agree well with the recorded pressure traces, showing the model's capability of capturing the different flashing processes. Note that the same coefficients were used to model the contribution of heterogeneous nucleation in all cases. In contrast, the relaxation time applied in the HRM* to fit the experimental data varies from $\theta = 0.04$ ms for the warmest test to $\theta = 2.82$ ms for the coldest test. The HFM furthermore predicts the pressure profile in the pipe more accurately than the HRM*. We note that for the coldest test, the HFM might benefit from a more refined model for the heterogeneous nucleation as the pressure is underestimated close to the open end of the pipe. Nevertheless, it is clear that by incorporating homogeneous nucleation in the mass-transfer model, the need for model tuning is significantly reduced and the predictive ability of the model is enhanced — which is vital for the application in engineering tools for safety evaluations, where flow estimates for unknown scenarios must be made a priori as data for fitting parameters may not be available.

5.4. Effect of the homogeneous and heterogeneous nucleation terms

In this section, we evaluate the importance and contribution of the heterogeneous and homogeneous nucleation models for the mass-transfer rate in the HFM, see Eq. (15). We conduct this study for the intermediate-temperature test case, Test 4, as this case is affected by both homogeneous and heterogeneous nucleation. Furthermore, the depressurization path does not cross the metastability limit so we can safely vary or omit different mass-transfer contributions without reaching the thermodynamically unstable area of the liquid phase.

In Fig. 19(a), we show the pressure evolution at $x = 28$ cm for the complete HFM and for the HFM omitting either the homogeneous or the heterogeneous nucleation model. When homogeneous nucleation is omitted, the modeled pressure undershoot becomes much too large, and the pressure increases too quickly. Interestingly, ignoring the heterogeneous nucleation term provides nearly no difference in the resulting pressure prediction at $x = 28$ cm from the open end for the time frame considered here. This suggests that homogeneous nucleation dominates the flashing process close to the open end of the pipe for this depressurization case.

In Fig. 19(b), we show the pressure profile along the pipe at $t = 20$ ms for the complete HFM and for the HFM omitting either the homogeneous nucleation terms or the heterogeneous nucleation terms. Most interestingly, when heterogeneous nucleation is ignored, the pressure from $x > 1$ m and up to the position of the fast-moving rarefaction wave is underestimated by up to 1 MPa. In this region, the local superheat is too small for a significant amount of bubbles to nucleate homogeneously, so the two-phase mixture area is not accurately predicted. The heterogeneous term ensures that the two-phase flow extends further into the pipe.

Fig. 20 shows the profile of the volume fraction of vapor 8 m along the pipe for the full HFM and the HFM where either homogeneous or heterogeneous nucleation is omitted. The recorded pressure profile at $t = 20$ ms suggests that there is two-phase flow up to around 4 m inside the pipe. The HFM without heterogeneous nucleation only predicts vapor 1.3 m into the pipe.

Based on the above results, we note the following on the effect of the homogeneous and heterogeneous nucleation terms on the pressure evolution inside the pipe:

- Homogeneous nucleation dominates near the open end of the pipe and limits the predicted pressure undershoot for the present case.
- Even though we are considering a relatively warm case, where homogeneous nucleation is expected to dominate, our results suggest that heterogeneous nucleation plays a major role in initiating (flash) boiling further inside the pipe.
- This means that both homogeneous and heterogeneous nucleation must be accurately accounted for to predict the flash boiling characteristics during pipe depressurizations of liquid CO_2 throughout the length of the pipe.

6. Conclusions

Accurate models for flashing flows can improve the efficiency and safe operation of several industrial systems including nuclear cooling systems, refrigeration units and CO_2 pipeline transportation systems in the context of CCS. In the present work, we propose and study a homogeneous flashing model (HFM) for transient, flashing flow, in which

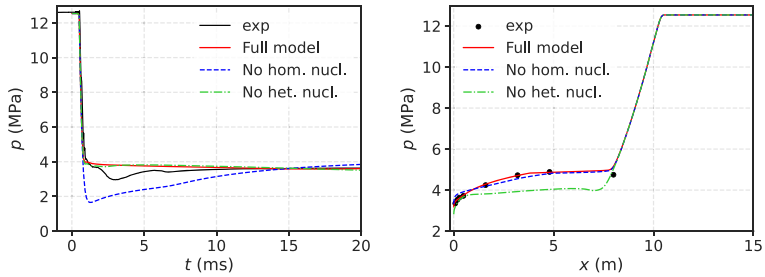

(a) Modeled and measured pressure at 28 cm from the open end of the pipe.

(b) Modeled and measured pressure along the pipe at t = 20 ms after disk rupture.

Fig. 19. Investigation of the effect on the HFM when the homogeneous nucleation model or the heterogeneous nucleation model is omitted.

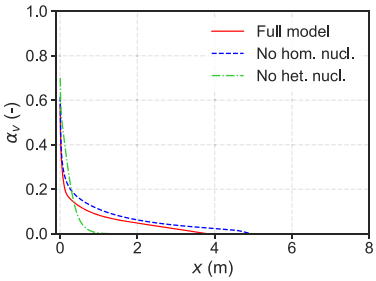

Fig. 20. Modeled volume fraction of vapor inside the pipe for the complete HFM and when either homogeneous nucleation or heterogeneous nucleation is ignored.

the physical phenomena of the flashing are taken into account: homogeneous and heterogeneous bubble nucleation, coalescence, break-up and growth. The flow equations of the HFM are the same as for the homogeneous chemical potential-relaxation model (HRM*), with the addition of transport equations for the bubble density in the flow and total interfacial area between liquid and vapor. Homogeneous nucleation is modeled using classical nucleation theory and heterogeneous nucleation is modeled with constant rates for bubble creation and mass transfer from liquid to vapor.

We have fitted and compared the HFM to experimental data from eight full-bore CO_2 pipe depressurization tests conducted at temperatures from approximately 5 °C to 40 °C and a pressure of about 12 MPa. The results were also discussed in relation to those of the HRM* with a standard HRM-type mass-transfer model. The relaxation parameter in the HRM-type model was set using an empirical correlation that has been tuned on a case-by-case basis for each experiment. The effect of the homogeneous and heterogeneous nucleation models in the HFM was also investigated. The results are summarized below:

- The average mean absolute percentage error of the HFM fit to the pressure recordings for four pressure sensors close to the pipe's open end over 20 ms of the depressurization tests was 6.0%, and for the HRM* it was 7.6%.
- The HFM was tuned to the experimental data using parameters related to the heterogeneous nucleation and bubble breakup. The parameters were tuned to the first 20 ms of the experimental data by visual inspection. The same parameter values provided a reasonable fit for all the experiments, i.e., it was not necessary to tune the model on a case-by-case basis. The results suggest that incorporating homogeneous nucleation in the flashing flow model enhances the predictive capabilities of the model.
- The pressure evolution calculated by the HFM was investigated in more detail for the warmest (40 °C), coldest (5 °C) and an intermediate temperature (21 °C) depressurization test from the experimental dataset. These experiments have very different flashing characteristics.
- For the warm and intermediate temperature depressurization tests, we found that homogeneous nucleation plays a main role in limiting the liquid superheat near the pipe's open end and heterogeneous nucleation plays a main role in initiating flashing further inside the pipe.
- For the coldest test, our results indicate that only heterogeneous nucleation caused flashing in the pipe. The HFM obtained a too low pressure near the open end for this case, suggesting that the constant-rate parameters for heterogeneous nucleation are too simple to capture the actual nucleation process.
- Heterogeneous nucleation must always be accounted for, both for cold and warm depressurization cases. If heterogeneous nucleation is neglected for warm cases, the pressure is underestimated further inside the pipe as homogeneous nucleation is not initiated there.

In summary, the HFM constitutes a promising step towards a fully predictive model for pipe depressurization with flashing.

Note that there are several interesting avenues for further work:

- In the present flow model, the temperatures of the phases are assumed to be equal, $T_v = T_\ell$, which is a simplification. The same mass-transfer model could be tested with flow models that allow for a temperature difference between the phases. This may improve the estimates of the evaporation/bubble growth model as well, as discussed in Section 5.2.1, which currently overestimates the mass transfer caused by evaporation.
- In order to improve the estimates of mass transfer caused by bubble growth, one may also test bubble growth models governed by heat transfer between the phases and/or the wall of the pipe.
- The model for heterogeneous nucleation in the HFM assumes constant rates of bubble nucleation and mass transfer. Although the model performed well for the cases considered here, this may not be the case in other situations or for longer times. As we have found heterogeneous nucleation to be essential in modeling the flashing inside the pipe for both cold and warm depressurization cases, more refined models for this kind of nucleation should be tested, accounting for, e.g., the activation of nucleation sites, bubble growth and bubble departure rate from these sites.

For the HFM to become fully predictive, an accurate model for heterogeneous bubble nucleation in real systems must be developed. To the authors' knowledge, such a model does not yet exist.

CRediT authorship contribution statement

Alexandra Metallinou Log: Conceptualization, Methodology, Software, Data curation, Formal analysis, Investigation, Visualization, Writing – original draft. **Morten Hammer:** Conceptualization, Software, Supervision, Writing – review & editing. **Svend Tollak Munkejord:** Conceptualization, Supervision, Writing – review & editing, Funding acquisition.

Declaration of competing interest

The authors declare that they have no known competing financial interests or personal relationships that could have appeared to influence the work reported in this paper.

Data availability

The experimental data recorded in this study can be downloaded from Zenodo (Log et al., 2023b). (The DOI will be activated at publication.) The data from the other tests conducted at the ECCSEL depressurization facility can also be downloaded from Zenodo (Munkejord et al., 2020a; Log et al., 2023a).

Acknowledgments

This publication has been produced with support from the NCCS Centre, performed under the Norwegian research programme Centres for Environment-friendly Energy Research (FME). The authors acknowledge the following partners for their contributions: Aker BP, Aker Carbon Capture, Allton, Ansaldo Energia, Baker Hughes, CoorsTek Membrane Sciences, Elkem, Eramet, Equinor, Gassco, Hafslund Oslo Celsio, Krohne, Larvik Shipping, Norcem Heidelberg Cement, Offshore Norge, Quad Geometrics, Stratum Reservoir, TotalEnergies, Vår Energi, Wintershall Dea and the Research Council of Norway (257579).

The construction of the ECCSEL Depressurization Facility was supported by the INFRASTRUKTUR programme of the Research Council of Norway (225868). We thank Dr. Kamal K. Botros for sharing data from CO_2 depressurization tests conducted at Nova chemicals. The data was used to estimate the points where flashing first occurred for these tests, as shown in Fig. 6.

References

Aasen, A., Wilhelmsen, Ø., Hammer, M., Reguera, D., 2023. Free energy of critical droplets – from the binodal to the spinodal. J. Chem. Phys. 158 (11), http://dx.doi.org/10.1063/5.0142533.

Alamgir, Md., Lienhard, J.H., 1981. Correlation of pressure undershoot during hot-water depressurization. J. Heat Transfer 103 (1), 52–55. http://dx.doi.org/10.1115/1.3244429.

Angielczyk, W., Bartosiewicz, Y., Butrymowicz, D., 2020. Development of delayed equilibrium model for CO_2 convergent-divergent nozzle transonic flashing flow. Int. J. Multiph. Flow 131, 103351. http://dx.doi.org/10.1016/j.ijmultiphaseflow.2020.103351.

Angielczyk, W., Bartosiewicz, Y., Butrymowicz, D., Seynhaeve, J.-M., 2010. 1-D modeling of supersonic carbon dioxide two-phase flow through ejector motive nozzle. In: International Refrigeration and Air Conditioning Conference. Purdue University, https://docs.lib.purdue.edu/iracc/1102/.

Angielczyk, W., Seynhaeve, J.M., Gagan, J., Bartosiewicz, Y., Butrymowicz, D., 2019. Prediction of critical mass rate of flashing carbon dioxide flow in convergent-divergent nozzle. Chem. Eng. Process. – Process Intensif. 143 (4), 107599. http://dx.doi.org/10.1016/j.cep.2019.107599.

Apfel, R.E., 1970. The role of impurities in cavitation-threshold determination. J. Acoust. Soc. Am. 48, 1179–1186. http://dx.doi.org/10.1121/1.1912258.

Atchley, A.A., Prosperetti, A., 1989. The crevice model of bubble nucleation. J. Acoust. Soc. Am. 86, 1065–1084. http://dx.doi.org/10.1121/1.398098.

Aursand, E., Dumoulin, S., Hammer, M., Lange, H.I., Morin, A., Munkejord, S.T., Nordhagen, H.O., 2016a. Fracture propagation control in CO_2 pipelines: Validation of a coupled fluid–structure model. Eng. Struct. 123, 192–212. http://dx.doi.org/10.1016/j.engstruct.2016.05.012.

Aursand, P., Gjennestad, M.A., Aursand, E., Hammer, M., Wilhelmsen, Ø., 2016b. The spinodal of single- and multi-component fluids and its role in the development of modern equations of state. Fluid Phase Equilib. 436, 98–112. http://dx.doi.org/10.1016/j.fluid.2016.12.018.

Aursand, P., Hammer, M., Lavrov, A., Lund, H., Munkejord, S.T., Torsæter, M., 2017. Well integrity for CO_2 injection from ships: Simulation of the effect of flow and material parameters on thermal stresses. Int. J. Greenh. Gas Control 62, 130–141. http://dx.doi.org/10.1016/j.ijggc.2017.04.007.

Banasiak, K., Hafner, A., 2013. Mathematical modelling of supersonic two-phase R744 flows through converging–diverging nozzles: The effects of phase transition models. Appl. Therm. Eng. (ISSN: 1359-4311) 51 (1), 635–643. http://dx.doi.org/10.1016/j.applthermaleng.2012.10.005.

Bankoff, S.G., 1958. Entrapment of gas in the spreading of a liquid over a rough surface. aichej 4, http://dx.doi.org/10.1002/aic.690040105.

Barták, J., 1990. A study of the rapid depressurization of hot water and the dynamics of vapour bubble generation in superheated water. Int. J. Multiph. Flow 16, 789–798. http://dx.doi.org/10.1016/0301-9322(90)90004-3.

Bartosiewicz, Y., Seynhaeve, J.-M., 2013. Delayed equilibrium model (DEM) of flashing flows relevant to LOCA. Multiphase Sci. Technol 25, 117–131. http://dx.doi.org/10.1615/MultScienTechn.v25.i2-4.50.

Bartosiewicz, Y., Seynhaeve, J.-M., 2014. Delayed equilibrium model (DEM) of flashing choked flows relevant to LOCA and implementation in system codes. In: Proceedings of the 2014 22nd International Conference on Nuclear Engineering. Prague, Czech Republic, Vol. 2B: Thermal Hydraulics. http://dx.doi.org/10.1115/ICONE22-30957, V02BT09A040.

Bejan, A., 1993. Heat Transfer. John Wiley & Sons, Inc., New York, ISBN: 0-471-50290-1.

Bilicki, Z., Kestin, J., 1990. Physical aspects of the relaxation model in two-phase flow. Proc. R. Soc. London Ser. A, Math. Phys. Sci. R. Soc. 428, 379–397. http://dx.doi.org/10.1098/rspa.1990.0040.

Blinkov, V.N., Jones, O.C., Nigmatulin, B.I., 1993. Nucleation and flashing in nozzles – 2. Comparison with experiments using a five-equation model for vapor void development. Int. J. Multiph. Flow 19 (6), 965–986. http://dx.doi.org/10.1016/0301-9322(93)90072-3.

Botros, K.K., Geerligs, J., Rothwell, B., Robinson, T., 2016. Measurements of decompression wave speed in pure carbon dioxide and comparison with predictions by equation of state. J. Press. Vess. – T. ASME 138 (3), http://dx.doi.org/10.1115/1.4031941.

Botros, K.K., Geerligs, J., Rothwell, B., Robinson, T., 2017. Effect of argon as the primary impurity in anthropogenic carbon dioxide mixtures on the decompression wave speed. Can. J. Chem. Eng. 95 (3), 440–448. http://dx.doi.org/10.1002/cjce.22689.

Botros, K.K., Geerligs, J., Rothwell, B., Robinson, T., 2017b. Measurements of decompression wave speed in binary mixtures of carbon dioxide mixtures and impurities. J. Press. Vess. – T. ASME 139 (2), http://dx.doi.org/10.1115/1.4034016.

Botros, K.K., Geerligs, J., Rothwell, B., Robinson, T., 2017c. Measurements of decompression wave speed in simulated anthropogenic carbon dioxide mixtures containing hydrogen. J. Press. Vess. – T. ASME 139 (2), http://dx.doi.org/10.1115/1.4034466.

Brown, S., Beck, J., Mahgerefteh, H., Fraga, E.S., 2013. Global sensitivity analysis of the impact of impurities on CO_2 pipeline failure. Reliab. Eng. Syst. Safe 115, 43–54. http://dx.doi.org/10.1016/j.ress.2013.02.006.

Brown, S., Martynov, S., Mahgerefteh, H., Chen, S., Zhang, Y., 2014. Modelling the non-equilibrium two-phase flow during depressurisation of CO_2 pipelines. Int. J. Greenh. Gas Control 30, 9–18. http://dx.doi.org/10.1016/j.ijggc.2014.08.013.

Brownsort, P., 2019. Briefing on Carbon Dioxide Specifications for Transport. Tech. rep., CCUS Projects Network, EU, https://www.ccusnetwork.eu/sites/default/files/TG3_Briefing-CO2-Specifications-for-Transport.pdf. Accessed 2023-10-17.

Chappell, M.A., Payne, S.J., 2007. The effect of cavity geometry on the nucleation of bubbles from cavities. J. Acoust. Soc. Am. 121, 853–862. http://dx.doi.org/10.1121/1.2404629.

Committee on Carbon Capture, Use, and Storage, 2019. Meeting the Dual Challenge: A Roadmap to At-Scale Deployment of Carbon Capture, Use, and Storage: Volume III – Analysis of CCUS Technologies. Tech. rep., National Petroleum Council, https://dualchallenge.npc.org/downloads.php. Accessed 2023-10-17.

Cosham, A., Jones, D.G., Armstrong, K., Allason, D., Barnett, J., 2014. Analysis of two dense phase carbon dioxide full-scale fracture propagation tests. In: 10th International Pipeline Conference, IPC2014. Calgary, Canada, Vol. 3. http://dx.doi.org/10.1115/IPC2014-33080.

De Lorenzo, M., Lafon, P., Seynhaeve, J.-M., Bartosiewicz, Y., 2017. Benchmark of delayed equilibrium model (DEM) and classic two-phase critical flow models against experimental data. Int. J. Multiph. Flow 92, 112–130. http://dx.doi.org/10.1016/j.ijmultiphaseflow.2017.03.004.

Debenedetti, P.G., 1997. Metastable Liquids: Concepts and Principles. Princeton University Press, ISBN: 9780691213941, http://dx.doi.org/10.1515/9780691213941.

Deligiannis, P., Cleaver, J., 1990. The role of nucleation in the initial phases of a rapid depressurization of a subcooled liquid. Int. J. Multiph. Flow 16 (6), 975–984. http://dx.doi.org/10.1016/0301-9322(90)90102-O.

Deligiannis, P., Cleaver, J., 1992. Determination of the heterogeneous nucleation factor during a transient liquid expansion. Int. J. Multiph. Flow 18 (2), 273–278. http://dx.doi.org/10.1016/0301-9322(92)90088-X.

DNV, 2021. Design and operation of carbon dioxide pipelines. recommended practise. DNV-RP-F104.

Downar-Zapolski, P., Bilicki, Z., Bolle, L., Franco, J., 1996. The non-equilibrium relaxation model for one-dimensional flashing liquid flow. Int. J. Multiph. Flow 22 (3), 473–483. http://dx.doi.org/10.1016/0301-9322(95)00078-X.

ECCSEL, 2021. Depressurization facility. https://www.eccsel.org/catalogue/113. Accessed 2023-05-23.

Edwards, A.R., O'Brien, T.P., 1970. Studies of phenomena connected with the depressurization of water reactors. J. Br. Nucl. Energy Soc. 9 (2), 125–135.

Elias, E., Chambré, P.L., 1993. Flashing Inception in Water During Rapid Decompression. J. Heat Transfer 115 (1), 231–238. http://dx.doi.org/10.1115/1.2910654.

Flechas, T., Laboureur, D.M., Glover, C.J., 2020. A 2-D CFD model for the decompression of carbon dioxide pipelines using the Peng-Robinson and the Span-Wagner equation of state. Process Saf. Environ. 140, 299–313. http://dx.doi.org/10.1016/j.psep.2020.04.033.

Friedel, L., 1979. Improved friction pressure drop correlations for horizontal and vertical two phase pipe flow. In: Proceedings, European Two Phase Flow Group Meeting. Ispra, Italy. Paper E2.

Gallo, M., Magaletti, F., Casciola, C.M., 2021. Heterogeneous bubble nucleation dynamics. J. Fluid Mech. 906 (A20), http://dx.doi.org/10.1017/jfm.2020.761.

Gungor, K.E., Winterton, R.H.S., 1987. Simplified general correlation for saturated flow boiling and comparisons of correlations with data. Chem. Eng. Res. Des. 65 (2), 148–156.

Hammer, M., Aasen, A., Wilhelmsen, Ø, 2023. Thermopack. https://github.com/thermotools/thermopack. Accessed 2023-06-14.

Hammer, M., Deng, H., Austegard, A., Log, A.M., Munkejord, S.T., 2022. Experiments and modelling of choked flow of CO_2 in orifices and nozzles. Int. J. Multiph. Flow 156, 104201. http://dx.doi.org/10.1016/j.ijmultiphaseflow.2022.104201.

Hansen, P.M., Gaathaug, A.V., Bjerketvedt, D., Vågsæther, K., 2019. Rapid depressurization and phase transition of CO_2 in vertical ducts – small-scale experiments and rankine-hugoniot analyses. J. Hazard. Mater. 365, 16–25. http://dx.doi.org/10.1016/j.jhazmat.2018.10.092.

Hesketh, R.P., Fraser Russel, T.W., Etchells, A.W., 1987. Bubble size in horizontal pipelines. AIChE J. 33 (4), 663–667. http://dx.doi.org/10.1002/aic.690330414.

Hibiki, T., Ishii, M., 2003. Active nucleation site density in boiling systems. Int. J. Heat Mass Transfersfer 46 (14), 2587–2601. http://dx.doi.org/10.1016/S0017-9310(03)00031-0.

IPCC, 2005. IPCC Special Report on Carbon Dioxide Capture and Storage. Prepared by Working Group III of the Intergovernmental Panel on Climate Change. IPCC, Cambridge University Press, Cambridge, United Kingdom and New York, NY, USA, https://www.ipcc.ch/site/assets/uploads/2018/03/srccs_wholereport-1.pdf. Accessed 2023-10-17.

Ivashnyov, O.E., Ivashneva, M.N., Smirnov, N.N., 2000. Slow waves of boiling under hot water depressurization. J. Fluid Mech. 413, 149–180. http://dx.doi.org/10.1017/S0022112000008417.

Kjelstrup, S., Bedeaux, D., 2008. Non-Equilibrium Thermodynamics of Heterogeneous Systems. World Scientific, http://dx.doi.org/10.1142/6672.

Klinkby, L., Nielsen, C.M., Krogh, E., Smith, I.E., Palm, B., Bernstone, C., 2011. Simulating rapidly fluctuating CO_2 flow into the Vedsted CO_2 pipeline, injection well and reservoir. In: Gale, J., Hendriks, C., Turkenberg, W. (Eds.), GHGT-10–10th International Conference on Greenhouse Gas Control Technologies. IEAGHGT, Energy Procedia, Vol. 4. The Netherlands, Amsterdam, pp. 4291–4298. http://dx.doi.org/10.1016/j.egypro.2011.02.379.

Kocamustafaogullari, G., Ishii, M., 1983. Interfacial area and nucleation site density in boiling systems. Int. J. Heat Mass Transfersfer 26 (9), 1377–1387. http://dx.doi.org/10.1016/S0017-9310(83)80069-6.

Kunz, O., Wagner, W., 2012. The GERG-2008 wide-range equation of state for natural gases and other mixtures: An expansion of GERG-2004. J. Chem. Eng. Data 57 (11), 3032–3091. http://dx.doi.org/10.1021/je300655b.

Le Martelot, S., Saurel, R., Nkonga, B., 2014. Towards the direct numerical simulation of nucleate boiling flows. Int. J. Multiph. Flow 66, 62–78. http://dx.doi.org/10.1016/j.ijmultiphaseflow.2014.06.010.

Lee, W.H., 1980. A pressure iteration scheme for two-phase flow modeling. In: Veziroglu, T.N. (Ed.), Multiphase Transport Fundamentals, Reactor Safety, Applications. Hemisphere Publishing Corporation, Washington DC, http://dx.doi.org/10.1142/9789814460286_0004.

LeVeque, R.J., 2002. Finite Volume Methods for Hyperbolic Problems. Cambridge University Press, Cambridge, UK, ISBN: 0-521-00924-3.

Levich, V.G., 1962. Physicochemical Hydrodynamics. Prentice-Hall, Englewood Cliffs, N.J, ISBN: 0136744400.

Liao, Y., Lucas, D., 2017a. Computational modelling of flash boiling flows: A literature survey. Int. J. Heat Mass Transfer 111, 246–265. http://dx.doi.org/10.1016/j.ijheatmasstransfer.2017.03.121.

Liao, Y., Lucas, D., 2017b. Possibilities and Limitations of CFD Simulation for Flashing Flow Scenarios in Nuclear Applications. Energy 10, http://dx.doi.org/10.3390/en10010139.

Liao, Y., Lucas, D., 2021. A review on numerical modelling of flashing flow with application to nuclear safety analysis. Appl. Therm. Eng. 182, 116002. http://dx.doi.org/10.1016/j.applthermaleng.2020.116002.

Lienhard, J.H., Alamgir, Md., Trela, M., 1978. Early response of hot water to sudden release from high pressure. J. Heat Trans. – T. ASME 100 (3), 473–479. http://dx.doi.org/10.1115/1.3450833.

Liu, B., Liu, X., Lu, C., Godbole, A., Michal, G., Tieu, A.K., 2017. Multi-phase decompression modeling of CO_2 pipelines. Greenh. Gas. Sci. Tech 7 (4), 665–679. http://dx.doi.org/10.1002/ghg.1666.

Liu, B., Liu, X., Lu, C., Godbole, A., Michal, G., Tieu, A.K., 2018. A CFD decompression model for CO_2 mixture and the influence of non-equilibrium phase transition. Appl. Energy 227, 516–524. http://dx.doi.org/10.1016/j.apenergy.2017.09.016.

Log, A.M., Hammer, M., Deng, H., Austegard, A., Hafner, A., Munkejord, S.T., 2023a. Depressurization of CO_2 in Pipes: Effect of Initial State on Non-Equilibrium Two-Phase Flow – Dataset. Zenodo, http://dx.doi.org/10.5281/zenodo.7669536.

Log, A.M., Hammer, M., Deng, H., Austegard, A., Hafner, A., Munkejord, S.T., 2024. Depressurization of CO_2 in pipes: Effect of initial state on non-equilibrium two-phase flow. Int. J. Multiph. Flow 170, 104624. http://dx.doi.org/10.1016/j.ijmultiphaseflow.2023.104624.

Log, A.M., Hammer, M., Munkejord, S.T., 2023b. A Flashing Flow Model for the Rapid Depressurization of CO_2 in a Pipe Accounting for Bubble Nucleation and Growth – Dataset. Zenodo, http://dx.doi.org/10.5281/zenodo.8164913.

Log, A.M., Munkejord, S.T., Hammer, M., Hafner, A., Deng, H., Austegard, A., 2022. Investigation of non-equilibrium effects during the depressurization of carbon dioxide. In: 15th IIR-Gustav Lorentzen Conference on Natural Refrigerants (GL2022). Proceedings. Trondheim, Norway, June 13-15th 2022. International Institute of Refrigeration (IIR). http://dx.doi.org/10.18462/iir.gl2022.0197.

Lund, H., 2012. A hierarchy of relaxation models for two-phase flow. SIAM J. Appl. Math. 72 (6), 1713–1741. http://dx.doi.org/10.1137/12086368X.

Michal, G., Østby, E., Davis, B.J., Røneid, S., Lu, C., 2020. An empirical fracture control model for dense-phase CO2 carrying pipelines. In: 13th International Pipeline Conference. IPC 2020, ASME, http://dx.doi.org/10.1115/IPC2020-9421.

Munkejord, S.T., Austegard, A., Deng, H., Hammer, M., Stang, H.G.J., Løvseth, S.W., 2020a. Depressurization of CO_2 in a Pipe: High-Resolution Pressure and Temperature Data and Comparison with Model Predictions – Dataset. Zenodo, http://dx.doi.org/10.5281/zenodo.3928227.

Munkejord, S.T., Austegard, A., Deng, H., Hammer, M., Stang, H.G.J., Løvseth, S.W., 2020b. Depressurization of CO_2 in a pipe: High-resolution pressure and temperature data and comparison with model predictions. Energy 211, 118560. http://dx.doi.org/10.1016/j.energy.2020.118560.

Munkejord, S.T., Deng, H., Austegard, A., Hammer, M., Skarsvåg, H.L., Aasen, A., 2021. Depressurization of CO_2-N_2 and CO_2-He in a pipe: Experiments and modelling of pressure and temperature dynamics. Int. J. Greenh. Gas Control 109, 103361. http://dx.doi.org/10.1016/j.ijggc.2021.103361.

Munkejord, S.T., Hammer, M., Løvseth, S.W., 2016. CO_2 Transport: Data and models – a review. Appl. Energy 169, 499–523. http://dx.doi.org/10.1016/j.apenergy.2016.01.100.

Nakagawa, M., Berana, M.S., Kishine, A., 2009. Supersonic two-phase flow of CO_2 through converging-diverging nozzles for the ejector refrigeration cycle. Int. J. Refrig. 32 (6), 1195–1202. http://dx.doi.org/10.1016/j.ijrefrig.2009.01.015.

Pelanti, M., 2022. Arbitrary-rate relaxation techniques for the numerical modeling of compressible two-phase flows with heat and mass transfer. Int. J. Multiph. Flow 153, 104097. http://dx.doi.org/10.1016/j.ijmultiphaseflow.2022.104097.

Pelanti, M., Shyue, K.-M., 2014. A mixture-energy-consistent six-equation two-phase numerical model for fluids with interfaces, cavitation and evaporation waves. J. Comput. Phys. 259, 331–357. http://dx.doi.org/10.1016/j.jcp.2013.12.003.

Pham, L.H.H.P., Rusli, R., 2016. A review of experimental and modelling methods for accidental release behaviour of high-pressurised CO_2 pipelines at atmospheric environment. Process Saf. Environ. 104, 48–84. http://dx.doi.org/10.1016/j.psep.2016.08.013.

Pinhasi, G.A., Ullmann, A., Dayan, A., 2005. Modeling of flashing two-phase flow. Rev. Chem. Eng. 21 (3–4), 133–264. http://dx.doi.org/10.1515/REVCE.2005.21.3-4.133.

Quinn, D., Stannard, D., Edwards, J., Botros, K.K., Johansen, C., 2022. Experimental visualization and characteristics of bubble nucleation during rapid decompression of supercritical and subcooled carbon dioxide. Int. J. Pres. Ves. Pip. 195, 104569. http://dx.doi.org/10.1016/j.ijpvp.2021.104569.

Rathjen, W., Straub, J., 1977. Temperature dependence of surface tension, coexisting curve, and vapor pressure of CO_2, $CClF_3$, $CBrF_3$, and SF_6. In: Hahne, E., Grigull, U. (Eds.), Heat Transfer in Boiling. Taylor & Francis Inc., ISBN: 0-123-14450-7, chap. 18.

Ringstad, K.E., Allouche, Y., Gullo, P., Ervik, Å., Banasiak, K., Hafner, A., 2020. A detailed review on CO_2 two-phase ejector flow modeling. Therm. Sci. Eng. Prog. 20, 100647. http://dx.doi.org/10.1016/j.tsep.2020.100647.

Riznic, J.R., Ishii, M., 1989. Bubble number density and vapor generation in flashing flow. Int. J. Heat Mass Transfer 32 (10), 1821–1833. http://dx.doi.org/10.1016/0017-9310(89)90154-3.

Saha, K., Som, S., Battistoni, M., 2017. Investigation of homogeneous relaxation model parameters and their implications for gasoline injectors. At. Sprays 27, 345–365. http://dx.doi.org/10.1615/AtomizSpr.2017016338.

Saurel, R., Petitpas, F., Abgrall, R., 2008. Modelling phase transition in metastable liquids: application to cavitating and flashing flows. J. Fluid Mech. 607, 313–350. http://dx.doi.org/10.1017/S0022112008002061.

Seynhaeve, J.-M., Crécy, A.D., Bartosiewicz, Y., 2015. Uncertainty analysis of delayed equilibrium model (dem) using the circe methodology. In: NURETH16. Chicago, USA. https://glc.ans.org/nureth-16/data/papers/12971.pdf. Accessed 2023-07-30.

Shin, T.S., Jones, O.C., 1993. Nucleation and flashing in nozzles – 1. A distributed nucleation model. Int. J. Multiph. Flow 19 (6), 943–964. http://dx.doi.org/10.1016/0301-9322(93)90071-2.

Skarsvåg, H.L., Hammer, M., Munkejord, S.T., Log, A.M., Dumoulin, S., Gruben, G., 2023. Towards an engineering tool for the prediction of running ductile fractures in CO_2 pipelines. Process Saf. Environ. 171, 667–679. http://dx.doi.org/10.1016/j.psep.2023.01.054.

Toro, E.F., Spruce, M., Speares, W., 1994. Restoration of the contact surface in the HLL-Riemann solver. Shock Waves 4 (1), 25–34.

Wilhelmsen, Ø., Aasen, A., 2022. Choked liquid flow in nozzles: Crossover from heterogeneous to homogeneous cavitation and insensitivity to depressurization rate. Chem. Eng. Sci. 248, 117176. http://dx.doi.org/10.1016/j.ces.2021.117176.

Wilhelmsen, Ø., Aasen, A., Skaugen, G., Aursand, P., Austegard, A., Aursand, E., Gjennestad, M.A., Lund, H., Linga, G., Hammer, M., 2017. Thermodynamic modeling with equations of state: Present challenges with established methods. Ind. Eng. Chem. Res. 56 (13), 3503–3515. http://dx.doi.org/10.1021/acs.iecr.7b00317.

Wilt, P.M., 1986. Nucleation rates and bubble stability in water-carbon dioxide solutions. J. Colloid Interf. Sci. 112 (2), 530–538. http://dx.doi.org/10.1016/0021-9797(86)90122-0.

Winters Jr., W.S., Merte, J.H., 1979. Experiments and Nonequilibrium Analysis of Pipe Blowdown. Nucl. Sci. Eng. 69 (3), 411–429. http://dx.doi.org/10.13182/NSE79-A19959.

Xiao, C., Lu, Z., Yan, L., Yao, S., 2020. Transient behaviour of liquid CO_2 decompression: CFD modelling and effects of initial state parameters. Int. J. Greenh. Gas Control 101, 103154. http://dx.doi.org/10.1016/j.ijggc.2020.103154.